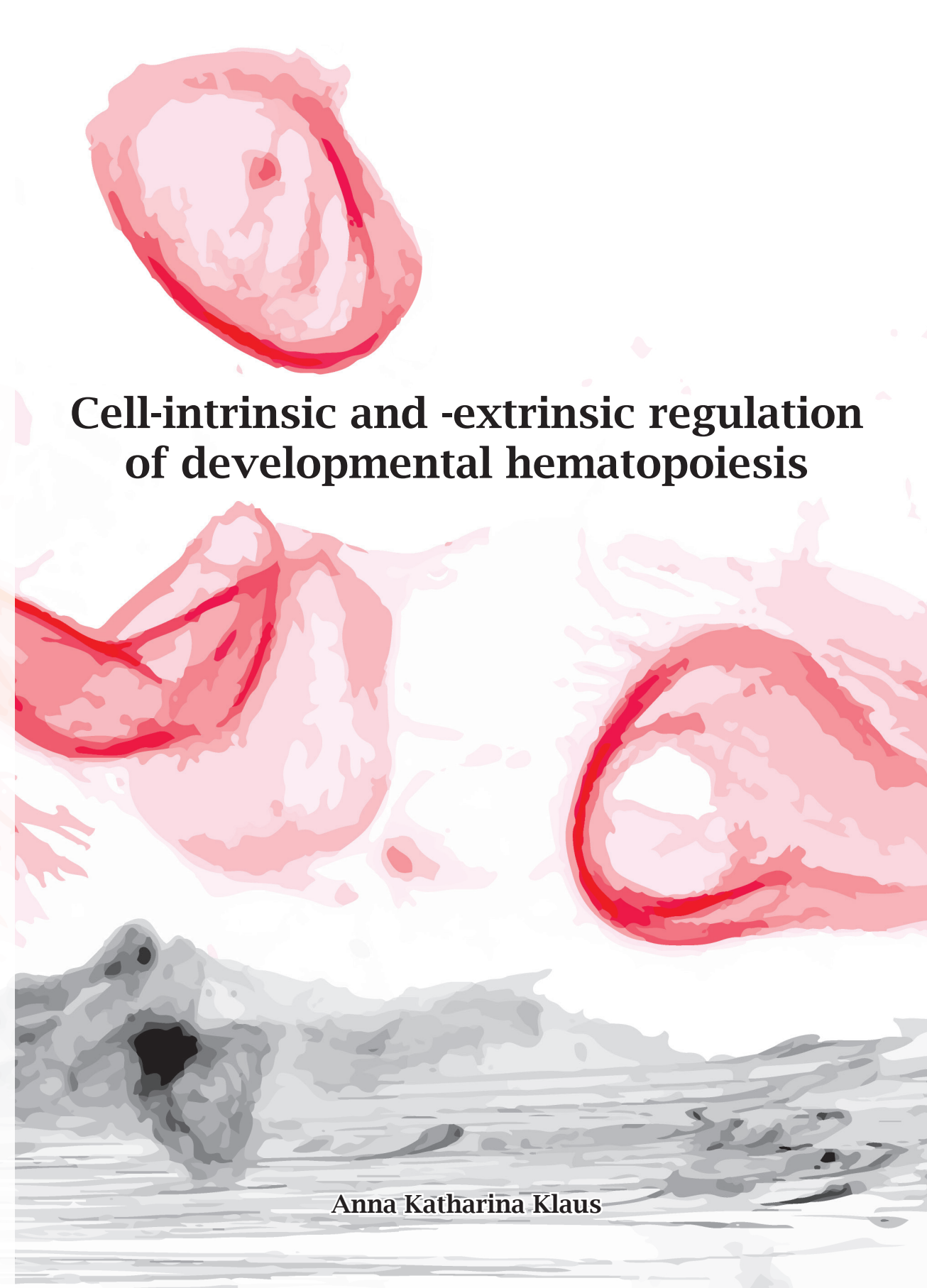


Cell-intrinsic and -extrinsic regulation of developmental hematopoiesis

Anna Klaus



## Cell-intrinsic and -extrinsic regulation of developmental hematopoiesis

Anna Katharina Klaus

Cell-intrinsic and -extrinsic regulation  
of developmental hematopoiesis

Anna Katharina Klaus



The work described in this thesis was performed at the Hubrecht Institute for Developmental Biology and Stem Cell Research (the Royal Netherlands Academy of Arts and Sciences, KNAW) within the framework of the research school Cancer, Stem Cells & Developmental Biology (CS&D), which is part of the Utrecht Graduate School of Life Sciences (Utrecht University).

Cover design: Anna Katharina Klaus and Kim de Luca

Layout: Anna Katharina Klaus

Printing: Ridderprint | [www.ridderprint.nl](http://www.ridderprint.nl)

ISBN: 978-94-6458-612-1

Copyright © 2022 by Anna Katharina Klaus. All rights reserved. No part of this book may be reproduced, stored in a retrieval system or transmitted in any form or by any means, without prior permission of the author.

# Cell-intrinsic and -extrinsic regulation of developmental hematopoiesis

Cel-intrinsieke en -extrinsieke regulatie van hematopoëse tijdens  
embryonale ontwikkeling

(met een samenvatting in het Nederlands)

Proefschrift

ter verkrijging van de graad van doctor aan de  
Universiteit Utrecht  
op gezag van de  
rector magnificus, prof.dr. H.R.B.M. Kummeling,  
ingevolge het besluit van het college voor promoties  
in het openbaar te verdedigen op

maandag 31 oktober 2022 des middags te 12.15 uur

door

**Anna Katharina Klaus**

geboren op 5 februari 1987  
te Braunschweig, Duitsland

Promotor:  
Prof. dr. A. van Oudenaarden

Copromotor:  
Dr. C. Robin

Beoordelingscommissie:  
Prof. dr. ir. J.P.W.M. Bakkers  
Prof. dr. M.M. Maurice  
Prof. dr. E. van Rooij  
Prof. dr. H.G.P. Raaijmakers  
Prof. dr. T. Jaffredo

The research described in this thesis was supported by a European Research Council grant (ERC, project number 220-H75001EU/HSCOrigin-309361), a TOP8861-subsidy from NWO/ZonMw (912.15.017), an Innovational Research Incentives Scheme (NWO-VIDI) grant (917-76-345) and a Landsteiner Foundation for Blood Transfusion Research (LSBR 1025) grant.

# Table of contents

	Outline of the thesis	8
Chapter 1	Introduction Embryonic hematopoiesis under microscopic observation	12
Chapter 2	Progressive maturation toward hematopoietic stem cells in the mouse embryo aorta	44
Chapter 3	Single-cell transcriptomics reveal the dynamic of haematopoietic stem cell production in the aorta	66
Chapter 4	Multispecies RNA tomography reveals regulators of hematopoietic stem cell birth in the embryo	106
Chapter 5	CLASP2 safeguards hematopoietic stem cell properties during mouse and fish development	152
Chapter 6	Clasp2 regulates secondary angiogenesis and lymphangiogenesis through extra-cellular matrix modulation during zebrafish development	196
Chapter 7	Discussion	218
Addendum	List of abbreviations	236
	Samenvatting in het Nederlands	240
	Zusammenfassung auf Deutsch	243
	List of publications	246
	Curriculum Vitae	247
	Acknowledgements	248
	Image Credits	256





„O Bär“, sagte der Tiger, „ist das Leben nicht unheimlich schön, sag!“  
„Ja“, sagte der kleine Bär, „ganz unheimlich und schön“.

Janosch - Post für den Tiger

# Outline of the thesis

## Cell-intrinsic and -extrinsic regulation of developmental hematopoiesis

**Chapter 1 Introduction** Hematopoietic stem cells (HSCs) are at the foundation of the hematopoietic system. Endowed with multi-lineage differentiation and long-term self-renewal properties, HSCs have the capacity to replenish the entire blood system, thereby meeting the constant need for short-lived blood cell types throughout life without exhaustion. In all vertebrates, the first HSCs originate during embryonic life. At embryonic day (E)9.5 of mouse development, specialized hemogenic endothelial cells bud from the endothelial lining of the main arteries, such as the aorta, to undergo an endothelial-to-hematopoietic transition (EHT). EHT leads to the formation of hematopoietic cells that organize in clusters (also referred to as intra-aortic hematopoietic clusters or IAHCs) that remain transiently attached to the endothelium. The number of IAHC cells peaks at E10.5, when the first HSCs start to be detected in the aorta. At E11, IAHCs contain very few HSCs and committed erythroid-myeloid progenitors, and are mainly composed of HSC precursors (pre-HSCs) that progressively mature towards fully transplantable HSCs. The decrease of IAHC cell number in the aorta coincides with the appearance of HSCs in the fetal liver (FL). Given the similar number of aortic pre-HSCs at E11.5 and HSCs in FL at E12.5, pre-HSCs most likely migrate from the aorta to the FL to complete their maturation process there. This wave of pre-HSC maturation, followed by expansion, leads to the formation of the adult HSC pool that will colonize the bone marrow (BM), the main site of hematopoiesis in adulthood. The restricted spatial and temporal production of HSCs during embryonic development is tightly regulated by a complex network of cell-intrinsic and -extrinsic factors. Obtaining a better understanding of HSC regulation is the main focus of this thesis.

**Chapter 2** IAHCs were previously described as composed of HSCs and more committed progenitor cells. However, we and others have shown that the vast majority of IAHC cells are, in fact, pre-HSCs (type I and II) that display their full engraftment potential only after a maturation process that can be induced either *in vitro* or after transplantation *in vivo* in a permissive microenvironment (i.e. neonate liver).

**Chapter 3** To understand the cell-intrinsic regulatory network and molecular events of IAHC formation and HSC generation in the aorta, we investigated the transcriptional landscape of phenotypically defined populations, including non-hemogenic endothelium, hemogenic endothelium, pre-HSCs type I, pre-HSCs type II and progenitor cells, by single-cell RNA-sequencing. Our goal was to better understand why HSC production in the aorta is spatiotemporally confined, i.e. while IAHCs are present in both sides of the aorta, HSC activity is restricted to the ventral side of the aorta, peaking at E10.5. We therefore identified which genes were differentially expressed in the aforementioned populations isolated at E10.5 and E11.5 (during the maturation process). We also investigated spatial distribution by evaluating gene expression in IAHCs isolated from the ventral and dorsal sides of the aorta, and found that they were molecularly very similar.

**Chapter 4** The stem cell environment or niche plays an important role in controlling IAHC cell formation, and therefore HSC production, in the aorta. As such, HSC potential is restricted to the ventral side of the aorta during embryonic hemato-

poiesis. To identify conserved cell-extrinsic molecular signals that are involved in the regulatory landscape of HSC generation, we performed RNA tomography-sequencing (tomo-seq) of different embryo species, i.e. human, mouse, chicken, and zebrafish, that were cryosectioned along the dorsoventral and anteroposterior axes of the embryo. Several genes active in the ventral aortic microenvironment were identified and their positive regulatory effect on HSC production was confirmed by performing loss- or gain-of-function (LOF, GOF) experiments in zebrafish, mouse and/or chicken models. We highlighted the vasodilator ADM and its receptor RAMP-2, as well as SVEP1, an adhesion molecule, as important and conserved microenvironmental cues for proper HSC generation in the embryonic aorta.

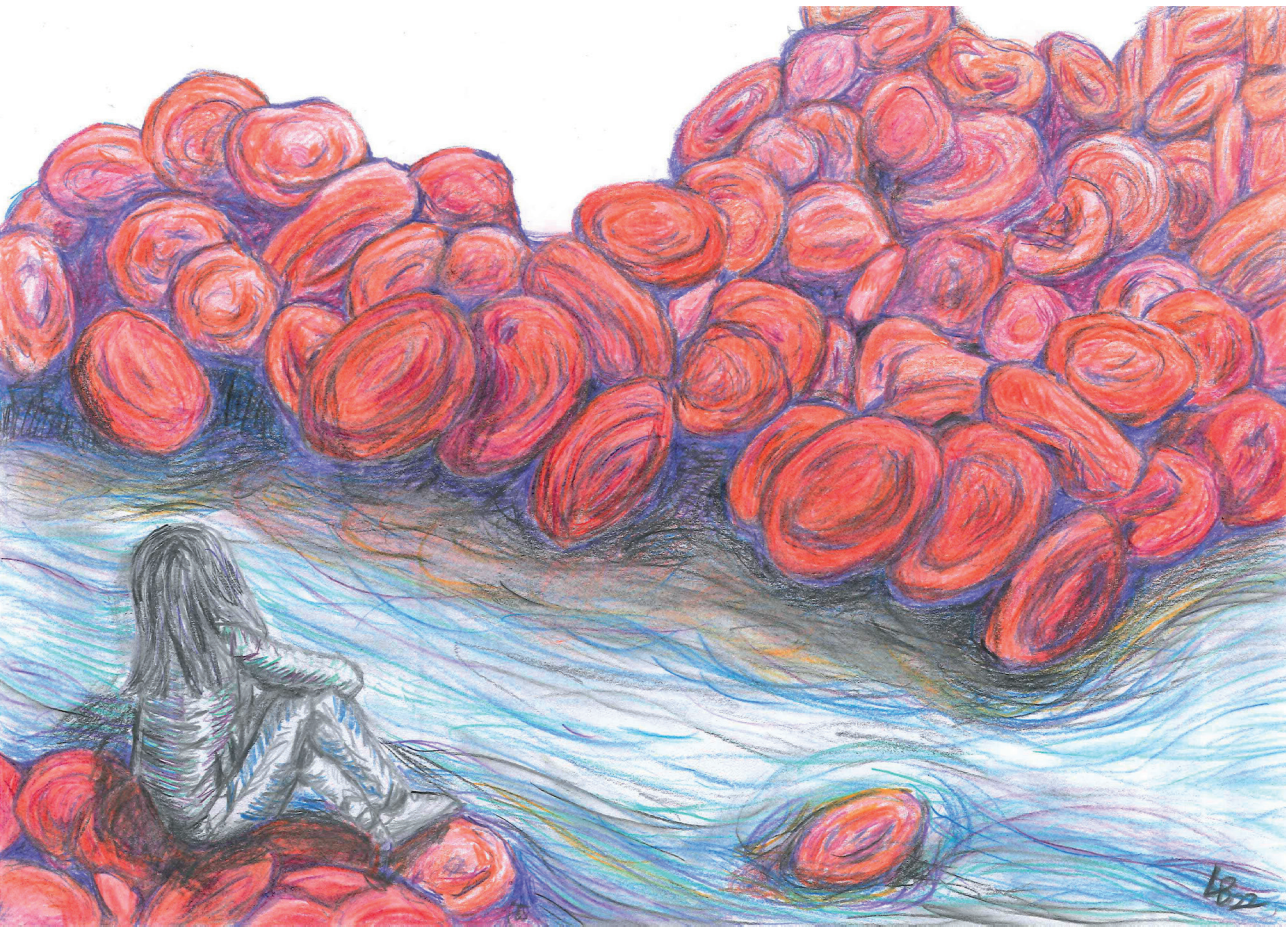
**Chapter 5** CLASP2 was previously shown to be a microtubule (MT) stabilizing factor required for the maintenance of adult HSCs in the bone marrow of adult mice. Through the analysis of mouse and zebrafish LOF models, we unravel the critical involvement of CLASP2 in guarding the stem cell properties of embryonic and fetal HSCs. While phenotypically comparable to WT HSCs, *Clasp2* knock-out HSCs are not endowed with self-renewing capacity and undergo premature differentiation into more lineage-committed blood cell types. Consequently, the HSC pool will ultimately be depleted. We found that the deficiency in self-renewal in *Clasp2* knockout HSCs is linked to impaired recycling of the c-Kit receptor to the plasma membrane, due to a defective Golgi network and increased lysosomal degradation. We describe, for the first time, a gradient of c-Kit expression (rather than a binary absence or presence) that strongly affects HSC self-renewal properties through interaction with the stem cell niche.

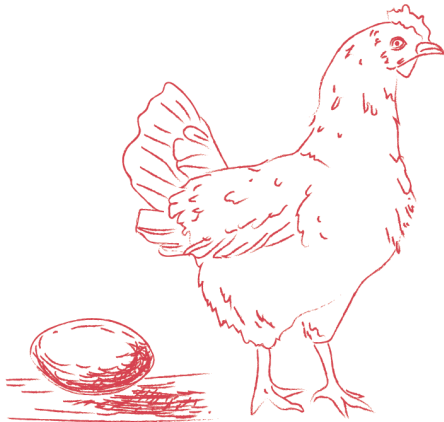
**Chapter 6** Clasp2 not only mediates c-Kit cell surface expression and thereby interaction of embryonic HSCs with their respective niche; we also revealed that Clasp2 modulates the dynamics of hematopoietic stem and progenitor cell (HSPC) emergence from the aortic endothelium. Using high-resolution live-cell imaging, we observed that loss of Clasp2 leads to extensive cellular protrusions that anchor cells to the endothelium of the aorta, altering their migratory behavior. Transcriptional analysis of the vascular endothelium in zebrafish *clasp2* mutant embryos supports a role of Clasp2 in the endo/lysosomal pathway and suggests a regulatory function in the remodeling of the extra-cellular matrix in venous/lymphatic endothelial cells. Consistent with these data, loss of Clasp2 impaired venous secondary sprouting and lymphangiogenesis. Modulation of the hyaluronan ECM network rescued different aspects of the venous/lymphatic phenotype in Clasp2-deficient embryos, indicating that Clasp2 is indeed involved in ECM turnover regulation. We report here a regulatory function of Clasp2 in the migratory behavior of specific endothelial cell populations through modulation of ECM composition and turnover.

**Chapter 7 Discussion** “How are functional HSCs generated during embryonic development and how is this process regulated?” is the central question of this thesis. The present work, together with other studies, begins to elucidate the complex regulatory network that controls HSC development at different levels. For instance, cell-intrinsic factors, such as molecular changes in the transcription factor network, allow for the transition from an endothelial to a hematopoietic program during EHT. At the cellular level, complex rearrangements of cytoskeletal elements are needed for the successful emergence from the endothelium. The maintenance of the initiated stem cell program is critically dependent on the interaction of the cell with the surrounding microenvironment and its ability to respond to gradients of soluble factors. Impaired intra-cellular trafficking of receptors such as c-Kit, which mediates



the cross-talk between HSCs and the niche factors, results in the loss of stem cell properties. Herein, the appropriate timing and number of receptors on the cellular surface—partly controlled by vesicular trafficking through the Golgi and degradation through the endo/lysosomal pathway—seems pivotal. Cell-extrinsic signals, such as secreted ligands from the immediate microenvironment, are another critical part of the regulatory landscape of HSC generation. The availability of those ligands in the extracellular space to bind to their cognate receptors at the cell surface is modulated by the extracellular matrix and its complexity. Understanding the regulatory network that allows for *de novo* generation of HSCs during embryonic development is crucial to improve our current efforts to produce these precious cells *in vitro*, with wider significance for stem cell therapies and regenerative medicine.





# Chapter

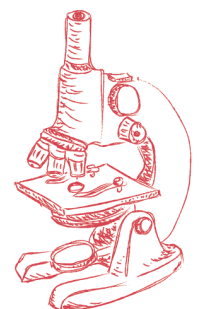
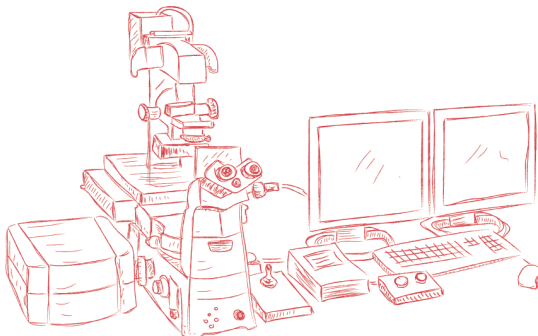
# 1

## Introduction

Part of this chapter has been published in:  
Developmental Biology, volume 428, issue 2, pp. 318-327 (2017)

Klaus, A., Robin, C.

### Embryonic hematopoiesis under microscopic observation



**H**ematopoietic stem cells (HSCs) are at the origin of adult hematopoiesis, providing an organism with all blood cell types needed throughout life. During embryonic development, a first wave of hematopoiesis (independent of HSCs) allows for the survival and growth of the embryo until birth. A second wave of hematopoiesis that will last into adulthood depends on the production of HSCs that begins at mid-gestation in large arteries such as the aorta. HSC production occurs through a hemogenic endothelial to hematopoietic transition (EHT) process and the formation of hematopoietic clusters in most vertebrate species. Advances in understanding EHT, cluster formation and HSC production were triggered by combined progresses made in the development of *in vivo* assays, microscopy, imaging and fluorescence tools. Here, we review the current knowledge on developmental hematopoiesis with a focus on the first step of HSC production in the aorta and how microscopic approaches have contributed to a better understanding of the vital process of blood cell formation.



## 1. A brief history of the hematopoietic/blood stem cell discovery

The initial discovery of blood-producing cells concurs with the progresses made in the field of microscopy in the early 20th century. Modern microscopes allowed direct visualization of individual cells and tissue structure, leading to important scientific dogma. For example, a close look at human and rabbit bone marrow (BM) saps has led Ernst E.C. Neumann to think that the BM was the seedbed of red blood cell (1) and leukocyte formation. He also suggested the existence of a unique cell at the foundation of the entire blood system. Decades of subsequent research proved the presence of such cells and their central role to replenish the entire blood system upon transplantation. The Russian scientist Alexander A. Maximow coined the term “hematopoietic stem cell” (HSC) for this very particular cell type (2).

The first experimental evidence in animals for the existence of single immature stem cells at the origin of all blood cells came from transplantation experiments done in the early 1960s. BM cells, transplanted into irradiated mouse recipients, gave rise to colonies composed of both erythroid and myeloid cells in the spleen (3-5). These cells were referred to as colony-forming-unit in the spleen or CFU-S. Retrospectively, CFU-S possess only limited multipotency and self-renewal abilities and are therefore not ‘true’ HSCs. Indeed, HSCs are endowed with a multilineage potential that allows single HSCs to produce all cells from erythroid, myeloid and lymphoid lineages. They are also able to self-renew to maintain a constant pool of HSCs throughout the entire existence of an organism. The experimental gold standard method to reveal both self-renewal and multipotent capacities of ‘true’ HSCs is to perform long-term *in vivo* transplantation assays in primary and secondary recipients (6). Herein, irradiated recipients are injected with the cells of interest together with cells that provide short-term blood supply (for the survival of the recipients). The degree of chimerism in all (erythro-myeloid and lymphoid) blood lineages present in all hematopoietic organs (i.e., peripheral blood, BM, spleen, thymus and lymph nodes) in primary and secondary recipients are the measurement to retrospectively prove the multilineage and self-renewal potential of HSCs.

As Neumann postulated, most adult HSCs reside in the BM in mammals. It is also the case in avians. However, HSCs reside in the kidney (referred to as kidney marrow) in fish. Yet, HSCs are initially generated during embryonic development where they transit through different anatomical sites before to reach the BM. While HSCs were long thought to be responsible for blood homeostasis, it was of late shown that a large number of long-lived progenitors would in fact be responsible for the steady-state blood production throughout life (7). Most recently this view was supported by lineage-tracing studies indicating that fetal hematopoiesis is also sustained by multipotent progenitors, rather than HSCs (8). Nevertheless, HSCs remain essential as they are the key cell type able to replenish defective HSCs and therefore the entire blood system in patients with blood-related diseases and disorders upon transplantation.

## 2. Exploring embryonic hematopoiesis

HSCs, which reside in the BM, are initially generated during embryonic development. Understanding and characterizing all the physiological steps of the birth of HSCs during developmental hematopoiesis holds great promise to improve the production of these cells *in vitro*. To this end, embryonic hematopoiesis has been extensively studied in various animal species, such as fish, amphibian, avian, rodent and other mammalian systems. In the following paragraphs, I will summarize the current knowledge of developmental hematopoiesis in the chronological order as it occurs *in vivo* in the embryo.

## 2.1. The yolk sac is the site of HSC-independent hematopoietic waves

The mesodermal layer of the extra-embryonic yolk sac (YS) is the site where the first waves of hematopoiesis occur in mouse and chicken embryos. This first wave, also referred to as primitive erythropoiesis, leads to the production of primitive erythroblasts in the blood islands, starting at embryonic day (E)2 of chicken and E7.25 of mouse development (2, 9-11). The mouse primitive erythroblasts, which express embryonic globins, are released in the circulation when the heart starts beating, and begin to enucleate at E12.5 to produce erythrocytes that continue to transiently circulate in pups after birth (12-14). The early production of primitive erythrocytes coincides with the need of a proper oxygenation of the growing embryo. Primitive megakaryocyte and macrophage progenitors are also produced at E7.25 in the mouse YS (15, 16). Megakaryocytes and platelets are found soon after, playing a role in the development of blood and lymphatic vasculatures during embryonic development (17). Primitive hematopoiesis transiently produces cells that do not last into adulthood, except for primitive macrophages that were recently shown to produce microglia in the brain of adult mice (18), as it is also the case in chicken (19). Long thought of as only able to produce primitive/transient hematopoietic waves, the YS also originates the definitive hematopoietic wave, with the production of erythroid progenitors (burst-forming unit erythroid or BFU-E) at E8.25 of mouse development (20). After colonization of the fetal liver (FL), BFU-E will produce the first definitive erythrocytes. Different types of myeloid progenitors (e.g., granulocyte-macrophage progenitors, mast cell progenitors, high proliferative potential colony-forming cells) also appear in the YS at E8.25, before colonizing the FL where they will produce mature cells after E10.5 (21). Erythro-myeloid progenitors (EMPs) start to emerge in the YS at E8 and will be responsible for the production of definitive erythrocytes, granulocytes and macrophages in the FL (22). Altogether, the YS primitive and definitive hematopoietic waves allow for the survival and growth of the embryo to term without the need of HSCs (23).

Hematopoiesis begins only 11 hours post fertilization (hpf) in the intra-embryonic lateral plate mesoderm in the zebrafish larvae. It is specified in a posterior region, giving rise to erythroid cells, and an anterior region generating macrophages (24). In concordance with other vertebrates, this initial blood cell production is followed by a wave of EMP hematopoiesis (25).

Importantly, besides the YS, the placenta (PL) is also a major source of progenitors during development (26, 27). Hematopoietic activity commences in the PL during mid-gestation, which occurs in parallel to the definitive potential in the aortic region that is detailed below. It is still not fully resolved whether the PL is capable of *de novo* HSC generation, as seen in the embryonic aorta (reviewed in (28)).

Until the 1970s, the YS blood islands were assumed to be at the origin of definitive hematopoiesis. This assumption was based on their capability to produce hematopoietic progenitors (15).

## 2.2. The aorta is the cradle of the first HSCs

The dogma of the YS as the source of definitive HSCs was challenged after graft experiments were performed in the avian and amphibian models, allowing for the first tracing of hematopoietic cells in developing embryos until adulthood. The creation of chicken/quail chimeras and the possibility to distinguish quail intra-embryonic cells (dark nuclei) (29) from chicken YS cells demonstrated the intra-embryonic origin of adult blood (30). Indeed, the early extra-embryonic YS progenitors (chicken origin) were short-lived and became gradually replaced by long-lived blood cells of intra-embryonic quail origin. It was confirmed in the amphibian model (*Xenopus*)

by using a similar grafting experimental approach (31, 32). In that case, the dorsal lateral plate (mesodermal region containing the dorsal aorta) mainly contributed to adult blood production while the ventral blood island region did not. These findings, supporting an intra-embryonic region comprising the aorta as the cradle of HSCs, contradicted the dogma of a YS HSC origin in mammals (15).

The use of organotypic *in vitro* cultures revealed the presence of multipotent precursors in the mouse intra-embryonic splanchnopleura region (before blood circulation) while it was not the case in the YS (33). This therefore demonstrated that the YS does not contribute to definitive hemopoiesis in the mouse. By means of transplantation assays, HSCs were first detected in the aorta of the aorta-gonad-mesonephros (AGM) region (which develops from the para-aortic splanchnopleura), as well as in the vitelline and umbilical arteries and the head at E10.5 (34-37). Starting at E11.0-E11.5, HSCs are also found in the YS, PL and FL (38-40). The PL and the FL become important HSC reservoirs at mid-gestation before HSCs start to colonize the BM at E17.5 (41).

### **2.3. The relationship between hemogenic endothelium, hematopoietic clusters and HSCs**

In the mouse embryo, clusters of round cells have been found tightly associated with the endothelial layer of large arteries, such as the aorta (Fig. 2), and the vitelline and umbilical arteries (42), and were therefore referred to as intra-aortic hematopoietic clusters (IAHCs). Similar clusters are also found in the vascular labyrinth of the PL (43), more precisely in the chorio-allantoic vasculature and the fetal vessels near the chorionic plate (44). Immunostaining on whole embryos or sections have shown that IAHC cells express numerous hematopoietic markers (e.g., c-Kit, CD41, CD45) also expressed by embryonic HSCs (26, 45-47). While the morphology and phenotype of IAHC cells strongly suggested a hematopoietic identity, the link between IAHC cells and HSCs was established after close observation of hematopoietic mutants lacking important transcription factors such as RUNX1. The fact that *Runx1*<sup>-/-</sup> mutant embryos, devoid of HSCs, also lack IAHCs formally linked HSCs and IAHCs (48-50).

Microscopic observations of the close spatial connection between IAHCs and the vessel wall led to the pioneer idea that the endothelium or specialized endothelial cells might give rise to IAHCs (51). Immunostaining of whole embryos or sections have shown that IAHC cells, besides hematopoietic markers, also express endothelial markers (e.g., VE-Cadherin, endomucin, CD31, CD34, endoglin, Tie2) (42, 45-47, 52). It therefore supported a developmental relationship between endothelial and hematopoietic lineages. The endothelium capable of generating hematopoietic cells was named hemogenic endothelium (Fig.1, right panel). The first functional proof of an endothelial origin of IAHC cells was obtained in chicken embryos (53). The aortic endothelium was labeled by injecting acetylated-low density lipoproteins (Ac-LDL) into the heart of a chicken embryo before IAHC emergence. Twenty-four hours later, all IAHC cells were labeled with this traceable dye, formally proving their endothelial origin.

Further experiments performed in the avian system have permitted a better comprehension of the organization and origin of the hemogenic endothelium in the aorta. Grafting experiments of mesodermal fragments between chicken and quail embryos suggested that the aortic endothelium derives from two distinct endothelial cell lineages. While the ventro-lateral portion of the aorta is derived from the splanchnopleural lateral mesoderm, the roof is derived from the paraxial mesoderm (54). It appeared that only the splanchnopleural-derived ventral endothelium is hemogenic, starting at E2.5 by thickening and expressing the pan-hematopoietic marker CD45 and progressively transforming into IAHCs (Fig.1, left panel). Non-hemogenic endothelial cells of somitic origin gradually replace the disappearing hemogenic endothe-

lium, which corresponds to the end of the hematopoietic production in the aorta (55). The precise location of the hemogenic endothelium and its progressive replacement regulate both in time and space IAHC production in the aorta. While part of IAHC cells is thought to be released in the lumen of the aorta, many cells also ingress into the underlying mesenchyme forming para-aortic foci of CD45+ hematopoietic cells (56, 57). These avian foci are considered as a mammalian FL equivalent (58, 59), providing a transient and maybe proliferative niche before the cells colonize definitive hematopoietic sites (i.e., spleen, thymus, BM, bursa of Fabricius) (60-62). The use of mouse embryonic stem cell (ESC) cultures confirmed the need for an endothelial step to produce hematopoietic cells from hemangioblasts (63, 64). Indeed, the continuous long-term single-cell imaging and tracking of mouse mesodermal cells allowed to directly observe hemogenic endothelial cells giving rise to round hematopoietic cells *in vitro* (63).

Various experimental approaches have been employed to prove the endothelial origin of IAHCs and HSCs *in vivo*. Cre recombinase was expressed under the control of the endothelial cell specific promoter VE-Cadherin and induced at a specific time-point of early development (65, 66). The stable genetic labeling of endothelial cells was detectable thereafter in the hematopoietic embryonic and adult progeny, clearly demonstrating the endothelial origin of HSCs. The conditional deletion of Runx1 in VE-Cadherin+ endothelial cells, leading to the absence of IAHC and HSC formation in mice, also confirmed the endothelial origin of both (67). Another molecule crucial for the EHT process are Gfi1 proteins. These proteins allow for the emergence of HSC through epigenetic downregulation of the endothelial program in HE cells (68).

Using an endothelial KDR-GFP transgenic reporter fish, the so-called endothelial-to-hematopoietic transition (EHT) could be observed for the first time *in vivo* in live zebrafish embryos. HSPCs were shown to emerge from the ventral aortic endothelium between 33 hpf and 54 hpf, with a peak at 48 hpf (69-71). HSPC emergence coincides with the expression of HSC markers, such as CD41, RUNX1, LMO2 and c-MYB. During EHT, hemogenic endothelial cells (HECs) start to bend away from the aortic endothelium towards the sub-aortic space (Fig.1, middle panel). Neighboring endothelial cells are thereby brought in proximity before HSPCs bud into the sub-aortic space, where they either divide or directly enter the circulation via the axial vein (70). Interestingly, HSPCs do not seem to bud into the aortic lumen as it is the case in other vertebrate species. Based on time-lapse imaging, an estimate of 3 HSPCs enter the vein circulation per hour (72), leading to approximately 60 HSPCs, 30 of them being true HSCs as they sustain definitive/adult hematopoiesis (69, 73, 74). Once HSPCs enter the blood stream, they migrate to the caudal hematopoietic tissue (CHT, the equivalent of the mammalian FL). There, HSPCs find a stem cell niche in which they amplify before colonizing the thymus and kidney marrow.

#### 2.4. Cell composition and role of intra-aortic hematopoietic clusters

During mouse embryonic development, IAHCs were first found at E9.5 in the vitelline, umbilical arteries and in the aorta (75). The number of IAHC cells (CD31+c-Kit+), counted after whole embryo staining, steadily increases until E10.5 (~700 IAHC cells/aorta) and remains numerous until E11.5 (~500 IAHC cells), concomitant with HSC emergence in the aorta (37, 42). Thereafter, the IAHC cell number gradually declines until E14.5, which coincides with an increase of HSPCs in the FL. IAHCs were long considered as composed solely of HSCs and committed progenitors. Surprisingly, only few HSCs (1-3 HSCs estimated per aorta at E10.5-E11.5 after performing limiting cell transplantation assays (38, 39, 76)) and committed progenitors (an average of 22 erythroid and myeloid progenitors estimated per aorta after clonogenic assays (77))



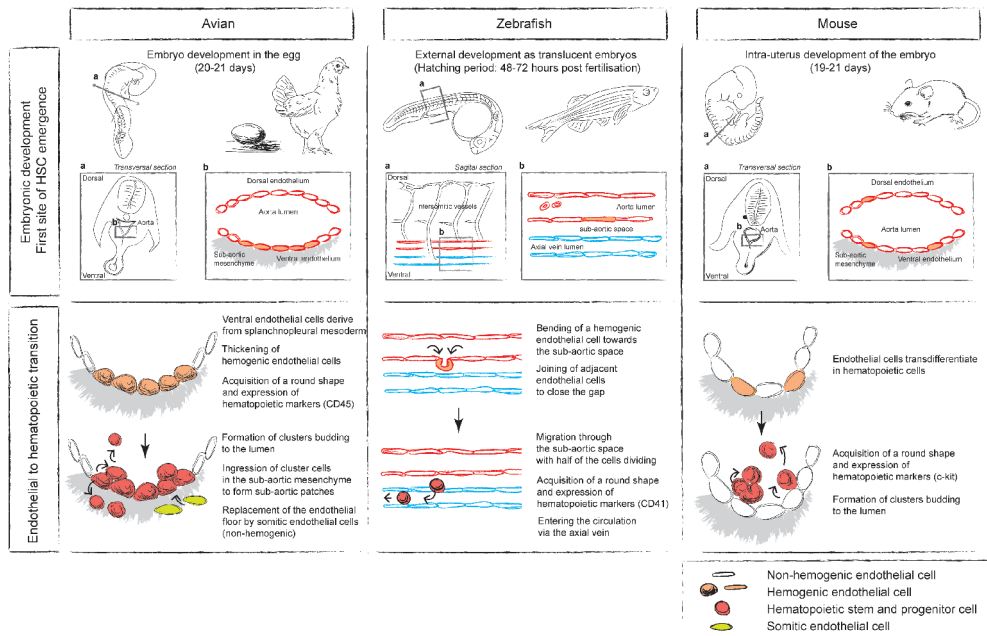


**Figure 1: Hematopoietic stem and progenitor cell formation across species.** Schematic representation of the embryonic development (top), first site of hematopoietic stem cell (HSC) emergence (middle) and the process of endothelial-to-hematopoietic transition (EHT) (bottom) in the avian, zebrafish and mouse embryo models (left to right). HSCs and intra-aortic cluster (IAHC) cells (in the case of avian and mice) are generated from hemogenic endothelial cells located in the aorta. EHT is restricted to the ventral aspect of the aorta in the avian and zebrafish, while it also occurs in the dorsal aspect of the aorta in mouse embryos. It is important to note that the EHT process differs between avian, zebrafish and mouse models..

are part of IAHCs that are composed of at least 25 times more cells at E10.5-E11.5 (42). IAHC cells are phenotypically heterogeneous, all cells expressing c-Kit but not all expressing CD45 or Ly-6A (SCA-1) at E10.5 (45, 77). This therefore suggests that an immature intermediate cell population between the hemogenic endothelium and HSCs might represent the majority of IAHC cells. The development of an *in vitro* culture assay, where AGMs are disaggregated and cells reagggregated in the presence of OP-9 cells and cultured for several days as explant reaggregates on the top of medium supplemented with cytokines, has permitted the identification of such population named HSC precursors (pre-HSCs) (47). Three types of successive pre-HSC populations have been identified thus far. Pro-HSCs (VE-cad+CD45- CD41<sup>low</sup>CD43-) are detected at E9.5 while Type I (VE- cad+CD45-CD41<sup>low</sup>) and Type II (VE-cad+CD45+) pre-HSCs are present in E10.5-E11.5 AGMs (78, 79). These pro/pre-HSCs sequentially and progressively mature into functional HSCs upon various periods of culture in reaggregates in presence of cytokines and/or stromal cell lines. The presence of pre-HSCs at earlier time points in the embryo and in IAHCs has also been demonstrated *in vivo* (80, 77), see chapter 2). A different type of *in vivo* transplantation assay has also been established to reveal the potential of these very immature cells, that are incapable to engraft adult recipients but can exert their HSC potential when transplanted in a more permissive environment (e.g. as the BM of immunodeficient mice or the liver of newborns) (80, 81). The repopulation efficiency of pre-HSCs could be linked to their proliferative status. In contrast to adult HSCs, pre-HSCs are highly proliferative displaying the highest potential in G2/M/S phase (82). Different transgenic reporter models were developed (such as Ly6a-GFP (83), Runx1+23GFP (84) and

Gfi1:H2B-Tomato (68) lines) to readily distinguish HE from non-HE cells and to dissect the EHT process and pre-HSC formation.

The properties and phenotype of maturing HSCs change as they transit through the successive anatomical niches, for instance from the aorta to FL, as described in detail below. In this process, CD41 (integrin  $\alpha\text{IIb}$ ) is one of the first cell surface markers expressed when HECs commit to a hematopoietic identity (26, 85-89). However, the use of this marker is limited, as it is only transiently and lowly expressed on embryonic and fetal HSCs (85). While adult HSCs lose CD41 expression, it is maintained on other more lineage-committed cell types and megakaryocytes. The opposite is true for the pan-hematopoietic marker CD45. When immature HSPCs initially emerge from the CD34, CD31 and VE-cadherin expressing endothelium, starting at E9.5 in mice, they are CD45 negative and will only gradually start to express this marker by E11.5 (90). Similarly, another marker of adult HSCs, Sca1 (Ly6a) (also marking HECs), is upregulated in IAHC cells between E10.5 and E11.5 (77, 90-92), see chapter 2). In contrast, the endothelial markers VE-cadherin is strongly expressed in emerging cells and in cells at the base of IAHCs, but will be gradually downregulated during further development (93-95). However, other cell surface markers, such as CD34, CD31 and c-Kit, maintain their expression into fetal and even adult stages (90, 96).

## 2.5. The formation of an embryonic HSC pool in the FL

The number of pre-HSCs present at E11.5 in the aorta matches the number of definitive HSCs detected at E12.5 in the FL, suggesting that the majority of IAHC pre-HSCs mature into HSCs after migration to the FL to generate the adult HSC pool that will colonize the BM before birth (97).

From E11.0-11.5, HSCs are also found in other highly blood perfused organs, i.e., YS, PL and FL (38-40). In fact, only very few HSCs are present in the entire mouse conceptus at this timepoint (4-11 cells). Strikingly, one day later this number amplifies to about 152 HSCs at E12.5, the majority of these cells residing in the FL and PL. HSCs will dramatically expand (~38 fold) from E12.5 to E16, with a peak at E14.5 (98) and subsiding numbers around 2-4 days postnatal (67, 96, 99-101). The FL herein represents an important transient niche for the maturation of pre-HSCs into HSCs and their subsequent amplification, becoming the main reservoir of HSCs at fetal stages.

At E11, HSCs start to colonize the FL under the influence of chemo attractive cytokines, such as CXCL12 (SDF1) (102), which is secreted from the forming niche and known to play an important role in HSC-niche interactions (homing, retention, survival) (41, 103-105). Importantly, CXCL12 is working synergistically with SCF to enhance HSC migration towards the FL niche (41). Apart from cytokines, other key factors mediating FL colonization are integrins like the  $\beta\text{1}$  integrin subunit (CD29). As such, chimeric  $\beta\text{1}^{-/-}$  embryos readily produce erythro-myeloid progeny, but HSCs fail to colonize the FL (106). Fetal HSCs express a variety of cell adhesion receptors and integrins that are potentially involved in direct cell-cell interactions with the microenvironment. HSPC trafficking to fetal tissues is for instance mediated by VE-Cadherin (CD144),  $\alpha\text{IIb}$  integrin (CD41), c-Kit and CXCR4 (85, 107). Of note, numerous extra cellular matrix (ECM) and cell adhesion molecules are also highly expressed by FL stromal cell lines, which support HSC maintenance/expansion *in vitro*, such as AFT024 (108-112).

More recently, a close physical interaction of seeding HSCs with endothelial cells (ECs) in the FL was shown (113). Through time-lapse imaging of FL explants, the seeding of c-Kit+ HSCs in the sinusoidal endothelial niche was captured. Upon arrival of the HSPC, endothelial cells start to virtually wrap around it, bringing the cell in proximity to supportive stromal cells and thereby facilitating their cell division

and amplification in the mouse FL and zebrafish CHT. FL ECs themselves support hematopoiesis via SCF expression. Perivascular Nestin expressing cells that associate with the portal vessel are a key component of the FL niche, as their depletion leads to reduced HSC numbers at E14 (114). Moreover, Nestin<sup>+</sup> perivascular stromal cells express *angptl2*, an important HSC expansion factor that is also expressed by the AFT024 supportive stromal cell line. Other stromal cell populations, for example stellate cells or hepatocytes, contribute to the HSC niche. Stellate cells appear around E11 in proximity to HSCs and express several supportive cytokines, including OSM, SCF and CXCL12 (115). Similarly, murine DLK1-positive hepatoblasts express cytokines that influence hematopoiesis and seem to be the main source of SCF, CXCL12 and ANGPTL2 (102, 116, 117). Importantly, from E12-E14, HSC expansion is proportional to the development of the vascular tree at this stage, suggesting that the availability of the niche restricts HSC expansion (114). Interestingly, after birth, the vascular tree of portal vessels undergoes differentiation from an arterial (Ephrin-B2<sup>+</sup>) to venous (EphrinB4<sup>+</sup>) identity, which coincides with the loss of Nestin<sup>+</sup> perivascular cells and the migration of HSCs to the BM (114).

## 2.6. HSC seeding of the BM

Transplantable HSCs are first detected in the BM, the adult site of hematopoiesis, at E17.5 (41). Interestingly, this first seeding of the BM also overlaps with the formation of vasculature at E16.5 (118). In order to seed the BM niche, HSCs need to migrate from the blood into the marrow. SDF-1/CXCL12 is critical for HSC chemoattraction to the BM. Binding of CXCL12 to its receptor CXCR4 expressed on HSCs activates multiple downstream pathways that are involved in colonization, but also retention of HSCs in the BM niche. Similar to the FL niche, the BM niche is built out of several cell types that regulate HSC maintenance. ECs not only play a role in the initial steps of homing during the trans-endothelial migration, but also contribute to the niche. For instance, the EC-specific depletion of the Notch ligand *Jag1* (using VE-cadherin-Cre) results in reduced HSC number in homeostasis and impairs recovery after irradiation (119). Likewise, SCF deletion in ECs (using *Tie2-Cre*) also reduces HSC numbers (120). Homeostasis and maintenance of HSCs in the BM is highly regulated and critically dependent on the stem cell niche. Cell-extrinsic signals from a heterogeneous population of cells such as the mentioned ECs, osteoblasts (121), Nestin<sup>-</sup> (122, 123), CAR<sup>-</sup> (124) and *LepR*<sup>-</sup> (120, 122) stromal cells, perivascular nerves (125) and hematopoietic cells [megakaryocytes (126-128); macrophages (129, 130) and neutrophils (131)] are pivotal to orchestrate hematopoiesis.

## 3. Molecular characterization of HSC emergence and maturation

In recent years, several studies have focused on a better understanding of the molecular events occurring during HEC specification, EHT and pre-HSC maturation into HSCs in the embryonic aorta by using single-cell transcriptomics approaches. Such studies support that IAHCs are mainly composed of pre-HSCs and have identified a complex transcriptional network controlling the downregulation of the endothelial program and upregulation of the hematopoietic program during EHT and pre-HSC maturation at E10.5 and E11.5 (132), Zhu (82).

Current efforts aim at the molecular characterization of the early stages of hematopoietic specification when conceptionally a vascular endothelial cell chooses a hematopoietic fate. This model remains controversial: some reports indicate that HECs and arterial ECs represent different cellular lineages with a distinct origin, defined by levels of Notch signaling. Recently Hou et al. transcriptionally defined two different

arterial EC populations at E9.5-E10.5, coinciding with the appearance of IAHCs in the aorta (133). Further enrichment by an EPCR+ Kit+ PK44 and also CD44+ signature purified a HE population with a dual potential: angiogenic and hematopoietic. Interestingly, vascular endothelial cells seem to face two cell fate choices, first an arterial and subsequently a hematopoietic fate. New cellular intermediate states, such as a pre-HE population has been recently revealed (134, 135). Importantly, a developmental bottleneck that is based on RUNX1 dosage controls the transition from pre-HECs to HECs (135). Moreover, this transition is marked by CD143 (ACE) expression (134). Upon acquisition of a hemogenic state, pre-HECs enter the active cell cycle. Of late, it was shown that the emergence of pre-HSCs is preceded by the generation of CD45+ lympho-myeloid biased progenitors (135). In line with this observation, two distinct HEC populations were identified in the aorta (136). Those are characterized by their CXCR4 expression levels that are important for stem cell-niche interactions. The first-specified CXCR4-negative HECs generate multipotent progenitors (MPPs) and only the later appearing CXCR4-positive HECs are capable of forming definitive HSCs. The HSC-competent CXCR4 positive HECs are characterized by the upregulation of the arterial program and stem-cell self-renewal genes.

Single-cell transcriptional profiling was also important for the identification of new markers, such as EPCR (Procr, CD201<sup>high</sup>) mentioned above, to further purify the pre-HSC populations *in silico* (82). Recently, the receptor for hyaluronan CD44 was identified as a novel marker of EHT cells, but also as functionally important since abrogation of the ligand-receptor interaction impaired the emergence of HSPCs (137). Vascular ECs are CD44 negative. Upon acquisition of the arterial identity, CD44 is up-regulated (low level) and will progressively increase to a high level in pre-HSCs type II.

#### **4. Cell-extrinsic regulation: How the surrounding microenvironment or niche influences HSC generation and fate**

The initial concept of a stem cell-surrounding microenvironment referred to as "niche" was proposed in 1978 by Schofield (138). He hypothesized that stem cells are located in close association with other cells that determine their fate. Such niche enables the self-renewal and prevents the differentiation of stem cells.

##### **4.1. Dorso-ventral regulation of aortic hematopoiesis**

IAHC emergence is increased in specific regions of the aorta in an antero-posterior manner. While most IAHCs are centrally located in the mouse and human aorta (42, 139), chicken has more IAHCs in the anterior region (140). This patterning is likely controlled by extrinsic factors from the microenvironment, but this regulatory landscape remains to be characterized. Recent studies shed some light onto the dorso-ventral regulation of IAHC formation. In most vertebrate species, the location of HECs and IAHCs is ventrally polarized. The mouse represents an exception with the formation of IAHCs in both ventral and dorsal sides of the aorta (Fig.2A). However, subdissection of the aortic region to separate the ventral and dorsal sides of the aorta revealed that while progenitors are found in both sides, transplantable HSCs reside only in the ventral side (141). Explant culture of AGM regions with ventral tissues (i.e., including the gut) enhanced the HSC potential while culture with dorsal tissues (i.e., including the neural tube) decreased the activity, suggesting that there is positional information in the microenvironment that is transmitted in the form of instructive cues (Fig.2B) (142).

At early E10, Hedgehog (Hh) proteins supplied in the explant medium had a comparably positive effect as the AGM co-culture with the gut (142). Sonic Hh is a key

inductive cue for VEGF signaling (Fig.2B) that controls angiogenesis during early embryonic development and plays a fundamental role in establishing and maintaining arterial identity of vessels, as shown in the zebrafish model (143). Accordingly, Hh maintains the arterial features of the roof of the aorta, while Bmp4 induces the Runx1-controlled hematopoietic specification in the ventral floor of the dorsal aorta (DA) in zebrafish embryos (Fig.2B) (144). BMP4 plays an important role in the induction of the hematopoietic potential from the mesoderm (145, 146). Deletion of Bmp4 leads to a loss of dorsal tissues identity and enhances ventral identity, including hematopoietic cell output. Similarly, overexpression of Bmp4 increases ventral cellular lineages (147). In explant or reaggregation culture, addition of BMP mostly enhances HSC activity (Fig.2B) (148, 149). However, scRNA-seq revealed that activation of BMPER via BMP4 is important for HSC maturation (150). During IAHC cell formation in mouse and human embryos, BMP4 is ventrally expressed by the immediate microenvironment, composed of mesenchymal and ECs that underly IAHCs. *In vivo*, all HSCs are activated by BMP in the aorta (151). In contrast, the use of *in vitro* explant cultures identified two distinguishable types of HSCs, i.e., BMP-activated and non-activated HSC populations (152). Interestingly, the latter is depending on Hh-mediated VEGF-signaling. Because of this close relationship of blood and vessel development, the contribution of angiogenic factors to hematopoiesis cannot easily be distinguished. However, VEGFa reduction in *Xenopus* embryos impairs HSC development while the arterial identity of the DA is correctly specified (153). Repression of VEGFa results in decreased Notch1 expression in the hemogenic endothelium. VEGFR-Notch signaling is not only pivotal for angiogenic sprouting and arterial EC identity, but also needs to be turned down at a precise developmental time to facilitate HSC emergence (Fig.2B). A threshold level of NOTCH is key for hematopoietic induction that downstream regulates crucial hematopoietic transcription factors such as GATA2 and RUNX1 (154). In a similar transient manner, the activity of the Wnt/beta-catenin pathway in neighboring ECs is needed for the emergence of HSCs in the aorta (155). Wnt signaling is acting in a signaling axis with retinoic acid (RA) to control HSC generation. Herein, RA positively stimulates HSC potential and is blocked by Wnt induction (Fig.2B) (156). Besides these EC-derived signals, the nervous system also provides hematopoietic cues. For instance, the sympathetic nervous system secretes catecholamines, which stimulate the newly emerging HSCs, blood flow independently (157). However, blood flow and the resulting shear stress activate the nitric oxide pathway. NO-signaling is capable of supporting HSC development in mouse and zebrafish, both *in vivo* and *in vitro* (158, 159). Embryonic HSC generation, survival and amplification are critically controlled by other growth factors present in the AGM, such as Flt3l and interleukin-3 (IL-3) (76). Together with stem cell factor (SCF) (Fig.2C), they support pre-HSC maturation in *ex vivo* reaggregate co-cultures (47) and are highly expressed by HSC-supportive stromal cell lines derived from the aorta microenvironment (112).

#### 4.2. Niche-HSC interaction, the example of SCF/c-Kit

During embryogenesis, HSCs transit through different anatomical locations and niches to specify, mature, expand and/or be maintained. As discussed above, specific growth factors and other signaling molecules mediate the niche interactions between the supportive environment and the nesting HSCs. Here, I will focus on one critical factor receptor-ligand pair for stem cell-niche communication, c-Kit and SCF (Fig.2C). The tyrosine kinase receptor c-Kit is expressed by all HSPCs. In 1987, c-Kit was identified as the cellular counterpart of the v-Kit oncogene (Hardy-Zuckerman 4 feline sarcoma virus), encoded by the white-spotting (W) locus (160). The ligand of c-Kit, SCF, is encoded in the Steel (Sl) locus (161). A manifold of loss-of-function studies described the crucial role of SCF/c-Kit signaling in primordial germ cell migration, fertility,



pigmentation and importantly also hematopoiesis. Various W mutations in the c-Kit locus have been identified. Most of them affect the intracellular kinase domain of c-Kit. These mutations are associated with different degrees of hematopoietic failure that are proportional to the level of impairment in kinase activity. For instance, in *W42* mutants, the aspartic acid 790 is substituted by asparagine, resulting in a severe reduction of kinase activity (162). *W42* homozygous mutants die perinatally and even *W42/+* heterozygous mutants suffer from a severe loss of long-term HSCs (163). However, *Kit W41* homozygous mice with a partial loss of function of c-Kit are viable, with merely a twofold reduction of long-term HSCs (164). Similarly, deletion of the membrane bound form of SCF (*Sld*) is sufficient to induce hematopoietic defects (165), indicating that SCF/c-Kit signaling that is mediated via cell-cell contact is required to maintain hematopoiesis (Fig.2C).

c-Kit, as a type III receptor tyrosine kinase (RTK), encompasses five extracellular immunoglobulin (Ig)-like N-terminal domains that mediate ligand binding. They are followed by a single-spanning transmembrane region. The intracellular domain consists of the juxta-membrane region and a split tyrosine kinase domain, interrupted by a kinase insert sequence and followed by the carboxyterminal tail. SCF binding to the extracellular domain induces the formation of c-Kit homodimers, bringing the two Ig-like domains of adjacent c-Kit molecules in close enough proximity to interact and stabilize the dimeric structure. In this state, the intracellular kinase domains are positioned in close proximity, allowing for their activation and subsequent transphosphorylation. Nine phosphorylation sites have been identified. Seven of these phosphorylated tyrosines serve as docking sites for signaling molecules with Src2 (SH2) domains. Next to the Src-signaling pathway, the Ras-Raf-MAP kinase cascade, JAK/STAT, phospholipase C and D signaling and phosphatidylinositol-3-kinase (PI3-K)/Akt pathway are also induced downstream of c-Kit activation. Thereby, the activated ligand-receptor complex relays signals along various important signaling pathways, inducing different cellular responses such as survival, proliferation, migration and protein trafficking (Fig.2C) (reviewed in (166)). As an example, PI3-K associates with the tyrosine 719 (murine c-Kit, Y719F) in the insert kinase domain. Mutation of Y719F in a myeloid cell line does not impair SCF-induced internalization. However, the receptor remained close to the membrane and was not processed in the endocytic pathway, suggesting that PI3-K is involved in c-Kit trafficking (167). In contrast, Src-kinase activity is necessary for c-Kit internalization (168).

It is not surprising that mutations in the proto-oncogene c-Kit, which render the kinase constitutively active, are driving the leukemic transformation in some myelodysplastic syndromes (169). Therefore, it is of crucial importance for the cells to control SCF/c-Kit signaling in intensity and duration. c-Kit downregulation is achieved by different means acting in concert (reviewed in (166)). First, the kinase domain is inactivated by either serine phosphorylation and/or tyrosine dephosphorylation. Second, c-Kit receptors are removed from the cellular surface followed by degradation through the endosomal pathway. Of note, phosphorylated c-Kit activates c-Cbl. Those active Cbl proteins then act as E3 ubiquitin ligases, targeting c-Kit for degradation by ubiquitination and thereby providing a negative feedback loop of the SCF/c-Kit signaling pathway (170). Upon clathrin-dependent internalization (168), the activated and ubiquitinated c-Kit complex is proteolytically degraded in lysosomes and partly in proteasomes (170-173). After downregulation, c-Kit levels are reestablished at the cell surface through synthesis of new receptor proteins and their vesicular transport to the plasma membrane (173, 174). However, cell surface receptor levels, especially RTKs, are also restored by recycling of the internalized proteins. They are either directly delivered back to the plasma membrane, or sorted in early endosomes. After a transit through other recycling compartments, such as the *trans*-Golgi, the internal-

zed receptors are transported back in vesicles to the cell surface (reviewed in (175)). In the embryonic aorta, all IAHC cells are characterized by c-Kit expression. Accordingly, all long-term HSC activity is restricted to the c-Kit<sup>+</sup>/c-Kit<sup>high</sup> fraction of cells in E11/E12 aorta and FL (176, 177). Concomitantly, the ligand SCF is expressed in those embryonic hematopoietic niches (178-180), suggesting an early role for SCF/c-Kit-signaling in embryonic hematopoiesis. However, abrogation of SCF/c-Kit-signaling by neutralizing antibodies or mutated forms of c-Kit, showed no requirement of this pathway for HSPC emergence (181, 182). Interestingly, IAHCs show a c-Kit gradient with low expressing cells at the base and c-Kit<sup>high</sup> cells more apical. Those c-Kit<sup>high</sup> cells were identified as highly proliferative pre-HSCs and maturation towards the HSC state required slowing of the cycling, suggesting that SCF/c-Kit signaling plays a role in the maturation process (183). *In vitro* reaggregation culture of AGMs in presence of various growth factors revealed that indeed SCF is the major driver of HSC maturation between E9.5 and E11.5 in the aorta (79). In this developmental timeframe, the YS produces EMPs that also express c-Kit at high levels (184). While SCF deficient Sl/Sl embryos have normal numbers of EMPs at E9.5, their number decreases significantly by E11.5 (185). Similarly, tissue resident macrophages and lympho-myeloid progenitors generated in the YS were affected, suggesting a requirement of SCF/c-Kit signaling prior to the emergence of HSCs in the aorta. This view was recently challenged as loss of c-Kit did not affect EMP production in the YS (186). The overall number of c-Kit<sup>+</sup> IAHC cells was decreased in the aorta of E10.5 Sl/Sl embryos, with a specific decrease of large IAHCs in the ventral side of the aorta. Upon transplantation, HSC activity was affected, indicating that SCF is an important EC-derived factor (185). Consistently, kit-ligand b (kitlb) has an important role in controlling HSPC emergence in the aorta and expansion in the CHT of zebrafish embryos (187, 188). Interestingly, the ECM protein Hapln1b, which links proteoglycans to hyaluronan polymers, seems to control the availability of the membrane-bound kitlb in the AGM and also CHT region. The complexity of the ECM network herein enables or hinders the binding of the ligand to the c-Kit receptor on the surface of HSPCs (188).

Membrane-bound SCF is also produced as a niche factor by FL ECs. c-Kit was recently shown to be required for early FL EMP expansion and transient-definitive hematopoiesis (186). Concomitantly, the FL of Sl/Sl mouse embryos contain dramatically reduced numbers of HSCs. The remaining fraction of HSCs was still able to self-renew, indicating a reduced ability to expand in absence of SCF (189). Importantly, SCF is amplifying the migratory response of FL HSCs to the chemokine CXCL12, while BM HSCs only respond to a CXCL12 gradient (41). Therefore, SCF in concert with CXCL12 might be important for HSC retaining in the FL.

*Sl/Sl* mutant mice that lack the membrane-bound form of SCF also display severe HSC defects in the BM, highlighting the role of SCF/c-Kit signaling via cell-cell contact for the maintenance of HSCs (190). Indeed, mice with mosaic expression of membrane-bound SCF on just some ECs had normal HSC maintenance in close proximity to those SCF-expressing cells (191). There are multiple cellular sources of SCF in the BM, such as perivascular stromal cells (Lepr<sup>+</sup>) and ECs (Tie2<sup>+</sup>) that form a perivascular niche (120). HSCs with lower c-Kit levels show enhanced self-renewal and long-term reconstitution ability compared to c-Kit<sup>high</sup> HSCs, which have an intrinsic megakaryocytic bias differentiation potential (192). c-Kit is also implicated in the maintenance of a quiescent HSC state and HSC survival (164). Upon differentiation, c-Kit starts to be downregulated and remains mainly co-expressed in the myeloid lineage with markers such as Mac-1 and Gr-1 (193). Indeed, common myeloid progenitors (CMPs) differentiate mainly into GMPs and megakaryocyte-erythroid progenitors that maintain c-Kit expression at rather high levels. Accordingly, c-Kit mutations lead to myeloid defects (194). However, if those are secondary to the critical role of c-Kit in HSCs is

difficult to determine.

Importantly, these local stem cell-niche interactions require the proper presentation of receptor ligand pairs on the cell surface. Membrane anchored proteins are transported to the plasma membrane via a vesicular machinery that utilizes a complex microtubule network for the transportation.

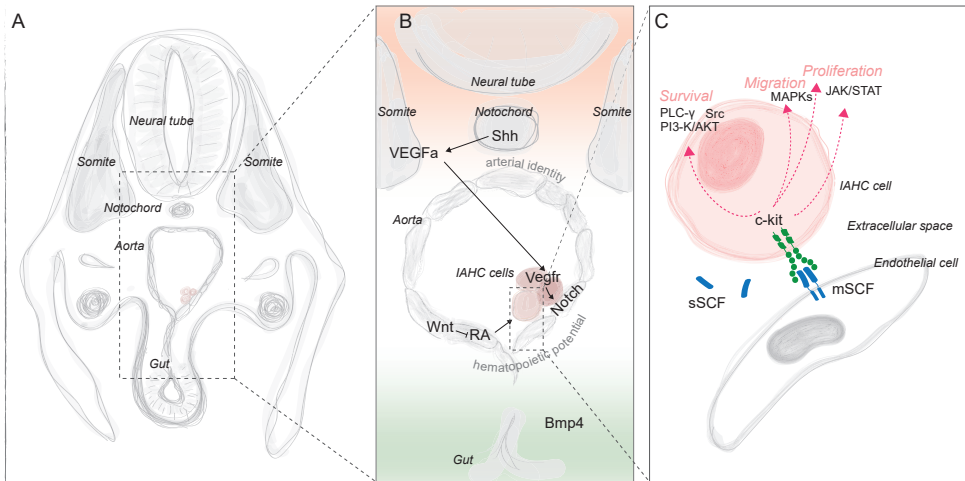


**Figure 2: Extrinsic regulation of IAHC cell formation.** A) Schematic overview of a cross section of an E10 mouse embryo. The neural tube, notochord, somites, aorta and gut are indicated. B) Hematopoietic potential is enriched (restricted to ventral ECs in other species) in the ventral endothelium. Pro-hematopoietic factors, such as BMP4 from the gut, are expressed ventrally (indicated in green), while inhibitory and pro-angiogenic factors are expressed dorsally (indicated in orange). In dorsal, Shh is expressed in the notochord and induces VEGFa expression from the somites. VEGFa is the ligand for VEGFR2 that is expressed on ECs and acts as powerful angiogenic factor. VEGF/VEGFR activation induces Notch signaling. Both pathways need to be balanced to allow IAHC cell formation. Furthermore, Wnt expressed by ECs is an inhibitor for the pro-angiogenic factor retinoic acid (RA). C) c-Kit is a receptor expressed by all IAHC cells. The ligand SCF is expressed and secreted by the aortic endothelium. Membrane-bound SCF binds to c-Kit and activates important signaling pathways downstream, such as PI3-K/Akt, PLC $\gamma$ , Src with ensure cellular survival. The MAPK pathway is activated, important for migration and proliferation, as well as the JAK/STAT pathway also controlling proliferation.

## 5. Cell-intrinsic regulation: Movement through the cell - the cytoskeleton and associated proteins

### 5.1. The cytoskeleton - microtubules

The cytoskeleton is built out of three types of filaments: microfilaments (actin), intermediate filaments and microtubules (MTs). Their different physical properties make them suitable for specific cellular functions.

In this thesis, I am focusing on MTs which can extend over long distances in a cell, while still being highly dynamic structures (reviewed in (195)). Motor proteins use MTs for long-range transports of cargo through the cell, e.g., vesicles containing cell surface receptors. Structurally, MTs are linear protofilaments, composed of  $\alpha$ - and  $\beta$ -tubulin subunits that form dimers. Thirteen laterally associated protofilaments form a hollow tubular structure with a diameter of about 25nm. The MT has intrinsic polarity since each protofilament has an  $\alpha$ -tubulin subunit at one end and a  $\beta$ -tubulin subunit at the other end, all protofilaments in a tubule having the same orientation.



$\alpha$ - and  $\beta$ -tubulin subunits are able to each bind a GTP, but only the  $\beta$ -subunits allow for the hydrolyzation. This more dynamic  $\beta$ -tubulin site of the MT is called the (+)-end, while the  $\alpha$ -tubulin site is called the (-)-end. In most vertebrate cells, MT nucleation is initiated at the MT-organizing centers (MTOCs), where the (-)-end is anchored (reviewed in (196)). Interphase cells have one prominent MTOC, the centrosome, located in the perinuclear region from which radial MTs are sent out with their (+)-end extending towards the periphery. Centrosomes consist of two centrioles surrounded by pericentriolar such as  $\gamma$ -tubulin. A  $\gamma$ -tubulin ring complex ( $\gamma$ -TuRC) serves as a ground structure for  $\alpha\beta$ -tubulin dimers to build onto during nucleation and anchors the (-)-end of the growing MTs. Overall, MTs are highly dynamic structures. At steady state, they are capable of treadmilling. Growing MTs are characterized by a cap of GTP-containing subunits at the (+)-end that is created by a delay between polymerization and hydrolysis. Thus, when the GTP in the terminal  $\beta$ -tubulins becomes more rapidly hydrolyzed than subunits are added, the cap is lost and the formerly blunt end will curl. This initiates the shrinkage of the MT in a process called catastrophe. However, a new GTP-cap can be formed by the new addition of GTP-binding dimers in a possibly stochastic event, then the growth of the MT continues. This transition from shrinkage to growth was termed rescue. During the catastrophe, the remaining GTP-tubulin in older sections of the MT get exposed and serve as a starting point for the rescue (197). This process of alternating phases of catastrophe and rescue is described as dynamic instability of MTs and allows for the rapid adaptability of the MT network.

## 5.2. Microtubule tracks for intracellular trafficking

The intracellular MT network plays a crucial role in intracellular vesicular trafficking of proteins, dynamics of membranes and localization and integrity of organelles (Fig.3) (reviewed in (198)). Trafficking occurs through the secretory pathway that transports soluble and membrane proteins on MTs to the plasma membrane and to the lysosome. The endocytic pathway does the opposite as it takes up substances from the surface and transports them to the inside of the cell. Both pathways employ vesicles to carry their cargo and transport them along the MT network to their destination. The key mechanistic features of both pathways are the budding of vesicles from a parental membrane and after transport, the fusion with the destination membrane. The budding is induced by the polymerization of coat complexes onto the membrane that provide the curvature. Interaction of the coatamers with the cytosolic domain of the transported transmembrane receptors further controls which cargo is transported. Moreover, different polymers coat vesicles headed for different destination organelles. Briefly, the secretory pathway transits through two major organelles. First, newly synthesized proteins translocate to the endoplasmic reticulum (ER), where they will be folded and covalently modified. In the second step, they are transported through the Golgi for further modification, such as glycosylation. Anterograde moving vesicles from the ER fuse to form *cis*-Golgi cisternae. The *cis*-cisternae undergo maturation and herein move via a *medial*-Golgi position towards the *trans*-Golgi side. The *trans*-Golgi network (TGN) is a major branchpoint, i.e., from here cargo-loaded vesicles are either transported to the surface for secretion/surface expression of their cargo or to the late endosomes for their degradation (Fig.3). Late endosomes also fuse with early endosomal vesicles that bud from the plasma membrane to bring membrane bound proteins into the cell for degradation or recycling (endocytic pathway).

### 5.3. Microtubule-associated proteins

MT assembly by polymerization is greatly catalyzed by MT-associated proteins (MAPs) *in vivo*. MAPs extrinsically regulate MT dynamics and kinetics as stabilizing or destabilizing factors. An important family of MAPs that influences MT dynamics are the (+)-end tracking proteins (+TIPs) that, as the name suggests, bind to the growing (+)-end of MTs (reviewed in (199-201)). +TIPs form dynamic networks among themselves that associate with the MT (+)-end. The first +TIP identified was the cytoplasmatic linker protein of 170kDa (CLIP-170) (202). A multitude of +TIP protein families have been described. They can be classified by the functional domains with which they interact with the MT (reviewed in (201)). One important class is the end-binding protein (EB) family whose specific binding domains enable it to interact with multiple other +TIPs positioning them as core components of +TIP networks. Another +TIP class contains TOG or TOG-like motifs that are arranged in tandem, which likely supports MT growth. Some +TIPs have several motifs that direct the protein to the MT and other subcellular regions. CLASPs belong to that category, as such they contain an SxIP motif next to TOG and TOG-like domains.

### 5.4. CLASPs

In the first study focusing on CLASP, it was shown to interact with CLIP-170, and CLIP-115 (203), hence the name of CLIP-associated protein (CLASP). CLASPs are an evolutionary conserved family of regulators of MT dynamics and organization. Orthologs have been identified in various species (*D. melanogaster* (Mast/Orbit) (204, 205), *S. cerevisiae* (Stu1) (206), *C. elegans* (cls-1 to -3) (207) and *A. thaliana* (CLASP) (208)). In mammals, there are two paralogs of CLASPs, CLASP1 and CLASP2, sharing 77% of identity. While CLASP1 is ubiquitously found, CLASP2 expression seems to be more confined with high expression in the brain and neural tissues (203).

Structurally, CLASPs can bind  $\alpha\beta$ -tubulin dimers with special helical repeat regions, the TOG domains (209, 210). Following the N-terminal TOG and TOG-like domains is a Serine-Arginine-Proline rich region. This SxIP motif is required for the interaction with EBs and targets CLASP to the tip of MTs (211). Mammalian CLASPs have an additional TOG3 domain binding to arched tubulin surfaces that mildly supports rescue events, but does not influence catastrophe. Lastly, C-terminal is a S/R-basic region that mediates lattice binding and importantly the interaction with other factors, such as CLIPs (203), the Golgi protein GCC185 (212), the cell cortex protein LL5 $\beta$  and the kinetochore-associated kinesin CENP-E (213, 214).

### 5.5. Roles of CLASP2

As the interactome with various proteins suggests, CLASPs physiological functions range from the stabilization of MTs, cytoskeletal remodeling, a role in cell polarity, to association with the kinetochore and mitotic spindle. I will focus below on the two roles that we further addressed in the following chapters of this thesis - persistent cell migration and secretory pathway at the Golgi apparatus.

#### CLASP role in cell migration

A prerequisite of cell migration is the establishment of polarity. CLASPs not only stabilize MTs at the leading edge of motile cells, but also support the formation of a polarized MT network in direction of the movement (203, 215, 216). Herein, CLASPs support the formation of Golgi-derived MTs in the direction of the leading edge, which will be discussed in detail below. The turnover of focal adhesions (FA), that are large multiprotein complexes linking the ECM to the actin-network at the cortex of a cell, is essential for cell movement. FA gather near the leading edge of the cell,

mature and then disassemble beneath the forward moving cell (Fig.3). CLASPs play a role in this FA turnover. They are recruited to the cortex at the leading edge of the cell through binding of LL5 $\beta$ , a phosphatidylinositol (3,4,5)-trisphosphate (PIP3)-binding protein (213, 217, 218). Through PI3-K signaling, CLASP2 is dephosphorylated, reinforcing its affinity to MTs and ultimately results in a polar and stabilized MT network at the migratory front of the cells (215). CLASPs not only mediate the MT tethering at FAs, but are also important in the disassembly process that involves ECM degradation. There, they ensure a local secretion pathway by coupling a stable MT network with directed exocytosis of vesicles whose content (likely metalloproteases) is essential for ECM degradation (217). This study places CLASPs at the center of a secretory pathway that modulates ECM-cell interaction in migrating cells (Fig.3).

### **CLASP and the Golgi apparatus**

Differentiated and polarized interphase cells often develop non-centrosomal MT arrays. These arrays require for their nucleation a cellular scaffold alternative to the pericentrosomal material. In many cells the Golgi, which is the major protein sorting and trafficking machinery, serves as such (Fig.3). Non-centrosomal MTs not only play an important role in polarized trafficking, but also support the integrity of the Golgi itself.

$\gamma$ -tubulin was found associated with the Golgi membrane. However, the  $\gamma$ -TuRCs template alone is insufficient to initiate the energetically unfavorable nucleation reaction (219). Additional factors in the Golgi-environment that would promote the MT polymerization or stabilization seem required. One of this key stabilizing factors is CLASP (Fig.3) (212). Both isoforms gather at the TGN. CLASP might be involved in the stabilization of the newly formed MT by coating and/or even function via its TOG domains already in the polymerization process. CLASP acts in concert with other factors. The AKAP protein complex has the capability to recruit the  $\gamma$ -TuRC, possibly to the *cis*-Golgi membrane (212) and either the seeds translocate towards the *trans*-Golgi side (220), or only those MTs that reach from their *cis*-nucleation side towards the TGN will be stabilized by CLASP (Fig.3) (221, 222). MT function is strongly dependent on their lifetime, and factors such as AKAP9 and CLASP are also capable of MT stabilization in that context (Fig.3) (203, 223, 224). It is clear that Golgi-derived MTs adapt a different function than centrosomal MT arrays and might also structurally and mechanically diverge. Enrichment of stabilizing factors such as CLASP on the lattice of Golgi-derived MTs (212, 225), as well as an accumulation of acetylated tubulin, might induce a more stable MT conformation (226).

During mitosis, the Golgi fragments into smaller vesicles that need to be reassembled once the division is completed. CLASP-dependent Golgi-anchored MTs play an important role in capturing these mini-Golgi stacks and pulling them in proximity to enable their fusion. Consequently, loss of CLASP leads to a dispersed Golgi morphology as reassembly to the characteristic ribbon structure fails (227). Since CLASPs are indispensable for the Golgi-derived MT network that enables the directional transport of vesicles to the leading edge of the cell, loss of CLASP also leads to loss of polarization and persistent migration. Of note, the efficiency of the secretory pathway remains unaffected, but the direction of trafficking to the plasma membrane is random (227). Therefore CLASPs, and particularly CLASP2, are key in securing Golgi integrity, polarized vesicular trafficking, and directed migration of cells.

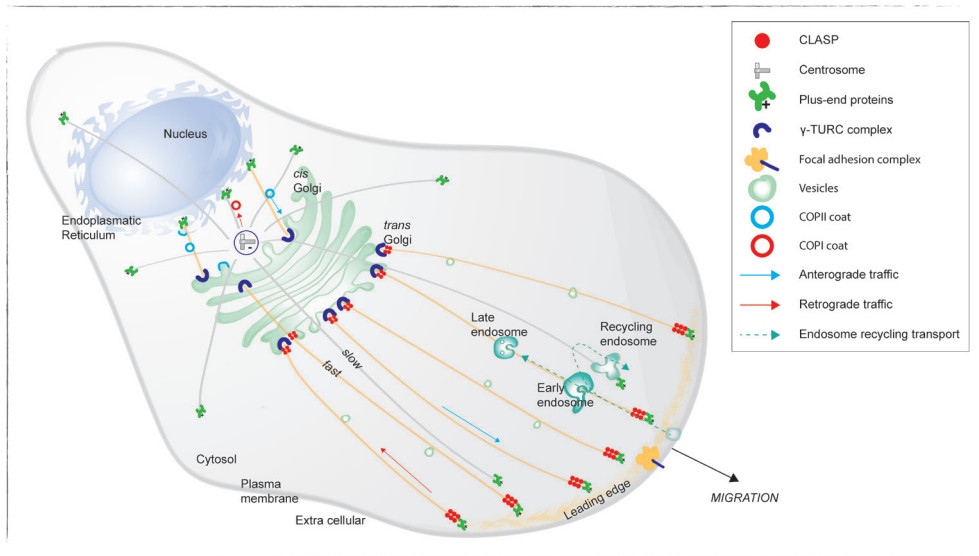


**Figure 3: CLASPs stabilize the acentrosomal microtubule network important for a polarized secretory pathway.** Schematic overview of the microtubule (MT) organization in a migrating cell and the interaction of MTs with the endoplasmic reticulum (ER), Golgi, the secretory pathway and the plasma membrane. ER and Golgi are directly linked through MTs that function as transport ways of vesicles. COPII coated vesicles transport cargo carried from the ER to the Golgi, as part of the anterograde traffic. COPI-coated vesicles transport their cargo in the opposite direction. The Golgi apparatus is at the center of the secretory pathway trafficking, but also functions as MTOC. It is closely located to the centrosome from which centrosomal MTs are emanating, but itself also possesses MT nucleating and capture ability. As such, the Golgi is the origin of an acentrosomal MT network directed towards the leading edge of the migrating cell. CLASPs play an important role in capturing MTs at the trans Golgi, but also in attaching MTs via interaction with LL5 $\beta$  to the cell cortex. Vesicles, carrying various cell surface targeted proteins, are formed at the Golgi and transported via MTs to the cell cortex. Endosomes that are required for the recycling but also through several maturation steps for lysosomal degradation of cell surface proteins, interact with MTs.

## 5.6. Cytoskeleton and hematopoiesis

Relatively little is known about the role of the cytoskeleton during embryonic hematopoiesis. Two recent studies in zebrafish embryos reveal new biomechanical characteristics of the EHT (228, 229). A critical step of successful emergence of HSPCs is the contractile and oscillatory force of an actomyosin ring at the basis of the cell that simultaneously extrudes the cell from the endothelial layer and brings adjacent cells in contact to close the hole. Inhibition of actin polymerization leads to less emergence events, incomplete extrusions and HSPCs bending towards the DA instead of extrusion towards the sub-aortic space (228). Interestingly, the abrogation of shear stress by blood flow also impairs the orientation of emergence (229).

A dynamic interplay of actin and MTs is at the basis of macrophage migration in *D. melanogaster*. Macrophages extend arms with a polarized array of MTs in their direction of migration. Upon the encounter of another macrophage, this extrusion mediates cell-cell repulsion to regulate the migratory behavior. Ablation of orbit/MAST (CLASP homolog) leads to defective polarity and loss of cell-cell repulsion to a similar extent as depolymerization of MTs (230).

Remarkably, human HSPCs extend protrusions when cultured *ex vivo* on a MSC feeder layer (reviewed in (231)). A lamellipodium is formed at the leading edge that expresses high levels of CXCR4, consistent with the attraction along a chemotactic

CXCL12 gradient. At the rear side, another microdomain, the uropod, is extruded at whose basis the MTOC is located. Thus, under these culture conditions, HSPCs adapt a highly polarized morphology and migrate by extending the lamellipodium and simultaneously retracting the uropod in a continuous cycle of attachment and detachment. The GTPase RhoA and the associated effector kinase ROCK1 are involved in MT destabilization in rear of the cell that is essential for polarization and uropod formation.

As seen above, CLASPs are crucial for the persistent migration of cells. In the absence of CLASP2, HSCs indeed home inefficiently to their niche in the BM and display disrupted MT network organization and overall stability (232). Loss of CLASP2 in mice causes an impaired HSC activity and downstream of this, a progressive pancytopenia with defects in megakaryopoiesis and erythropoiesis. Of note, *Clasp2*<sup>-/-</sup> HSCs express reduced levels of *c-Mpl*, the thrombopoietin receptor, known to be crucial for HSC maintenance in the BM niche. Despite a round cellular morphology, HSCs are polarized with Golgi and centrosomes clearly localizing to one side of the cell. Since CLASPs play a crucial role in polarization and proper attachment in other cell types, the authors hypothesized that HSC homing is impaired due to defects in attachment and/or migration in the absence of CLASP2. This lack of stem cell - niche interactions then impact signaling cascades (i.e., TPO - c-MPL signaling) important for HSC maintenance and then ultimately results in the loss of stem cell properties.

## 6. Development of the vascular system in zebrafish

Developmental hematopoiesis is highly dependent on the formation of a functional vascular network. As such, hematopoiesis cannot fully be investigated without assessing the endothelial development and vascular integrity first. In this section I will describe the vascular construction during zebrafish development. The formation of the vascular network is a multistep process that commences with the differentiation of mesodermal precursor cells into ECs in zebrafish. These ECs will form the DA and posterior cardinal vein (PCV) during vasculogenesis in the early embryo. This process is followed by sprouting angiogenesis, secondary angiogenesis and lymphangiogenesis, forming a complex vascular network (Fig.4).

### 6.1. Vasculogenesis

The *de novo* formation of vessels starts at about 12hpf in zebrafish embryos. Specific cells from the lateral plate mesoderm (LPM) develop an angioblast identity. They then migrate to the midline of the embryo to form the medial vascular rod by 22hpf (233, 234). Until rather recently, it was debated whether aortic or venous fate was pre-determined prior to migration. Live-imaging approaches revealed that arterial fated angioblasts migrate first, followed by venous destined cells about 3h later (235). This indicates an early distinction between DA- and PCV-angioblasts within the lateral plate mesoderm. Angioblasts contributing to the DA display active Notch- (236) and Erk-signaling (237).

### 6.2. Primary arterial angiogenesis

Subsequent to the formation of the major axial vessel by 22hpf, primary sprouting angiogenesis from ECs of the DA begins, ultimately forming the inter-somitic vessels (ISVs). The dynamics of this process is controlled by Notch- and Vegfa-Kdr1/Kdr- signaling. The cells guiding the sprout along the somite boundaries are called tip-cells. They are characterized by exploratory filopodia and high *dll4* expression (238-240). Dll4 then activates Notch in the following cells, called stalk cells, which in

turn suppresses Vegfa/Kdr/Kdrl signaling (241-244). The sprouts migrate dorsally where they fuse to form the dorsal longitudinal anastomosis vessel (DLAV) at 28-30hpf. Neighboring sprouts connect through anastomosis of their leading cells and the vessel forms a lumen (245).

Vegf-signaling is critical for angiogenesis. The ligand Vegfa binds to dimers of Kdrl and Kdr (zebrafish Vegfr2) to direct angiogenesis (Fig.4D). Mutants of either component reduce primary angiogenic sprouting and result in mis-patterning of the vessel (246, 247). Double mutants for *kdr/kdrl* (248) or mutants for downstream effectors, such as *plc-γ* (249, 250), display a complete block of arterial angiogenesis. Interestingly, mitosis in the post-tip cell might asymmetrically distribute Vegfr activity to the daughter cells, thereby reestablishing tip versus stalk cell identity. In this case, the mitotic spindle will be positioned closer to the proximal site of the tip cells, resulting in an unequal split of the cytoplasm (251).

### 6.3. Secondary venous angiogenesis and lymphangiogenesis

Starting at 32hpf, cells of the PCV start to sprout (245). These venous sprouts begin to migrate dorsally where they either form a successful anastomosis with the arterial ISV (aISV), or migrate even further to the height of the horizontal myoseptum (Fig.4A). Once the connection between a venous sprout and the ISV is perfused, the blood stream will support the migration of venous ECs from the PCV into the newly formed vISV. Ultimately, they will replace the upwards migrating arterial ECs (252). Strikingly, the formation of these venous ISVs (vISV) by anastomosis is influencing the overall arterial-venous specification throughout the embryo. While the identity of the first and last ISVs is commonly determined, all other ISVs stochastically adopt an arterial or venous identity. However, in total, aISVs and vISVs are equally distributed in number. When one ISV specifies towards a venous identity, the adjacent ISVs have a high probability to remain arterial (245, 253).

ECs that do not anastomose localize to the horizontal myoseptum where they accumulate transiently as a parachordal pool of lymphatic ECs (parachordal lymphangioblasts, PL) (Fig.4A) (253, 254). At 2.5dpf, PLs migrate from the myoseptum along the arteries, both ventral and dorsal (253, 255). The migrating lymphatic ECs (LECs) express Cxcr4a that interacts with its receptor Cxcr12a expressed in the horizontal myoseptum and Cxcr12b expressed by aISVs (255). LECs will proceed to form the major lymphatic network with the thoracic duct (TD) and the intersegmental lymphatic vessels (Fig.4C) (reviewed in (256)). Venous and lymphatic vessel development is tightly intertwined, Vegfc-Flt4 signaling being crucial for all secondary angiogenesis and required for the sprouting of ECs from the PCV (Fig.4E, F) (245, 257-260). More recently, an early distinction between venous and lymphatic progenitor cells was suggested even before secondary angiogenesis begins. Prox1, a key lymphatic transcription factor, is expressed in a portion of cells in the dorsal wall of the PCV before the sprouting starts (Fig.4D) (261-263). Interestingly, these cells will divide and while one daughter cell maintains prox1a expression and migrates dorsally, the other one will downregulate the expression and remains in the PCV, maintaining its structure. However, not all of the dorsally prox1a expressing cells contribute to the lymphatic vasculature, indicating that there is a degree of plasticity between lymphatic and venous fate (261).



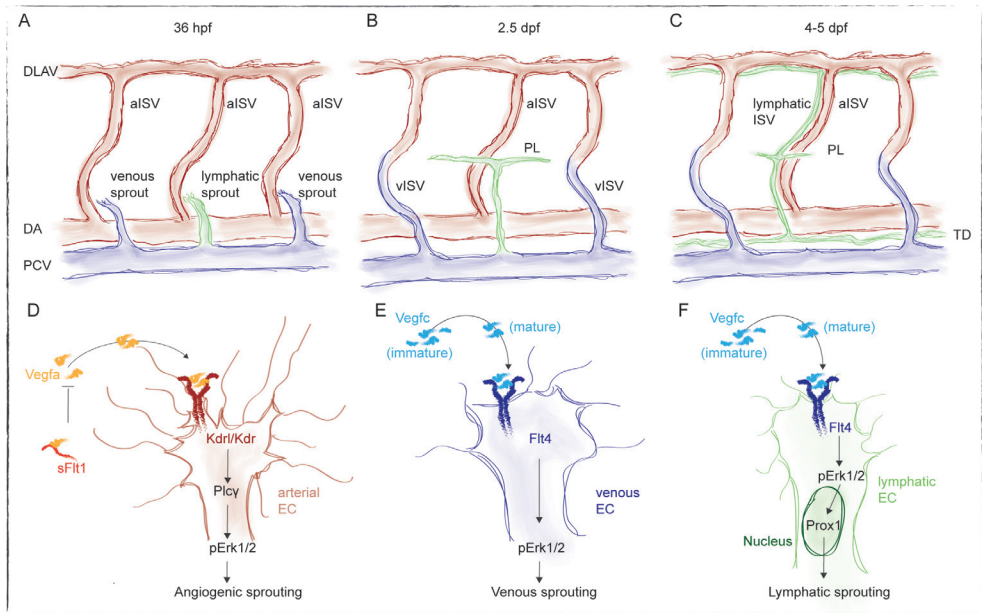


**Figure 4: Secondary angiogenesis and lymphangiogenesis during zebrafish development.** A) Venous (blue) and lymphatic (green) sprouts emerge from the PCV at 36hpf. B) At 2.5dpf, venous sprouts anastomose with the arterial ISVs. The lymphatic sprouts, that did not form such connection, migrate further to the horizontal myoseptum and form the parachordal lymphangioblasts (PL) C) At 4-5dpf, lymphatic progenitors migrate further and prepare to fuse into a lymphatic network consisting out of lymphatic ISVs, thoracic duct (TD) and dorsal longitudinal lymphatic vessel. D) Arterial EC sprouting is driven by Vegfa binding to Kdr/Kdr. Ligand activation induces Erk1/2 phosphorylation via Plc $\gamma$ . Vegfa availability is negatively regulated by soluble Flt1 (sFlt1). E, F) Secondary angiogenesis and lymphangiogenesis is guided by Vegfc signals. The mature form of Vegfc, which is secreted by the DA and hypochord, binds to Flt4 receptor. E) In venous ECs, ligand binding leads to pErk1/2 activation and venous sprouting. F) The expression of Prox1, an essential factor for lymphangiogenesis, is induced in lymphatic ECs.

#### 6.4. VEGF and hyaluronan signaling

As highlighted in the previous paragraphs, Vegf-signaling is an essential regulator of angiogenesis in zebrafish development. While primary arterial angiogenesis requires Vegfa, secondary sprouting from the PCV is controlled by Vegfc and both activate pErk1/2 signaling downstream (237, 260) (Fig.4D-F). The MAP kinase pathway is induced by Vegfa, after which plc- $\gamma$  mediates arterial specific Erk phosphorylation (250) (Fig.2C). This phosphorylation is inhibited by PI3K/AKT signaling, another effector of Vegf signaling (264) (Fig.2C). *In vitro*, ERK1/2 co-immunoprecipitates with the hyaluronan (HA) receptors (HARE, Stablin 2 [Stab2]) for endocytosis. Upon binding of HA to Stab2, the receptor becomes Tyr-phosphorylated, inducing Erk phosphorylation (265).

Stabilins are characterized as scavenger receptors removing waste products from the blood. As such, Stab2 also mediates endocytosis of acetylated-LDL, chondroitin sulfate, heparin, dextrane sulfate (266) and other anionic particles (267). *stab2* is specifically expressed by ECs of the developing vasculature in zebrafish (Fig. 5). During angiogenesis, *stab2* expression is first increased in the arterial endothelium where it progressively becomes downregulated after 24hpf, becoming more restricted to the

venous endothelium (268). Morpholino-mediated knockdown of *Stab2* in zebrafish embryos results in disturbed arterial-venous specification (268) and lymphangiogenesis (269). *stab2* morphants have reduced pErk in arterial ECs. Furthermore, Vegf seems to provide a negative feedback system by inhibiting *stab2* expression (268), while *Hoxc9* positively regulates *stab2* expression in lymphatic ECs (269) (Fig.5).

HA is a glycosaminoglycan that can form long, linear polymers out of repeating disaccharide units, GlcNAc and GlcUA (reviewed in (270)) (Fig.5). These polymers can reach a molecular weight of 1000-6000kDa and have a high affinity for water (1000 times its weight). This property allows HA to act as pericellular buffer and integral component of the ECM. HA polymers are produced by Has enzymes (Has1-3), Has2 being the main producer during development (271, 272) (Fig.5). Specific hyaluronidases, such as Tmem2, control the depolymerization into smaller forms of low-molecular weight (10-250kDa) and o-HA (HA oligomers, <10kDa) (Fig.5) (273). Interestingly, the turnover rate of HA is high, i.e., about 30% of HA is replaced daily *in vivo* (274). HA function strongly depends on its length. While molecules with high molecular weight inhibit EC proliferation, are anti-inflammatory (275) and anti-angiogenic (276), shorter HA forms stimulate immune responses (277) and act as pro-angiogenic factors (278). Shorter forms can directly bind to cell-surface receptors, such as CD44, RHAMM and TLR-4 (279), thereby inducing EC proliferation, migration and sprouting angiogenesis. These processes are stimulated by Vegf that is released in response to o-HA binding to CD44 (280, 281) (Fig.5). Furthermore, HA glycosaminoglycans have been reported to act as traps for cytokines, such as VEGF (282) (Fig.5).

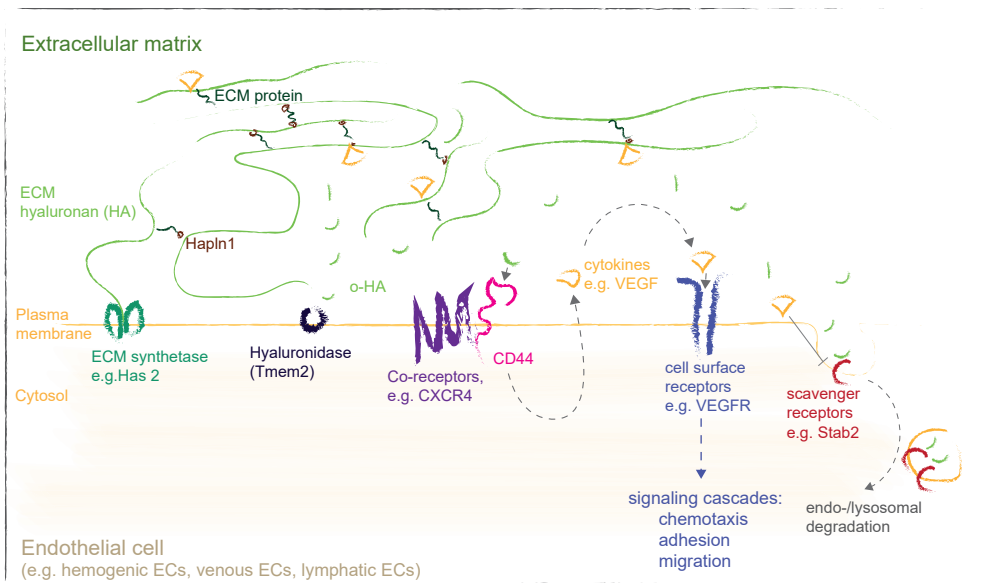


**Figure 5: Interplay of VEGF-VEGFR and hyaluronan signaling in endothelial cells.** Hyaluronan (HA) is synthesized by HA synthases (Has2) into the extra-cellular space. Together with other proteins, HA forms there a network, the extracellular matrix (ECM). Hapln1 is one of the proteins involved in binding cytokines to the HA-network. Hyaluronidases (Tmem2) depolymerizes HA into smaller forms (o-HA). These smaller forms can bind to CD44, a co-receptor of for instance CXCR4, and thereby induce the release of VEGFa. VEGFa is sequestered by the ECM. Upon binding of VEGFa to VEGFR2, downstream signaling cascades important for chemotaxis, cell adhesion and migration, are induced. HA is removed from the extracellular space by scavenger receptors (e.g., Stab2) and then degraded in the endo-/lysosomal pathway. VEGF has a negative regulatory effect on Stab2 expression.



## References

1. E. Neumann, in *Centralblatt für die Med. Wissenschaft.* (1868), vol. Band 44, chap. 689.
2. A. Maximow, in *Arch. Mikroskop. Anat.* (1909), pp. 444-561.
3. J. E. Till, E. A. McCulloch, A direct measurement of the radiation sensitivity of normal mouse bone marrow cells. *Radiat Res* 14, 213-222 (1961).
4. L. Siminovitch, E. A. McCulloch J. E. Till, The distribution of colony-forming cells among spleen colonies. *J Cell Comp Physiol* 62, 327-336 (1963).
5. A. J. BECKER, E. A. McCULLOCH, J. E. TILL, Cytological demonstration of the clonal nature of spleen colonies derived from transplanted mouse marrow cells. *Nature* 197, 452-454 (1963).
6. M. R. Harrison et al., In-utero transplantation of fetal liver haemopoietic stem cells in monkeys. *Lancet* 2, 1425-1427 (1989).
7. D. Sun et al., Epigenomic Profiling of Young and Aged HSCs Reveals Concerted Changes during Aging that Reinforce Self-Renewal. *Cell Stem Cell* 14, 673-688 (2014).
8. B. A. Ulloa et al., Definitive hematopoietic stem cells minimally contribute to embryonic hematopoiesis. *Cell Rep* 36, 109703 (2021).
9. J. L. Haar, G. A. Ackerman, A phase and electron microscopic study of vasculogenesis and erythropoiesis in the yolk sac of the mouse. *Anat Rec* 170, 199-223 (1971).
10. J. J. Owen, M. A. Moore, G. A. Harrison, Chromosome marker studies in the graft-versus-host reaction in the chick embryo. *Nature* 207, 313-315 (1965).
11. T. Jaffredo, L. Yvernogeu, How the avian model has pioneered the field of hematopoietic development. *Exp Hematol* 42, 661-668 (2014).
12. T. Fraser, J. Isern, M. H. Baron, Maturation and enucleation of primitive erythroblasts during mouse embryogenesis is accompanied by changes in cell-surface antigen expression. *Blood* 109, 343-352 (2007).
13. P. D. Kingsley, J. Malik, K. A. Fantauzzo, J. Palis, Yolk sac-derived primitive erythroblasts enucleate during mammalian embryogenesis. *Blood* 104, 19-25 (2004).
14. P. M. Wong, S. W. Chung, S. M. Reicheld, D. H. Chui, Hemoglobin switching during murine embryonic development: evidence for two populations of embryonic erythropoietic progenitor cells. *Blood* 67, 716-721 (1986).
15. M. A. Moore, D. Metcalf, Ontogeny of the haemopoietic system: yolk sac origin of *in vivo* and *in vitro* colony forming cells in the developing mouse embryo. *Br J Haematol* 18, 279-296 (1970).
16. J. Xu M et al., Evidence for the presence of murine primitive megakaryocytopoiesis in the early yolk sac. *Blood* 97, 2016-2022 (2001).
17. C. C. Bertozzi et al., Platelets regulate lymphatic vascular development through CLEC-2-SLP-76 signaling. *Blood* 116, 661-670 (2010).
18. F. Ginhoux et al., Fate mapping analysis reveals that adult microglia derive from primitive macrophages. *Science* 330, 841-845 (2010).
19. M. A. Cuadros, P. Coltey, M. Carmen Nieto, C. Martin, Demonstration of a phagocytic cell system belonging to the hemopoietic lineage and originating from the yolk sac in the early avian embryo. *Development* 115, 157-168 (1992).
20. K. E. McGrath et al., A transient definitive erythroid lineage with unique regulation of the  $\beta$ -globin locus in the mammalian embryo. *Blood* 117, 4600-4608 (2011).
21. J. Palis, S. Robertson, M. Kennedy, C. Wall, G. Keller, Development of erythroid and myeloid progenitors in the yolk sac and embryo proper of the mouse. *Development* 126, 5073-5084 (1999).
22. J. Y. Bertrand et al., Three pathways to mature macrophages in the early mouse yolk sac. *Blood* 106, 3004-3011 (2005).
23. J. Palis, Hematopoietic stem cell-independent hematopoiesis: emergence of erythroid, megakaryocyte, and myeloid potential in the mammalian embryo. *FEBS Lett* 590, 3965-3974 (2016).
24. H. W. Detrich et al., Intraembryonic hematopoietic cell migration during vertebrate development. *Proc Natl Acad Sci U S A* 92, 10713-10717 (1995).
25. J. Y. Bertrand et al., Definitive hematopoiesis initiates through a committed erythromyeloid progenitor in the zebrafish embryo. *Development* 134, 4147-4156 (2007).
26. C. Corbel, P. Vaigot, J. Salaün, (alpha)IIb Integrin, a novel marker for hemopoietic progenitor cells. *Int J Dev Biol* 49, 279-284 (2005).
27. H. K. a. Mikkola, C. Gekas, S. H. Orkin, F. Dieterlen-Lievre, Placenta as a site for hematopoietic stem cell development. *Experimental hematology* 33, 1048-1054 (2005).
28. N. Azevedo Portilho, M. Pelajo-Machado, Mechanism of hematopoiesis and vasculogenesis in mouse placenta. *Placenta* 69, 140-145 (2018).
29. N. Le Douarin, in *Bull Biol Fr Belg.* (1969), vol. 103, pp. 435-452.
30. F. Dieterlen-Lievre, On the origin of haemopoietic stem cells in the avian embryo: an experimental approach. *Journal of embryology and experimental morphology* 33, 607-619 (1975).
31. A. Ciau-Uitz, M. Walmsley, R. Patient, Distinct origins of adult and embryonic blood in *Xenopus*. *Cell* 102, 787-796 (2000).
32. J. B. Turpen, C. M. Knudson, P. S. Hoefen, The early ontogeny of hematopoietic cells stud-

- ied by grafting cytogenetically labeled tissue anlagen: localization of a prospective stem cell compartment. *Developmental biology* 85, 99-112 (1981).
33. a. Cumano, F. Dieterlen-Lievre, I. Godin, Lymphoid potential, probed before circulation in mouse, is restricted to caudal intraembryonic splanchnopleura. *Cell* 86, 907-916 (1996).
  34. M. F. de Bruijn, N. a. Speck, M. C. Peeters, E. Dzierzak, Definitive hematopoietic stem cells first develop within the major arterial regions of the mouse embryo. *The EMBO journal* 19, 2465-2474 (2000).
  35. Z. Li et al., Mouse embryonic head as a site for hematopoietic stem cell development. *Cell Stem Cell* 11, 663-675 (2012).
  36. a. Medvinsky, E. Dzierzak, Definitive hematopoiesis is autonomously initiated by the AGM region. *Cell* 86, 897-906 (1996).
  37. A. M. Müller, A. Medvinsky, J. Strouboulis, F. Grosveld, E. Dzierzak, Development of hematopoietic stem cell activity in the mouse embryo. *Immunity* 1, 291-301 (1994).
  38. C. Gekas, F. Dieterlen-lièvre, S. H. Orkin, H. K. A. Mikkola, N.-s. Marne, Hematopoietic Stem Cells. 8, 365-375 (2005).
  39. P. Kumaravelu et al., Quantitative developmental anatomy of definitive haematopoietic stem cells/long-term repopulating units (HSC/RUs): role of the aorta-gonad-mesonephros (AGM) region and the yolk sac in colonisation of the mouse embryonic liver. *Development* 129, 4891-4899 (2002).
  40. K. Ottersbach, E. Dzierzak, The murine placenta contains hematopoietic stem cells within the vascular labyrinth region. *Developmental cell* 8, 377-387 (2005).
  41. J. L. Christensen, D. E. Wright, A. J. Wagers, I. L. Weissman, Circulation and chemotaxis of fetal hematopoietic stem cells. *PLoS Biol* 2, E75 (2004).
  42. T. Yokomizo, E. Dzierzak, Three-dimensional cartography of hematopoietic clusters in the vasculature of whole mouse embryos. *Development* 3661, 3651-3661 (2010).
  43. K. E. Rhodes et al., The emergence of hematopoietic stem cells is initiated in the placental vasculature in the absence of circulation. *Cell Stem Cell* 2, 252-263 (2008).
  44. N. Azevedo Portilho, P. Tavares Guedes, B. A. Croy, M. Pelajo-Machado, Localization of transient immature hematopoietic cells to two distinct, potential niches in the developing mouse placenta. *Placenta* 47, 1-11 (2016).
  45. J.-C. Boisset et al., *In vivo* imaging of haematopoietic cells emerging from the mouse aortic endothelium. *Nature* 464, 116-120 (2010).
  46. J. A. Garcia-Porrero et al., Antigenic profiles of endothelial and hemopoietic lineages in murine intraembryonic hemogenic sites. *Developmental & Comparative Immunology* 22, 303-319 (1998).
  47. S. Taoudi et al., Extensive hematopoietic stem cell generation in the AGM region via maturation of VE-cadherin+CD45+ pre-definitive HSCs. *Cell stem cell* 3, 99-108 (2008).
  48. T. North et al., Cbfa2 is required for the formation of intra-aortic hematopoietic clusters. *Development (Cambridge, England)* 126, 2563-2575 (1999).
  49. T. Okuda, J. van Deursen, S. W. Hiebert, G. Grosveld, J. R. Downing, AML1, the target of multiple chromosomal translocations in human leukemia, is essential for normal fetal liver hematopoiesis. *Cell* 84, 321-330 (1996).
  50. Q. Wang et al., Disruption of the Cbfa2 Gene Causes Necrosis and Hemorrhaging in the Central Nervous System and Blocks Definitive Hematopoiesis. 93, 3444-3449 (1996).
  51. W. Dantschakoff, Untersuchungen über die Entwicklung von Blut und Bindegewebe bei Vögeln. *Archiv für mikroskopische Anatomie* 73, 117-181 (1908).
  52. G. Brachtendorf et al., Early expression of endomucin on endothelium of the mouse embryo and on putative hematopoietic clusters in the dorsal aorta. *Developmental dynamics: an official publication of the American Association of Anatomists* 222, 410-419 (2001).
  53. T. Jaffredo, R. Gautier, a. Eichmann, F. Dieterlen-Lièvre, Intraortic hemopoietic cells are derived from endothelial cells during ontogeny. *Development (Cambridge, England)* 125, 4575-4583 (1998).
  54. L. Pardanaud et al., Two distinct endothelial lineages in ontogeny, one of them related to hemopoiesis. *Development* 122, 1363-1371 (1996).
  55. C. Pouget, R. Gautier, M.-A. Teillet, T. Jaffredo, Somite-derived cells replace ventral aortic hemangioblasts and provide aortic smooth muscle cells of the trunk. *Development (Cambridge, England)* 133, 1013-1022 (2006).
  56. F. Dieterlen-Lièvre, C. Martin, Diffuse intraembryonic hemopoiesis in normal and chimeric avian development. *Dev Biol* 88, 180-191 (1981).
  57. T. Jaffredo, R. Gautier, V. Brajeul, F. Dieterlen-Lièvre, Tracing the progeny of the aortic hemangioblast in the avian embryo. *Developmental biology* 224, 204-214 (2000).
  58. P. T. Guedes et al., Histological analyses demonstrate the temporary contribution of yolk sac, liver, and bone marrow to hematopoiesis during chicken development. *PLoS One* 9, e90975 (2014).
  59. J. W. Kingsbury, M. Alexanderson, E. S. Kornstein, The development of the liver in the chick. *Anat Rec* 124, 165-187 (1956).
  60. D. Dunon, N. Allioli, O. Vainio, C. Ody, B. A. Imhof, Renewal of thymocyte progenitors and emigration of thymocytes during avian development. *Dev Comp Immunol* 22, 279-287 (1998).
  61. D. Dunon, N. Allioli, O. Vainio, C. Ody, B. A. Imhof, Quantification of T-cell progenitors during ontogeny: thymus colonization depends on blood delivery of progenitors. *Blood*

- 93, 2234-2243 (1999).
62. O. Lassila, J. Eskola, P. Toivanen, F. Dieterlen-Lièvre, Lymphoid stem cells in the intraembryonic mesenchyme of the chicken. *Scand J Immunol* 11, 445-448 (1980).
  63. H. M. Eilken, S.-I. Nishikawa, T. Schroeder, Continuous single-cell imaging of blood generation from haemogenic endothelium. *Nature* 457, 896-900 (2009).
  64. C. Lancrin et al., The haemangioblast generates haematopoietic cells through a haemogenic endothelium stage. *Nature* 457, 892-895 (2009).
  65. E. Oberlin, B. El Hafny, L. Petit-Cocault, M. Souyri, Definitive human and mouse hematopoiesis originates from the embryonic endothelium: a new class of HSCs based on VE-cadherin expression. *The International journal of developmental biology* 54, 1165-1173 (2010).
  66. A. C. Zovein et al., Article Fate Tracing Reveals the Endothelial Origin of Hematopoietic Stem Cells. *Stem Cell* 3, 625-636 (2008).
  67. M. J. Chen, T. Yokomizo, B. M. Zeigler, E. Dzierzak, N. a. Speck, Runx1 is required for the endothelial to haematopoietic cell transition but not thereafter. *Nature* 457, 887-891 (2009).
  68. R. Thambyrajah et al., GFI1 proteins orchestrate the emergence of haematopoietic stem cells through recruitment of LSD1. *Nat Cell Biol* 18, 21-32 (2016).
  69. J. Y. Bertrand et al., Haematopoietic stem cells derive directly from aortic endothelium during development. *Nature* 464, 108-111 (2010).
  70. K. Kissa, P. Herbomel, Blood stem cells emerge from aortic endothelium by a novel type of cell transition. *Nature* 464, 112-115 (2010).
  71. E. Y. N. Lam, C. J. Hall, P. S. Crosier, K. E. Crosier, M. V. Flores, Live imaging of Runx1 expression in the dorsal aorta tracks the emergence of blood progenitors from endothelial cells. *Blood* 116, 909-914 (2010).
  72. K. Kissa et al., Live imaging of emerging hematopoietic stem cells and early thymus colonization. *Blood* 111, 1147-1156 (2008).
  73. D. Ma, J. Zhang, H.-f. Lin, J. Italiano, R. I. Handin, The identification and characterization of zebrafish hematopoietic stem cells. *Blood* 118, 289-297 (2011).
  74. J. Henninger et al., Clonal fate mapping quantifies the number of haematopoietic stem cells that arise during development. *Nature Cell Biology* 19, 17-27 (2017).
  75. A. D. Yzaguirre, N. A. Speck, Extravascular endothelial and hematopoietic islands form through multiple pathways in midgestation mouse embryos. *Developmental Biology* 415, 111-121 (2016).
  76. C. Robin et al., An unexpected role for IL-3 in the embryonic development of hematopoietic stem cells. *Dev Cell* 11, 171-180 (2006).
  77. J. C. Boisset et al., Progressive maturation toward hematopoietic stem cells in the mouse embryo aorta. *Blood* 125, 465-469 (2015).
  78. S. Rybtsov et al., Hierarchical organization and early hematopoietic specification of the developing HSC lineage in the AGM region. *The Journal of experimental medicine* 208, 1305-1315 (2011).
  79. S. Rybtsov et al., Tracing the origin of the HSC hierarchy reveals an SCF-dependent, IL-3-independent CD43(-) embryonic precursor. *Stem cell reports* 3, 489-501 (2014).
  80. M. C. Yoder, K. Hiatt, Engraftment of embryonic hematopoietic cells in conditioned newborn recipients. *Blood* 89, 2176-2183 (1997).
  81. a. Cumano, J. C. Ferraz, M. Klaine, J. P. Di Santo, I. Godin, Intraembryonic, but not yolk sac hematopoietic precursors, isolated before circulation, provide long-term multilineage reconstitution. *Immunity* 15, 477-485 (2001).
  82. F. Zhou et al., Tracing haematopoietic stem cell formation at single-cell resolution. *Nature* 533, 487-492 (2016).
  83. X. Ma et al., Expression of the Ly-6A (Sca-1) lacZ transgene in mouse haematopoietic stem cells and embryos. *Br J Haematol* 116, 401-408 (2002).
  84. T. Bee et al., The mouse Runx1 +23 hematopoietic stem cell enhancer confers hematopoietic specificity to both Runx1 promoters. *Blood* 113, 5121-5124 (2009).
  85. J. C. Boisset, T. Clapes, R. Van Der Linden, E. Dzierzak, C. Robin, Integrin  $\alpha$ IIb (CD41) plays a role in the maintenance of hematopoietic stem cell activity in the mouse embryonic aorta. *Biol Open* 2, 525-532 (2013).
  86. C. Corbel, J. Salaün,  $\alpha$ IIb integrin expression during development of the murine hematopoietic system. *Dev Biol* 243, 301-311 (2002).
  87. M. J. Ferkowicz, CD41 expression defines the onset of primitive and definitive hematopoiesis in the murine embryo. *Development* 130, 4393-4403 (2003).
  88. H. K. Mikkola, Y. Fujiwara, T. M. Schlaeger, D. Traver, S. H. Orkin, Expression of CD41 marks the initiation of definitive hematopoiesis in the mouse embryo. *Blood* 101, 508-516 (2003).
  89. M. T. Mitjavila-Garcia et al., Expression of CD41 on hematopoietic progenitors derived from embryonic hematopoietic cells. *Development* 129, 2003-2013 (2002).
  90. A. Matsubara et al., Endomucin, a CD34-like sialomucin, marks hematopoietic stem cells throughout development. *J Exp Med* 202, 1483-1492 (2005).
  91. M. F. T. R. D. Bruijn et al., to the Endothelial Cell Layer in the Midgestation Mouse Aorta. *Blood* 100, 673-683 (2002).
  92. G. J. Spangrude, S. Heimfeld, I. L. Weissman, Purification and characterization of mouse

- hematopoietic stem cells. *Science* 241, 58-62 (1988).
93. S. T. Fraser, M. Ogawa, R. T. Yu, S. Nishikawa, M. C. Yoder, Definitive hematopoietic commitment within the embryonic vascular endothelial-cadherin(+) population. *Exp Hematol* 30, 1070-1078 (2002).
  94. I. Kim, O. H. Yilmaz, S. J. Morrison, CD144 (VE-cadherin) is transiently expressed by fetal liver hematopoietic stem cells. *Blood* 106, 903-905 (2005).
  95. S. Taoudi et al., Progressive divergence of definitive haematopoietic stem cells from the endothelial compartment does not depend on contact with the foetal liver. *Development* 132, 4179-4191 (2005).
  96. C. I. Baumann et al., PECAM-1 is expressed on hematopoietic stem cells throughout ontogeny and identifies a population of erythroid progenitors. *Blood* 104, 1010-1016 (2004).
  97. S. Rybtsov, A. Ivanovs, S. Zhao, A. Medvinsky, Concealed expansion of immature precursors underpins acute burst of adult HSC activity in foetal liver. *Development (Cambridge)* 143, 1284-1289 (2016).
  98. H. Ema, H. Nakauchi, Expansion of hematopoietic stem cells in the developing liver of a mouse embryo. *Blood* 95, 2284-2288 (2000).
  99. S. J. Morrison, H. D. Hemmati, a. M. Wandycz, I. L. Weissman, The purification and characterization of fetal liver hematopoietic stem cells. *Proceedings of the National Academy of Sciences of the United States of America* 92, 10302-10306 (1995).
  100. J. Lessard, A. Faubert, G. Sauvageau, Genetic programs regulating HSC specification, maintenance and expansion. *Oncogene* 23, 7199-7209 (2004).
  101. O. V. Payushina, Hematopoietic Microenvironment in the Fetal Liver: Roles of Different Cell Populations. *ISRN Cell Biology* 2012, 1-7 (2012).
  102. S. Chou, H. F. Lodish, Fetal liver hepatic progenitors are supportive stromal cells for hematopoietic stem cells. *Proceedings of the National Academy of Sciences of the United States of America* 107, 7799-7804 (2010).
  103. T. Ara et al., Long-term hematopoietic stem cells require stromal cell-derived factor-1 for colonizing bone marrow during ontogeny. *Immunity* 19, 257-267 (2003).
  104. T. Sugiyama, H. Kohara, M. Noda, T. Nagasawa, Maintenance of the hematopoietic stem cell pool by CXCL12-CXCR4 chemokine signaling in bone marrow stromal cell niches. *Immunity* 25, 977-988 (2006).
  105. A. Greenbaum et al., CXCL12 in early mesenchymal progenitors is required for haematopoietic stem-cell maintenance. *Nature* 495, 227-230 (2013).
  106. E. Hirsch, A. Iglesias, A. J. Potocnik, U. Hartmann, R. Fässler, Impaired migration but not differentiation of haematopoietic stem cells in the absence of beta1 integrins. *Nature* 380, 171-175 (1996).
  107. I. B. Mazo, S. Massberg, U. H. von Andrian, Hematopoietic stem and progenitor cell trafficking. *Trends Immunol* 32, 493-503 (2011).
  108. J. A. Nolte et al., The AFT024 stromal cell line supports long-term *ex vivo* maintenance of engrafting multipotent human hematopoietic progenitors. *Leukemia* 16, 352-361 (2002).
  109. P. Charbord et al., Comparative study of stromal cell lines derived from embryonic, fetal, and postnatal mouse blood-forming tissues. *Exp Hematol* 30, 1202-1210 (2002).
  110. P. Charbord et al., A systems biology approach for defining the molecular framework of the hematopoietic stem cell niche. *Cell Stem Cell* 15, 376-391 (2014).
  111. R. A. Oostendorp et al., Embryonal subregion-derived stromal cell lines from novel temperature-sensitive SV40 T antigen transgenic mice support hematopoiesis. *J Cell Sci* 115, 2099-2108 (2002).
  112. R. A. Oostendorp et al., Stromal cell lines from mouse aorta-gonads-mesonephros subregions are potent supporters of hematopoietic stem cell activity. *Blood* 99, 1183-1189 (2002).
  113. Owen J. Tamplin et al., Hematopoietic Stem Cell Arrival Triggers Dynamic Remodeling of the Perivascular Niche. *Cell* 160, 241-252 (2015).
  114. J. A. Khan et al., Fetal liver hematopoietic stem cell niches associate with portal vessels. *Science* 351, 176-180 (2016).
  115. K. S. Tan, K. Kulkeaw, Y. Nakanishi, D. Sugiyama, Expression of cytokine and extracellular matrix mRNAs in fetal hepatic stellate cells. *Genes Cells* 22, 836-844 (2017).
  116. D. Sugiyama, K. Kulkeaw, C. Mizuochi, TGF-beta-1 up-regulates extra-cellular matrix production in mouse hepatoblasts. *Mech Dev* 130, 195-206 (2013).
  117. D. Sugiyama, T. Sasaki, *Stem Cell Niche*. 1035, 57-65 (2013).
  118. S. Coşkun et al., Development of the fetal bone marrow niche and regulation of HSC quiescence and homing ability by emerging osteolineage cells. *Cell Rep* 9, 581-590 (2014).
  119. M. G. Poulos et al., Endothelial Jagged-1 is necessary for homeostatic and regenerative hematopoiesis. *Cell Rep* 4, 1022-1034 (2013).
  120. L. Ding, T. L. Saunders, G. Enikolopov, S. J. Morrison, Endothelial and perivascular cells maintain haematopoietic stem cells. *Nature* 481, 457-462 (2012).
  121. L. M. Calvi et al., Osteoblastic cells regulate the haematopoietic stem cell niche. *Nature* 425, 841-846 (2003).
  122. N. Asada et al., Differential cytokine contributions of perivascular haematopoietic stem cell niches. *Nat Cell Biol* 19, 214-223 (2017).
  123. S. Méndez-Ferrer et al., Mesenchymal and haematopoietic stem cells form a unique bone

- marrow niche. *Nature* 466, 829-834 (2010).
124. Y. Omatsu et al., The essential functions of adipo-osteogenic progenitors as the hematopoietic stem and progenitor cell niche. *Immunity* 33, 387-399 (2010).
  125. Y. Katayama et al., Signals from the sympathetic nervous system regulate hematopoietic stem cell egress from bone marrow. *Cell* 124, 407-421 (2006).
  126. I. Bruns et al., Megakaryocytes regulate hematopoietic stem cell quiescence through CXCL4 secretion. *Nat Med* 20, 1315-1320 (2014).
  127. A. Nakamura-Ishizu, K. Takubo, M. Fujioka, T. Suda, Megakaryocytes are essential for HSC quiescence through the production of thrombopoietin. *Biochem Biophys Res Commun* 454, 353-357 (2014).
  128. M. Zhao et al., Megakaryocytes maintain homeostatic quiescence and promote post-injury regeneration of hematopoietic stem cells. *Nat Med* 20, 1321-1326 (2014).
  129. A. Chow et al., Bone marrow CD169+ macrophages promote the retention of hematopoietic stem and progenitor cells in the mesenchymal stem cell niche. *J Exp Med* 208, 261-271 (2011).
  130. I. G. Winkler et al., Bone marrow macrophages maintain hematopoietic stem cell (HSC) niches and their depletion mobilizes HSCs. *Blood* 116, 4815-4828 (2010).
  131. M. Casanova-Acebes et al., Rhythmic modulation of the hematopoietic niche through neutrophil clearance. *Cell* 153, 1025-1035 (2013).
  132. C. S. Baron et al., Single-cell transcriptomics reveal the dynamic of haematopoietic stem cell production in the aorta. *Nature Communications* 9, (2018).
  133. S. Hou et al., Embryonic endothelial evolution towards first hematopoietic stem cells revealed by single-cell transcriptomic and functional analyses. *Cell Res* 30, 376-392 (2020).
  134. M. Z. Fadlullah et al., Murine AGM single-cell profiling identifies a continuum of hemogenic endothelium differentiation marked by ACE. *Blood*, (2021).
  135. Q. Zhu et al., Developmental trajectory of prehematopoietic stem cell formation from endothelium. *Blood* 136, 845-856 (2020).
  136. T. Dignun et al., Multipotent progenitors and hematopoietic stem cells arise independently from hemogenic endothelium in the mouse embryo. *Cell Rep* 36, 109675 (2021).
  137. M. Oatley et al., Single-cell transcriptomics identifies CD44 as a marker and regulator of endothelial to haematopoietic transition. *Nature Communications* 11, 1-18 (2020).
  138. R. Schofield, The relationship between the spleen colony-forming cell and the haemopoietic stem cell. *Blood cells* 4, 7-25 (1978).
  139. M. Tavian et al., Aorta-associated CD34+ hematopoietic cells in the early human embryo. *Blood* 87, 67-72 (1996).
  140. L. Yvernogeu, C. Robin, Restricted intra-embryonic origin of bona fide hematopoietic stem cells in the chicken. *Development* 144, 2352-2363 (2017).
  141. S. Taoudi, A. Medvinsky, Functional identification of the hematopoietic stem cell niche in the ventral domain of the embryonic dorsal aorta. *Proceedings of the National Academy of Sciences of the United States of America* 104, 9399-9403 (2007).
  142. M. Peeters et al., Ventral embryonic tissues and Hedgehog proteins induce early AGM hematopoietic stem cell development. *Development (Cambridge, England)* 136, 2613-2621 (2009).
  143. N. D. Lawson, A. M. Vogel, B. M. Weinstein, sonic hedgehog and vascular endothelial growth factor act upstream of the Notch pathway during arterial endothelial differentiation. *Dev Cell* 3, 127-136 (2002).
  144. R. N. Wilkinson et al., Hedgehog and Bmp polarize hematopoietic stem cell emergence in the zebrafish dorsal aorta. *Developmental cell* 16, 909-916 (2009).
  145. G. Q. Zhao, Consequences of knocking out BMP signaling in the mouse. *Genesis* 35, 43-56 (2003).
  146. S. Pearson, P. Sroczynska, G. Lacaud, V. Kouskoff, The stepwise specification of embryonic stem cells to hematopoietic fate is driven by sequential exposure to Bmp4, activin A, bFGF and VEGF. *Development* 135, 1525-1535 (2008).
  147. S. Gupta, H. Zhu, L. I. Zon, T. Evans, BMP signaling restricts hemato-vascular development from lateral mesoderm during somitogenesis. *Development* 133, 2177-2187 (2006).
  148. C. Durand et al., Embryonic stromal clones reveal developmental regulators of definitive hematopoietic stem cells. *Proceedings of the National Academy of Sciences of the United States of America* 104, 20838-20843 (2007).
  149. P. G. Kim et al., Flow-induced protein kinase A-CREB pathway acts via BMP signaling to promote HSC emergence. *Journal of Experimental Medicine* 212, 633-648 (2015).
  150. A. C. McGarvey et al., A molecular roadmap of the AGM region reveals BMPER as a novel regulator of HSC maturation. *J Exp Med* 214, 3731-3751 (2017).
  151. M. Crisan et al., BMP signalling differentially regulates distinct haematopoietic stem cell types. *Nature Communications* 6, 1-8 (2015).
  152. M. Crisan et al., BMP and Hedgehog Regulate Distinct AGM Hematopoietic Stem Cells *Ex vivo*. *Stem Cell Reports* 6, 383-395 (2016).
  153. A. Ciau-Uitz, P. Pinheiro, R. Gupta, T. Enver, R. Patient, Tel1/ETV6 specifies blood stem cells through the agency of VEGF signaling. *Dev Cell* 18, 569-578 (2010).
  154. C. E. Burns, D. Traver, E. Mayhall, J. L. Shepard, L. I. Zon, Hematopoietic stem cell fate is established by the Notch-Runx pathway. *Genes & development* 19, 2331-2342 (2005).



155. C. Ruiz-Herguido et al., Hematopoietic stem cell development requires transient Wnt/ $\beta$ -catenin activity. *J Exp Med* 209, 1457-1468 (2012).
156. B. Chanda, A. Ditadi, N. N. Iscove, G. Keller, Retinoic acid signaling is essential for embryonic hematopoietic stem cell development. *Cell* 155, 215-227 (2013).
157. S. R. Fitch et al., Signaling from the sympathetic nervous system regulates hematopoietic stem cell emergence during embryogenesis. *Cell Stem Cell* 11, 554-566 (2012).
158. T. E. North et al., Hematopoietic stem cell development is dependent on blood flow. *Cell* 137, 736-748 (2009).
159. L. Adamo et al., Biomechanical forces promote embryonic haematopoiesis. *Nature* 459, 1131-1135 (2009).
160. E. N. Geissler, M. A. Ryan, D. E. Housman, The dominant-white spotting (W) locus of the mouse encodes the c-kit proto-oncogene. *Cell* 55, 185-192 (1988).
161. E. Huang et al., The hematopoietic growth factor KL is encoded by the *c-kit* locus and is the ligand of the c-kit receptor, the gene product of the *W* locus. *Cell* 63, 225-233 (1990).
162. J. C. Tan, K. Nocka, P. Ray, P. Traktman, P. Besmer, The dominant W42 spotting phenotype results from a missense mutation in the c-kit receptor kinase. *Science* 247, 209-212 (1990).
163. Y. Sharma, C. M. Astle, D. E. Harrison, Heterozygous kit mutants with little or no apparent anemia exhibit large defects in overall hematopoietic stem cell function. *Exp Hematol* 35, 214-220 (2007).
164. L. A. Thorén et al., Kit regulates maintenance of quiescent hematopoietic stem cells. *J Immunol* 180, 2045-2053 (2008).
165. J. G. Flanagan, D. C. Chan, P. Leder, Transmembrane form of the kit ligand growth factor is determined by alternative splicing and is missing in the *Sld* mutant. *Cell* 64, 1025-1035 (1991).
166. J. Lennartsson, L. Rönnstrand, Stem cell factor receptor/c-Kit: from basic science to clinical implications. *Physiol Rev* 92, 1619-1649 (2012).
167. J. L. Gommerman, R. Rottapel, S. A. Berger, Phosphatidylinositol 3-kinase and Ca<sup>2+</sup> influx dependence for ligand-stimulated internalization of the c-Kit receptor. *J Biol Chem* 272, 30519-30525 (1997).
168. V. C. Broudy et al., Signaling via Src family kinases is required for normal internalization of the receptor c-Kit. *Blood, The Journal of the American Society of Hematology* 94, 1979-1986 (1999).
169. H. Celik et al., Enforced differentiation of *Dnmt3a*-null bone marrow leads to failure with c-Kit mutations driving leukemic transformation. *Blood, The Journal of the American Society of Hematology* 125, 619-628 (2015).
170. S. Zeng, Z. Xu, S. Lipkowitz, J. B. Longley, Regulation of stem cell factor receptor signaling by *Cbl* family proteins (*Cbl-b/c-Cbl*). *Blood* 105, 226-232 (2005).
171. D. D'Allard et al., Tyrosine kinase inhibitors induce down-regulation of c-Kit by targeting the ATP pocket. *PLoS One* 8, e60961 (2013).
172. Z. Orinska et al., *I787* provides signals for c-Kit receptor internalization and functionality that control mast cell survival and development. *Blood* 116, 2665-2675 (2010).
173. T. Jahn et al., Analysing c-kit internalization using a functional c-kit-EGFP chimera containing the fluorochrome within the extracellular domain. *Oncogene* 21, 4508-4520 (2002).
174. Y. Shimizu, L. K. Ashman, Z. Du, L. B. Schwartz, Internalization of Kit together with stem cell factor on human fetal liver-derived mast cells: new protein and RNA synthesis are required for reappearance of Kit. *J Immunol* 156, 3443-3449 (1996).
175. L. K. Goh, A. Sorkin, Endocytosis of receptor tyrosine kinases. *Cold Spring Harbor perspectives in biology* 5, a017459 (2013).
176. M.-J. Sánchez, A. Holmes, C. Miles, E. Dzierzak, Characterization of the first definitive hematopoietic stem cells in the AGM and liver of the mouse embryo. *Immunity* 5, 513-525 (1996).
177. C. S. Vink et al., Iterative Single-Cell Analyses Define the Transcriptome of the First Functional Hematopoietic Stem Cells. *Cell Rep* 31, 107627 (2020).
178. E. Keshet et al., Embryonic RNA expression patterns of the c-kit receptor and its cognate ligand suggest multiple functional roles in mouse development. *The EMBO Journal* 10, 2425-2435 (1991).
179. Y. Matsui, K. M. Zsebo, B. L. M. Hogan, Embryonic expression of a haematopoietic growth factor encoded by the *SI* locus and the ligand for c-kit. *Nature* 347, 667-669 (1990).
180. C. Souilhoh et al., Inductive interactions mediated by interplay of asymmetric signalling underlie development of adult haematopoietic stem cells. *Nature Communications* 7, 1-13 (2016).
181. M. Ogawa et al., Expression and function of c-Kit in fetal hemopoietic progenitor cells: transition from the early c-Kit-independent to the late c-Kit-dependent wave of hemopoiesis in the murine embryo. *Development* 117, 1089-1098 (1993).
182. F. Bernex et al., Spatial and temporal patterns of c-kit-expressing cells in *WlacZ/+* and *WlacZ/WlacZ* mouse embryos. *Development* 122, 3023-3033 (1996).
183. A. Batsivari et al., Understanding Hematopoietic Stem Cell Development through Functional Correlation of Their Proliferative Status with the Intra-aortic Cluster Architecture. *Stem Cell Reports* 8, 1549-1562 (2017).

184. K. E. McGrath et al., Distinct Sources of Hematopoietic Progenitors Emerge before HSCs and Provide Functional Blood Cells in the Mammalian Embryo. *Cell Reports* 11, 1892-1904 (2015).
185. E. Azzoni et al., Kit ligand has a critical role in mouse yolk sac and aorta-gonad-mesonephros hematopoiesis. *EMBO Rep* 19, (2018).
186. A. Fantin et al., KIT Is Required for Fetal Liver Hematopoiesis. *Frontiers in Cell and Developmental Biology* 9, 1908 (2021).
187. C. B. Mahony, C. Pasche, J. Y. Bertrand, Oncostatin M and Kit-Ligand Control Hematopoietic Stem Cell Fate during Zebrafish Embryogenesis. *Stem Cell Reports* 10, 1920-1934 (2018).
188. C. B. Mahony et al., Hapln1b, a central organizer of the extracellular matrix, modulates kit signalling to control developmental haematopoiesis. *Blood Adv*, (2021).
189. K. Ikuta, I. L. Weissman, Evidence that hematopoietic stem cells express mouse c-kit but do not depend on steel factor for their generation. *Proceedings of the National Academy of Sciences* 89, 1502 (1992).
190. J. E. Barker, Sl/Slid hematopoietic progenitors are deficient in situ. *Exp Hematol* 22, 174-177 (1994).
191. N. S. Wolf, Dissecting the Hematopoietic Microenvironment. *Cell Proliferation* 11, 325-334 (1978).
192. J. Y. Shin, W. Hu, M. Naramura, C. Y. Park, High c-Kit expression identifies hematopoietic stem cells with impaired self-renewal and megakaryocytic bias. *Journal of Experimental Medicine* 211, 217-231 (2014).
193. M. Ogawa et al., Expression and function of c-kit in hemopoietic progenitor cells. *The Journal of experimental medicine* 174, 63-71 (1991).
194. V. C. Broudy, Stem cell factor and hematopoiesis. *Blood, The Journal of the American Society of Hematology* 90, 1345-1364 (1997).
195. E. Nogales, Structural Insights into Microtubule Function. *Annual Review of Biochemistry* 69, 277-302 (2000).
196. A. D. Sanchez, J. L. Feldman, Microtubule-organizing centers: from the centrosome to non-centrosomal sites. *Current opinion in cell biology* 44, 93-101 (2017).
197. A. Dimitrov et al., Detection of GTP-tubulin conformation *in vivo* reveals a role for GTP remnants in microtubule rescues. *Science* 322, 1353-1356 (2008).
198. L. Fourriere, A. J. Jimenez, F. Perez, G. Boncompain, The role of microtubules in secretory protein transport. *J Cell Sci* 133, (2020).
199. A. Akhmanova, M. O. Steinmetz, Tracking the ends: A dynamic protein network controls the fate of microtubule tips. *Nature Reviews Molecular Cell Biology* 9, 309-322 (2008).
200. A. Akhmanova, M. O. Steinmetz, Microtubule +TIPs at a glance. *Journal of Cell Science* 123, 3415-3419 (2010).
201. N. Galjart, Plus-end-tracking proteins and their interactions at microtubule ends. *Current Biology* 20, R528-R537 (2010).
202. F. Perez, G. S. Diamantopoulos, R. Stalder, T. E. Kreis, CLIP-170 Highlights Growing Microtubule Ends *In vivo*. *Cell* 96, 517-527 (1999).
203. A. Akhmanova et al., CLASPs Are CLIP-115 and -170 Associating Proteins Involved in the Regional Regulation of Microtubule Dynamics in Motile Fibroblasts. 104, 923-935 (2001).
204. Y. H. Inoue et al., Mutations in orbit/mast reveal that the central spindle is comprised of two microtubule populations, those that initiate cleavage and those that propagate furrow ingression. *J Cell Biol* 166, 49-60 (2004).
205. C. L. Lemos et al., Mast, a conserved microtubule-associated protein required for bipolar mitotic spindle organization. *Embo j* 19, 3668-3682 (2000).
206. D. Pasqualone, T. C. Huffaker, STU1, a suppressor of a beta-tubulin mutation, encodes a novel and essential component of the yeast mitotic spindle. *J Cell Biol* 127, 1973-1984 (1994).
207. E. B. Espiritu, L. E. Krueger, A. Ye, L. S. Rose, CLASPs function redundantly to regulate astral microtubules in the *C. elegans* embryo. *Developmental Biology* 368, 242-254 (2012).
208. J. C. Ambrose, T. Shoji, A. M. Kotzer, J. A. Pighin, G. O. Wasteneys, The Arabidopsis CLASP Gene Encodes a Microtubule-Associated Protein Involved in Cell Expansion and Division. *The Plant Cell* 19, 2763-2775 (2007).
209. J. Al-Bassam, N. A. Larsen, A. A. Hyman, S. C. Harrison, Crystal Structure of a TOG Domain: Conserved Features of XMAP215/Dis1-Family TOG Domains and Implications for Tubulin Binding. *Structure* 15, 355-362 (2007).
210. K. C. Slep, The role of TOG domains in microtubule plus end dynamics. *Biochem Soc Trans* 37, 1002-1006 (2009).
211. Y. Mimori-Kiyosue et al., CLASP1 and CLASP2 bind to EB1 and regulate microtubule plus-end dynamics at the cell cortex. *The Journal of cell biology* 168, 141-153 (2005).
212. A. Efimov et al., Asymmetric CLASP-dependent nucleation of noncentrosomal microtubules at the *trans*-Golgi network. *Developmental cell* 12, 917-930 (2007).
213. G. Lansbergen et al., CLASPs attach microtubule plus ends to the cell cortex through a complex with LL5beta. *Developmental cell* 11, 21-32 (2006).
214. S. Maffini et al., Motor-Independent Targeting of CLASPs to Kinetochores by CENP-E Promotes Microtubule Turnover and Poleward Flux. *Current Biology* 19, 1566-1572 (2009).

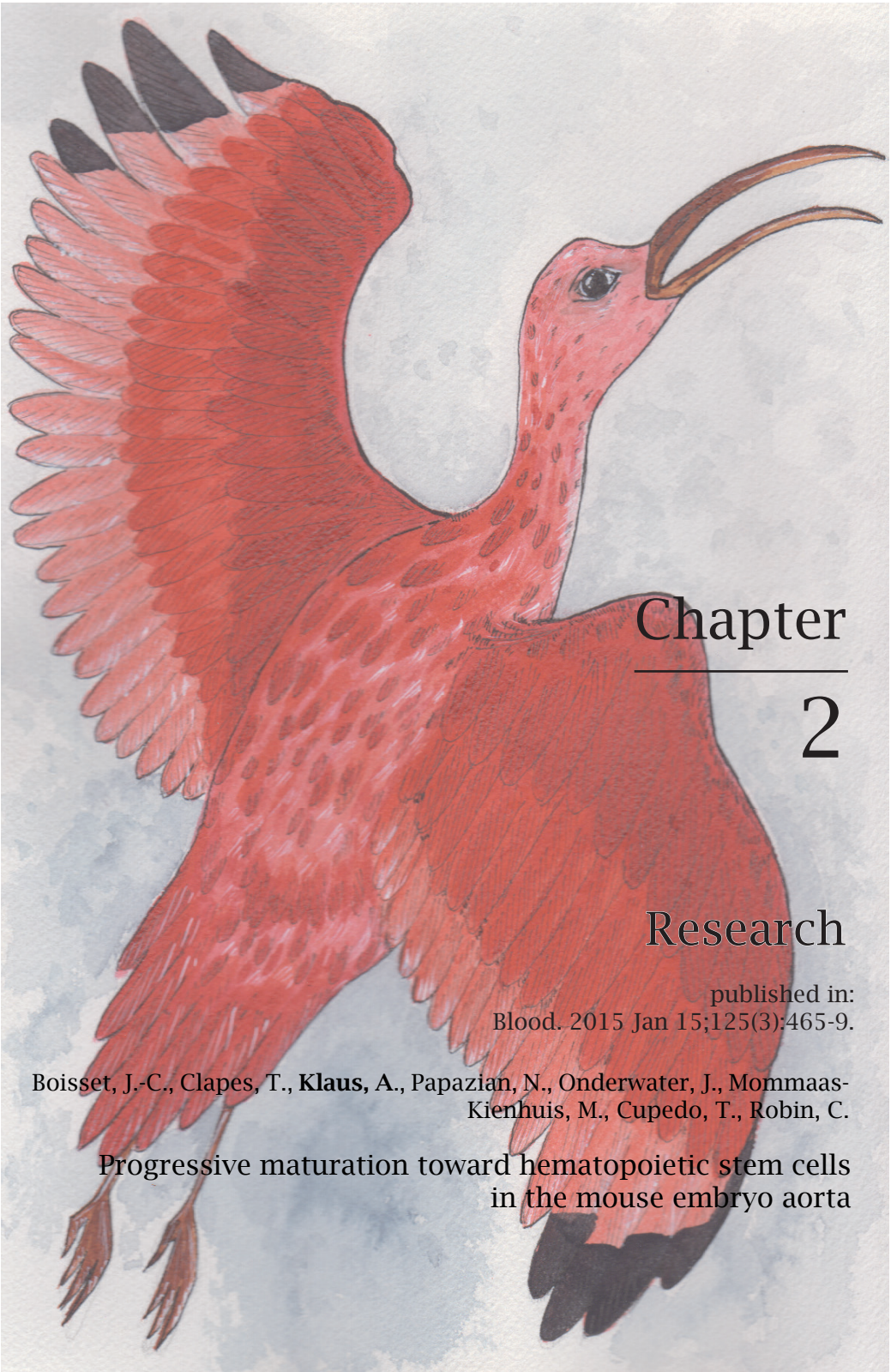


215. K. Drabek et al., Role of CLASP2 in microtubule stabilization and the regulation of persistent motility. *Current biology : CB* 16, 2259-2264 (2006).
216. T. Wittmann, C. M. Waterman-Storer, Spatial regulation of CLASP affinity for microtubules by Rac1 and GSK3 $\beta$  in migrating epithelial cells. *Journal of Cell Biology* 169, 929-939 (2005).
217. S. J. Stehbens et al., CLASPs link focal-adhesion-associated microtubule capture to localized exocytosis and adhesion site turnover. *Nature cell biology* 16, 561-573 (2014).
218. S. Basu et al., CLASP2-dependent microtubule capture at the neuromuscular junction membrane requires LL5 $\beta$  and actin for focal delivery of acetylcholine receptor vesicles. *Molecular Biology of the Cell* 26, 938-951 (2015).
219. M. Wieczorek, S. Bechstedt, S. Chaaban, G. J. Brouhard, Microtubule-associated proteins control the kinetics of microtubule nucleation. *Nat Cell Biol* 17, 907-916 (2015).
220. D. J. Stephens, Functional coupling of microtubules to membranes - implications for membrane structure and dynamics. *J Cell Sci* 125, 2795-2804 (2012).
221. T. Vinogradova, P. M. Miller, I. Kaverina, Microtubule network asymmetry in motile cells: role of Golgi-derived array. *Cell Cycle* 8, 2168-2174 (2009).
222. C. Sütterlin, A. Colanzi, The Golgi and the centrosome: building a functional partnership. *J Cell Biol* 188, 621-628 (2010).
223. M. C. Larocca, M. Jin, J. R. Goldenring, AKAP350 modulates microtubule dynamics. *Eur J Cell Biol* 85, 611-619 (2006).
224. L. Hurtado et al., Disconnecting the Golgi ribbon from the centrosome prevents directional cell migration and ciliogenesis. *J Cell Biol* 193, 917-933 (2011).
225. A. Aher et al., CLASP Suppresses Microtubule Catastrophes through a Single TOG Domain. *Developmental Cell* 46, 40-58.e48 (2018).
226. K. Chabin-Brion et al., The Golgi complex is a microtubule-organizing organelle. *Mol Biol Cell* 12, 2047-2060 (2001).
227. P. M. Miller et al., Golgi-derived CLASP-dependent microtubules control Golgi organization and polarized trafficking in motile cells. *Nature cell biology* 11, 1069-1080 (2009).
228. N. Pouillet et al., Mechanical instabilities of aorta drive blood stem cell production: a live study. *Cell Mol Life Sci* 77, 3453-3464 (2020).
229. M. Lancino et al., Anisotropic organization of circumferential actomyosin characterizes hematopoietic stem cells emergence in the zebrafish. *Elife* 7, (2018).
230. B. Stramer et al., Clasp-mediated microtubule bundling regulates persistent motility and contact repulsion in *Drosophila* macrophages *in vivo*. *Journal of Cell Biology* 189, 681-689 (2010).
231. A. V. Fonseca, D. Corbeil, The hematopoietic stem cell polarization and migration: A dynamic link between rhoa signaling pathway, microtubule network and ganglioside-based membrane microdomains. *Communicative and Integrative Biology* 4, 201-204 (2011).
232. K. Drabek et al., The microtubule plus-end tracking protein CLASP2 is required for hematopoiesis and hematopoietic stem cell maintenance. *Cell reports* 2, 781-788 (2012).
233. B. Fouquet, B. M. Weinstein, F. C. Serluca, M. C. Fishman, Vessel patterning in the embryo of the zebrafish: guidance by notochord. *Dev Biol* 183, 37-48 (1997).
234. L. Sumoy, J. B. Keasey, T. D. Dittman, D. Kimelman, A role for notochord in axial vascular development revealed by analysis of phenotype and the expression of VEGF-2 in zebrafish *flh* and *ntl* mutant embryos. *Mech Dev* 63, 15-27 (1997).
235. V. Kohli, J. A. Schumacher, S. P. Desai, K. Rehn, S. Sumanas, Arterial and venous progenitors of the major axial vessels originate at distinct locations. *Dev Cell* 25, 196-206 (2013).
236. A. Quillien et al., Distinct Notch signaling outputs pattern the developing arterial system. *Development (Cambridge, England)* 141, 1544-1552 (2014).
237. M. Shin et al., Vegfa signals through ERK to promote angiogenesis, but not artery differentiation. *Development* 143, 3796-3805 (2016).
238. I. B. Lobov et al., Delta-like ligand 4 (Dll4) is induced by VEGF as a negative regulator of angiogenic sprouting. *Proc Natl Acad Sci U S A* 104, 3219-3224 (2007).
239. L. Jakobsson et al., Endothelial cells dynamically compete for the tip cell position during angiogenic sprouting. *Nat Cell Biol* 12, 943-953 (2010).
240. B. Ubezio et al., Synchronization of endothelial Dll4-Notch dynamics switch blood vessels from branching to expansion. *Elife* 5, (2016).
241. M. Hellström et al., Dll4 signalling through Notch1 regulates formation of tip cells during angiogenesis. *Nature* 445, 776-780 (2007).
242. J. D. Leslie et al., Endothelial signalling by the Notch ligand Delta-like 4 restricts angiogenesis. *Development (Cambridge, England)* 134, 839-844 (2007).
243. A. F. Siekmann, N. D. Lawson, Notch signalling limits angiogenic cell behaviour in developing zebrafish arteries. *Nature* 445, 781-784 (2007).
244. S. Suchting et al., The Notch ligand Delta-like 4 negatively regulates endothelial tip cell formation and vessel branching. *Proceedings of the National Academy of Sciences of the United States of America* 104, 3225-3230 (2007).
245. S. Isogai, N. D. Lawson, S. Torrealday, M. Horiguchi, B. M. Weinstein, Angiogenic network formation in the developing vertebrate trunk. *Development (Cambridge, England)* 130, 5281-5290 (2003).
246. L. D. Covassin, J. a. Villefranc, M. C. Kacergis, B. M. Weinstein, N. D. Lawson, Distinct ge-

- netic interactions between multiple Vegf receptors are required for development of different blood vessel types in zebrafish. *Proceedings of the National Academy of Sciences of the United States of America* 103, 6554-6559 (2006).
247. H. Habeck, B. Walderich, H.-m. Maischein, S. Schulte-merker, A. P. Exelisis, Analysis of a Zebrafish VEGF Receptor Mutant Reveals Specific Disruption of Angiogenesis. *Development* 12, 1405-1412 (2002).
  248. N. Bahary et al., Duplicate VegfA genes and orthologues of the KDR receptor tyrosine kinase family mediate vascular development in the zebrafish. *Blood* 110, 3627-3636 (2007).
  249. L. D. Covassin et al., A genetic screen for vascular mutants in zebrafish reveals dynamic roles for Vegf/Plcg1 signaling during artery development. *Developmental biology* 329, 212-226 (2009).
  250. N. D. Lawson, J. W. Mugford, B. A. Diamond, B. M. Weinstein, phospholipase C gamma-1 is required downstream of vascular endothelial growth factor during arterial development. *Genes & development* 17, 1346-1351 (2003).
  251. G. Costa et al., Asymmetric division coordinates collective cell migration in angiogenesis. *Nature cell biology* 18, 1292-1301 (2016).
  252. B. Weijts et al., Blood flow-induced Notch activation and endothelial migration enable vascular remodeling in zebrafish embryos. *Nat Commun* 9, 5314 (2018).
  253. J. Bussmann et al., Arteries provide essential guidance cues for lymphatic endothelial cells in the zebrafish trunk. *Development (Cambridge, England)* 137, 2653-2657 (2010).
  254. B. M. Hogan et al., Ccbe1 is required for embryonic lymphangiogenesis and venous sprouting. *Nat Genet* 41, 396-398 (2009).
  255. Y. R. Cha et al., Chemokine signaling directs trunk lymphatic network formation along the preexisting blood vasculature. *Developmental cell* 22, 824-836 (2012).
  256. A. v. Impel, S. Schulte-Merker, A fish-eye view on lymphangiogenesis. *Developmental Aspects of the Lymphatic Vascular System*, 153-165 (2014).
  257. A. M. K uchler et al., Development of the zebrafish lymphatic system requires VEGFC signaling. *Curr Biol* 16, 1244-1248 (2006).
  258. K. Yaniv et al., Live imaging of lymphatic development in the zebrafish. *Nat Med* 12, 711-716 (2006).
  259. B. M. Hogan et al., Vegfc/Flt4 signalling is suppressed by Dll4 in developing zebrafish intersegmental arteries. *Development* 136, 4001-4009 (2009).
  260. M. Shin et al., Vegfc acts through ERK to induce sprouting and differentiation of trunk lymphatic progenitors. *Development* 143, 3785-3795 (2016).
  261. K. Koltowska et al., Vegfc Regulates Bipotential Precursor Division and Prox1 Expression to Promote Lymphatic Identity in Zebrafish. *Cell Rep* 13, 1828-1841 (2015).
  262. J. Nicenboim et al., Lymphatic vessels arise from specialized angioblasts within a venous niche. *Nature* 522, 56-61 (2015).
  263. S. Baek et al., The alternative splicing regulator Nova2 constrains vascular Erk signaling to limit specification of the lymphatic lineage. *Developmental cell* 49, 279-292 (2019).
  264. S. Blum et al., An inhibitory role of the phosphatidylinositol 3-kinase-signaling pathway in vascular endothelial growth factor-induced tissue factor expression. *Journal of Biological Chemistry* 276, 33428-33434 (2001).
  265. S. V. Kyosseva, E. N. Harris, P. H. Weigel, The hyaluronan receptor for endocytosis mediates hyaluronan-dependent signal transduction via extracellular signal-regulated kinases. *J Biol Chem* 283, 15047-15055 (2008).
  266. E. N. Harris, J. A. Weigel, P. H. Weigel, Endocytic function, glycosaminoglycan specificity, and antibody sensitivity of the recombinant human 190-kDa hyaluronan receptor for endocytosis (HARE). *Journal of Biological Chemistry* 279, 36201-36209 (2004).
  267. F. Campbell et al., Directing Nanoparticle Biodistribution through Evasion and Exploitation of Stab2-Dependent Nanoparticle Uptake. *ACS Nano* 12, 2138-2150 (2018).
  268. M. S. Rost, S. Sumanas, Hyaluronic acid receptor Stabilin-2 regulates Erk phosphorylation and arterial-venous differentiation in zebrafish. *PLoS One* 8, e88614 (2014).
  269. S. J. Stoll, S. Bartsch, J. Kroll, HOXC9 regulates formation of parachordal lymphangioplasts and the thoracic duct in zebrafish via stabilin 2. *PLoS One* 8, e58311 (2013).
  270. S. Garantziotis, R. C. Savani, Hyaluronan biology: A complex balancing act of structure, function, location and context. *Matrix Biol* 78-79, 1-10 (2019).
  271. P. H. Weigel, Hyaluronan Synthase: The Mechanism of Initiation at the Reducing End and a Pendulum Model for Polysaccharide Translocation to the Cell Exterior. *International journal of cell biology* 2015, 367579-367579 (2015).
  272. J. Bakkers et al., Has2 is required upstream of Rac1 to govern dorsal migration of lateral cells during zebrafish gastrulation. *Development* 131, 525-537 (2004).
  273. J. E. De Angelis et al., Tmem2 Regulates Embryonic Vegf Signaling by Controlling Hyaluronic Acid Turnover. *Dev Cell* 40, 123-136 (2017).
  274. V. Bourguignon, B. Flamion, Respective roles of hyaluronidases 1 and 2 in endogenous hyaluronan turnover. *The FASEB Journal* 30, 2108-2114 (2016).
  275. A. C. Petrey, C. A. de la Motte, Hyaluronan, a crucial regulator of inflammation. *Frontiers in immunology* 5, 101-101 (2014).
  276. R. Deed et al., Early-response gene signalling is induced by angiogenic oligosaccharides of hyaluronan in endothelial cells. Inhibition by non-angiogenic, high-molecular-weight hyaluronan. *Int J Cancer* 71, 251-256 (1997).

277. P. W. Noble, Hyaluronan and its catabolic products in tissue injury and repair. *Matrix Biol* 21, 25-29 (2002).
278. F. Gao, C. X. Yang, W. Mo, Y. W. Liu, Y. Q. He, Hyaluronan oligosaccharides are potential stimulators to angiogenesis via RHAMM mediated signal pathway in wound healing. *Clin Invest Med* 31, E106-116 (2008).
279. S. P. Evanko, M. I. Tammi, R. H. Tammi, T. N. Wight, Hyaluronan-dependent pericellular matrix. *Advanced Drug Delivery Reviews* 59, 1351-1365 (2007).
280. J. F. Murphy et al., Engagement of CD44 modulates cyclooxygenase induction, VEGF generation, and cell proliferation in human vascular endothelial cells. *The FASEB journal* 19, 1-17 (2005).
281. L. S. Rodgers et al., Depolymerized hyaluronan induces vascular endothelial growth factor, a negative regulator of developmental epithelial-to-mesenchymal transformation. *Circ Res* 99, 583-589 (2006).
282. S. Nandadasa et al., The versican-hyaluronan complex provides an essential extracellular matrix niche for Flk1+ hematoendothelial progenitors. *Matrix Biology* 97, 40-57 (2021).





## Chapter

---

# 2

## Research

published in:  
Blood. 2015 Jan 15;125(3):465-9.

Boisset, J.-C., Clapes, T., **Klaus, A.**, Papazian, N., Onderwater, J., Mommaas-Kienhuis, M., Cupedo, T., Robin, C.

Progressive maturation toward hematopoietic stem cells  
in the mouse embryo aorta

Clusters of cells attached to the endothelium of the main embryonic arteries were first observed a century ago. Present in most vertebrate species, such clusters or IAHCs (intra-aortic hematopoietic clusters) derive from specialized hemogenic endothelial cells and contain the first few hematopoietic stem cells (HSCs) generated during embryonic development. However, some discrepancies remained concerning the spatio-temporal appearance and the numbers of IAHCs and HSCs. Therefore, the exact cell composition and function of IAHCs remain unclear to date. We show here that IAHCs contain pre-HSCs (or HSC precursors) that can mature into HSCs *in vivo* (as shown by the successful long-term multilineage reconstitution of primary neonates and secondary adult recipients). Such IAHC pre-HSCs could contribute to the HSC pool increase observed at mid-gestation. The novel insights in pre-HSC to HSC transition represent an important step towards generating transplantable HSCs *in vitro* that are needed for autologous HSC transplantation therapies.

## Introduction

All blood cell production throughout adult life originates from Hematopoietic Stem Cells (HSCs) that are initially produced during embryonic development. HSCs are first detected in the aorta of the Aorta-Gonad-Mesonephros (AGM) region at embryonic day(E)10.5 of mouse development (1). They most likely reside in cell clusters (Intra-Aortic Hematopoietic Clusters, IAHCs) tightly attached to the endothelium. Indeed, both HSCs and IAHC cells express similar markers (e.g. c-kit (2)) and are absent in *Runx1*<sup>-/-</sup> embryos<sup>3</sup>. IAHCs, first described a century ago (4), are present in most vertebrate species and believed to derive from the underlying endothelium (4). The so-called hemogenic endothelial origin of IAHCs and HSCs was shown in chicken (5) and mouse embryos (6-9). It was definitively confirmed after we and others observed the endothelial to hematopoietic transition directly in the aorta by time-lapse confocal microscopy, *ex vivo* in thick mouse embryo slices (10) and *in vivo* in zebrafish embryos (11,12).

Some discrepancies remain when HSCs and IAHCs are compared: (1) IAHCs appear one day before HSCs (E9.5 and E10.5, respectively) (1,2); (2) the number of IAHC cells largely exceeds the number of HSCs estimated per AGM (~600 IAHC cells and <0.1 HSC at E10.5; ~500 IAHC cells and <2 HSCs at E11.5 (1,2,13)); (3) while IAHCs are located in both sides of the aorta, HSCs are restricted to the ventral side (14). To determine the exact cell composition and function of IAHCs, we analyzed the phenotypic evolution and function of IAHC cells before and during HSC detection. Here we show that IAHCs contain pre-HSCs (or HSC precursors) capable of long-term multilineage reconstitution in newborn recipients at a time when HSCs are not detected yet. We demonstrate that IAHC pre-HSCs mature towards a HSC fate by performing secondary transplantations in adults and *ex vivo* time-lapse live confocal imaging.

## Results and discussion

To observe in details the structure of IAHCs, we imaged by scanning electron microscopy E10 (Figure 1A-C, Supplementary Figure 1C-G) and E11 (Supplementary Figure A,B) embryo slices. IAHCs, endothelium and sub-aortic mesenchyme were clearly visible (Figure 1C). In addition to single cells (Supplementary Figure 1B), we observed spheroid (Figure 1C), stack (Supplementary Figure 1C) and 'mushroom' (Supplementary Figure 1D) IAHC shapes. Most cells were spherical with surface microvilli (Supplementary Figure 1E-G). As control, no IAHCs were visible in *Runx1*<sup>-/-</sup> embryo slices (Supplementary Figure 1H,I).

The functional characterization of IAHCs has been hindered by the difficulty to isolate IAHC cells to purity. All IAHC cells express c-kit but contaminating c-kit<sup>+</sup> cells are also present in the circulating blood and outside the aorta (2,15). To circumvent this issue, directly labeled antibodies against c-kit were injected inside the aorta of non-fixed E10 embryo, prior AGM dissection/dissociation. Our procedure allows flushing out the blood from the aorta, staining all IAHCs (10,16) and isolating IAHC cells only (Figure 1D). When the AGM is dissociated before staining, contaminating c-kit<sup>+</sup> cells will also be stained (Figure 1E). Therefore, c-kit intra-aortic staining allows IAHC cells isolation to purity.

c-kit<sup>+</sup> IAHC cells express several endothelial and hematopoietic surface markers (Supplementary Figure 2A-D (E10) and 2E-H (E11)). Ly6a-GFP and CD45 were clearly differentially expressed in IAHCs (2,10,16,17). It revealed four phenotypically distinct populations (c-kit+Ly6a-GFP-CD45-, c-kit+Ly6a-GFP+CD45-, c-kit+Ly6a-GFP-CD45+ and c-kit+Ly6a-GFP+CD45+), as shown by flow cytometry or confocal micros-

copy at E10 (Figure 1F, Supplementary Figure 3; Supplementary Movie 1) and E11 (Supplementary Figure 4A).

To test whether IAHCs contain committed hematopoietic progenitors and whether these progenitors might be restricted to a particular phenotype, IAHC cells were tested *in vitro* in three different clonogenic assays for the presence of erythroid/myeloid progenitors, pre-B lymphoid progenitors or Megakaryocyte progenitors (CFU-Mk). We found that IAHCs contained very few erythroid/myeloid progenitors ( $13 \pm 3$  erythroid/myeloid progenitors/E10 AGM,  $n=3$ , Figure 1G;  $19 \pm 4$  erythroid/myeloid progenitors/E11 AGM,  $n=3$ , Supplementary Figure 4B), very few CFU-Mk ( $9 \pm 2$  CFU-Mk/E10 AGM,  $n=2$ ) and no pre-B progenitors (neither in E10 c-kit<sup>+</sup> yolk sac sorted cells, data not shown). As positive control, adult bone marrow cells produced pre-B progenitors in our culture system (data not shown). Noteworthy, B progenitors were previously reported in the AGM, but only after a culture step on stromal cell lines (18). The number and types of myeloid progenitors were similar in the four-sorted IAHC cell populations, indicating that a particular phenotype does not correlate with a specific type of progenitors at E10. Interestingly, most erythroid/myeloid progenitors at E10 and E11 were not present in IAHCs but in the AGM circulating blood (enriched in the c-kit+Ly6a-GFP-CD45+ fraction) (Supplementary Figure 4C,D and 4E,F, respectively). They are most likely coming from the yolk sac (19). Altogether, our data show that HSCs and committed progenitors do not account for the high IAHC cell number.

We then tested whether IAHCs contained pre-HSCs (or HSC-precursors). Pre-HSCs were previously reported in pre-cultured E8 Para-aortic Splanchnopleura (P-Sp, prospective AGM area) (20), and E9.0 yolk sac and P-Sp (21,22). These cells, unable to reconstitute adult irradiated WT recipients, could reconstitute more permissive recipients (e.g. busulfan conditioned WT neonates, immunodeficient adult). Secondary transplantations performed in WT adult recipients also confirmed the self-renewal potential of the pre-HSCs (21). Pre-HSCs were also identified after an *in vitro* AGM dissociated/reaggregated culture (23,24). We performed transplantations of c-kit+ IAHC cells isolated from early E10 (prior to HSC detection) and mid-E10 (beginning of HSC detection) AGMs into the liver of *Rag2*<sup>-/-</sup>*γc*<sup>-/-</sup> or WT neonates (Table 1). Early E10 IAHC cells long-term reconstituted both *Rag2*<sup>-/-</sup>*γc*<sup>-/-</sup> and WT neonate recipients after the minimum injection of 100 and 200 cells, respectively. Mid-E10 IAHC cells reconstituted both types of recipients with as few as 50 cells. All reconstitutions were multilineage with donor contribution in myeloid, T and B lymphoid lineages (Figure 1H; Supplementary Figure 5). Thus IAHCs contain pre-HSCs and their frequency increases between early and mid-E10. Based on the number of c-kit<sup>+</sup> cells (~200 and 600 c-kit<sup>+</sup> cells/aorta at early E10 and mid-E10, respectively) (2) and our neonate transplantation data (all recipients reconstituted when injected with 100 and 50 c-kit<sup>+</sup> cells from early E10 and mid-E10 embryos, respectively), we estimate that there is an average of 2 pre-HSCs/aorta at early E10. This number increases to 12 pre-HSCs at mid-E10, which largely exceeds the number of HSCs estimated at this stage (~0.1 HSC) (1,13). All four c-kit+ IAHC sub-populations reconstituted *Rag2*<sup>-/-</sup>*γc*<sup>-/-</sup> neonates (Table 1). Therefore, pre-HSCs in IAHCs are not restricted to a specific phenotype at E10, based on Ly6a-GFP and CD45 expression. Both markers are thus not useful to enrich in pre-HSCs at E10 but are indicative of pre-HSC maturation into a HSC fate (since all HSCs are Ly6a-GFP+CD45+ at E11.5).

Our data shows that pre-HSCs not only derive from Ly6a-GFP<sup>+</sup> hemogenic endothelial cells (25) but also from Ly6a-GFP<sup>-</sup> hemogenic endothelial cells (not visible by fluorescent live confocal imaging (10)). Ly6a-GFP is thus very unlikely to be an exclusive marker of hemogenic endothelial cells. To date, only Runx1 seems to mark endothelial cells endowed with the potential of producing blood cells (6). To deter-



mine whether IAHC pre-HSC maturation occurs *in vivo*, secondary transplantations were performed in adult recipients (*Rag2*<sup>-/-</sup>*γc*<sup>-/-</sup> and/or WT) with bone marrow and spleen cells isolated from primary reconstituted recipients (identified by “e” and “g” in Table 1) (Supplementary Table 1). In both cases, long-term multilineage reconstitution was observed in bone marrow, spleen and peripheral blood of the recipients. Therefore, IAHC pre-HSCs can mature into fully potent HSCs *in vivo*. Time-lapse confocal microscopy of E10 *Ly6a*-GFP embryo slices (stained with CD31 and c-kit antibodies prior to imaging) revealed that while most IAHC cells were *Ly6a*-GFP<sup>-</sup>, they all started to express GFP during the course of imaging (Figure 1I, Supplementary Movie 2), indicative of maturation towards a HSC fate (all HSCs are *Ly6a*-GFP<sup>+</sup>) (17). To test whether cell proliferation occurred in IAHCs, embryo slices were stained for Phospho-Histone H3.3 (PHH3), CD31 and c-kit (Supplementary Figure 6A,B) and proliferating IAHC cells (c-kit<sup>+</sup>PHH3<sup>+</sup>) were counted to determine the mitotic index (percentage of IAHC proliferating cells per total IAHC cells; Figure 1J). Only few IAHC cells proliferated at early, mid and late E10 stages. Thus, the majority of IAHC cells mature towards a putative HSC state with low proliferation. The hemogenic endothelium does not directly form fully potent HSCs, but an intermediate cell population organized in IAHCs. Concomitant to HSC detection (mid-E10), IAHCs already contain an average of 12 pre-HSCs and 22 committed progenitors. The vast majority of IAHC cells is therefore not identified yet, but could be very immature pre-HSCs not able to reconstitute neonate recipients yet. We hypothesize that IAHC cells will progressively become pre-HSCs, maturing towards an HSC fate via successive steps initiated inside the aorta and possibly completed in the fetal liver (FL, main HSC reservoir at mid-gestation) (Supplementary Figure 8). We indeed observed three phenotypically defined IAHC pre-HSC populations in E12 FL (Supplementary Figure 7A,B). To which extent the pre-HSC populations described so far in different hematopoietic sites are related remains to be determined.

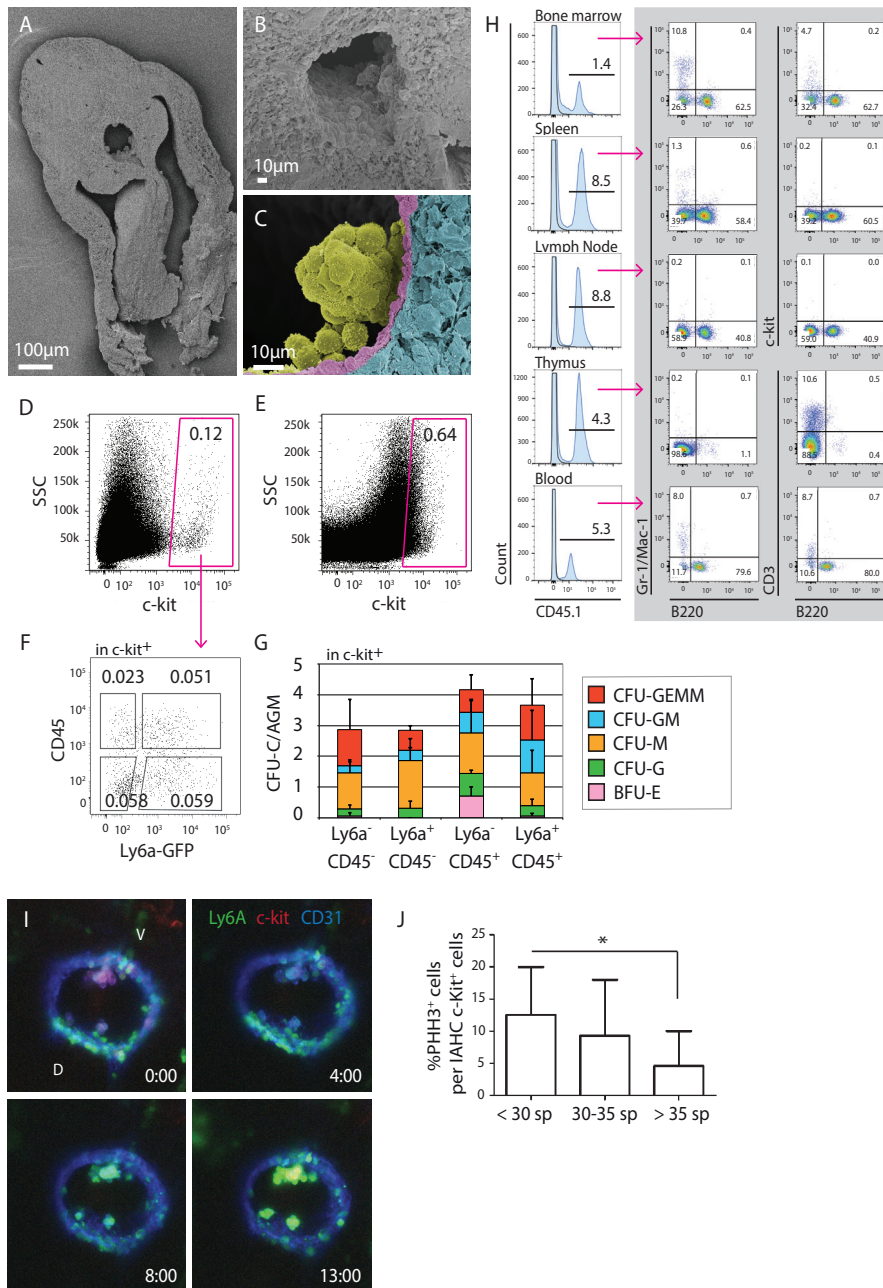


**Figure 1. Intra-Aortic Hematopoietic Clusters (IAHCs) at E10 are phenotypically heterogeneous, contain very few progenitors but contain pre-HSCs able of long-term multilineage hematopoietic reconstitution after transplantation in WT neonates.** (A-C) Scanning electron microscopy of E10 (28-34 somite pairs, sp) thick embryo slices. Before tissue fixation, the circulating blood was flushed out of the aorta to ascertain that attached IAHCs and not circulating cells were observed. (A) Whole E10 embryo slice. (B) Close-up view of the aorta where IAHCs are visible inside the aorta. (C) Close-up view of a IAHC with sphere shape in the aorta of E10 embryos. IAHC (yellow), endothelium (pink) and sub-aortic mesenchyme (blue) were artificially colored to show the delimitation between the structures. Top, dorsal side; Bottom: ventral

side. No morphologic heterogeneity was observed in the cells within single IAHCs or between IAHCs. (D, E) Flow cytometry analysis of AGM cells (E10 embryos) stained with c-kit antibody by intra-aortic injection before AGM dissociation (D) or on dissociated AGM cells (E). (F) CD45 and Ly6a-GFP expression within c-kit<sup>+</sup> AGM cells from E10 Ly6a-GFP embryos. Percentages of viable cells are indicated inside the gates. The absolute numbers of each population per ee are 216 ± 114 (c-kit<sup>+</sup>Ly6a-GFP-CD45<sup>-</sup>); 52 ± 16 (c-kit<sup>+</sup>Ly6a-GFP+CD45<sup>-</sup>), 37 ± 17 (c-kit<sup>+</sup>Ly6a-GFP-CD45<sup>+</sup>), 49 ± 23 (c-kit<sup>+</sup>Ly6a-GFP+CD45<sup>+</sup>) (n=4, Mean ± Standard Deviation). (G) CFU-C assays for the four IAHC cell populations isolated from E10 AGMs (28-34 somite pairs) and sorted based on (F) (n=3). Bars, Mean ± Standard Deviation. The number of CFU-C is indicated per flushed AGM. (H) Analysis of a WT neonate recipient (CD45.2) transplanted with 50 IAHC c-kit<sup>+</sup> cells from mid-E10 (33-38 sp) AGM (CD45.1) up to 4 months post-transplantation. FACS analysis show donor cell contribution (CD45.1) in bone marrow, spleen, lymph nodes, thymus and blood represented in histogram on the left panel (CD45.1: blue, Control: black line). Lines indicate the percentages of donor contribution in the whole tissue. Multilineage donor contribution (dot plots on grey background) was analyzed in all organs for myeloid (Gr-1/Mac-1) and B cells (B220), in bone marrow and spleen for hematopoietic stem/progenitor cells (c-kit), and in blood and thymus for T cells (CD3). Percentages of each donor population are indicated per quadrant. The analyzed reconstituted mouse is shown in Table 1 (“f”). (I) Time-lapse series pictures from Supplementary Movie 2 (Example 1) showing the maturation of IAHC cells. All CD31+c-kit+Ly6a-GFP<sup>-</sup> in IAHCs progressively express Ly6a-GFP during the time-lapse imaging (13h). V, ventral; D, dorsal; Ly6a-GFP, green; c-kit, red; CD31, blue. (J) Percentages of proliferating (c-kit+PHH3+) cells per IAHC (c-kit+) cells (or mitotic index) in the aorta of early E10 (<30 sp), mid-E10 (30-35 sp) and late E10 (>35 sp) embryos. Bars, Means ± Standard Deviation. \*p-value <0.05. To note, we controlled that the intra-aortic staining procedure did not detach IAHCs by performing whole-embryo c-kit staining of flushed compared to non-flushed embryos. We found no significant differences in the number of c-kit<sup>+</sup> (IAHC) cells in the aorta or in the shape of IAHCs (data not shown).

## Table

**Table 1. Intra-aortic hematopoietic clusters contain pre-HSCs.**

Embryo stage	Sorted cells	Cell number injected/recipient	Neonate recipients <sup>c</sup>	
			<i>Rag2</i> <sup>-/-</sup> <i>γc</i> <sup>-/-</sup>	WT
Early E10 (25-32 sp)	c-kit <sup>+</sup> <sup>a</sup>	10	0/1	0/9
		50	-	0/4
		100	2/2	0/2
		150	-	-
		200	-	3 <sup>d</sup> /5
		750	1 <sup>e</sup> /1	-
		1350	1/1	-
	c-kit <sup>+</sup> GFP <sup>+</sup> CD45 <sup>-</sup> <sup>b,h</sup>	1000-2500	3/3	-
	c-kit <sup>+</sup> GFP <sup>+</sup> CD45 <sup>-</sup>	250-550	3/4	-
c-kit <sup>+</sup> GFP <sup>+</sup> CD45 <sup>+</sup>	150-350	1/4	-	
c-kit <sup>+</sup> GFP <sup>+</sup> CD45 <sup>+</sup>	250-650	3/4	-	
Mid-E10 (33-38 sp)	c-kit <sup>+</sup> <sup>a</sup>	10	0/1	0/6
		50	2/2	2 <sup>f,g</sup> /12
		100	-	1/3
		150	2/2	-
		200	-	1/1

- a) n=5 independent experiments.
- b) n=3 independent experiments.
- c) Number of repopulated recipients per injected neonate recipients 4-5 months post-injection. Mice were considered repopulated when donor derived cells (>0.01%) were detected in both bone marrow and spleen, by flow cytometry of the H2kk and Ly6a-GFP donor markers (for Rag2-/- $\gamma$ c-/- recipients) or of the CD45.1 donor marker (for wild-type (WT) recipients).
- d) Multilineage reconstitution is shown in Supplementary Figure 5.
- e,g) Primary recipients used for secondary transplantations (see Supplementary Table 1).
- f) Multilineage reconstitution is shown in Figure 1H.
- h) The doses of c-Kit+GFP-CD45-, c-kit+GFP+CD45-, c-kit+GFP-CD45+ and c-kit+GFP+CD45+ cells injected per recipient correspond to 5-12, 5-11, 4-9 and 5-13 ee injected per recipients, respectively.
- (-) Not done.

## Methods

IAHCs were analyzed by scanning electron microscopy or after immunostaining on embryo (slices or whole). Sorted IAHC cells were tested *in vitro* in hematopoietic progenitor assays and *in vivo* after primary long-term transplantation in Rag2-/- $\gamma$ c-/- or WT newborns. Secondary transplantations were performed in adult Rag2-/- $\gamma$ c-/- or WT recipients. Donor chimerism was analyzed by flow cytometry 4-5 months upon transplantation.

## Acknowledgments

We thank the experimental animal center (Experimental Dieren Centrum, Erasmus MC) for mouse care and the Optical Imaging Center of the Erasmus MC for confocal microscope access. We thank Reinier van der Linden and Julien Karrich for help with cell sorting, Elize Haasdijk for initial help with the vibratome, Niels Galjart (Erasmus MC) for access to the Velocity software, Fanny Sage for her help in editing the movies, and Jacqueline Deschamps (Hubrecht Institute) for careful reading of the manuscript. This work was supported by the ERC grant (project number 220-H75001 EU/ HSCOrigin - 309361). C.R. and J.-C.B. were partly supported by NWO (VIDI) grant (917-76-345), and T. Clapes was supported by Landsteiner Foundation for Blood Transfusion Research (LSBR 1025).

C.R. and J.-C.B. conceived ideas and designed the research. J.-C.B. performed most experiments with the help of C.R., T. Clapes and A.K.. J.O. performed scanning electron microscopy, supervised by M.M. N.P. performed the initial neonate transplantations, supervised by T. Cupedo. J.-C.B. and C.R. analyzed the data, interpreted the experiments, made the figures and wrote the paper. All authors discussed the results and commented on the manuscript.

## Disclosure of conflicts of interest

The authors declare no financial or commercial conflicts of interest.

## References

1. Muller AM, Medvinsky A, Strouboulis J, Grosveld F, Dzierzak E. Development of hematopoietic stem cell activity in the mouse embryo. *Immunity* 1994;1(4):291-301.
2. Yokomizo T, Dzierzak E. Three-dimensional cartography of hematopoietic clusters in the vasculature of whole mouse embryos. *Development* 2010;137(21):3651-3661.
3. Cai Z, de Bruijn M, Ma X, et al. Haploinsufficiency of AML1 affects the temporal and spatial generation of hematopoietic stem cells in the mouse embryo. *Immunity* 2000;13(4):423-431.
4. Dantschakoff V. Untersuchungen über die Entwicklung von Blut und Bindegewebe bei Vögeln. Das lockere Bindegewebe des Huhnchens in Fetalen Leben. *Arch f mikr Anat.* 1909;73:117-181.
5. Jaffredo T, Gautier R, Eichmann A, Dieterlen-Lievre F. Intraaortic hemopoietic cells are derived from endothelial cells during ontogeny. *Development* 1998;125(22):4575-4583.
6. Chen MJ, Yokomizo T, Zeigler BM, Dzierzak E, Speck NA. Runx1 is required for the endothelial to haematopoietic cell transition but not thereafter. *Nature* 2009;457(7231):887-891.
7. Eilken HM, Nishikawa S, Schroeder T. Continuous single-cell imaging of blood generation from haemogenic endothelium. *Nature* 2009;457(7231):896-900.
8. Lancrin C, Sroczynska P, Stephenson C, Allen T, Kouskoff V, Lacaud G. The haemangioblast generates haematopoietic cells through a haemogenic endothelium stage. *Nature* 2009;457(7231):892-895.
9. Zovein AC, Hofmann JJ, Lynch M, et al. Fate tracing reveals the endothelial origin of hematopoietic stem cells. *Cell Stem Cell* 2008;3(6):625-636.
10. Boisset JC, van Cappellen W, Andrieu-Soler C, Galjart N, Dzierzak E, Robin C. *In vivo* imaging of haematopoietic cells emerging from the mouse aortic endothelium. *Nature* 2010;464(7285):116-
11. Bertrand JY, Chi NC, Santoso B, Teng S, Stainier DY, Traver D. Haematopoietic stem cells derive directly from aortic endothelium during development. *Nature* 2010;464(7285):108-111.
12. Kissa K, Herbomel P. Blood stem cells emerge from aortic endothelium by a novel type of cell transition. *Nature* 2010;464(7285):112-115.
13. Gekas C, Dieterlen-Lievre F, Orkin SH, Mikkola HK. The placenta is a niche for hematopoietic stem cells. *Dev Cell* 2005;8(3):365-375.
14. Taoudi S, Medvinsky A. Functional identification of the hematopoietic stem cell niche in the ventral domain of the embryonic dorsal aorta. *Proc Natl Acad Sci U S A* 2007;104(22):9399-9403.
15. Zovein AC, Turlo KA, Ponc RM, et al. Vascular remodeling of the vitelline artery initiates extravascular emergence of hematopoietic clusters. *Blood* 2010;116(18):3435-3444.
16. Boisset JC, Andrieu-Soler C, van Cappellen WA, Clapes T, Robin C. *Ex vivo* time-lapse confocal imaging of the mouse embryo aorta. *Nat Protoc* 2011;6(11):1792-1805.
17. de Bruijn MF, Ma X, Robin C, Ottersbach K, Sanchez MJ, Dzierzak E. Hematopoietic stem cells localize to the endothelial cell layer in the midgestation mouse aorta. *Immunity* 2002;16(5):673-683.
18. Ohmura K, Kawamoto H, Fujimoto S, Ozaki S, Nakao K, Katsura Y. Emergence of T, B, and myeloid lineage-committed as well as multipotent hematopoietic progenitors in the aortogonad-mesonephros region of day 10 fetuses of the mouse. *J Immunol* 1999;163(9):4788-4795.
19. Lux CT, Yoshimoto M, McGrath K, Conway SJ, Palis J, Yoder MC. All primitive and definitive hematopoietic progenitor cells emerging before E10 in the mouse embryo are products of the yolk sac. *Blood* 2008;111(7):3435-3438.
20. Cumano A, Ferraz JC, Klaine M, Di Santo JP, Godin I. Intraembryonic, but not yolk sac hematopoietic precursors, isolated before circulation, provide long-term multilineage reconstitution. *Immunity* 2001;15(3):477-485.
21. Yoder MC, Hiatt K, Dutt P, Mukherjee P, Bodine DM, Orlic D. Characterization of definitive lymphohematopoietic stem cells in the day 9 murine yolk sac. *Immunity* 1997;7(3):335-344.
22. Yoder MC, Hiatt K, Mukherjee P. *In vivo* repopulating hematopoietic stem cells are present in the murine yolk sac at day 9.0 postcoitus. *Proc Natl Acad Sci U S A* 1997;94(13):6776-6780.
23. Taoudi S, Gonneau C, Moore K, et al. Extensive hematopoietic stem cell generation in the AGM region via maturation of VE-cadherin+CD45+ pre-definitive HSCs. *Cell Stem Cell* 2008;3(1):99-108.
24. Rybtsov S, Sobiesiak M, Taoudi S, et al. Hierarchical organization and early hematopoietic specification of the developing HSC lineage in the AGM region. *J Exp Med* 2011;208(6):1305-1315.
25. Chen MJ, Li Y, De Obaldia ME, et al. Erythroid/myeloid progenitors and hematopoietic stem cells originate from distinct populations of endothelial cells. *Cell Stem Cell* 2011;9(6):541-552.

## Supplemental information

### Supplemental Methods

#### Embryo generation

Mouse embryos were generated from timed matings. Observation of vaginal plugs was considered as day 0 of embryonic development. WT embryos were generated in the C57BL/6, Ly5.1 or FVB/NJ backgrounds. *Ly6a*-GFP embryos (1) were generated by crossing *Ly6a*-GFP<sup>+/-</sup> males with (C57BL/10 x CBA) females, and *Rag2*<sup>-/-</sup>*γc*<sup>-/-</sup> pups by crossing *Rag2*<sup>-/-</sup>*γc*<sup>-/-</sup> males and females. Animals were housed according to institutional guidelines, and procedures were performed in compliance with Standards for Care and Use of Laboratory Animals with approval from the Erasmus MC ethical review board.

#### Scanning electron microscopy

E10 (28-34 sp) and E11 WT C57BL/6 (or E10 *Runx1*<sup>-/-</sup>) embryos were separated from placenta, yolk sac and amnion. Head and tail were cut. Blood in the aorta of the remaining caudal half was removed through injection of PBS/FCS (PBS supplemented with 10% fetal calf serum, penicillin (100 U/ml) and streptomycin (100 mg/ml)) inside the dorsal aorta using a pulled glass capillary and a glass syringe. Next, the embryo caudal parts were fixed overnight in osmium tetroxide, washed several times in PBS and subsequently sectioned with a Lancer Vibratome Series 1000 (Technical Products International) into transversal sections of 200 μm. Sections were fixed in 1.5% glutaraldehyde in 0.1M cacodylate buffer, dehydrated in a graded ethanol series, critical point dried over CO<sub>2</sub>, sputter-coated with gold-palladium and viewed in a Jeol JSM 7600F Scanning Electron Microscope at 5 kV.

#### Confocal microscopy of non-fixed embryos (slices or whole)

Tissue preparation was as previously described (2,3). Briefly, E10 (32-35 somite pairs, s.p.) and E11 *Ly6a*-GFP embryos were freed from placenta, yolk sac, amnion, head and tail. Non-fixed embryo trunks were stained by intra-aortic injection of antibodies or only PBS/FCS (to remove blood), and either cut into 200 μm transversal slices with a tissue chopper (McIlwain) or dissected to remove the dorsal tissues (for whole aorta floor observation). The comparison of whole-embryo c-kit staining of injected and non-injected embryos confirmed that no IAHC cells were detached after the intra-aortic injection procedure (no significant differences in c-kit<sup>+</sup> cell numbers inside the aorta or in IAHCs shape) (data not shown).

Tissues (slices or whole) were embedded in agarose gel and observed by confocal microscopy (Leica Microsystem). In the case of *ex vivo* time-lapse imaging, embryos were stained with AlexaFluor647 anti-CD31 and PE anti-c-kit antibodies before slicing. After slicing and embedding, the embryo slices were observed for 13 h. Time-lapse videos were reconstructed using ImageJ. For multicolor z-stack pictures, thick embryo slices were stained after cutting by incubation with Pacific Blue or APC anti-CD34 (RAM34), PE anti-c-kit (2B8), PE anti-flk-1 (Avas12α1), APC anti-CD45 (30-F11), PE anti-CD41 (MWRreg30), PE anti-Tie2 (TEK4), AlexaFluor 647 anti-CD31 (MEC13.3), AlexaFluor 647 anti-VE-Cadherin (eBioBV13) antibodies (from BD Pharmingen, eBioscience, Invitrogen, Santa Cruz, BioLegend), and observed by confocal microscopy. Images were edited with the Leica Analysis Software, or with Volocity (Perkin Elmer) for 3D images or video reconstructions. For video 2 and 3, E10 (30-34 sp) *Ly6a*-GFP embryos were used.



### **Embryonic tissue isolation and cell preparation**

Pregnant mice were sacrificed by cervical dislocation to collect E10 and E11 embryonic tissues. *Ly6a*-GFP embryos were checked under the fluorescent microscope for GFP expression. All embryonic tissues were dissected and enzymatically dissociated as previously described<sup>4</sup>. Briefly, after removal of the mother uterus, the embryos were isolated. Intra-embryonic AGM and fetal liver were further carefully dissected away from all other embryonic tissues. The intra-aortic blood was removed by intra-aortic injection of PBS/FCS, or by the injection of antibodies (in the case of intra-aortic staining) with a glass capillary. The flushed blood was collected and filtered on a 40  $\mu\text{m}$  mesh. Flushed AGM were enzymatically digested in a 0.125% collagenase solution in PBS/FCS for 1 hour at 37°C. Fetal livers were crushed through a 40  $\mu\text{m}$  nylon cell strainer. Single cell suspensions were used for flow cytometry analysis, clonogenic assays and/or transplantations.

### **Flow cytometry analysis and cell sorting**

After tissue isolation and dissociation, cells were counted after Trypan Blue staining to exclude the dead cells in a Bürker Türk counting chamber. Cells were then stained with PE anti-c-kit (2B8) and APC anti-CD45 (30-F11) antibodies for 30 minutes at 4 °C and washed. Alternatively PE anti-c-kit antibodies were injected intra- aorta with a glass capillary prior to AGM dissection and dissociation. Cells were analyzed and sorted with an Aria III flow cytometer (Becton Dickinson). 7- aminoactinomycin D (7-AAD) (Invitrogen) or Hoechst 33258 (Invitrogen, Molecular probes) were added to the cell suspension to discriminate dead from alive cells.

### **Hematopoietic progenitor assays**

For myeloid progenitor clonogenic assay, different doses of cells were plated in methylcellulose (M3434; StemCell Technologies). After 12 days of culture at 37°C, colonies were identified and counted by microscopic observation. This assay allows identifying five types of clonogenic progenitors: CFU-GEMM (Colony Forming Unit-Granulocytes Erythrocytes Macrophages Megakaryocytes), CFU-GM (CFU- Granulocytes Macrophages), CFU-M (CFU-Macrophages), CFU-G and BFU-E (Burst Forming Unit-Erythroid). For pre-B progenitor clonogenic assay, different doses of cells were plated in methylcellulose (M3630; StemCell Technologies) and the colonies were counted after 7 days of culture. For Megakaryocyte progenitor (CFU-MK) assay, cells were transferred into MegaCult®-C Medium (StemCell Technologies Inc.; Vancouver, Canada) supplemented with recombinase human- Thrombopoietin (rh-TPO, 50 ng/ml) and recombinase murine-Interleukin-3 (rm-IL-3, 10 ng/ml). Cultures were prepared according to the manufacturer's instructions and incubated in humidified 5% CO<sub>2</sub> incubator at 37°C. After 8 days of culture, slides were fixed in cold acetone (15 min), stained, and CFU-MK colonies were scored. CFU-MKs were identified by the detection of acetylcholinesterase activity of megakaryocytes. A CFU-MK colony was defined as a cluster of three or more MK cells detected by light microscopy.

### **Intra-liver newborn transplantations, analysis, and secondary transplantations**

After sort, IAHC cells were washed and suspended in 15-20  $\mu\text{L}$  of PBS before injection in the liver of 1-5 days old *Rag2*<sup>-/-</sup>*γc*<sup>-/-</sup> or WT irradiated newborns (3 and 5Gy respectively, 137 Cs-source). After up to 5 months, donor chimerism was analyzed on bone marrow, spleen and peripheral blood (red blood cells were lysed with IOTest® 3 Lysing Solution, Beckman Coulter) of the grown-up neonates. Thymus and lymph nodes were only analyzed in WT recipients. The presence of donor contribution was determined by flow cytometry (LSR II, Becton Dickinson) after staining with APC anti-H2kk antibody (H100-27.R55) and by *Ly6a*-GFP expression (both of donor origin) for

*Rag2*<sup>-/-</sup>*yc*<sup>-/-</sup> recipients (H2kd), or PE anti-CD45.1 antibody for WT recipients (CD45.2). Dead cells were excluded with DAPI or Hoechst 33258 (Invitrogen, Molecular probes). Expression of H2kd (recipient) and H2kk (donor) were tested in BALB/c mice (same background as the recipient *Rag2*<sup>-/-</sup>*yc*<sup>-/-</sup> mice) (data not shown). In addition, bone marrow, spleen and peripheral blood cells were analyzed by semi-quantitative Polymerase Chain Reaction (PCR) for the presence of the *Ly6a*-GFP transgene (data not shown). Multilineage analyses were carried out on bone marrow, spleen and peripheral blood of the transplanted grown-up neonates by using APC-Cy7 or APC efluor780 anti-Mac-1 (M1/70), APC-Cy7 anti-Gr-1 (RB6-8C5), AlexaFluor 700 anti-B220 (RA3-6B2), PE-Cy7 anti-CD45 (30-F11), APC anti-CD3 and Per-CP-Cy5.5 anti-c-kit (2B8) antibodies (from BD Pharmingen, eBioscience, BioLegend).

For secondary transplantations, bone marrow and spleen cells from primary reconstituted recipients were isolated and suspended in PBS for injection in either adult irradiated *Rag2*<sup>-/-</sup>*yc*<sup>-/-</sup> or WT (C57Bl/10 x CBA, or C57Bl/6) recipients (3 Gy and 9 Gy split dose, respectively). 2x10<sup>5</sup> (C57Bl/10 x CBA, or C57Bl/6) spleen cells were co-injected in the WT recipients. After up to 5 months, secondary recipients were analyzed as described previously for primary recipients. (C57Bl/10 x CBA) recipients were only analyzed for GFP expression by semi-quantitative PCR (as previously described<sup>5</sup>) on bone marrow, spleen and peripheral blood (since they express H2kk as the donor cells). A mouse was considered repopulated when both bone marrow and spleen contained at least 0.01% of donor contribution.

#### **Confocal microscopy of thick fixed embryo slices for IAHC proliferation assay**

FVB/NJ embryos were dissected at early E10 (<30 sp), mid-E10 (30-35 sp) and late E10 (>35 sp). The head and tail were removed and the aortic blood was flushed away. The remaining non-fixed embryo trunk was cut into 200  $\mu$ m slices with a tissue chopper. Slices were fixed 30 minutes in 2% Para-Formaldehyde at 4 °C, washed in PBS and dehydrated in methanol. After rehydration, slices were sequentially incubated with anti-c-kit (2B8)/AlexaFluor 647 anti-rat IgG, biotin anti-CD31 (MEC13.3)/AlexaFluor 594 streptavidin and anti-phospho-Histone H3.3 (PHH3)/AlexaFluor 488 anti-rabbit IgG antibodies as previously described<sup>6</sup>. Slices were cleared with a benzyl alcohol benzyl benzoate (BABB) solution and observed by confocal microscopy (Leica Microsystem). z-stack images of the aorta were obtained with a 20x Epiplan-Neofluar dry lens. Whole mount embryo slices were imaged in 3D (xyz). The number of intra-aortic c-kit+PHH3- (non proliferative) and c-kit+PHH3low/+ (proliferative) cells was manually counted using the Leica Analysis Software. IAHC cells in focus were counted per each xyz-stack (3  $\mu$ m in depth) for all z-stack images constituting the embryo slices. 56 c-kit+PHH3+/409 c-kit+ total cells (14 embryo slices), 72 c-kit+PHH3+/769 c-kit+ total cells (27 embryo slices), 18 c-kit+PHH3+/362 c-kit+ total cells (7 embryo slices) were counted at early, mid and late E10, respectively. Student's t test was used to determine statistical significance. \*p-value <0.05 was considered significant.

## Supplemental references

1. Ma X, Robin C, Ottersbach K, Dzierzak E. The Ly-6A (Sca-1) GFP transgene is expressed in all adult mouse hematopoietic stem cells. *Stem Cells* 2002;20(6):514-521.
2. Boisset JC, van Cappellen W, Andrieu-Soler C, Galjart N, Dzierzak E, Robin C. *In vivo* imaging of haematopoietic cells emerging from the mouse aortic endothelium. *Nature* 2010;464(7285):116-120.
3. Boisset JC, Andrieu-Soler C, van Cappellen WA, Clapes T, Robin C. *Ex vivo* time-lapse confocal imaging of the mouse embryo aorta. *Nat Protoc* 2011;6(11):1792-1805.
4. Robin C, Dzierzak E. Hematopoietic stem cell enrichment from the AGM region of the mouse embryo. *Methods Mol Med.* 2005;105:257-272.
5. de Bruijn MF, Ma X, Robin C, Ottersbach K, Sanchez MJ, Dzierzak E. Hematopoietic stem cells localize to the endothelial cell layer in the midgestation mouse aorta. *Immunity* 2002;16(5):673-683.
6. Yokomizo T, Yamada-Inagawa T, Yzaguirre AD, Chen MJ, Speck NA, Dzierzak E. Whole-mount three-dimensional imaging of internally localized immunostained cells within mouse embryos. *Nat Protoc* 2012;7(3):421-431.

## Supplemental movie legends

**Video 1.** This movie shows the phenotypic heterogeneity of IAHCs imaged on the aortic floor of a E10 Ly6a-GFP embryo. All IAHC cells are c-kit<sup>+</sup> (red) but they differentially express Ly6a-GFP (green) and CD45 (blue). (20x lens; floor of the aorta imaged from a dorsal perspective).

**Video 2.** This movie shows two examples of the maturation of CD31+c-kit+Ly6a- GFP- cells in CD31+c-kit+Ly6a-GFP+ cells in IAHCs (20x lens; green, Ly-6a-GFP; red, c-kit; blue, CD31). Example 1: Ventral side, top right; Dorsal side, bottom left. Example 2: Ventral side, top left; Dorsal side, bottom right.

## Supplemental table

**Table S1. IAHC pre-HSCs are able to reconstitute secondary adult recipients.**

Primary neonate recipient initially injected with:	Secondary recipients <sup>a</sup>			
	(Number repopulated/Number injected) <sup>b</sup>			
	<i>Rag2</i> <sup>-/-</sup> $\gamma$ <i>c</i> <sup>-/-</sup> injected with cells from:		wt injected with cells from:	
	Bone marrow	Spleen	Bone marrow	Spleen
750 c-Kit <sup>+</sup> cells from early E10 AGM (25-32 sp)	1/1	1/1	1/1	1/1
50 c-Kit <sup>+</sup> cells from mid-E10 AGM (33-38 sp)	-	-	3/3	3/3

<sup>a</sup>Secondary recipients injected with cells from primary recipients (indicated with "e" and "g" in Table 1).

<sup>b</sup>Number of repopulated recipients per injected recipients 4-5 months post-injection. Mice were considered repopulated when donor derived cells were detected in both bone marrow and spleen, by flow cytometry of the H2k<sup>k</sup> and Ly6a-GFP donor markers, and semi-quantitative PCR of the *Ly6a-GFP* transgene.

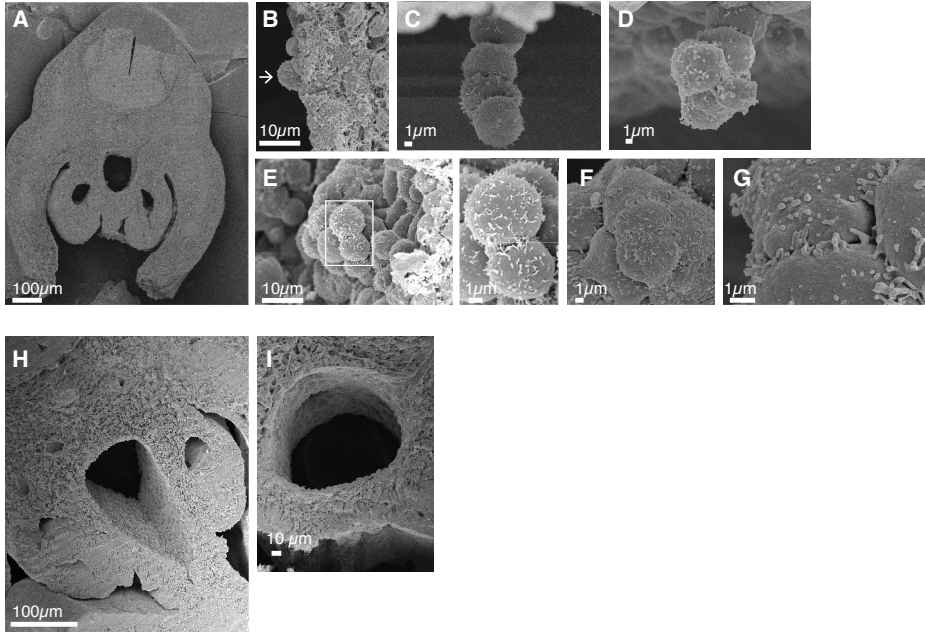


**Figure S1. IAHC cells are seemingly alike at E10 and E11.** (A-I) Scanning electron microscopy of E10 (C-I) and E11 (A,B) thick embryo slices (Wild-type: A-G; *Runx1*<sup>-/-</sup>: H,I). (A) Whole E11 embryo slice where IAHCs are visible inside the aorta. (B) Close-up view of a single hematopoietic cell (arrow) attached to the aortic endothelium. (C,D) Close-up views of IAHCs with stack (C) and “mushroom-like” (D) shapes in the aorta of E10 embryos. (E-G) All cells look alike in IAHCs. The white box in E (left panel) is shown in E (right panel). (H,I) Close-up of *Runx1*<sup>-/-</sup> embryo slices show, as expected, the absence of IAHCs inside the aorta. It validates our technique and proves that the IAHCs observed in wild-type embryo slices are not artifacts or circulating cells. Scale bars are indicated for each panel.

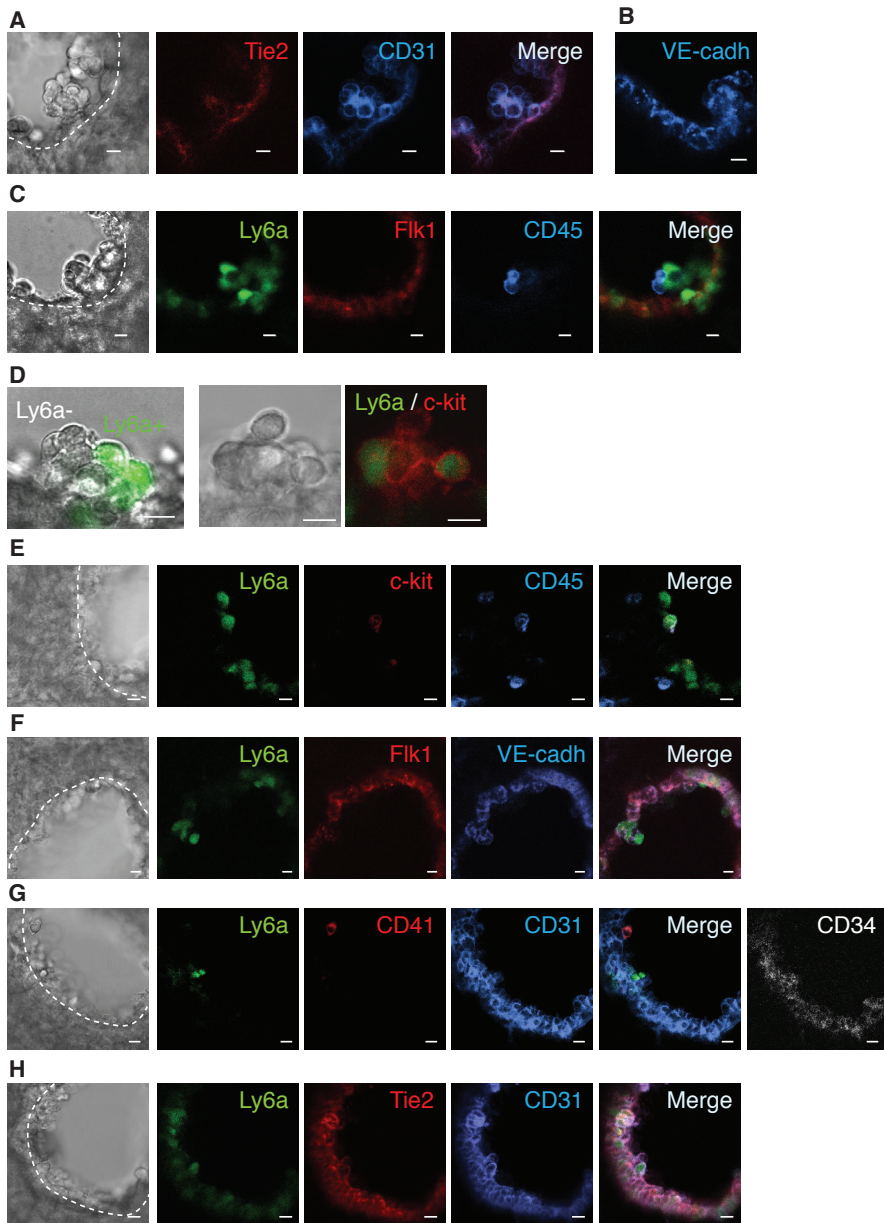


**Figure S2. IAHC cells express various endothelial and hematopoietic surface markers.** Visualization of IAHC cells by confocal imaging on non-fixed E10 (A-D) and E11 (E-H) Ly6a-GFP embryo slices (except for A, B: WT embryos). Ly6a-GFP (green) embryo slices stained with the indicated antibodies directly labeled with phycoerythrin (red), APC (blue), Alexafluor647 (blue) or pacific blue (grey). Image orientation: ventral side of the embryo downward. Left panels: transmitted light, middle panels: individual fluorescent signals, right panels: merged fluorescent signals. Scale bar, 10  $\mu$ m. Dashed line: aortic endothelium location. To note, (A) and (B) show two different embryo slices. The phenotypic heterogeneity within and between IAHCs was independent of IAHC size and shape.



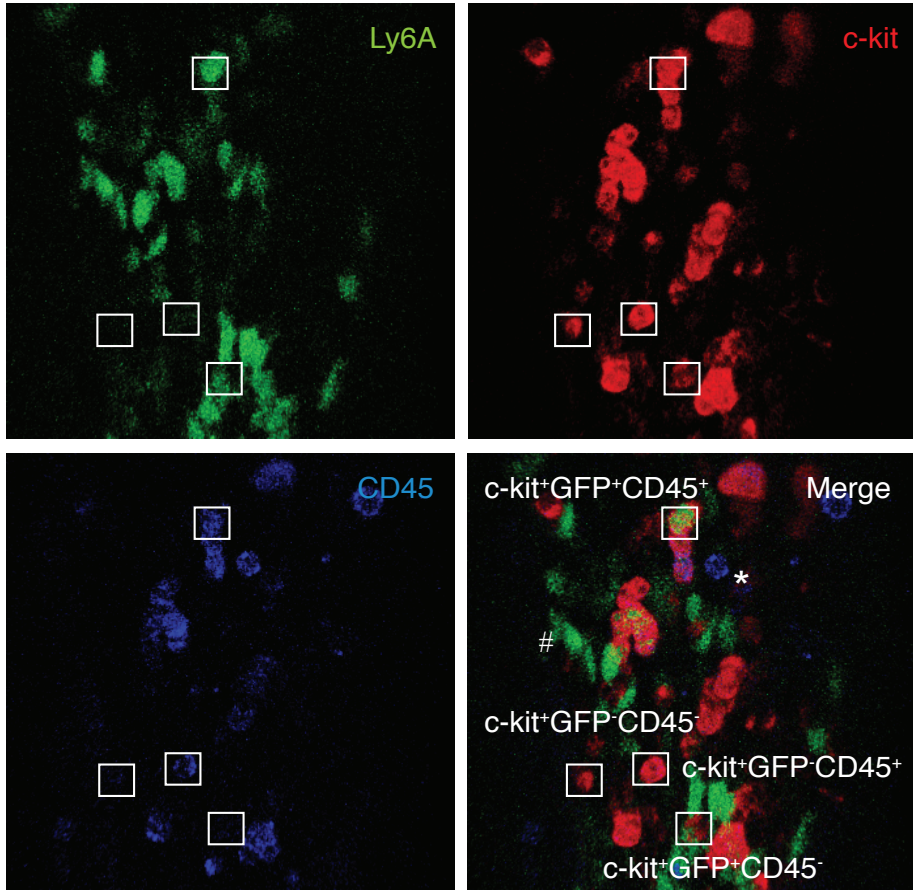


**Figure S3. IAHC cells differentially express Ly6a-GFP and CD45.**

Confocal imaging of the aortic endothelium and IAHCs on the floor of a non-fixed E10 Ly6a-GFP (green) embryo. The aorta was stained with antibodies against c-kit (red) and CD45 (blue). White boxes show examples of the four IAHC cell populations expressing c-kit but differentially expressing Ly6a-GFP and CD45 on the merged fluorescent signal panel. The three-dimensional reconstitution of the aortic floor is shown in Supplemental Movie 1.

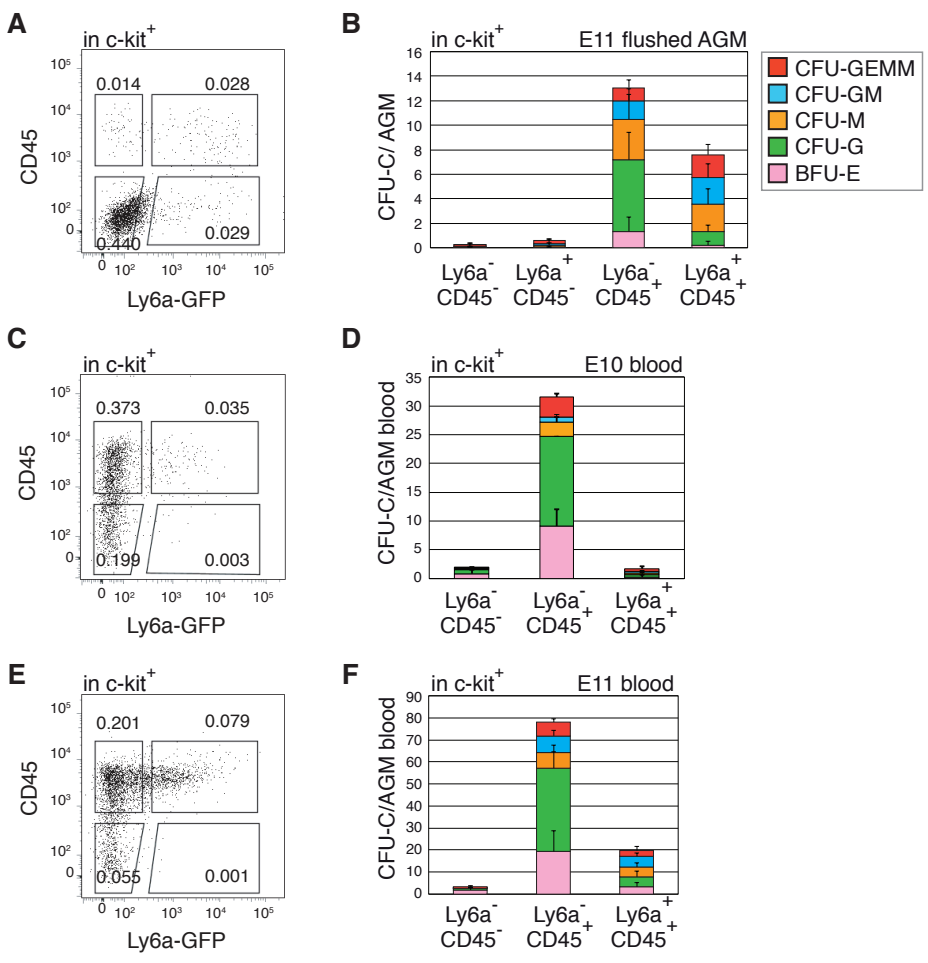


**Figure S4. Most hematopoietic progenitors are in the blood circulation at E10 and E11.** (A,C,E) Flow sorting and (B,D,F) CFU-C assays. (A, B) CFU-C assay of four IAHC cell populations (c-kit+Ly6a-GFP-CD45-, c-kit+Ly6a-GFP+CD45-, c-kit+Ly6a-GFP-CD45+, c-kit+Ly6a-GFP+CD45+) sorted from E11 flushed AGMs (n=3). (C,F) CFU-C assays of three cell populations (c-kit+Ly6a-GFP-CD45-, c-kit+Ly6a-GFP-CD45+, c-kit+Ly6a-GFP+CD45+) isolated from E10 (C,D, n=2) and E11 (E,F, n=3) flushed AGM blood. Percentages of viable cells are indicated inside the dot plot gates (A,C,E). Total number of CFU-C is indicated per flushed AGM (blood flushed out) (B) or by the equivalent of the blood flushed out of 1 AGM (D,F). Bars, Means of CFU-C ± Standard Deviation. n= independent experiments.

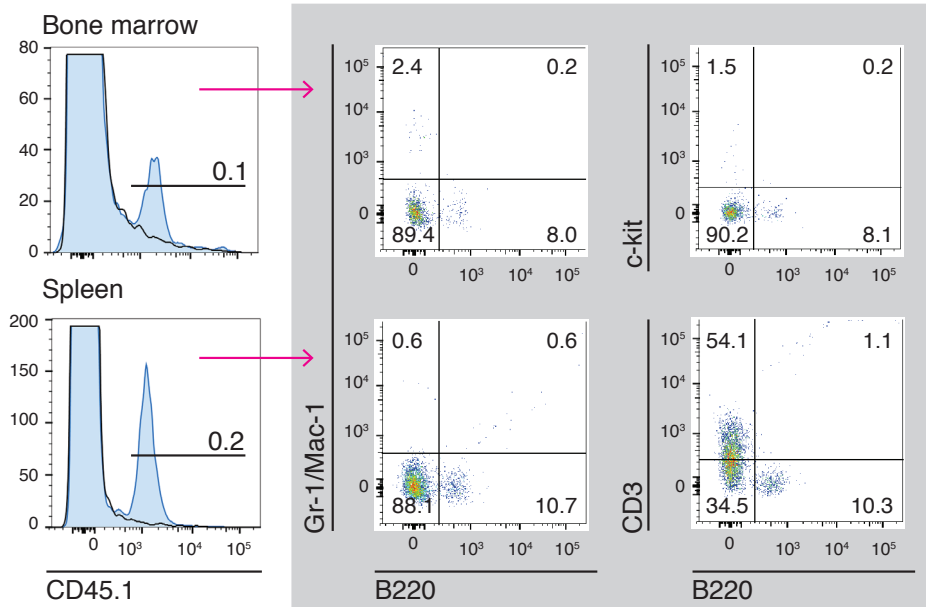


**Figure S5. IAHCs from early E10 embryos contain pre-HSCs able of long-term multilineage hematopoietic reconstitution after transplantation in WT neonates.** Analysis of a WT neonate recipient (CD45.2) transplanted with 200 IAHC c-kit<sup>+</sup> cells from early-E10 (25-32 sp) AGM (CD45.1) up to 4 months post-transplantation. FACS analyses show donor cell contribution (CD45.1) in bone marrow and spleen represented in histogram on the left panel (CD45.1: blue, Control: black line). Lines indicate the percentages of donor contribution in the whole tissue. Multilineage donor contribution (dot plots on grey background) was analyzed in bone marrow and spleen for myeloid (Gr-1/Mac-1) and B cells (B220), in bone marrow for hematopoietic stem/progenitor cells (c-kit), and in spleen for T cells (CD3). Percentages of each donor population are indicated per quadrant. The analyzed reconstituted mouse is shown in Table 1 (“d”).

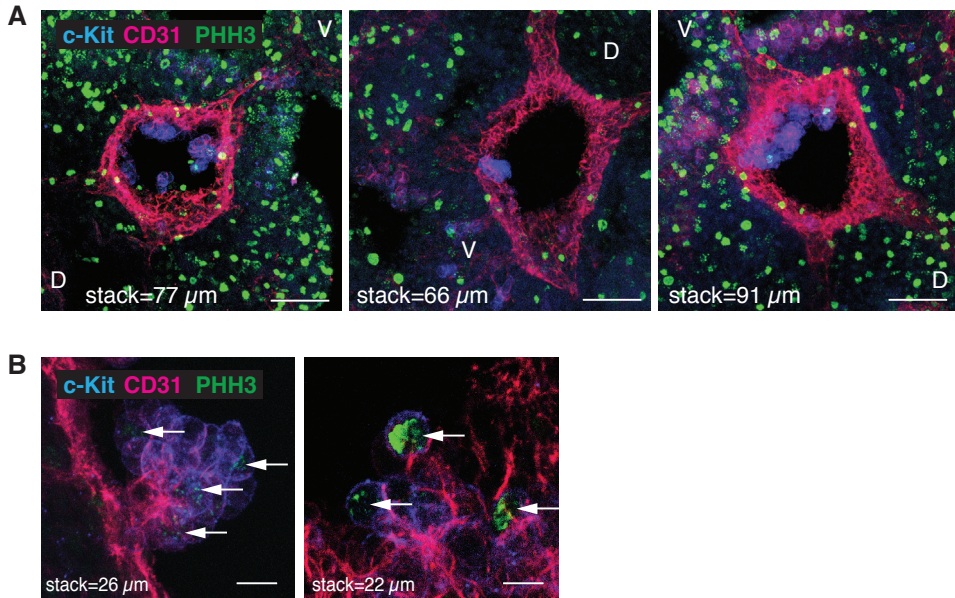


**Figure S6. Few IAHC cells proliferate in the aorta.** (A,B) Visualization of IAHC cells by confocal imaging on fixed thick E10 WT embryo slices. Embryo slices were stained with c-kit (blue), CD31 (red) and PHH3 (green). (A) Views of the aorta and surrounding mesenchyme show cell proliferation mainly outside of the aorta. Scale bar, 50 μm. (B) Close-up of IAHCs showing PHH3+ cells (arrows). Scale bar, 10 μm. V, ventral; D, dorsal.

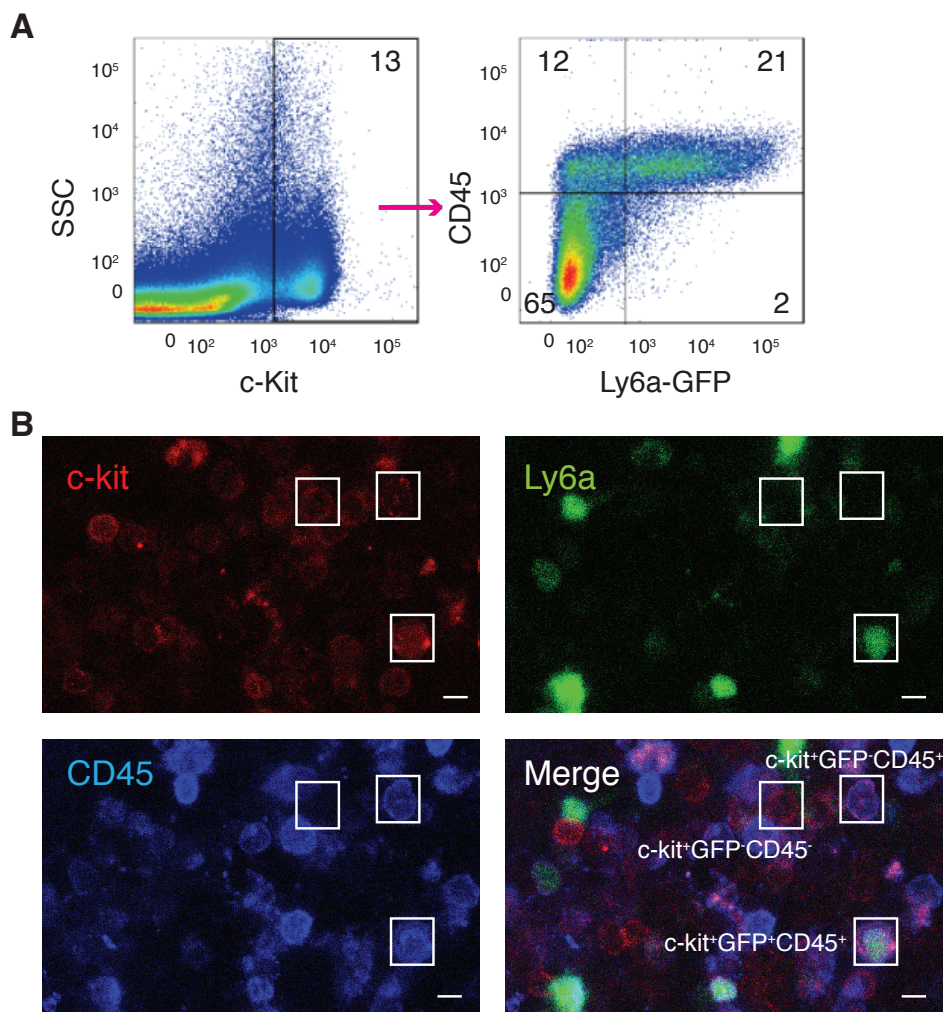



**Figure S7. Phenotypically defined pre-HSCs are present in the fetal liver.** (A,B) Visualization of phenotypically defined pre-HSCs by FACS and confocal imaging on fixed thick Ly6a-GFP liver slices. (A) FACS analysis of fetal liver cells isolated from E12 Ly6a-GFP embryos, after staining with c-kit and CD45 antibodies. Percentages of viable cells are indicated per gate and quadrant. (B) E12 Ly6a-GFP (green) non-fixed fetal liver slices stained with c-kit (red) and CD45 (blue). White boxes show examples of the three c-kit<sup>+</sup> cell populations differentially expressing Ly6a-GFP and CD45 on the merged fluorescent signal panel. Scale bar, 10  $\mu$ m.

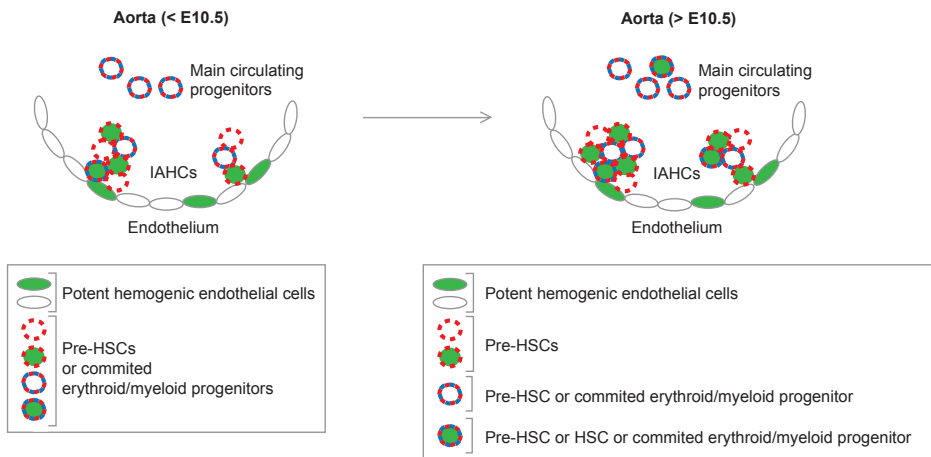


**Figure S8. Schematic summary.** Hemogenic endothelial cells (Ly6a-GFP+ or Ly6a-GFP-) generate IAHCs containing pre-HSCs and progenitors, not distinguishable based on Ly6a-GFP and CD45 expression at early E10. After E10.5, the first HSCs appear (c-Kit+Ly6a-GFP+CD45+) and the progenitors are mainly restricted in the c-Kit+Ly6a-GFP+CD45+ and c-Kit+Ly6a-GFP-CD45+ fractions. The main populations of progenitors observed in the circulating blood are also represented at both time points. Green: *Ly6a*-GFP expression; Blue: CD45 expression; red: c-Kit expression.





# Chapter

---

# 3

## Research

published in:  
Nat Commun 9, 2517 (2018).

Baron, C.S.\*, Kester, L.\*, Klaus, A., Boisset, J.-C., Thambyrajah, R.,  
Yvernogeu, L., Kouskoff, V., Lacaud, G., van Oudenaarden, A. & Robin, C.

Single-cell transcriptomics reveal the dynamic of  
haematopoietic stem cell production in the aorta

**H**aematopoietic stem cells (HSCs) are generated from haemogenic endothelial (HE) cells via the formation of intra-aortic haematopoietic clusters (IAHCs) in vertebrate embryos. The molecular events controlling endothelial specification, endothelial to haematopoietic transition (EHT) and IAHC formation, as it occurs *in vivo* inside the aorta, are still poorly understood. To gain insight in these processes, we performed single-cell RNA-sequencing of non-HE cells, HE cells, cells undergoing EHT, IAHC cells and whole IAHCs isolated from mouse embryo aortas. Our analysis identified the genes and transcription factor networks activated during the endothelial-to-haematopoietic switch and IAHC cell maturation towards a HSC fate. Our study provides an unprecedented complete resource to study in depth HSC generation *in vivo*. It will pave the way for improving HSC production *in vitro* to address the growing need for tailor-made HSCs to treat patients with blood-related disorders.

## Introduction

Haematopoietic stem cells (HSCs) produce billions of blood cells every day throughout life, owing to their multipotency and self-renewal properties. In the clinic, HSC transplantations are common practice to treat patients with blood related genetic disorders and malignancies. However, finding match donor HSCs for the increasing number of transplantations has become an issue. Intensive years of research have focused on the possibility to generate HSCs *in vitro* that would serve as a potential alternative source for these life-saving cells. An unlimited access to *in vitro* patient derived HSCs would also facilitate drug screening and allow studying the development of blood related diseases such as leukaemia. The fundamental finding that all HSCs derive from “haemogenic” endothelial cells during embryonic development has paved the way to recent advancements in the generation of transplantable HSCs *in vitro* (1-4). However, the molecular mechanism of the endothelial specification and its conversion into HSCs as it occurs *in vivo* in the course of embryonic life is still poorly understood. Such knowledge would certainly help to improve the production of bona fide transgene-free HSCs, which remains the optimal choice for therapies.

During mouse embryonic development, HSCs are first detected in the main arteries (such as the aorta of the aorta-gonad-mesonephros (AGM) region), starting at embryonic day (E)10.5, as shown by long-term *in vivo* transplantation assays (5-7). HSCs reside in intra-aortic haematopoietic clusters (IAHCs) attached to the wall of the aorta between E9.5 and E14.9. IAHCs are found in the ventral side of the aorta in most vertebrate species, with the exception of the mouse where low numbers of IAHCs are also present in the dorsal side (10). IAHCs express haematopoietic stem and progenitor cell (HSPC) markers (e.g. c-kit, CD41) (11-13) and are completely absent in mouse models devoid of HSCs (e.g. *Runx1*<sup>-/-</sup> mice) (14-16). Beside haematopoietic characteristics, IAHCs also express endothelial markers (e.g. CD31 (PECAM1), VE-Cadherin (CDH5, CD144), Tie2, CD34) (8,9,17), which supported a presumptive endothelial origin (18). This has since been proven in various animal models by performing live confocal imaging and *in vivo/in vitro* lineage tracing experiments (12,16,19-24). Altogether these studies established that HSPCs and IAHCs are generated from a transient subset of endothelial cells, named haemogenic endothelial (HE) cells, through an endothelial to haematopoietic transition (EHT). Although numerous IAHC cells (~700 IAHC cells at E11) are present in the aorta (9), they contain only very few HSCs (~1-3 HSCs/AGM) (25,26). IAHCs also contain very few committed progenitors (~22 progenitors/AGM). Most of them are indeed in the circulating blood, coming from the yolk sac (YS) (8,27,28). Finally, IAHCs also contain few HSC precursors (~12-18 pre-HSCs/AGM, capable of long-term multilineage reconstitution upon transplantation in newborn recipients or after a step of *in vitro* culture on stroma cell line prior transplantation) (8,29). In fact, most IAHC cells are probably very immature pre-HSCs (with no transplantable capacity yet) that progressively mature towards a HSC fate. Accordingly, numerous type I pre-HSCs (CDH5+CD45<sup>-</sup>) able to mature into type II pre-HSCs (CDH5+CD45<sup>+</sup>) and then into functional HSCs have been identified in an *in vitro* AGM dissociated/reaggregated culture system (30,31). Since the number of E11.5 AGM pre-HSCs correlates with E12.5 foetal liver HSCs, it strongly suggests that IAHC cells form the adult HSC pool after migration and maturation in the foetal liver (32). However, the exact cell composition of IAHCs *in vivo*, their putative heterogeneity, and the molecular steps leading to the generation of IAHCs and HSCs from the endothelium remain poorly understood. Novel approach that does not rely on functional *in vitro/in vivo* assays would need to be deployed to answer these questions.

In this study, we identified the molecular changes occurring during endothelial specification, EHT and IAHC formation, by using single-cell mRNA-sequencing (scRNA-seq). This technique allows to *in silico* purify IAHC cells, therefore removing any contamination from the dataset. We established that IAHCs are composed of pre-HSCs (type I and II) and committed progenitors, discernible by opposing gradients of endothelial and haematopoietic transcripts. We identified the genes and transcription factor (TF) networks activated for the silencing of the endothelial program and the initiation of the haematopoietic program during EHT as it occurs *in vivo* in the aorta of E10 and E11 embryos. Finally, we developed a new technique to isolate single whole IAHCs (wIAHCs) in the ventral and dorsal side of the aorta and demonstrated that they have similar transcriptomes, at both E10 and E11. Overall, we provide an unprecedented complete resource to study in depth the molecular changes occurring in the successive steps leading to HSC formation.

## Results

### scRNA-seq allows *in silico* purification of IAHC cells

To determine which staining procedure allows IAHC cell isolation to the highest purity, several approaches were compared (Supplementary Fig. 1). Cells were stained with anti-c-kit antibodies alone or in combination with anti-CD31 antibodies, either after dissociation of the whole AGM (total staining, TS) (9) or directly inside the aorta prior to AGM dissection (intra-aorta staining, IAS) (8,12,33). Single c-kit<sup>+</sup> cells (TS, Supplementary Fig. 1a; IAS, Supplementary Fig. 1b) or c-kit<sup>+</sup> cells with CD31 index recording (IAS; Supplementary Fig. 1c) were sorted. Besides composing IAHCs (Supplementary Fig. 1d, arrow heads), c-kit<sup>+</sup> cells are also present in the aorta surrounding mesenchyme (Supplementary Fig. 1d, asterisks) (9,12). To evaluate the possible contamination by non-IAHC c-kit<sup>+</sup> cells, anti-c-kit-PE antibodies were injected inside the aorta, AGMs were then dissected, dissociated, and cells were stained with APC-anti-c-kit, FITC-anti-CD31 and anti-CD45 antibodies. Single non-IAHC cells were then sorted (c-kit-PE-c-kit-APC+CD31-CD45<sup>-</sup> cells, thereafter referred to as c-kit<sup>+</sup> cells, mesenchyme staining or MS; Supplementary Fig. 1e).

scRNA-seq was performed on a total of 542 c-kit<sup>+</sup> (TS, IAS, MS), c-kit<sup>+</sup>CD31<sup>+</sup> and c-kit<sup>+</sup>CD31<sup>-</sup> (IAS) cells using CEL-seq (34,35) (Fig. 1a). RaceID (34), an algorithm developed for rare cell type identification in complex populations of single cells, identified six main clusters (Fig. 1b). Cells had varying levels of *Kit*, *Pecam1* (*CD31*) and *Ptprc* (*CD45*) mRNA expression (Fig. 1c, and Supplementary Fig. 1f). Part of the c-kit<sup>+</sup> cells (IAS) and most c-kit<sup>+</sup>CD31<sup>+</sup> cells (IAS) were in clusters 4 and 5 (Fig. 1b). They expressed known IAHC markers such as *Gpr56*, *CD34*, *Runx1* and *Gata2* (12,15,36,37) (Fig. 1d). Noteworthy, some cells in clusters 4 and 5 did not express IAHC markers but markers for haematopoietic cells located in sub-aortic patches such as *Gata3* and *Cdkn1c* (*P57*, *Kip2*) (38,39) (Supplementary Fig. 2a,b). In contrast, the other part of c-kit<sup>+</sup> cells (IAS) and most c-kit<sup>+</sup>CD31<sup>-</sup> cells (IAS) and c-kit<sup>+</sup> cells (TS) clustered together with the c-kit<sup>+</sup> cells (MS), forming the clusters 1, 2, 3 and 6 (Fig. 1b). These cells did not express IAHC markers (Fig. 1d). Cells in clusters 1, 2 and 3 expressed genes related to mesenchymal lineages (40) (e.g. *Crabp1*, *Cxcl12*, *Pdgfrb*, *Sox11*, *Ptprd*, *Col3a1* and *Epha7*; Supplementary Fig. 2c-i). Accordingly, they were located in the mesenchyme in close proximity to the aortic endothelium, as shown by single-molecule (sm)RNA-FISH (e.g. *Epha7*; Supplementary Fig. 2j). Cluster 6 expressed genes related to erythro-myeloid progenitors (EMPs) (41-43) (e.g. cells expressing *Csf1r* and *Fcgr3* (CD16) but not *Myb* transcripts; Supplementary Fig. 2k-m).



**Figure 1. scRNA-Seq allows *in silico* purification of IAHC cells from E11 AGM.** (a-d) t-SNE maps displaying as coloured dots 542 single cells isolated from the aorta-gonad-mesonephros (AGMs) region of E11 embryos. (a) t-SNE map displaying 37 c-kit+ cells sorted after total staining (brown dots), 215 c-kit+ cells sorted after intra-aorta staining (purple dots), c-kit+ cells sorted with CD31 fluorescence intensity index after intra-aorta staining (92 c-kit+CD31- cells, blue dots; 198 c-kit+CD31+ cells, green dots), and 114 c-kit-PE-c-kit-APC+CD31-CD45- cells (pink dots). (b) t-SNE map displaying single cells from (a) in clusters identified after RaceID analysis. Different numbers and colours highlight the different RaceID clusters. (c) *Kit* and (d) *Gpr56*, *CD34*, *Runx1* and *Gata2* marker genes projected on t-SNE maps. Colour bars, number of transcripts. Dim, dimension. (e) t-SNE map displaying *in silico* selected IAHC cells (in red) and excluded non-IAHC cells (in black).

The optimal IAHC cell purity was obtained after IAS based on c-kit and CD31 expression (97% of c-kit+CD31+ cells expressed *Gpr56* transcripts; Fig. 1d, Table 1). However, 25% of IAHC cells (*Gpr56*+ ) would be lost in the c-kit+CD31- fraction after sorting of the c-kit+CD31+ fraction (Table 1). Therefore, it is technically difficult to isolate all IAHC cells as a pure population due to unavoidable limitations related to antibody staining procedure, the difficulty to set up optimal sorting gates and cell sorting errors. However, scRNA-seq represents a powerful tool to correct for cell

contamination by *in silico* purifying IAHC cells based on specific marker gene expression. To study pure IAHC cells, we therefore selected the cells that had more than one *Gpr56* transcript and filtered out the cells that had more than two transcripts of one or more of the non-IAHC genes (Fig. 1e).

**Table 1. Percentages of IAHC cells (identified by *Gpr56* expression) after different antibody staining and cell sorting strategies.**

Sorted cells (staining strategy)	Percentage of cells with <i>Gpr56</i> transcripts
c-kit <sup>+</sup> cells (total staining)	6
c-kit <sup>+</sup> cells (intra-aorta staining)	53
c-kit <sup>+</sup> CD31 <sup>-</sup> (intra-aorta staining)	25
c-kit <sup>+</sup> CD31 <sup>+</sup> (intra-aorta staining)	97
c-kit-PE <sup>-</sup> c-kit-APC <sup>+</sup> CD31 <sup>-</sup> CD45 <sup>-</sup> (mesenchyme staining)	0

3

### Isolation of successive cell populations during EHT

To analyse the molecular steps leading to IAHC formation, different cell populations were sorted based on the differential expression of the transcriptional repressors *Gfi1* and *Gfi1b*, and *c-kit* (12,44). Single non-HE cells (*Cdh5*+*Gfi1*-*Gfi1b*-*c-kit*-), HE cells (*Cdh5*+*Gfi1*+*Gfi1b*-*c-kit*-) and cells undergoing EHT (*Cdh5*+*Gfi1*+*Gfi1b*-*c-kit*+) were sorted from E11 and E10 AGMs and sequenced (Supplementary Fig. 3a,b, respectively). In addition, sorted E11 and E10 IAHC cells were *in silico* purified (Fig. 1f). Finally, type I pre-HSCs (*c-kit*+*Cdh5*+*CD45*-) and type II pre-HSCs (*c-kit*+*Cdh5*+*CD45*+) were sorted from E11 AGMs (Supplementary Fig. 3c). For comparison, *c-kit*+ HSPCs were also sorted from E11 and E10 YSs (Supplementary Fig. 3d,e, respectively). The transcriptomes of the single cells from the different populations were then compared to each other at E11 and E10 (Fig. 2a and 3a, left panels; respectively).

The Monocle algorithm (45) was used to arrange the single cell expression profiles on a developmental axis. Both at E11 and E10, the different populations aligned along a pseudotime axis that followed the successive steps of the *in vivo* EHT process (Fig. 2a and 3a, right panels; respectively). The concomitant loss of the endothelial program and initiation of the haematopoietic program during developmental progression was illustrated by the decreased expression of *Vwf* and *Cdh5* (endothelial marker genes) and the increased expression of *Kit*, *Runx1*, *Mpo* and *Mt1* (haematopoietic marker genes) (Fig. 2b (E11) and Fig. 3b (E10)). The most extensive transcriptome remodelling occurred during EHT, where over 250 genes significantly changed their expression (Fig. 2c). For example, endothelial cells highly expressed gap junction transcripts (e.g. *Gja 4* and *Gja 5*, Supplementary Fig. 4a,b) that were down regulated when cells underwent EHT. HE cells expressed *Prom1* (46), *Sox17* and *Gfi1* (Supplementary Fig. 4c-e) while *Kit*, *Runx1*, *Sfp1* and *Gpr56* expression increased as cells underwent EHT (Supplementary Fig. 4f-i) and remained expressed in IAHC cells. The proliferation of IAHC cells was recently reported (32,47). Using the KEGG database, we analysed the “cell cycle” pathway according to pseudotime and indeed detected many genes of this pathway in most cell populations of our E11 dataset (Supplementary Fig.5). Importantly, the gene expression observed in the different populations (as reported above) did not change after correction for cell cycle and proliferation genes. Overall, our analysis validated the identity of the various sorted cell populations chosen



based on the expression of expected marker genes. Furthermore, this dataset represents a unique and reliable resource to examine gene expression changes during the development of endothelial cells into IAHC cells.

### IAHCs contain pre-HSCs and progenitors at E11 and E10

RaceID analysis, performed to identify the different cell types present in IAHCs, divided IAHC cells into two main clusters at E11 (Fig. 2d; clusters 1 and 2). Part of

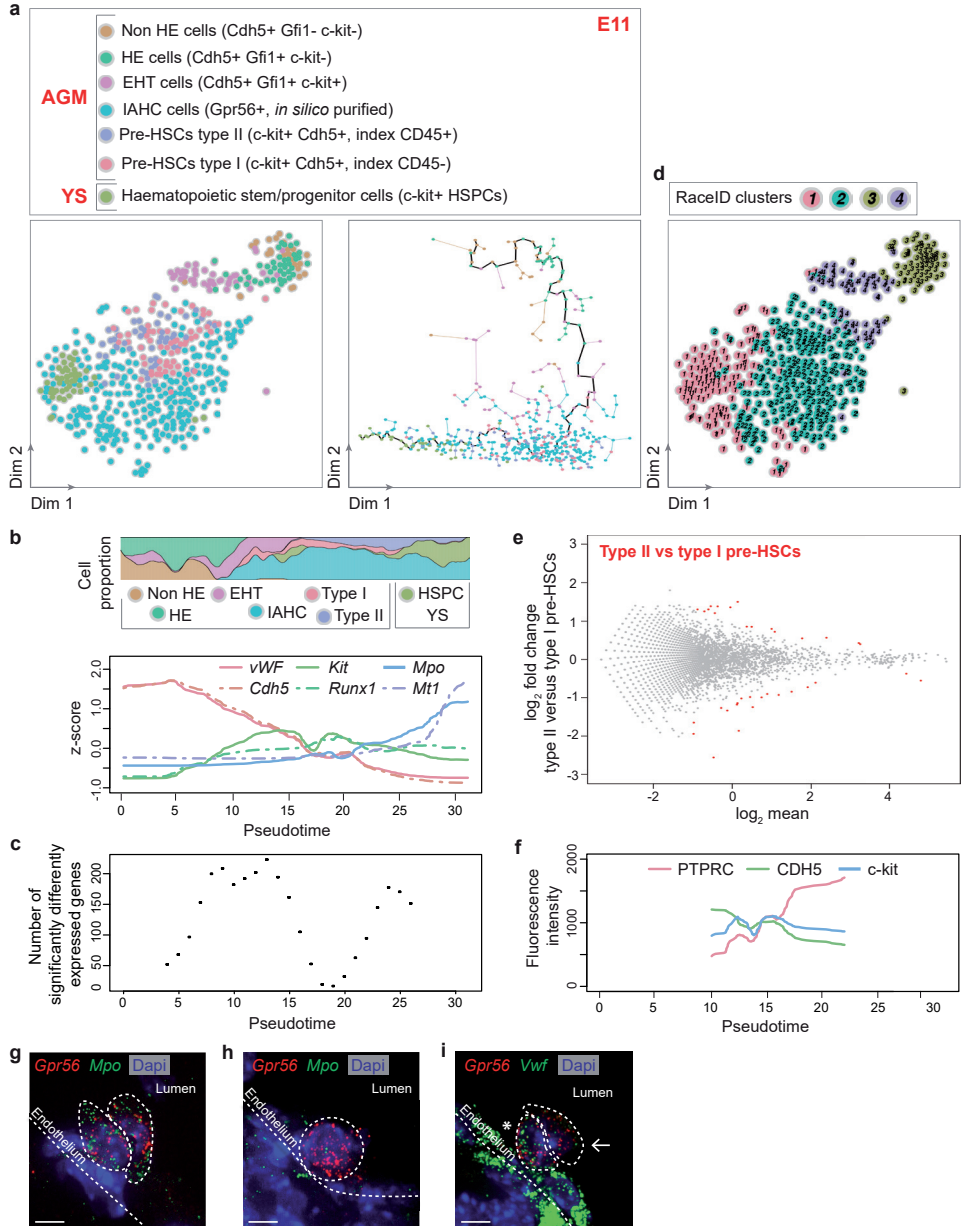


**Figure 2. Pre-HSCs and progenitors are discernible by opposing gradients of endothelial and haematopoietic transcripts in E11 IAHCs.** (a) t-SNE map of 554 single cells isolated from E11 embryo AGM and yolk sac (YS). (a, left panel) t-SNE map displaying 27 sorted non haemogenic endothelial cells (non HE cells, *Cdh5*+*Gfi1*-*c-kit*-, brown dots), 45 haemogenic endothelial cells (HE cells, *Cdh5*+*Gfi1*+*c-kit*-, green dots), 43 cells undergoing endothelial to haematopoietic transition (EHT cells, *Cdh5*+*Gfi1*+*c-kit*+, purple dots), 282 IAHC cells (turquoise dots; *c-kit*+ cells *in silico* purified based on *Gpr56* expression from Fig. 1a), and HSC precursors (58 pre-HSCs type I [*c-kit*+*Cdh5*+, index *CD45*-, pink dots] and 55 type II [*c-kit*+*Cdh5*+, index *CD45*+, violet dots] from AGMs. 44 *c-kit*+ cells were also sorted from YS (haematopoietic stem and progenitor cells, HSPCs, khaki dots). (a, right panel) Pseudotime analysis by Monocle algorithm of the cells shown in (a, left panel) (same colour code). (b) Top panel, proportion of each cell type shown in (a) along pseudotime; Bottom panel, endothelial and haematopoietic marker gene expression along pseudotime (*Vwf* [von Willebrand factor], *Cdh5* [VE-cadherin], *Kit*, *Runx1*, *Mpo* [Myeloperoxidase], *Mt1* [Metallothionein 1]). (c) Number of significantly differentially expressed genes along pseudotime. (d) t-SNE plot displaying the single cells shown in (a) in clusters identified by RaceID analysis. (e) DE-seq analysis showing the differential gene expression between type I and type II pre-HSCs (36 genes were significantly differentially expressed, red dots). (f) Fluorescence intensity of markers used to sort pre-HSCs along pseudotime (PTPRC [CD45], CDH5, *c-kit*). (g-i) E11 embryo cryosections hybridized with smFISH probes against *Gpr56* (red dots) (g-i) and *Mpo* (green dots) (g,h) or *Vwf* (green dots) (i). IAHC cells (*Gpr56*+) expressing high (asterisk) or low/no levels (arrow) of *Vwf* in (i). Dash lines delimitate the position of the aortic endothelium and IAHC cells. Dapi marks the nuclei (blue).

IAHC cells clustered with YS HSPCs (cluster 1) while the other part clustered with sorted pre-HSCs (cluster 2). Most cells in cluster 1 expressed haematopoietic markers such as *Rac2* and *Mpo* (Supplementary Fig. 6a,b) and some cells also expressed committed erythroid lineage transcripts (e.g. *Klf1*, *Gata1* and *Mt1*; Supplementary Fig. 6c-e). On the other hand, cells in cluster 2 expressed endothelial transcripts (e.g. *Vwf*, *Cdh5*, *Pecam1* (*CD31*), *Tie1* and *Eng* (*CD105*)) (17,48,49) (Supplementary Fig. 6f-j) and *Procr* (*CD201*), a gene recently described as a type I pre-HSC marker (29) that we found also highly expressed in EHT and HE cells (Supplementary Fig. 6k). This suggests the presence of two populations in IAHCs at E11, namely committed haematopoietic progenitors and pre-HSCs, which are discernible by opposing endothelial and haematopoietic signatures (Supplementary Fig. 6l). RaceID analysis also identified these two populations in IAHCs at E10 (clusters 1 (pre-HSCs) and cluster 2 (committed progenitors); Fig. 3c,d). To determine whether these populations are similar at E11 and E10, RaceID was performed on the combined dataset (Supplementary Fig. 7a,b). This showed that both E10 and E11 committed progenitors (cluster 1, cells expressing *Rac2*, Supplementary Fig. 7b,c) and E10 and E11 pre-HSCs (cluster 2, cells expressing *Cdh5*, Supplementary Fig. 7b,d) clustered together. Overall, progenitors and pre-HSCs are already present in IAHCs at E10, with a similar transcriptome than at E11.

Our scRNA-seq data were further analyzed to examine the transcriptome of type I and type II pre-HSCs in E11 IAHCs. Interestingly, the two populations clustered together (cluster 2, Fig. 2d). DE-Seq analysis (50) revealed that only 36 genes (out of 18,735 genes) were significantly differentially expressed between type I and type II pre-HSCs (Fig. 2e; Supplementary Data 1), confirming that phenotypically defined pre-HSCs (based on CD45 differential expression) are very similar at the transcriptome level *in vivo*. We then looked at the fluorescence intensities recorded during flow cytometry sorting of type I and type II pre-HSCs along the pseudotime axis (Fig. 2f). Although *Kit* expression was stable, a decreased expression of CDH5 and increased expression of PTPRC (CD45) were observed along the pseudotime axis. This therefore further validates the *in vivo* developmental order of events, with the maturation of type I pre-HSCs into type II pre-HSCs within IAHCs *in vivo*. Flow cytometry analysis also confirmed the lower abundance of phenotypically defined type I pre-HSCs at E11 compared to E10 (Supplementary Fig. 3c,f, respectively).

Zhou and colleagues recently performed scRNA-seq analysis on four populations sorted from E11 AGM based on CD31 and CD45 but also CD41 and CD201 expres-

sion (according to Zhou et al. nomenclature: t1 CD201<sup>low</sup> [CD31+CD45-CD41<sup>low</sup> c-kit+CD201<sup>low</sup>]; t1 CD201<sup>high</sup> [CD31+CD45-CD41<sup>low</sup> c-kit+CD201<sup>high</sup>]; t2 CD41<sup>low</sup> [CD31+CD45+CD41<sup>low</sup>]; t2 CD201<sup>high</sup> [CD31+CD45+c-kit+CD201<sup>high</sup>]) (29). We compared the genes differentially expressed between our cell populations (Fig. 2a) to the genes differentially expressed between their four populations. The analysis confirmed the identity of our pre-HSCs type I, which had a significant high overlap with the t1 CD201<sup>high</sup> population (enriched in pre-HSCs type I) (Supplementary Fig. 8a [left panel] and 8b [42% of genes in common]), but not with the t2 CD41<sup>low</sup> population (enriched in pre-HSCs type II) (29) (Supplementary Fig. 8a [left panel] and 8c (7% of genes in common)). The analysis also confirmed the identity of our pre-HSCs type II, which had a significant overlap with both t1 CD201<sup>high</sup> (although lower than with pre-HSCs type I) (Supplementary Fig. 8a [right panel] and 8d (27% of genes in common)) and t2 CD41<sup>low</sup> populations (Supplementary Fig. 8a [right panel] and 8e (21% of genes in common)). Accordingly, t1 CD201<sup>high</sup> cells (similar to our pre-HSCs type I) expressed *Gpr56*, *Pecam1* and *Kit* but not yet *Ptprc* (Supplementary Fig. 8f). t2 CD41<sup>low</sup> cells (similar to our pre-HSCs type II) expressed *Gpr56*, *Pecam1*, *Kit* and *Ptprc* (Supplementary Fig. 8f). As expected, our pre-HSCs had a significant overlap with AGM t2 CD201<sup>high</sup>, E12 fetal liver (Lin-Sca1+Mac1<sup>low</sup>CD201+) and adult BM HSCs (29) (Supplementary Fig. 8a). Of note, Zhou and colleagues mentioned that the t2 CD41<sup>low</sup> population was contaminated by committed progenitors (29). Indeed, this population had a significant high overlap with our progenitor cells (Supplementary Fig. 8g and 8h (21% of genes in common)). To further confirm the committed progenitor identity of cluster 1 cells (Fig. 2d), four populations were sorted from E11 AGMs and tested in clonogenic assays (c-kit+CD31+Cdh5-CD45+ and c-kit+CD31+Cdh5-CD45- cells (both in cluster 1), and c-kit+CD31+Cdh5+CD45+ and c-kit+CD31+Cdh5+CD45- cells (both in cluster 2)). All fractions produced erythroid and/or myeloid colonies (Supplementary Fig. 8i; n=6 independent experiments). However, such progenitors were highly enriched in the c-kit+CD31+Cdh5-CD45+ fraction (29.9±7.4 progenitors/100 sorted cells) (Supplementary Fig. 8j), therefore confirming that cluster 1 encompass the committed progenitors. The t1 CD201<sup>low</sup> population, shown to have no transplantation potential<sup>29</sup>, could be identified as non-IAHC cells since they highly overlap with this population (Supplementary Fig. 8k and 8l (28% of genes in common)) but not with our pre-HSCs (Supplementary Fig. 8a). Accordingly, t1 CD201<sup>low</sup> cells did not express *Gpr56* and *Ptprc* (Supplementary Fig. 8f). Altogether, our data and comparative analysis confirmed the committed progenitor identity of cluster 1 cells and the pre-HSC identity of cluster 2 cells at E11. Moreover, our datasets provide complementary information and the possibility to perform comparative analyses with previously published datasets (29), independently of the markers used for cell sorting strategy.

smRNA-FISH for *Gpr56* and *Mpo* or *Vwf* was performed on E11 embryo cryosections to localize committed progenitors and pre-HSCs in IAHCs, respectively. Cells with high amounts of *Mpo* transcripts (Fig. 2g), corresponding to committed progenitors, or with few to no *Mpo* transcripts, corresponding to pre-HSCs (Fig. 2h), were visible in *Gpr56*+ IAHCs. As expected, *Vwf* transcripts were abundantly detected in aortic endothelial cells (17) (Fig. 2i). Similar to *Mpo*, the expression level of *Vwf* in *Gpr56*+ IAHC cells was variable, with cells expressing *Vwf* transcripts being closer to the endothelium (Fig. 2i, asterisk). Overall, our analyses demonstrated that IAHCs are very similar at E10 and E11, containing pre-HSCs and committed progenitors expressing opposing gradients of endothelial (up-regulated in pre-HSCs) and haematopoietic (up-regulated in committed progenitors) transcripts.

## Non-HE and HE cells have very similar transcriptomes

To further analyse the first steps leading to IAHC formation, non-HE, HE and EHT cells were compared at both E11 and E10. RaceID analysis clustered most EHT cells together, which allows studying genes specifically expressed in this population evolving from an endothelial to a haematopoietic state. DE-Seq analysis revealed that fewer genes were differentially expressed between HE and EHT cells at E11 (370 genes) than at E10 (572 genes) (Fig. 3e; Supplementary Data 2 and 3). Interestingly, some pre-HSCs and HE cells clustered with EHT cells at both E11 (cluster 4, Fig. 2d) and E10 (cluster 1, Fig. 3c), reflecting the continuum of differentiation occurring between these successive related populations.

RaceID analysis clustered non-HE and HE cells together at E11 (cluster 3, Fig. 2d) but not at E10 (clusters 4 and 3, respectively, Fig. 3c). However, DE-Seq analysis showed that very few genes were differentially expressed between non-HE and HE cells at both time points (30 and 109 genes at E11 and E10, respectively; Fig. 3f, Supplementary Data 4 and 5). Nevertheless, some genes were nicely significantly differentially expressed in between non-HE, HE, EHT cells and IAHC cells. For example, at both E10 and E11, non-HE cells expressed *Mgp* while HE cells did not (Supplementary Fig. 9a). Furthermore, non-HE and HE cells expressed *Epas1* and *Id3* transcripts while EHT cells did not (Supplementary Fig. 9b,c). On the other hand, only EHT cells expressed *Mycn* transcripts (Supplementary Fig. 9d). To reinforce the relevance of the genes highlighted in our study, we performed different immunostaining techniques on AGM cells from E10 or E11 embryos for a selection of three new markers. IKZF2 (Helios), PROM1 (CD133) and GJA5 (Connexin 40) were chosen for their differential expression in our populations of interest (endothelium versus IAHC cells) and for the commercial availability of antibodies. As predicted by our scRNA-seq data, IKZF2 was much highly expressed at the protein level in c-kit+CD31+ IAHC cells (86.6%) than in endothelial cells (15.8%), as shown by flow cytometry analysis (Supplementary Fig. 10 a,b). On the other hand, PROM1 and GJA5 were expressed by CD31+ endothelial cells but not by IAHC cells (c-kit+CD31+ or Runx1+CD31+ cells, Supplementary Fig. 10c-g [immunostaining on E11 live thick embryo slices] and Supplementary Fig. 10h-l [immunostaining on E10 embryo cryosections], respectively). Therefore there is a good correlation between scRNA-seq data and protein expression, which consolidates our datasets. Such datasets will be useful to study the functionality of specific genes of interest in specific populations of the aorta or to test their usefulness as new surface markers for specific cell isolation in the future.

To identify the pathways active in the aortic populations, we performed a KEGG pathway analysis on our E11 dataset. As expected, specific genes related to the BMP pathway (e.g. *Bmp4*, *Bmpr1a*, *Bmpr2*, *Smad 6*, *Smad 7*), Notch pathway (e.g. *Dll1*, *Dll4*, *Notch1*, *Notch 3*, *Notch 4*, *Jag1*) and mTORC2 pathway (e.g. *Rictor*, *mTor*, *Deptor*, *Tti1*) were expressed. We then examined in more details the KEGG cytokine pathway. A heatmap was generated where genes present in each cytokine pathway (according to KEGG analysis) were on the y-axis and E11 single cells (ordered along the pseudotime axis) were on the x-axis (Supplementary Fig. 11a). It revealed the dynamic expression of some known important regulators, including c-kit (51) and IL-3 (through IL-3R) (26). Three groups of cytokines/growth factors were more active in endothelium, IAHC cells or committed progenitors. A KEGG pathway analysis performed on these three datasets highlighted the involvement of interleukins, TGF, chemokines and/or BMP in the endothelium and IAHC cells (Supplementary Fig. 11b,c). Pathways involving hemostasis and cell surface interactions at the vascular wall were active in the committed progenitor group, possibly reflecting the detachment of these cells to the circulation (Supplementary Fig. 11d). Molecules involved in the immune system/

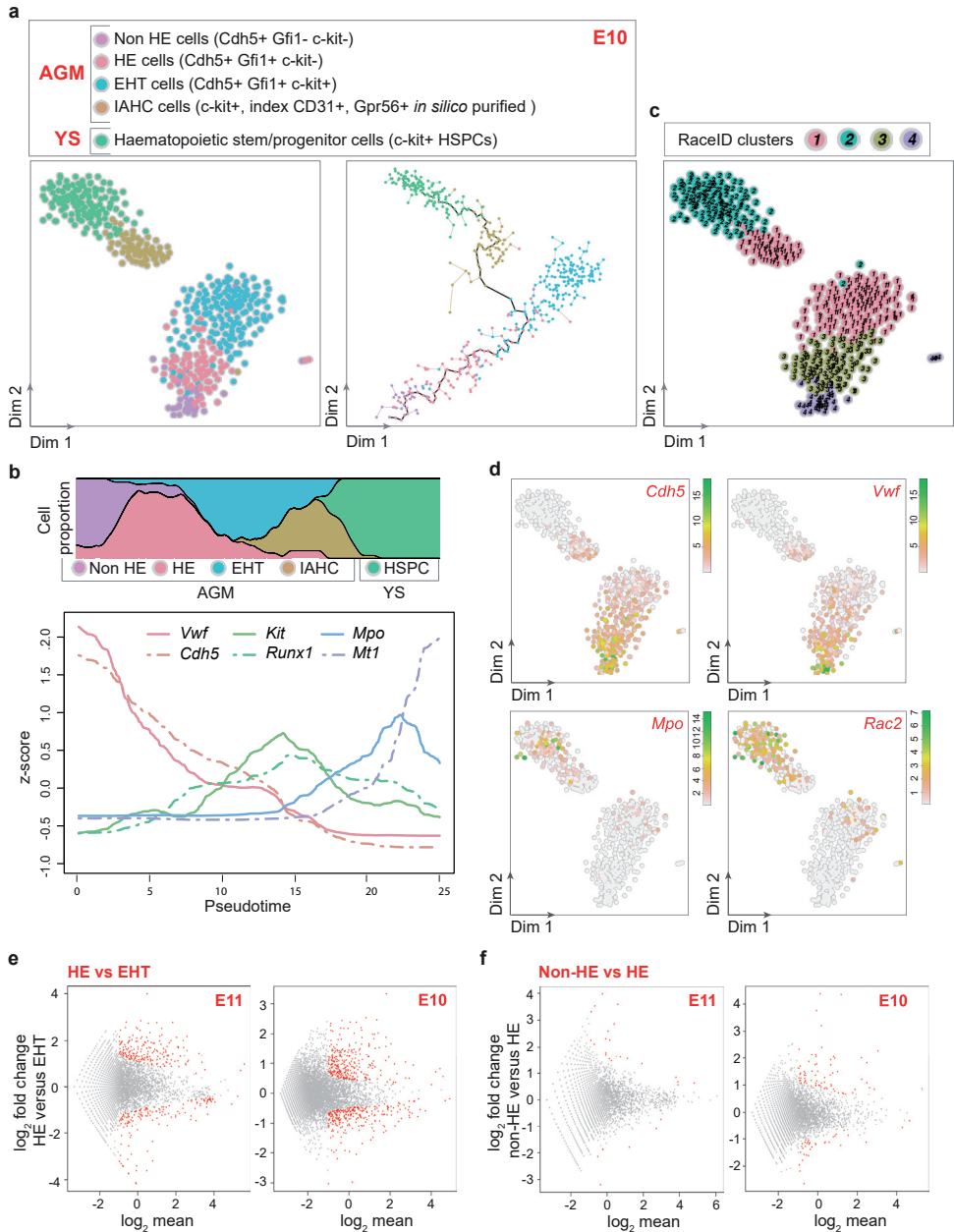


**Figure 3. Non-HE and HE cells have different transcriptome at E10.** (a) t-SNE map displaying 464 single cells isolated from E10 embryo AGM. (a, left panel) t-SNE map displayed 39 sorted non hemogenic endothelial (HE) cells (purple dots), 96 HE cells (pink dots), 116 EHT cells (blue dots) and 73 IAHC cells (*in silico* purified on Gpr56 expression; brown dots) from E10 AGM, and 140 HSPCs from E10 YS (green dots). (a, right panel) Pseudotime analysis by Monocle algorithm of the sorted cells shown in (a, left panel) (same colour code). (b) Top panel, proportion of each cell type shown in (a) along pseudotime; Bottom panel, endothelial and haematopoietic marker gene expression along pseudotime (*Vwf*, *Cdh5*, *Kit*, *Runx1*, *Mpo*, *Mt1*). (c) t-SNE plot displaying single cells from (a) in clusters identified by RaceID analysis. Different numbers and



colours highlight different RaceID clusters. (d) Expression of *Cdh5*, *Vwf*, *Mpo* and *Rac2* marker genes projected on t-SNE maps. Colour bars, number of transcripts. Dim, dimension. (e) DE-seq analysis showing the differential gene expression between HE and EHT cells at E11 (e, left panel, 370 genes significantly differentially expressed, red dots) and E10 (e, right panel, 572 genes). (f) DE-seq analysis showing the differential gene expression between non-HE and HE cells at E11 (f, left panel, 30 genes) and E10 (f, right panel, 109 genes). Non-significantly differentially expressed genes, grey dots.

inflammation were also active in the three groups (i.e. TNF, IL-6), in accordance to the literature where the inflammatory process was recently reported as an important key regulator of HSC development (52). Our datasets will be useful to investigate in the future the requirement for specific cytokines and growth factors at specific time points during endothelial specification and HSC characteristic acquisition.

### TF network involved in IAHC formation at E11 and E10

To get insight in the transcriptional program involved in EHT and IAHC formation, we analysed the expression profiles of all TFs expressed in our datasets (53). 127 and 88 TFs were detected at E11 and E10, respectively (Supplementary Fig. 12a and 13a). Hierarchical clustering of the expression profiles identified three distinct clusters of TFs (I, II and III), with their expression peaking in early, intermediate and late pseudotime, respectively (Fig. 4a (E11) and 4b (E10)). Cluster I contained TFs highly expressed in endothelial cells (e.g. *Sox17*, *Hey2*) (54,55) (Fig. 4a,b; Supplementary Fig. 12b,c and 13b,c) and TFs up-regulated in HE cells (e.g. *Elk3*, *Jun*, *Mecom*) (37). Gene Set Enrichment Analysis (GSEA) indicates that cluster I TFs were involved in processes such as the regulation of vasculature development, vasculogenesis or dorsal aorta morphogenesis (Supplementary Fig. 12d and 13d). Cluster II contained TFs expressed in EHT cells and pre-HSCs (Fig. 4a,b). GSEA indicates that these TFs were involved in stem cell differentiation, haematopoiesis or in the regulation of stem cell maintenance (e.g. *Gfi1*, *Sfpi1*, *Dnmt3a*, *Ikzf2*) (37,44) (Supplementary Fig. 12e-g and 13e-g). Finally, cluster III contained TFs that were up-regulated in IAHC pre-HSCs and/or progenitors and YS HSPCs (Fig. 4a,b). These TFs were involved in definitive haematopoiesis, negative regulation of cell growth, as for example *Zfpml1*, which is involved in megakaryocytic and erythroid differentiation (Supplementary Fig. 12h-j and 13h-j). Of note, a large proportion of TFs were common between E10 and E11 in each cluster (48.6% in Cluster I, 33.4% in Cluster II and 30.3% in Cluster III) (Fig. 4c).

Transcriptional regulatory networks were built based on the Pearson correlations between all TFs at E11 and E10 (Fig. 4d and e, respectively). The TFs up-regulated in non-HE and HE cells highly correlated with each other and with some of the TFs up-regulated in EHT cells that still had an active endothelial program. The rest of TFs up-regulated in EHT cells correlated with TFs up-regulated in IAHC pre-HSCs, and were most likely involved in the initiation of the haematopoietic program. Finally, some TFs up-regulated in IAHC pre-HSCs correlated with TFs up-regulated in YS HSPCs that exhibited a strong haematopoietic signature. Overall, the TF regulatory networks can be used to explore the TFs involved in the continuous progression of non-HE to HE cells to EHT cells and finally into IAHC resident pre-HSCs and progenitors.

### Ventral and dorsal IAHCs have similar transcriptomes

Mouse embryos differs from other vertebrate embryos by the presence of IAHCs in both ventral and dorsal sides of the aorta (10). To compare the transcriptome of IAHCs according to their position within the aorta (ventral versus dorsal side), we



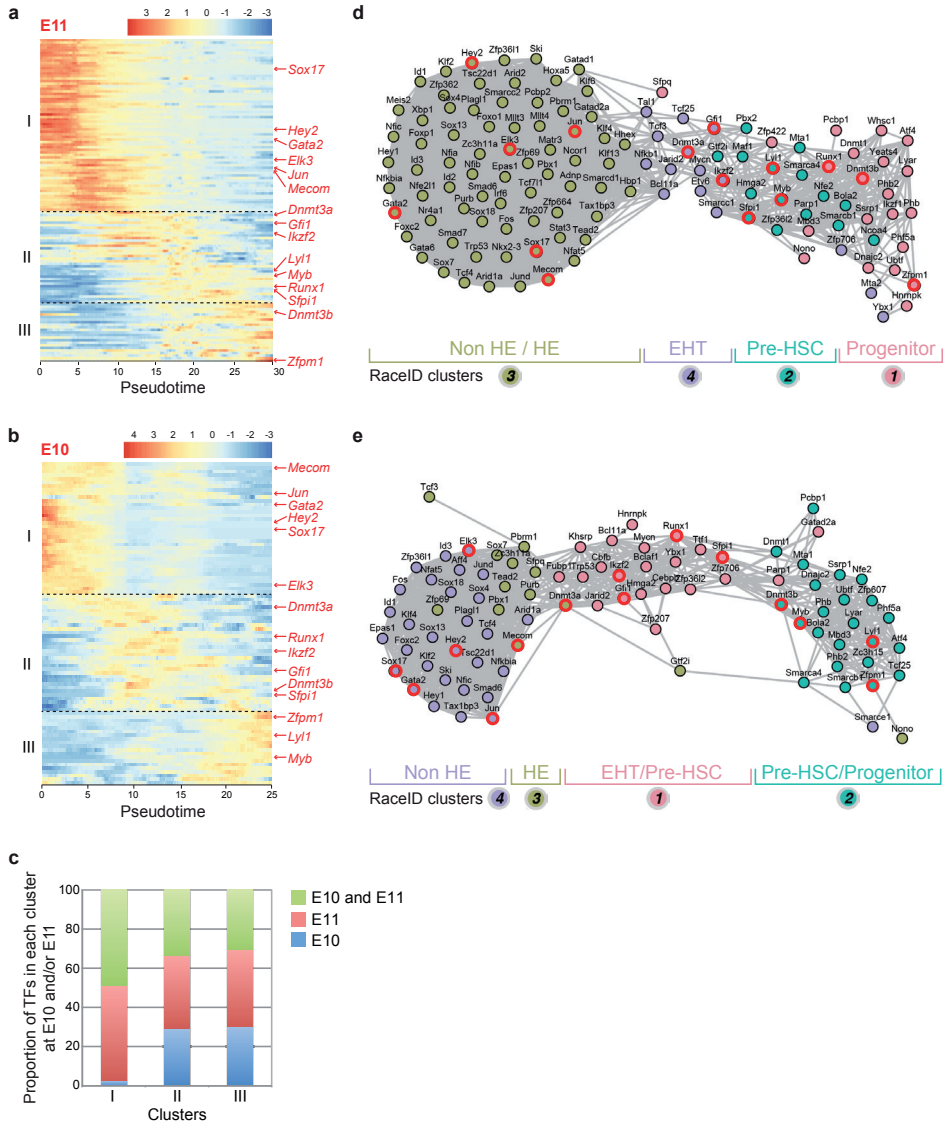


**Figure 4. Transcription factor networks involved during IAHc formation at E11 and E10.** (a,b) Heatmap of differentially expressed transcription factors (TFs) at (a) E11 and (b) E10 between the different cell types (non HE, HE, EHT, IAHc cells and YS HSPCs), according to pseudotime. Three distinct expression patterns are identified as clusters I, II and III. (c) Proportion of transcription factors that are present in clusters I, II or III at both E10 and E11, only at E11 or only at E10. (d,e) Network of TFs related to different expression patterns as determined in (a) and (b), respectively. Colour-coded circles are related to RaceID analysis shown in Fig. 2d and 3c, respectively. TFs mentioned in the results section are outlined in red.

developed a new technique to mechanically pick-up single whole IAHcs (wIAHCs) in the aorta of E10 and E11 embryo slices (Fig. 5a,b). An automated cell picker (CellCelector™) (Supplementary Fig. 14a) was used to aspirate single c-kit+ wIAHCs directly from thick embryo slices (Fig. 5c-d). wIAHCs were then placed in a drop of medium (Fig. 5e,f), picked-up a second time to isolate pure wIAHCs (Fig. 5g) and

finally dropped in a tube cap for scRNA-seq (Supplementary Fig. 14b-f; see Methods for details). To determine the purity of the single wIAHCs and therefore to validate the isolation procedure, the transcriptome of single wIAHCs and single aortic cells (Fig. 1b) were correlated (Supplementary Fig. 14g). The analysis showed that wIAHCs were not contaminated with non-IAHC cells, as it was the case for IAHC cells sorted by flow cytometry. Then, the contribution of each RaceID cluster (Fig. 2d (E11); Fig. 3c (E10)) to each picked wIAHC was calculated. At both E11 and E10, all single wIAHCs were solely composed of IAHC and EHT cells (Fig. 5h,i, respectively). No or negligible endothelial contribution to wIAHCs was observed at E11 and E10. Therefore, our technique allows the isolation of pure single wIAHCs at both E10 and E11, without contamination by non-IAHC cells or endothelial cells.

The transcriptome of E11 and E10 single wIAHCs was then correlated to the transcriptome of E11 and E10 single aortic cells ordered along the pseudotime axis (Fig. 5j-m). At E11, single wIAHCs were projecting mainly between pseudotime points 15 and 25 where IAHC pre-HSCs were present (Fig. 5j,l). At E10, wIAHC projected mainly between pseudotime points 10 and 20 where EHT and IAHC cells were located (Fig. 5k,m). Of note, the number of cells per single wIAHCs (numbers close to the y-axis inside the graph shown in Fig. 5j,k) did not influence their cell composition at both E10 and E11, meaning that larger wIAHCs were not enriched in a specific cell type but were composed of a more heterogeneous group of cells. Overall, wIAHCs are mainly composed of pre-HSCs with less haematopoietic progenitors and EHT cells as embryonic development progresses.

We then compared the transcriptome of ventral and dorsal wIAHCs collected at E10 and E11 (Supplementary Fig. 14f) by clustering on the correlations. Most wIAHCs had similar transcriptome (Fig. 6a). Only three wIAHCs had a low correlation to the rest of wIAHCs (Fig. 6a, bottom left corner of the heatmap). These three wIAHCs had high expression levels of haemoglobin genes, suggesting that they mainly contained erythroid progenitors. DE-Seq analysis was then performed to determine the differentially expressed genes between E11 and E10 ventral and dorsal wIAHCs. Interestingly, only very few genes (out of 18,735 genes) were found differentially expressed (51 genes between E11 and E10 dorsal wIAHCs (Fig. 6b; Supplementary Data 6); 199 genes between E11 and E10 ventral wIAHCs (Fig. 6c; Supplementary Data 7); 2 genes between E11 ventral and dorsal wIAHCs (Fig. 6d; Supplementary Data 8); 16 genes between E10 ventral and dorsal wIAHCs (Fig. 6g; Supplementary Data 9)). In agreement with these data, the contribution of E11 single IAHC cells (Fig. 2d) to E11 ventral and dorsal wIAHCs (Fig. 6e,f, respectively) was similar, with a majority of pre-HSCs. The contribution of E10 single aortic cells (Fig. 3c) to E10 ventral and dorsal wIAHCs (Fig. 6h,i, respectively) demonstrated that pre-HSCs, progenitors and EHT cells similarly contributed to both ventral and dorsal E10 wIAHCs. Overall, our analysis revealed that ventral and dorsal wIAHCs are very similar in term of cellular composition and transcriptome at both E10 and E11. Most transcriptome changes occurred in ventral wIAHCs between E10 and E11, suggesting that these genes might be involved in the pre-HSC maturation process.

## Discussion

The molecular events regulating endothelial specification, IAHC formation and their consecutive maturation into HSCs remain poorly understood. Using scRNA-seq, we established that IAHCs contain pre-HSCs and committed progenitors (similar to the ones found in YS). The spatial and temporal comparison of single aortic cells (*in silico* purified IAHC cells, non-HE and HE cells, cells undergoing EHT) and dorsal/ventral wIAHCs revealed that most transcriptome changes occur between E10 and

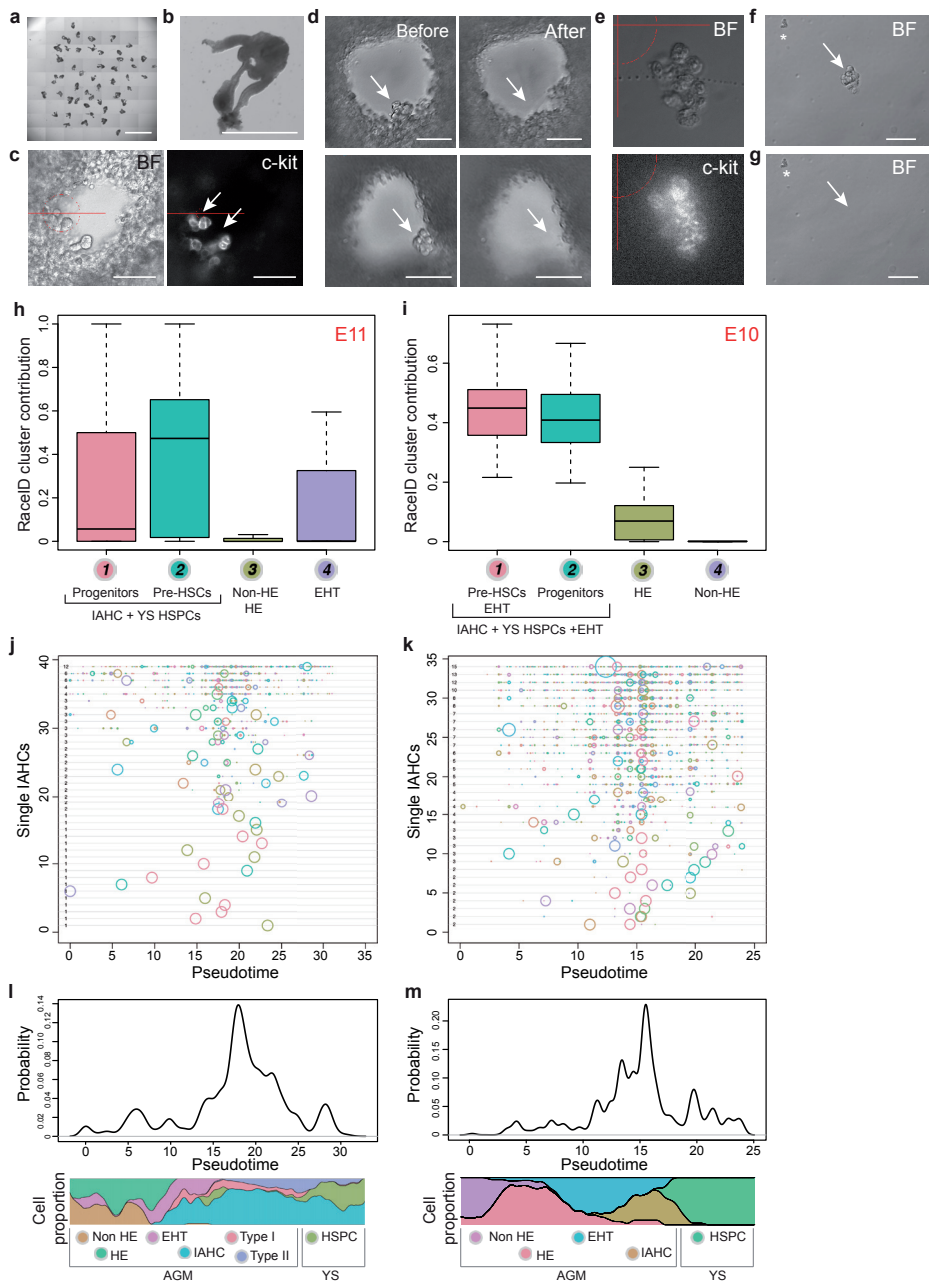


**Figure 5. Transcriptome comparison of pure whole IAHCs mechanically picked-up inside the aorta.** (a) E10 embryo slices embedded in agarose. Scale bar, 5 mm. (b) Close-up showing an embryo slice. Scale bar, 1 mm. (c) Close-up showing *c-kit*<sup>+</sup> IAHCs attached to the aortic endothelium of an E10 embryo slice (left panel, bright filter (BF); right panel, *c-kit* fluorescence). Scale bar, 50  $\mu$ m. (d) Two examples (upper and lower panels) of single IAHCs mechanical pick-up. Before pick-up, IAHCs were attached to the ventral side of the aorta (left panel, arrow). After pick-up, IAHCs were no longer visible in the aorta (right panel, arrow). (e) Example of a single mechanically picked-up IAHC (whole IAHC or wIAHC). Upper panel, BF; lower panel, *c-kit* fluorescence. (f) Presence of a wIAHC (arrow) and contaminating single cells (asterisk) after

wIAHC first pick-up. (g) The wIAHC was picked-up a second time to eliminate the contaminating cells that remained in the medium drop (asterisk). (h,i) Box plots showing the RaceID cluster contribution to E11 (h) and E10 (i) wIAHCs. Colour-coded boxes are related to RaceID analysis shown in Fig. 2d and Fig. 3c, respectively. (j,k) Probability for each cell to contribute to single wIAHCs at E11 (j) and E10 (k). Each horizontal line depicts a single wIAHC. The size of the circle is proportional to the probability for the cell at that position in pseudotime to contribute to that particular wIAHC. The number (next to the y-axis, inside the graph) depicts the total number of cells present in that particular wIAHC. (l,m) Probability density along pseudotime for contributing to wIAHCs.

E11 (in ventral IAHCs), concomitant with EHT and pre-HSC maturation. We provide here an unprecedented resource to study in great details the genes expressed or repressed during endothelial haemogenic specification, EHT, IAHC formation and pre-HSC maturation towards a HSC fate, as it originally occurs *in vivo* in the aorta of the mouse embryo.

To determine the transcriptome of IAHC cells, cell isolation to high purity is required. However, isolating an entire IAHC cell population to purity was technically impossible. Therefore, precautions must be taken when analyses are performed on bulk cell measurements, as it does not take into account cell heterogeneity. Consequently, data might reflect the molecular content of contaminating cells (from the mesenchyme or circulating blood) rather than IAHC cells per se. Nevertheless, scRNA-seq appeared as an excellent tool to *in silico* purify IAHC cells based on the expression of known IAHC transcripts such as *Gpr56* (37).

We performed scRNA-seq to study cell and gene expression heterogeneity in IAHCs at single-cell resolution (56-58), since it has been previously successfully used to examine the transcriptome of rare cell populations (34,59-61). The comparative transcriptome analysis of *in silico* purified IAHC cells, sorted AGM pre-HSCs and YS HSPCs, as well as clonogenic experiments, directly addressed the controversial question about the cell composition of IAHCs. Indeed, the discrepancies reported so far about IAHCs were inherent to the different approaches used in different laboratories, the *in vitro/in vivo* assays being ultimately limited. Moreover, most studies analysed total AGM or subdissected aorta cells but rarely the IAHC population itself. We found that IAHCs contain committed progenitors and pre-HSCs (in accordance to our previous findings (8)), and more surprisingly also EMP-like cells. EMPs were described so far only in the YS between E8.5 and E11.5 (41,43). Since EMPs circulate in the blood stream between E10.5 and E12.5 and the EMP-like cells we observed do not express *Gpr56* (and do not cluster with committed progenitors), these cells are most likely circulating YS EMPs that attached to IAHCs and were subsequently picked-up in our analysis. Whether the other progenitors (identified in the clonogenic assay and scRNA-seq analysis) emerged inside the aorta or originated from the YS (as EMPs) and attached to IAHCs while passing through the blood stream remains difficult to ascertain. Others and we have previously demonstrated the presence of few pre-HSCs in IAHCs (~12-18 pre-HSCs/aorta), capable of long-term multilineage reconstitution upon direct transplantation in neonates (8) or in adult wild type recipients after 6 days of co-culture on stromal cells (29). However a large number of type I and type II pre-HSCs, able to produce transplantable HSCs, have been identified *in vitro* in dissociated/reaggregated culture of E10.5/E11.5 AGMs (30,31,51). Based on immunostaining observations, IAHCs seem to mostly contain type II pre-HSCs (type I pre-HSCs localizing mainly to the aorta subluminal area) (30,31). However, scRNA-seq data revealed that both type I and type II pre-HSCs are present in IAHCs, as recently reported (47). Maturing pre-HSCs accumulated at E11, with less type I pre-HSCs at E11 than at E10. Finally, type I and type II pre-HSCs have a very similar transcriptome (only 36 genes differentially expressed out of 18,735 genes). Future research will be necessary to determine whether some of these genes might be involved in pre-HSC

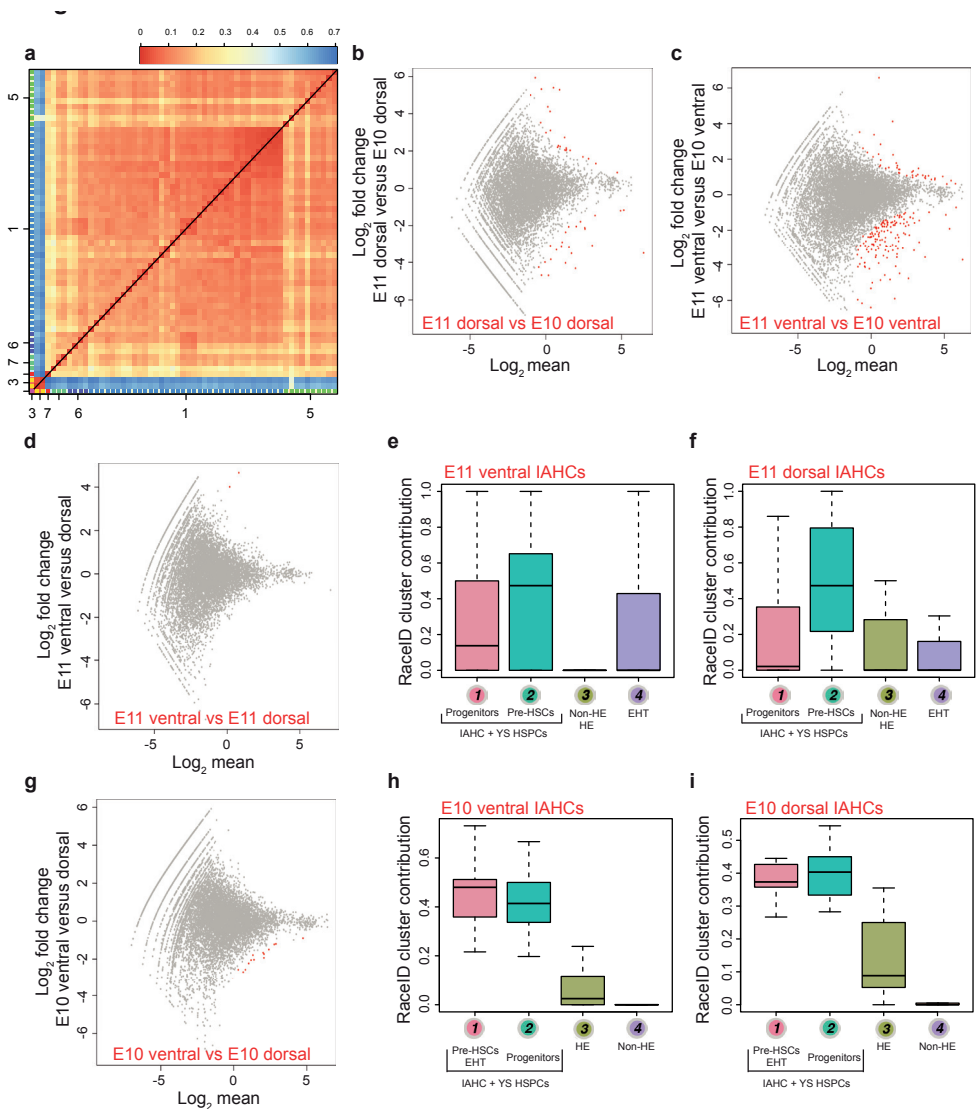


**Figure 6. Ventral and dorsal wIAHCs have a similar transcriptome at E10 and E11.** (a) Heatmap representing the transcriptome similarities measured by the Euclidean distance of the transcriptome correlation matrix for single E10 and E11 wIAHCs. Cluster numbers are shown along the axis for the major clusters. (b-d.g) DE-seq analysis showing the differential gene expression between E11 and E10 dorsal wIAHCs (51 genes significantly differentially expressed as shown by red dots) (b), between E11 and E10 ventral wIAHCs (199 genes) (c), between E11 ventral and dorsal wIAHCs (2 genes) (d) and between E10 ventral and dorsal wIAHCs (16 genes) (g). (e, f) Box plots of the RaceID cluster contribution to E11 ventral (e) and dorsal (f) wIAHCs. Colour-coded boxes are related to RaceID analysis shown in Fig. 2d. (h, i) Box plots of the RaceID cluster contribution to E10 ventral (h) and dorsal (i) wIAHCs. Colour-coded boxes are related to RaceID analysis shown in Fig. 3c.

maturation and/or the acquisition of transplantation potential.

Transcriptome comparison of wIAHCs, according to their location inside the aorta (ventral versus dorsal side) at different time points in development, was impossible thus far. The challenge was to access wIAHCs in situ and to detach them from the aortic endothelium without cell damage, wIAHC integrity loss and/or cell contami-



nation (from the surrounding endothelium and mesenchyme tissue). Our mechanical picking technique inside the aorta of non-fixed thick embryo slices allowed the isolation of single and pure wIAHCs. Functional analysis of the sub-dissected aorta initially revealed that HSC activity was restricted to the ventral side of the aorta while clonogenic haematopoietic activity was associated with both ventral and dorsal sides (10). However, the presence of pre-HSCs and functional HSC activity in both dorsal and ventral side of the aorta was recently reported (62). Accordingly, we found very few differences in the transcriptome of ventral and dorsal wIAHCs (at both E10 and E11). In agreement with our comparative analysis of single IAHC cells, most transcriptional changes were observed between E10 and E11, mainly in the ventral wIAHCs, which is concomitant with pre-HSC maturation.

More transcriptome changes occurred at E10 (compared to E11) between non-HE, HE and EHT cells, with more than 500 genes differentially expressed between HE and EHT cells. EHT cells also largely contributed to wIAHCs at E10. One could hypothesize that EHT is particularly active at E10, which would be consistent with the number of IAHC cells peaking at E10.5 (9) and the emergence of proliferating type I pre-HSCs at E10.5 (32,47). Further analysis will be needed to determine which genes among those might be involved in the induction of a haemogenic potential in endothelial cells and subsequent EHT. The transcriptional changes, associated with the progressive down-regulation of the endothelial program and up-regulation of the haematopoietic program, were increased in EHT cells. The endothelial to haematopoietic switch, needed for haematopoietic commitment, has been previously reported by performing a functional and transcriptional analysis of single 23GFP+ HE cells (isolated from *Runx1*+23 enhancer-reporter transgenic embryos) (63). The switch initiated before the detection of HSCs in E9.5 CD41- 23GFP+ HE cells that were still embedded in the endothelial wall, strongly suggesting that haematopoietic specification occurs before EHT. One explanation would be that successive transcriptional switches take place (e.g. in HE cells, EHT cells, pre-HSCs), all being necessary to complete full HSC fate commitment and maturation.

How regulatory programs control cell decision towards a HSC fate remains a central question. The fundamental finding that all HSCs derive from specialized HE cells during embryonic development has paved the way to improve the generation of HSC-like cells *in vitro* (1,46,64). More recently, mouse adult endothelial cells (2) and human pluripotent stem cells (3) were converted into transplantable HSCs (via a HE intermediate) by enforced expression of selected TFs and usage of a vascular niche. Interestingly, we found a very similar expression pattern of the TFs used in the above-mentioned studies by looking at our transcriptional regulatory networks and the one from Zhou *et al.* (29). As expected, *Runx1*, *Spi1* and *Gfi1* were expressed in EHT cells and most cluster cells (pre-HSCs and/or progenitors). However, some TFs were either weakly (*Hoxa5*, *Hoxa9*, *Hoxa10*, *Fosb*) or not (*Erg*, *Lcor*) detected. TF requirement might differ *in vivo* and *in vitro* because the culture conditions developed to generate HSCs *in vitro* do not recreate a complete *in vivo* microenvironment but instead reproduces few of its elements so far (e.g. addition of cytokines or vascular-niche-derived angiocrine factors, activation/inhibition of specific pathways) (2,3). Shear stress and 3D cell-cell contact are also obvious regulatory elements that are not (yet) optimally reproduced *in vitro*. Therefore, some TFs might be needed *in vitro* but not *in vivo* due to a redundant role with other TFs *in vivo*. On the other hand, some factors that need to be discovered are obviously still missing to obtain the generation of HSCs that are fully functional and molecularly similar to bona fide HSCs. Studying gene expression in the physiological context of the aorta is thus essential to understand the *in vivo* context of HSC production and to lead the way to improve *in vitro* HSC production. In conclusion, we provide here a reliable resource of data available for the scientific



community to further explore the key factors and pathways involved in the initiation of the HSC program as it occurs physiologically in the aorta *in vivo*. It is of crucial importance to improve the challenging HSC production *in vitro* for clinical transplantation purpose.

## Methods

### Embryo generation

Wild type mouse embryos were generated from timed matings between C57BL/6 females and males (> 8 weeks). Observation of vaginal plugs was considered as embryonic day (E)0 of development. Animals were housed according to institutional guidelines, and procedures were performed in compliance with Standards for Care and Use of Laboratory Animals, with approval from the Dutch Animal Experiment Committee. Wild type ICR females were mated to *Gfi+tomato/ Gfi1b+/GFP* males (ICR strain) (44). All animal work in Manchester was performed under regulations governed by UK Home Office Legislation under the Animals (Scientific Procedures) Act 1986 and was approved by the Animal Welfare and Ethics Review Body (AWERB) of the Cancer Research UK Manchester Institute.

### Embryonic tissue isolation

Embryos surrounded by the YS were removed from the mother uterus. YS were carefully collected and vitelline vessels were cut off. Embryos were precisely staged according to the day of isolation, the number of somite pairs (sp) and/or based on Thelie criteria. Embryos were collected at embryonic day (E)10 (between 28 and 32 sp) and E11 (>40 sp) of development in PBS supplemented with 10% of Foetal Calf Serum and 5% of Penicillin/Streptomycin (PBS/FCS/PS). The blood was flushed away by injecting PBS/FCS/PS with a glass capillary directly inside the aorta of the embryo trunk, after removal of the head and tail<sup>33</sup>.

### Flow cytometry analysis and cell sorting

\* IAHC cells were stained by using different procedures (Supplementary Fig. 1). For the total staining procedure (TS) (Supplementary Fig. 1a), Aorta-Gonad-Mesonephros (AGM) regions were dissected, pooled and dissociated by collagenase treatment (0.125% collagenase type I in PBS/FCS/PS) for 1 hour at 37°C. After dissociation, cells were washed, stained with PE anti-c-kit (CD117) antibodies (BD Pharmingen, 553355, 1/100) and sorted. For the intra-aorta staining procedure (IAS) (Supplementary Fig. 1b,c), embryos were injected with PE anti-c-kit antibodies (and/or AF647 anti-PECAM (CD31) antibodies [BioLegend, 102516, 1/100], CD31 index sorting (65)) directly inside the aorta (12,33). Non-injected embryos were used as control. After 30 minutes of staining, AGMs were dissected, pooled and dissociated by collagenase treatment for 1 hour. After dissociation, cells were washed and kept on ice for further analysis. For the c-kit mesenchymal staining (Supplementary Fig. 1e), PE anti-c-kit antibodies were directly injected inside the aorta. AGMs were then dissected and digested, and cells were washed and further stained with FITC anti-CD31 (BD Pharmingen, 553372, 1/100), FITC anti-CD45 (BD Pharmingen, 553080, 1/200) and APC anti-c-kit (BD Pharmingen, 553356, 1/400) antibodies for 30 minutes. Cells were then washed and kept on ice for further analysis.

\* For clonogenic assays, PE anti-c-kit and FITC anti-CD31 antibodies were directly injected inside the aorta. AGMs were then dissected and digested, and cells were washed and further stained with APC anti-CD45 (BD Pharmingen, 559864, 1/300) and PE-Cy7 anti-Cdh5 (CD144, BioLegend, 138015, 1/200) antibodies.

\* For type I and type II pre-HSCs isolation, APC anti-c-kit antibodies were directly

injected inside the aorta. AGMs were then dissected and digested, and cells were washed and further stained with FITC anti-CD45 and PE anti-Cdh5 (eBioscience, 12-1441-82, 1/40) antibodies for 30 minutes at 4°C (CD45 index sorting).

\* YS cells were stained after enzymatic digestion with PE anti-c-kit antibodies for 30 minutes at 4°C.

\* For non-HE, HE and EHT cells, AGMs were dissected, digested and cells were stained with APC-eFluor780 anti-c-kit (eBioscience, 47-1171-82, 1/200), APC anti-Cdh5 (eBioscience, 17-1441-82, 1/200) and PerCP Cy5.5 anti-CD45 (BioLegend, 103132, 1/200) antibodies for 30 minutes and washed (44).

\* For intra-cytoplasmic staining, cells were stained in surface with APC anti-c-kit and FITC anti-CD31 antibodies for 30 minutes, washed, fixed and permeabilised with BD Cytofix/Cytoperm solution kit according to the manufacturer's instructions (Thermo Fisher) and then stained with PE anti-Ikzf2 (BioLegend, 137206, 1/100).

For all sort and flow cytometry analysis, Hoechst or 7AAD was added to exclude dead cells (except for intra-cytoplasmic staining). Cells were analysed or sorted with a FACSCalibur and an Aria III flow cytometer (BD Biosciences), respectively.

### **Mechanical pick-up of single wIAHCs**

Single whole (w)IAHCs were mechanically picked-up by using a CellCelector™ (A.L.S) (Supplementary Fig. 14a). This micromanipulation system combines a motor-operated inverse microscope with a precise robot system to harvest, image, and store parameters and images (e.g. before and after pick-up). The robot platform is equipped with a harvesting module (Supplementary Fig. 14b), usually used to isolate single cells or cell colonies with high precision (66,67). We adapted the automated robotic system for wIAHC pick-up and manually calibrated the machine by defining parameters for optimal pick-up (e.g. volume and speed for aspiration and for tipping out the harvested material).

The blood was flushed away from the aorta of non-fixed embryo trunk and IAHC cells were stained by intra-aorta injection of anti-c-kit antibodies (12, 33). Embryo trunks were then transversally cut in thick slices of 200µm with a tissue chopper to visualize c-kit+ IAHC cells inside the aorta (Fig. 5a-c). Slices were transferred into the well of a 6-well plate and immobilized with 0.7% low melting point agarose. When polymerized, the agarose gel was covered with PBS/FCS/PS. The 6-well plate was placed on the motor-operated stage of an inverse Olympus microscope connected to a high definition CCD Olympus camera and to the robotic platform of the CellCelector™. All embryo slices were manually screened for the presence of c-kit+ IAHCs (Fig. 5c). Bright field and fluorescence images of embryo slices were taken before and after each wIAHC pick-up (two before/after pick-up examples are shown in Fig. 5d). All pictures and picture information were transmitted to the imaging software and stored. wIAHCs were mechanically harvested one by one, by gentle aspiration with a calibrated glass capillary (Micropipets, Origio Inc.) containing PBS and connected to a syringe placed on a robotic arm (SingleCell-modul) (Supplementary Fig. 14b,c). The aspirated IAHC was then automatically transported to an empty well of a 6-well plate (Supplementary Fig. 14d, left red arrow; Fig. 5e). The deposit drop was screened for pick-up control (e.g. wIAHC integrity, no apparent contaminating cells attached). To avoid any contamination of the collected sample (c-kit+ wIAHC; Fig. 5f, arrow) with c-kit- cells that might detach from the embryo slice during aspiration (Fig. 5f, asterisk), a second pick-up was performed (Supplementary Fig. 14d, right red arrow; Fig. 5g, arrow). For this step, single wIAHCs were transferred directly in the cap of a 0.2ml tube (Supplementary Fig. 14e) that was immediately closed, spun down and stored at -80°C. wIAHCs were collected at E10 and E11 in the ventral and dorsal side of the aorta for sc-RNA-seq (Supplementary Fig. 14f).

### **RNA extraction from single IAHC cells and single wIAHCs**

Single cells were sorted in the wells of 96-well PCR plates, each well containing 100  $\mu$ l of TRIzol reagent and 0.2  $\mu$ l of a 1:250,000 dilution of ERCC spike ins (Thermo Fisher). wIAHCs were collected after pick-up in tubes containing the above solution. Total RNA was extracted from single cells, according to TRIzol manufacturer's instructions (Thermo Fisher) with few alterations. GlycoBlue reagent (0.2  $\mu$ l) was added to each sample to facilitate RNA precipitation. After overnight isopropanol precipitation, RNA pellets were air dried for up to 15 minutes, and suspended in CEL-Seq first-strand primer solution.

### **CEL-Seq library preparation**

Single wIAHCs and single cells were processed according to the CEL-Seq protocol (34). Briefly, single cells (or wIAHCs) RNA obtained after TRIzol extraction was suspended in primer solution, denatured at 70 °C for 2 minutes and quickly chilled. First strand synthesis was carried out at 42 °C for 1 hour followed by a second strand synthesis step at 16 °C for 1 hour. cDNA was cleaned-up and *in vitro* transcription was set-up overnight at 37 °C. Amplified RNA was fragmented and cleaned-up for 3' adapter ligation, reverse transcription reaction and PCR amplification. Libraries were sequenced with an Illumina NextSeq 2500 by using 75 bp paired end sequencing.

### **CEL-Seq data analysis**

Initial analysis was performed using the RaceID2 algorithm, which is a part of StemID (68). On average, 12,000 unique transcripts were detected per cell. The sequenced cells were down sampled to 5,000 unique transcripts. All other cells were discarded from the analysis. Monocle analysis (45) was performed using default parameters. For the dimensionality reduction of Monocle, all genes expressing in at least 1 cell with at least 5 transcripts were included. For the differentially expressed genes along pseudotime, a sliding window of 10 Pseudotime arbitrary units was used. The first 5 units in this window were compared to the second 5 units to assess the number of differentially expressed genes within the window. For the TF network analysis, the Fantom5 mouse TFs was used. To cope with drop-out effects due to the low expression of most TFs, we included all TFs that were expressed in at least 1 cell with at least 1 transcript after smoothening of the data along Pseudotime. GSEA analyses were performed using EnrichR (69,70), with default parameters.

### **Comparison of single IAHC cells and wIAHCs**

Comparison of single IAHC cells to wIAHCs was performed by using a Markov-Chain Monte Carlo (MCMC) approach. For each wIAHC, a random number of cells corresponding to the number of cells present in that particular wIAHC was chosen from the single IAHC cells (artificial wIAHC). The collective transcriptome of this artificial wIAHC was then compared to the transcriptome of the wIAHC based on Pearson correlation. Then, 10,000 random swaps of cells within the artificial wIAHC were performed to obtain the set of single cells that had the highest correlation to that particular wIAHC. This entire process was repeated 100 times using different starting cells to ascertain that the starting population of cells did not influence the outcome of the MCMC.

### **Single-molecule FISH on embryo cryosections**

Probe libraries were designed (for *Gpr56*, *CD34*, *Kit*, *Epha7*, *Mpo* and *Vwf*) and fluorescently labelled with Cy5, Alexa Fluor 594 or TMR fluorophores. All probe libraries consisted of 20 to 39 oligonucleotides of 20 bp lengths complementary to the coding sequence of the genes of interest. Cryosections (8  $\mu$ m) were obtained and mounted

on poly-l-lysine coated cover glass. Cryosections were then fixed in 4% paraformaldehyde for 15 minutes and dehydrated in 70% ethanol for a minimum of 2 hours. Embryo cryosections were washed and hybridized overnight with selected probes at 30°C. DAPI staining was done after washes to visualize nuclei. Images were acquired on a Perkin Elmer spinning disc confocal microscope with a 100× oil-immersion objective. Images were processed and combined using Image J.

### **Immunostaining on live thick embryo slices and cryosections**

\* Prom1 (CD133) staining was performed on live thick E11 embryo slices<sup>12,33</sup>. Briefly, the blood was flushed out of the aorta and FITC anti-CD31, PE anti-CD133 (BioLegend, 141203, 1/100) and APC anti-c-kit antibodies were injected directly inside the aorta. After 30 minutes of incubation, the embryos were transversally cut in thick slices, embedded in agarose gel and imaged with a Zeiss LSM700 confocal microscope.

\* Gja5 (Connexin 40) staining was performed on embryo cryosections (10 μm). Briefly, E10 embryos were fixed (4% paraformaldehyde, PFA), cryoprotected in 15% sucrose buffer and frozen in liquid nitrogen. Sections were collected on Superfrost slides (Thermo), rehydrated in PBS, blocked with PBS/1% BSA/0.1% Triton-X100 for 1 hour. Sections were incubated overnight at 4°C with primary antibodies (purified anti-Connexin 40 (Gja5, ThermoFisher, 37-8900, 1/250) and purified anti-Runx (Abcam, Ab92336, 1/250)). After several washes in PBS, sections were incubated for 90 minutes at room temperature with secondary antibodies (Alexa 647 Goat anti-mouse IgG1 [ThermoFisher, A21240, 1/250] to reveal Connexin 40 and Alexa 488 Goat anti-rabbit [ThermoFisher, A11008, 1/250] to reveal Runx). After several washes in PBS, sections were incubated for 1 hour at room temperature with PE anti-CD31 antibody. After wash, sections were stained with DAPI to visualize nuclei.

### ***In vitro* clonogenic assay**

AGM cells isolated from E11 embryos and sorted based on c-kit, CD31, CD45 and Cdh5 differential expression, were plated in methylcellulose (M3434; StemCell Technologies). After 12 days of culture at 37°C, colonies were counted after microscopic observation. Five types of clonogenic progenitors were identified: CFU-GEMM (Colony Forming Unit-Granulocytes Erythrocytes Macrophages Megakaryocytes), CFU-GM (CFU-Granulocytes Macrophages), CFU-M (CFU-Macrophages), CFU-G and BFU-E (Burst Forming Unit-Erythroid).

### **Data availability**

The datasets generated during and/or analysed during the current study are available in the Gene Expression Omnibus (GEO) repository, with the series record GSE112642, [<https://www.ncbi.nlm.nih.gov/geo/query/acc.cgi?acc=GSE112642>].

The authors declare that all data supporting the findings of this study are available within the manuscript or its supplementary files or are available from the corresponding author upon reasonable request.

### **Code availability**

The transcriptome analysis was performed using RaceID2 available at <https://github.com/dgrun>.

### **Acknowledgments**

The authors thank the lab members for helpful discussion and various technical help. We would like to thank Jens Eberhardt and Michael Hollstein for their help to develop the automated cell picking of wIAHCs with the CellCollector™. We also thank the Animal Facility for mouse care and the Optical Imaging Center for confocal

microscope access (both at the Hubrecht Institute). We thank Reinier van der Linden (Hubrecht Institute), and Jeroen van Velzen and Pien van der Burgh (UMC Utrecht) for help with cell sorting. This work was supported in CR lab by a European Research Council grant (ERC, project number 220-H75001EU/HSCOrigin-309361), a TOP-subsidy from NWO/ZonMw (912.15.017) and the UMC Utrecht “Regenerative Medicine & Stem Cells” priority research program, in G.L. and V.K. labs by the Medical Research Council (MR/P000673/1), the Biotechnology and Biological Sciences Research Council (BB/I001794/1), Bloodwise (12037), the European Union’s Horizon 2020 (GA6586250) and Cancer Research UK (C5759/A20971), and in A. v O. lab by a TOP-subsidy NWO/CW (714.016.001).

## Author contributions

Contribution: C.R. conceived ideas and designed the research; C.R performed embryo dissections with the help of C.B. and A.K.; C.B. performed AGM IAHC cells and YS cells staining and sorting, and wIAHC mechanical pick-up. V.K and G.L. contributed to the design of sorts for non-HE, HE and EHT cells. R.T. performed AGM non-HE, HE and EHT cell staining and sorting. L.K. and C.B. performed scRNA-seq. C.B. performed smFISH experiments with the help of L.K.; L.Y. performed immunostaining and flow cytometry experiments; L.K analysed all scRNA-seq data with the help of A.vO., C.R., C.B. and J-C.B.; A.K. performed cell sorting and *in vitro* clonogenic assays. J-C.B. contributed to initial experimental design and experiments. C.R analysed and interpreted the experiments with the help of the other authors. C.R. created the figures and wrote the paper. All authors commented on the manuscript.

## Author information

Reprints and permissions information is available at [www.nature.com/reprints](http://www.nature.com/reprints).

The authors declare no competing financial interests.

Correspondence and material requests should be addressed at Catherine Robin, Hubrecht Institute-KNAW & and University Medical Center Utrecht, Uppsalalaan 8, 3584 CT, Utrecht, The Netherlands; e-mail: [c.robin@hubrecht.eu](mailto:c.robin@hubrecht.eu).

## References

1. Sandler, V.M. et al. Reprogramming human endothelial cells to haematopoietic cells requires vascular induction. *Nature* 511, 312-318 (2014).
2. Lis, R. et al. Conversion of adult endothelium to immunocompetent haematopoietic stem cells. *Nature* 545, 439-445 (2017).
3. Sugimura, R. et al. Haematopoietic stem and progenitor cells from human pluripotent stem cells. *Nature* 545, 432-438 (2017).
4. Pearson, S., Cuvertino, S., Fleury, M., Lacaud, G. & Kouskoff, V. In vivo repopulating activity emerges at the onset of hematopoietic specification during embryonic stem cell differentiation. *Stem Cell Reports* 4, 431-444 (2015).
5. Medvinsky, A. & Dzierzak, E. Definitive hematopoiesis is autonomously initiated by the AGM region. *Cell* 86, 897-906. (1996).
6. Muller, A.M., Medvinsky, A., Strouboulis, J., Grosveld, F. & Dzierzak, E. Development of hematopoietic stem cell activity in the mouse embryo. *Immunity* 1, 291-301. (1994).
7. de Bruijn, M.F., Speck, N.A., Peeters, M.C. & Dzierzak, E. Definitive hematopoietic stem cells first develop within the major arterial regions of the mouse embryo. *Embo J* 19, 2465-2474. (2000).
8. Boisset, J.C. et al. Progressive maturation toward hematopoietic stem cells in the mouse embryo aorta. *Blood* 125, 465-469 (2015).
9. Yokomizo, T. & Dzierzak, E. Three-dimensional cartography of hematopoietic clusters in the vasculature of whole mouse embryos. *Development* 137, 3651-3661 (2010).
10. Taoudi, S. & Medvinsky, A. Functional identification of the hematopoietic stem cell niche in the ventral domain of the embryonic dorsal aorta. *Proc Natl Acad Sci U S A* 104, 9399-9403 (2007).
11. Robin, C., Ottersbach, K., Boisset, J.C., Oziemlak, A. & Dzierzak, E. CD41 is developmen-



- tally regulated and differentially expressed on mouse hematopoietic stem cells. *Blood* 117, 5088-5091 (2011).
12. Boisset, J.C. et al. In vivo imaging of haematopoietic cells emerging from the mouse aortic endothelium. *Nature* 464, 116-120 (2010).
  13. Mikkola, H.K., Fujiwara, Y., Schlaeger, T.M., Traver, D. & Orkin, S.H. Expression of CD41 marks the initiation of definitive hematopoiesis in the mouse embryo. *Blood* 101, 508-516 (2003).
  14. Cai, Z. et al. Haploinsufficiency of AML1 affects the temporal and spatial generation of hematopoietic stem cells in the mouse embryo. *Immunity* 13, 423-431 (2000).
  15. North, T. et al. Cbfa2 is required for the formation of intra-aortic hematopoietic clusters. *Development* 126, 2563-2575 (1999).
  16. Chen, M.J., Yokomizo, T., Zeigler, B.M., Dzierzak, E. & Speck, N.A. Runx1 is required for the endothelial to haematopoietic cell transition but not thereafter. *Nature* 457, 887-891 (2009).
  17. Garcia-Porrero, J.A. et al. Antigenic profiles of endothelial and hemopoietic lineages in murine intraembryonic hemogenic sites. *Dev Comp Immunol* 22, 303-319 (1998).
  18. Dantschakoff, V. Untersuchungen über die Entwicklung von Blut und Bindegewebe bei Vögeln. Das lockere Bindegewebe des Huhnhens in Fetalen Leben. *Arch. f. mikr. Anat.* 73, 117-181 (1909).
  19. Bertrand, J.Y. et al. Haematopoietic stem cells derive directly from aortic endothelium during development. *Nature* 464, 108-111 (2010).
  20. Eilken, H.M., Nishikawa, S. & Schroeder, T. Continuous single-cell imaging of blood generation from haemogenic endothelium. *Nature* 457, 896-900 (2009).
  21. Jaffredo, T., Gautier, R., Eichmann, A. & Dieterlen-Lievre, F. Intraaortic hemopoietic cells are derived from endothelial cells during ontogeny. *Development* 125, 4575-4583 (1998).
  22. Kissa, K. & Herbomel, P. Blood stem cells emerge from aortic endothelium by a novel type of cell transition. *Nature* 464, 112-115 (2010).
  23. Lancrin, C. et al. The haemangioblast generates haematopoietic cells through a haemogenic endothelium stage. *Nature* 457, 892-895 (2009).
  24. Zovein, A.C. et al. Fate tracing reveals the endothelial origin of hematopoietic stem cells. *Cell Stem Cell* 3, 625-636 (2008).
  25. Kumaravelu, P. et al. Quantitative developmental anatomy of definitive haematopoietic stem cells/long-term repopulating units (HSC/RUs): role of the aorta-gonad- mesonephros (AGM) region and the yolk sac in colonisation of the mouse embryonic liver. *Development* 129, 4891-4899. (2002).
  26. Robin, C. et al. An unexpected role for IL-3 in the embryonic development of hematopoietic stem cells. *Dev Cell* 11, 171-180 (2006).
  27. Lancrin, C. et al. GFI1 and GFI1B control the loss of endothelial identity of hemogenic endothelium during hematopoietic commitment. *Blood* 120, 314-322 (2012).
  28. Lux, C.T. et al. All primitive and definitive hematopoietic progenitor cells emerging before E10 in the mouse embryo are products of the yolk sac. *Blood* 111, 3435-3438 (2008).
  29. Zhou, F. et al. Tracing haematopoietic stem cell formation at single-cell resolution. *Nature* 533, 487-492 (2016).
  30. Rybtsov, S. et al. Hierarchical organization and early hematopoietic specification of the developing HSC lineage in the AGM region. *J Exp Med* 208, 1305-1315 (2011).
  31. Taoudi, S. et al. Extensive hematopoietic stem cell generation in the AGM region via maturation of VE-cadherin+CD45+ pre-definitive HSCs. *Cell Stem Cell* 3, 99-108 (2008).
  32. Rybtsov, S., Ivanovs, A., Zhao, S. & Medvinsky, A. Concealed expansion of immature precursors underpins acute burst of adult HSC activity in foetal liver. *Development* 143, 1284-1289 (2016).
  33. Boisset, J.C., Andrieu-Soler, C., van Cappellen, W.A., Clapes, T. & Robin, C. Ex vivo time-lapse confocal imaging of the mouse embryo aorta. *Nat Protoc* 6, 1792-1805 (2011).
  34. Grun, D. et al. Single-cell messenger RNA sequencing reveals rare intestinal cell types. *Nature* 525, 251-255 (2015).
  35. Hashimshony, T., Wagner, F., Sher, N. & Yanai, I. CEL-Seq: single-cell RNA-Seq by multiplexed linear amplification. *Cell Rep* 2, 666-673 (2012).
  36. Pimanda, J.E. et al. Gata2, Fli1, and Scl form a recursively wired gene-regulatory circuit during early hematopoietic development. *Proc Natl Acad Sci U S A* 104, 17692-17697 (2007).
  37. Solaimani Kartalaei, P. et al. Whole-transcriptome analysis of endothelial to hematopoietic stem cell transition reveals a requirement for Gpr56 in HSC generation. *J Exp Med* 212, 93-106 (2015).
  38. Manaia, A. et al. Lmo2 and GATA-3 associated expression in intraembryonic hemogenic sites. *Development* 127, 643-653 (2000).
  39. Mascarenhas, M.I., Parker, A., Dzierzak, E. & Ottersbach, K. Identification of novel regulators of hematopoietic stem cell development through refinement of stem cell localization and expression profiling. *Blood* 114, 4645-4653 (2009).
  40. Charbord, P. et al. A systems biology approach for defining the molecular framework of the hematopoietic stem cell niche. *Cell Stem Cell* 15, 376-391 (2014).
  41. Gomez Perdiguero, E. et al. Tissue-resident macrophages originate from yolk-sac-derived erythro-myeloid progenitors. *Nature* 518, 547-551 (2015).



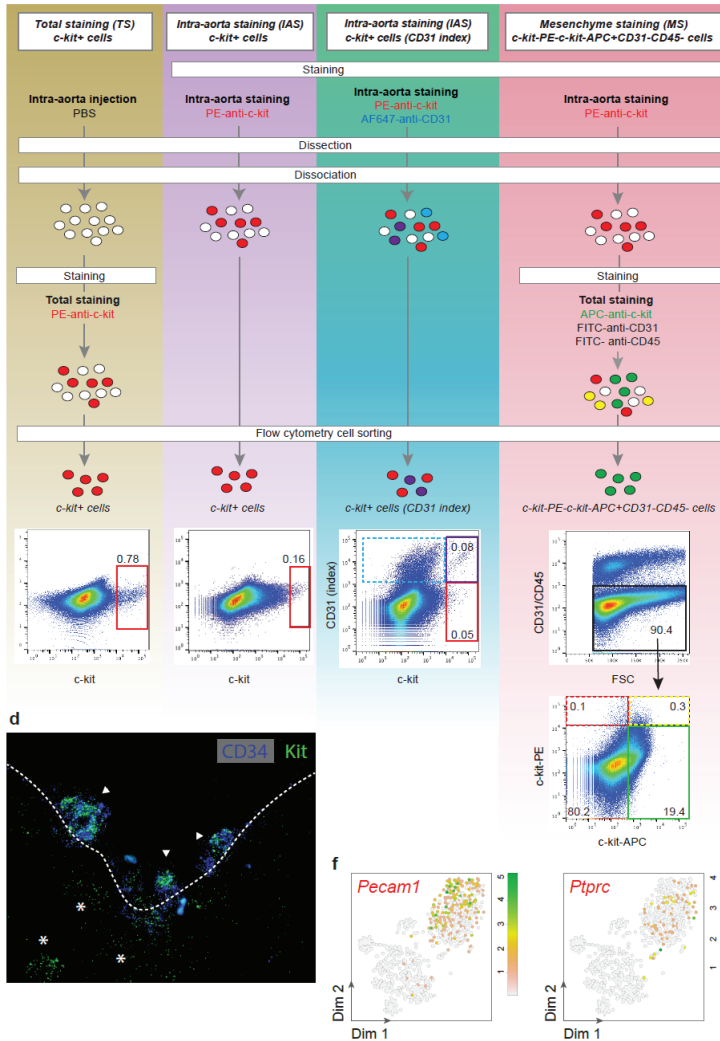
42. Hoeffel, G. et al. C-Myb(+) erythro-myeloid progenitor-derived fetal monocytes give rise to adult tissue-resident macrophages. *Immunity* 42, 665-678 (2015).
43. McGrath, K.E. et al. Distinct Sources of Hematopoietic Progenitors Emerge before HSCs and Provide Functional Blood Cells in the Mammalian Embryo. *Cell Rep* 11, 1892-1904 (2015).
44. Thambyrajah, R. et al. GFI1 proteins orchestrate the emergence of haematopoietic stem cells through recruitment of LSD1. *Nat Cell Biol* 18, 21-32 (2016).
45. Trapnell, C. et al. The dynamics and regulators of cell fate decisions are revealed by pseudotemporal ordering of single cells. *Nat Biotechnol* 32, 381-386 (2014).
46. Pereira, C.F. et al. Hematopoietic Reprogramming In Vitro Informs In Vivo Identification of Hemogenic Precursors to Definitive Hematopoietic Stem Cells. *Dev Cell* 36, 525-539 (2016).
47. Batsivari, A. et al. Understanding Hematopoietic Stem Cell Development through Functional Correlation of Their Proliferative Status with the Intra-aortic Cluster Architecture. *Stem Cell Reports* 8, 1549-1562 (2017).
48. Migueles, R.P. et al. Transcriptional regulation of Hhex in hematopoiesis and hematopoietic stem cell ontogeny. *Dev Biol* 424, 236-245 (2017).
49. Roques, M. et al. Endoglin expression level discriminates long-term hematopoietic from short-term clonogenic progenitor cells in the aorta. *Haematologica* 97, 975-979 (2012).
50. Muraro, M.J. et al. A Single-Cell Transcriptome Atlas of the Human Pancreas. *Cell Syst* 3, 385-394 e383 (2016).
51. Rybtsov, S. et al. Tracing the origin of the HSC hierarchy reveals an SCF-dependent, IL-3-independent CD43(-) embryonic precursor. *Stem Cell Reports* 3, 489-501 (2014).
52. Espin-Palazon, R., Weijts, B., Mulero, V. & Traver, D. Proinflammatory Signals as Fuel for the Fire of Hematopoietic Stem Cell Emergence. *Trends Cell Biol* 28, 58-66 (2018).
53. Abugessaisa, I. et al. FANTOM5 transcriptome catalog of cellular states based on Semantic MediaWiki. Database (Oxford) 2016 (2016).
54. Corada, M. et al. Sox17 is indispensable for acquisition and maintenance of arterial identity. *Nat Commun* 4, 2609 (2013).
55. Rowlinson, J.M. & Gering, M. Hey2 acts upstream of Notch in hematopoietic stem cell specification in zebrafish embryos. *Blood* 116, 2046-2056 (2010).
56. Kolodziejczyk, A.A., Kim, J.K., Svensson, V., Marioni, J.C. & Teichmann, S.A. The technology and biology of single-cell RNA sequencing. *Mol Cell* 58, 610-620 (2015).
57. Picelli, S. et al. Full-length RNA-seq from single cells using Smart-seq2. *Nat Protoc* 9, 171-181 (2014).
58. Wang, Y. & Navin, N.E. Advances and applications of single-cell sequencing technologies. *Mol Cell* 58, 598-609 (2015).
59. Durruthy-Durruthy, R. et al. Reconstruction of the mouse otocyst and early neuroblast lineage at single-cell resolution. *Cell* 157, 964-978 (2014).
60. Treutlein, B. et al. Reconstructing lineage hierarchies of the distal lung epithelium using single-cell RNA-seq. *Nature* 509, 371-375 (2014).
61. Jaitin, D.A. et al. Massively parallel single-cell RNA-seq for marker-free decomposition of tissues into cell types. *Science* 343, 776-779 (2014).
62. Souilhol, C. et al. Inductive interactions mediated by interplay of asymmetric signalling underlie development of adult haematopoietic stem cells. *Nat Commun* 7, 10784 (2016).
63. Swiers, G. et al. Early dynamic fate changes in haemogenic endothelium characterized at the single-cell level. *Nat Commun* 4, 2924 (2013).
64. Batta, K., Florkowska, M., Kouskoff, V. & Lacaud, G. Direct reprogramming of murine fibroblasts to hematopoietic progenitor cells. *Cell Rep* 9, 1871-1884 (2014).
65. Schulte, R. et al. Index sorting resolves heterogeneous murine hematopoietic stem cell populations. *Exp Hematol* 43, 803-811 (2015).
66. Haupt, S. et al. Automated selection and harvesting of pluripotent stem cell colonies. *Biotechnol Appl Biochem* 59, 77-87 (2012).
67. Neumann, M.H. et al. Isolation and characterization of circulating tumor cells using a novel workflow combining the CellSearch(R) system and the CellCelector. *Biotechnol Prog* (2016).
68. Grun, D. et al. De Novo Prediction of Stem Cell Identity using Single-Cell Transcriptome Data. *Cell Stem Cell* 19, 266-277 (2016).
69. Chen, E.Y. et al. Enrichr: interactive and collaborative HTML5 gene list enrichment analysis tool. *BMC Bioinformatics* 14, 128 (2013).
70. Kuleshov, M.V. et al. Enrichr: a comprehensive gene set enrichment analysis web server 2016 update. *Nucleic Acids Res* 44, W90-97 (2016).

## **End notes**

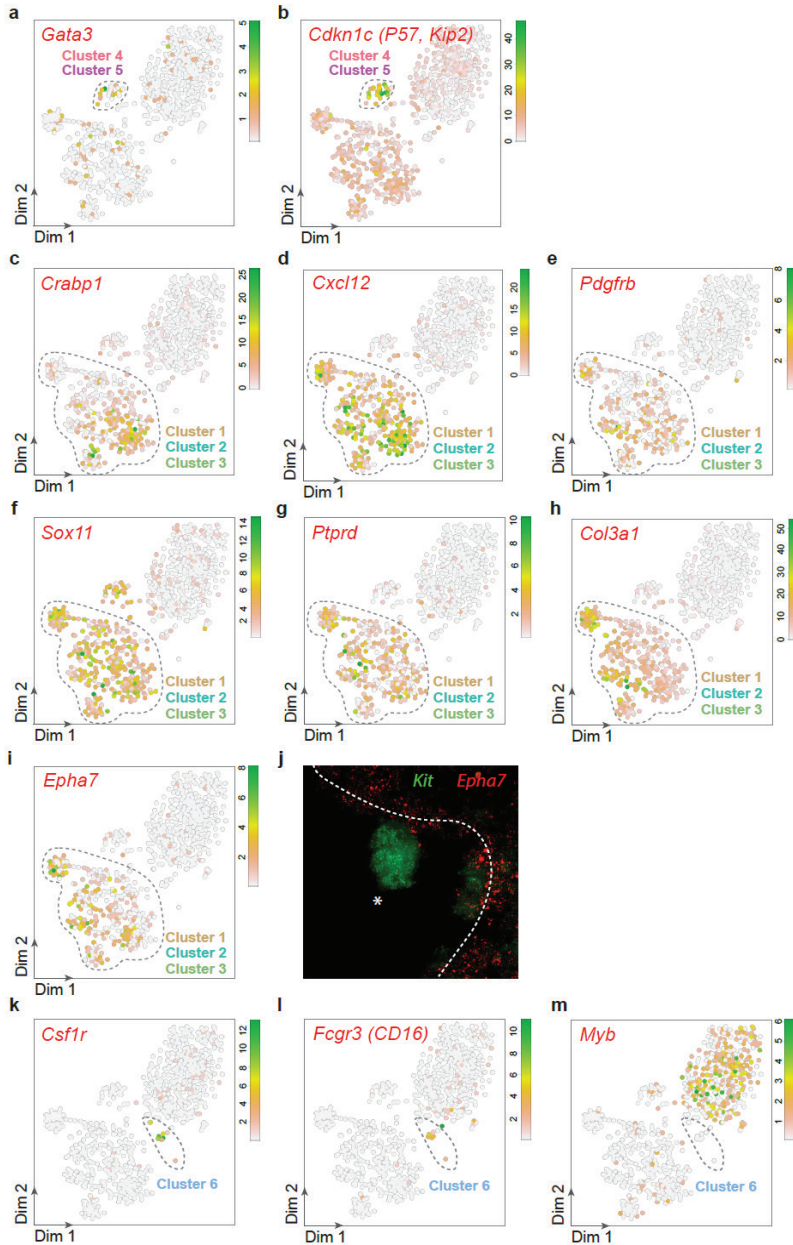
### **Supplementary information**

Supplementary information is linked to the online version of the paper at [www.nature.com/nature](http://www.nature.com/nature).

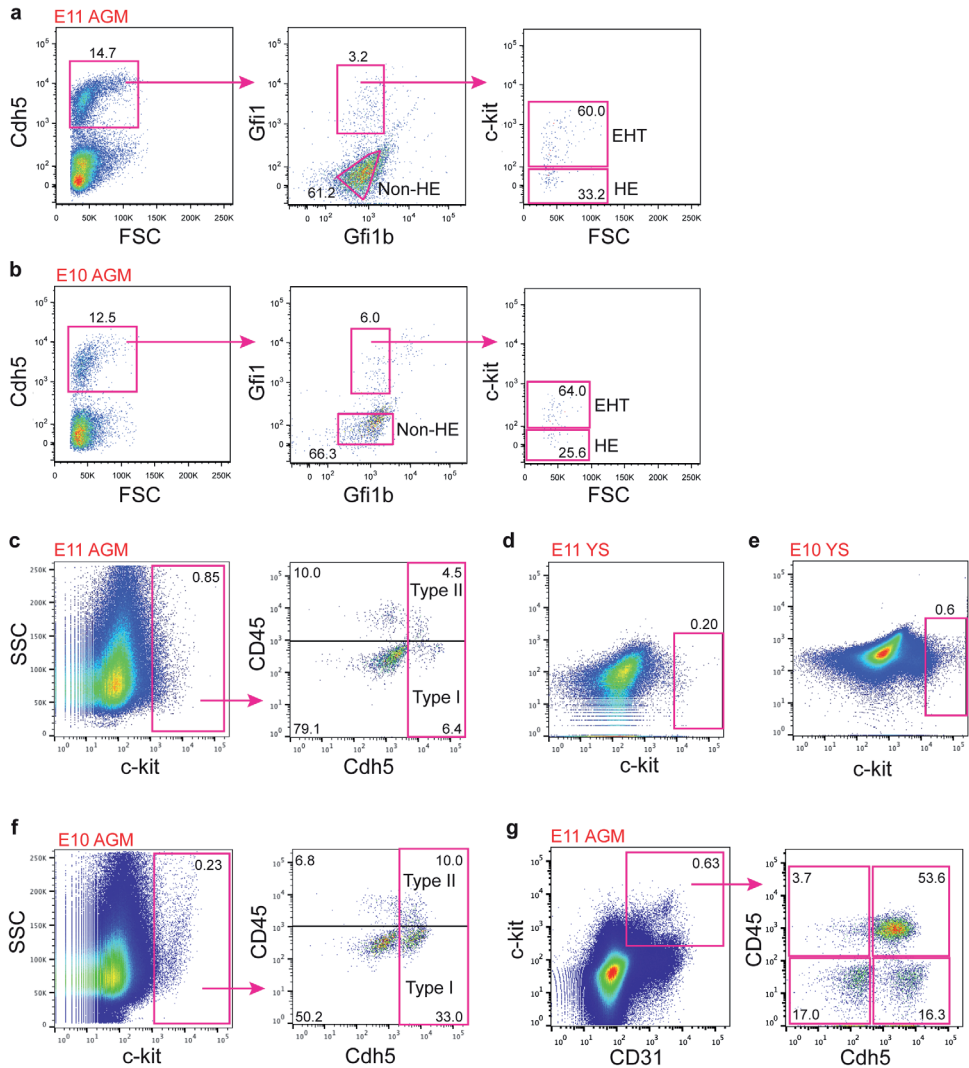
## Supplementary figures



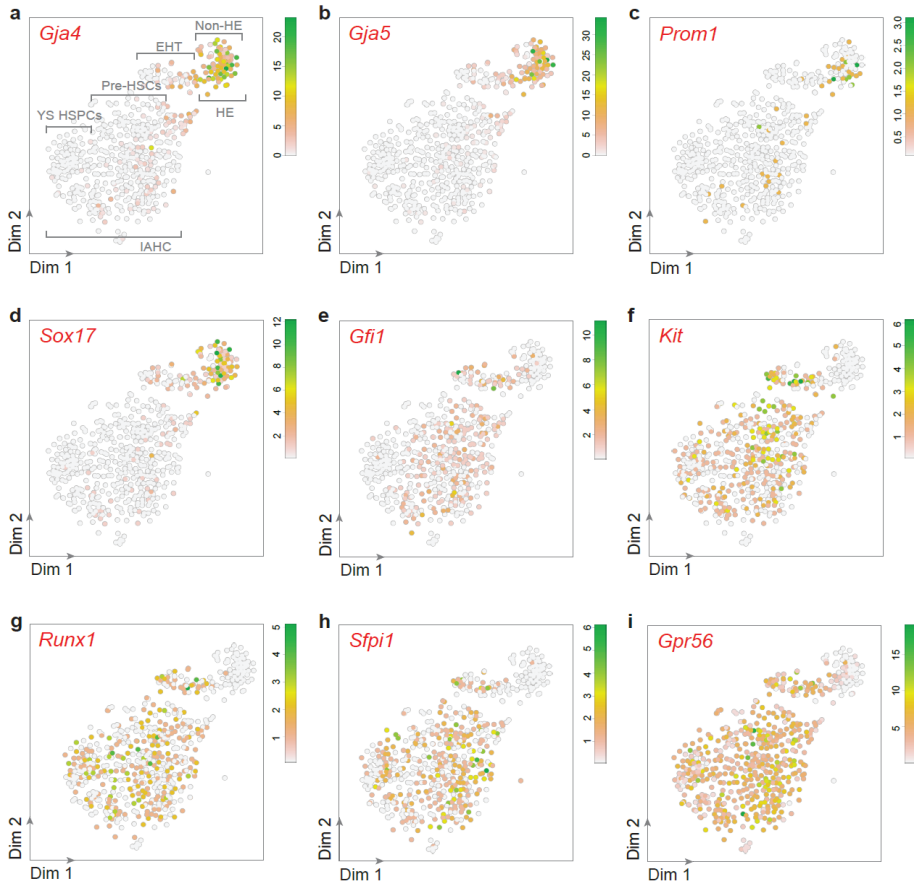
**Supplementary Figure 1 (related to Figure 1). Antibody staining and cell sorting strategies to isolate IAHC cells from E11 AGMs.** (a) After intra-aortic injection of PBS (to flush the blood out), AGMs were dissected, dissociated and cells were stained with PE anti-c-kit antibodies (procedure referred to as total staining or TS). c-kit<sup>+</sup> cells were sorted by flow cytometry (red gate in FACS plot) (cells depicted as brown dots in Fig. 1a). (b) Cells were stained after intra-aortic injection of PE anti-c-kit antibodies in the aorta (procedure referred to as intra-aortic staining or IAS). AGMs were dissected, dissociated and c-kit<sup>+</sup> cells were sorted (red gate in FACS plot) (cells depicted as purple dots in Fig. 1a). (c) Cells were stained after intra-aorta injection of PE anti-c-kit and AF647 anti-CD31 antibodies. AGMs were then dissected, dissociated and c-kit<sup>+</sup> cells were sorted with CD31 sorting index (red and purple gates in FACS plot) (c-kit<sup>+</sup>CD31<sup>+</sup> cells and c-kit<sup>+</sup>CD31<sup>-</sup> cells depicted as green and blue dots in Fig. 1a, respectively). (d) Single-molecule fluorescent in situ hybridization (smFISH) on an E11 embryo cryosection with probes against CD34 (blue dots) and Kit (green dots). Cells expressing Kit transcripts are present in IAHCs (arrow heads) and in the mesenchyme underneath the aortic endothelium (asterisks). (e) Cells were stained after intra-aorta injection of PE anti-c-kit antibodies. AGMs were dissected, dissociated and cells were stained with APC anti-c-kit, FITC anti-CD31 and FITC anti-CD45 antibodies. PE-c-kit-APC<sup>+</sup>c-kit<sup>-</sup>CD31<sup>-</sup>CD45<sup>-</sup> cells were sorted (green gate in FACS plot) (cells depicted as pink dots in Fig. 1a). Percentages of viable cells are indicated in the gates. (f) Expression of *Pecam1* and *Ptprc* marker genes projected on t-SNE maps. Dim, dimension.



**Supplementary Figure 2 (related to Figure 1). Marker gene expression reveals the presence of contaminating non-IAHC cells among the sorted IAHC cells.** (a-i; k-m) The transcript count of selected marker genes is projected on t-SNE maps. Shown are maps for sub-aortic patches markers *Gata3* and *Cdkn1c* (a, b), for mesenchymal marker genes *Crabp1* (c), *Cxcl12* (d), *Pdgfrb* (e), *Sox11* (f), *Ptprd* (g), *Col3a1* (h), *Epha7* (i), and for erythro-myeloid progenitors *Csf1r* (k), *Fcgr3* (l) and *Myb* (m). The expression of the above mentioned transcripts identify few cells in RaceID clusters 4 and 5, and all cells in RaceID clusters 1, 2 and 3 in Fig. 1b. Dim, dimension. (j) smFISH on an E11 embryo cryosection with probes against *Kit* (green dots) and *Epha7* (red dots). Cells in IAHC (asterisk) expressed *Kit* but not *Epha7* while cells from the underlying mesenchyme expressed *Epha7*.

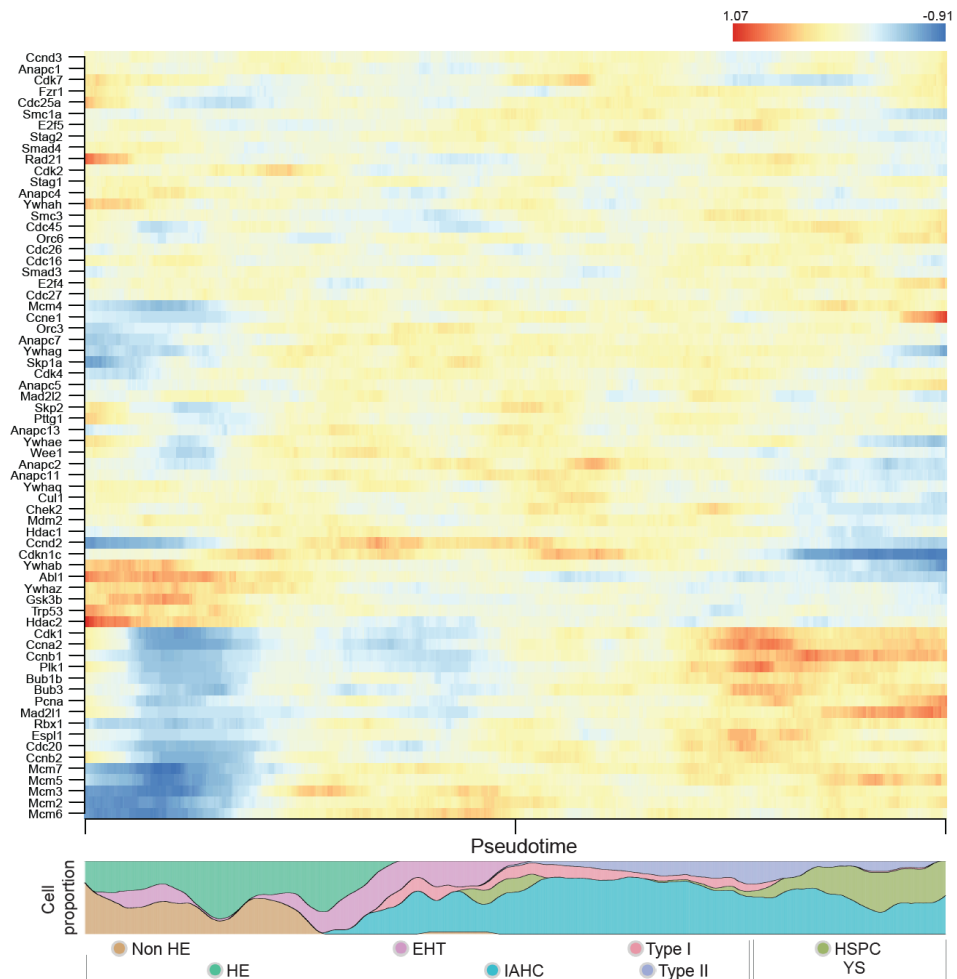


**Supplementary Figure 3 (related to Figures 2 and 3). Different aortic cell populations sorted from E10 and E11 AGMs and YSS.** (a-g) Examples of cell sorting and gating strategies. (a) Cdh5+Gfi1-Gfi1b-c-kit- non haemogenic endothelial (HE) cells, Cdh5+Gfi1+Gfi1b-c-kit- HE cells, and Cdh5+Gfi1+Gfi1b-c-kit+ cells undergoing endothelial to haematopoietic transition (EHT) sorted from E11 AGMs for scRNA-seq analysis. (b) Non-HE cells, HE cells and EHT cells sorted from E10 AGMs for scRNA-seq analysis. (c) Cdh5+c-kit+ cells sorted with CD45 index (CD45-, type I pre-HSCs; CD45+, type II pre-HSCs) from E11 flushed AGMs for scRNA-seq analysis. (d, e) c-kit+ HSPCs sorted from E11 (d) or E10 (e) YSS for scRNA-seq analysis. (f) Cdh5+c-kit+ cells sorted with CD45 index (CD45-, type I pre-HSCs; CD45+, type II pre-HSCs) from E10 flushed AGMs for scRNA-seq analysis. (g) Cells sorted based on c-kit, CD31, Cdh5 and CD45 differential expression from E11 flushed AGMs for *in vitro* clonogenic assays.

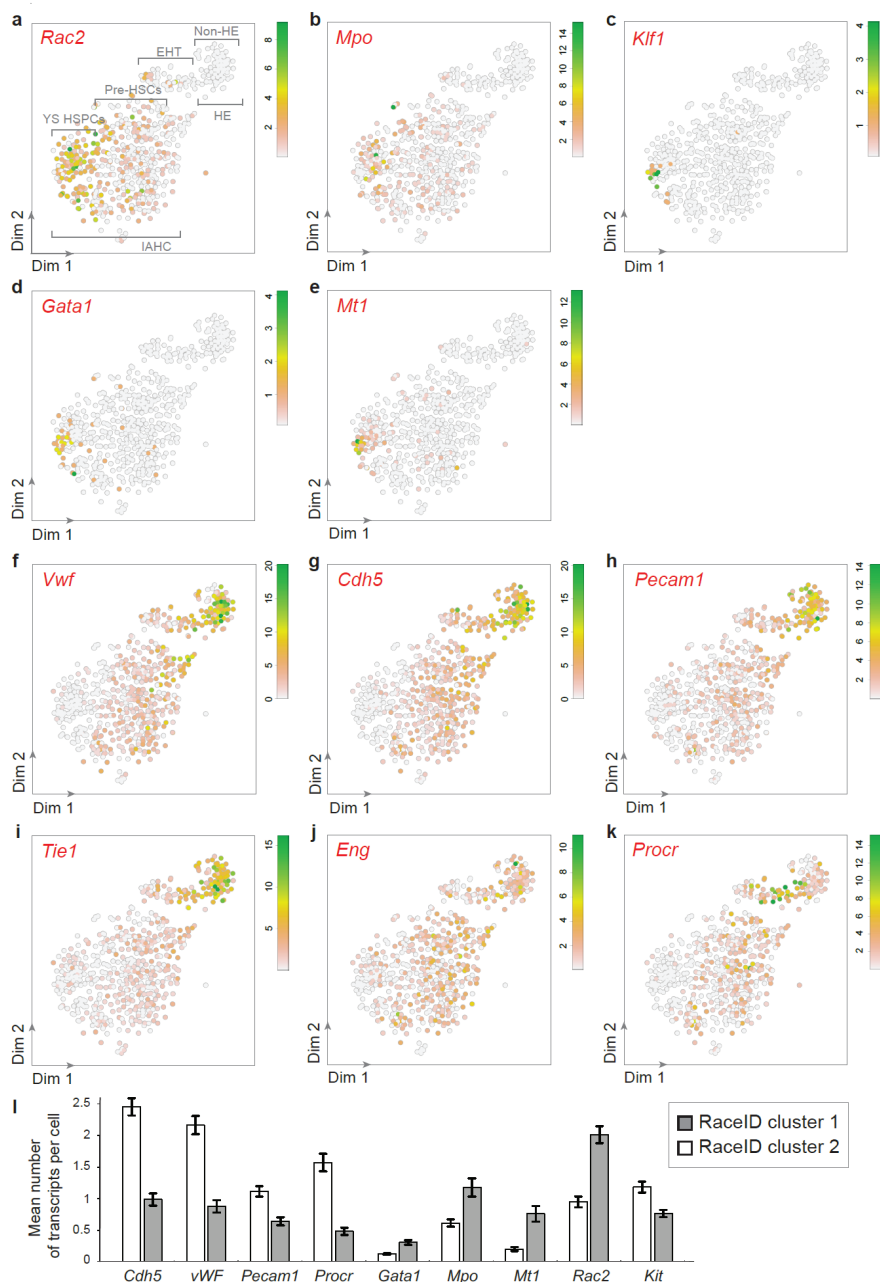


**Supplementary Figure 4 (related to Figure 2). Evolution of selected marker genes during EHT and IAHC formation at E11.** (a-i) The transcript count of selected marker genes is projected on t-SNE maps. Shown are maps for *Gja4* (a), *Gja5* (b), *Prom1* (c), *Sox17* (d), *Gfi1* (e), *Kit* (f), *Runx1* (g), *Sfp1* (h) and *Gpr56* (i).

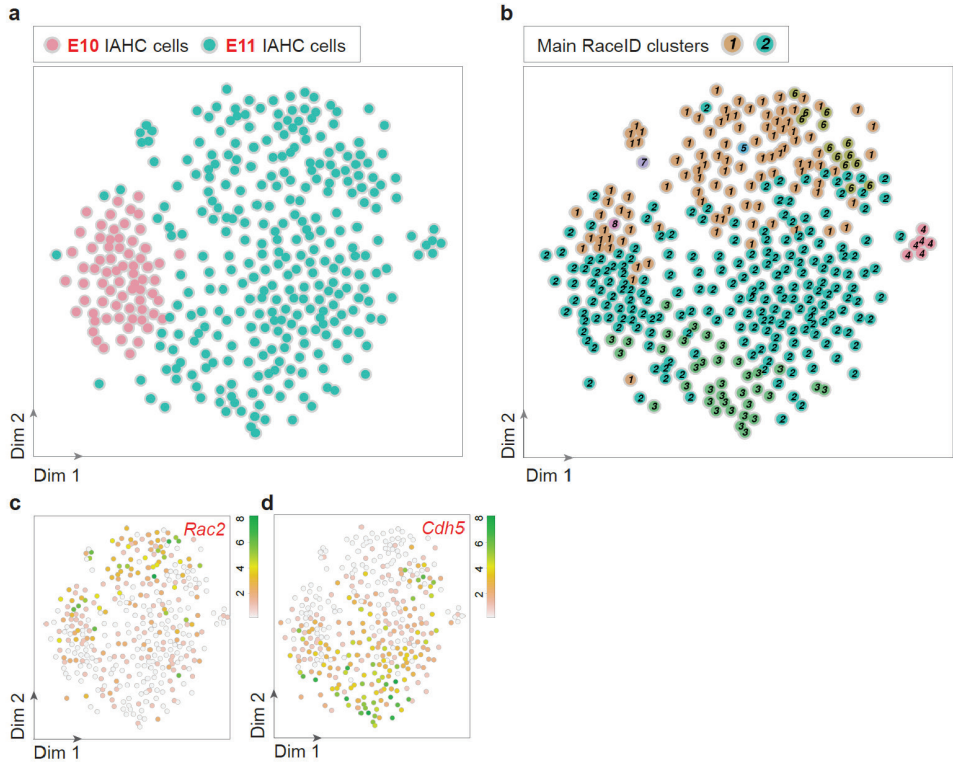




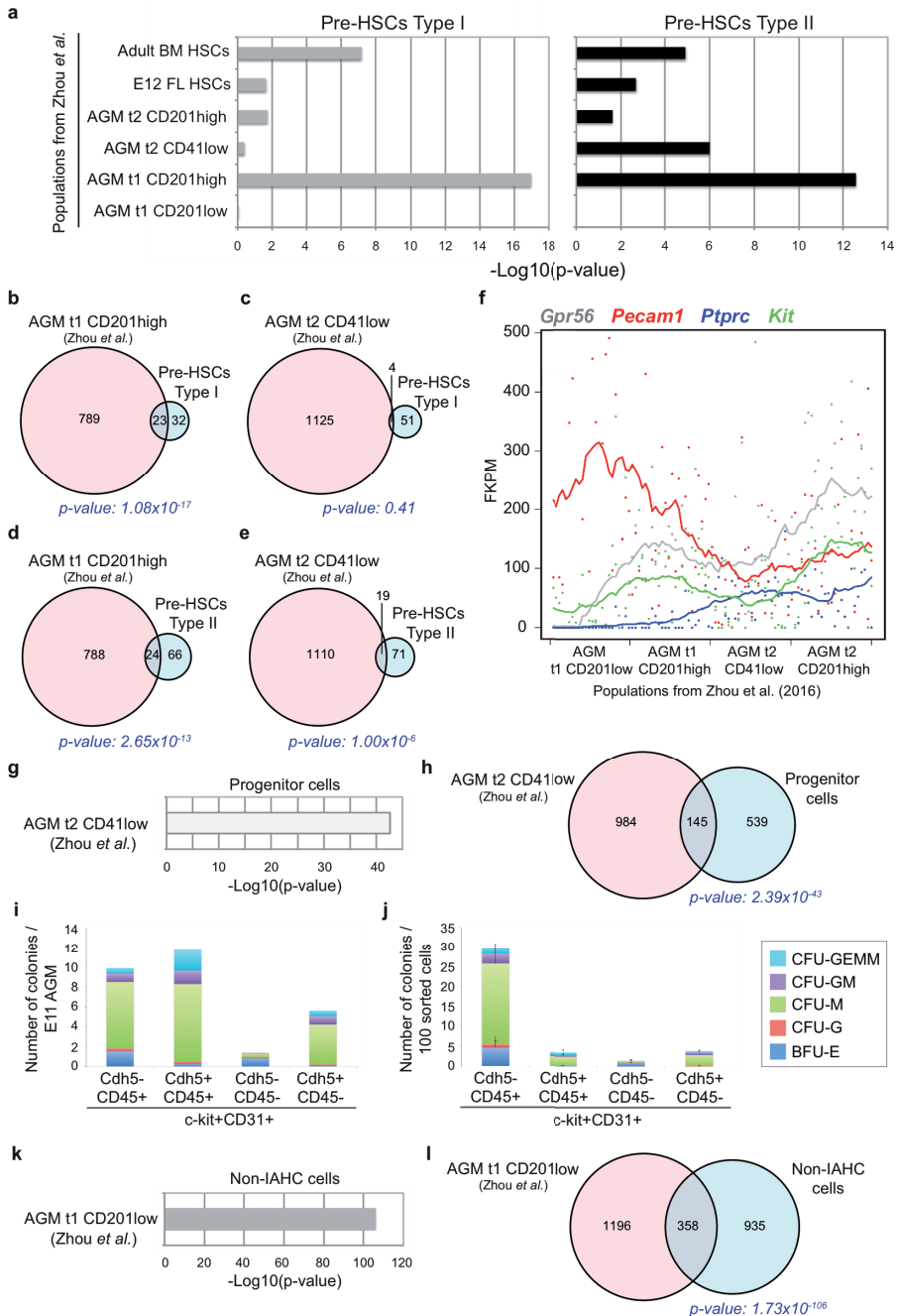
**Supplementary Figure 5 (related to Figure 2).** Dynamic and fluctuant expression of cell cycle related genes at E11, according to pseudotime. Heatmap depicting on the y-axis the genes related to the KEGG cell cycle pathway and on the x-axis the E11 single cells ordered along the pseudotime axis.



**Supplementary Figure 6 (related to Figure 2). Oposing gradients of endothelial and haematopoietic transcripts identify committed haematopoietic progenitors and pre-HSCs as the two cell populations composing IAHCs.** (a-k) The transcript count of selected marker genes is projected on t-SNE maps. (a-e) Shown are maps for *Rac2* (a), *Mpo* (b), *Klf1* (c), *Gata1* (d) and *Mt1* (e) (that identify committed haematopoietic progenitors in RaceID cluster 1 in Fig. 2d). (f-k) Shown are maps for *Vwf* (f), *Cdh5* (g), *Pecam1* (h), *Tie1* (i), *Eng* (j) and *Procr* (k) (that identify pre-HSCs in RaceID clusters 2 in Fig. 2d). (l) Histogram representing the average numbers of transcripts per cell in RaceID clusters 1 and 2 for the designated genes. Data are represented as mean  $\pm$  SEM.

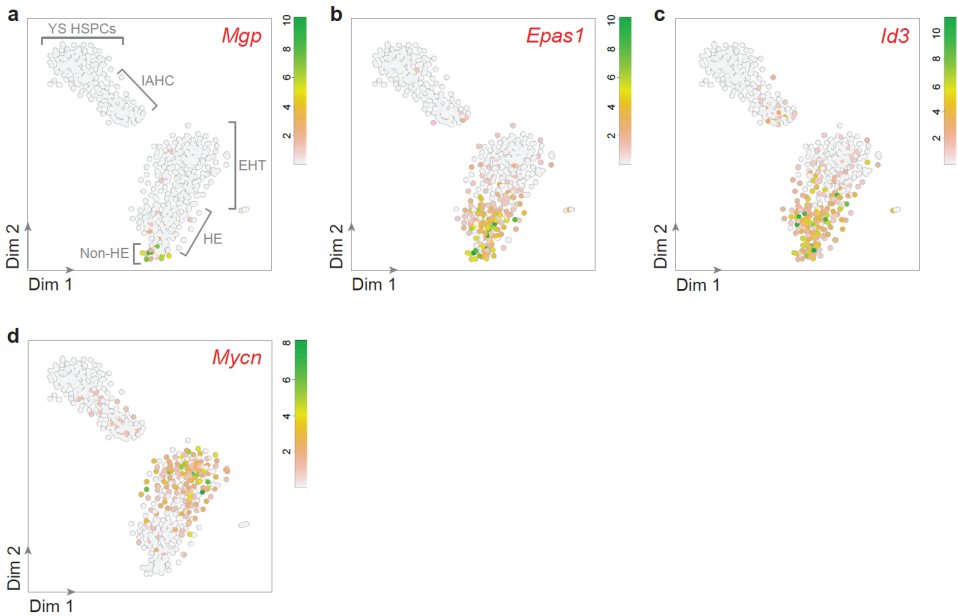


**Supplementary Figure 7 (related to Figures 2 and 3). Both E10 and E11 IAHCs contain committed progenitors and pre-HSCs.** (a) t-SNE map displaying single IAHC cells isolated from E10 (pink dots) and E11 (green dots) embryo AGMs. (b) t-SNE plot displaying single cells from (a) in clusters identified by RaceID. Different numbers and colours highlight different RaceID clusters. Cluster 1 contained IAHC progenitors, while cluster 2 contained pre-HSCs. (c,d) Distribution of selected marker gene expression in t-SNE maps. *Rac2* expression is restricted to cluster 1 (c) while *Cdh5* expression is restricted to cluster 2 (d).

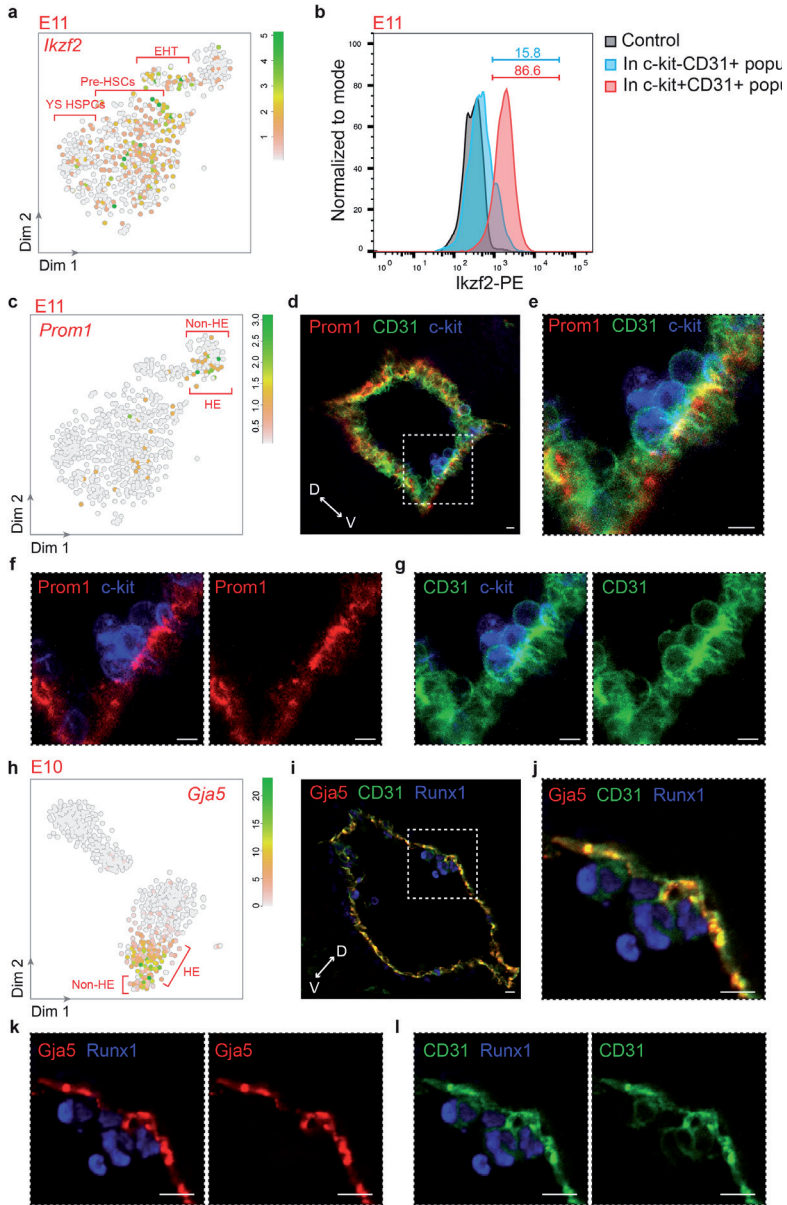


**Supplementary Figure 8 (related to Figure 2). Confirmation of pre-HSC and committed progenitor identities in E11 IAHCs.** (a, g, k) The genes differentially expressed between each E11 AGM population from Zhou et al.<sup>29</sup> and the genes differentially expressed between each of our E11 AGM populations (Fig. 1a and 2a) were compared. The p-values representing the significance of the overlap between the Zhou populations and the pre-HSCs type I and type II are depicted as column bars ( $-\text{Log}_{10}(\text{p-value})$ ) in (a). (b-e) Venn diagrams showing shared and distinct genes between (b) AGM t1 CD201<sup>high</sup> and pre-HSCs type I, (c) AGM t2 CD41<sup>low</sup> and pre-HSCs type I, (d)

AGM t1 CD201<sup>high</sup> and pre-HSCs type II, (e) AGM t2 CD41<sup>low</sup> and pre-HSCs type II. (f) Fragments per kilobase of exon per million reads mapped (FPKM) values for *Gpr56*, *Pecam1*, *Ptprc* and *Kit* in each E11 AGM population from Zhou et al. (29). (g) The p-values representing the significance of the overlap between the Zhou populations and the progenitor cells are depicted as column bars (-Log<sub>10</sub>(p-value)). (h) Venn diagrams showing shared and distinct genes between AGM t2 CD41<sup>low</sup> and progenitor cells. (i) *In vitro* clonogenic analyses of E11 AGM cells sorted based on c-kit, CD31, Cdh5 and CD45 differential expression. Bars, number of colonies/E11 AGM embryo equivalent for each indicated sorted population ± SD. n=6 independent experiments. CFU-GEMM: CFU-Granulocyte-Erythroid- Macrophage-Megakaryocyte; CFU-GM: CFU- Granulocyte-Macrophage; CFU-M: CFU-Macrophage; CFU-G: CFU-Granulocyte; BFU-E: Burst-Forming Unit-Erythroid. (j) Clonogenic data shown in (i) represented in number of colonies/100 sorted cells (for each population indicated on the x-axis). (k) The p-values representing the significance of the overlap between the Zhou populations and the non-IAHC cells are depicted as column bars (-Log<sub>10</sub>(p-value)). (l) Venn diagrams showing shared and distinct genes between AGM t1 CD201<sup>low</sup> and non-IAHC cells.

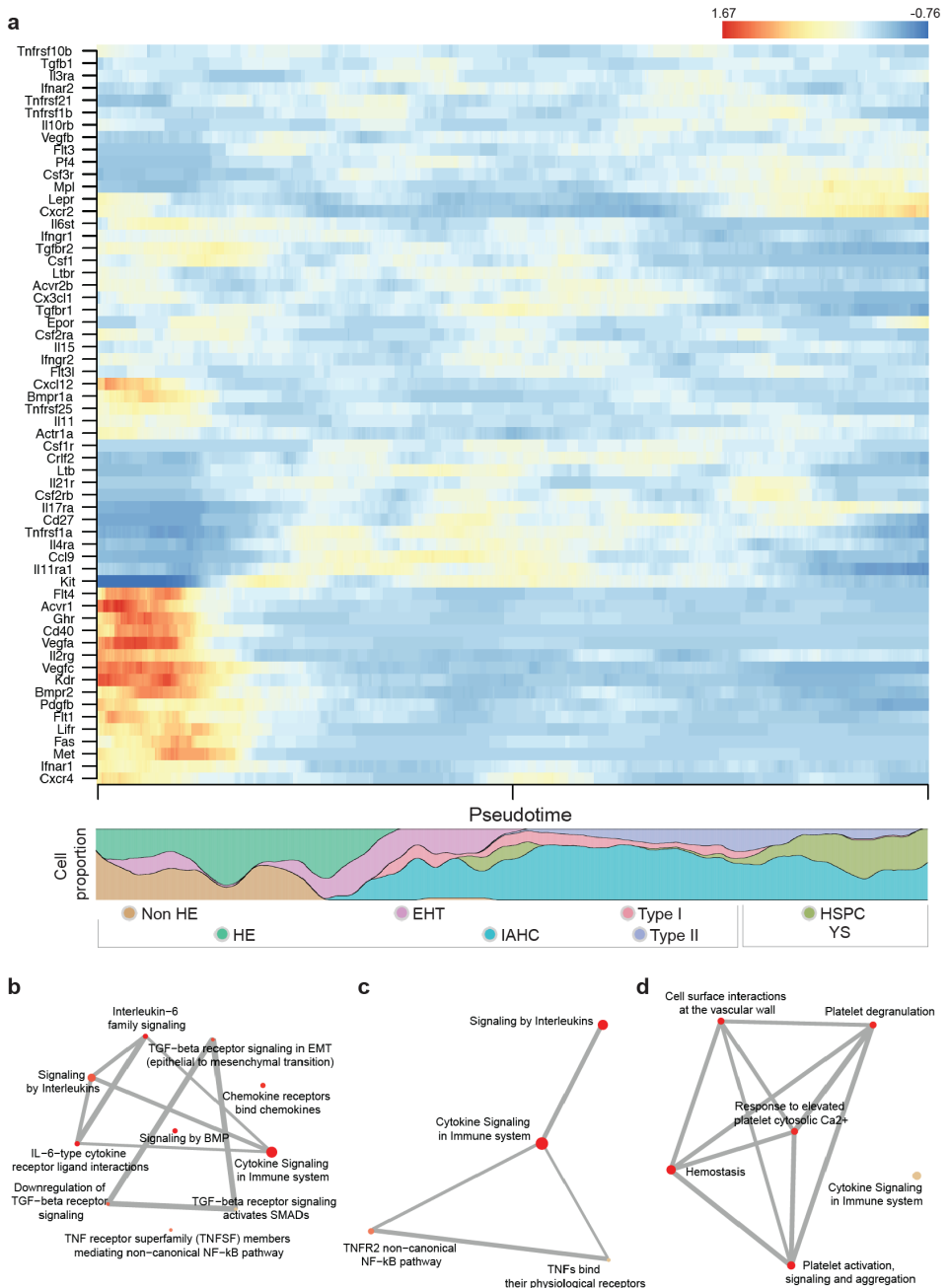


**Supplementary Figure 9 (related to Figure 3). Evolution of selected marker genes during EHT at E10.** (a-d) The transcript count of selected marker genes is projected on t-SNE maps. Shown are maps for *Mgp* (a), *Epas1* (b), *Id3* (c) and *Mycn* (d).

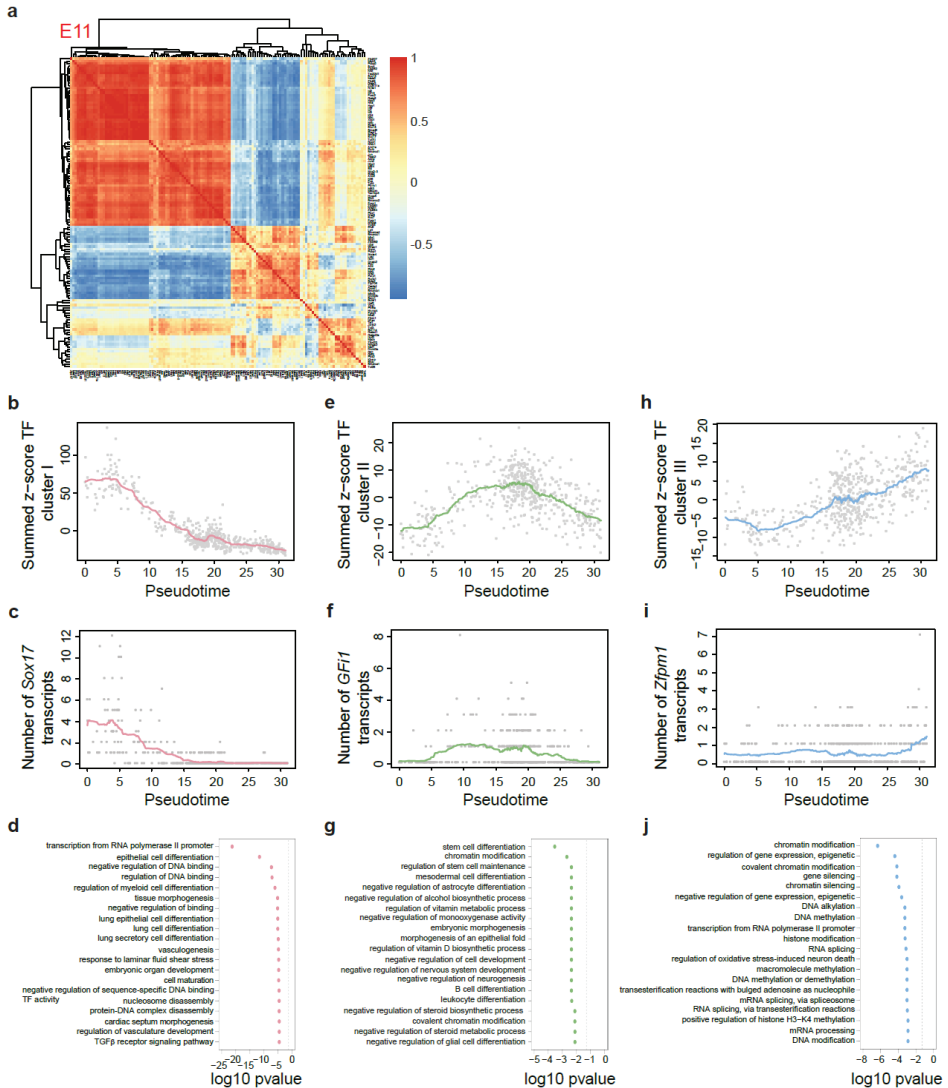


**Supplementary Figure 10 (related to Figures 2 and 3). Correlation between protein expression patterns and scRNA-seq data for IKZF2, PROM1 and GJA5.** (a, c, h) Distribution of selected marker gene expression in t-SNE maps. *Ikzf2* expression is mainly in IAHC cells (a) while *Prom1* (c) and *Gja5* (h) expression is restricted to endothelial cells. (b) Flow cytometry analysis shows IKZF2 expression in c-kit-CD31+ endothelial cells (blue) and c-kit+CD31+ IAHC cells (red) represented in histogram. Control: grey. Lines indicate the percentages of IKZF2+ cells in each live population. (d-g) Immunostaining on an E11 live thick embryo slice with antibodies against c-kit (blue), CD31 (green) and PROM1 (red). c-kit+CD31+ IAHC cells do not express Prom1 while c-kit-CD31+ endothelial cells do express Prom1. (e-g) Dashed white box in (d) is enlarged in (e-g). (i-l) Immunostaining on an E10 embryo cryosection with antibodies against RUNX1 (blue), CD31 (green) and GJA5 (red). RUNX1+CD31+ IAHC cells do not express GJA5 while RUNX1-CD31+ endothelial cells do express GJA5. Dashed white box in (i) is enlarged in (j-l). Scale bars, 10  $\mu$ m. V: ventral side of the embryo. D: dorsal side of the embryo.

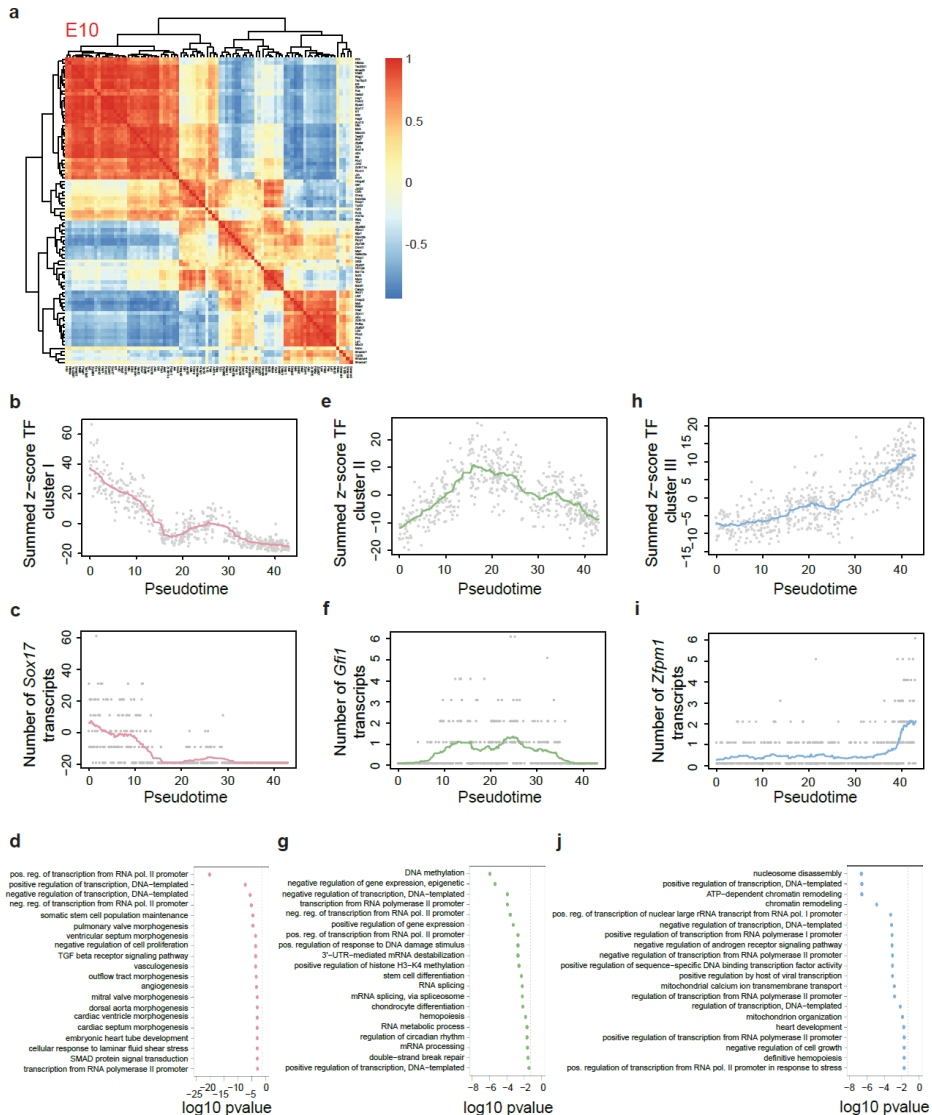




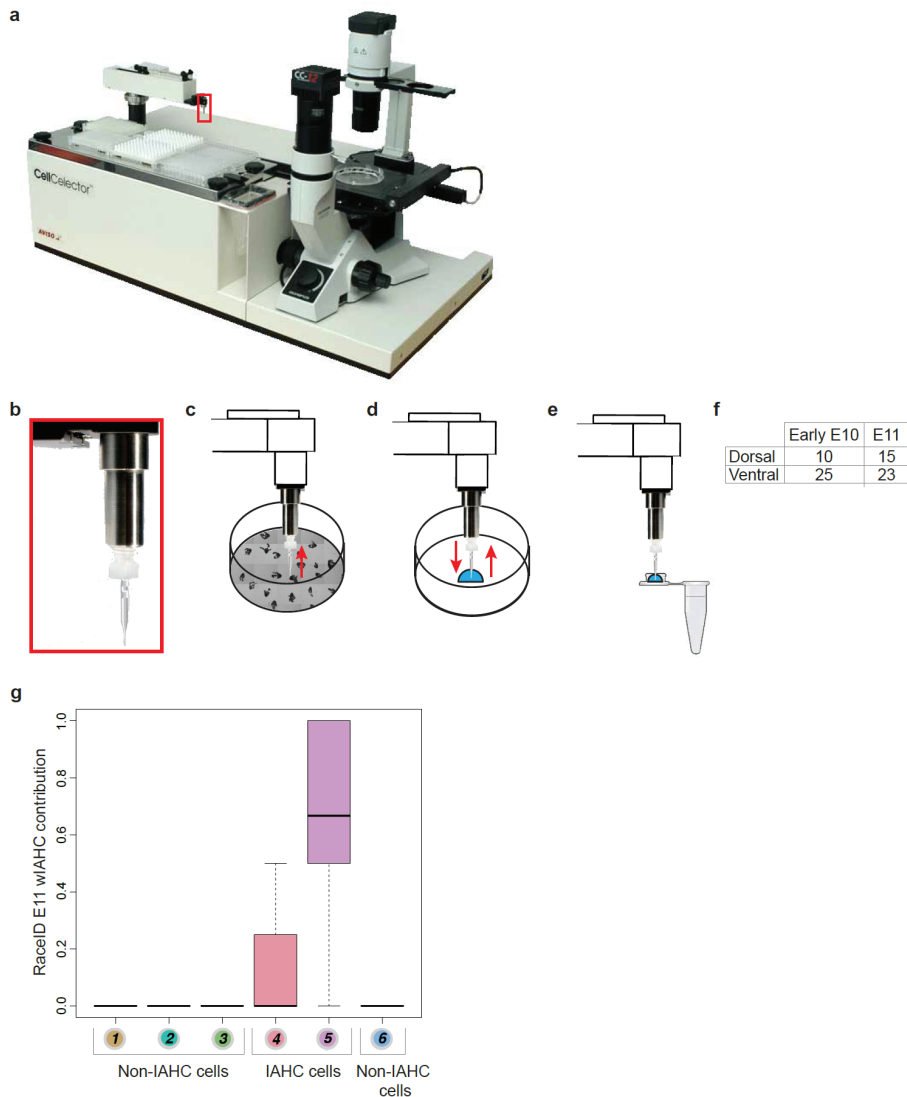
**Supplementary Figure 11 (related to Figure 2). Dynamic and fluctuant expression of cytokine/growth factor related genes at E11, according to pseudotime. (a)** Heatmap depicting on the y-axis the genes present in each pathway according to KEGG cytokine pathway and on the x-axis the E11 single cells ordered along the pseudotime axis. **(b-d)** KEGG pathway analysis on genes related to the cytokine pathways (shown in (a)), in **(b)** endothelial cells (non HE, HE), **(c)** EHT and IAHC cells (pre-HSCs type I and II), and **(d)** committed progenitors.



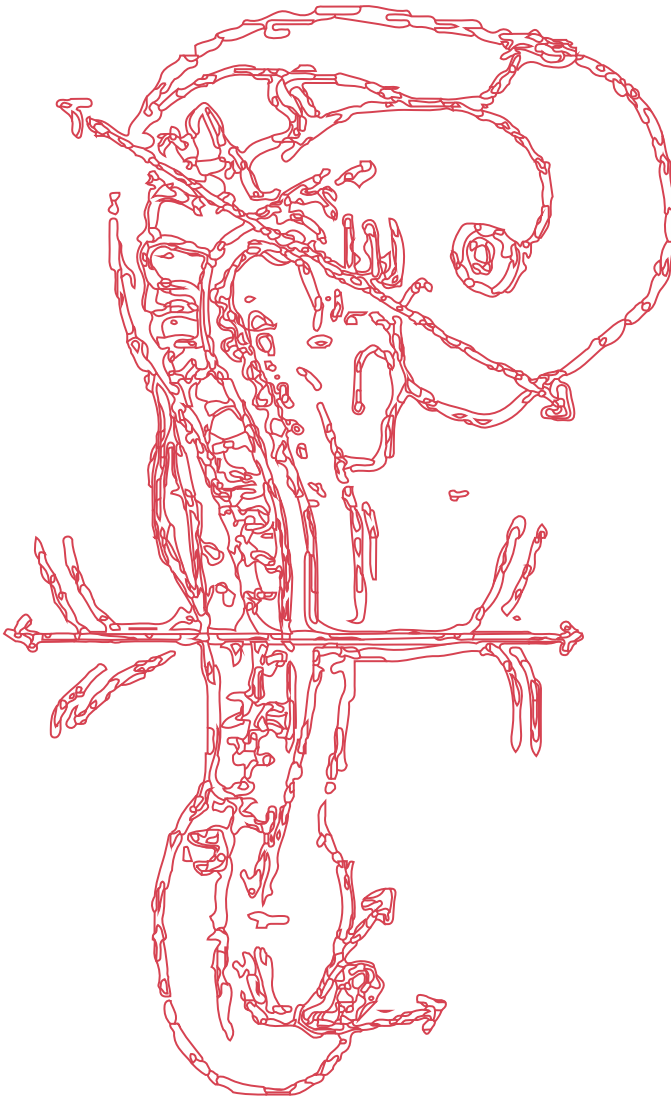
**Supplementary Figure 12 (related to Figures 2 and 4). Transcription factor expression during EHT and IAHC formation at E11.** (a) Heatmap depicting Euclidean distances between the 127 transcription factors (TFs) obtained in our set of E11 data. (b, e, h) Mean z-score of TFs in heatmap clusters I (b), II (e) and III (h) according to Monocle pseudotime. (c, f, i) Mean number of *Sox17* (c), *Gfi1* (f) and *Zfp1* (i) transcripts per cell according to pseudotime. Grey dots: single cells. (d, g, j) Major biological process GO terms enriched in heatmap clusters I (d), II (g) and III (j).



**Supplementary Figure 13 (related to Figures 3 and 4). Transcription factor expression during EHT and IAH formation at E10.** (a) Heatmap depicting Euclidean distances between the 88 transcription factors (TFs) obtained in our set of E10 data. (b, e, h) Mean z-score of TFs in heatmap clusters I (b), II (e) and III (h) according to Monocle pseudotime. (c, f, i) Mean number of *Sox17* (c), *Gfi1* (f) and *Zfpml1* (i) transcripts per cell according to pseudotime. Grey dots: single cells. (d, g, j) Major biological process GO terms enriched in heatmap clusters I (d), II (g) and III (j).



**Supplementary Figure 14 (related to Figures 1, 5 and 6). Mechanical pick-up of pure wIAHCs in embryo aorta thick slices.** (a) Automated cell picker CellCollector™. (b) Close-up of the harvesting module composed of a glass capillary connected to a syringe, associated with the CellCollector™ robotic arm (red box shown in (a)). (c-e) Steps of single wIAHC pick-up (see Methods for details). (c) The first pick-up allowed harvesting of single wIAHCs from the aorta of embryo slides immobilized in agarose in a 6-well plate. (d) wIAHCs were deposited (left arrow) and picked-up a second time (right arrow) to eliminate the presence of non-IAHC cells. (e) Pure single wIAHCs were collected in individual cap tubes. (f) Number of wIAHCs mechanically picked-up in the dorsal and ventral side of the aorta from E10 and E11 embryo slices. (g) Box plots of the RaceID cluster contribution to mechanically picked-up E11 wIAHCs. All wIAHCs were only composed of IAHC cells (identified by RaceID clusters 4 and 5) and no contaminating non-IAHC cells (identified by RaceID clusters 1, 2, 3 and 6). Colour-coded boxes are related to RaceID analysis shown in Fig. 1b.



## Chapter

---

# 4

## Research

published in:  
Blood, 2020; 136 (7): 831-844.

Yvernogeu, L., **Klaus, A.**, Maas, J., Morin-Poulard, I., Weijts, B.,  
Schulte-Merker, S., Berezikov, E., Junker, J.-P., Robin, C.

Multispecies RNA tomography reveals regulators of  
hematopoietic stem cell birth in the embryonic aorta

The defined location of a stem cell within a niche regulates its fate, behavior and molecular identity via a complex extrinsic regulation far from being fully elucidated yet. To explore the molecular characteristics and key components of the aortic microenvironment, where the first hematopoietic stem cells (HSCs) are generated during development, we performed genome-wide RNA tomography sequencing on zebrafish, chicken, mouse and human embryos. The resulting anterior-posterior and dorsal-ventral transcriptional maps provided a powerful resource for exploring genes and regulatory pathways active in the aortic microenvironment. By performing inter-species comparative RNA-seq analyses and functional assays, we explored the complexity of the aortic microenvironment landscape and the fine-tuning of various factors interplaying to control HSC generation both in time and space *in vivo*, including the ligand-receptor couple ADM-RAMP2 and SVEP1. Understanding the regulatory function of the local environment will pave the way for improved stem cell production *in vitro* and clinical cell therapy.



## Introduction

The constant production of short-lived hematopoietic cells throughout life relies on hematopoietic stem cells (HSCs) (1). Defects in HSCs lead to various blood-related disorders and cancers that are partly treated by HSC transplantations. Efforts have been made to generate bona fide HSCs *in vitro* to circumvent the limited supply of donor compatible HSCs for clinical use. Despite progress (2-4), HSC culture protocols are sub-optimal in mimicking the HSC surrounding microenvironment or niche, which is needed to induce HSC formation and to preserve HSC properties. A better knowledge of the regulatory factors and pathways involved in HSC formation *in vivo* is therefore important and required to improve *in vitro* culture protocols and HSC engineering (5,6).

HSCs are initially generated during embryonic development (7-9). They derive from hemogenic endothelial cells, via an endothelial to hematopoietic transition (EHT), in the aorta of the aorta-gonad-mesonephros (AGM) region of vertebrate embryos (10-18). The mechanism of HSC emergence is highly conserved and regulated both in time and space, with few species-specific differences (7). While HSC generation is polarized and restricted to the ventral side of the aorta in chicken, zebrafish and human embryos, EHT also occurs in the dorsal part of the aorta in mouse (although to a less extent) (6,17,19-23). HSCs are generated through the formation of intra-aortic hematopoietic clusters in chicken, mouse and human embryos but not in zebrafish where single cells emerge underneath the aorta (17,21,22,24). HSC production is also temporally regulated, starting at around 26 hours post-fertilization (hpf) with a peak at 40hpf in zebrafish and at embryonic day (E)2.25 with a peak at E3 in the anterior portion of the chicken aorta (16,17,21). Cluster emergence occurs between day 27 and day 42 in the middle portion of the aorta in human embryos (6,19,22,25). Similarly, emergence starts at E9.5 in the mouse aorta with cluster number and HSC activity peaking at E10.5 and E11.5, respectively (11,20).

The spatio-temporal restriction of hematopoietic emergence clearly indicates the presence of specific molecular cues in the surroundings of the aorta at defined locations and time points, instructing the aortic hemogenic endothelium and driving EHT and HSC production. How the AGM niche regulates these essential processes *in vivo* is still poorly understood. HSC regulation by extrinsic signals is indeed a complex process that occurs via direct cell-cell contact or long-range distribution of secreted molecules, acting directly or by inducing secondary signals (26). Our knowledge relies on the knockdown of specific ligands/receptors, *in vitro* experiments (e.g. co-culture of mouse/human HSCs with AGM-derived stromal cell lines, AGM explant culture with selected growth factors) and transcriptional comparison of supportive and less supportive stromal cell lines (27-29). Several important factors and signaling pathways regulating HSC generation, survival and/or maturation in the AGM niche have been identified (28,30-36).

RNA tomography (tomo-seq) was developed to provide spatially resolved transcriptomics, meaning information about any gene expressed along a pre-determined axis of a whole tissue or embryo, and at a precise time point of tissue isolation or embryonic development (37). This powerful approach, which combines cryosectioning and low input RNA sequencing, allowed to generate a high-resolution genome-wide atlas of gene expression patterns in the zebrafish embryo (37). We performed tomo-seq on embryos of the four different species classically used to study developmental hematopoiesis, i.e. chicken, zebrafish, mouse and human. Whole embryos and/or transversal sections were collected along the anterior-posterior and/or dorsal-ventral embryo axes at the developmental time points of HSC production. We generated spatial gene expression maps to investigate the molecular regulation of HSC generation in the

embryonic aorta. To create a more in-depth analysis between the niche and HSCs, we combined our AGM microenvironment tomo-seq datasets with cluster datasets (from mouse (35) and chicken (present study) embryos). This led to the identification of the ligand/receptor interactions active between the aortic microenvironment and clusters. Within our data, we unraveled a new conserved extrinsic HSC regulator, ADM and its receptor RAMP2, that we functionally validated *in vivo*. We also identified SVEP1 as the first extrinsic regulator of both cluster cellularity and cluster cell fate towards an HSC fate reported thus far. Overall, our findings emphasize the complexity of the aortic microenvironment landscape at the time of HSC formation and provides insights on the fine-tuning of various factors interplaying to control HSC production both in time and space as it occurs *in vivo*.

## Results

### Molecular landscape of the (ventral) aortic microenvironment in human, chicken, mouse and zebrafish embryos.

To study the molecular landscape of the aortic microenvironment where cluster and hematopoietic stem and progenitor cell (HSPC) emergence is spatially restricted, we focused on the four species classically used to study developmental hematopoiesis, i.e. chicken, human, mouse and zebrafish (Fig.1A-D). For tomo-seq, we collected samples from the different species at the time points of HSC production, (i) E3 chicken embryo slices, (ii) 35-day old human embryo slices, (iii) E10.5 and E11.5 mouse embryo slices, and (iv) 28hpf and 40hpf whole zebrafish embryos and trunks (including the aorta and yolk sac elongation) (Supplemental Table 1, Supplemental Fig.1A,B). To confirm the presence of cluster cells and HSPCs in the aorta at the indicated time points and location (6,17,19-23), we performed immunostainings on slices that were adjacent to the ones collected for tomo-seq (ventral cluster cells in chicken [MEP21+CD45+RUNX1+; Fig.1E] and human [CD34+CD45+RUNX1+; Fig.1F], ventral and dorsal (arrows) cluster cells in mouse [CD31+KIT+; Fig.1G], single HSPCs in zebrafish [*kdrl+cd41+*; Fig.1H,I] were observed). All thick slices and trunks (Fig.1J-L,N) were cryosectioned along the dorsal-ventral axis while whole embryos (Fig.1M) were cryosectioned along the anterior-posterior axis of the embryo, all cryosections being then processed for tomo-seq (Supplemental Fig.1A,B, Supplemental Tables 5-8).

To define our regions of interest within the tomo-seq data, we used the expression of genes restricted to specific tissues or cells. In chicken, the tomo-seq trace of *MPL*, whose expression is restricted to the cluster cells, precisely demarcated the ventral aortic region (Fig.1O, red area [R1], Fig.1P). As expected, *MPL* transcripts were not detected in the dorsal region of the aorta where clusters are absent, a region delimited by *SHH* expression (Fig.1O, blue area [R2], Fig.1Q, *SHH* is expressed by the notochord and floor plate). For human, we processed two slices for tomo-seq (slice #1, Fig.1K; slices #1 and #2, Supplemental Fig.2A,B). Hierarchical clustering of gene expression traces validated the reproducibility of the tomo-seq technique since three similar clusters [I to III], with expression maxima along the dorsal-ventral axis, were observed in both slices (Supplemental Fig.2C,D). Of note, an extra cluster (IV) was observed in slice #2, corresponding to the gut tissue that remained attached to this slice (Supplemental Fig.2B,D). *BMP4* and *GATA2* traces were used to demarcate the ventral aortic region (Fig.1R, Supplemental Fig.2E, red area [R1]). The *WWP2* trace detected in the cryosections containing the notochord/sclerotome area delimited the dorsal region of the aorta (Fig.1R, Supplemental Fig.2E, blue area [R2]). The traces of *Bmp4* and *Gata2* were also used for E10.5 and E11.5 mouse slices where they are

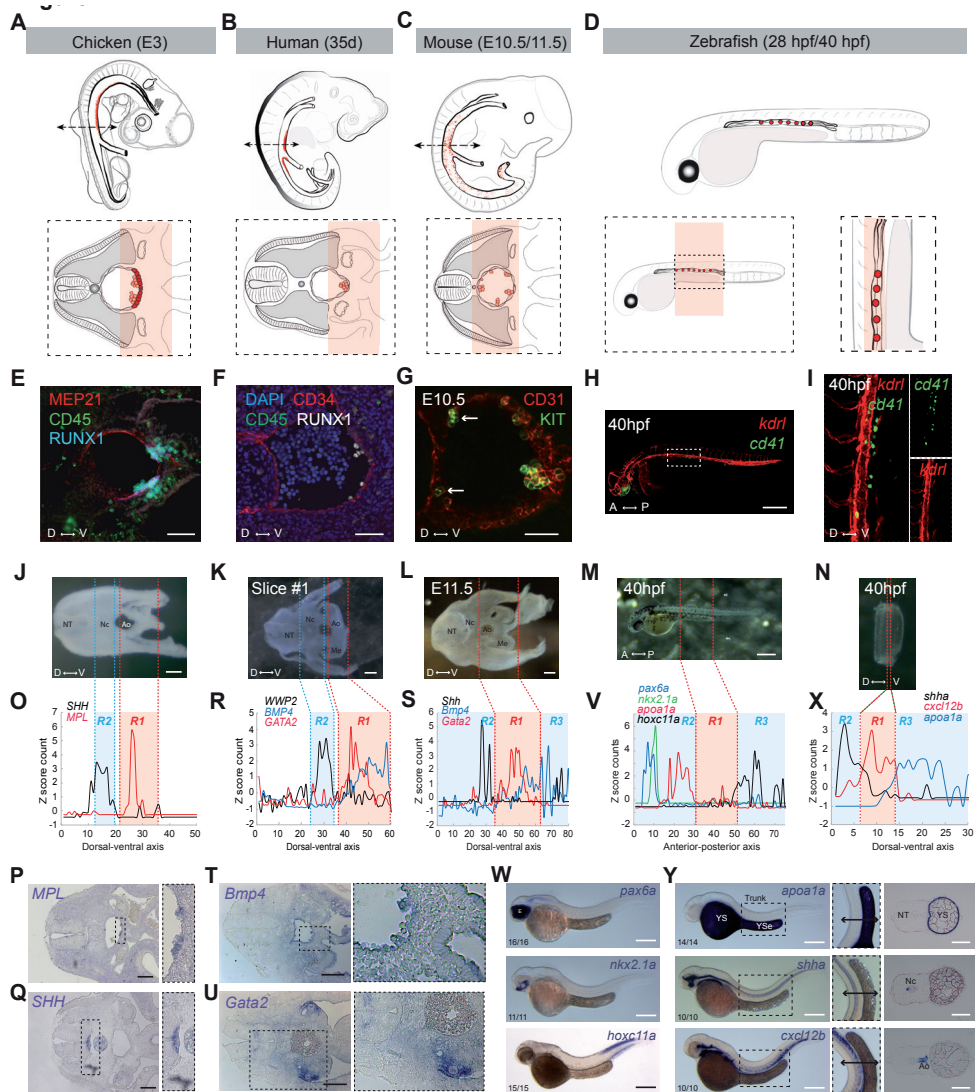


**Figure 1. Tomo-seq allows the identification of specific gene expression patterns restricted to the (ventral) aortic microenvironment.** (A-D) Schemes of the embryo species (upper panels) and samples (lower panels) used for tomo-seq analysis, i.e. E3 chicken anterior slices (A), 35-day old human slices (B), E10.5 and E11.5 mouse slices (C), 28hpf and 40hpf whole zebrafish embryos (D, left panel) and, 28hpf and 40hpf zebrafish trunks (D, right panel). The red areas mark the (ventral) aortic region where cluster and HSC emergence occurs. (E-G) Immunostainings of chicken (E), human (F), and mouse (G) embryo slices showing the location of clusters in the aorta. (E) Thick transversal slice of an E3 chicken embryo (slice adjacent to the one used for tomo-seq) stained with anti-MEP21 (red), anti-CD45 (green) and anti-RUNX1 (blue) antibodies. (F) Aorta of the human embryo slice #1 stained with anti-CD34 (red), anti-CD45 (green), anti-RUNX1 (white) antibodies and DAPI (blue). (G) Aorta of an E10.5 thick mouse embryo slice stained with anti-CD31 (red) and anti-KIT (green) antibodies. Arrows, dorsal clusters. (H) Global view of a *Tg(kdrl:mCherry;cd41:eGFP)* reporter zebrafish embryo at 40hpf; mCherry fluorescence highlights the whole vasculature, GFP fluorescence highlights hematopoietic stem/progenitor cells (HSPCs). (I) Trunk region containing the aortic region and yolk sac elongation of the 40hpf zebrafish embryo shown in H (dashed boxed area). Single fluorescent pictures (right panels). (J-L) Thick slices from E3 chicken (J), 35 day-old human (K) and E11.5 mouse (L) embryos used for tomo-seq. (M) Whole 40hpf zebrafish embryo used for tomo-seq. (N) Dissected trunk region of a 40hpf zebrafish embryo used for tomo-seq. (O) Tomo-seq traces for *MPL* (red) and

*SHH* (black) along the dorsal-ventral axis of the E3 chicken embryo slice shown in J. Colored areas corresponding to the ventral part of the aorta (R1, red) or to the dorsal part of the aorta (R2, blue). Of note, the numbers on the x axes of z score plots represent sequential individual section numbers (in Figure 1O, R, S, V, X). (P, Q) ISH for *MPL* (P) and *SHH* (Q) on transversal sections of E3 chicken embryo, showing the restricted expression of *MPL* and *SHH* to clusters and notochord, respectively. Dashed boxed areas are shown enlarged in the right panels. (R) Tomo-seq traces for *BMP4* (blue), *GATA2* (red) and *WPP2* (black) along the dorsal-ventral axis of the human embryo slice #1 shown in K. Colored areas corresponding to the ventral part of the aorta (R1, red) or to the dorsal part of the aorta (R2, blue). (S) Tomo-seq traces for *Gata2* (red), *Bmp4* (blue) and *Shh* (black), along the dorsal-ventral axis of the E11.5 mouse embryo slice shown in L. Colored areas corresponding to the aortic region (R1, red) or to the regions flanking the aorta (R2 and R3, blue). (T, U) ISH for *Bmp4* (T) and *Gata2* (U) on E11.5 mouse embryo transversal sections. Dashed boxed areas are shown enlarged in the right panels. (V) Tomo-seq traces for *pax6a* (blue), *nkx2.1a* (green), *hoxc11a* (black) and *apo1a* (red) along the posterior-anterior axis of the 40hpf zebrafish embryo shown in M. (W) WISH showing the expression patterns of *pax6a*, *nkx2.1a* and *hoxc11a* in 40hpf zebrafish embryos. (X) Tomo-seq traces for *apo1a* (blue), *shha* (black) and *cxcl12b* (red) along the dorsal-ventral axis of the 40hpf zebrafish embryo trunk shown in N. Red area (R1): slices corresponding to the yolk sac elongation region (including the aorta) (V) or the aortic region (X). Blue areas (R2 and R3): slices corresponding to regions flanking the aorta region. (Y) WISH showing the expression patterns of *apo1a*, *shha* and *cxcl12b* in 40hpf zebrafish embryos (left panels). Dashed boxed areas (trunk regions) are enlarged in the middle panels. Embryos were cryosectioned post-ISH to show the expression pattern of *apo1a*, *shha* and *cxcl12b* along the dorsal-ventral axis of the embryo trunks (right panels). The total numbers of embryos analyzed for WISH are indicated on the pictures. A, anterior; P, posterior; D, dorsal; V, ventral; R, region. NT, neural tube; Nc, notochord; Ao, aorta; Me, mesonephros; YS, yolk sac; YSe, yolk sac elongation. hpf; hours post-fertilization. Scale bars: 50µm (E, F, G, Y [right panels]), 100µm (J, P, Q), 150µm (L, T, U), 200µm (H, K, M, W, Y [left panels]).

expressed in the middle part of the slices (Fig.1S-U, Supplemental Fig.2F,G, red area [R1]). Since clusters are present in both dorsal and ventral sides of the aorta, we choose a larger region around the entire aorta to prevent the exclusion of any positive HSC regulators that might be present also in the dorsal side of the aorta. In zebrafish, we used specific gene expression patterns that clearly mark the different parts of the embryo, both at 28hpf and 40hpf (Fig.1V,X, Supplemental Fig.2H-L). For example, traces of *pax6a*, *nkx2.1a*, *apo1a* and *hoxc11a* indicated the cryosections containing the head, yolk sac and tail in the whole embryo, respectively (Fig.1V,W, Supplemental Fig.2K). *Shha*, *cxcl12b* and *apo1a* indicated the cryosections containing the dorsal (including notochord), middle (aorta) and ventral (yolk sac elongation) regions of the trunks, respectively (Fig.1X,Y, Supplemental Fig.2L).

Our initial goal was to identify, with the highest confidence, genes expressed in the microenvironment and involved in HSPC emergence. To this end, we applied the most stringent filtering strategy possible to extract genes that were more highly expressed in the (ventral) aortic region (red region R1) than in the dorsal aortic region and/or the rest of the embryo (blue regions R2 and R3) (Fig.1O,R,S,V,X, Supplemental Fig.2E,G,K,L) (see Methods for the strategy details). We identified 990 genes and 1,249 genes specifically upregulated in the ventral side of the chicken and human aorta, respectively (Supplemental Tables 5 and 6, “ventral selection” sheets), and 229 and 448 genes in the mouse aortic region at E10.5 and E11.5, respectively (Supplemental Table 7, “selection” sheet). Finally, we identified 645 and 276 genes for 28hpf and 40hpf whole zebrafish embryos, and 147 and 199 genes for 28hpf and 40hpf trunks, respectively (Supplemental Table 8, “AP selection” and “DV selection” sheets). By using a comparative tomo-seq approach on four species, we were thus able to identify the genes that are expressed in the (ventral) aortic region of chicken, human, mouse and zebrafish embryos (Supplemental Tables 5-8, respectively). Further comparative molecular analysis of the selective genes is now possible to unravel exclusive or conserved regulators of HSPC emergence.



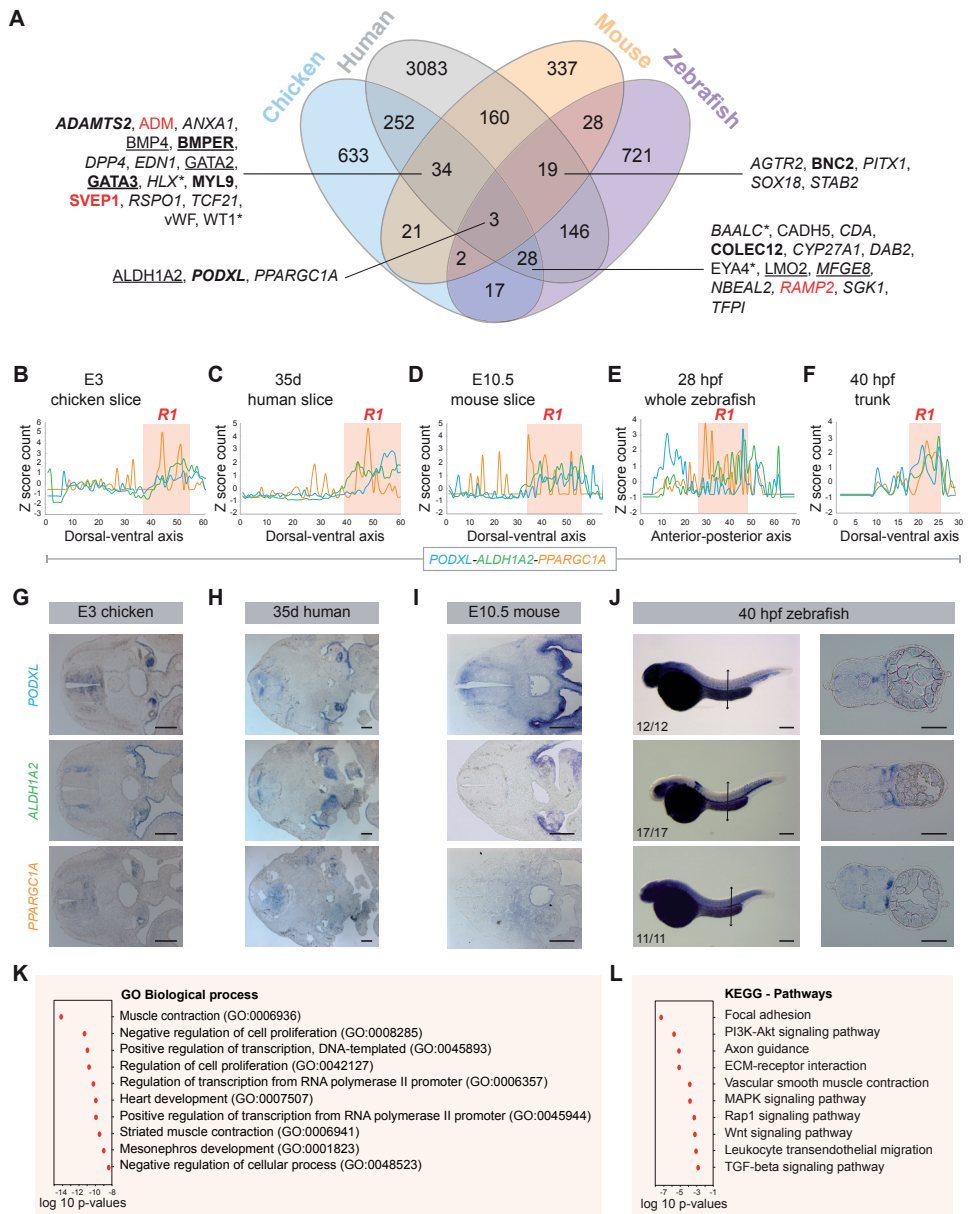


**Figure 2. Comparative analysis of tomo-seq datasets identifies species restricted and inter-species conserved gene expression in the aortic HSC supportive microenvironment.** (A) Venn diagram showing shared and distinct ventrally expressed genes between chicken, human, mouse and zebrafish tomo-seq datasets. Genes in bold: up-regulated (mRNA level) in HSPC supportive stromal cell line UG26.1B6 compared to non/less supportive stromal cell line UG26.3B5 isolated from the embryonic AGM (according to <http://stemniche.snv.jussieu.fr/> (29)); Genes underlined: known HSPC regulators in the embryonic aorta; Genes in italic: connected to hematopoiesis; Genes with\*: connected to leukemia. (B-F) Tomo-seq traces for *PODXL* (blue), *ALDH1A2* (green) and *PPARGC1A* (orange) in the (ventral) aortic region (R1) of E3 chicken slice (B), 35-day old human slice (C), E10.5 mouse slice (D), 28hpf whole zebrafish (E) and 40hpf zebrafish trunk (F). (G-J) ISH showing the specific expression patterns of *PODXL*, *ALDH1A2* and *PPARGC1A* in the (ventral) aortic region (R1) of E3 chicken anterior slice (G), 35-day old human

slice (H), E10.5 mouse slice (I), 40hpf whole zebrafish embryo (J, left panel) and zebrafish trunk slice (J, right panel). The total numbers of embryos analyzed for WISH are indicated on the pictures. (K, L) Ten first biological processes GO terms (K) and most relevant KEGG pathways (L) enriched in at least two species tomo-seq datasets (i.e. two, three and four species datasets). Scale bars: 150µm (G, I, J [left panels]), 200µm (H), 50µm (J [right panels]).

### **Species-restricted and inter-species gene expression, biological processes and pathways in the aortic HSC supportive microenvironment.**

Comparative data analysis identified genes that were species restricted, or common to two or more species (Fig.2A, Supplemental Table 9). The goal of this strategy was to identify the genes most likely involved in HSC regulation, and not to provide a complete account of all genes present in the aortic microenvironment. Consequently, only three genes (*Podxl*, *Aldh1a2* and *Ppargc1a*) were found conserved among the four species, but strikingly all of them were previously reported as HSPC regulators (40,41,42). However, it is important to note that, due to potential false negatives caused by e.g. species-dependent differences in expression levels, we cannot rule out that the real overlap between the species is higher. These genes that nicely displayed tomo-seq traces in R1 (Fig.2B-F) were indeed expressed in the aortic region of all species. *Podxl* was expressed mainly in the mesonephros and ventral epithelium, *Aldh1a2* was expressed on the lateral sides of the aorta, close to the cardinal veins and in the lateral epithelium, and *Ppargc1a* was lowly detected in the (ventral) aortic region (Fig.2G-J). Pathway analysis of genes that were at least common to more than two species revealed their involvement in cell proliferation, transcription, muscle and mesonephros development (Fig.2K, Supplemental Fig.3A). Some of these genes (Fig.2A) were either previously reported as being more highly expressed in HSPC embryonic supportive compared to non/low supportive stromal cell lines (in bold), connected to HSPC formation and/or regulation (in italic), connected to leukemia (with \*) and/or involved in HSC generation/regulation in the embryonic aorta (underlined) (28,36,43-46). In accordance, KEGG pathway analysis underlined different pathways known to be important for EHT and/or HSC formation, such as WNT and TGFβ (47,48) (Fig.2L, Supplemental Fig.3B). Interestingly, the analysis of the GO biological process or KEGG pathways of each species revealed a high degree of similarity, particularly in between chicken and human species (Supplemental Fig.4 and 5). Overall, through a stringent filtering strategy, we identified the aortic gene landscape specific or common to multiple species that is most likely involved in the formation of the first HSCs during embryonic development.

### **Ligand-receptor crosstalk between the microenvironment and HSCs.**

Crosstalk between the aortic microenvironment and clusters can occur through direct cell-cell contact mediated through ligand-receptor signaling. We therefore examined our datasets to identify spatial interactions of signaling pathways and secretory proteins/receptors (based on genes encoding annotated ligands-receptors, see Method Details). We used our previously published mouse cluster dataset (35), which we complemented with a chicken cluster dataset. This set was generated by FACS sorting CD45+ cluster cells from E3 chicken embryos after specific intra-aortic staining with anti-CD45 antibodies (38) and sequenced as bulk using the CEL-seq protocol (49,50) (Supplemental Fig.6, Supplemental Table 10). We first compared the mouse (35) and chicken cluster datasets and then compared them with the microenvironment dataset common to at least two species (Supplemental Table 9). This approach resulted into an insight full map of potential ligand-receptor interactions occurring between the aortic microenvironment and cluster cells (Fig.3A). Through pathway



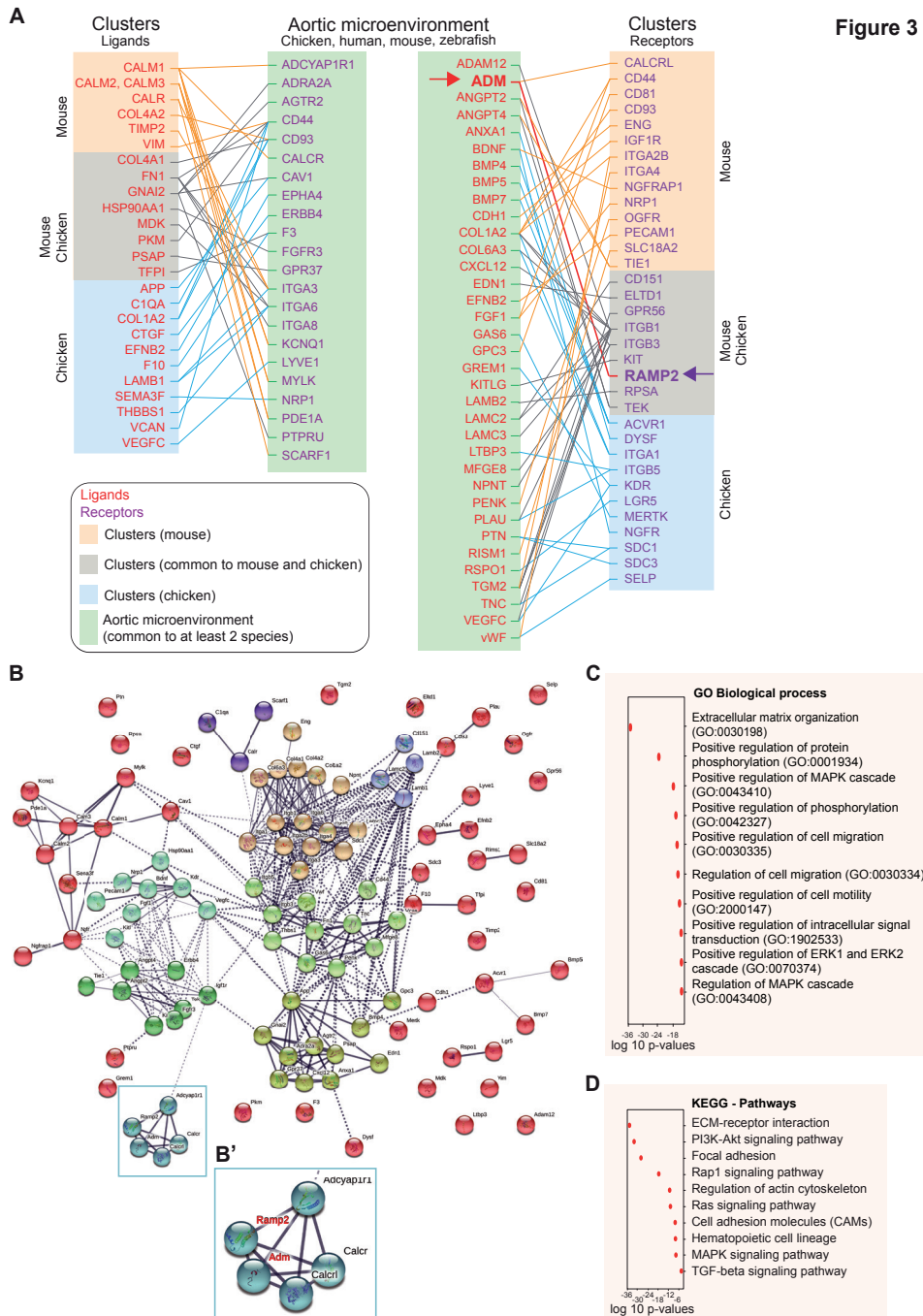


**Figure 3**

**Figure 3. Ligands-receptors interactions, biological processes and pathways active during the crosstalk between the cluster cells and the aortic microenvironment. (A) Distribution of the ligands and their corresponding receptors in the aortic microenvironment and clusters based on the microenvironment dataset (common to at least two species, Supplemental Table 9), the chicken cluster dataset (Supplemental Table 10) and a mouse cluster dataset (35). (B) Secretomics analysis using the microenvironment dataset (common to at least two species)**

and the chicken/mouse cluster datasets. Of note, not all molecules are linked because we used stringent active interaction sources (experiments and database) for better readability of the k-means clustering network. (B') Enlarged view of the blue node shown in the box in B. (C, D) Ten first biological processes GO terms (C) and most relevant KEGG pathways (D) enriched in the ligand-receptor datasets.

analysis, we found that these ligands-receptors were mainly involved in processes like EHT and HSPC survival, attachment, maturation and/or expansion, including INTEGRIN (ITG), WNT, BMP and FGF. Several partners were also connected to important HSPC regulators and pathways such as BMP and NOTCH signaling (ACVR1, GREM1, APP, CDH1, ITGB3), catecholamines (ADRA2A) and inflammation (ANXA1, CXCL12, SELP) (Fig.3A). Protein-protein interaction network visualized by STRING and k-mean clustering revealed intricate nodes of query proteins and first shell of interactors (Fig.3B). The analysis of the GO biological process and KEGG pathways emphasized a role of these molecules forming the major interconnected nodes in the extracellular matrix organization (i.e. collagens, integrins, laminins), hematopoietic cell lineage (KIT, KITL, KDR), cell migration/adhesion (Ephrins, FN1, GPR56, PECAM1) and cytoskeleton rearrangement (TEK) (Fig.3C,D). The ligand-receptor partners were also involved in various cellular processes (protein phosphorylation, intracellular protein transduction, ERK and MAPK cascades) and specific pathways (Pi3K-AKT, MAPK, ERK, RAP1, RAS) (Fig.3C,D). Overall, our comparative analysis of the multi-species microenvironment and cluster datasets revealed common ligands and receptors present in the microenvironment of the aorta or cluster cells at the time of HSPC emergence and therefore potentially involved in EHT, cluster cell survival, maturation, adhesion and/or migration.

### ADM and its receptor RAMP2 regulates HSPC production.

To further explore and validate our ligand-receptor data, we focused on two candidates with thus far an unknown hematopoietic role, i.e. ADM and its receptor RAMP2 (Adrenomedullin-Receptor Activity Modifying Protein 2, Fig.2A (in red), Fig.3A [arrows], Fig.3B,B' [blue node]). Our tomo-seq data and cluster data (from chicken [present study] and mouse (35)) predicted that ADM is expressed in the (ventral) aortic microenvironment while RAMP2 is expressed by the ventral aortic endothelium and cluster cells/HSPCs. We confirmed these expression patterns for ADM in human, mouse and zebrafish embryos (Fig.4A) and for RAMP2 in mouse (Fig.4B1), chicken (Fig.4B2) and zebrafish embryos (Fig.4B, bottom panel), by performing immunostaining and (W)ISH experiments. To determine whether ADM and RAMP2 play a role in HSPC production *in vivo*, we performed morpholino oligonucleotide (MO) knockdown in zebrafish embryos. ATG (MO\_ATG) and splice blocking (MO\_SB) morpholinos were injected in one-cell stage embryos. For controls, embryos were either not injected or injected with mismatch MO. After validation of the MO knockdown (Supplemental Fig.7A,B), we determined the effect of each gene knockdown on hematopoietic production by counting the number of *runx1+* or *cmyb1+* cells in the floor of the dorsal aorta by whole-mount *in situ* hybridization (WISH) in 40hpf and 48hpf zebrafish embryos, respectively (Fig.4C-F). The numbers of both *runx1+* and *cmyb1+* cells were statistically decreased in *adm* (Fig.4C,E) and *ramp2* (Fig.4D,F) morphants compared to controls. Additionally, knockdown of *adm* or *ramp2* in *Tg(kdrl:mCherry;cd41:eGFP)* embryos resulted in a decrease in *cd41+* HSPCs (Fig.4G,H). Importantly, the ablation of *adm* or *ramp2* did not result in an obvious vascular defect (*kdrl:mCherry+*) (Fig.4G,H) nor did it affect the arterial specification as visualized by *ephrinb2a* expression (Fig.4I,J).

To determine whether ADM is also involved in HSPC production in other species, we tested the active form of ADM (human ADM [13-52]) and its antagonist (human ADM

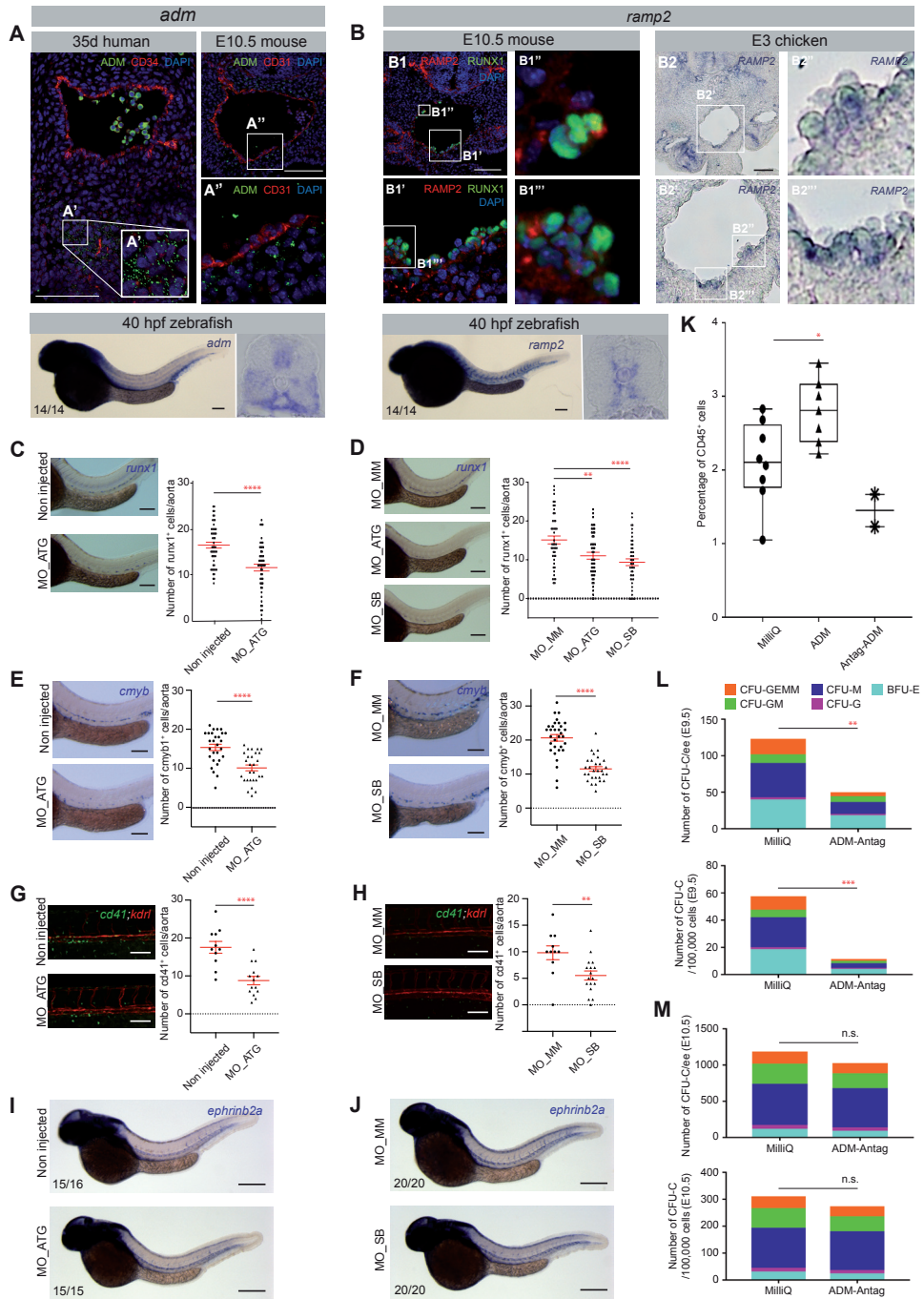


**Figure 4. ADM and its receptor RAMP2 are new and conserved HSPC regulators.** (A) Top left panel: Cryosection of 35-day old human embryo stained with anti-ADM (green) and anti-CD34 (red) antibodies and DAPI (blue). (A') Inset shows ADM expression in the ventral aortic microenvironment. Top right panels: Cryosection of E10.5 mouse embryo stained with anti-ADM (green) and anti-CD31 (red) antibodies and DAPI (blue). (A'') Boxed area is presented enlarged

to show immunostainings for ADM in the ventral aortic microenvironment closed to budding hematopoietic cells. Bottom panels: WISH showing the expression pattern of *adm* in 40hpf zebrafish embryos (left panel). Embryos were cryosectioned post-ISH to show the expression pattern of *adm* along the dorsal-ventral axis of the embryo trunks (right panel). (B) Top left panels (B1): Cryosection of E10.5 mouse embryo stained with anti-RAMP2 (red) and anti-RUNX1 (green) antibodies and DAPI (blue). (B1', B1'', B1''') Boxed areas are presented enlarged to show immunostainings for RAMP2 in the ventral endothelium and clusters. Top right panels (B2): ISH showing the expression patterns of *RAMP2* in an E3 chicken embryo cryosection. (B2', B2'', B2''') Boxed areas are shown enlarged to show *RAMP2* expression in the ventral aortic endothelium and clusters. Bottom panels: WISH showing the expression pattern of *ramp2* in 40hpf zebrafish embryos (left panel). Embryos were cryosectioned post-ISH to show the expression pattern of *ramp2* along the dorsal-ventral axis of the embryo trunks (right panel). The total numbers of embryos analyzed for WISH are indicated on the pictures. (C, D) The number of *runx1*+ HSPC cells was counted per aorta after WISH in non-injected embryos, embryos injected with mismatch MOs (controls) and in embryos injected with blocking MOs (ATG and/or SB) for *adm* (C, right panels) and *ramp2* (D, right panels). Representative cases of WISH for *runx1* expression in controls and *adm* (C), *ramp2* (D) injected MOs, analyzed at 40hpf (left panels). Graphs represent the average number ( $\pm$  SEM) of *runx1*+ cells in the dorsal aorta in each condition (n=3 independent experiments, n $\approx$ 50 zebrafish embryos each). (E, F) Number of *cmyb*+ HSPCs per aorta in embryos non-injected, injected with mismatch MOs (MO\_MM) or blocking MOs (MO\_ATG or MO\_SB) for *adm* (E) and *ramp2* (F). Example of WISH for *cmyb* in controls and *adm* (E) and *ramp2* (F) injected MOs, analyzed at 48hpf (left panels). Graphs represent the average number ( $\pm$  SEM) of *cmyb*+ cells in the aorta (n=3 independent experiments, n $\approx$ 30 embryos for each condition). (G, H) Number of *cd41*+ HSPCs per aorta in embryos non-injected, injected with mismatch MOs (MO\_MM) or blocking MOs (MO\_ATG or MO\_SB) for *adm* (G) and *ramp2* (H). Fluorescent pictures of controls and *adm* (G) and *ramp2* (H) injected MOs in the *Tg(kdrl:mCherry;cd41:eGFP)* fish background, analyzed at 40hpf (left panels). Graphs represent the average number ( $\pm$  SEM) of *cd41*+ cells in the aorta (n=2 independent experiments, 11 to 18 embryos for each condition). (I, J) WISH for *ephrinB2a* (arterial marker) in controls and *adm* (I) and *ramp2* (J) injected MOs, analyzed at 40hpf. (K) Graph represents the percentage of CD45+ hematopoietic cells in E3 chicken trunks after intra-cardiac injection of MilliQ water (control), adrenomedullin (ADM) or ADM antagonist (ADM-Antag). n=2 independent experiments. Dot: 2 to 3 trunks pooled. (L, M) *In vitro* clonogenic assay with cells isolated from E9.5 (L) or E10.5 (M) wild-type AGMs cultured as explant with MilliQ (control) or ADM antagonist (ADM-Antag). Top graphs represent the number of CFU-Cs per AGM embryo equivalent (ee). Bottom graphs represent the number of CFU-Cs per 100,000 AGM explant cells. One representative experiment of n=2 independent experiments. Scale bars: 100 $\mu$ m (A, B, C-H), 200 $\mu$ m (I, J). \*\*\*\*P<0.0001, \*\*\*P<0.001, \*\*P<0.01, \*P<0.05 (Student's t-test). n.s., not significant. CFU-GEMM: CFU-Granulocyte-Erythroid-Macrophage-Megakaryocyte; CFU-GM: CFU-Granulocyte-Macrophage; CFU-M: CFU-Macrophage; CFU-G: CFU-Granulocyte; BFU-E: Burst Forming Unit-Erythroid.

[22-52] trifluoroacetate salt, referred to as ADM-Antag) in chicken embryos *in vivo*. ADM [13-52] is the ADM fragment that possesses vasodilatory activity. ADM-Antag is a putative ADM receptor antagonist that inhibits the production of cAMP elicited by ADM. Intra-cardiac injections of either ADM, ADM-Antag or MilliQ water as a control (used to desolve ADM) were performed in E2 chicken embryos *in ovo*. Embryo trunks were isolated at E3 and the percentage of CD45+ hematopoietic cells was evaluated after flow cytometry analysis (Fig.4K, n=2). While ADM increased the percentage of CD45+ cells in the aorta *in vivo*, the ADM-Antag decreased this percentage (when compared to controls). Therefore ADM promotes HSPC activity also in the chicken embryo species. We then tested whether the effect of ADM was conserved in the mouse species. For this purpose, E9.5 and E10.5 AGMs were cultured as explant in presence of Antag-ADM or the same amount of MilliQ water (as a control) in the explant medium. After 3 days of explant, AGM cells were tested *in vitro* in a clonogenic assay (CFU-C). While ADM-Antag had no effect on cell viability, it decreased the number of CFU-Cs at E9.5 but to a much less extend at E10.5 (Fig.4L and M, respectively, n=2). These data thus reveal an early role of ADM in HSPC production in the mouse embryonic aorta.

Overall, our tomo-seq and RNA-seq inter-species comparative analyses and functional validations identified ADM and RAMP2 as an important conserved ligand-receptor couple involved in HSPC production *in vivo*.



## SVEP1 regulates the cellularity and fate of intra-aortic clusters.

Besides direct ligand-receptor interactions between the microenvironment and HSCs, single secreted growth factors and modulators of the extracellular environment might also be important components to modulate or fine-tune HSC development. Our transcriptomics analyses identified SVEP1 (Fig.2A, in bold red), which is a secreted factor known to modulate the extracellular environment to facilitate sprouting and migration of venous endothelial cells (51). Interestingly, cells producing SVEP1 are in immediate contact with the endothelium, including the dorsal aorta (51). These cells are most likely mesenchymal cells since HSPCs, endothelial cells, muscle pioneer cells and neurons do not express SVEP1 (51). Our tomo-seq traces and ISH in E3 chicken, 35-day old human and E10.5 mouse embryos supported an expression pattern restricted to the aortic region (Supplemental Fig.8A-C). To determine whether SVEP1 plays a role on HSPC production, we quantified the number of cluster cells in the aorta of *Svep1*<sup>+/+</sup> and *Svep1*<sup>-/-</sup> mouse embryos<sup>51</sup> by performing whole-mount immunostaining. Even though no significant differences were found at both E10.5 and E12.5 in the numbers of cluster cells (CD31+KIT+RUNX1+) per aorta (Fig.5A,B, respectively), nor in their distribution along the aorta (Supplemental Fig.8D,E), the cellularity per cluster differed. Indeed, very large clusters were observed in *Svep1*<sup>-/-</sup> compared to *Svep1*<sup>+/+</sup> aortas at both time points (Fig.5C,D). The cellularity of *Svep1*<sup>-/-</sup> clusters was significantly increased when compared to *Svep1*<sup>+/+</sup> clusters at both E10.5 and E12.5 (Fig.5E,F). *Svep1*<sup>-/-</sup> aortas contained clusters composed of up to 80 cells while clusters never contained more than 20 cells in *Svep1*<sup>+/+</sup> aortas. Accordingly, the total number of clusters was lower (Fig.5G,H). To determine whether the presence of large clusters in *Svep1*<sup>-/-</sup> aortas was due to an increased cell proliferation, staining for phosphorylated histone H3 (PHH3) and Ki67 were performed on E10.5 *Svep1*<sup>+/+</sup> and *Svep1*<sup>-/-</sup> embryo thick slices (Supplemental Fig.9A and B, respectively). No differences were observed in the mitotic PHH3<sup>+</sup> cells (Supplemental Fig.9C, D) or in cells in M phase (Ki67<sup>high</sup>), in G1, S or G2 phase (Ki67<sup>int</sup>) or G0 phase (Ki67<sup>neg</sup>) (Supplemental Fig.9E-G) in all clusters or large clusters (>5 cells). Thus, the increased cellularity observed in *Svep1*<sup>-/-</sup> clusters is not due to an abnormal cell proliferation.

To test whether the increased cluster cellularity might affect the HSC activity, AGM cells from E11 *Svep1*<sup>+/+</sup> and *Svep1*<sup>-/-</sup> embryos (CD45.2 background) were transplanted into adult irradiated wild-type recipients (CD45.1 background). Two cell doses were injected (0.3 and 1 embryo equivalent (e.e.)/recipient) and long-term multilineage analysis was performed at 4 months post-transplantation. A lower percentage of reconstituted recipients was observed when *Svep1*<sup>-/-</sup> AGM cells were transplanted, with a lower chimerism (Fig.5I,J). The frequency of HSCs in *Svep1*<sup>+/+</sup> and *Svep1*<sup>-/-</sup> AGMs was determined by applying Poisson statistics (Fig.5K), and the absolute number of HSCs was calculated. While *Svep1*<sup>+/+</sup> AGMs contain 2.04 HSCs (frequency=1 HSC/142,036 AGM cells), a number in accordance with previous studies (31,52,53), *Svep1*<sup>-/-</sup> AGMs contained only 1.17 HSCs (frequency=1 HSC/248,563 AGM cells). Nonetheless, the *Svep1*<sup>-/-</sup> HSCs were functional since we obtained normal proportions of T cells (CD4<sup>+</sup>/CD8<sup>+</sup>), B cells (B220<sup>+</sup>) and myeloid cells (CD11b<sup>+</sup>/GR1<sup>+</sup>) in all reconstituted recipients, indicating multilineage reconstitutions at 4 months (Fig.5L) that was maintained one-year post transplantation (data not shown). To test the self-renewal ability of *Svep1*<sup>-/-</sup> HSCs, secondary transplantations were performed. No differences in the long-term multilineage reconstitution were observed in the secondary recipients injected either with bone marrow cells from primary recipients initially reconstituted with *Svep1*<sup>+/+</sup> or *Svep1*<sup>-/-</sup> AGM cells (Fig.5M,N). Therefore, the loss of SVEP1 resulted in a reduced number of clusters that contained more cells but fewer

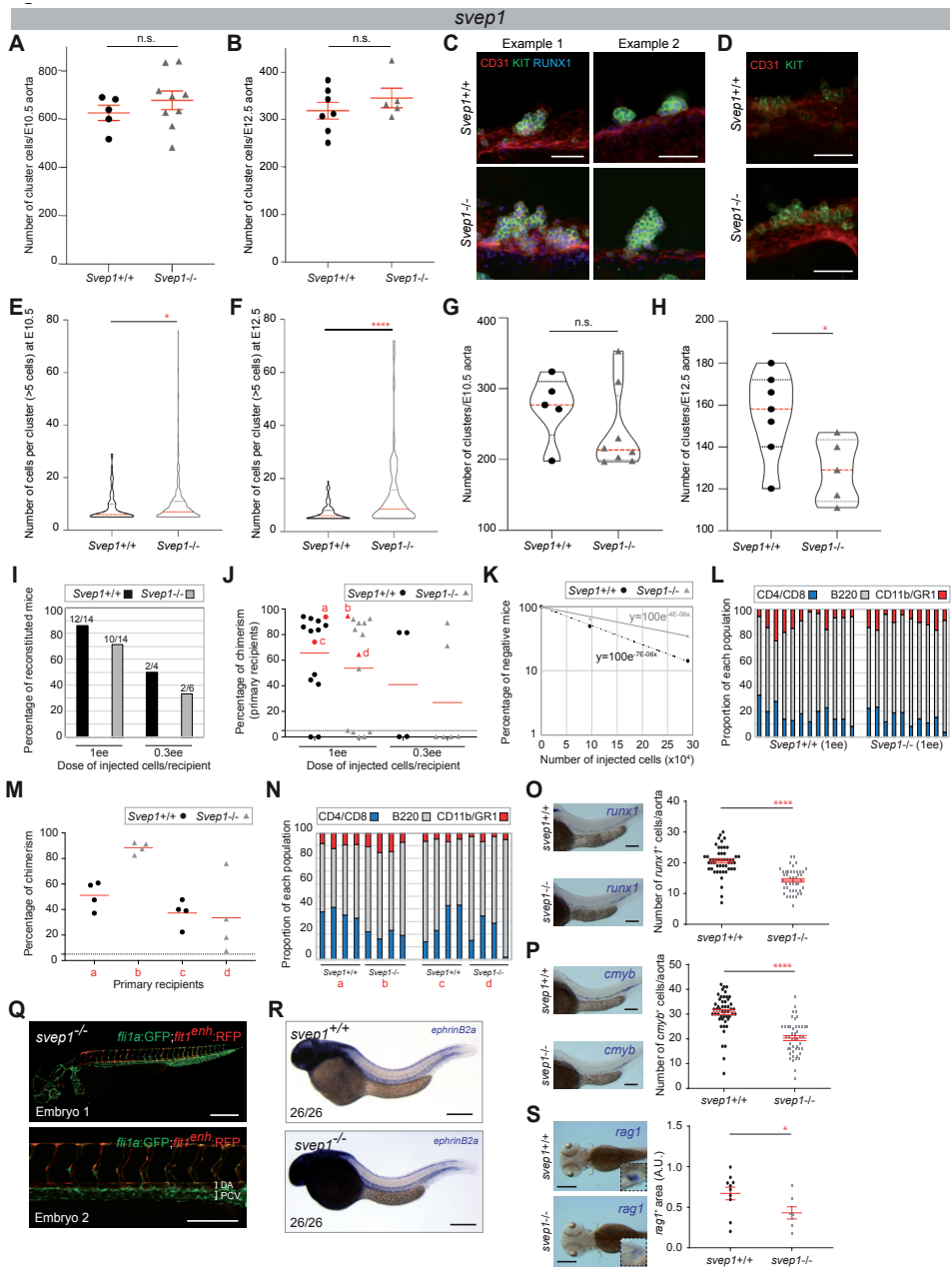


**Figure 5. *Svep1* regulates the cellularity and fate of clusters.** (A, B) Number of cluster cells per E10.5 (A) and E12.5 (B) *Svep1*<sup>+/+</sup> and *Svep1*<sup>-/-</sup> aortas (at E10.5: n=5 and 9 *Svep1*<sup>+/+</sup> and *Svep1*<sup>-/-</sup> embryos, respectively; at E12.5: n=7 and 5 *Svep1*<sup>+/+</sup> and *Svep1*<sup>-/-</sup> embryos, respectively; n= 3 independent experiments). Bars represent mean  $\pm$  SEM. (C, D) Examples of clusters observed in close-up after maximal projection of E10.5 (C) and E12.5 (D) *Svep1*<sup>+/+</sup> (upper panels) and *Svep1*<sup>-/-</sup> (lower panels) aortas stained with anti-CD31 (endothelial and hematopoietic marker, red), anti-KIT (hematopoietic marker, green) and anti-RUNX1 (hemogenic endothelium and hematopoietic marker, blue) antibodies. (E, F) Number of cells per clusters composed of more than 5 cells in E10.5 (E) and E12.5 (F) *Svep1*<sup>+/+</sup> and *Svep1*<sup>-/-</sup> aortas. (G, H) Number of clusters per E10.5 (G) and E12.5 (H) *Svep1*<sup>+/+</sup> and *Svep1*<sup>-/-</sup> aortas. (I) Hematopoietic repopulation analyses after



injection of AGM cells isolated from *Svep1*<sup>+/+</sup> and *Svep1*<sup>-/-</sup> E11 embryos (n=1 to 3 independent experiments). Numbers above columns indicate the number of mice repopulated/number of mice injected. Dose of injected cells is indicated as embryo equivalent (ee). (J) Percentage of chimerism in peripheral blood for each injected mouse (shown in I), 4 months post-transplantation. Dot: one transplanted mouse. Red dots: mice used to perform secondary transplantations (thereafter named a to d). Dashed line: limit of positivity (>5% of chimerism by flow cytometry). Red line: chimerism average. (K) HSC frequency determined based on the transplantation results (shown in I). HSC frequency per AGM was estimated by Poisson statistics applied to the percentage of non-repopulated recipients (y-axis) and the number of injected cells (x-axis). (L) Long-term donor-derived lymphoid (T cells: CD4<sup>+</sup>, CD8<sup>+</sup>; B cells: B220<sup>+</sup>) and myeloid (CD11b<sup>+</sup>, GR1<sup>+</sup>) contribution in the blood of reconstituted recipients (shown in J). Each bar represents a single recipient. (M) Percentage of chimerism in peripheral blood for each secondary recipient mouse transplanted with 3x10<sup>6</sup> bone marrow cells isolated from the primary reconstituted recipients (a to d, indicated as red dots in J) at 4 months post-transplantation. Dot: one transplanted mouse. Dashed line: limit of positivity (>5% of chimerism by flow cytometry). Red line: chimerism average. (N) Long-term donor-derived lymphoid (T cells: CD4<sup>+</sup>, CD8<sup>+</sup>; B cells: B220<sup>+</sup>) and myeloid (CD11b<sup>+</sup>, GR1<sup>+</sup>) contribution in the blood of secondary reconstituted recipients (shown in M). Each bar represents a single recipient. (O, P) Number of *runx1*<sup>+</sup> (O) and *cmyb*<sup>+</sup> (P) HSPCs per aorta at 40hpf and 48hpf, respectively, were determined after WISH in *svep1*<sup>+/+</sup> and *svep1*<sup>-/-</sup> zebrafish embryos. Representative cases of WISH for *runx1* and *cmyb* expressions in *svep1*<sup>+/+</sup> and *svep1*<sup>-/-</sup> zebrafish embryos (left side of each graph). Graphs represent the average number (± SEM) of *runx1*<sup>+</sup> and *cmyb*<sup>+</sup> cells in the dorsal aorta (n≈50 zebrafish embryos each). (Q) Fluorescent pictures of two *svep1*<sup>-/-</sup> (*fli1a:GFP;flt1enh:RFP*) embryos analyzed at 40hpf. Global view (upper panel, embryo #1) and a close-up of the dorsal aorta area (lower panel, embryo #2) are shown. (R) WISH for *ephrinb2a* in *svep1*<sup>+/+</sup> (upper panel) and *svep1*<sup>-/-</sup> (lower panel) embryos, analyzed at 40hpf. The total numbers of embryos analyzed for WISH are indicated on the pictures. (S) The *rag1*<sup>+</sup> thymic areas at 4 dpf were determined after WISH in *svep1*<sup>+/+</sup> and *svep1*<sup>-/-</sup> zebrafish embryos. Representative cases of WISH for *rag1* expression in *svep1*<sup>+/+</sup> and *svep1*<sup>-/-</sup> zebrafish embryos (left panels). Graphs represent the average of *rag1*<sup>+</sup> thymic area (± SEM) (n≈10 zebrafish embryos). \*\*\*\*P<0.0001, \*\*\*P<0.001, \*\*P<0.01, \*P<0.05 (Student's t-test). n.s., not significant. Scale bars: 50µm (C, D), 100µm (O, P, Q), 200µm (R, S).

functional HSCs. We found that the percentage of CD45<sup>+</sup> cells in E11.5 *Svep1*<sup>+/+</sup> and *Svep1*<sup>-/-</sup> embryos was similar indicating that the reduced HSC activity was not due to a premature differentiation of cluster cells in *Svep1*<sup>-/-</sup> embryos (Supplemental Fig.9H,I).

To test whether the regulatory role of SVEP1 was conserved, we analyzed HSPC production in *svep1* mutant fish lines (51). Similar to chicken, mouse and human, *svep1* is expressed in the aortic region and in the caudal hematopoietic tissue (CHT) of 40hpf zebrafish embryos (Supplemental Fig.8F). Zebrafish mutants had a significant reduction in *runx1*<sup>+</sup> and *cmyb*<sup>+</sup> cells in the floor of the dorsal aorta at 40hpf and 48hpf, respectively (Fig.5O,P), while arterial development and specification were unaffected (Fig.5Q,R). The hematopoietic defect persisted since we observed a significant reduction in *rag1*<sup>+</sup> lymphocytes in the thymus of the mutants at 4dpf (Fig.5S). SVEP1, which was predicted as a potential conserved HSPC regulator of the aortic microenvironment based on our transcriptomics analysis, indeed regulates HSPC production in mouse and zebrafish embryos.

## Discussion

We generated genome-wide datasets to identify spatial gene expression patterns along the developmental axes of four embryo species, i.e. chicken, human, mouse and zebrafish. By combining tomo-seq and RNA-seq dataset analyses, supervised filtering strategies and *in vivo* functional assays, we disclosed the complexity of the (ventral) aortic microenvironment landscape at the time of HSC emergence. We especially highlighted three new and conserved regulators required for proper cluster and HSC formation, i.e. ADM and its receptor RAMP2, and SVEP1.

Secretomics analysis and comparison of the aortic microenvironment datasets (common to at least 2 species) and cluster datasets (from chicken [present study] and mouse (35)) identified a myriad of interesting ligand-receptor partners. This emphasizes the complex cross-talk occurring between cluster cells and their proximal (i.e. endothelium, sub-aortic mesenchyme) and distal (e.g. UGR) microenvironment. GO term and K-mean clustering analyses identified nodes of molecules involved in different biological processes and pathways that would support the successive steps leading to HSC formation, i.e. regulation of actin cytoskeleton (for EHT and cluster formation), hematopoietic cell lineage (for cluster maturation), focal adhesion/regulation of cell motility (for cluster cell attachment/detachment/migration). The ligand-receptor ADM-RAMP2 specifically caught our attention as it might provide a potential signaling route that senses hemodynamic shear stress in the environment and transfers this signal to the hemogenic endothelium and/or to HSPCs. Normal blood flow is essential for HSC development and its absence severely impairs hematopoiesis (54-58). However, the molecular mechanism underlying shear stress sensing is not fully understood yet. One could speculate that the absence of ADM, which is a known hypotensive and vasodilator agent involved in tube formation (59), might affect the potential of hemogenic endothelial cells to produce HSPCs *in vivo* (as we reported here). Similarly, the absence of RAMP2, which transports the calcitonin gene-related peptide type 1 receptor (CALCRL) to the plasma membrane and acts as a receptor for ADM together with CALCRL, would also interfere on HSPC formation.

Beside ligands-receptors, single factors are also active in the aortic microenvironment. Among them, we identified SVEP1 as a new and conserved HSC regulator. SVEP1 is the first extrinsic factor identified in the aortic microenvironment that regulates cluster cellularity and fate in the mouse embryo. While less clusters were formed in absence of SVEP1, they were composed of more cells resulting in a normal number of cluster cells per aorta. However, the HSC activity was affected. The presence of large clusters does not seem to result of abnormal cluster cell proliferation or adhesion, or to an increase of EHT events. Double deficiency for the two NOTCH targets, HES1 (expressed in the aortic endothelium and clusters) and HES5, also leads to the formation of large clusters but no functional progenitors and HSCs (60). DLL4 was recently shown to control cell recruitment into the clusters, which blockage increased the number of cells in clusters that acquire an HSC activity (61). The presence of large clusters and the decrease of HSC activity in *Svep1*<sup>-/-</sup> embryos unlikely result from *Notch* deregulation since preliminary data indicated that *Hes1* and *Hes5* were similarly expressed in *Svep1*<sup>+/+</sup> and *Svep1*<sup>-/-</sup> embryos (data not shown). This might indicate that the cluster cellularity is controlled by another pathway that remains to be identified. While the same amount of cluster cells were present in *Svep1*<sup>+/+</sup> and *Svep1*<sup>-/-</sup> mouse embryos, less HSPCs were produced in *svep1*<sup>-/-</sup> zebrafish embryos. It might look contradictory and the result of differences between species that produce HSPCs via clusters or single cells. But overall, both species have a functional HS(P)C defect in absence of SVEP1, showing its conserved regulatory role. How does *Svep1* regulate cluster cellularity will be the subject of future research in both species. Moreover, a better identification of the different cell types composing the aortic microenvironment (poorly described thus far) will be needed to ascertain specific regulatory functions to specific cell types. It will also help to decipher whether the extrinsic regulation is a direct or indirect event occurring either in close contact to the hemogenic endothelium and clusters (e.g. by cell-cell contact, paracrine factors) or at distance (e.g. via a gradient of expression).

All our RNA-seq datasets are available to the community, providing the possibility to perform further analyses by changing any parameters (e.g. for a less stringent filtering approach, by increasing the size of the regions of interest and/or by decreasing the thresholds). Our tomo-seq datasets can also be more broadly used by the scientific community to identify gene expression patterns and to perform gene expression comparisons along the embryo axes (as shown for example for the chicken embryo in Supplemental Fig.10). To this end, we developed an interactive website (<http://multi-species.embryos.tomoseq.genomes.nl>), allowing (i) to compare with precision the expression pattern of any given gene of interest in any structure or microenvironment along the posterior-anterior (zebrafish, chicken) and/or dorsal-ventral embryo axes (all four species), (ii) to identify molecular signals that are potentially involved in tissue patterning (e.g. induction signal from neural tube/somite, notochord/somite) or (iii) to identify new genes that follow an expression pattern similar to that of a known gene used to define a region of interest (e.g. further genes involved in the AGM region, genes involved in neural crest cell, sclerotomal cell or mesonephros development). In the near future, the ability to integrate spatial transcriptomics with for example advanced (live) tissue imaging techniques and computational/theoretical models will open new horizons to further understand stem cell regulation in a physiological situation (e.g. regulatory networks, spatial gradients of gene expression). Understanding the native (hematopoietic) stem cell niche will offer novel approaches to promote stem cell activity and tissue regeneration, as for example after injury, irradiation, chemotherapy or upon aging. This will also provide insights in healthy versus cancer stem cell niches for drug testing, disease modelling and therapy.

## Methods

### Embryo generation

Human embryos and embryonic tissues were obtained from the Cupedo laboratory (Erasmus MC, Rotterdam, Netherlands) and Chuva de Sousa Lopes laboratory (LUMC, Leiden, Netherlands). The Medical Ethical Committee of LUMC (P08.087) approved all procedures regarding the collection and use of human embryonic material. The gestational age was calculated from the crown-rump length (CRL) of the fetus (before medical procedure by obstetric ultrasonography). Human fetal tissues were donated for research with informed consent from elective abortions without medical indication. The Medical Ethical Committee of the Erasmus MC approved the use of human embryonic and fetal tissues (fetal liver, bone marrow donors). Samples were used to titrate human antibodies and ISH probes. The use of these human tissues was contingent on informed consent in accordance with the Dutch Fetal tissue act. Fetal tissues were obtained from elective abortions, and informed consent was obtained after the decision to abort was finalized.

Details for animal housing, procedures, use of laboratory animal approvals, and embryo generation are in Supplemental Methods.

### Analyses and procedures

#### Whole embryo collection, embryo dissection and embryo slicing

Embryos and embryo slices were prepared as previously described (15,38) (Supplemental Methods).

#### RNA tomography (Tomo-sequencing)

Sample preparation for tomo-seq and sequencing libraries preparation were performed as described in<sup>37</sup> (Supplemental Methods).

Sample orientation and cryosections thickness are listed in Supplemental Table 1.

### **Filtering strategies**

Filtering strategies applied to determine gene expression in chicken, human, mouse and zebrafish (ventral) aortic environments are detailed in Supplemental Methods.

### **Whole-mount embryo, thick embryo slice and human paraffin section immunostainings**

Whole embryo and thick embryo slices were prepared and stained as previously described<sup>15,20</sup> (Supplemental Methods).

### **Whole in situ hybridization (WISH)**

Primers used for partial CDS amplification are listed in Supplemental Table 2 (Supplemental Methods).

### **Microinjections of morpholinos (MOs) in zebrafish embryos**

Sequences (Supplemental Table 3) and concentrations used for each MO and morpholino knockdown validation details are in Supplemental Methods.

### **Quantitative real time PCR**

Protocols and primer sequences are in Supplemental Methods and Supplemental Table 4, respectively.

### **Flow cytometry analysis and cell sorting**

Chicken cluster cell sorting

Cluster cells were stained by injecting PE anti-CD45 directly inside the aorta (as described in (15, 20), Supplemental Methods).

### **Secretomics analysis**

The annotation between ligand-receptor was downloaded from FANTOM39. The protein-protein interaction network was visualized by STRING (Supplemental Methods).

### **Data sharing statement**

Datasets generated during and/or analyzed during the current study are available in the Gene Expression Omnibus (Accession number GSE128350).

## **Acknowledgments**

The authors thank the lab members for helpful discussion and in particular Carla Kroon-Veenboer and Rutger Wielink for technical help. We thank Alexander van Oudenaarden for very helpful discussion at the beginning of the project. We thank Jacqueline Deschamps and Jean-Charles Boisset for useful comments on the manuscript. We thank Romualdo Ciau-Uitz (from Roger Patient's Laboratory) for kindly sharing zebrafish ISH probes. We would like to thank the Animal Facility for mouse and zebrafish care and the Optical Imaging Center for confocal microscope access (Hubrecht Institute). We thank Stefan van der Elst (Hubrecht Institute) for help with cell sorting and Mauro Muraro for technical help and advice (Single Cell Discoveries bv). We also thank the Utrecht Sequencing Facility (USF), subsidized by the University Medical Center Utrecht, Hubrecht Institute and Utrecht University. We thank Eugene Berezikov's lab for improving the chicken genome annotation. We thank Kelly McNagny (Vancouver) for the anti-chicken MEP21 supernatant. We thank Tom Cupedo

(Erasmus MC, Rotterdam) and Susana Chuva de Sousa Lopes (LUMC, Leiden) for providing human material samples. This work was supported in CR lab by a European Research Council grant (ERC, project number 220-H75001EU/HSCOrigin-309361), a TOP-subsidy from NWO/ZonMw (912.15.017) and the UMC Utrecht “Regenerative Medicine & Stem Cells” priority research program.

### **Authorship contributions**

C.R. and L.Y. conceived ideas and designed the research; C.R. and L.Y. performed mouse embryo dissections for transplantation experiments; C.R. performed the transplantations. L.Y. analyzed the transplanted mice by flow cytometry. L.Y. performed all embryo dissections and prepared all samples for tomo-seq experiments; L.Y. performed tomo-seq with the help of A.K., I.M-P and J.P.J.; L.Y., A.K. and I.M-P. performed morpholino injections; L.Y. and J.M. performed ISHs; L.Y. and C.R. analyzed all tomo-seq data with the help of J.P.J.; B.W. and J.M. performed RT-qPCR; A.K. performed explant cultures and CFU-C assay. L.Y. performed chicken embryo injections and analyses. L.Y. performed staining and quantification for Ki67 and PHH3 experiments. E.B. made the website. S.S-M provided the *Svep1* fish and mouse lines. L.Y. and C.R. analyzed and interpreted the experiments. L.Y. and C.R. created the Figures and wrote the paper with the help of A.K and B.W. All authors commented on the manuscript.

### **Conflict of interest disclosure**

The authors declare no competing financial interests.

## References

1. Orkin SH, Zon LI. Hematopoiesis: an evolving paradigm for stem cell biology. *Cell*. 2008;132(4):631-644.
2. Sugimura R, Jha DK, Han A, et al. Haematopoietic stem and progenitor cells from human pluripotent stem cells. *Nature*. 2017;545(7655):432-438.
3. Barcia Duran JG, Lis R, Lu TM, Rafii S. In vitro conversion of adult murine endothelial cells to hematopoietic stem cells. *Nat Protoc*. 2018;13(12):2758-2780.
4. Lis R, Karrasch CC, Poulos MG, et al. Conversion of adult endothelium to immunocompetent haematopoietic stem cells. *Nature*. 2017;545(7655):439-445.
5. Rowe RG, Mandelbaum J, Zon LI, Daley GQ. Engineering Hematopoietic Stem Cells: Lessons from Development. *Cell Stem Cell*. 2016;18(6):707-720.
6. Ivanovs A, Rybtsov S, Ng ES, Stanley EG, Elefanty AG, Medvinsky A. Human haematopoietic stem cell development: from the embryo to the dish. *Development*. 2017;144(13):2323-2337.
7. Klaus A, Robin C. Embryonic hematopoiesis under microscopic observation. *Dev Biol*. 2017;428(2):318-327.
8. Boisset JC, Robin C. On the origin of hematopoietic stem cells: progress and controversy. *Stem Cell Res*. 2012;8(1):1-13.
9. Dzierzak E, Bigas A. Blood Development: Hematopoietic Stem Cell Dependence and Independence. *Cell Stem Cell*. 2018;22(5):639-651.
10. Medvinsky A, Dzierzak E. Definitive hematopoiesis is autonomously initiated by the AGM region. *Cell*. 1996;86(6):897-906.
11. Muller AM, Medvinsky A, Strouboulis J, Grosveld F, Dzierzak E. Development of hematopoietic stem cell activity in the mouse embryo. *Immunity*. 1994;1(4):291-301.
12. Tavian M, Robin C, Coulombel L, Peault B. The human embryo, but not its yolk sac, generates lympho-myeloid stem cells: mapping multipotent hematopoietic cell fate in intraembryonic mesoderm. *Immunity*. 2001;15(3):487-495.
13. Ivanovs A, Rybtsov S, Welch L, Anderson RA, Turner ML, Medvinsky A. Highly potent human hematopoietic stem cells first emerge in the intraembryonic aorta-gonad-mesonephros region. *J Exp Med*. 2011;208(12):2417-2427.
14. Jaffredo T, Gautier R, Eichmann A, Dieterlen-Lievre F. Intraaortic hemopoietic cells are derived from endothelial cells during ontogeny. *Development*. 1998;125(22):4575-4583.
15. Boisset JC, van Cappellen W, Andrieu-Soler C, Galjart N, Dzierzak E, Robin C. In vivo imaging of haematopoietic cells emerging from the mouse aortic endothelium. *Nature*. 2010;464(7285):116-120.
16. Bertrand JY, Chi NC, Santoso B, Teng S, Stainier DY, Traver D. Haematopoietic stem cells derive directly from aortic endothelium during development. *Nature*. 2010;464(7285):108-111.
17. Kissa K, Herbomel P. Blood stem cells emerge from aortic endothelium by a novel type of cell transition. *Nature*. 2010;464(7285):112-115.
18. Lam EY, Hall CJ, Crosier PS, Crosier KE, Flores MV. Live imaging of Runx1 expression in the dorsal aorta tracks the emergence of blood progenitors from endothelial cells. *Blood*. 2010;116(6):909-914.
19. Mascarenhas MI, Parker A, Dzierzak E, Ottersbach K. Identification of novel regulators of hematopoietic stem cell development through refinement of stem cell localization and expression profiling. *Blood*. 2009;114(21):4645-4653.
20. Yokomizo T, Dzierzak E. Three-dimensional cartography of hematopoietic clusters in the vasculature of whole mouse embryos. *Development*. 2010;137(21):3651-3661.
21. Yvernogeu L, Robin C. Restricted intra-embryonic origin of bona fide hematopoietic stem cells in the chicken. *Development*. 2017;144(13):2352-2363.
22. Tavian M, Coulombel L, Luton D, Clemente HS, Dieterlen-Lievre F, Peault B. Aorta-associated CD34+ hematopoietic cells in the early human embryo. *Blood*. 1996;87(1):67-72.
23. Taoudi S, Medvinsky A. Functional identification of the hematopoietic stem cell niche in the ventral domain of the embryonic dorsal aorta. *Proc Natl Acad Sci U S A*. 2007;104(22):9399-9403.
24. Boisset JC, Clapes T, Klaus A, et al. Progressive maturation toward hematopoietic stem cells in the mouse embryo aorta. *Blood*. 2015;125(3):465-469.
25. Tavian M, Peault B. Embryonic development of the human hematopoietic system. *Int J Dev Biol*. 2005;49(2-3):243-250.
26. Peeters M, Ottersbach K, Bollerot K, et al. Ventral embryonic tissues and Hedgehog proteins induce early AGM hematopoietic stem cell development. *Development*. 2009;136(15):2613-2621.
27. Oostendorp RA, Harvey KN, Kusadasi N, et al. Stromal cell lines from mouse aorta-gonad-mesonephros subregions are potent supporters of hematopoietic stem cell activity. *Blood*. 2002;99(4):1183-1189.
28. Durand C, Robin C, Bollerot K, Baron MH, Ottersbach K, Dzierzak E. Embryonic stromal clones reveal developmental regulators of definitive hematopoietic stem cells. *Proc Natl Acad Sci U S A*. 2007;104(52):20838-20843.
29. Charbord P, Pouget C, Binder H, et al. A systems biology approach for defining the molec-



- ular framework of the hematopoietic stem cell niche. *Cell Stem Cell*. 2014;15(3):376-391.
30. Orelia C, Haak E, Peeters M, Dzierzak E. Interleukin-1-mediated hematopoietic cell regulation in the aorta-gonad-mesonephros region of the mouse embryo. *Blood*. 2008;112(13):4895-4904.
  31. Robin C, Ottersbach K, Durand C, et al. An unexpected role for IL-3 in the embryonic development of hematopoietic stem cells. *Dev Cell*. 2006;11(2):171-180.
  32. Rybtsov S, Batsivari A, Bilotkach K, et al. Tracing the origin of the HSC hierarchy reveals an SCF-dependent, IL-3-independent CD43(-) embryonic precursor. *Stem Cell Reports*. 2014;3(3):489-501.
  33. Robin C, Durand C. The roles of BMP and IL-3 signaling pathways in the control of hematopoietic stem cells in the mouse embryo. *Int J Dev Biol*. 2010;54(6-7):1189-1200.
  34. Gao X, Xu C, Asada N, Frenette PS. The hematopoietic stem cell niche: from embryo to adult. *Development*. 2018;145(2).
  35. Baron CS, Kester L, Klaus A, et al. Single-cell transcriptomics reveal the dynamic of haematopoietic stem cell production in the aorta. *Nat Commun*. 2018;9(1):2517.
  36. Fitch SR, Kimber GM, Wilson NK, et al. Signaling from the sympathetic nervous system regulates hematopoietic stem cell emergence during embryogenesis. *Cell Stem Cell*. 2012;11(4):554-566.
  37. Junker JP, Noel ES, Guryev V, et al. Genome-wide RNA Tomography in the zebrafish embryo. *Cell*. 2014;159(3):662-675.
  38. Boisset JC, Andrieu-Soler C, van Cappellen WA, Clapes T, Robin C. Ex vivo time-lapse confocal imaging of the mouse embryo aorta. *Nat Protoc*. 2011;6(11):1792-1805.
  39. Ramiłowski JA, Goldberg T, Harshbarger J, et al. A draft network of ligand-receptor-mediated multicellular signalling in human. *Nat Commun*. 2015;6:7866.
  40. Doyonnas R, Nielsen JS, Chelliah S, et al. Podocalyxin is a CD34-related marker of murine hematopoietic stem cells and embryonic erythroid cells. *Blood*. 2005;105(11):4170-4178.
  41. Chanda B, Ditadi A, Iscove NN, Keller G. Retinoic acid signaling is essential for embryonic hematopoietic stem cell development. *Cell*. 2013;155(1):215-227.
  42. Basu S. A complex interplay between PGC-1 co-activators and mTORC1 regulates hematopoietic recovery following 5-fluorouracil treatment. *Stem Cell Res*. 2014;12(1):178-193.
  43. Genthe JR, Clements WK. R-spondin 1 is required for specification of hematopoietic stem cells through Wnt16 and Vegfa signaling pathways. *Development*. 2017;144(4):590-600.
  44. McGarvey AC, Rybtsov S, Souilhoul C, et al. A molecular roadmap of the AGM region reveals BMPER as a novel regulator of HSC maturation. *J Exp Med*. 2017;214(12):3731-3751.
  45. de Pater E, Kaimakis P, Vink CS, et al. Gata2 is required for HSC generation and survival. *J Exp Med*. 2013;210(13):2843-2850.
  46. Gao X, Johnson KD, Chang YI, et al. Gata2 cis-element is required for hematopoietic stem cell generation in the mammalian embryo. *J Exp Med*. 2013;210(13):2833-2842.
  47. Ruiz-Herguido C, Guiu J, D'Altri T, et al. Hematopoietic stem cell development requires transient Wnt/beta-catenin activity. *J Exp Med*. 2012;209(8):1457-1468.
  48. Lempereur A, Canto PY, Richard C, et al. The TGFbeta pathway is a key player for the endothelial-to-hematopoietic transition in the embryonic aorta. *Dev Biol*. 2018;434(2):292-303.
  49. Hashimshony T, Wagner F, Sher N, Yanai I. CEL-Seq: single-cell RNA-Seq by multiplexed linear amplification. *Cell Rep*. 2012;2(3):666-673.
  50. Grun D, van Oudenaarden A. Design and Analysis of Single-Cell Sequencing Experiments. *Cell*. 2015;163(4):799-810.
  51. Karpanen T, Padberg Y, van de Pavert SA, et al. An Evolutionarily Conserved Role for Polydom/Svep1 During Lymphatic Vessel Formation. *Circ Res*. 2017;120(8):1263-1275.
  52. Kumaravelu P, Hook L, Morrison AM, et al. Quantitative developmental anatomy of definitive haematopoietic stem cells/long-term repopulating units (HSC/RUs): role of the aorta-gonad-mesonephros (AGM) region and the yolk sac in colonisation of the mouse embryonic liver. *Development*. 2002;129(21):4891-4899.
  53. Gekas C, Dieterlen-Lievre F, Orkin SH, Mikkola HK. The placenta is a niche for hematopoietic stem cells. *Dev Cell*. 2005;8(3):365-375.
  54. Adamo L, Naveiras O, Wenzel PL, et al. Biomechanical forces promote embryonic haematopoiesis. *Nature*. 2009;459(7250):1131-1135.
  55. North TE, Goessling W, Peeters M, et al. Hematopoietic stem cell development is dependent on blood flow. *Cell*. 2009;137(4):736-748.
  56. Diaz MF, Li N, Lee HJ, et al. Biomechanical forces promote blood development through prostaglandin E2 and the cAMP-PKA signaling axis. *J Exp Med*. 2015;212(5):665-680.
  57. Jing L, Tamplin OJ, Chen MJ, et al. Adenosine signaling promotes hematopoietic stem and progenitor cell emergence. *J Exp Med*. 2015;212(5):649-663.
  58. Kim PG, Nakano H, Das PP, et al. Flow-induced protein kinase A-CREB pathway acts via BMP signaling to promote HSC emergence. *J Exp Med*. 2015;212(5):633-648.
  59. Karpinich NO, Hoopes SL, Kechele DO, Lenhart PM, Caron KM. Adrenomedullin Function in Vascular Endothelial Cells: Insights from Genetic Mouse Models. *Curr Hypertens Rev*. 2011;7(4):228-239.
  60. Guiu J, Shimizu R, D'Altri T, et al. Hes repressors are essential regulators of hematopoietic stem cell development downstream of Notch signaling. *J Exp Med*. 2013;210(1):71-84.

61. Porcheri C, Golan O, Calero-Nieto FJ, et al. Notch ligand Dll4 impairs cell recruitment to aortic clusters and limits blood stem cell generation. *EMBO J.* 2020; e104270.

## Supplemental Data

### Supplemental Methods

#### Embryo generation

All animals were housed according to institutional guidelines, and procedures were performed in compliance with Standards for Care and Use of Laboratory Animals with approval from the Hubrecht Institute ethical review board. All animal experiments were approved by the Animal Experimentation Committee (DEC) of the Royal Netherlands Academy of Arts and Sciences.

We strictly follow the three Rs (3Rs) rules in order to use the minimum number of animals needed to obtain reliable results.

#### Mouse embryos

Mouse embryos were generated from timed matings. Observation of vaginal plugs was considered as day 0 of embryonic development. Mouse embryos were collected at embryonic day (E)10.5 and E11.5. Embryos were precisely staged based on the number of somite pairs. C57BL/6 wild-type embryos were used for tomo-seq. *Polydom/Svep1* mutant line was kindly provided by the Schulte-Merker laboratory (WWU, Munster, Germany)<sup>1</sup>.

#### Zebrafish embryos

Zebrafish were maintained and propagated according to standard laboratory conditions. *Tg(kdrl:mCherry;cd41:eGFP)* reporter fish line was used for tomo-seq (*kdrl:mCherry* (ZFIN ID: ZDB-TGCONSTRUCT-110127-23); *cd41:eGFP* (Lin et al., 2005)). *polydom/svep1* mutant fish line was kindly provided by the Schulte-Merker laboratory (WWU, Munster, Germany) (1). Of note, the *polydom/svep1* mutant line is in a *fli1a:GFP;flt1enh:RFP* double transgenic background. Zebrafish were used at 28- and 40-hours post-fertilization (hpf). AB fish line (EZRC) was used for morpholino injections. Of note, both *polydom/svep1* knock-out zebrafish and mouse lines are embryonic lethal or sub-viable due to abnormal lymphatic vessel development leading to critical edemas. Fish were kept according to FELASA guidelines<sup>2</sup>.

#### Chicken embryos

Fertilized chicken eggs (Bovans Brown) were obtained from Het Anker poultry (Ochten, The Netherlands). Eggs were incubated at  $37\pm 1^\circ\text{C}$  in a humidified atmosphere until they reached the appropriate developmental stage. Embryos were staged according to the embryonic day. E3 and E4 embryos were used.

#### Whole embryo collection, embryo dissection and embryo slicing

##### Mouse embryos

Briefly, embryos were removed from the uterus and yolk sac, and washed in PBS/FCS (PBS supplemented with 10% fetal calf serum). Head and tail were cut off with needles. Blood was flushed out of the aorta by using a borosilicate needle containing PBS/FCS. Embryos were then cut transversally into thick slices (200 $\mu\text{m}$ ) with a tissue chopper. Individual embryo slices were collected in PBS/FCS medium.

##### Chicken embryos

Embryos and embryo slices were prepared as previously described for mouse<sup>3-5</sup>. Head and tail were cut off the embryo, and the blood was flushed out of the aorta with PBS/FCS. Embryos were then transversally sliced into thick slices with a tissue chopper.

### **Zebrafish embryos**

Whole zebrafish or the embryo trunk including the aorta and the yolk sac elongation were used.

### **Human embryos**

The embryo was transversally cut into thick slices with a tissue chopper (as described above for chicken and mouse embryos).

### **RNA Tomography (Tomo-sequencing)**

Embryo thick slices, trunk and subdissected aorta embedding in O.C.T and cryosectioning. Whole embryos (zebrafish), dissected trunks (zebrafish) and thick slices (mouse, chicken, human) were placed into a plastic tissue dispomolds (Adamas Instrumenten bv) using a 3.5ml transfer pipette (Sarstedt) and carefully straightened. The excess of PBS was removed using a tip and the samples were immediately embedded in O.C.T freezing medium (Tissue-Tek). Samples were oriented (for sectioning along the anterior-posterior axis or along the dorsal-ventral axis), quickly frozen on dry ice and stored at  $-80^{\circ}\text{C}$  prior cryosectioning. Of note, it is technically very challenging to collect the first cryosections from small samples such as the thick slices. To avoid losing the first cryosections of the tissue, we usually collected several cryosections before seeing the tissue in the block. These cryosections will not contain tissues and therefore no RNA (0 read). As easily understandable, the number of empty cryosections will vary from one sample to another one. However, this is not an issue for our analysis since we do not select the regions of interests arbitrary or by using the same number of slices for the different samples. For our analyses, we always defined the regions of interests (Rs) by looking for genes with well-defined expression patterns (e.g. *Shh*). It allows to precisely locate the different parts of the section. Therefore, we do not have to adjust for the variability in our replicates and it does not affect the analysis. Each cryosection was sequentially collected in Eppendorf LoBind tubes and immediately transferred to dry ice.

### **Sequencing libraries preparation**

Total RNA was isolated from individual cryosection using TRIzol reagent (Ambion), according to the manufacturer's manual. RNA extraction, amplification and sequencing libraries were performed as described in<sup>6</sup>. Briefly, RNA samples were treated according to the CEL-seq protocol<sup>7</sup>. Illumina sequencing libraries were prepared with the TruSeq small RNA sample prep kit (Illumina) and sequenced paired-end either at 50 bp read length on HiSeq or 75 bp read length on NextSeq.

### **Data analysis**

The sequencing data were aligned to the reference transcriptomes and normalized to the same number of reads per section as previously described<sup>6</sup>. For similarity rankings (Supplemental Fig.10) and hierarchical clustering (Supplemental Fig.2C,D), tomo-seq traces were z-score transformed to normalize against differences in total expression levels between genes. Only genes expressed above a threshold of  $>4$  reads in  $>1$  section were retained for analysis. Similarity rankings were calculated based on Euclidean distance of z-score transformed tomo-seq traces across all sections. Hierarchical clustering was performed on all genes with a detected spatial expression peak (Z score  $>1$  in  $>4$  consecutive sections of smoothed tomo-seq traces). Identification of differentially expressed genes between regions of interest (R) within the same tomo-seq sample was performed by comparing mean expression levels inside and outside the R, using fold-expression thresholds as described in the main text. Bioinformatic analyses were performed with Matlab.

## Filtering strategies

*Gene expression in chicken ventral aortic environment* - The tomo-seq trace of MPL was used as a reference to indicate our region of interest, i.e. the ventral region of the anterior part of the aorta (Fig.1O, Region R1). The region where clusters were absent and where MPL expression was not detected was also defined, i.e. in the dorsal side of E3 anterior slices (Fig.2O, R2). The supervised filtering strategy was performed on E3 anterior chicken slices, by selecting the genes with a total sum of reads in R1 that was 1.5 times higher compared to the total sum of reads in R2. Since three E3 anterior chicken slices were used, we decided to select genes that were present in 2 out of the 3 resulting lists, i.e. 990 genes (Supplemental Table 5). Genes were then ranked using MPL as a reference.

*Gene expression in human ventral aortic environment* - Regions of interest were defined in the ventral and dorsal side of the aorta for both human embryo slices (Fig.1R, Supplemental Fig.2E; R1 and R2, respectively). Genes with a total sum of reads in R1 that was 1.5 times higher than the total sum of reads in R2 were then selected for both slices (similar to the filtering strategy applied on chicken slices, see above). At last, 1,249 genes passed the filtering criteria in both samples. These genes were ranked according to the similarity between their expression profile and the *GATA2* expression profile (used as reference)<sup>8</sup> (Supplemental Table 6).

*Gene expression in mouse aortic environment* - A different supervised filtering strategy than reported above for chicken and human samples was applied since cluster emergence is not ventrally restricted and mostly occurs in the middle portion of the mouse aorta<sup>9-11</sup>. Indeed, cluster cells (CD31+KIT+/RUNX1+) are also found in the dorsal part of the mouse aorta (although in lower numbers) (Fig.1G, arrows). Therefore, we first defined a broad region around the aorta using *Bmp4* and *Gata2* expression as a reference (Fig.1S, Supplemental Fig.2G, R1) and two regions flanking R1 (Fig.1S, Supplemental Fig.2G, R2 and R3). Genes with a total sum of reads in R1 that was 2 times higher than the total sum of reads in R2 and R3 were selected. The analysis was run 3 times independently for both E10.5 and E11.5 samples. Genes that were common in at least 2 out of the 3-resulting lists were selected. This filtering strategy led to two shortlists of 229 and 448 genes at E10.5 and E11.5, respectively (Supplemental Table 7).

*Gene expression in zebrafish ventral aortic environment* - Regions located along the yolk sac elongation in whole embryos (low *apo1a* expression) and between the notochord and the yolk sac elongation in the trunk samples (*cxcl12b* expression) were demarcated (Fig.1V,X, Supplemental Fig.2K,L, R1) as well as regions outside R1 (Fig.1V,X, Supplemental Fig.2K,L, R2 and R3). Genes with a total sum of reads in the defined R1 that was twice higher than the total sum of reads in R2 and R3 were selected. The analysis was run 3 times independently for the 28hpf whole embryos and 2 times independently for the other samples. The filtering strategy provided four short lists of genes. We obtained 645 genes for 28hpf whole embryo and 276 genes for 40hpf whole embryo (the selected genes were common in at least 2 out of the 3-resulting lists or common in the 2-resulting lists, respectively). For the trunk, 147 genes (28hpf) and 199 genes (40hpf) were obtained (the selected genes were common in the 2-resulting lists) (Supplemental Table 8).

The expression threshold (i.e. 1.5-fold, 2-fold) was determined empirically based on the resolution of the tomo-seq traces. The resolution of tomo-seq traces depends on the type of samples. In cases where the tissue of interest constitutes a relatively large

part of the sections, a 2-fold cut-off was used. In cases where more unrelated tissue is contained in the sections, we lowered the threshold to 1.5-fold to be able to extract the relevant genes. Our criterion for determining the threshold value was whether or not known marker genes were recovered by our analysis.

### **Whole-mount embryo, thick embryo slice and human paraffin section immunostainings**

Briefly, mouse and chicken embryos were injected with PBS to flush out the blood from the aorta. Chicken embryos were perfused in the heart with anti-MEP21 antibody12 to stain the whole vasculature5. Embryos were then washed three times in PBS before fixation in 4% PFA during 20 minutes at 4°C. Embryos were washed again in PBS before dehydration-rehydration step in methanol. Embryos were then blocked in a PBS-MT (1% skim milk, 0.4% TritonX-100, 0.2%BSA, 0.1% goat serum) solution for 1 hour at 4°C. Mouse embryos were stained with (i) purified anti-CD117 antibody (KIT, clone 2B8, ebiosciences, Thermofisher) or purified anti-CD45 antibody (PTPRC, BD Pharmingen, Invitrogen), (ii) biotin anti-CD31 (PECAM) antibody (MEC133, BD Bioscience), and (iii) purified anti-RUNX1 antibody (ab92336, Abcam). Alexa Fluor 647 goat anti-rat, Alexa Fluor 555 Streptavidin and Alexa Fluor 488 goat anti-rabbit antibodies (Life Technologies) were used to reveal CD117, CD31 and RUNX1 antibodies, respectively. For immunostainings on sections, purified anti-ADM antibody (PA5-36524, Invitrogen) and anti-RAMP2 antibody (MAB6500, R&D Systems) were used.

For proliferation status experiments, E10.5 *Svep1*<sup>+/+</sup> and *Svep1*<sup>-/-</sup> mouse embryo thick slices were stained with either human purified anti-Ki67 antibody (clone B56, BD Pharmingen, Invitrogen) or purified anti-PHH3 antibody (06-570, Millipore). Alexa Fluor 555 goat anti-mouse and Alexa Fluor 647 goat anti-rabbit antibodies were used to reveal Ki67 and PHH3 antibodies, respectively. For Ki67 and PHH3 experiments, biotin anti-CD34 antibody (BD Pharmingen, Invitrogen) and purified anti-CD117 (KIT, clone 2B8, ebiosciences, Thermofisher) antibody were used to stain the endothelium of the aorta and the hematopoietic cluster cells, respectively.

Chicken embryos were stained with purified anti-CD45 (HisC7, Cedi-Diagnostics B.V.) and anti-RUNX1 antibodies. Alexa Fluor 647 goat anti-mouse IgG1, Alexa Fluor 555 goat anti-mouse IgG2a and Alexa Fluor 488 goat anti-rabbit antibodies were used to reveal MEP21, CD45 and RUNX1 antibodies, respectively. Each antibody (primary and secondary) incubation was performed overnight at 4°C in PBS-MT followed by several washes in PBS-MT the following day. At the end of the staining, embryos were washed in PBS-T (0.4% TritonX-100) several times for 20 minutes. Then, embryos were dehydrated in methanol, cleared progressively via successive passages into a Methanol/50% BABB (benzyl alcohol:benzylbenzoate, 1:2) and 100% BABB solutions. Transparent embryos were mounted between slide and coverslip using Fast Well (Grace Bio-Labs) and imaged with a Zeiss LSM700 confocal microscope.

Human sections were stained with purified anti-CD45 (clone 555480, BD Biosciences), biotin anti-CD34 (ab30375, Abcam), anti-ADM antibody (PA5-36524, Invitrogen), anti-RAMP2 antibody (MAB6500, R&D Systems) and purified anti-RUNX1 antibodies. Antigen retrieval was performed by heating slides containing aorta sections at 85°C in 10mM sodium citrate buffer (pH6) for 20 minutes. Alexa Fluor 647 goat anti-mouse IgG1, Alexa Fluor 555 Streptavidin and Alexa Fluor 488 goat anti-rabbit secondary antibodies were used to reveal CD45 or RAMP2, CD34 and RUNX1 or ADM antibodies, respectively.

### **Whole in situ hybridization (WISH)**

ISH probe constructs were generated by PCR amplification of partial coding sequence (CDS) from cDNA, and subsequent ligation into PCS2 vector (Addgene). EcoRI and



XhoI restriction sites were added to the primers for selective ligation into the PCS2 vector. Probe plasmids were linearized and riboprobes transcribed from linearized template in the presence of digoxigenin-11-UTP. Zebrafish embryos were fixed in 4% PFA overnight, and dehydrated stepwise into methanol before storage at -20°C. Embryos were rehydrated stepwise to PBST (PBS supplemented with 0.1% Tween20, Sigma-Aldrich), and embryos were incubated for 10 minutes with Proteinase K (10µg/ml) followed by 20 minutes post-fixation in 4% PFA. Embryos were prehybridized in Hyb- buffer for at least 1 hour at 70°C. Riboprobes were diluted 1/200 in Hyb- buffer supplemented with transfer RNA and heparin, and embryos were incubated in probe solution overnight at 70°C. Following probe removal, embryos were washed stepwise from hybridization buffer into 2X SSC, then from 0.2X SSC into PBST. Embryos were blocked in PBST with BSA and Sheep Serum for at least 1 hour, and incubated with anti-digoxigenin AP antibody overnight at 4°C. Following antibody incubation embryos were washed extensively in PBST and transferred into TBST. Probe detection was carried out using NBT/BCIP. Embryos were fixed in 4% PFA and then either washed stepwise to PBS/Glycerol (80%) for whole embryo pictures or processed for freezing/cryosectioning (for transversal section pictures). Zebrafish *runx1*, *cmyb* and *rag1* probes were a gift from Romualdo Ciau-Uitz (Patient's Laboratory)<sup>13</sup>. For chicken and mouse WISH, the zebrafish WISH protocol was applied with few adjustments. For instance, embryos were incubated for 15 minutes with Proteinase K (20µg/ml), prehybridized in Hyb- buffer containing Dextran Sulfate (10X final concentration), Denhart (1X final concentration) and CHAPS (1%) solutions, and extensively washed in MABT (pH7.5) solution before probe detection.

### **Microinjections of morpholinos (MOs) in zebrafish embryos**

The morpholinos (MOs) were selected against *adm* and *ramp2*. Antisense (ATG) MOs, splice-blocking (SB) MOs and mismatch (MM) MOs were purchased from GeneTools, LCC. Typically, 1nl total volume of MO was injected in 1-cell stage embryos. MO-injected fish were fixed at 40hpf and processed for *runx1* ISH. All morpholinos were from GeneTools, LCC.

### **Morpholino knockdown validation**

To determine the efficiency of the *adm* MO, we replaced the transcriptional start site of mScarlet with 15bp upstream and 15bp downstream of the transcriptional start site of *adm* (which contained the *adm* ATG MO target sequence). It was then cloned into the pCS2+ plasmid. One-cell stage zebrafish embryos were injected with 100pg linearized plasmid with or without *adm* ATG MO. mScarlet expression was analyzed by fluorescence microscopy at 30hpf.

### **Quantitative real-time PCR**

Zebrafish embryos were dissolved in RLT buffer and total RNA was extracted according to manufacturers' instructions using the RNeasy Mini Kit (Qiagen, cat #74106). cDNA was synthesized with SuperScript IV Reverse Transcriptase (Qiagen, cat#18090010) with random hexamer primers (Thermo Scientific, cat#SO142). Quantitative PCR was performed on a MyiQ cycler (Bio-Rad) using SYBRgreen chemistry (Bio-Rad). Two reference genes were used (*tbp* and  $\beta$ -actin). MIQE standards were applied to our protocols (14).

### **Flow cytometry analysis and cell sorting**

#### **Chicken cluster cell sorting**

Non-injected embryos were used as control. After 30 minutes of staining, AGMs were dissected, pooled and dissociated by collagenase treatment for 1 hour. After dissoci-

ation, cells were washed, Hoechst 33258 was added to exclude dead cells, and CD45+ cluster cells were sorted in bulk using an Aria III flow cytometer (BD Biosciences). The sorted cells were then treated according to the CEL-seq protocol (7).

### Secretomics analysis

K-mean clustering analysis was performed to reveal nodes of the query proteins and first shell of interactors. The proteins were functionally linked based on text mining, experimental/biochemical data and association in curated databases, the color saturation of the lines representing the confidence score of a functional association.

### Intra-cardiac injection of ADM in chicken embryo and flow cytometry analysis

E2 chicken embryos were injected with either 5 $\mu$ g of the human ADM active form ([13-52], H-4936.0500, BACHEM), 5 $\mu$ g of the human ADM antagonist (22-52, H-4144.0500, BACHEM, hereafter called ADM-Antag) or with 1 $\mu$ l of MilliQ into the heart. The next day, embryos were dissected. Briefly, the heart and tail part (after the vitelline artery-aorta connection) were cut off. Two to 3 embryo trunks were pooled and dissociated by collagenase treatment (0.12% w/v, type I, Sigma) for 1 hour at 37°C. After dissociation, cells were washed, stained with PE anti-CD45 antibody (clone LT40, Southern Biotech) and 7-Aminoactinomycin D (7-AAD) was added to exclude dead cells. Flow cytometry analyses were performed on a FACS Calibur. Data were analyzed using the FlowJo software (TreeStar).

### Proliferation assays

The proliferation status of cluster cells from E10.5 *Svep1*<sup>+/+</sup> and *Svep1*<sup>-/-</sup> mouse embryos was tested after two different staining procedures, PHH3 and Ki67 staining. Proliferating IAHC cells (PHH3+, Ki67<sup>neg</sup>, Ki67<sup>int</sup> or Ki67<sup>high</sup>) were counted to determine either the mitotic index (MI=number of PHH3+ cluster cells/total number of cluster cells\*100) or the proliferation status (PS= [number of Ki67<sup>neg</sup> or Ki67<sup>int</sup> or Ki67<sup>high</sup>]/total number of cluster cells\*100).

### AGM explant cultures

AGMs were isolated from E9.5 and E10.5 embryos. The blood was flushed away from E10.5 aortas. AGMs were cultured as explants at 37°C in 5% CO<sub>2</sub> for 3 days. Briefly, the AGMs were placed onto a filter (Durapore 0.65  $\mu$ m, Millipore) carried by a steel mesh grid, aiding to culture the explants at the liquid-air interface of the Myelocult culture medium (M5300, StemCell Technologies). The medium was supplemented with 10<sup>-6</sup> M hydrocortisone succinate (Sigma) and either MilliQ water as control or 5 x 10<sup>-6</sup> M of human Adrenomedullin [22-52] trifluoroacetate salt (4028071, Bachem). The compounds were refreshed after 30 hours of culture. After three days of culture, the AGM explants were scraped from the filter and dissociated with collagenase as previously described (15).

### Hematopoietic progenitor assay

For myeloid progenitor colony forming unit (CFU-) assay, cells from 0.67-1 embryo equivalent (e.e.) (E9.5) or 0.05 e.e. (E10.5) of AGM explants were plated in Methocult medium (M3434, StemCell Technologies). After 12 days of culture at 37°C and 5% CO<sub>2</sub>, colonies were counted by microscopic observation. Five different types of colonies were categorized: erythroid colonies (Burst Forming Unit; BFU-E), granulocyte-, macrophage- or granulocyte-macrophage colonies (CFU-G, CFU-M and CFU-GM), and granulocyte, erythroid, macrophage, megakaryocyte colonies (CFU-GEMM).

### **Long-term transplantation and multilineage analysis**

AGMs from E11 *Svep1*<sup>+/+</sup> and *Svep1*<sup>-/-</sup> embryos (*Polydom/Svep1* mutant line (C57BL/6, CD45.2)) were dissected and dissociated by collagenase treatment (0.12% w/v, type I, Sigma) for 1 hour<sup>15</sup>. Cell suspensions were injected in the tail vein of irradiated adult recipients (B6.SJL-Ptprca Pepcb/BoyJ (C57BL/6, CD45.1), The Jackson Laboratory). Recipients were exposed to a split dose of 9.5 Gy of  $\gamma$ -irradiation (137 Cs source) and injected with two dilutions of cells (0.3 or 1 embryo equivalent [e.e.]). 2x10<sup>5</sup> spleen cells (C57BL/6, CD45.1) were co-injected to promote short-term survival. After injection, the mice were maintained on 0.16% neomycin (Sigma, 1405-10-3) water. Peripheral blood was collected into tubes containing EDTA (Micro tube 1.3ml K3E, Sarstedt) at 4 months (and 1 year) post transplantation and analyzed for long-term hematopoietic repopulation. Chimerism level of CD45.1 recipients (C57BL/6) injected with CD45.2 cells was determined by flow cytometry after staining of the blood samples with anti-CD45.1-APC (clone A20, BD Biosciences) and anti-CD45.2-FITC (clone 104, BD Biosciences) antibodies, and 7-AAD (Life Technologies) to exclude dead cells. Erythrocytes were depleted using a cell lysing buffer (IOtest 3 Lysing Solution, Beckman Coulter, A07799). The percentage of donor CD45.2 cells in each recipient was analyzed using a FACS Calibur and the FlowJo software (TreeStar). Multilineage hematopoietic contribution was determined in the peripheral blood at 4 months (and 1 year) post transplantation in the CD45.2+ population after staining with lineage-specific monoclonal antibodies for CD11b-PE, GR1-PE, CD4-PE, CD8-PE, B220-APC (all from BD Biosciences). Primary recipient bone marrow cells were injected into secondary irradiated recipients to assess self-renewal capacity (3x10<sup>6</sup> cells injected per recipient). Recipients were considered repopulated when the chimerism was greater than 5% (16,17).

### **Quantification and statistical analysis**

Quantification and statistical analyses were performed using the Prism6 software (GraphPad Software, Inc.). Data are represented as mean  $\pm$  SD or SEM when specified. Statistical analyses between 2 groups were conducted using the 2-tailed unpaired or paired Student t-test. Comparison among >2 groups was performed using a 2-way analysis of variance with Bonferroni's post hoc test. P value <0.05, 0.01, 0.001, 0.0001 was interpreted to denote statistical significance \*, \*\*, \*\*\*, \*\*\*\*, respectively.

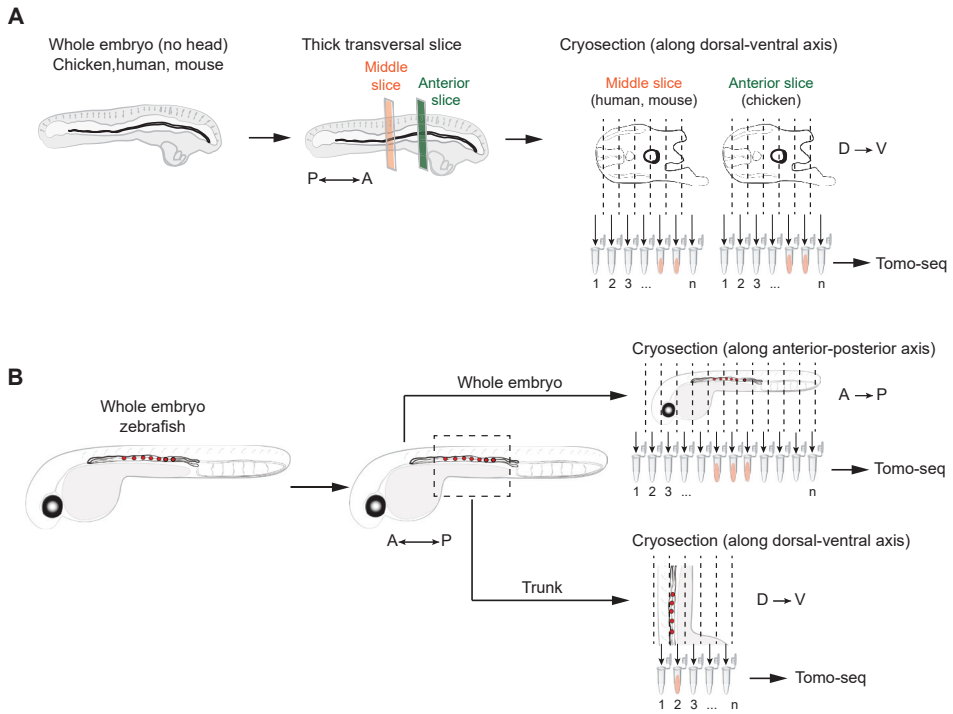
### **Data and software availability**

The authors declare that all data supporting the findings of this study are available within the manuscript or its supplemental data or are available from the corresponding author upon reasonable request.

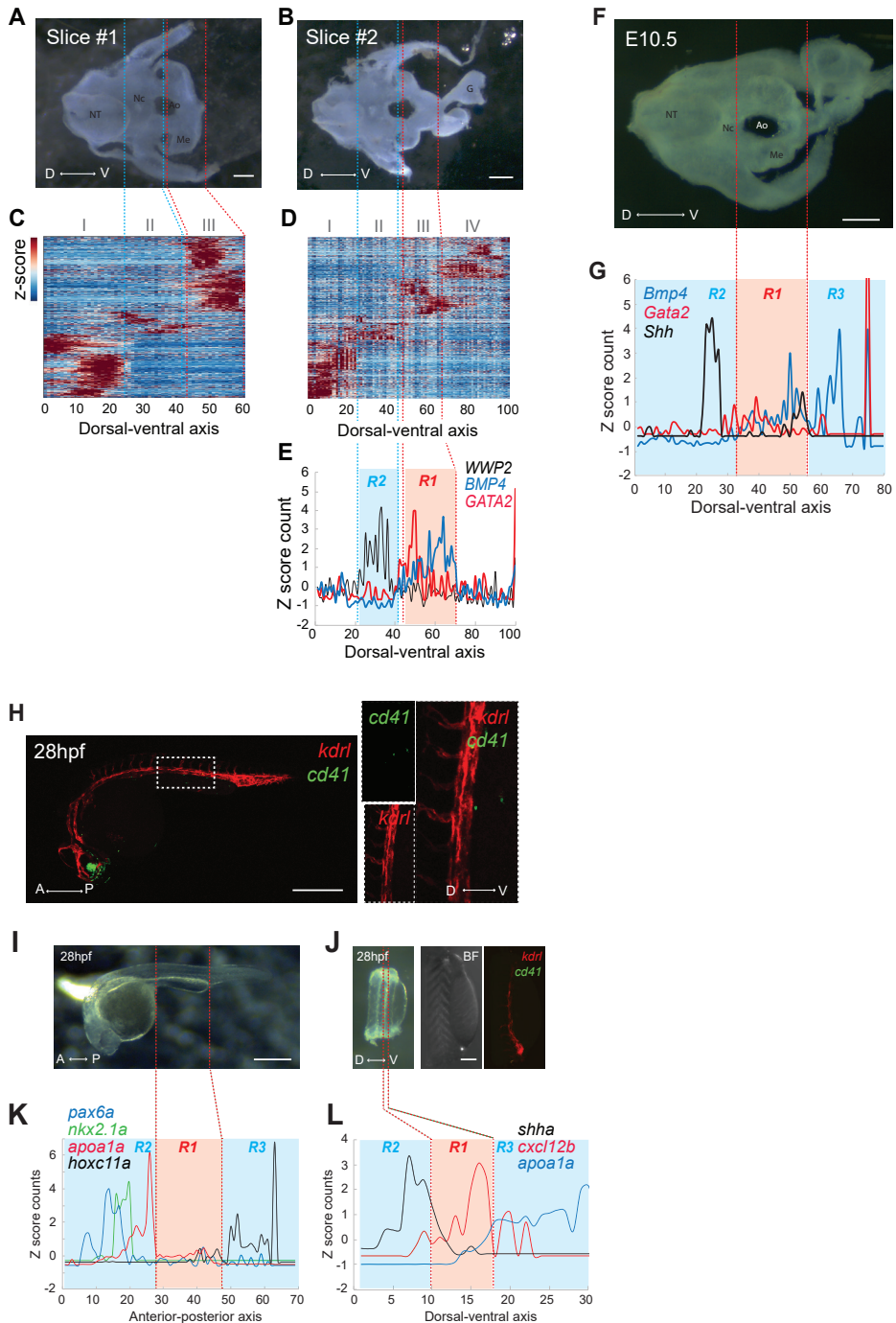
## Supplemental References

1. Karpanen T, Padberg Y, van de Pavert SA, et al. An Evolutionarily Conserved Role for Polydom/Svep1 During Lymphatic Vessel Formation. *Circ Res*. 2017;120(8):1263-1275.
2. Alestrom P, D'Angelo L, Midtlyng PJ, et al. Zebrafish: Housing and husbandry recommendations. *Lab Anim*. 2019;23677219869037.
3. Boisset JC, Andrieu-Soler C, van Cappellen WA, Clapes T, Robin C. Ex vivo time-lapse confocal imaging of the mouse embryo aorta. *Nat Protoc*. 2011;6(11):1792-1805.
4. Boisset JC, van Cappellen W, Andrieu-Soler C, Galjart N, Dzierzak E, Robin C. In vivo imaging of haematopoietic cells emerging from the mouse aortic endothelium. *Nature*. 2010;464(7285):116-120.
5. Yvernogeu L, Robin C. Restricted intra-embryonic origin of bona fide hematopoietic stem cells in the chicken. *Development*. 2017;144(13):2352-2363.
6. Junker JP, Noel ES, Guryev V, et al. Genome-wide RNA Tomography in the zebrafish embryo. *Cell*. 2014;159(3):662-675.
7. Hashimshony T, Wagner F, Sher N, Yanai I. CEL-Seq: single-cell RNA-Seq by multiplexed linear amplification. *Cell Rep*. 2012;2(3):666-673.
8. Pimanda JE, Ottersbach K, Knezevic K, et al. Gata2, Fli1, and Scl form a recursively wired gene-regulatory circuit during early hematopoietic development. *Proc Natl Acad Sci U S A*. 2007;104(45):17692-17697.
9. Mascarenhas MI, Parker A, Dzierzak E, Ottersbach K. Identification of novel regulators of hematopoietic stem cell development through refinement of stem cell localization and expression profiling. *Blood*. 2009;114(21):4645-4653.
10. Taoudi S, Medvinsky A. Functional identification of the hematopoietic stem cell niche in the ventral domain of the embryonic dorsal aorta. *Proc Natl Acad Sci U S A*. 2007;104(22):9399-9403.
11. Yokomizo T, Dzierzak E. Three-dimensional cartography of hematopoietic clusters in the vasculature of whole mouse embryos. *Development*. 2010;137(21):3651-3661.
12. McNagny KM, Pettersson I, Rossi F, et al. Thrombomucin, a novel cell surface protein that defines thrombocytes and multipotent hematopoietic progenitors. *J Cell Biol*. 1997;138(6):1395-1407.
13. Gering M, Patient R. Hedgehog signaling is required for adult blood stem cell formation in zebrafish embryos. *Dev Cell*. 2005;8(3):389-400.
14. Bustin SA, Benes V, Garson JA, et al. The MIQE guidelines: minimum information for publication of quantitative real-time PCR experiments. *Clin Chem*. 2009;55(4):611-622.
15. Robin C, Dzierzak E. Hematopoietic stem cell enrichment from the AGM region of the mouse embryo. *Methods Mol Med*. 2005;105:257-272.
16. Mirshekar-Syahkal B, Haak E, Kimber GM, et al. Dlk1 is a negative regulator of emerging hematopoietic stem and progenitor cells. *Haematologica*. 2013;98(2):163-171.
17. Zhou J, Xu J, Zhang L, et al. Combined Single-Cell Profiling of lncRNAs and Functional Screening Reveals that H19 Is Pivotal for Embryonic Hematopoietic Stem Cell Development. *Cell Stem Cell*. 2019;24(2):285-298 e285.

## Supplemental Figures



**Supplemental Figure 1. Tomo-seq experimental design for chicken, human, mouse and zebrafish species.** (A) Scheme of the experimental procedure. Thick transversal embryo slices were collected in the middle part of human and mouse embryos, or in the anterior part of chicken embryos. Of note, clusters are not restricted to the anterior portion of the aorta in human and mouse embryos (in contrast to chicken embryos). The anterior part of the embryo where the chicken thick slices were isolated (thereafter referred to as anterior slices) was defined as the region between the head and the vitelline artery-aorta connection. Slices were then cryosectioned along the dorsal-ventral axis and then processed for RNA-seq. (B) Scheme of the experimental procedure. Whole zebrafish embryos were either cryosectioned along the anterior-posterior axis (top panel), or the trunk was dissected and subsequently cryosectioned along the dorsal-ventral axis (bottom panel). All cryosections were then processed for RNA-seq.



**Supplemental Figure 2. Tomo-seq analysis of human embryo slices, E10.5 mouse embryo slices, and 28hpf zebrafish embryo and trunk.** (A, B) Two thick slices collected in the middle part of a thirty-five-day-old human embryo (of note, picture in A is also shown in Fig.1K) and used for tomo-seq. (C, D) Hierarchical clustering of z-score normalized tomo-seq gene expression traces (slice #1 (C) and #2 (D)). Distinct gene expression clusters (I to IV) corres-



pond to different regions of the slice. Of note, an extra cluster (IV) was observed in slice #2, corresponding to the gut tissue that remained attached to this slice (visible in B). (E) Tomo-seq traces for *BMP4* (blue), *GATA2* (red) and *WWP2* (black) along the dorsal-ventral axis of slice #2 (shown in B). Colored areas corresponding to the ventral part of the aorta (R1, red) or to the dorsal part of the aorta (R2, blue). (F) Thick transversal slice collected in the middle part of an E10.5 embryo used for tomo-seq. (G) Tomo-seq traces for *Gata2* (red), *Bmp4* (blue) and *Shh* (black), along the dorsal-ventral axis of the E10.5 embryo slice (shown in F). Colored areas corresponding to the aortic region (R1, red) or to the regions flanking the aorta region (R2 and R3, blue). (H) Global view of a *Tg(kdrl:mCherry;cd41:eGFP)* reporter zebrafish embryo at 28hpf; mCherry fluorescence highlights the whole vasculature, GFP fluorescence highlights hematopoietic stem/progenitor cells (HSPCs). The dashed boxed areas are shown in the right panels for single and double fluorescence (enlarged view). (I) Whole 28hpf zebrafish embryos used for tomo-seq. (J) Dissected trunk region containing the aortic region and yolk sac elongation of 28hpf zebrafish embryos, used for tomo-seq (left panel). Transmitted light (middle panel) and fluorescent pictures (right panel) of the dissected trunk. (K) Tomo-seq traces for *pax6a* (blue), *nkx2.1a* (green), *hoxc11a* (black) and *apo1a* (red) along the posterior-anterior axis of the 28hpf zebrafish embryo (shown in I). (L) Tomo-seq traces for *apo1a* (blue), *shha* (black) and *cxcl12b* (red) along the dorsal-ventral axis of the 28hpf zebrafish embryo trunk (shown in J). Red area (R1): slices corresponding to the yolk sac elongation region including the aorta (K) or the aortic region (L). Blue areas (R2 and R3): slices corresponding to regions flanking the aortic region. A, anterior; P, posterior; D, dorsal; V, ventral; R, region. NT, neural tube; Nc, notochord; Ao, aorta. G, gut; Me, mesonephros. hpf, hours post-fertilization; BF, bright field. Scale bars: 200 $\mu$ m (A, B, H, I), 150 $\mu$ m (F), 50 $\mu$ m (J).

**A****GO Biological process****Muscle contraction**

*RYR1;MYO1;SMPX;LMO1;ACTG2;MYO2;MYO3;MYLK;SGCA;DMD;MYH11;CACNG1;CHRN1;ACTN3;TNNC1;TNNC2;NEB;KLHL41;ACTA2;ACTC1;MYL7;MYL1;TNNT1;MYOT;TNNT3;CASQ2;HRC;MYL9;CRYAB*

**Negative regulation of cell proliferation**

*PTPRU;CDKN1A;BTG2;IFITM1;GATA3;GATA2;AIF1;PBLD;SLC9A3R1;DUSP10;ERBB4;FRZB;ADAMTS1;HNF4A;PDPN;MARVELD3;TP53INP1;SPEG;ZNF503;SOX7;S100A11;NKX3.1;ZBTB7C;MYOG;LYN;KLF10;TESC;IGFBP3;MAGI2;WNT5A;TBX5;SMAD6;BMP5;GREM1;BMP4;FABP3;SFRP1;WT1;DL1;ALDH1A2;ID2;PTPN6;IRF6*

**Positive regulation of transcription, DNA-templated**

*TCF21;IKZF1;FGF1;IRF2BPL;IKBKB;HHEX;RPS6KA5;SFR1;SOX18;CDH1;HNF4A;PITX2;NKX3.1;MYOG;LMO1;KLF10;MKL2;OSR2;FOXD2;EDN1;TESC;OSR1;LMO2;WNT5A;HNF1B;RUNX2;PAX2;GREM1;TOX2;SFRP1;ELF3;PAX8;MDFIC;MYOD1;HAND2;IRF2;ITGA6;MAPRE3;IRF6;PLCB1;ZFPM2;PPARA;MET;ATF3;CEBPB;EPAS1;GATA6;GLIS3;GATA5;GATA4;GATA3;GATA2;GLIS1;PPP3R1;ERBB4;EPCAM;PRDM16;TP53INP1;ALX1;NDP;MEF2D;PPARGC1A;WNT2;WNT4;JUN;FZD5;JUP;ESRRB;IGF1;GDF6;TBX5;SMARCA1;GRHL1;MEIS2;BMP7;PHOX2B;FOSL2;HIPK2;BMP5;BMP4;CDK7;DAB2;NFIA;WT1;ID2;MYF6*

**Regulation of cell proliferation**

*VPTPRU;CDKN1A;BTG2;IFITM1;LAMC2;FGF1;FGF9;ADAMTS1;HNF4A;SPEG;CTSH;SOX7;NKX3.1;MYOG;KLF10;OSR2;EDN1;SYK;EDN3;TESC;IGFBP3;MAGI2;ADAM10;ADRA2A;KLHL41;GREM1;SFRP1;ALDH1A2;KIT;IRF6;SGK1;PTGFR;CTF1;NPR3;GATA3;PTN;DPP4;EFNB2;SLC9A3R1;ERBB4;FRZB;EPCAM;PDGFD;PDPN;TP53INP1;ZNF503;STX3;WNT2;S100A11;ZBTB7C;LYN;JUN;JUP;VEGFC;IGF1;TBX5;SMAD6;TBX3;BMP5;BMP4;FABP3;WT1;DL1;PTPN6;FGFR3*

**Regulation of transcription from RNA polymerase II promoter**

*AMHR2;IKZF1;FGF1;RPS6KA5;SOX18;PITX2;LMO1;OSR2;MSX2;OSR1;LMO2;USP2;WNT5A;ARID5B;HNF1B;DKK1;RUNX2;ZFPM2;EZR;ATF3;TSHZ3;EPAS1;TSHZ2;GATA6;GLIS3;GATA5;FOXO6;GATA4;AEBP1;GATA3;GATA2;ZBTB4;GLIS1;PPP3R1;PRDM16;ALX1;PPARGC1A;WNT2;JUN;FZD5;JUP;CAV1;ESRRB;SMAD9;IGF1;GDF6;SMAD6;BMP7;PHOX2B;FOSL2;BMP5;BMP4;CDK7;MYF6;ZCCHC12;CDKN1A;TCF21;PCSK6;IRF2BPL;IKBKB;HHEX;HNF4A;NFBIZ;ZNF366;DACT1;NKX3.1;MYOG;KLF10;MKL2;FOXD2;EDN1;ITGA3;ANXA4;PAX2;GREM1;TOX2;ELF3;PAX8;MYOD1;HAND2;CRY2;KIT;IRF2;ITGA6;IRF6;PPARA;MET;CEBPB;CUX2;EPCAM;CREG1;CRYM;MEF2D;IRX1;ATP2B4;TBX5;GRHL1;MEIS2;TBX3;HIPK2;NFIA;WT1*

**Heart development**

*RAMP2;GATA6;GATA5;GATA4;GATA3;GATA2;CDH5;ERBB4;SOX18;MEF2D;SGCG;STRA6;OSR1;MICAL2;TBX5;BMP7;BMP5;BMP4;TH;WT1;DL1;HAND2;PKP2;TEK;ZFPM2*

**Positive regulation of transcription from RNA polymerase II promoter**

*TCF21;IKZF1;FGF1;IRF2BPL;IKBKB;HHEX;RPS6KA5;SOX18;HNF4A;PITX2;NKX3.1;MYOG;LMO1;KLF10;MKL2;OSR2;FOXD2;EDN1;OSR1;LMO2;WNT5A;HNF1B;RUNX2;PAX2;GREM1;TOX2;PAX8;MYOD1;HAND2;IRF2;ITGA6;IRF6;ZFPM2;PPARA;MET;ATF3;CEBPB;EPAS1;GLIS3;GATA5;GATA4;GATA3;GATA2;GLIS1;PPP3R1;EPCAM;PRDM16;ALX1;MEF2D;PPARGC1A;WNT2;JUN;FZD5;JUP;ESRRB;SMAD9;MICAL2;IGF1;TBX5;GRHL1;MEIS2;PHOX2B;FOSL2;HIPK2;BMP5;BMP4;CDK7;NFIA;MYF6*

**Striated muscle contraction**

*CHRNA1;MYO1;SMPX;TNNC1;TNNC2;ATP1B1;RCS1;MYO2;KLHL41;MYO3;TNNT1;KCNQ1;TNNT3;CASQ2;DMD;SCN1B*

**Mesonephros development**

*BMP4;OSR2;PAX8;OSR1;GATA3;FGF1;BMP7;PAX2*

**Negative regulation of cellular process**

*PTPRU;CDA;CDKN1A;BTG2;IFITM1;NPR1;GATA3;WISP1;SLC9A3R1;BRINP1;ERBB4;FRZB;PODXL;ADAMTS1;HNF4A;PDPN;TP53INP1;DACT2;SPEG;LPXN;ZNF503;SLIT3;SOX7;S100A11;NKX3.1;ZBTB7C;MYOG;LYN;KLF10;TESC;CAV1;IGFBP3;MAGI2;ADAM10;TBX5;SMAD6;BMP7;PAX2;BMP5;BMP4;FABP3;SFRP1;WT1;DL1;ALDH1A2;PTPN6;IRF6;AGTR2*

**B****KEGG - Pathways****Focal adhesion**

*LAMC3;TNC;PIK3CD;LAMC2;THBS4;MYLK4;MYLK;PDGFD;RAC2;VAV3;JUN;VWF;LAMB2;ITGA3;CAV1;VEGFC;IGF1;PARVB;COL1A2;MYL7;ITGA8;COL6A3;ITGA6;MYL9;MET*

**PI3K-Akt signaling pathway**

*CDKN1A;LAMC3;TNC;PIK3CD;LAMC2;FGF1;THBS4;IKBKB;GHR;FGF9;ERBB4;PDGFD;ANGPT4;ANGPT2;SYK;VWF;BDNF;LAMB2;ITGA3;MAGI2;VEGFC;IGF1;COL1A2;PPP2R2B;KIT;ITGA8;COL6A3;ITGA6;TEK;SGK1;FGFR3;MET*

**Axon guidance**

*EPHA4;NRP1;TRPC4;WNT5A;CAMK2A;PIK3CD;UNC5C;BMP7;GNAI1;EFNB2;PPP3R1;ABLIM2;CXCL12;RAC2;SLIT3;LRRRC4;NEO1;MYL9;MET;WNT4*

**ECM-receptor interaction**

*VWF;LAMC3;LAMB2;ITGA3;TNC;LAMC2;NPNT;THBS4;COL1A2;ITGA8;COL6A3;ITGA6;CD44*

**Vascular smooth muscle contraction**

*RAMP2;EDN1;CALCRL;EDN3;NPR1;ADM;ACTG2;MYLK4;MYLK;ACTA2;KCNMA1;MYH11;PLCB1;MYL9;PRKG1*

**MAPK signaling pathway**

*ANGPT4;DUSP5;JUN;ANGPT2;IL1R1;BDNF;CACNA2D1;VEGFC;IGF1;FGF1;IKBKB;PPP3R1;RPS6KA5;DUSP10;FGF9;ERBB4;PDGFD;KIT;RAC2;PTPN7;TEK;CACNG1;FGFR3;MET*

**Rap1 signaling pathway**

*ANGPT4;ANGPT2;MAGI2;PIK3CD;VEGFC;IGF1;FGF1;RAP1GAP;GNAI1;FGF9;CDH1;PDGFD;KIT;RAC2;TEK;PLCB1;FGFR3;MET*

**Wnt signaling pathway**

*JUN;FZD5;WNT5A;CAMK2A;DKK1;WNT6;SFRP1;PPP3R1;DAAM2;RAC2;ROR1;RSPO1;PLCB1;WNT2;WNT4*

**Leukocyte transendothelial migration**

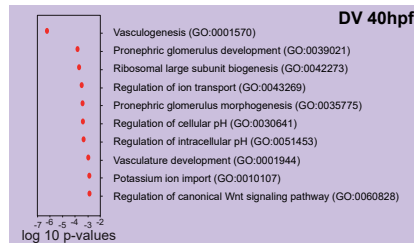
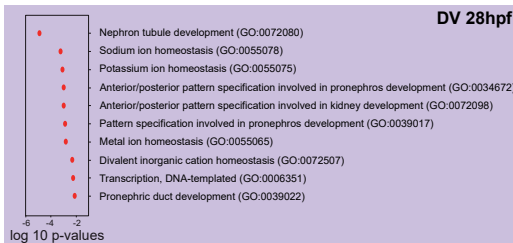
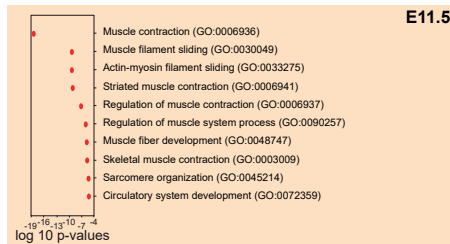
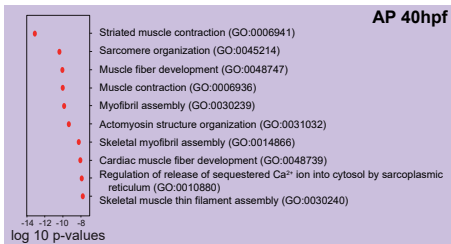
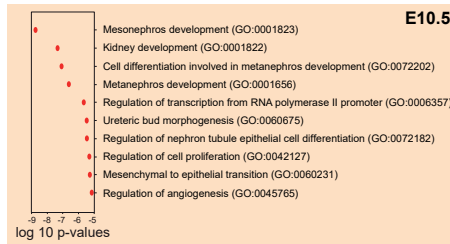
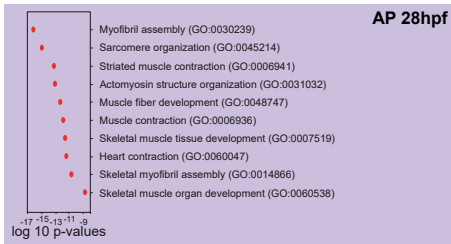
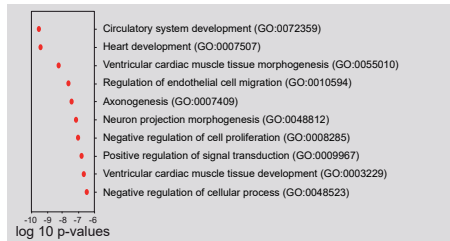
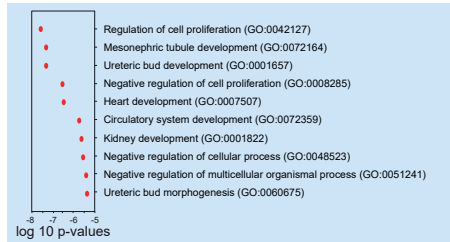
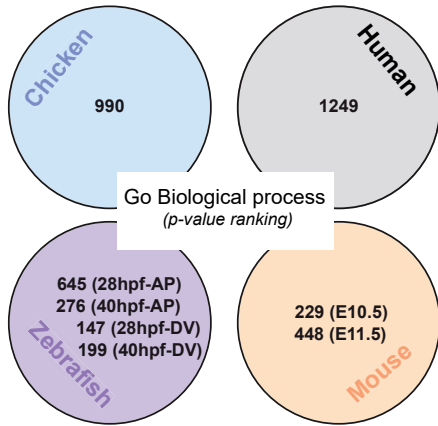
*VAV3;CDH5;OCLN;CXCL12;MYL7;CLDN15;RAC2;PIK3CD;F11R;EZR;MYL9;GNAI1*

**TGF-beta signaling pathway**

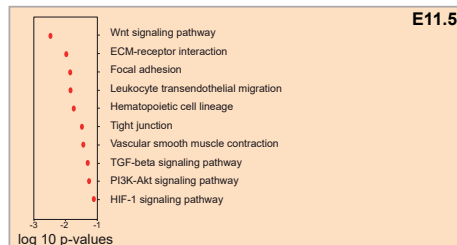
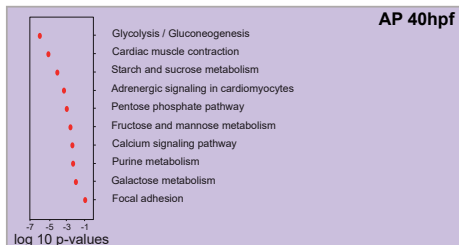
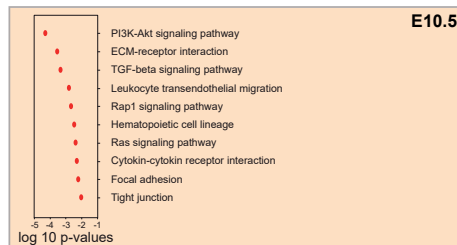
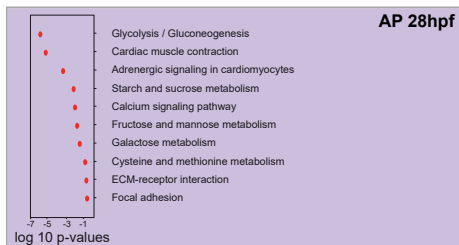
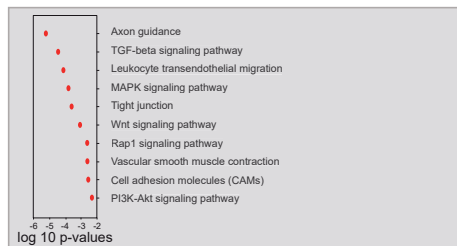
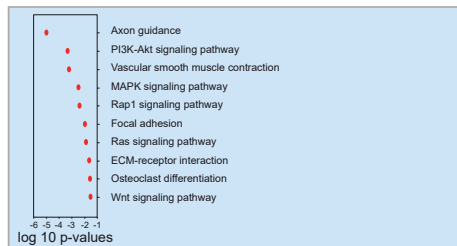
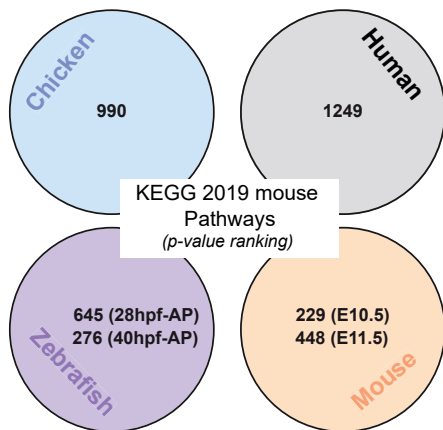
*BMP4;AMHR2;ID2;SMAD9;PITX2;GDF6;SMAD6;NEO1;BMP7;BMP5*

**Supplemental Figure 3. Common genes active in the ventral aortic microenvironment. (A)** Genes involved in the ten first biological processes GO terms enriched in at least two species (shown in Fig.2A,K). **(B)** Genes involved in the most relevant KEGG pathways enriched in at least two species (shown in Fig.2A,L).

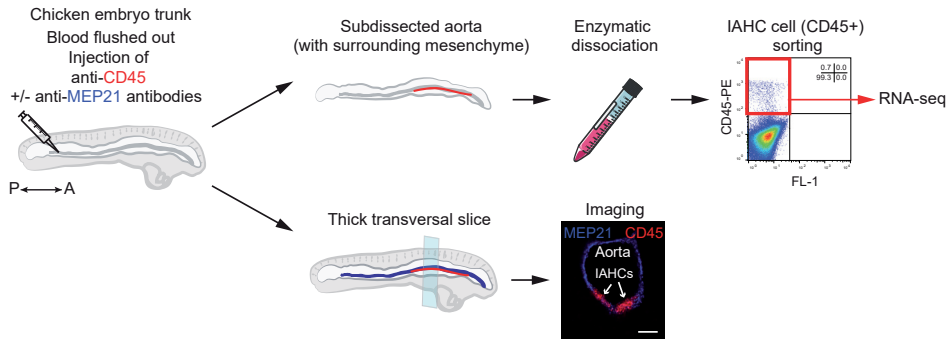
4



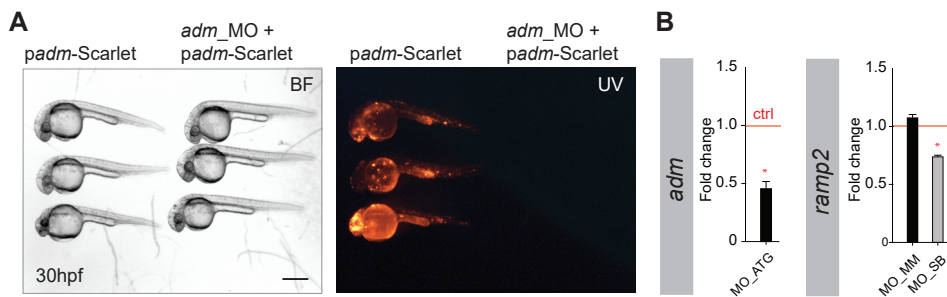
**Supplemental Figure 4. GO biological processes for each individual species (chicken, human, mouse, zebrafish).** Ten first biological processes GO terms enriched in the chicken (blue panel), human (grey panel), zebrafish (purple panels) and mouse (orange panels). A, anterior; P, posterior; D, dorsal; V, ventral; E, embryonic day; hpf, hour post-fertilization.



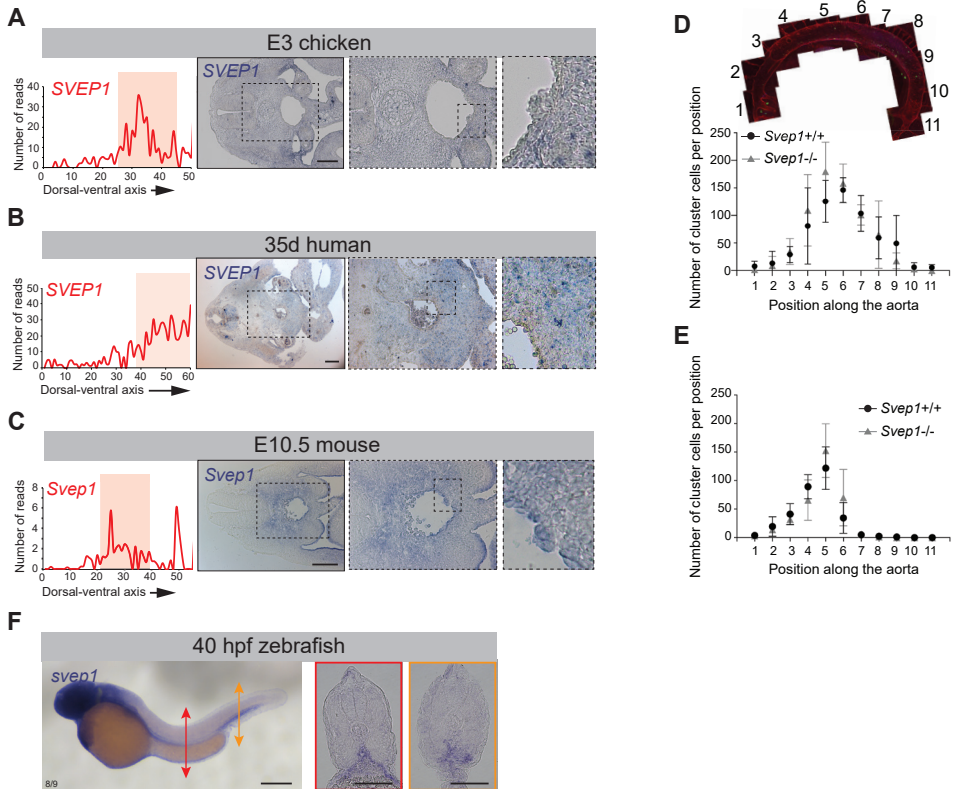
**Supplemental Figure 5. KEGG pathway analysis for each individual species (chicken, mouse, zebrafish).** KEGG pathways enriched in the chicken (blue panel), human (grey panel), zebrafish (purple panels) and mouse (orange panels). A, anterior; P, posterior; D, dorsal; V, ventral; E, embryonic day; hpf, hour post-fertilization.



**Supplemental Figure 6. Protocol scheme for the isolation of CD45+ intra-aortic hematopoietic cluster cells from chicken embryo.** The blood from an E3 chicken embryo (with no head) was flushed away. Anti-CD45 (pan-hematopoietic marker) and/or anti-MEP21 (endothelial and hematopoietic marker) antibodies were injected directly inside the aorta. Top panel: the aorta (with the surrounding mesenchyme) was dissected, dissociated and live 7AAD-CD45+ cluster cells were sorted in bulk for RNA-seq. Bottom panel: thick transversal embryo slices were collected and imaged by confocal microscopy. Of note, imaging shows the restricted CD45 staining to cluster cells. Scale bar: 50µm.

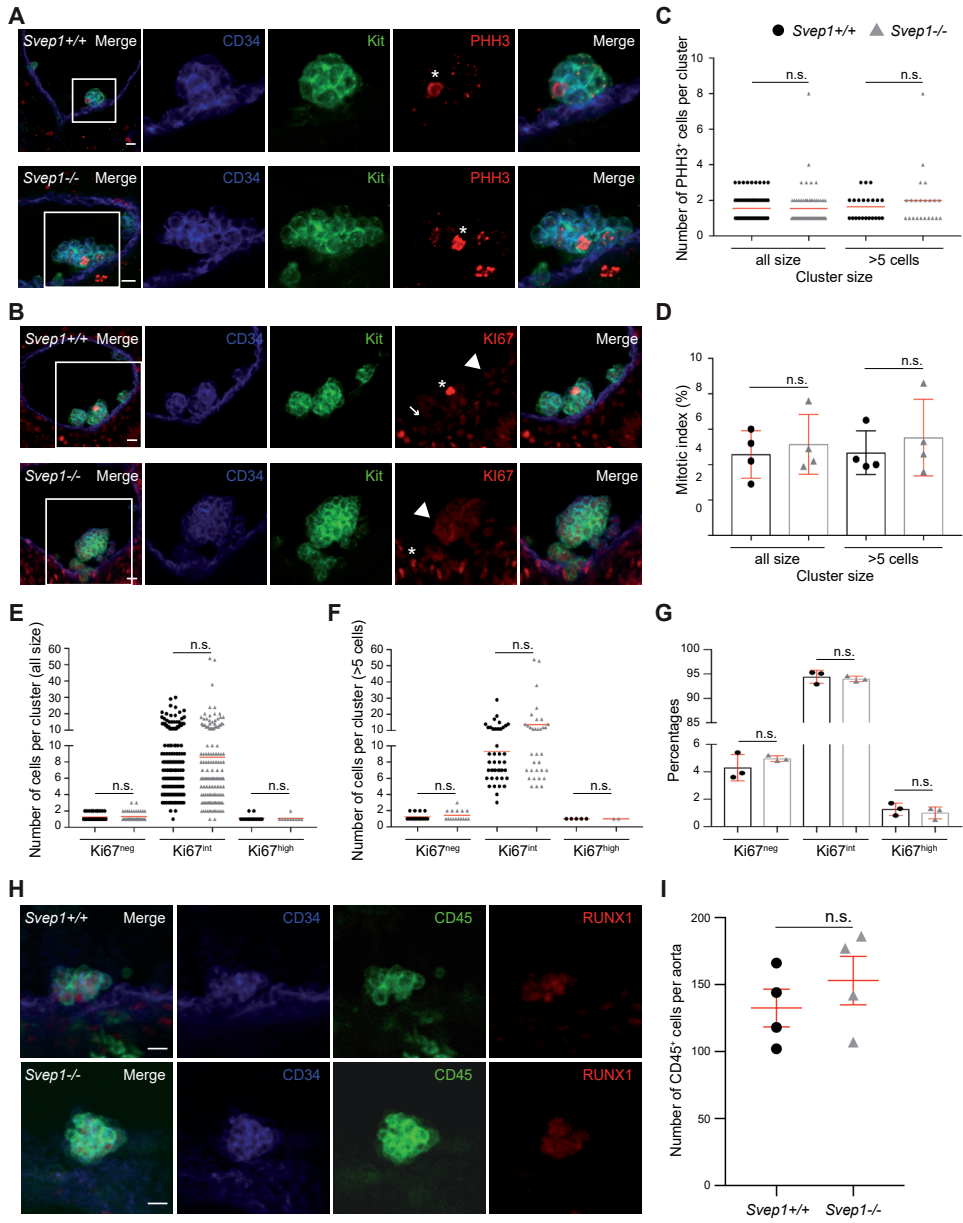


**Supplemental Figure 7. Validations of morpholino experiments.** (A) Validation of the ADM morpholino efficiency by fusion Scarlet plasmid injection. Global view of zebrafish embryos (left panel) injected either with the *padm*-Scarlet plasmid alone (embryos on the left) or with the *padm*-Scarlet plasmid+*adm*\_MO (embryos on the right) observed in bright field (BF) at 30hpf. Global view of the same zebrafish embryos observed under UV light (right panel). (B) RT-qPCR on 40hpf zebrafish embryos that were previously injected either with *adm*\_ATG or *ramp2*\_SB MO showing a decrease of expression for the targeted genes. \*P<0.05 (Mann-whitney U). Scale bar: 200µm (A).

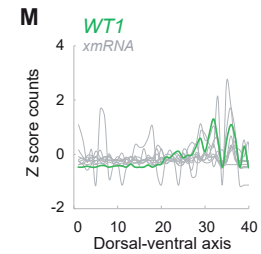
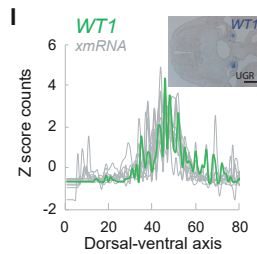
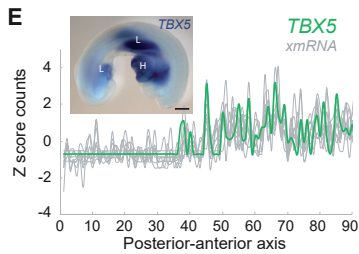
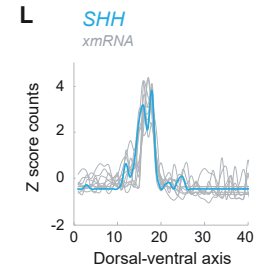
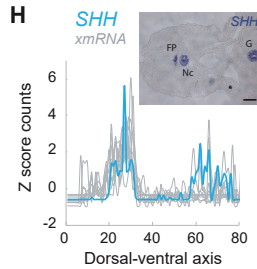
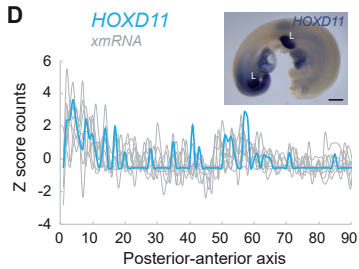
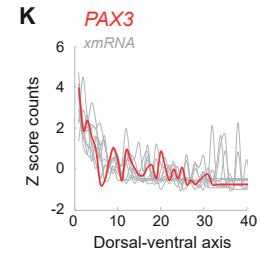
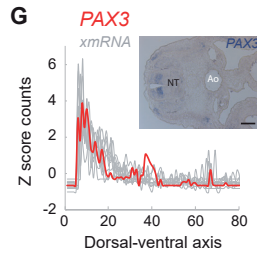
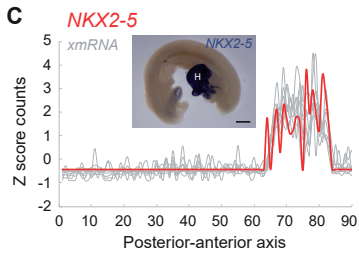
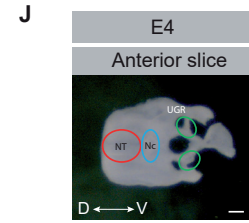
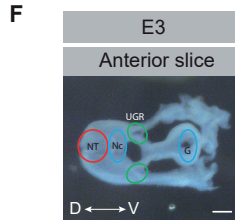
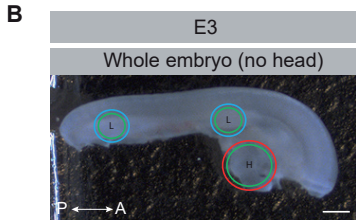
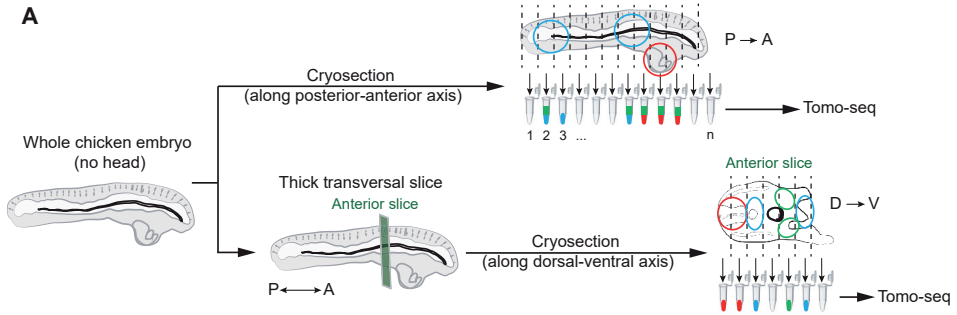


**Supplemental Figure 8. *Svep1* expression pattern among the four species and repartition of cluster cells in mouse *Svep1*<sup>+/+</sup> and *Svep1*<sup>-/-</sup> embryo aorta.** (A-C) ISH showing *SVEP1* expression pattern in E3 chicken (A, middle panel), 35-day old human (B, middle panel), E10.5 mouse (C, middle panel). Dashed boxed areas are shown enlarged in the right panels in A-C. Tomo-seq traces for *svep1* are shown in A-C (left panels, red area: slices corresponding to the aortic region). (D, E) (D, upper panel), maximal projection of the aorta stained with anti-CD31 (red) and anti-KIT (green) antibodies. The aorta is virtually subdivided into positions (along the anterior to posterior axis, 1 to 11 positions). (D, lower panel) Number of cluster cells per aorta position showing the repartition of cluster cells along E10.5 (D) and E12.5 (E) *Svep1*<sup>+/+</sup> and *Svep1*<sup>-/-</sup> aortas. Bar: SD. (F) WISH for *svep1* on 40hpf zebrafish embryos (left panel). Zebrafish embryos were cryosectioned post-ISH to show *svep1* expression in the aortic region and CHT (right panels, red and orange arrows and boxes, respectively). The total number of embryos analyzed for WISH is indicated on the picture. Scale bars: 100 $\mu$ m (A, F [right panel]), 200 $\mu$ m (B, F [left panel]), 150 $\mu$ m (C).





**Supplemental Figure 9. Proliferative status of *Svep1*<sup>+/+</sup> and *Svep1*<sup>-/-</sup> intra-aortic clusters.** (A) Thick slices of E10.5 *Svep1*<sup>+/+</sup> (top panels) and *Svep1*<sup>-/-</sup> (bottom panels) embryos were stained using anti-CD34 (blue), anti-KIT (green) and anti-PHH3 (red) antibodies. Asterisk, PHH3+ cell. Boxed areas are shown enlarged for single and merged fluorescence in intra-aortic clusters. (B) Thick slices of E10.5 *Svep1*<sup>+/+</sup> (top panels) and *Svep1*<sup>-/-</sup> (bottom panels) embryos were stained using anti-CD34 (blue), anti-KIT (green) and anti-Ki67 (red) antibodies. Asterisk, Ki67<sup>high</sup> cell; arrow head, Ki67<sup>int</sup> cell; arrow, Ki67<sup>neg</sup> cell. Boxed areas are shown enlarged for single and merged fluorescence in intra-aortic clusters. (C) Graph showing the number of PHH3+ cells per cluster in all clusters or in clusters >5 cells in E10.5 *Svep1*<sup>+/+</sup> and *Svep1*<sup>-/-</sup> aortas. n= 4 *Svep1*<sup>+/+</sup> (2256 total cluster cells counted) and n=4 *Svep1*<sup>-/-</sup> (1938 total cluster cells counted) embryos; 7-11 slices counted per embryo. Dot: count in one slice. Red line: mean. (D) Mitotic index. Red bar: mean ± SD. (E, F) Graphs showing the number of Ki67<sup>neg</sup>, Ki67<sup>int</sup>, and Ki67<sup>high</sup> cells in all clusters (E) or in clusters > 5 cells (F) in E10.5 *Svep1*<sup>+/+</sup> and *Svep1*<sup>-/-</sup> aortas. n= 3 *Svep1*<sup>+/+</sup> (1427 total cluster cells counted) and n=3 *Svep1*<sup>-/-</sup> (1295 total cluster cells counted) embryos; 9-12 slices counted per embryo. Dot: count in one slice. Red line: mean. (G) Percentages of Ki67<sup>neg</sup>, Ki67<sup>int</sup>, and Ki67<sup>high</sup> cells in all clusters. Red bar: mean ± SD. (H) Pictures of clusters after whole-mount immunostaining of *Svep1*<sup>+/+</sup> (top panels) and *Svep1*<sup>-/-</sup> (bottom panels) embryos by using anti-CD34 (blue), anti-CD45 (green) and anti-RUNX1 (red) antibodies. (I) Graph showing the number of CD45+ cells per E11.5 *Svep1*<sup>+/+</sup> and *Svep1*<sup>-/-</sup> aortas. Dot: one embryo. Red bar: mean ± SEM. n=2 independent experiments. Scale bars: 10µm. n.s., not significant.



**Supplemental Figure 10. Tomo-seq identifies specific gene expression patterns along the posterior-anterior and dorsal-ventral axes of the chicken embryo.** (A) Scheme of the experimental procedures. Whole E3 chicken embryos (head removed) were either cryosectioned along the posterior-anterior axis (top panel), or cut into thick transversal slices that were subsequently cryosectioned along the dorsal-ventral axis (bottom panel). All cryosections were then processed for RNA-seq. (B) Whole E3 chicken embryo (head removed) used for tomo-seq. (C-E) Tomo-seq traces for *NKX2-5* (C, red), *HOXD11* (D, blue) and *TBX5* (E, green) along the posterior-anterior axis of the embryo shown in (B), and the 10 most similar genes (shown as example) as determined by Euclidean distance of Z score transformed expression traces (xmRNA, grey traces). Insets show expression patterns of the respective genes by WISH. (F) Thick slice collected in the anterior part of an E3 chicken embryo used for tomo-seq. (G-I) Tomo-seq traces for *PAX3* (G, red), *SHH* (H, blue) and *WT1* (I, green) along the dorsal-ventral axis of the slice shown in (F), and for the 10 most similar genes (xmRNA, grey traces). Insets show expression patterns of the respective genes by ISH. (J) Thick slice collected in the anterior part of an E4 chicken embryo used for tomo-seq. (K-M) Tomo-seq traces for *PAX3* (K, red), *SHH* (L, blue) and *WT1* (M, green) along the dorsal-ventral axis of the slice shown in (J), and for the 10 most similar genes (xmRNA, grey traces). A, anterior; P, posterior; D, dorsal; V, ventral. NT, neural tube; Nc, notochord; Ao, aorta; L, limb, H, heart; FP, floor plate, G, gut; UGR, urogenital ridges. Scale bars: 500µm (B-E), 100µm (F-I), 150µm (J).

## Supplemental Tables

**Supplemental Table 1. Samples for tomography-sequencing.**

Species	Samples <sup>§</sup>	Sample orientation*	Cryosection thickness (µm)	Number of sequenced cryosections
Chicken	Whole E3 embryo (head removed)	P → A	60	95
	E3 anterior slice #1	D → V	14	64
	E3 anterior slice #2	D → V	14	84
	E3 anterior slice #3	D → V	14	84
	E4 anterior slice #1	D → V	20	43
Mouse	E10.5 slice #1	D → V	14	82
	E10.5 slice #2	D → V	14	82
	E10.5 slice #3	D → V	14	56
	E11.5 slice #1	D → V	18	83
	E11.5 slice #2	D → V	18	83
	E11.5 slice #3	D → V	18	76
Human	35-day old embryo slice #1	D → V	20	60
	35-day old embryo slice #2	D → V	20	100
Zebrafish	40 hpf whole embryo #1	A → P	40	76
	40 hpf whole embryo #2	A → P	40	82
	28 hpf whole embryo #1	A → P	30	69
	28 hpf whole embryo #2	A → P	30	71
	28 hpf whole embryo #3	P → A	30	69
	40 hpf trunk #1	D → V	12	29
	40 hpf trunk #2	D → V	12	32
	28 hpf trunk #1	D → V	10	31
	28 hpf trunk #2	D → V	10	32

<sup>§</sup>Each slice was isolated from different embryos (except for the human samples).

\*P → A: posterior-anterior axis; D → V: dorsal-ventral axis; A → P: anterior-posterior axis

**Supplemental Table 2. Sequences of primers used for ISH probe synthesis.**

Species	Genes	Sequences (5' → 3')	Size (pb)
Chicken	Mpl	Fw GGAGAATTCCGCCATACACCGTTCTACT	718
		Rv AGGCTCGAGGAAGAGCTCATGGGTGCTGT	
	Svep1	Fw GGAGAATTCTCTGGTGGGAAGCAGTATCC	436
		Rv AGGCTCGAGATCCTGGATGTTTGCCTCC	
	Shh	Fw GGAGAATTCACAGCGACTTCCTCACCTTC	511
		Rv AGGCTCGAGAGGAGCCGTGAGTACCAATG	
	Ramp2	Fw GGAGAATTCAGCCAGCCAGACAGGATTTAAA	418
		Rv AGGCTCGAGCGAAGGACTCCCAGCAGTAG	
	Nkx2-5	Fw GGAGAATTCGGCGGACAAGAAAGAACTGTG	612
		Rv AGGCTCGAGAAGTCCCCACGCTGAAGTTCA	
	Hoxd11	Fw GGAGAATTCACAGGGTGCCTTATTACGTC	564
		Rv AGGCTCGAGTCTTCTCTGCAACAGCCTCA	
	Tbx5	Fw GGAGAATTCGTGGGACGGAGATGATCAT	607
Rv AGGCTCGAGTCTGTCTCACTGTGCTCTGT			
Pax3	Fw GGAGAATTCACAGTTTCCAAAAGTCCGC	558	
	Rv AGGCTCGAGAGTTTGGCTCTTTGTGCGAG		
Wt1	Fw GGAGAATTCGATCACAGAGGGATGGCAG	534	
	Rv AGGCTCGAGGCATTCCAGTTGTGACGTCA		
Podxl	Fw GGAGAATTCATGCCACAGTCAACAACCAC	630	
	Rv AGGCTCGAGGTGACAGCAGCCGTAGATTG		
Aldh1a2	Fw GGAGAATTCGAAGTTGACACGGACAAGG	566	
	Rv AGGCTCGAGTGCACATGAGATGCTATTG		
Ppargc1a	Fw GGAGAATTCAGAACTTGACCTCTCCGA	432	
	Rv AGGCTCGAGGTTTCGATGGTTTTGTGTGC		
Mouse	Svep1	Fw GGAGAATTCCTTCGCTCAACTTCAGCTT	578
		Rv AGGCTCGAGAGCGATGCTGCAATAGGTCT	
	Bmp4	Fw GGAGAATTCAGGGCTCCACCGTATAAA	369
		Rv AGGCTCGAGATGCTTGGGACTAGCTTTGG	
	Gata2	Fw GGAGAATTCAGCTCATGACTATGGCAGCA	398
		Rv AGGCTCGAGTCATGGTCAGTGGCCTGTTA	
	Podxl	Fw GGAGAATTCAGCTTTCTCCTAAGGCCGT	589
Rv AGGCTCGAGTTGTGAGGAGGGAGACAACC			
Aldh1a2	Fw GGAGAATTCGTTGGACAAGCTTGCAGAC	561	
	Rv AGGCTCGAGCCAGGGTCACTCTCTCAGG		
Ppargc1a	Fw GGAGAATTCAGCCTCTTTGCCAGATCTT	327	
	Rv AGGCTCGAGCAGGCATGGAGGAAGGACTG		
Zebrafish	Pax6a	Fw GGAGAATTCGCTGATGCAAAGTCCAAG	559
		Rv AGGCTCGAGAGTGCATTCCTTTGCAGTT	
	Nkx2.1a	Fw GGAGAATTCCTTCGAGCTCCACTCAAAC	633
		Rv AGGCTCGAGCCATGCCTTTACCAACATCC	
	Hoxc11a	Fw GGAGAATTCAGTGTGTACAGCCACCACCA	594
		Rv AGGCTCGAGATAACAGGCAACGCCATTTTC	
	Apoa1a	Fw GGAGAATTCCTAATTTGTCCAGGCTGAT	520
		Rv AGGCTCGAGGGCACAACCTTTGGACTTGGT	
	Shha	Fw GGAGAATTCCTACTACGAGGGAAGAGCTG	529
		Rv AGGCTCGAGTTAAGCTGGCCGCTATCAT	
	Cxcl12b	Fw GGAGAATTCATTGCCAAGCTGAAGAACA	769
		Rv AGGCTCGAGCCACAAAGCAAGCATTAGCA	
	Svep1	Fw GGAGAATTCGGTGACACCCGTTCTAAACC	899
Rv AGGCTCGAGGAGAGCCATGCTGTGATGAA			
Podxl	Fw GGAGAATTCAGAGACTGAACGCGGAGAA	596	
	Rv AGGCTCGAGTCTTGCTTCGCTGGACTGTA		



	Aldh1a2	Fw <b>GGAGAATTCGGTGGAGAGACAGTGCTT</b> Rv <i>AGGCTCGAGGCCTGTTCTAATGCCAGCTC</i>	606
	Ppargc1a	Fw <b>GGAGAATTCGGTGCTTGCATCTCATCTG</b> Rv <i>AGGCTCGAGTGGTGCTGTCTCGTTTTGTG</i>	
Human	Podxl	Fw <b>GGAGAATTC</b> CCACAGACCTCACATCCACT	550
		Rv <i>AGGCTCGAGAATTTCTCATCCGAAGCGCC</i>	
	Aldh1a2	Fw <b>GGAGAATTC</b> AAAGGGGACGTCTGTTGGAT	548
		Rv <i>AGGCTCGAGTCTTCCAGCTGCTTCTTGA</i>	
	Ppargc1a	Fw <b>GGAGAATTC</b> CTGGCGTCATTCAGGAGCT	549
		Rv <i>AGGCTCGAGTGCATGGTTCTGGGTA</i> CTGA	
	Svep1	Fw <b>GGAGAATTC</b> ACACACACAGGCCATTTT	584
		Rv <i>AGGCTCGAGCACTGGCTGTTTCCTTGA</i>	

Rv: Reverse; Fw: Forward. EcoRI restriction sites are indicated in bold; XhoI restriction sites are indicated in italic.

### Supplemental Table 3. Sequences of morpholinos

Morpholino	Sequences (5' → 3')
ATG-Adm	GCAGGATCAGTTGCATCTTGATTGA
ATG-Ramp2	GGCCATTCTGCTTTAATCCAGGCTT
SB-Ramp2	ATAAAATGAGCACATCTCACCACAG
MM-Ramp2	ATAAATTC AAGCACATGTCTCGACAG

### Supplemental Table 4. Primer sequences for quantitative real time PCR

Gene name	Forward	Reversed
tbp	TCACCCCTATGACGCCTATC	CAAGTTGCACCCCAAGTTT
β-actin	CGTCTGGATCTAGCTGGTCGTGA	CAATTTCTCTTTCGGCTGTGGTG
Ramp2	GACTCCATGAACAGTACAGACTGG	GTCAGCAACAGTCTCAGTGC
Adm	GACAGTGCGAAGCATGACC	CGTCTGGTCTGACAAACTGC

**Supplemental Table 5** (Excel). Tomo-seq datasets for all chicken embryo samples cryosectioned along the anterior-posterior or dorsal-ventral axis, and the shortlist of potent candidate genes (ventrally expressed) obtained after applying a supervised filtering strategy. See <https://figshare.com/s/f354f53ab02e17358b39>

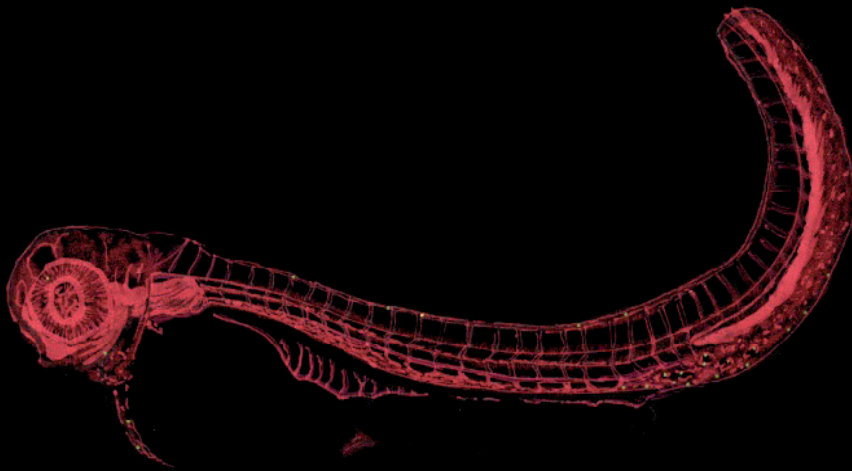
**Supplemental Table 6** (Excel). Tomo-seq datasets for human samples cryosectioned along the dorsal-ventral axis and shortlists of potent candidate genes (ventrally expressed) obtained after applying a supervised filtering strategy. See <https://figshare.com/s/a78b5dd681a878b4de3b>

**Supplemental Table 7** (Excel). Tomo-seq datasets for all mouse embryo samples (E10.5; E11.5) cryosectioned along the dorsal-ventral axis and shortlists of potent candidate genes obtained after applying a supervised filtering strategy. See <https://figshare.com/s/11766a92dc7269244a14>

**Supplemental Table 8** (Excel). Tomo-seq datasets for all zebrafish embryo samples (28hpf; 40hpf) cryosectioned along the anterior-posterior or dorsal-ventral axis and shortlists of potent candidate genes obtained after applying a supervised filtering strategy. See <https://figshare.com/s/746a8653e2628817417e>

**Supplemental Table 9** (Excel). List of genes common to two, three or four species, obtained after applying a supervised filtering strategy. See <https://figshare.com/s/b34bd97233f950d6e0e4>

**Supplemental Table 10** (Excel). E3 chicken cluster cell RNA dataset.  
See <https://figshare.com/s/88f0ed0ee947ef560534>

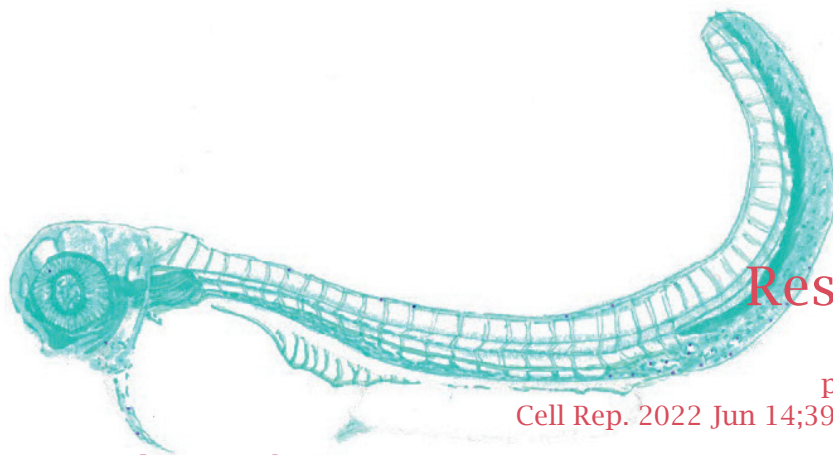


## Chapter

---

# 5

## Research



published in:  
Cell Rep. 2022 Jun 14;39(11):110957

**Klaus, A., Clapes, T., Yvernogeu, L.\***, Basu, S.\*, Weijts, B.\*, Maas, J., Smal, I., Galjart, N., Robin, C.

**CLASP2 safeguards hematopoietic stem cell properties during mouse and fish development**

**H**ematopoietic stem cells (HSCs) express a large variety of cell-surface receptors that are associated with the acquisition of self-renewal and multipotent properties. The correct expression of these receptors depends on a delicate balance between cell surface trafficking, re-cycling, and degradation, and is controlled by the microtubule network and Golgi apparatus, whose role has hardly been explored during embryonic/fetal hematopoiesis. Here we show that in the absence of CLASP2, a microtubule-associated protein, the overall production of HSCs is reduced while the produced HSCs fail to self-renew and maintain their stemness throughout mouse and zebrafish development. This phenotype can be attributed to a decreased cell surface expression of the hematopoietic receptor c-Kit, which originates from an increased lysosomal degradation in combination with a reduction in trafficking to the plasma membrane. A dysfunctional Golgi apparatus in CLASP2-deficient HSCs seems to be the underlying cause of the c-Kit expression and signaling imbalance.

## Introduction

Endowed with multilineage differentiation and long-term self-renewal properties, hematopoietic stem cells (HSCs) have the capacity to replenish the entire blood system throughout life without exhaustion. In all vertebrates, the first HSCs originate during embryonic life (1, 2). Starting at embryonic day (E)9.5 of mouse development, hemogenic endothelial cells first bud from the endothelium lining the main arteries, through an endothelial-to-hematopoietic transition (EHT) (3, 4), and subsequently form intra-aortic hematopoietic clusters (IAHCs) (5, 6), whose number peaks at E10.5, when the first HSCs start to be detected in the aorta of the aorta-gonad-mesonephros region (AGM) (6-8). At E11, IAHCs contain few HSCs and committed erythroid-myeloid progenitors (5, 9, 10); instead they are mainly composed of HSC precursors (pre-HSCs type I and type II) that progressively mature towards fully transplantable HSCs (5, 11-16). IAHC cell maturation starts in the aorta and is completed after pre-HSCs migrate to the fetal liver (FL) (9, 17). This wave of maturation followed by expansion yields a FL-based HSC pool with adult HSC properties, and these HSCs will colonize the bone marrow (BM), the main site of hematopoiesis in adulthood.

An ever-growing body of evidence emphasizes niche interactions as key for functional HSC production and maintenance. Among signaling molecules acting at the plasma membrane, c-Kit, a tyrosine kinase receptor, and stem cell factor (SCF), its ligand, are crucial for blood development and for the maintenance of adult HSCs, safeguarding their survival and quiescence (18-22). SCF is highly expressed by arterial endothelial and perivascular cells, which provide a vascular niche supporting the self-renewal of adult c-Kit expressing HSCs (23, 24). Hematopoiesis in the embryonic niches such as the yolk sac (YS), AGM and placenta is also regulated through the c-Kit/SCF signaling axis (25, 26). For instance, SCF is an important factor for the maturation of AGM pre-HSCs *in vitro* (27).

The journey of an HSC through the successive anatomical niches involves various processes that rely on the ability of HSCs to dynamically modulate intracellular organelles and protein trafficking. This is partly regulated by the microtubule (MT) network, whose behavior and organization are controlled by MT-associated proteins (28-30). Surprisingly, while the role of MTs in adult human and mouse hematopoietic stem and progenitor cells (HSPCs) has been investigated (31-34), no studies explored MT function in embryonic/fetal hematopoiesis, although pathway analyses of multi-dimensional sequencing have highlighted the potential involvement of cytoskeleton regulation, organization and biogenesis, in the mouse embryonic aorta and zebrafish caudal hematopoietic tissue (CHT), which is the zebrafish equivalent of the FL (35-37). Mammalian CLIP-associating protein (CLASP) 1 and CLASP2 are two conserved proteins that bind and stabilize MTs in specific areas of the cell, such as the cellular cortex and kinetochores (38-42). CLASPs are also involved in non-centrosomal MT nucleation at the Golgi apparatus (43) and in the regulation of Golgi morphology itself (44). CLASPs are required in various cellular processes, including directed cell motility (45), focal adhesion turnover and directional vesicle transport (46), and mitosis (47, 48). We previously described a function for CLASP2 in the maintenance of HSCs in the mouse adult BM *in vivo* (34). However, it remains unknown whether CLASP2 is involved during embryonic or fetal hematopoiesis for the generation, maturation and/or expansion of the first HSCs. Here we show that CLASP2 is important to maintain a proper amount of c-Kit at the plasma membrane of pre-HSCs and HSCs, which is crucial to safeguard their stem cell properties and fate throughout mouse and zebrafish development.

## Results

### CLASP2 regulates IAHC dynamics, pre-HSC maturation and HSC activity in the aorta of mouse embryos

To determine whether CLASP2 plays a role during embryonic HSC development, we counted the number of CD31+c-Kit+ IAHC cells in *Clasp2*<sup>-/-</sup> and *Clasp2*<sup>+/+</sup> (wild-type, WT) littermates at different time points (Figure 1A). Compared to WT littermates, *Clasp2*<sup>-/-</sup> embryos had less IAHC cells at E10.5, the age at which numbers normally peak (6). This decrease was not due to cell death (Figure S1A, S1B) or defects in proliferation (Figure S1C). IAHC cell production peaked one day later, at E11.5, in *Clasp2*<sup>-/-</sup> aortas reaching a similar number as in *Clasp2*<sup>+/+</sup> littermates (Figure 1A). Accordingly, an increased proliferation of *Clasp2*<sup>-/-</sup> IAHC cells occurred at E11.5 (Figure S1D), with no increase in cell death (Figure S1E). Despite this increase in proliferation, the peak of *Clasp2*<sup>-/-</sup> IAHC cells at E11.5 remained lower than the one in *Clasp2*<sup>+/+</sup> at E10.5 (Figure 1A).

To decipher whether the delay in IAHC production interfered with cell fate and function, we examined the pre-HSC populations (5, 12, 13, 27) by flow cytometry in freshly dissected E11 and E12 AGMs (referred to as 'day 0'), when the numbers of IAHC cells were similar in *Clasp2*<sup>+/+</sup> and *Clasp2*<sup>-/-</sup> aortas (Figure 1B; Figure S2A (controls) and S2B). We constantly observed higher percentages of phenotypically defined type I pre-HSCs (c-Kit+CD31+VE-cad+CD45-) and lower percentages of type II pre-HSCs (c-Kit+CD31+VE-cad+CD45+) in E11 and E12 *Clasp2*<sup>-/-</sup> compared to *Clasp2*<sup>+/+</sup> AGMs in each experiment performed, as shown by the lower type II versus type I ratios (Figure 1C [left panel]). This partial blockage of pre-HSC maturation was also observed in E12 FLs where maturation mainly takes place (17) (Figure 1C [left panel], Figure S2C). The blockage was amplified after *in vitro* explant culture of E10 and E11 AGMs with cytokines, which normally promotes pre-HSC maturation (Figure 1C [right panel]; Figure S2D).

To test whether the pre-HSC maturation block impaired HSC activity, we performed *in vivo* long-term transplantations of E11 *Clasp2*<sup>+/+</sup> and *Clasp2*<sup>-/-</sup> AGM cells. Only 15% of recipients were reconstituted with *Clasp2*<sup>-/-</sup> cells compared to 57% with *Clasp2*<sup>+/+</sup> cells (Figure 1D [red lines: mean of chimerism]). Moreover, the reconstitution was not multilineage but lymphoid-biased (Figure S3A, upper and middle panels: injected with *Clasp2*<sup>+/+</sup> or *Clasp2*<sup>-/-</sup> cells [mouse A marked with a red dot in Figure 1D], respectively). Failure to reconstitute secondary recipients revealed a defect in the self-renewal capacity of *Clasp2*<sup>-/-</sup> cells *in vivo* (Figure S3B). Functional HSCs were thus absent in E11 *Clasp2*<sup>-/-</sup> aortas. We conclude that CLASP2 controls the timing of IAHC production and pre-HSC maturation to initiate the formation of functional HSCs in the aorta.

### Conserved role of *Clasp2* in hematopoietic stem and progenitor cell emergence

To determine whether the role of *Clasp2* in HSC production was conserved among species, we generated two zebrafish mutant lines using CRISPR/Cas9 genome editing. We targeted an exon common to most of the *clasp2* variants found in fish, causing a frame shift and a premature STOP codon (Figure S4A, S4B; mutant fish lines are referred to as *clasp2*mut[-4bp] and [-10bp]). Both *clasp2*mut lines displayed a robust downregulation of *clasp2* isoforms (Figure S4C, S4D). On average, 25% of embryos from a cross of heterozygous *clasp2*mut displayed a curved body at 3 days post-fertilization (dpf) (Figure S4E, S4F), and genotyping revealed that these represented homozygous *clasp2*mut embryos. The curved body phenotype was recapit-



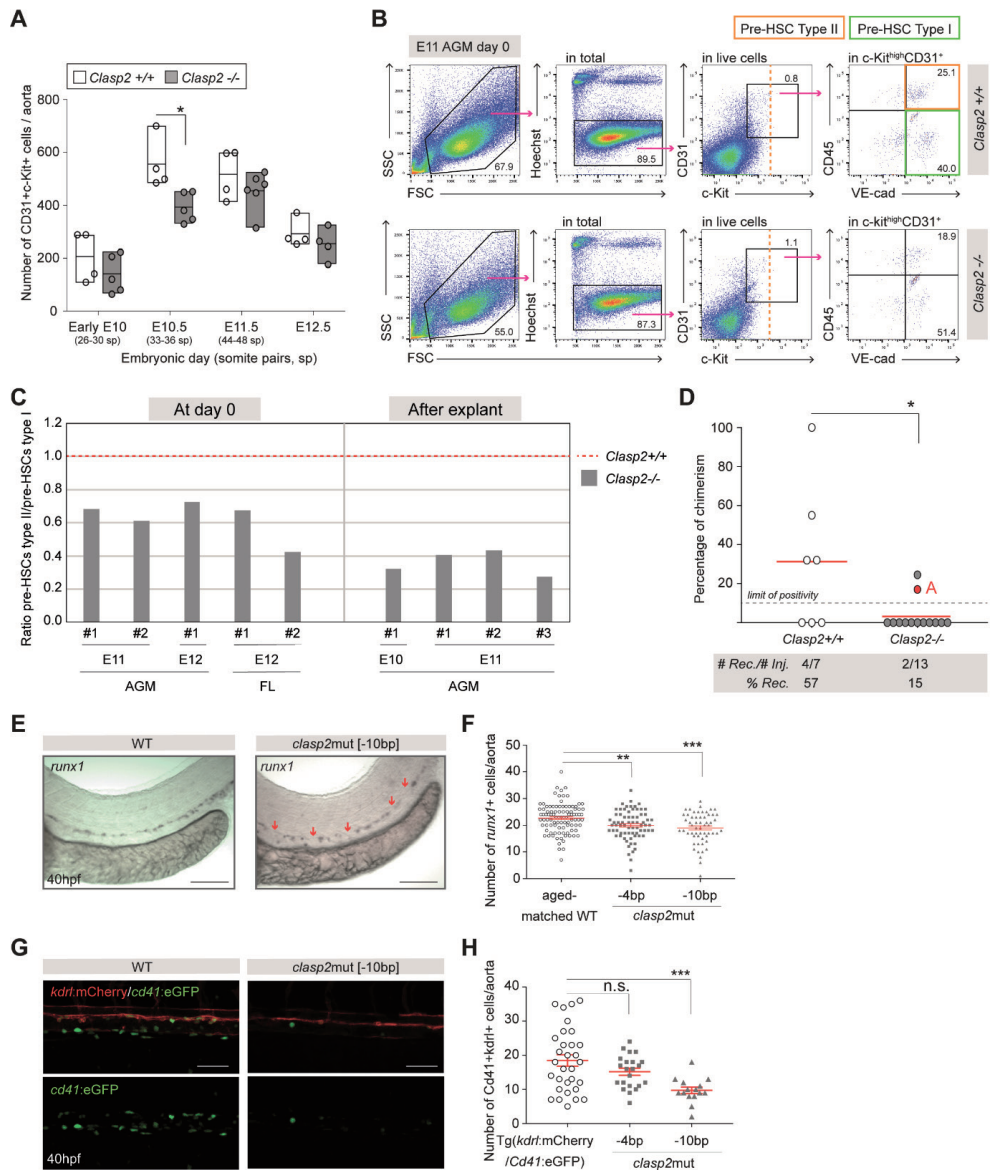


**Figure 1. CLASP2 regulates HSPC production in the aorta of mouse and zebrafish embryos.** (A) Number of CD31+c-Kit+ IAHC cells per early E10, E10.5, E11.5 and E12.5 *Clasp2*<sup>+/+</sup> and *Clasp2*<sup>-/-</sup> aortas (16 *Clasp2*<sup>+/+</sup>, 20 *Clasp2*<sup>-/-</sup> embryos, n=4). One dot: one embryo. (B) Representative flow cytometry analyses of type I (green gate, c-Kit+CD31+VE-cad+CD45-) and type II (orange gate, c-Kit+CD31+VE-cad+CD45+) pre-HSC populations at day 0 in E11 AGMs isolated from *Clasp2*<sup>+/+</sup> (top panels) and *Clasp2*<sup>-/-</sup> (bottom panels) embryos (14 *Clasp2*<sup>+/+</sup>, 8 *Clasp2*<sup>-/-</sup>, n=3). (C) Ratio between the percentages of type II and type I pre-HSCs at day 0 in E11 (n=2) and E12 (n=1) AGMs and E12 FLs (n=2) (left panel), and after explant culture of E10 (n=1) and E11 (n=3) AGMs of *Clasp2*<sup>+/+</sup> and *Clasp2*<sup>-/-</sup> embryos. #, independent experiments. Ratio for *Clasp2*<sup>+/+</sup> set at 1. Average fold decrease: at day 0 (E11/E12): 1.7±0.4; after explant (E10/E11): 2.9±0.6. (D) Hematopoietic repopulation (percentage of chimerism) after injection of E11 *Clasp2*<sup>+/+</sup> and *Clasp2*<sup>-/-</sup> AGM cells (n=6; 1 embryo equivalent/mouse). Dot: one transplanted mouse. Dashed line: limit of positivity (>10% of chimerism in blood). Red line: chimerism aver-

age. (E) Representative images of WISH for *runx1* expression in WT and *clasp2mut*[-10bp] zebrafish embryos (40hpf). Red arrows: areas with no *runx1*<sup>+</sup> cells. (F) Number of *runx1*<sup>+</sup> cells in the aorta of WT, *clasp2mut*[-4bp] and *clasp2mut*[-10bp] embryos (40hpf) (n=5; 97 WT, 71 *clasp2mut*[-4 bp], 57 *clasp2mut*[-10 bp]). (G) Representative merge and single GFP fluorescent images of *Tg(cd41:eGFP/kdrl:mCherry)* (WT) and *clasp2mut*[-10bp] embryos (background *Tg(cd41:eGFP/kdrl:mCherry)*) at 40hpf. (H) Number of *cd41+kdrl+* HSPCs per aorta in WT, *clasp2mut*[-4bp] and *clasp2mut*[-10bp] embryos at 40hpf (n=3; 31 WT, 25 *clasp2mut*[-4bp], 20 *clasp2mut*[-10bp]). Line, mean (A, D). Error bars, mean ± SEM (F, H). \*\*\*P<0.001, \*\*P<0.01, \*P<0.05, n.s., not significant, Mann-Whitney U test (A, D, F, H). Scale bars: 100µm (E, G). IAHc, intra-aortic hematopoietic cluster; sp, somite pair; WT, wild-type; E, embryonic day; AGM, aorta-gonad-mesonephros; hpf, hour post-fertilization; WISH, whole in situ hybridization; # Rec, number of reconstituted mice; # Inj, number of injected mice; % Rec, percentage of reconstituted recipients. See also Figures S1-S4.

tulated when we injected a *clasp2* morpholino oligonucleotide (MO) into embryos (Figure S4G). RT-PCRs showed intron retention in the *clasp2* morphants, indicating that *clasp2* mRNA splicing is blocked (Figure S4H). The rescue of the curved body axis phenotype by injection of WT *clasp2* mRNA in *clasp2mut* (Figure S4I, S4J) confirmed that it was due to the loss of *clasp2*. Since the curved body axis is specific for the loss of Clasp2 and a convenient mutant screening method, we used it to distinguish *clasp2mut* from aged-matched WT embryos for the rest of the study. Of note, *clasp2mut* begin to die at 5dpf. Moreover, many acridine orange<sup>+</sup> cells, likely apoptotic cells, were observed in the *clasp2mut* neural tube, reflecting an essential role of Clasp2 in fish neuronal development (Figure S5A). By contrast, no difference in acridine orange staining was detected in *cd41+kdrl+* HSPCs in the aorta of *clasp2mut* compared to WT embryos (Figure S5B).

To determine whether *clasp2* loss-of-function interfered with HSPC production in the embryonic aorta, the number of *runx1*<sup>+</sup> cells was counted after whole in situ hybridization (WISH) in *clasp2mut* and WT embryos (Figure 1E, 1F). The number of HSPCs [*cd41+kdrl+*] was also determined after crossing *clasp2mut* lines with a reporter line for HSPCs and vascular endothelium (*Tg(cd41:eGFP/kdrl:mCherry)*) (Figure 1G, 1H). In both experiments, the number of HSPCs was reduced in *clasp2mut* compared to WT at 40 hours post fertilization (hpf) (Figure 1F, 1H). Thus, Clasp2 has a role in the formation of the first HSPCs in the aorta of both mouse and zebrafish embryos.

## CLASP2 regulates HSC self-renewal and prevents HSC exhaustion throughout mouse development

To determine whether CLASP2 is involved in hematopoietic regulation after IAHc emergence, we examined FLs at E14. The phenotypically defined LSK Slam HSC population (*Lin*<sup>low</sup>/*-CD48*<sup>low</sup>/*-SCA-1+c-Kit+CD150+*) was present in *Clasp2*<sup>-/-</sup> FLs (Figure 2A), although less numerous (5,637±1,249 versus 4,290±578 cells per *Clasp2*<sup>+/+</sup> and *Clasp2*<sup>-/-</sup> FLs, respectively). No increase of pre-apoptotic (Annexin-V+7-AAD-) or dead (7-AAD+) c-Kit<sup>+</sup> cells was observed in *Clasp2*<sup>-/-</sup> FLs (Figure S1F-H). However, transplantation of 0.001 and 0.005 embryo equivalent (ee) of *Clasp2*<sup>-/-</sup> FL cells reconstituted only 1 recipient out of 8 (Mouse B, red dot) with a low chimerism (Figure 2B, 2C [red lines: mean of chimerism]), respectively. The reconstitution of Mouse B was lymphoid-biased (Figure S3A, bottom panel) and none of the secondary recipients were reconstituted (Figure S3B), as reported above for AGM cells. In contrast, all recipients injected with *Clasp2*<sup>+/+</sup> cells were repopulated with 100% of chimerism (Figure 2B, 2C). Thus, *Clasp2*<sup>-/-</sup> embryos are depleted in multipotent and self-renewing HSCs in both the AGM and FL.

We next tested whether *Clasp2*<sup>-/-</sup> FL HSCs were progressively exhausted through self-renewal defects by performing a long-term culture-initiating cell (LTC-IC) assay. The ability of sorted E14 FL LSK cells to produce hematopoietic progenitors (CFU-Cs) was tested up to 4 weeks after co-culture with the supportive stromal cell line MS-5

(Figure 2D). While the numbers of CFU-Cs produced by *Clasp2*<sup>+/+</sup> and *Clasp2*<sup>-/-</sup> LSK cells were similar after 1 and 2 weeks of culture, this number started to decrease after 3 weeks, with almost no CFU-Cs produced at 4 weeks in the *Clasp2*<sup>-/-</sup> culture

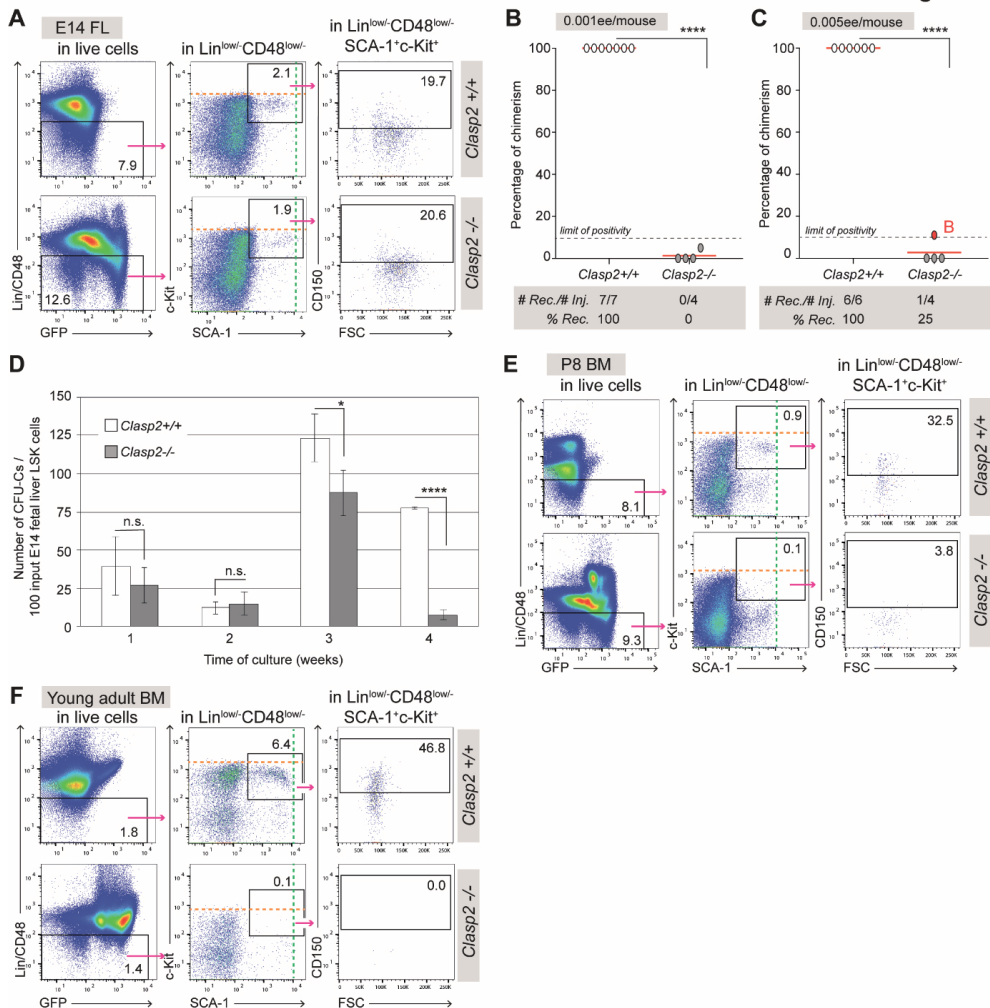


**Figure 2. CLASP2 is required to maintain HSC activity throughout mouse development.** (A) Gating strategy to analyze phenotypically defined HSCs ( $Lin^{low}SCA-1+c-Kit+CD150+CD48^{-/low}$ ) in E14 FLs (n=3; 8 *Clasp2*<sup>+/+</sup>, 7 *Clasp2*<sup>-/-</sup>). (B, C) Hematopoietic repopulation analyses after injection of 0.001ee (B, n=3) and 0.005ee (C, n=3) of E14 *Clasp2*<sup>+/+</sup> and *Clasp2*<sup>-/-</sup> FL cells. Red dot: mouse B. (D) Average of CFU-Cs produced weekly per 100  $Lin-SCA-1+c-Kit+$  (LSK) input cells sorted from *Clasp2*<sup>+/+</sup> and *Clasp2*<sup>-/-</sup> E14 FLs and cultured in LTC-IC culture system for up to 4 weeks. Representative experiment of n=2. Error bars, mean  $\pm$  SD between triplicates. (E, F) Gating strategy to analyze phenotypically defined HSCs in the BM of *Clasp2*<sup>+/+</sup> (upper panels) and *Clasp2*<sup>-/-</sup> (lower panels) P8 mice (n=3) (E) and young adult mice (4.5 weeks old, n=3) (F). Orange and green dashed lines: highest level of c-Kit and SCA-1 fluorescence, respectively (A, E, F). Of note, *Clasp2*<sup>-/-</sup> cells express GFP (as seen in the bottom left plots of (A, E, F); also see Star Methods). Error bars: mean  $\pm$  SD (D). \*\*\*\*P<0.0001, \*P<0.05, n.s., not significant, Mann-Whitney U test (B, C), Student's t-test (D). FL, fetal liver; BM, bone marrow; # Rec, number of reconstituted mice; # Inj, number of injected mice; % Rec, percentage of reconstituted recipients. See also Figures S1 and S3.

(Figure 2D). In comparison, *Clasp2*<sup>+/+</sup> LSK cells continued to produce CFU-Cs, confirming a self-renewal defect and therefore the progressive loss of *Clasp2*<sup>-/-</sup> LSK cells in culture.

Flow cytometry analyses revealed that the progressive exhaustion of HSCs observed in E14 FLs continued *in vivo* in the BM of *Clasp2*<sup>-/-</sup> neonates (P8) and young adults (4.5 weeks old) (Figure 2E, 2F). The defect was intrinsic to HSCs and not the result of a defective HSC BM niche, as demonstrated by the successful *in vivo* transplantation of total BM cells or LSK-sorted cells from WT donors into irradiated *Clasp2*<sup>-/-</sup> recipients (Figure S3C, S3D). Of note, sorted LSK cells were transplanted to rule out any possible engraftment of WT derived BM microenvironment cells that could support WT HSCs. WT HSCs provided a high-level multilineage reconstitution in primary (Figure S3C, S3D) and secondary recipients (Figure S3E, S3F), proving their capacity to self-renew in the *Clasp2*<sup>-/-</sup> BM microenvironment. Overall, our *in vitro* and *in vivo* experiments demonstrate an essential intrinsic role of CLASP2 in proper self-renewal and maintenance of functional HSCs throughout mouse development.

### Clasp2 maintains the HSPC pool throughout zebrafish development

After emergence, HSPCs migrate to the CHT in zebrafish embryos (54, 55) before colonizing the thymus (56, 57) and ultimately the kidney marrow (BM equivalent in fish) (55, 58-60). As *clasp2*<sup>mut</sup> begin to die at 5dpf, our analyses were restricted to earlier time points. We observed a progressive loss of *cd41*<sup>+</sup> HSPCs in the CHT of *clasp2*<sup>mut</sup> compared to aged-matched WT (*Tg(cd41:eGFP/kdrl:mCherry)*) at both 52hpf (Figure 3A, 3B) and 3dpf (Figure 3C, 3D). These data were confirmed by the decrease of *cmyb*<sup>+</sup> cells after WISH in the CHT of *clasp2*<sup>mut</sup> compared to WT siblings (Figure 3E, 3F). A partial hematopoietic phenotype rescue was observed after injection of WT *clasp2* mRNA in *clasp2*<sup>mut</sup>, confirming that the hematopoietic defect is indeed due to the loss of *clasp2* (Figure 3G). The HSPC deficiency was also recapitulated in *clasp2* morphants that drastically lose the *cmyb*<sup>+</sup> population in the CHT at 3dpf (Figure 3H). By 5dpf, the number of *cd41*<sup>+</sup> cells per *clasp2*<sup>mut</sup> thymus was markedly decreased (Figure 3I, 3J), as expected since the early seeding of the thymus is dependent on HSPCs generated in AGM and CHT (55, 59). These data were confirmed by a reduced or a complete absence of thymic area (*rag1*<sup>+</sup> T-cell) in *clasp2*<sup>mut</sup> compared to WT siblings at 5dpf (Figure 3K). Similar to mice, the progressive loss of HSPCs in *clasp2*<sup>mut</sup> zebrafish was not the result of apoptosis, as very few acridine orange<sup>+</sup> apoptotic cells were observed in the aortic region at 40hpf, and in the CHT at both 52hpf and 3dpf (Figure S5B). Overall, our data demonstrate that Clasp2 also regulates HSPC maintenance throughout zebrafish development.

### CLASP2 prevents premature HSPC differentiation

Coinciding with the severe loss of HSPCs in the CHT, we observed a significant increase in neutrophils (Mpx<sup>+</sup>) but not macrophages (Mpeg<sup>+</sup>) in 3dpf *clasp2*<sup>mut</sup> zebrafish (Figure S6A, S6B), potentially pointing to premature HSPC differentiation. As primitive and definitive hematopoiesis cannot be easily discriminated in *clasp2*<sup>mut</sup> since they die after 5dpf, we focused on our mouse model to investigate how *Clasp2*<sup>-/-</sup> cells might prematurely differentiate. We performed clonogenic assays to examine the production of CFU-Cs in *Clasp2*<sup>+/+</sup> and *Clasp2*<sup>-/-</sup> E11 AGMs, E14 FLs and P8 BMs. The numbers and types of progenitors and the cellularity were similar in *Clasp2*<sup>-/-</sup> and *Clasp2*<sup>+/+</sup> AGMs at day 0 (Figure 4A, 4B). However, more progenitors were present in *Clasp2*<sup>-/-</sup> AGMs after explant culture despite a lower cellularity (Figure 4C, 4D). These results reflect the *in vivo* situation observed in E14 FLs (Figure 4E, 4F). Importantly,



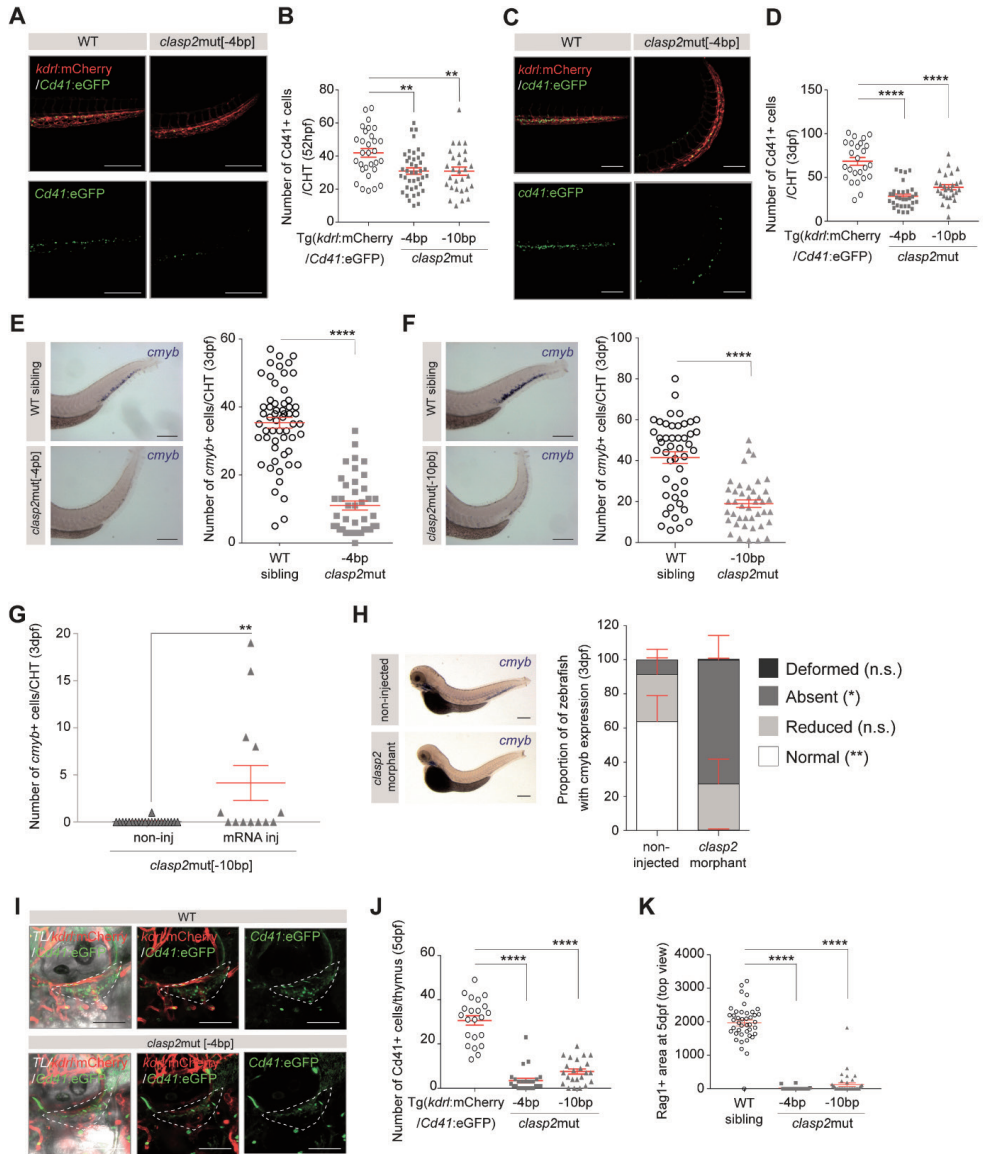


**Figure 3. CLASP2 is required to maintain HSPC activity throughout zebrafish development.** (A) Representative merge (top panels) and single GFP fluorescent (bottom panels) images of *Tg(cd41:eGFP/kdr1:mCherry)* (WT) and *clasp2mut[-4bp]* zebrafish CHTs (background *Tg(cd41:eGFP/kdr1:mCherry)*), at 52hpf (n=3). (B) Number of Cd41+ cells in the CHT of WT, *clasp2mut[-4bp]* and *clasp2mut[-10bp]* zebrafish embryos at 52hpf (n=4-5; 30 WT, 41 *clasp2mut[-4bp]*, 29 *clasp2mut[-10bp]* embryos). (C) Representative merge (top panels) and single GFP fluorescent (bottom panels) images of *Tg(cd41:eGFP/kdr1:mCherry)* and *clasp2mut[-4bp]* zebrafish CHTs, at 3dpf (n=3). (D) Number of Cd41+ cells in the CHT of WT, *clasp2mut[-4bp]* and *clasp2mut[-10bp]* zebrafish embryos at 3dpf (n=4; 25 WT, 32 *clasp2mut[-4bp]*, 27 *clasp2mut[-10bp]*). (E, F) Representative WISHs and graphs showing the number of *cmyb*+ cells in the CHT of WT sibling, *clasp2mut[-4bp]* (E) and *clasp2mut[-10bp]* (F) embryos at 3dpf (n=4, with a total of 57 WT (sibling), 40 *clasp2mut[-4bp]*, 46 WT (sibling) and 42 *clasp2mut[-10bp]* embryos). Representative images of WISH for *cmyb* expression are shown in the left side of the panels. (G) Number of *cmyb*+ cells per CHT of *clasp2mut[-10bp]* embryos either non-injected

(non-inj) or injected (inj) with WT *clasp2* mRNA for rescue and analyzed at 3dpf. (H) Proportion of zebrafish embryos with a normal, reduced or absence of *cmyb* expression in the CHT, or deformity at 3dpf, after non-injection or injection of *clasp2* morpholinos. Representative cases of WISH for *cmyb* expression are shown in the left side of the panel. n=5, with a total of 155 non-injected and 239 injected embryos. (I) Representative merge (left panels), double (middle panels) and single GFP (right panels) fluorescent images of *Tg(cd41:eGFP/kdrl:mCherry)* (WT) and *clasp2mut[-4bp]* (background *Tg(cd41:eGFP/kdrl:mCherry)*) zebrafish thymus (dashed area), at 5dpf. (J) Number of Cd41+ cells in the thymus (dashed areas shown in (I)) of WT, *clasp2mut[-4bp]* and *clasp2mut[-10bp]* embryos at 5dpf (n=3; 22 WT, 25 *clasp2mut[-4bp]*, 23 *clasp2mut[-10bp]*). (K) Rag1+ area (arbitrary unit) from the top view of the thymus (sum of both thymus) at 5dpf in WT sibling, *clasp2mut[-4bp]* and *clasp2mut[-10bp]* embryos (n=2; 42 WT, 20 *clasp2mut[-4bp]*, 39 *clasp2mut[-10bp]*). Green, GFP; Red, mCherry (A, C, I). Mean  $\pm$  SEM (B, D-H, J, K). \*\*\*\* $p < 0.0001$ , \*\* $p < 0.01$ , \* $p < 0.05$ , n.s., not significant, Mann-Whitney U test (B, D-H, J, K). Scale bars: 200 $\mu$ m (A, C), 100 $\mu$ m (I). WT, wild-type; CHT, caudal hematopoietic tissue. hpf, hour post-fertilization; dpf, day post-fertilization. See also Figures S4 and S5.

the high number of progenitors in FLs was not due to an increased influx of progenitors produced in the YS since this number was similar in *Clasp2*<sup>-/-</sup> and *Clasp2*<sup>+/+</sup> YSs (Figure 4G). Because *Clasp2* is highly expressed in the YS, especially in the CD31+ endothelial population (Figure 4H), the generation of progenitors in the YS appears to be independent of CLASP2. Thus, the increase of progenitors in FL is most likely due to a premature differentiation of pre-HSCs, which are partially blocked towards an HSC fate as shown above (Figure 1C), and which instead directly differentiate into committed progenitors. In support of a progressive exhaustion of the HSPC pool, the number of progenitors drastically decreased in the BM of P8 *Clasp2*<sup>-/-</sup> mice (Figure 4I). This is consistent with the LTC-IC data (Figure 2D) and with the pancytopenia previously reported in *Clasp2*<sup>-/-</sup> adult mice (34). Thus, CLASP2 maintains the pool of self-renewing HSCs by preventing premature differentiation.

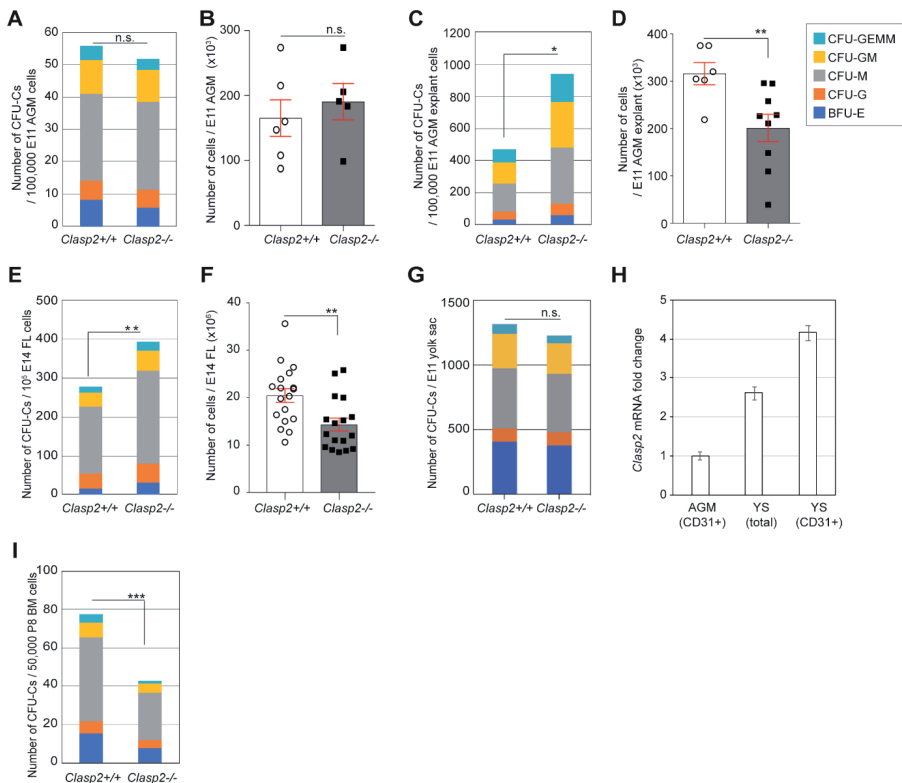




**Figure 4. Premature hematopoietic differentiation in *Clasp2*<sup>-/-</sup> embryos compared to *Clasp2*<sup>+/+</sup> embryos.** (A) Number of CFU-Cs per 100,000 AGM cells of E11 *Clasp2*<sup>+/+</sup> and *Clasp2*<sup>-/-</sup> embryos. (B) Graph representing the number of total cells per E11 AGM of *Clasp2*<sup>+/+</sup> and *Clasp2*<sup>-/-</sup> embryos at day 0. (C) Number of CFU-Cs per 100,000 E11 AGM cells obtained after 3 days of explant culture. (D) Graph representing the number of total cells per E11 AGM after explant culture. (E) Number of CFU-Cs per 105 E14 FL cells. (F) Graph representing the number of total cells per E14 FLs. (G) Number of CFU-Cs per one embryo equivalent of E11 YS cells. (H) Graph showing the fold change of *clasp2* (alpha) mRNA in total cells and sorted CD31+ endothelial cells from E11 WT YSs compared to sorted CD31+ endothelial cells from E11 WT AGMs (value set at 1), after RT-qPCR. (I) Number of CFU-Cs per 50,000 BM cells obtained from P8 neonates. For E11 AGM at day 0, n=3 [10 *Clasp2*<sup>+/+</sup>, 12 *Clasp2*<sup>-/-</sup>]; E11 AGM explant, n=5 [12 *Clasp2*<sup>+/+</sup>, 16 *Clasp2*<sup>-/-</sup>]; E14 FL, n=3 [3 *Clasp2*<sup>+/+</sup>, 4 *Clasp2*<sup>-/-</sup>]; E11 YS, n=3 [10 *Clasp2*<sup>+/+</sup> and 12 *Clasp2*<sup>-/-</sup>]; P8 BM neonates, n=2 [2 *Clasp2*<sup>+/+</sup>, 2 *Clasp2*<sup>-/-</sup>]. Data are represented as mean ± SEM (B, D, F) and mean ± SE (H). \*\*\*P<0.001, \*\*P<0.01, \*P<0.05, n.s., not significant, Mann-Whitney U test. CFU-GEMM: Colony Forming Unit-Granulocyte-Erythroid-Macrophage-Megakaryocyte; CFU-GM: CFU-Granulocyte-Macrophage; CFU-M: CFU-Macrophage; CFU-G: CFU-Granulocyte; BFU-E: Burst-Forming Unit-Erythroid; E, embryonic day; AGM, aorta-gonad-mesonephros; FL, fetal liver; YS, yolk sac; BM, bone marrow. See also Figure S6.

### CLASP2 regulates HSPC production by controlling c-Kit plasma membrane levels

To determine how CLASP2 might influence the fate of HSCs, we examined important hematopoietic markers, such as SCA-1 and c-Kit that are known to play a role in the differentiation, proliferation and survival of hematopoietic (stem) cells (61-63). Flow cytometry analyses of IAHC cells revealed a slight decrease of the c-Kit mean fluorescence intensity (MFI) in *Clasp2*<sup>-/-</sup> embryos at E11 (Figure 5A). By measuring the average fluorescence intensity of c-Kit along the circumference of IAHC cells after whole mount immunostaining with c-Kit antibody, using a customized Fiji plug-in, we confirmed the reduced levels of c-Kit at the plasma membrane of *Clasp2*<sup>-/-</sup> IAHC cells (Figure 5B-D). The decrease, not yet visible at E10, started at E10.5 and persisted at E12 (Figure 5E). Flow cytometry analyses of E14 FL, neonate and adult BM cells and phenotypically defined HSCs also revealed the progressive decrease in c-Kit MFI in *Clasp2*<sup>-/-</sup> mice (Figure 5F, left panel; Figure 2A, 2E, 2F, maximum level of fluorescence intensity indicated with orange dashed lines), which was not the case for SCA-1 and Lin (Figure 5F, middle and right panels; Figure 2A, 2E, 2F, green dashed lines for SCA-1), suggesting a specific sensitivity of c-Kit to the absence of CLASP2. Western blot (WB) experiments performed on Lin- E14 FL cells showed that c-Kit protein levels were strongly decreased in *Clasp2*<sup>-/-</sup> compared to *Clasp2*<sup>+/+</sup> embryos (Figure 5G), while we did not detect a difference in c-Kit at the transcriptional level (Figure 5H). These results suggest a CLASP2 dependent post-translational regulation of c-Kit.

### CLASP2 regulates Golgi morphology and lysosome number in IAHCs and fetal liver HSPCs

Since CLASP2 plays a role in Golgi organization *in vitro* (44), and the *trans*-Golgi network is a key relay station for vesicular trafficking to the cell surface (64, 65), we examined whether the decreased c-Kit expression at the cell surface might be linked to a potential Golgi defect in *Clasp2*<sup>-/-</sup> IAHCs. To this end, we co-stained for c-Kit and the Golgi marker GM130 and found an increased Golgi scattering in *Clasp2*<sup>-/-</sup> IAHC cells, compared to *Clasp2*<sup>+/+</sup> embryos (Figure 6A-C). This aberrant Golgi-morphology included the *trans*-Golgi network, as shown by the Golgi reassembly-stacking protein GRASP55 staining (Figure S7A-C). Remarkably, a similar aberrant Golgi morphology was also observed in HSPCs in the CHT of *clasp2*mut[-10bp] zebrafish embryos (Figure S7D-F), suggesting a universal *in vivo* function for CLASP2 in Golgi organization and integrity in HSPCs.

The removal of proteins from the surface by lysosomal degradation plays an impor-

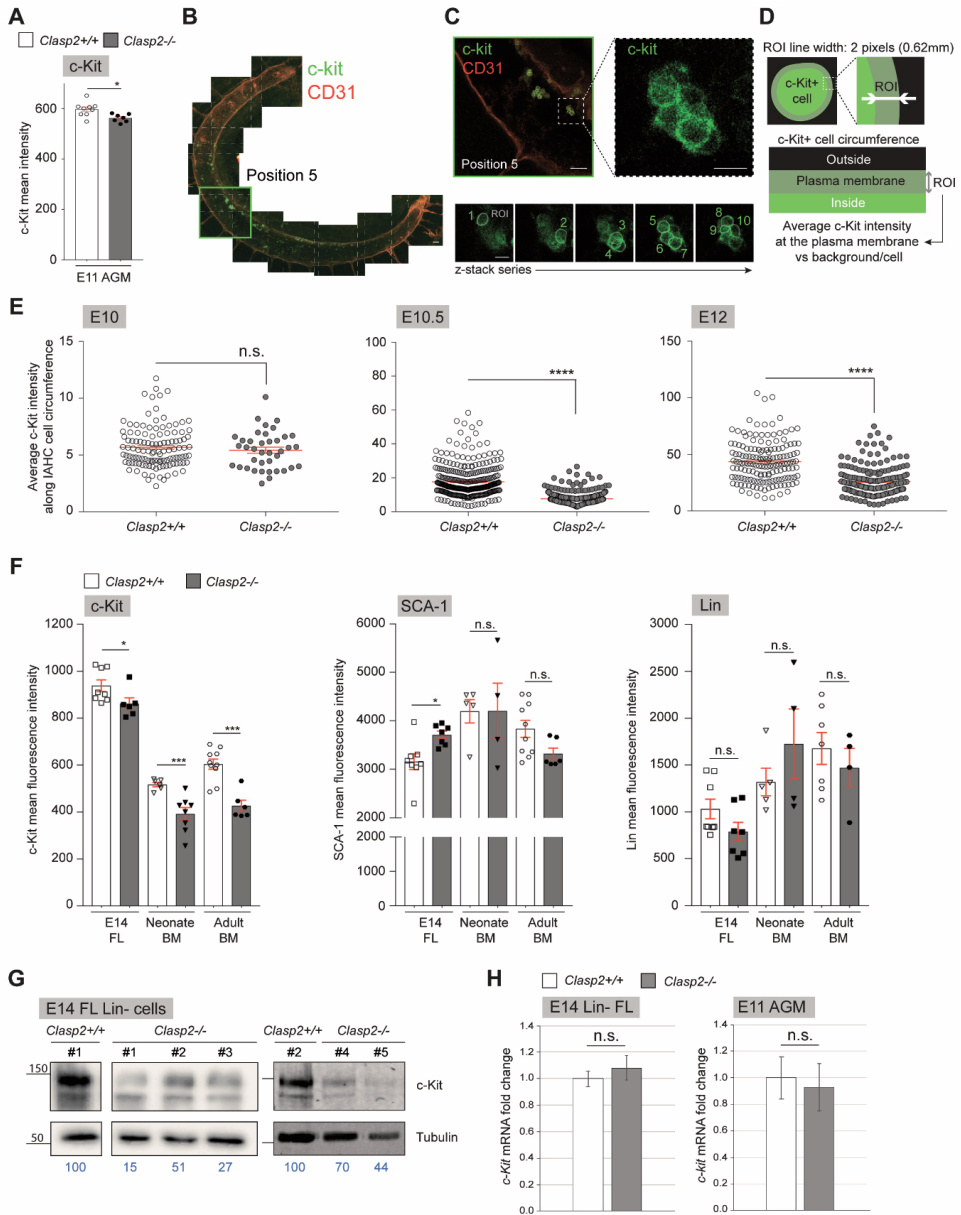


**Figure 5. Progressive loss of c-Kit at the plasma membrane of *Clasp2*<sup>-/-</sup> cells throughout development.** (A) Mean fluorescence intensity of c-Kit measured by flow cytometry in E11 *Clasp2*<sup>+/+</sup> and *Clasp2*<sup>-/-</sup> AGMs (9 *Clasp2*<sup>+/+</sup>, 7 *Clasp2*<sup>-/-</sup>, n=7). (B) Tile scale image reconstruction of a whole E10.5 *Clasp2*<sup>+/+</sup> embryo stained with c-Kit (green) and CD31 (red) antibodies. (C) Enlarged image of position 5 shown in (B), with dashed box outlining inset, which is shown enlarged to the right, and which reveals c-Kit fluorescence (green) in an IAHc. Bottom panels: images of this IAHc in various focal planes to draw ROIs at the maximal fluorescence intensity along the circumference of IAHc cells through a z-stack series. (D) Illustration of a IAHc cell with the ROI (2 pixels width) to measure the average c-Kit fluorescence intensity. (E) Average mean fluorescence intensity of c-Kit along the plasma membrane circumference of IAHc cells in the aorta of E10, E10.5 and E12 *Clasp2*<sup>+/+</sup> and *Clasp2*<sup>-/-</sup> embryos after whole mount immunostaining with c-Kit antibody (E10: 1 *Clasp2*<sup>+/+</sup>, 2 *Clasp2*<sup>-/-</sup>; E10.5: 1 *Clasp2*<sup>+/+</sup>, 1 *Clasp2*<sup>-/-</sup>;

E12: 1 *Clasp2*<sup>+/+</sup>, 1 *Clasp2*<sup>-/-</sup>). (F) Mean fluorescence intensity of c-Kit, SCA-1 and Lin markers measured by flow cytometry in E14 FL, neonate and adult BM cells isolated from *Clasp2*<sup>+/+</sup> and *Clasp2*<sup>-/-</sup> embryos and mice (E14 FLs [8 *Clasp2*<sup>+/+</sup>, 6 *Clasp2*<sup>-/-</sup> embryos], n=3; P8 BM [6 *Clasp2*<sup>+/+</sup>, 8 *Clasp2*<sup>-/-</sup>], n=6; adult BM [10 *Clasp2*<sup>+/+</sup>, 6 *Clasp2*<sup>-/-</sup>], n=7). (G) Western blots for c-Kit and tubulin (loading control) on lysates of E14 *Clasp2*<sup>+/+</sup> and *Clasp2*<sup>-/-</sup> Lin- FL cells (2 *Clasp2*<sup>+/+</sup>, 5 *Clasp2*<sup>-/-</sup>, n=2). c-Kit intensity is indicated in blue below the gel images, *Clasp2*<sup>+/+</sup> culture band set at 100. (H) RT-qPCR for c-Kit on Lin- FL cells and total AGM cells from *Clasp2*<sup>+/+</sup> and *Clasp2*<sup>-/-</sup> embryos isolated at E14 and E11, respectively. Error bars: mean  $\pm$  SEM (A, E, F). Mean  $\pm$  SD (H). \*\*\*\*P<0.0001, \*\*\*P<0.001, \*P<0.05, n.s., not significant, Mann-Whitney U test (A, E, F), Unpaired t-test (H). E, embryonic day; AGM, aorta-gonad-mesonephros; FL, fetal liver. Scale bars: 100 $\mu$ m (B, C), 10 $\mu$ m (C, close-up).

tant role in maintaining the proper levels at the plasma membrane. Immunostainings for the lysosomal-associated membrane protein 1 (LAMP-1) showed an increase of lysosomal vesicles in E10.5 *Clasp2*<sup>-/-</sup> IAHC cells (Figure 6D, 6E), suggesting lysosomal defects in addition to Golgi abnormalities in HSPCs lacking CLASP2. In agreement, we did not detect any differences in LAMP-1 at E10 when no difference in levels of c-Kit at the plasma membrane was observed between *Clasp2*<sup>+/+</sup> and *Clasp2*<sup>-/-</sup> embryos (Figure 6F, Figure 5E, left panel). Combined, these data are supportive of abnormal trafficking towards the plasma membrane and/or an increase in c-Kit protein degradation as a basis for c-Kit defects in *Clasp2*<sup>-/-</sup> HSPCs.

To examine the possibility of increased lysosomal degradation of c-Kit, we cultured E14 FL Lin- cells overnight, either untreated or treated with SCF (c-Kit ligand) or with Bafilomycin A1 (BafA, pharmacological inhibitor of lysosomal activity), or with both SCF and BafA, and measured c-Kit MFI by flow cytometry (Figure 6G). Binding of SCF to c-Kit led to the internalization of c-Kit in both *Clasp2*<sup>+/+</sup> and *Clasp2*<sup>-/-</sup> cells as measured by a decrease of c-Kit MFI, suggesting that c-Kit maintains its functionality in the absence of CLASP2. Inhibition of lysosomal activity through BafA treatment restored the c-Kit levels in *Clasp2*<sup>-/-</sup> cells to *Clasp2*<sup>+/+</sup> levels, indicating that c-Kit undergoes abnormal lysosomal degradation in the absence of CLASP2. Treatment with both SCF and BafA increased c-Kit MFI in *Clasp2*<sup>+/+</sup> cells in comparison to SCF alone, but not in *Clasp2*<sup>-/-</sup> cells. These data suggest that upon rapid SCF-mediated c-Kit internalization, the inhibition of lysosomal degradation is not sufficient to restore c-Kit cell-surface levels (as with BafA-only treatment), indicating a limited capacity of *Clasp2*<sup>-/-</sup> cells to recycle (and/or to target newly synthesized) c-Kit to the plasma membrane.

### CLASP2 regulates intracellular turnover of c-Kit

Due to the limited number of FL cells, we turned to *Clasp2*<sup>+/+</sup> and *Clasp2*<sup>-/-</sup> mouse embryonic stem cells (ESCs), which can be easily expanded, and which express c-Kit when cultured in conditions that maintain the ground state (66). *Clasp2*<sup>-/-</sup> ESCs display similar Golgi defects (Figure S7G, S7H), as in *Clasp2*<sup>-/-</sup> mouse and zebrafish embryos. In addition, c-Kit internalization and lysosomal degradation showed similar dynamics in *Clasp2*<sup>-/-</sup> ESCs (Figure 7A, 7B) as in FL cells (Figure 5G, 6G), i.e., less c-Kit protein under steady state conditions, reduced c-Kit degradation after BafA treatment, internalization and degradation of c-Kit after SCF treatment (Figure 7A), and no significant restoration of c-Kit levels in *Clasp2*<sup>-/-</sup> ESCs when treated with SCF followed by BafA (Figure 7B), indicating a rapid degradation of c-Kit prior to the inhibition of lysosomal activity. Thus, ESCs appear to be a suitable *in vitro* stem cell model for further analysis of c-Kit.

The imbalance in c-Kit trafficking and degradation in the absence of CLASP2 might originate from an altered c-Kit biosynthesis. N-terminal signal sequences are crucial for targeting the nascent protein to the endoplasmic reticulum (ER) (67). Concomitant with synthesis and transfer through the ER membrane, asparagine-linked glyco-

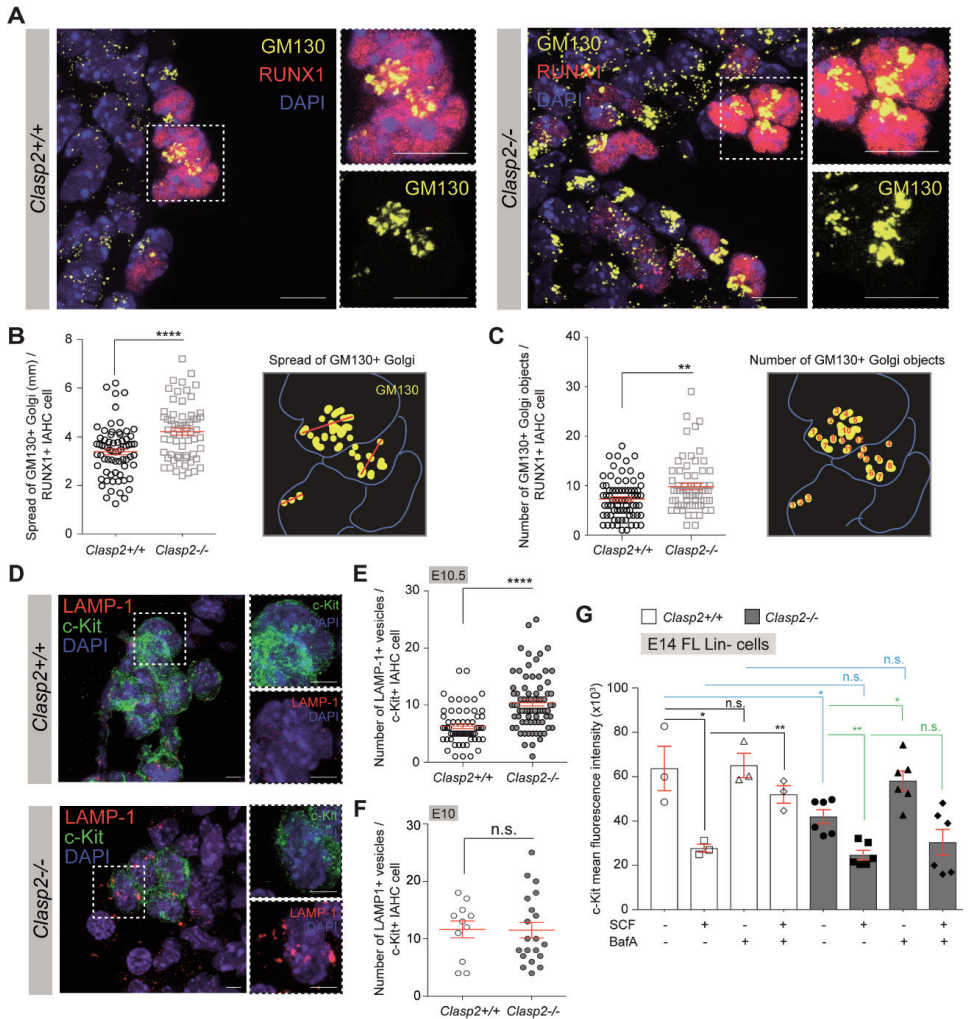


**Figure 6. Increased c-Kit degradation and defective trafficking to the plasma membrane in *Clasp2*<sup>-/-</sup> IAHC cells and Lin<sup>-</sup> fetal liver cells.** (A) Representative images of IAHCs in E10.5 *Clasp2*<sup>+/+</sup> and *Clasp2*<sup>-/-</sup> embryos after staining with anti-GM130 (yellow), anti-RUNX1 (red) and DAPI (blue). Dashed boxes are shown enlarged on the right of each main panel, with merge or single (GM130, yellow) fluorescence. (B, C) Spread (B) and number (C) of GM130+ Golgi per RUNX1+ IAHC cells in E10.5 *Clasp2*<sup>+/+</sup> and *Clasp2*<sup>-/-</sup> embryos (n=3). A schematic to the right side of each graph explains how the spread of Golgi (red lines) or the number of Golgi objects were measured. (D) Representative images of IAHCs in E10.5 *Clasp2*<sup>+/+</sup> and *Clasp2*<sup>-/-</sup> embryos after staining with anti-c-Kit (green), anti-LAMP-1 (red) and DAPI (blue). Dashed boxes are shown enlarged on the right of each main panel, with merges of (DAPI [blue] and either c-Kit [green] or LAMP-1 [red]) fluorescence. (E, F) Number of LAMP-1+ vesicles per c-Kit+ IAHC cell in E10.5 (E) and E10 (F) *Clasp2*<sup>+/+</sup> and *Clasp2*<sup>-/-</sup> embryos (n=2-3). (G) Mean fluorescence intensity of c-Kit measured by flow cytometry in E14 *Clasp2*<sup>+/+</sup> and *Clasp2*<sup>-/-</sup> Lin<sup>-</sup> FL cells cultured overnight, either alone, with stem cell factor (SCF, c-Kit ligand) or Bafilomycin A1 (BaFa), or with both SCF and BaFa (all in triplicates). Data are represented as mean ± SEM (B, C, E-G). \*\*\*\*P<0.0001, \*\*P<0.01, \*P<0.05, n.s., not significant, Mann-Whitney U test (B, C, E, F). Unpaired t-test (G). Scale bars: 10µm (A), 5µm (D). See also Figure S7.

sylation occurs in the ER lumen by a membrane-associated enzyme complex, which deposits an oligosaccharide group to the eight asparagine linked glycosylation sites in its N-terminal domain (68). Trafficking of c-Kit from the ER to the Golgi results

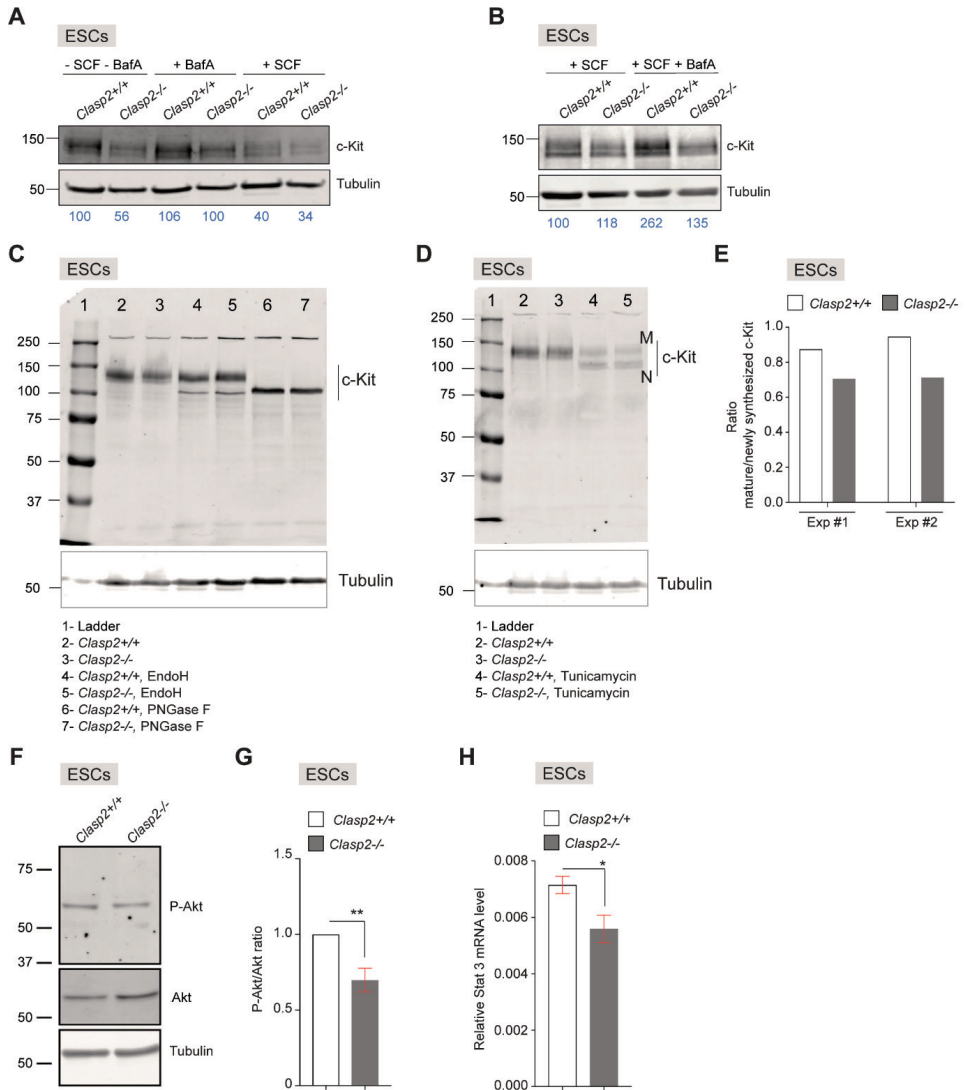


**Figure 7. Disturbed c-Kit degradation and trafficking affect downstream targets in *Clasp2*<sup>-/-</sup> mouse embryonic stem cells.** (A) Western blots for c-Kit and tubulin (loading control) on lysates of *Clasp2*<sup>+/+</sup> and *Clasp2*<sup>-/-</sup> mouse embryonic stem cells (mESCs) cultured overnight alone or with either BafA or SCF. (B) Western blots for c-Kit and tubulin (loading control) on lysates of *Clasp2*<sup>+/+</sup> and *Clasp2*<sup>-/-</sup> mESCs cultured overnight with SCF or SCF followed by BafA. In (A) and (B) the c-Kit band intensities were quantified using tubulin as control, these normalized intensities are indicated in blue below gel images, with the left lanes (*Clasp2*<sup>+/+</sup> culture (A) or *Clasp2*<sup>+/+</sup> culture with SCF (B)) set at 100 and the other intensities calculated relative to these values. (C) Mouse *Clasp2*<sup>+/+</sup> and *Clasp2*<sup>-/-</sup> ESC lysates were treated with either EndoH or Pngase F and examined by western blot using antibodies against the indicated proteins (Tubulin, loading control). Representative blot of n=2. (D) *Clasp2*<sup>+/+</sup> and *Clasp2*<sup>-/-</sup> mESCs were treated overnight with tunicamycin and lysates were examined by western blot using antibodies against the indicated proteins (Tubulin, loading control). M, mature c-Kit; N, newly synthesized c-Kit. Representative blot of n=2. (E) Ratio of mature c-Kit levels versus newly synthesized c-Kit measured by quantifying M and N c-Kit band intensities on western blot in *Clasp2*<sup>+/+</sup> and *Clasp2*<sup>-/-</sup> mESC lysates in 2 independent experiments (Exp #1 (shown in (D)), and #2). (F) Western blots containing *Clasp2*<sup>+/+</sup> and *Clasp2*<sup>-/-</sup> mESC lysates were probed with antibodies against total Akt and



phospho-Akt (P-Akt), and against Tubulin, which served as loading control. Representative blot of n= 4, with two independent sets of biological replicates. (G) Graph representing the relative levels of phospho-Akt to total Akt, after normalization to the tubulin loading control. (H) Graph representing the relative mRNA levels of *Stat3* in *Clasp2*<sup>+/+</sup> and *Clasp2*<sup>-/-</sup> mESCs. RT-qPCR was performed using *Stat3* primers and *Gapdh*, used as a housekeeping control. n=3 with 3 biological replicates per condition. \*\*P<0.01, \*P<0.05, Mann-Whitney U test, Mean ± SEM (G, H). ESC, embryonic stem cell.

in enzymatic modification of the sugar chains to the so-called “high mannose”, “hybrid”, or “complex” type sugars. As these modifications largely occur in the Golgi, and this organelle is affected in *Clasp2*<sup>-/-</sup> ESCs, we first tested whether glycosylation defects might occur in c-Kit in *Clasp2*<sup>-/-</sup> ESCs. Neither treatment of cell lysates with EndoH1 (an enzyme that cleaves “high mannose” type sugars from glycosylated proteins), nor treatment with PNGase F (which cleaves “hybrid” and “complex” type sugars) revealed an obvious difference in c-Kit glycosylation pattern between *Clasp2*<sup>+/+</sup> and *Clasp2*<sup>-/-</sup> ESCs (Figure 7C). Of note, EndoH1 hardly cleaved sugars off c-Kit while PNGase F was very efficient, indicating that most of the N-linked sugars on steady state c-Kit in ESCs are of the “hybrid” or “complex” type.

Next, we tested the effect of tunicamycin, which impairs N-linked ER glycosylation (69); (70) and thereby prevents trafficking of N-linked glycosylated proteins towards the Golgi complex due to misfolding (68). Tunicamycin treatment caused the appearance of two lower molecular weight bands of c-Kit on WB (marked with N, Figure 7D), which represent newly synthesized non-glycosylated isoforms (of note, Ribo-Seq analysis of c-Kit translation in ESCs cultured in 2iL confirmed expression of two isoforms (71)). In addition, we detected mature c-Kit (marked with M, Figure 7D), which was synthesized prior to the tunicamycin treatment. No difference in the levels of newly synthesized c-Kit was observed between *Clasp2*<sup>-/-</sup> and *Clasp2*<sup>+/+</sup> ESCs (Figure 7D, similar N band intensities, indicating similar biosynthesis rates of c-Kit), while the ratio of mature versus newly synthesized c-Kit was lower in *Clasp2*<sup>-/-</sup> ESCs (Figure 7E), indicating that while synthesis of c-Kit is not affected, degradation (and hence disappearance of mature c-Kit) is increased in *Clasp2*<sup>-/-</sup> ESCs. Consistent with the decreased expression of c-Kit at the cell surface of *Clasp2*<sup>-/-</sup> ESCs, we observed a reduction in the phosphorylation of AKT (P-Akt), a well-known downstream target of c-Kit (Figure 7F, 7G) (67). Furthermore, mRNA levels of *Stat3*, another c-Kit target, were also decreased (Figure 7H) (67); (72).

Taken together, our data indicate that the loss of CLASP2 affects overall Golgi integrity, including the *trans*-Golgi network, in addition to an enhanced lysosomal degradation of c-Kit and affected trafficking of c-Kit to the plasma membrane, causing reduced downstream signaling, such as AKT and *Stat3*. Therefore, CLASP2 is important to maintain a proper amount of c-Kit at the plasma membrane, which is crucial to safeguard the properties and fate of pre-HSCs and HSCs throughout development.

## Discussion

Understanding how HSCs acquire and maintain their stem cell properties *in vivo* is essential for improving HSC production *in vitro*. Here we show that CLASP2, a MT binding and Golgi organizing protein, is a key and conserved regulator of HSC formation during embryonic and fetal vertebrate development. Our data demonstrate that CLASP2 is involved in the regulation of successive steps such as EHT dynamics, pre-HSC maturation and the proper balance between HSC self-renewal and differentiation. Our data furthermore suggest that CLASP2 acts in all these steps by controlling c-Kit levels and hence, c-Kit signaling.



CLASP2 is involved in the first steps of HSC generation in the aorta by regulating EHT dynamics. Defects at this stage might influence subsequent fate decisions and contribute to the partial blockage of pre-HSC maturation and the absence of functional HSCs in *Clasp2*<sup>-/-</sup> AGM, FL and BM. The requirement for CLASP2 is cell-intrinsic and conserved in zebrafish species. The absence of apoptotic markers in the aorta suggests an alternative pre-HSC fate trajectory in *Clasp2*<sup>-/-</sup> embryos, “skipping” the acquisition of a functional HSC identity and prematurely differentiating into more lineage-committed cells. This hypothesis is supported by the lymphoid-biased reconstitution of *Clasp2*<sup>-/-</sup> AGM and FL cells upon transplantation and the increase in erythroid and myeloid progenitor production after AGM explant and in FLs. Erythro-myeloid progenitors (EMPs) and HSCs emerge from distinct populations of hemogenic endothelial cells in the YS and AGM, respectively (73). Our data indicate that CLASP2 is specifically required in HSC- but not in EMP-generating hemogenic endothelium. Overall, we hypothesize that CLASP2 safeguards the HSC state by preventing exhaustion through defective self-renewal and premature differentiation.

All aortic and FL HSCs reside within the c-Kit<sup>high</sup> population (74). We propose that reduced c-Kit expression on the surface of *Clasp2*<sup>-/-</sup> HSPCs causes at least part of the self-renewal phenotype, as well as progressive exhaustion during development. In support of our hypothesis and in concordance with our data, a decrease in the number of large IAHCs and type II pre-HSCs was reported in *Kit1* knockouts (*Kit1* encodes SCF), indicating that c-Kit/SCF signaling within the aortic niche regulates this maturation step (25). In addition, *kitb* knockdown in zebrafish embryos results in the specification of fewer aortic *runx1*-expressing HSPCs (75). Thus, the c-Kit surface level in pre-HSCs/HSCs seems to influence the self-renewal/differentiation choice. c-Kit is downregulated upon cell lineage differentiation where it is mainly co-expressed with myeloid markers (e.g., Mac-1, Gr1) in the BM (61). This might explain the lymphoid-biased reconstitution potential of *Clasp2*<sup>-/-</sup> AGM and FL cells upon transplantation. Modulating the expression of key receptors is an interesting concept to explore whether the generation and maintenance of HSC properties could be improved *in vitro*.

To maintain an optimal level of c-Kit at the cell surface, a balance of c-Kit synthesis, trafficking to the plasma membrane, and degradation is crucial (67). Upon ligand binding most receptor tyrosine kinases, such as c-Kit, are endocytosed and then either degraded or recycled back to the cell surface. The choice between lysosomal degradation or recycling is made in early endosomes, and recycling proteins can then pass through the *trans*-Golgi network on their way back to the cell surface (76). As the Golgi apparatus, including the *trans*-Golgi network, is affected in *Clasp2*<sup>-/-</sup> cells, both the trafficking of newly synthesized as well as recycling c-Kit could be affected in the absence of CLASP2. Inhibition of the lysosomal activity in E14 FL cells by BafA treatment restored the levels of c-Kit at the plasma membrane of *Clasp2*<sup>-/-</sup> cells almost to those of *Clasp2*<sup>+/+</sup> cells treated with BafA. This result is consistent with the notion of enhanced lysosomal degradation of c-Kit in *Clasp2*<sup>-/-</sup> cells, and with a somewhat impaired delivery of newly synthesized c-Kit. Importantly, upon SCF-mediated internalization of c-Kit, inhibition of lysosomal activity was not sufficient to restore c-Kit levels, suggesting that in addition to increased degradation, c-Kit plasma membrane recycling is reduced in the absence of CLASP2. We have previously reported that CLASP2 is involved in the delivery of acetylcholine receptors to the postsynaptic membrane of the neuro-muscular junction (77-79) and, more recently, in modulating cardiac sodium channel NaV1.5 activity at the intercalated disk of cardiomyocytes (80). In these studies, as well as in our previous work on the role of CLASP2 in the maintenance of adult HSCs (34), we focused on the MT-stabilizing function of CLASP2. A novel finding in embryonic (pre-)HSCs lacking CLASP2 is that

the trafficking defect of c-Kit is coupled to enhanced c-Kit degradation, which correlates with a higher lysosome number in *Clasp2*<sup>-/-</sup> cells. Thus, CLASP2 regulates cell surface levels of important proteins in different cell types. Whether all the phenotypes documented here and in other studies are eventually due to a MT-stabilizing and/or growth-promoting role of CLASP2 or whether this fascinating protein has additional activities needs to be examined in future studies.

CLASP2 has been shown to be involved in Golgi organization in cultured cells (44), and to play a critical role in nucleation of MTs at the *trans*-Golgi (81), thereby aiding in vesicular transport of constitutive secretory pathway components (43). Our data reveal, for the first time, a role for CLASP2 in Golgi organization *in vivo*. This function is conserved in mice and zebrafish, as we observe more Golgi scattering in mouse IAHc cells and zebrafish HSPCs in the absence of *Clasp2*. We hypothesize that an aberrant Golgi function affects c-Kit trafficking, both of newly synthesized as well as of recycling protein. In addition, Golgi perturbation seems to affect the lysosomal compartment and cause enhanced degradation of c-Kit in the absence of CLASP2. Overall, our findings bring new insights into the important conserved role of CLASP2 in the proper formation of functional HSCs *in vivo*.

## Experimental model and subject details

### Animals

All animals were housed and bred according to institutional guidelines, and procedures were performed in compliance with Standards for Care and Use of Laboratory Animals with approval from the Erasmus MC and Hubrecht Institute ethical review board. All animal experiments were approved by the Animal Experimentation Committee (DEC) of the Royal Netherlands Academy of Arts and Sciences.

*Mice and embryos* - *Clasp2*<sup>+/-</sup> animals (34) were backcrossed more than 20 generations in the C57BL/6 background. Of note, the second exon common to all known isoforms of CLASP2 was interrupted by insertion of an EGFP-loxP-pMC1NEO-loxP cassette to generate the *Clasp2* mutant mice (34). *Clasp2*<sup>+/+</sup> and *Clasp2*<sup>-/-</sup> embryos were generated by timed mating of *Clasp2* heterozygous transgenic males and females. The day of an observed vaginal plug was considered as embryonic day 0 (E0). Embryos were collected at early E10 (26-32 somite pairs (sp)), E10.5 (33-36 sp), E11.5 (44-48 sp), E12.5 and E14. E10.5 and E11.5 embryos were staged based on the number of sp. Postnatally sacrificed newborn animals were staged based on the day post birth (P8). Young adult mice were 4.5 weeks old and adult mice were >8 weeks old.

*Zebrafish and embryos* - Zebrafish were maintained and propagated according to the standard laboratory conditions of the Hubrecht Institute and FELASA guidelines. For microscopic observations *clasp2* mutants (*clasp2*<sup>mut</sup> with [-4bp] and [-10bp] mutations) and wild-type fish of the reporter line *Tg(kdrl:mCherry/cd41:eGFP)* were used (*kdrl:mCherry* (ZFIN ID: ZDB-TGCONSTRUCT-110127-23); *cd41:eGFP* (49)). *In situ* hybridizations were done on *clasp2*<sup>mut</sup> in wild-type TL/AB (EZRC), *Tg(kdrl:mCherry)* or *Tg(kdrl:mCherry/cd41:eGFP)* background. For flow cytometry, embryos of the *Tg(mpeg1.4:mCherry/mpx:eGFP)* line (*Tg(mpeg1.4:mCherry-F)ump2* (50), and *TgBAC(mpx:GFP)i114* (51)) were used. Zebrafish embryos were raised in E3 medium and staged as described in (52, 53) to obtain 40 hours post-fertilization (hpf), 52hpf, 3 days post-fertilization (dpf) and 5dpf embryos. For *in situ* hybridization and imaging, embryos were grown from 24hpf onwards in E3 with 0.003% 1-phenyl-2-thiourea to inhibit pigment formation (52).

## Acknowledgements

The authors thank the present and past lab members for helpful discussion and technical help, especially Jean-Charles Boisset, Carla Kroon, Trung Bui and Rutger Wielink. We also thank the Jeroen den Hertog and Jeroen Bakkers labs for providing reagents, zebrafish lines and expertise in genome-editing and the Catherine Rabouille lab for antibodies. We thank Romualdo Ciau-Uitz (Prof. Roger Patient's Laboratory) for kindly providing ISH probes. We thank Umut Akinci and Alex Maas (Department of Cell Biology, Erasmus MC) for derivation of the *Clasp2*<sup>-/-</sup> ESCs. We thank the Animal Facility for mouse and zebrafish care and the Optical Imaging Center for confocal microscope access (Hubrecht Institute). We thank Reinier van der Linden (Hubrecht Institute) for help with cell sorting. This work was supported in the CR and NG labs by a Landsteiner Stichting voor Bloedtransfusie Research (LSBR 1025), in the NG lab by an NWO-TTW grant (15511), and in the CR lab by a European Research Council grant (ERC, project number 220-H75001EU/HSCOrigin-309361), a TOP-subsidy from NWO/ZonMw (912.15.017) and an UMC Utrecht "Regenerative Medicine & Stem Cells" priority research program.

## Author contributions

C.R. and N.G. conceived ideas and designed the research with the help of the authors; C.R., T.C., A.K. and L.Y. performed mouse embryo dissections; C.R. transplanted the mice and T.C. analyzed the mice; T.C. and A.K. performed clonogenic assays; T.C. performed LTC-IC cultures and A.K. performed explant cultures; T.C. and A.K. performed flow cytometry analyses on mouse embryos; L.Y. performed whole mount immunostainings and intra-aortic hematopoietic cluster counts; A.K. generated the *clasp2* mutant fish lines and performed all analyses on zebrafish with the help of L.Y. for flow cytometry analyses; A.K. performed mouse IF staining with guidance of L.Y. and analyzed the data with C.R., S.B. and N.G.; B.W. performed all RT-qPCR on mouse and cloned the *clasp2* zebrafish construct for the rescue experiments; S.B. performed western blots and all experiments with ESCs; C.R. performed c-Kit mean intensity measurements; I.S. designed c-Kit intensity measurement and helped with statistical analyses; J.M. did *runx1* WISH; C.R. analyzed and interpreted the experiments with the help of all authors; C.R. created the figures and wrote the paper with the main help of A.K. and N.G. All authors commented on the manuscript.

## Declaration of interests

The authors declare no competing financial interests.

## References

1. E. Dzierzak, A. Bigas, Blood Development: Hematopoietic Stem Cell Dependence and Independence. *Cell stem cell* 22, 639-651 (2018).
2. A. Klaus, C. Robin, Embryonic hematopoiesis under microscopic observation. *Dev Biol* 428, 318-327 (2017).
3. J. C. Boisset et al., *In vivo* imaging of haematopoietic cells emerging from the mouse aortic endothelium. *Nature* 464, 116-120 (2010).
4. T. Jaffredo, R. Gautier, A. Eichmann, F. Dieterlen-Lievre, Intraaortic hemopoietic cells are derived from endothelial cells during ontogeny. *Development* (Cambridge, England) 125, 4575-4583 (1998).
5. J. C. Boisset et al., Progressive maturation toward hematopoietic stem cells in the mouse embryo aorta. *Blood* 125, 465-469 (2015).

6. T. Yokomizo, E. Dzierzak, Three-dimensional cartography of hematopoietic clusters in the vasculature of whole mouse embryos. *Development (Cambridge, England)* 137, 3651-3661 (2010).
7. A. Medvinsky, E. Dzierzak, Definitive hematopoiesis is autonomously initiated by the AGM region. *Cell* 86, 897-906. (1996).
8. A. M. Muller, A. Medvinsky, J. Strouboulis, F. Grosveld, E. Dzierzak, Development of hematopoietic stem cell activity in the mouse embryo. *Immunity* 1, 291-301. (1994).
9. P. Kumaravelu et al., Quantitative developmental anatomy of definitive haematopoietic stem cells/long-term repopulating units (HSC/RU): role of the aorta-gonad- mesonephros (AGM) region and the yolk sac in colonisation of the mouse embryonic liver. *Development (Cambridge, England)* 129, 4891-4899. (2002).
10. C. Robin et al., An unexpected role for IL-3 in the embryonic development of hematopoietic stem cells. *Dev Cell* 11, 171-180 (2006).
11. C. S. Baron et al., Single-cell transcriptomics reveal the dynamic of haematopoietic stem cell production in the aorta. *Nat Commun* 9, 2517 (2018).
12. S. Rybtsov et al., Hierarchical organization and early hematopoietic specification of the developing HSC lineage in the AGM region. *J Exp Med* 208, 1305-1315 (2011).
13. S. Taoudi et al., Extensive hematopoietic stem cell generation in the AGM region via maturation of VE-cadherin+CD45+ pre-definitive HSCs. *Cell stem cell* 3, 99-108 (2008).
14. F. Zhou et al., Tracing haematopoietic stem cell formation at single-cell resolution. *Nature* 533, 487-492 (2016).
15. C. S. Vink et al., Iterative Single-Cell Analyses Define the Transcriptome of the First Functional Hematopoietic Stem Cells. *Cell Rep* 31, 107627 (2020).
16. Q. Zhu et al., Developmental trajectory of pre-hematopoietic stem cell formation from endothelium. *Blood* 136, 845-856 (2020).
17. S. Rybtsov, A. Ivanovs, S. Zhao, A. Medvinsky, Concealed expansion of immature precursors underpins acute burst of adult HSC activity in foetal liver. *Development (Cambridge, England)* 143, 1284-1289 (2016).
18. Y. Sharma, C. M. Astle, D. E. Harrison, Heterozygous kit mutants with little or no apparent anemia exhibit large defects in overall hematopoietic stem cell function. *Exp Hematol* 35, 214-220 (2007).
19. L. A. Thoren et al., Kit regulates maintenance of quiescent hematopoietic stem cells. *J Immunol* 180, 2045-2053 (2008).
20. C. L. Li, G. R. Johnson, Stem cell factor enhances the survival but not the self-renewal of murine hematopoietic long-term repopulating cells. *Blood* 84, 408-414 (1994).
21. D. Lee, D. W. Kim, J. Y. Cho, Role of growth factors in hematopoietic stem cell niche. *Cell Biol Toxicol* 36, 131-144 (2020).
22. J. Y. Shin, W. Hu, M. Naramura, C. Y. Park, High c-Kit expression identifies hematopoietic stem cells with impaired self-renewal and megakaryocytic bias. *J Exp Med* 211, 217-231 (2014).
23. L. Ding, T. L. Saunders, G. Enikolopov, S. J. Morrison, Endothelial and perivascular cells maintain haematopoietic stem cells. *Nature* 481, 457-462 (2012).
24. C. Xu et al., Stem cell factor is selectively secreted by arterial endothelial cells in bone marrow. *Nat Commun* 9, 2449 (2018).
25. E. Azzoni et al., Kit ligand has a critical role in mouse yolk sac and aorta-gonad-mesonephros hematopoiesis. *EMBO Rep* 19, (2018).
26. T. Sasaki et al., Regulation of hematopoietic cell clusters in the placental niche through SCF/Kit signaling in embryonic mouse. *Development (Cambridge, England)* 137, 3941-3952 (2010).
27. S. Rybtsov et al., Tracing the origin of the HSC hierarchy reveals an SCF-dependent, IL-3-independent CD43(-) embryonic precursor. *Stem Cell Reports* 3, 489-501 (2014).
28. H. V. Goodson, E. M. Jonasson, Microtubules and Microtubule-Associated Proteins. *Cold Spring Harb Perspect Biol* 10, (2018).
29. S. Bodakuntla, A. S. Jijumon, C. Villablanca, C. Gonzalez-Billault, C. Janke, Microtubule-Associated Proteins: Structuring the Cytoskeleton. *Trends Cell Biol* 29, 804-819 (2019).
30. A. Akhmanova, M. O. Steinmetz, Control of microtubule organization and dynamics: two ends in the limelight. *Nat Rev Mol Cell Biol* 16, 711-726 (2015).
31. S. Biedzinski et al., Microtubules control nuclear shape and gene expression during early stages of hematopoietic differentiation. *EMBO J* 39, e103957 (2020).
32. C. Schwan, R. Grosse, A tight grip on differentiation: Nuclear constriction by microtubules regulates hematopoietic stem cells. *EMBO J* 39, e107086 (2020).
33. A. V. Fonseca, D. Corbeil, The hematopoietic stem cell polarization and migration: A dynamic link between RhoA signaling pathway, microtubule network and ganglioside-based membrane microdomains. *Commun Integr Biol* 4, 201-204 (2011).
34. K. Drabek et al., The microtubule plus-end tracking protein CLASP2 is required for hematopoiesis and hematopoietic stem cell maintenance. *Cell Rep* 2, 781-788 (2012).
35. L. Yvernogeu et al., Multispecies RNA tomography reveals regulators of hematopoietic stem cell birth in the embryonic aorta. *Blood* 136, 831-844 (2020).
36. M. I. Mascarenhas, A. Parker, E. Dzierzak, K. Ottersbach, Identification of novel regulators of hematopoietic stem cell development through refinement of stem cell localization and expression profiling. *Blood* 114, 4645-4653 (2009).

37. Y. Xue et al., A 3D Atlas of Hematopoietic Stem and Progenitor Cell Expansion by Multi-dimensional RNA-Seq Analysis. *Cell Rep* 27, 1567-1578 e1565 (2019).
38. H. Giroto et al., CLASP2 binding to curved microtubule tips promotes flux and stabilizes kinetochore attachments. *J Cell Biol* 219, (2020).
39. H. Maiato et al., Human CLASP1 is an outer kinetochore component that regulates spindle microtubule dynamics. *Cell* 113, 891-904 (2003).
40. E. Logarinho et al., CLASPs prevent irreversible multipolarity by ensuring spindle-pole resistance to traction forces during chromosome alignment. *Nat Cell Biol* 14, 295-303 (2012).
41. A. Akhmanova et al., Clasps are CLIP-115 and -170 associating proteins involved in the regional regulation of microtubule dynamics in motile fibroblasts. *Cell* 104, 923-935 (2001).
42. G. Lansbergen et al., CLASPs attach microtubule plus ends to the cell cortex through a complex with LL5beta. *Dev Cell* 11, 21-32 (2006).
43. P. M. Miller et al., Golgi-derived CLASP-dependent microtubules control Golgi organization and polarized trafficking in motile cells. *Nat Cell Biol* 11, 1069-1080 (2009).
44. T. Matsui et al., PAR3 and aPKC regulate Golgi organization through CLASP2 phosphorylation to generate cell polarity. *Mol Biol Cell* 26, 751-761 (2015).
45. K. Drabek et al., Role of CLASP2 in microtubule stabilization and the regulation of persistent motility. *Curr Biol* 16, 2259-2264 (2006).
46. S. J. Stehbens et al., CLASPs link focal-adhesion-associated microtubule capture to localized exocytosis and adhesion site turnover. *Nat Cell Biol* 16, 561-573 (2014).
47. S. Maffini et al., Motor-independent targeting of CLASPs to kinetochores by CENP-E promotes microtubule turnover and poleward flux. *Curr Biol* 19, 1566-1572 (2009).
48. A. L. Pereira et al., Mammalian CLASP1 and CLASP2 cooperate to ensure mitotic fidelity by regulating spindle and kinetochore function. *Mol Biol Cell* 17, 4526-4542 (2006).
49. H. F. Lin et al., Analysis of thrombocyte development in CD41-GFP transgenic zebrafish. *Blood* 106, 3803-3810 (2005).
50. A. Bernut et al., Mycobacterium abscessus cording prevents phagocytosis and promotes abscess formation. *Proc Natl Acad Sci U S A* 111, E943-952 (2014).
51. S. A. Renshaw et al., A transgenic zebrafish model of neutrophilic inflammation. *Blood* 108, 3976-3978 (2006).
52. M. Westerfield, *The Zebrafish Book. A Guide for the Laboratory Use of Zebrafish (Danio rerio)*. 4th ed., Univ. of Oregon Press, Eugene., (2000).
53. C. B. Kimmel, W. W. Ballard, S. R. Kimmel, B. Ullmann, T. F. Schilling, Stages of embryonic development of the zebrafish. *Dev Dyn* 203, 253-310 (1995).
54. Y. Xue et al., The Vascular Niche Regulates Hematopoietic Stem and Progenitor Cell Lodgment and Expansion via *klf6a-ccl25b*. *Dev Cell* 42, 349-362 e344 (2017).
55. E. Murayama et al., Tracing hematopoietic precursor migration to successive hematopoietic organs during zebrafish development. *Immunity* 25, 963-975 (2006).
56. K. Kissa et al., Live imaging of emerging hematopoietic stem cells and early thymus colonization. *Blood* 111, 1147-1156 (2008).
57. J. Y. Bertrand et al., Definitive hematopoiesis initiates through a committed erythromyeloid progenitor in the zebrafish embryo. *Development (Cambridge, England)* 134, 4147-4156 (2007).
58. D. Traver et al., Transplantation and *in vivo* imaging of multilineage engraftment in zebrafish bloodless mutants. *Nat Immunol* 4, 1238-1246 (2003).
59. J. Y. Bertrand, A. D. Kim, S. Teng, D. Traver, CD41+ *cmyb*+ precursors colonize the zebrafish pronephros by a novel migration route to initiate adult hematopoiesis. *Development (Cambridge, England)* 135, 1853-1862 (2008).
60. H. Jin, J. Xu, Z. Wen, Migratory path of definitive hematopoietic stem/progenitor cells during zebrafish development. *Blood* 109, 5208-5214 (2007).
61. M. Ogawa et al., Expression and function of c-kit in hemopoietic progenitor cells. *J Exp Med* 174, 63-71 (1991).
62. S. Okada et al., Enrichment and characterization of murine hematopoietic stem cells that express c-kit molecule. *Blood* 78, 1706-1712 (1991).
63. P. Paral et al., Cell cycle and differentiation of Sca-1(+) and Sca-1(-) hematopoietic stem and progenitor cells. *Cell Cycle* 17, 1979-1991 (2018).
64. Y. Ravichandran, B. Goud, J. B. Manneville, The Golgi apparatus and cell polarity: Roles of the cytoskeleton, the Golgi matrix, and Golgi membranes. *Curr Opin Cell Biol* 62, 104-113 (2020).
65. Y. Guo, D. W. Sirkis, R. Schekman, Protein sorting at the trans-Golgi network. *Annu Rev Cell Dev Biol* 30, 169-206 (2014).
66. F. Todaro et al., Regulation of Kit Expression in Early Mouse Embryos and ES Cells. *Stem Cells* 37, 332-344 (2019).
67. J. Lennartsson, L. Ronnstrand, Stem cell factor receptor/c-Kit: from basic science to clinical implications. *Physiol Rev* 92, 1619-1649 (2012).
68. S. Mohanty, B. P. Chaudhary, D. Zoetewey, Structural Insight into the Mechanism of N-Linked Glycosylation by Oligosaccharyltransferase. *Biomolecules* 10, (2020).
69. A. D. Elbein, Inhibitors of the biosynthesis and processing of N-linked oligosaccharides. *CRC Crit Rev Biochem* 16, 21-49 (1984).
70. A. Heifetz, R. W. Keenan, A. D. Elbein, Mechanism of action of tunicamycin on the UDP-



- GlcNAc:dolichyl-phosphate Glc-NAC-1-phosphate transferase. *Biochemistry* 18, 2186-2192 (1979).
71. Y. Atlasi et al., The translational landscape of ground state pluripotency. *Nat Commun* 11, 1617 (2020).
  72. A. Chaix et al., Mechanisms of STAT protein activation by oncogenic KIT mutants in neoplastic mast cells. *J Biol Chem* 286, 5956-5966 (2011).
  73. M. J. Chen et al., Erythroid/myeloid progenitors and hematopoietic stem cells originate from distinct populations of endothelial cells. *Cell stem cell* 9, 541-552 (2011).
  74. M. J. Sanchez, A. Holmes, C. Miles, E. Dzierzak, Characterization of the first definitive hematopoietic stem cells in the AGM and liver of the mouse embryo. *Immunity* 5, 513-525 (1996).
  75. C. B. Mahony, C. Pasche, J. Y. Bertrand, Oncostatin M and Kit-Ligand Control Hematopoietic Stem Cell Fate during Zebrafish Embryogenesis. *Stem Cell Reports* 10, 1920-1934 (2018).
  76. P. J. Cullen, F. Steinberg, To degrade or not to degrade: mechanisms and significance of endocytic recycling. *Nat Rev Mol Cell Biol* 19, 679-696 (2018).
  77. S. Basu et al., CLASP2-dependent microtubule capture at the neuromuscular junction membrane requires LL5beta and actin for focal delivery of acetylcholine receptor vesicles. *Mol Biol Cell* 26, 938-951 (2015).
  78. S. Basu et al., Acetylcholine receptor (AChR) clustering is regulated both by glycogen synthase kinase 3beta (GSK3beta)-dependent phosphorylation and the level of CLIP-associated protein 2 (CLASP2) mediating the capture of microtubule plus-ends. *J Biol Chem* 289, 30857-30867 (2014).
  79. N. Schmidt et al., Agrin regulates CLASP2-mediated capture of microtubules at the neuromuscular junction synaptic membrane. *J Cell Biol* 198, 421-437 (2012).
  80. G. A. Marchal et al., Targeting the Microtubule EB1-CLASP2 Complex Modulates Nav1.5 at Intercalated Discs. *Circ Res*, (2021).
  81. A. Efimov et al., Asymmetric CLASP-dependent nucleation of noncentrosomal microtubules at the trans-Golgi network. *Dev Cell* 12, 917-930 (2007).
  82. F. Pouthas et al., In migrating cells, the Golgi complex and the position of the centrosome depend on geometrical constraints of the substratum. *J Cell Sci* 121, 2406-2414 (2008).
  83. B. Weijts, E. Tkachenko, D. Traver, A. Groisman, A Four-Well Dish for High-Resolution Longitudinal Imaging of the Tail and Posterior Trunk of Larval Zebrafish. *Zebrafish* 14, 489-491 (2017).
  84. J. A. Gagnon et al., Efficient mutagenesis by Cas9 protein-mediated oligonucleotide insertion and large-scale assessment of single-guide RNAs. *PLoS One* 9, e98186 (2014).
  85. C. Robin, E. Dzierzak, Hematopoietic stem cell enrichment from the AGM region of the mouse embryo. *Methods in molecular medicine* 105, 257-272 (2005).
  86. J. C. Boisset, C. Andrieu-Soler, W. A. van Cappellen, T. Clapes, C. Robin, *Ex vivo* time-lapse confocal imaging of the mouse embryo aorta. *Nature protocols* 6, 1792-1805 (2011).
  87. J. Schindelin et al., Fiji: an open-source platform for biological-image analysis. *Nat Methods* 9, 676-682 (2012).
  88. C. Robin, K. Ottersbach, J. C. Boisset, A. Oziemlak, E. Dzierzak, CD41 is developmentally regulated and differentially expressed on mouse hematopoietic stem cells. *Blood* 117, 5088-5091 (2011).
  89. U. K. Laemmli, Cleavage of structural proteins during the assembly of the head of bacteriophage T4. *Nature* 227, 680-685 (1970).



## STAR METHODS

### KEY RESOURCES TABLE

REAGENT or RESOURCE	SOURCE	IDENTIFIER
<b>Antibodies</b>		
PE-anti-TER119	BD Biosciences	Cat#: 553673
APC-anti-TER119	BD Biosciences	Cat#: 557909
PE-anti-B220 (RA3-6B2)	BD Biosciences	Cat#: 553089
APC-anti-B220 (RA3-6B2)	BD Biosciences	Cat#: 553092
PE-anti-Gr1 (RB6-8C5)	BD Pharmingen	Cat#: 553128
PE-anti-CD48 (HM48-1)	BD Pharmingen	Cat#: 557485
PE-anti-CD3e (17A2)	BD Pharmingen	Cat#: 555275
APC-anti-CD150 (TC15)	Biolegend	Cat#: 115909
PE-Cy7-anti-SCA-1 (D7)	BD Biosciences	Cat#: 558162
Alexa Fluor 700-anti-SCA-1	eBioscience	Cat#: 56-5981-82
APC-eFluor 780-anti-c-Kit (CD117) (2B8)	eBioscience	Cat#: 47-1171-82
APC-anti-c-Kit (2B8)	BD Biosciences	Cat#: 553356
Purified anti-c-Kit	Abcam	Cat#: ab256345
PE-Cy7 anti-CDH5 (CD144, VE-cadherin)	BioLegend	Cat#: 138015
APC-Ki67 (20Raj1)	eBioscience	Cat#: 17-5699-42
APC anti-CD45	BD Pharmingen	Cat#: 559864
APC-Cy7-anti-Ly-6G and Ly-6C (RB6-8C5)	BD Pharmingen	Cat#: 557661
PE-anti-CD8a (53-6.7)	BD Biosciences	Cat#: 553032
PE-anti-CD4 (Gk1.5)	BD Pharmingen	Cat#: 557308
PE-anti-CD31 (MEC 13.3)	BD Biosciences	Cat#: 553373
PE-Annexin V	BD Biosciences	Cat#: 556421
Purified-anti-c-Kit (2B8)	eBioscience	Cat#: 14-1171-85
Purified-anti-c-Kit (D13A2)	Cell Signaling Technology	Cat#: 3074
Purified-anti-c-Kit (rabbit)	Abcam	Cat#: ab256345
Purified anti-GM130	BD Biosciences	Cat#: 610825
Anti-GRASP55 Rich	Kind gift from Dr. Bekier and Prof. Rabouille (Hubrecht Institute)	N/A
Anti-tubulin (rat)	Abcam	Cat#: ab6160
Anti- $\beta$ -tubulin (mouse)	Sigma	Cat#: T8328
biotinylated anti-CD31 (MEC 13.3)	BD Biosciences	Cat#: 553371
Anti-phospho-AKT-Ser473	Cell Signaling	Cat#: 4060
Anti-pan-AKT	Cell Signaling	Cat#: 4691
Alkaline phosphatase Anti-Digoxigenin-AP, Fab fragments	Roche	Cat#: 11093274910
Alexa Fluor™ 647 goat anti-rabbit IgG (H+L)	Life Technologies Europe BV	Cat#: A21245
Alexa Fluor™ 488 goat anti-rabbit IgG (H+L)	Life Technologies Europe BV	Cat#: A11008
Alexa Fluor™ 594 goat anti-rat IgG (H+L)	Life Technologies Europe BV	Cat#: A11042
Streptavidin Alexa Fluor® 555 conjugate	Life Technologies Europe BV	Cat#: S-21381
Horseradish Peroxidase (HRP) -conjugated secondary antibodies	GE Healthcare	Cat#: NA934 (donkey anti-Rabbit), Cat#: NA931 (sheep-anti mouse), Cat#: NA935 (goat - anti rat)
EasySep™ Mouse Hematopoietic Progenitor Cell Isolation Kit (FL custom-made kit, not containing antibodies against CD11b)	STEMCELLtechnology	Cat#: BM #19856

REAGENT or RESOURCE	SOURCE	IDENTIFIER
<b>Chemicals, Peptides, and Recombinant Proteins</b>		
Neomycin Sulfate	Sigma	Cat#: 1405-10-3
IOtest® 3 Lysing Solution	Beckman Coulter	Cat#: A07799
Hoechst 33258, pentahydrate (bis-benzimide)	Invitrogen	Cat#: H3569
7-AAD	Invitrogen	Cat#: A1310
Recombinant murine IL-3	BD Pharmingen	Cat#: 554579
Recombinant Murine SCF	Peprotech	Cat#: 250-03
Recombinant Murine SCF	Stem Cell Technologies	Cat#: 78064
Recombinant Murine Flt3-Ligand	Peprotech	Cat#: 250-31L 10ug
1-phenyl-2-thiourea, PTU	Sigma-Aldrich	Cat#: P7629-25G
NotI GQ, 1,000u	Promega	Cat#: R6435
Ethyl 3-aminobenzoate methanesulfonate salt Tricaine, MS-222	Sigma-Aldrich	Cat#: A5040-25G
Ethyl 3-aminobenzoate methanesulfonate	Sigma	Cat#: E10521
UltraPure™ Agarose	Invitrogen	Cat#: 16500-500
Paraformaldehyde (PFA)	Sigma-Aldrich	Cat#: P-6148
TWEEN 20	Sigma-Aldrich	Cat#: P1379 100ML
Proteinase K, 100 mg	Promega	Cat#: V3021
Bovine serum albumin (BSA)	Sigma-Aldrich	Cat#: A3294-100G
Glycerol, 'Baker Analyzed'	Boom Laboratoriumleverancier	Cat#: M BAK7044.2500
Acridine orange (AO)	Kind gift from Prof. Bakkers (Hubrecht Institute)	N/A
Penicillin-Streptomycin (5,000 U/mL)	Life Technologies	Cat#: 15070063
Collagenase	Sigma-Aldrich	Cat#: C0130-1G
Trypan Blue Solution, 0.4%	Life Technologies Europe BV	Cat#: 15250-061
Goat serum	Sigma-Aldrich	Cat#: S26-LITER
TrypLE	Gibco	Cat#: 12604054
EDTA	Hubrecht Institute	N/A
1X protease inhibitor (EDTA-free)	Roche	Cat#: 11836145001
DAPI	Sigma-Aldrich	Cat#: D954210MG
RQ1 RNase-Free DNase, 1,000u	Promega	Cat#: M6101
GoTaq G2 Flexi DNA Polymerase, 500u	Promega	Cat#: M7805
iQ™ SYBR® Green Supermix	Bio-Rad	Cat#: 1708880
iTaq Universal SYBR Green Supermix	Bio-Rad	Cat#: 1725122
SYBR Green	Roche	Cat#: 04707516001
Hydrocortisone 21-hemisuccinate sodium salt	Sigma-Aldrich	Cat#: H2270- 100MG
0.8% low-melting agarose	Invitrogen	Cat#: 16520050
PBS Dulbecco's Phosphate Buffered Saline	Sigma-Aldrich	Cat#: D8537
NBT	Sigma-Aldrich	Cat#: 11383213001

REAGENT or RESOURCE	SOURCE	IDENTIFIER
<b>Chemicals, Peptides, and Recombinant Proteins</b>		
BCIP	Sigma-Aldrich	Cat#: 11383221001
OCT medium	Sakura	Cat#: 4583
HEPES	ThermoFisher	Cat#: 15630080
Protease Inhibitor Cocktail	Thermo Scientific	Cat#: A32955
Bafilomycin A1 (BafA, 100nM)	Invitrogen	Cat#: tlr1-baf1
Tunicamycin	Sigma-Aldrich	Cat#: T7765
Fetal calf serum	Sigma	Cat#: F7524
L-Glutamine 200 mM (100ml)	Life Technologies	Cat#: 25030-024
L-Glutamine	Invitrogen	Cat#: 25030-032
Sodium pyruvate	ThermoFisher	Cat#: 11360070
Sodium pyruvate	Invitrogen	Cat#: 11360-039
2-mercaptoethanol (0.1mM)	Gibco	Cat#: 11528926
Non-fat powder milk	Sigma	Cat#: 70166-500G
PVDF membranes	Millipore	Cat#: IPVH00010
LIF	Sigma-Aldrich	Cat#: PD0325901
CHIR	Tocris Biochemicals	Cat#: 4423-10
PD	Stemgent	Cat#: 04-0006
Endo H	NEB	Cat#: P0702S
Pngase F	NEB	Cat#: P0704S
IRDyes 800CW and 600CW	Li-cor	N/A
Enhanced chemiluminescence detection (ECL)	GE Healthcare	Cat#: RPN2236
Fluorescent detection (Odyssey Imaging System)	Licor	Cat#: 926-68071 (goat anti-rabbit, IR dye 680 CW) Cat#: 926-32210 (goat anti-mouse, IR dye 800 CW)
Ambion MEGAscript T7 transcription kit	Life Technologies	Cat#: AM1333
pCS2-nCas9n plasmid	Addgene	Cat#: 47929
Clasp2 morpholino	GeneTools, LCC	N/A
pCS2+ plasmid	Kind gift from Prof. den Hertog (Hubrecht Institute)	N/A
BD Cytofix/Cytoperm™	BD Bioscience	Cat#: 554714
RNeasy Mini kit	Qiagen	Cat#: 74104
SuperScript® III Reverse Transcriptase	Life Technologies	Cat#: 18080044
SuperScript® IV Reverse Transcriptase	Thermo Fisher	Cat#: 18-090-050
GFP-GM130 mRNA	(82) mRNA kindly provided by Prof. Bakkers (Hubrecht Institute)	N/A

REAGENT or RESOURCE	SOURCE	IDENTIFIER
<b>Experimental Models: Organisms/Strains</b>		
Mouse: C57BL/6J (CD45.2)	The Jackson Laboratory	JAX: 000664
Mouse: Clasp2 <sup>+/+</sup> (C57BL/6)	Kind gift from Prof. Galjart (ErasmusMC, Rotterdam, NL)	(34)
Zebrafish: <i>mpeg1.4:mCherry/mpx:eGFP</i>	This paper	N/A
Zebrafish: <i>Kdrl:mcherry/cd41:eGFP</i>	This paper	N/A
Zebrafish: <i>Kdrl:mcherry/cd41:eGFP/Clasp2mut[-4bp]</i>	This paper	N/A
Zebrafish: <i>Kdrl:mcherry/cd41:eGFP/Clasp2mut[-10bp]</i>	This paper	N/A
Zebrafish: <i>Clasp2mut[-4bp]</i>	This paper	N/A
Zebrafish: <i>Clasp2mut[-10bp]</i>	This paper	N/A
Zebrafish: <i>AB</i>	EZRC	Item #: 1175.1
Zebrafish: <i>TL</i>	EZRC	Item #: 1174.1
MS-5 stromal line	Kind gift from Drs. Dusanter and Lauret (Cochin Institute)	N/A
<b>Oligonucleotides</b>		
Morpholinos	GeneTools, LCC	N/A
Primers for genotyping, CRISPR/Cas9 genome editing, semi-quantitative PCR, RT-qPCR, RT-PCR, ISH, see <b>Table S1</b>	IDT	N/A
<b>Medium</b>		
E3 medium	Hubrecht Institute	N/A
MethoCult™ M3434 medium	StemCell Technologies	Cat#: 03434
MyeloCult M5300	StemCell Technologies	Cat#: 05350
α-MEM	Gibco	Cat#: 12571063
DMEM (Dulbecco's modified Eagle's medium)	Gibco	Cat#: 31331-028
1x MEM non-essential amino acids	Gibco	Cat#: 12084947
<b>Software and Algorithms</b>		
Excel	Microsoft	N/A
Fiji (ImageJ)	Fiji	<a href="https://fiji.sc">https://fiji.sc</a>
FlowJo	FlowJo	<a href="https://www.flowjo.com/">https://www.flowjo.com/</a>
Prism7	GraphPad Software	GraphPad Software
Imaris X	Oxford Instruments	N/A
CellQuest software	BD Bioscience	N/A
CytExpert software	Beckman Coulter	N/A
Chopchop	N/A	<a href="https://chopchop.cbu.uib.no/">https://chopchop.cbu.uib.no/</a>
SnapGene	GSL Biotech LLC	N/A
Ensembl	EMBL-EBI	<a href="https://www.ensembl.org/index.html">https://www.ensembl.org/index.html</a>

REAGENT or RESOURCE	SOURCE	IDENTIFIER
<b>Other</b>		
LSM700 Confocal Microscope	Zeiss	N/A
Leica fluorescent stereomicroscope MZ 16 FA	Leica	N/A
Leica SP8 confocal microscope	Leica	N/A
Aria III flow cytometer	BD Bioscience	N/A
FACSCalibur	BD Bioscience	N/A
Jazz BD FACSJazz	BD Bioscience	N/A
FACSDiva	BD Bioscience	N/A
BD Influx Cell Sorter	BD Bioscience	N/A
CytoFLEX benchtop flow cytometer	Beckman Coulter	N/A
Hamamatsu Flash4 LT digital camera	Hamamatsu	N/A
BIO-RAD C1000 Touch Thermal Cycler, CFX384TM Real-Time System	BIO-RAD	N/A
ThermalSealRT™	Greiner	Cat#: 676044
SAPPHIRE MICROPLATE, 384 WELL	Greiner	Cat#: 785201
Mmessage Mmachine Sp6 Kit	Thermo Fisher Scientific	Cat#: 10086184
Four-well imaging dish (Muwells)	(83)	N/A
Cell strainers 40 um Blue	VWR	Cat#: 734-0002
Adhesion slides, SuperFrost Plus	VWR	Cat#: 631-0108
Durapore® Membrane Filters (0.65 µm)	Millipore	Cat#: DVPP02500

## Contact for reagent and resource sharing

Further information and requests for resources and reagents should be directed to and will be fulfilled by the Lead Contact, Catherine Robin (c.robin@hubrecht.eu).

## Method details

### Generation of *clasp2* mutant lines by CRISPR/Cas9-mediated mutagenesis

Using chopchop web tool (<https://chopchop.cbu.uib.no/>), sgRNAs were designed to target exon 3 in iso1 *clasp2*-001 or -205 (ensemble ENSDART00000144557.3) NM\_207072, exon 8 in iso2 *clasp2*-002 or -202 (ENSDART00000136873.3) NM\_001328259, exon 2 in iso8 *clasp2*-008 or -208 (ENSDART00000151086.2) and exon 1 in iso4 *clasp2*-004 or -204 (ENSDART00000139109.3). The sgRNA (GGATG-GAAGCAGGCCGTCAT) was chosen. SgRNA were generated strictly following the guidelines previously described in (84); the Ambion MEGAscript T7 kit (Life Technologies) was used for synthesis. The capped *Cas9*-mRNA was generated from pCS2-*nCas9n* (Addgene) plasmid by linearization with NotI enzyme (Promega) and synthesized using the SP6 mMessage Machine kit (Thermo Fisher Scientific). CRISPR mutants were generated by co-microinjection of the purified sgRNA (25ng/µl) and *Cas9* mRNA (150ng/µl) into the cell of a one-cell-stage embryo. Successful editing was assayed in the F1 offspring (F0 founder outcrossed to wild-type) by PCR (primers: 5'-cctttctgctgcagcttatgtca-3'; 5'-ggttaattgggcaatcattgct-3') and sequencing of the target sequence. We obtained two *clasp2* mutants with frame-shift mutations (-4bp, -10bp). All analyses were performed on generations >F2. *clasp2*mutant[-4bp] and [-10bp] lines were maintained and bred as described above for further analysis.

## Zebrafish genotyping

DNA was isolated from embryos or fin clips of adult single fish and genotyped by PCR with primers amplifying the genomic region containing exon 3 and one designed complementary to the edited region (primers see above, and 5'-GAAGCAGGCCGT-CATCGGC-3').

## Morpholino and mRNA injections

The morpholino (MO) targeting the exon 1/2/3/8 splice site of *Clasp2* (sequence: ACTACGGTCTACAAGAAGCAGTGAG) was purchased from GeneTools, LCC. The 1nl [5ng/embryo] MO was microinjected in the yolk of 1-2 cell stage embryos. Splice-blocking MO-mediated knockdown was validated by RT-PCR for intron retention. Full length zebrafish *clasp2* (NM\_207072) was cloned in the pCS2+ (kind gift from Prof. den Hertog's laboratory, Hubrecht Institute) and fused C-terminally to mScarlet. Full length mRNA was synthesized using the SP6 message machine kit (thermofisher) and 1nl of a 1000 ng/μl solution was injected in *clasp2* mutants for rescue experiments. Successfully injected embryos were selected based on mScarlet expression at 24hpf. The embryos were analyzed at 3dpf for a curved body axis and imaged with Leica stereomicroscope MZ16FA with a Hamamatsu Flash4 LT digital camera and fixed for *cmyb* WISH. One nl of a 50-100ng/μl solution GFP-GM130 (82) mRNA (kindly provided by the Bakkers' laboratory, Hubrecht Institute) was injected at one cell stage into WT and *clasp2* mutant embryos. Embryos were selected based on GFP fluorescence at 28hpf and imaged at 2dpf embedded in a four-well imaging dish (Muwells) with a Leica SP8 confocal microscope and a 63x/1.4 oil lens. Golgi integrity was analyzed using Fiji measurement and cell counting plugins on a single plane fluorescent image.

## Confocal fluorescence imaging of live zebrafish embryos

Fluorescent confocal microscopy images were acquired using a Zeiss LSM700 or Leica SP8 microscope. Embryos were anesthetized with 1x tricaine (0.16 mg/ml ethyl 3-aminobenzoate methanesulfonate; Sigma E10521), mounted in 0.8% low-melting agarose (Invitrogen) in a 35mm glass bottom dish and covered with E3 solution containing 1x tricaine. For higher magnifications, embryos were placed into a modified Four-Well WillCo dish (83) covered with 0.8 % low-melting agarose and imaged with a 63x objective.

## Whole-mount in situ hybridization on zebrafish embryos

The zebrafish antisense in situ hybridization (ISH) probes *runx1*, *cmyb* and *rag1* were kindly provided by Dr. Romualdo Ciau-Uitz (Prof. Roger Patient's Laboratory) and Prof. den Hertog's Laboratory. All other ISH probes (e.g., for *clasp2*) were generated by PCR amplification of a part of the coding region from template cDNA and subsequently cloned into pCS2+ plasmid (Addgene). After linearization, riboprobes were transcribed from the T7 promoter incorporating digoxigenin-11-UTP for detection via antibodies. Briefly, zebrafish embryos were collected, fixed overnight in 4% paraformaldehyde (PFA, Sigma-Aldrich) and then stepwise dehydrated in methanol before storage at -20°C. For the ISH, embryos were stepwise rehydrated in PBS with 0.1% Tween20 (PBST, Sigma-Aldrich), incubated for 3-10 minutes (min.) in Proteinase K (10μg/ml, Promega) solution and re-fixed in 4% PFA for 20 min. The overnight incubation at 70°C with the anti-sense riboprobe in hybridization buffer (hyb) with tRNA and heparin was preceded by equilibration in hyb for >1h. After hybridization, the embryos were stepwise washed into Sodium Salt Citrate (SSC) and then PBST, followed by a blocking step with BSA (Sigma-Aldrich) and sheep serum for 1h. Incubation with anti-digoxigenin antibody conjugated to alkaline phosphatase was performed



overnight at 4°C, followed by extensive washing with PBST and transfer into PBST. For the enzymatic detection, embryos were moved in NBT/BCIP substrate buffer. Stained embryos were fixed in 4% PFA, washed and stepwise transferred into 80% glycerol/PBS for imaging and storage. Embryos were imaged using a Leica stereomicroscope MZ16FA with a Hamamatsu Flash4 LT digital camera.

### **Acridine Orange staining**

To visualize apoptotic cells in living embryos, embryos were stained at 40hpf, 52hpf and 3dpf with the vital dye acridine orange (AO [Sigma], kindly provided by Prof. Bakkers' Laboratory, Hubrecht Institute). Embryos were placed in AO solution (10ug/ml) in E3 medium for 30 min. and then repeatedly washed with E3 medium before embedding and imaging with the Zeiss LSM700 confocal microscope.

### **Mouse embryo collection, tissue dissection and cell preparation**

E11 AGM regions and E14 FLs were dissected and dissociated as previously described in (85). Briefly, embryos were removed from the uterus and separated from the placenta and YS. Dissections were performed in PBS supplemented with 10% fetal calf serum (FCS), penicillin (100 U/ml, Life Technologies) and streptomycin (100 mg/ml, Life Technologies) (PBS/FCS/PS). For AGM isolation, head and tail were cut from the trunk with needles, the peripheral blood was flushed from the aorta and the AGM was dissected. YS were separated from vitelline vessels. AGM and YS were digested 1h in a 0,125% collagenase solution (Sigma-Aldrich) at 37°C and dissociated by multi-pipetting to obtain a single-cell suspension. FLs were mechanically crushed through 40µm mesh cell strainers (VWR) and resuspended in PBS/FCS/PS. P8 neonates were euthanized and dissected in PBS/FCS/PS to isolate the limb bones and spleen. BM cells were isolated from femur, tibiae, pelvic bones and humerus by gently squeezing the entire marrow out of the bone after carefully removing muscles, tendons, and periosteum from its surface. Cells were filtered through 40µm mesh cell strainers and resuspended in PBS/FCS/PS. The BM of young and adult mice was obtained from femur and tibiae by cutting the bone and flushing the BM out by means of a syringe with PBS/FCS/PS. Spleens, lymph nodes and thymus were mechanically crushed through 40µm mesh cell strainers and resuspended in PBS/FCS/PS. Cells were then washed and counted after Trypan Blue (Life Technologies Europe BV) addition (to exclude dead cells) in a Bürker Türk chamber.

### **Whole-mount immunostaining on mouse embryos**

The developmental stage of the embryos was precisely determined by counting the numbers of somite pairs (according to the Edinburgh Mouse Atlas). E10.5 embryos were fixed, stained and mounted as previously described (6). Briefly, embryo caudal halves were dissected and the blood present in the dorsal aorta flushed out as described in (86). Caudal halves were fixed in PBS/PFA (2%) solution for 20 min. at 4°C, washed twice in PBS and dehydrated in 100% methanol. Immunostainings were performed in PBS containing 1% skimmed milk, 0.2% bovine serum albumin, 0.4% TritonX-100 and 0.1% goat serum (PBS-MT, Sigma-Aldrich). Stainings were performed with anti-c-Kit (2B8) and biotinylated anti-CD31 (MEC 13.3) primary antibodies, and goat anti-rat Alexa Fluor 647 and Alexa Fluor 555-streptavidin secondary antibodies. All antibodies used in this study (including the source and catalogue numbers) are listed in the key resources table.

### **Immunostaining of mouse embryo cryosections**

Embryos were isolated at E10.5. Head and tail were cut off and the blood flushed out of the aorta as described above. After fixation in 4% PFA for 1h, embryos were

washed in PBS and incubated in 15% sucrose buffer overnight for cryoprotection. Embryos were transferred in 7.5% gelatin/15% sucrose solution and incubated at 37°C before placing them in a mold and freezing them in an isopentane bath on liquid nitrogen. Cryosections were cut at 10µm thickness and collected on Superfrost slides (VWR). They were rehydrated in PBS and incubated for 1h at 37°C for gelatin removal. Antigen-retrieval was achieved by heating the slides in 10mM sodium citrate buffer (pH6) at 85°C for 20 min with another 20 min cool-down. For immunofluorescence of cell surface proteins (e.g., c-Kit), E10.5 embryos were fixed for 30 min in 2% PFA, washed in PBS and incubated in 15% sucrose buffer overnight for cryoprotection. Embryos were then transferred into OCT medium and frozen in a 100% ethanol bath on liquid nitrogen. Cryosections were cut at 10µm thickness and collected on Superfrost slides (Thermo). No antigen-retrieval was required. The sections were first washed in PBS demi, then permeabilized in a 0.1% Tween20 (Sigma)/PBS demi solution and blocked in PBS-block (0.4% TritonX-100, 0.2% BSA, 0.1% goat serum) solution for 1 hour. The primary antibody (e.g., c-Kit) was incubated overnight in PBS-block at 4°C. After a washing step in PBS demi, the secondary antibody (e.g., Alexa Fluor 488 goat anti-rabbit) was incubated for 1h at room temperature (RT) in the dark. Sections were washed, stained in DAPI (Thermo Scientific) solution, and mounted in 50% Glycerol/PBS.

### **Confocal microscopy imaging of mouse whole-mount embryos and cryosections**

Microscopic observations of whole-mount embryo caudal halves were performed using a Zeiss LSM700 confocal microscope (Carl Zeiss), equipped with a ×10.0 fluar dry lens (numerical aperture 0.5 M27). Images were obtained using sequential scans. The Alexa Fluor 555 (AF555) fluorescence was detected using a 10.0 mW diode 555 nm and a 560–635 band pass emission filter. The Alexa Fluor 647 (AF647) fluorescence was detected using a 5.0 mW diode 639 nm and a dichromatic beam splitters 640 long pass filter. Embryo caudal halves were stained with individual antibody to check that no fluorescent signals were detected in the other channels. c-Kit expressing cells inside the aorta (delimited by CD31 expression) were counted and scored as cluster cells with the Zeiss Blue software.

The immunostained cryosections were imaged with a Leica SP8 or SP5 confocal microscope using a 63x oil lens (HC PL APO CS2 6 x/1.40 oil). Images were analyzed using Fiji (ImageJ) software tools (87) to measure the spread and number of objects of GM130 and GRASP55 signals.

### **Generation of *Clasp2*<sup>-/-</sup> embryonic stem cells (ESCs)**

For the generation of *Clasp2*<sup>-/-</sup> ESCs, E3.5 blastocysts were flushed out from the uterus of *Clasp2*<sup>+/-</sup> females crossed with *Clasp2*<sup>+/-</sup> males. Each blastocyst was transferred to a single well of a 96-well plate seeded with irradiated feeder MEFs. After 6 days, cells were trypsinized and expanded into a 24-well plate with feeders. Four days later, cells were expanded into 12-well plates, and simultaneously used for extraction of genomic DNA followed by PCR to determine the genotype. After confirmation of genotype, cells were further expanded for one more passage prior to karyotyping and freezing down. 2i was added to the medium at all times.

### **GM130, GRASP55, LAMP-1 and c-Kit immunostaining and quantification.**

Spread and/or number of GM130+ and GRASP55+ Golgi objects, and LAMP-1 lysosomal vesicles, were measured and counted using the Fiji measuring tool and plugin cell counter on immunofluorescent images of the respective antibody staining. For measuring Golgi size, in ESCs (GM130 staining), confocal z-stacks were first converted to maximum intensity projections to capture the entire Golgi network. The Golgi

was outlined manually as a ROI using the freehand selection tool in Fiji and the total area of this ROI was then calculated.

Image quantifications for c-Kit were done in Fiji on confocal acquired z-stacks of whole-mount embryos stained with c-Kit and CD31 antibodies. All images were acquired with identical settings. The entire membrane surface of each IAHC cell as stained by c-Kit inside the aorta (CD31+), was outlined using a segmented line ROI of width 2 pixels (0.62 $\mu$ m) to include the plasma membrane, as well as 1 pixel on either side of it. The average c-Kit fluorescence intensities were measured using a custom-made ImageJ plugin, which facilitated manual annotation of the circumference of IAHC cells and automatic estimation of parameters such as background intensity around a cell, average intensity along the circumference (within a narrow band with a thickness of 0.62 $\mu$ m) and minimum intensity within the cells (the corresponding regions are marked as “outside”, “plasma membrane” and “inside” in Figure 5). For each developmental time point, cells were manually annotated in 3D image stacks. For each cell, the annotation was done in its focal plane (the corresponding z-slice of the 3D image stack, also checking the CD31 signal) by drawing a 2D contour (as a region of interest (ROI)) and adding to the ImageJ’s ROI Manager. All the ROIs were further automatically processed to extract the abovementioned parameters using a custom-made plugin. For intersecting ROIs, the overlapping parts of the contours were properly accounted for while computing the averages.

### **Flow cytometry analysis and cell sorting**

For zebrafish - Embryos were sorted at 3dpf based on transgene expression and anesthetized using tricaine. Most of the yolk was mechanically removed with needles before collection. The remaining residues were stripped by incubation and pipetting in calcium free Ringer’s solution and washing with PBS0. Embryos were then dissociated by incubation in TrypLE (Gibco), shaking at 800 rpm for 1h at 32°C and subsequent pipetting. Before flow cytometry analysis, cells were resuspended in PBSMQ containing 2mM EDTA, 2% sterile filtered FCS and 0.5 $\mu$ g/ml DAPI (Sigma-Aldrich). Samples were acquired on a CytoFLEX cytometer and reanalyzed using the FlowJo software.

For mouse - Flow cytometry analysis and cell sorting were performed on a FACScalibur, AriaIII, Jazz BD FACSJazz, BD Influx Cell Sorter (BD Bioscience) or CytoFLEX benchtop flow cytometer (Beckman Coulter) with CellQuest (BD Bioscience), FACSDiva, BD FACS and CytExpert (Beckman Coulter) software, respectively. Stainings were performed in PBS/FCS/PS for 30 min. at 4°C. Cells were washed, suspended in PBS/FCS/PS and stained with 7-AAD (1 mg/ml, Invitrogen) or Hoechst 33258 (1 mg/ml, Invitrogen) to exclude dead cells. Isotype-matched control antibodies were used for controls. The following monoclonal antibodies (BD Pharmingen, eBioscience, Invitrogen) were used: Lin cocktail (PE-anti-Ter119, PE-anti-B220, PE-anti-Gr1, PE-anti-CD3e); PE-anti-CD48; APC-anti-CD150, Alexa Fluor 700-anti-SCA-1 or PE-Cy7-anti-SCA-1, APC-eFluor 780-anti-c-Kit or APC-Cy7-anti-c-Kit or APC-anti-c-Kit, PE-anti-CD31, and PE-anti-Ter119. For multilineage repopulation analysis, spleen cells were stained with APC-anti-B220, PE-anti-CD8a and PE-anti-CD4; BM cells were stained with APC-anti-Ly6C and PE-anti-CD31. Doublets and dead cells were excluded from the analyses. IAHC cells were stained by injecting APC-Cy7-anti-c-Kit and PE-anti-CD31 directly in the aorta and incubated 30 min before dissection.

For type I and type II pre-HSC staining, cells were additionally stained with APC anti-CD45 and PE-Cy7 anti-CDH5 (CD144, VE-cadherin) antibodies after dissociation. Flow cytometry analyses were performed within 1h after the end of the staining.

For cell cycle analysis, cells were isolated and stained as mentioned above. After completing the cell surface staining, cells were fixed and permeabilized with BD Cy-

tofix/Cytoperm kit according to manufacturer's instructions (BD Bioscience). Subsequently, fixed cells were stained with APC-Ki67 for 1h before washing in 0.1% PBS/Triton-X solution with 0.5 µg/ml DAPI. Cells were incubated at least 45 min in the DAPI solution before analysis on a BD Influx Cell Sorter.

For pre-apoptotic analysis, E14 FL or neonate BM cell suspensions were incubated for 20 min. at 4°C with directly labeled antibodies, i.e., APC anti-c-Kit. Single cell suspensions were washed twice in cold PBS and resuspended in 1X binding buffer (10mM HEPES/NaOH, pH 7.4, 140 mM NaCl, 2.5 mM CaCl<sub>2</sub>). To evaluate cell viability and the apoptotic status, cells were stained with Annexin V-PE and 7-AAD during 20 min. at RT. Flow cytometry analyses were performed within 1h after the end of the staining on a FACScalibur (BD) and analyzed with the FlowJo software.

The mean fluorescence intensity (MFI) was analyzed with the FlowJo software.

### **Magnetic depletion of lineage marker positive cells**

Lineage positive cells were depleted from E14 FL, P8 BM and young adult BM by using and following the manufacturer's instructions of the EasySep™ Mouse Hematopoietic Progenitor Cell Isolation Kit. Briefly, cells are first incubated with biotinylated antibodies (CD5, ±CD11b, CD19, CD45R/B220, Ly6G/C(Gr-1), TER119, 7-4), which bind to the lineage positive cells to be depleted. Second, streptavidin-coated magnetic particles are added to attach to the biotinylated antibodies. Using a magnet, the lineage positive cells remain in the tube while the lineage negative enriched cells are released in a new tube and kept for further flow cytometry staining or snap freezing for RT-qPCR or Western Blot analysis.

### **RT-PCR and RT-qPCR**

For zebrafish - the yolk of the zebrafish embryos was removed, and the head region was cut. One sample typically contained 15-20 embryo tails.

For mouse - AGM and FL samples, cells were pelleted by centrifugation and the supernatant was removed.

All samples were snapfrozen in liquid nitrogen and stored at -80°C. The RNA content was isolated using the RNeasy Mini kit (Qiagen) according to manufacturers' instructions, followed by the removal of genomic DNA through DNaseI digestion (Thermo Scientific) for 30 min. at 37°C and heat-inactivation at 65°C. SuperScript III First-Strand cDNA Synthesis Kit (Invitrogen) was used for cDNA synthesis. For ESC RNA isolation, ESCs were washed with PBS and then collected in TRI Reagent (Sigma). RNA was isolated using the RNeasy Mini Kit (Qiagen). For RT-qPCR, cDNA was generated using Random Primers (Invitrogen) and Superscript IV reverse transcriptase (Thermo Fisher) according to the manufacturer's instructions. PCR reactions were run on a C1000 Thermal Cycler (Bio-Rad).

RT-PCR was performed by using GoTaq-polymerase (Promega) with the listed primers in Table S1.

For RT-qPCR, SYBR Green qPCR SuperMix (Life Technologies) was used with the primers listed in Table S1.

### **LTC-IC assay**

The MS-5 stromal cell line was maintained on 25 cm<sup>2</sup> flasks in α-MEM medium supplemented with 10% FCS, 1% PS, 1mM L-glutamine (culture medium) at 37°C and 5% CO<sub>2</sub> in a humidified incubator. Four days before long-term culture (LTC), MS-5 stromal cells were plated into the wells of 24 well plates in culture medium. Cell confluence was reached after 48h of culture. The day of LTC, the culture medium was removed and replaced by myeloid long-term medium (M5300, Stemcell Technologies) supplemented with hydrocortisone (10<sup>-6</sup> M, Sigma-Aldrich). Two hundred Lin-SCA-

1+c-Kit+ (LSK) cells isolated either from *Clasp2*<sup>+/+</sup> and *Clasp2*<sup>-/-</sup> E14 FLs were added per well on the top of MS-5. Cultures were maintained at 37°C and 5% CO<sub>2</sub> in a humidified incubator. The medium was changed once a week. The cultures were harvested every week and replated in bulk into MethoCult™ M3434 medium (StemCell Technologies) supplemented with PS to address the presence of CFU-C. All CFU-C values were normalized to initial 100 LSK cells seeded into cultures.

#### ***In vitro* clonogenic assay (CFU-C)**

Colony formation capacity was tested in MethoCult M3434 medium (StemCell Technologies) supplemented with PS. Different dilutions of cells isolated from freshly dissociated AGM, AGM explants, YS, FL, or BM from *Clasp2*<sup>+/+</sup> and *Clasp2*<sup>-/-</sup> embryos or P8 neonates were mixed with MethoCult. The medium was then dispensed into culture dishes (triplicates) by using a syringe and blunt end needle. Plates were incubated in a humidified incubator at 37°C and 5% CO<sub>2</sub>. Colonies were scored after 12 days using an inverted microscope and gridded scoring dishes.

#### **Long-term *in vivo* transplantation assay**

Cell suspensions corresponding to the embryo equivalent (ee) of one AGM or 0.001-0.005 ee of FL from *Clasp2*<sup>+/+</sup> or *Clasp2*<sup>-/-</sup> male embryos were intravenously co-injected with 2x10<sup>5</sup> WT spleen cells into sub-lethally irradiated WT female recipients (C57BL/6, irradiated with a 9 Gy split-dose, 137Cs-source). The blood of the transplanted recipients was analyzed 4 months post-transplantation for the presence of donor cell markers (*Clasp2* and/or *ymt*) by semi-quantitative polymerase chain reaction (PCR). Signal quantitation was measured by DNA normalization (myogenin [*myo*] and *Clasp2* and/or *ymt* control DNA dilutions (0 to 100% donor marker). Recipients were considered repopulated when the chimerism in the peripheral blood was >10%.

For multilineage repopulation analysis, hematopoietic organs from primary reconstituted recipients (lymph nodes, thymus, BM, and spleens) were dissected. Erythroid, myeloid, T and/or B cells were sorted from recipient BM and spleen after antibody staining as previously described (88). To assess self-renewal capacity, BM cells isolated from primary reconstituted recipients were injected into secondary sub-lethally irradiated recipients (3x10<sup>6</sup> cells/recipient). Percentages of chimerism in the blood were determined as previously described by semi-quantitative PCR at 4 months post-transplantation.

#### **AGM explant culture**

E11 AGMs were cultured as explants at 37°C in 5% CO<sub>2</sub> for 3-4 days as previously described (7). Briefly, AGMs were cultured on a filter (Durapore 0.65 µm, Millipore) on the top of a steel mesh grid at the medium-air interface. The Myelocult medium (M5300, StemCell Technologies) was supplemented with 10<sup>-6</sup>M hydrocortisone succinate (Sigma) and 100ng/ml SCF, Flt3L (Peprotech) and IL-3 (BD Pharmingen). After 3-4 days of culture, AGM explants were collected from the filter with a scalpel and dissociated with collagenase as previously described (7).

#### **Culture and treatment of Lin<sup>-</sup> fetal liver cells and/or embryonic stem cells (ESCs), c-Kit and glycosylation analyses**

Lineage negative cells were isolated from E14 FLs by negative selection using the EasySep™ Mouse Hematopoietic Progenitor Cell Isolation Kit (as described above). The cells were cultured overnight in triplicates at 75,000 cells per well of a 24-well plate in Myelocult medium (M5300, StemCell Technologies). The medium was supplemented with 10<sup>-6</sup> M hydrocortisone succinate (Sigma). Cells were cultured untre-



ated, or in the presence of either 50ng/ml SCF (Peprotech) or Bafilomycin A1 (BafA, 100nM, Invitrogen), or both SCF and BafA. After culture, cells were harvested, stained with APC-anti-c-Kit (2B8, BD Bioscience) and analyzed by flow cytometry analysis as described above. c-Kit mean fluorescence intensities (MFI) were analyzed with the FlowJo software.

ESCs were cultured without feeders on plastic coated with 0.2% gelatin, and replated every 2-3 days at a split ratio of 1:5 following dissociation with Trypsin-EDTA. Cells were cultured in DMEM (Dulbecco's modified Eagle's medium) supplemented with 7.5% fetal calf serum (BioWest), 2mM L-glutamine, 1mM sodium pyruvate (both from Invitrogen), 0.1mM  $\beta$ mercaptoethanol, 1x MEM non-essential amino acids (Gibco), 100 units/ml LIF, PD (1 $\mu$ M, PD0325901, Stemgent), CHIR (3 $\mu$ M, CHIR99021, Tocris Biochemicals). Recombinant mouse SCF (Stem Cell Technologies) was added to cultures overnight at 50ng/ml. In some experiments, BafA (Invitrogen) was added at 100nM for 6 hours in conjunction with SCF. Tunicamycin (Sigma) was added to cells overnight, at a concentration of 1 $\mu$ g/mL before harvesting and western blotting was performed. For the glycosylation enzyme treatment, ESCs from 3x10cm dishes were harvested and lysed in 200 $\mu$ l lysis buffer containing 20mM Tris (pH7.5), 150mM KCL, 0.5% TritonX-100, 0.2%SDS, 10% Glycerol, 1X protease inhibitor (Roche, EDTA-free), followed by clarification at 5000rpm for 10 min at 40°C. Forty  $\mu$ l of clarified lysate was used for each enzymatic reaction. Endo H and Pngase F (both from NEB) were added according to the manufacturer's instructions and reactions were incubated for 1 hour at 37°C. Treated samples were then boiled with an equal volume of SDS sample buffer and western blotting was performed as described below.

### Western Blotting

E14 FL cells were washed in PBS after sorting, and cell pellets were snap frozen and stored in -80°C until use. Pellets were lysed in SDS sample Buffer (89) containing 2% SDS, 10% glycerol, 5%  $\beta$ -mercaptoethanol, 33mM Tris pH 6.8, and Protease Inhibitor Cocktail (Roche, according to manufacturers' instructions). ESCs were scraped directly from 3.5 mm dishes in SDS sample buffer and denatured by boiling. Proteins were separated by SDS-PAGE and transferred to PVDF membranes (Millipore). Membranes were blocked in 5% non-fat powder milk (Sigma) in PBS with 0.1% Tween 20 (PBS-T) and incubated with primary antibodies overnight at 4°C. After 3 washes, membranes were incubated with Horseradish Peroxidase (HRP)-conjugated secondary antibodies (GE Healthcare) at 1:10,000 dilution or IR dyes (800CW and 600CW, Licor) at 1:15,000 dilution for one hour. Blots were visualized by enhanced chemiluminescence detection (ECL, GE Healthcare), or fluorescent detection (Odyssey Imaging System, Licor). Band intensity on blots was analyzed using the Gel Analysis Plugin in Fiji. Intensities were normalized to tubulin (loading control) intensity in each lane on the blots and in each blot the *Clasp2*<sup>+/+</sup> sample at the left was considered as 100.

### Quantification and statistical analysis

For all quantifications and statistical analyses Prism7 software (GraphPad Software, Inc.) was used. Results were expressed as mean  $\pm$  SEM or mean  $\pm$  SD. RT-qPCR data are shown as mean  $\pm$  SD. Student's t-test or Mann-Whitney U test were applied to determine the level of significance between two groups. Welch's t-test was applied when the two samples to compare had unequal variances and/or unequal sample sizes.  $P < 0.05$ , 0.01, 0.001 and 0.0001 were considered statistically significant and marked as \*, \*\*, \*\*\*, and \*\*\*\*, respectively.



# SUPPLEMENTARY FIGURES

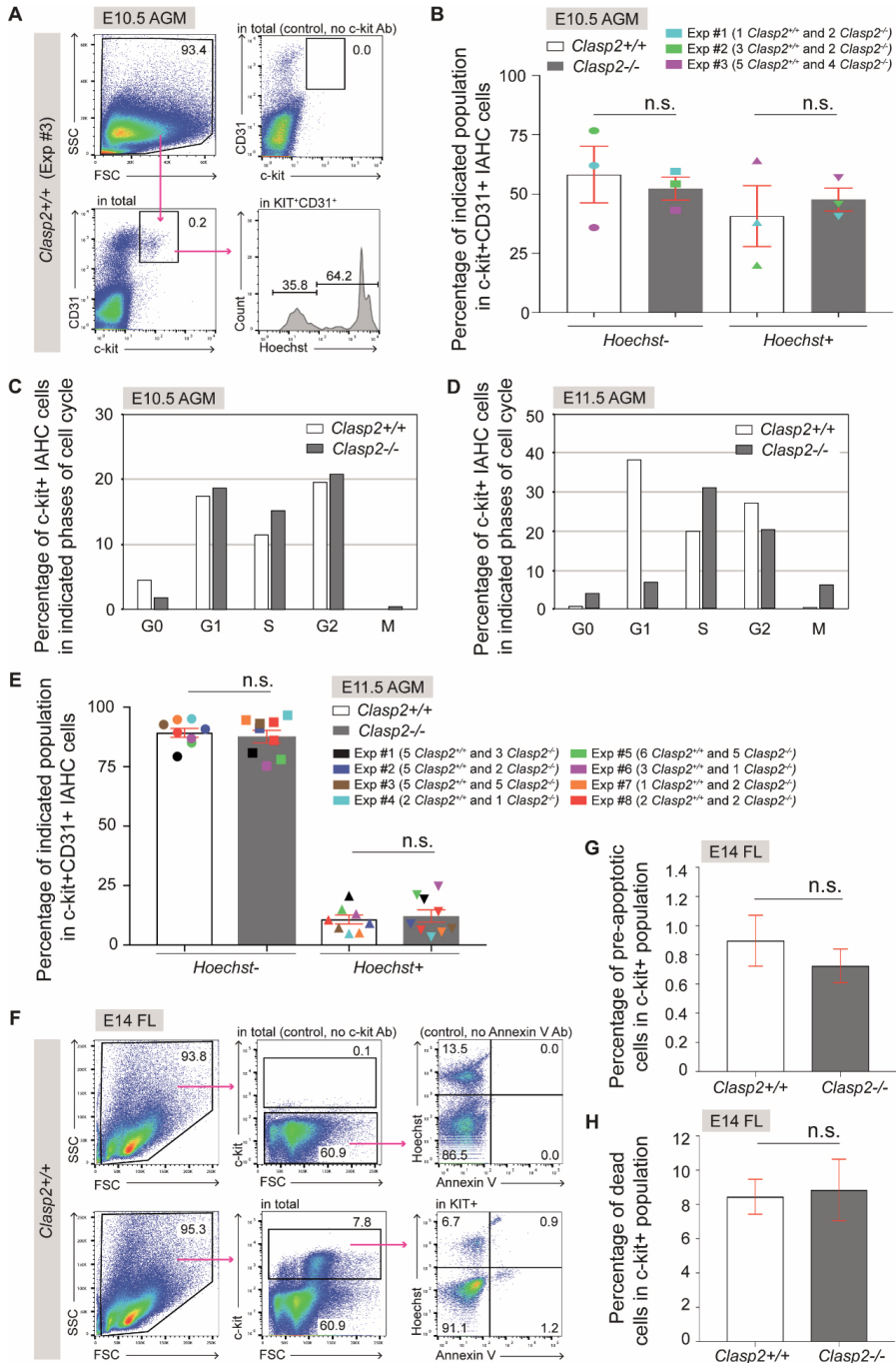


**Figure S1 (related to Figures 1 and 2). Apoptotic and cell cycle status of E10.5 and E11.5 IAHC cells and E14 FL cells from *Clasp2*<sup>+/+</sup> and *Clasp2*<sup>-/-</sup> embryos.** (A) Representative flow cytometry analysis of Hoechst expression in the c-Kit+CD31<sup>+</sup> IAHC population at day 0 in E10.5 *Clasp2*<sup>+/+</sup> AGMs. Percentages of populations are indicated in the gates and correspond to Exp#3 shown in (B). Control with no c-Kit antibody (upper right plot). (B) Percentages of live (Hoechst<sup>-</sup>) and dead (Hoechst<sup>+</sup>) cells in CD31+c-Kit+ IAHC cells from E10.5 *Clasp2*<sup>+/+</sup> and *Clasp2*<sup>-/-</sup> embryos (n=3 [Exp. 1 to 3]; 9 *Clasp2*<sup>+/+</sup>, 8 *Clasp2*<sup>-/-</sup>). (C, D) Percentages of c-Kit+ IAHC cells from E10.5 (C) and E11.5 (D) *Clasp2*<sup>+/+</sup> and *Clasp2*<sup>-/-</sup> embryos in G0, G1, S, G2 and M phases of cell cycle, as determined by Ki67 and DAPI staining (at E10.5, n=1 [4 *Clasp2*<sup>+/+</sup>, 5 *Clasp2*<sup>-/-</sup>]; at E11.5, n=1 [4 *Clasp2*<sup>+/+</sup>, 3 *Clasp2*<sup>-/-</sup>]). (E) Percentages of live (Hoechst<sup>-</sup>) and dead (Hoechst<sup>+</sup>) cells in CD31+c-Kit+ IAHC cells from E11.5 *Clasp2*<sup>+/+</sup> and *Clasp2*<sup>-/-</sup> embryos (n=8 [29 *Clasp2*<sup>+/+</sup>, 21 *Clasp2*<sup>-/-</sup>]). (F) Representative flow cytometry analysis of pre-apoptotic (AnnexinV+Hoechst<sup>-</sup>) and dead (AnnexinV+Hoechst<sup>+</sup>) cells in the c-Kit+ population of E14 *Clasp2*<sup>+/+</sup> and *Clasp2*<sup>-/-</sup> FLs (n=3 [11 *Clasp2*<sup>+/+</sup>, 11 *Clasp2*<sup>-/-</sup>]). Percentages of populations are indicated in the gates. Controls with no c-Kit and no AnnexinV antibodies (upper plots). (G, H) Percentages of pre-apoptotic (G) and dead (H) cells in the c-Kit+ population of E14 *Clasp2*<sup>+/+</sup> and *Clasp2*<sup>-/-</sup> FLs (n=3 [11 *Clasp2*<sup>+/+</sup>, 11 *Clasp2*<sup>-/-</sup>]). Error bars, mean ± SEM (B, E, G, H). n.s., not significant, Mann-Whitney U test (B, E, G, H). IAHC, intra-aortic hematopoietic cluster; AGM, aorta-gonad-mesonephros; FL, fetal liver; E, embryonic day; Exp., experiment.

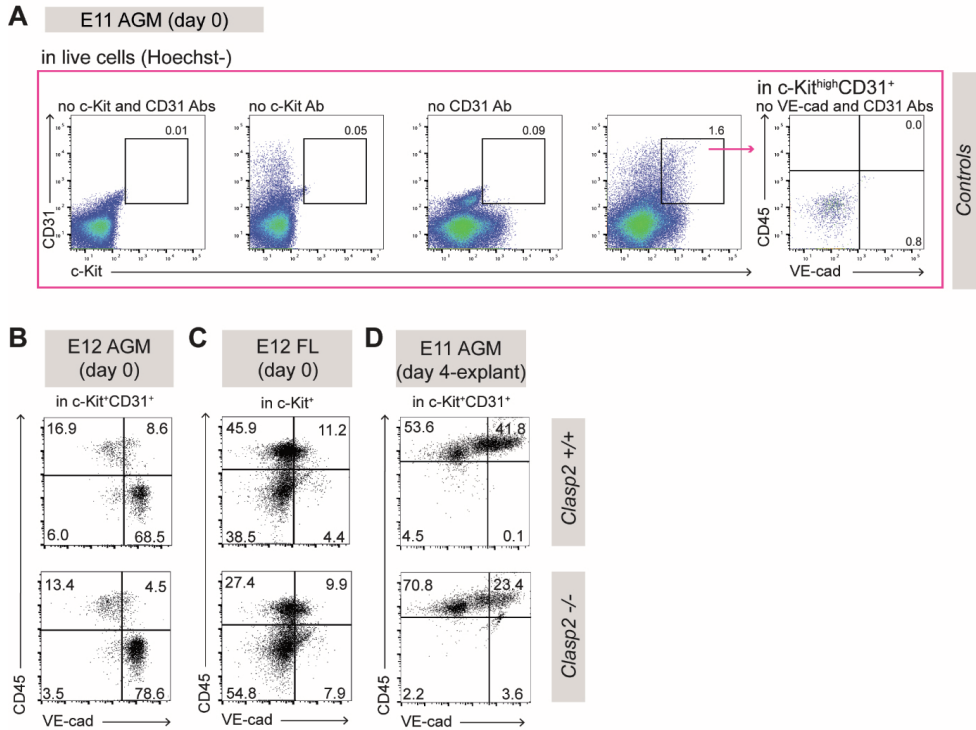


**Figure S2 (related to Figure 1). Partial blockage of pre-HSC maturation in *Clasp2*<sup>-/-</sup> embryos.** (A) Representative flow cytometry control plots with no c-Kit and/or no CD31, and no CD45 and VE-cadherin (VE-cad) antibodies, are shown in the live population in the pink box. (B-D) Representative flow cytometry analyses of the type I and type II pre-HSC populations at day 0 in E12 AGMs (B), at day 0 in E12 FL (C), and after explant culture of E11 AGMs (D) isolated from *Clasp2*<sup>+/+</sup> (top panels) and *Clasp2*<sup>-/-</sup> (bottom panels) embryos (E12 at day 0, n=2 [11 *Clasp2*<sup>+/+</sup>, 9 *Clasp2*<sup>-/-</sup>]; E12 FL at day 0, n=2 [11 *Clasp2*<sup>+/+</sup>, 9 *Clasp2*<sup>-/-</sup>]; E11 after explant, n=2 [5 *Clasp2*<sup>+/+</sup>, 7 *Clasp2*<sup>-/-</sup>]). Percentages of populations are indicated in the gates. Type I pre-HSC: c-Kit+CD31+VE-cad+CD45<sup>-</sup>; type II pre-HSC: c-Kit+CD31+VE-cad+CD45<sup>+</sup>. AGM, aorta-gonad-mesonephros; FL, fetal liver; E, embryonic day.

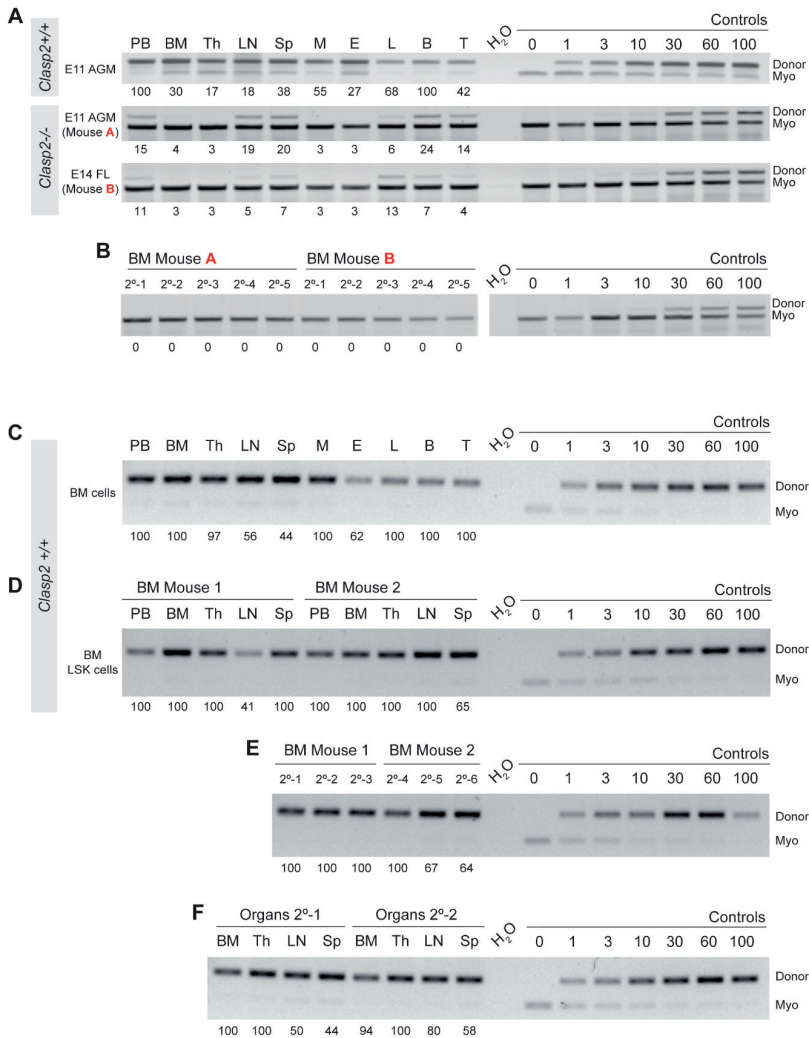


**Figure S3 (related to Figures 1 and 2). Cell-autonomous multilineage and self-renewal defects of *Clasp2*<sup>-/-</sup> cells.** (A) Representative semi-quantitative PCR analyses of whole hematopoietic tissues and sorted cell DNA isolated 4 months post-transplantation from primary recipients injected with 1e6 of E11 *Clasp2*<sup>+/+</sup> AGM cells (upper panel), E11 *Clasp2*<sup>-/-</sup> AGM cells (Mouse A, middle panel), and 0.005e6 of E14 *Clasp2*<sup>-/-</sup> FL (Mouse B, lower panel). (B) Representative semi-quantitative PCR analysis of peripheral blood DNA collected at 4 months post-transplantation from five secondary recipients (2<sup>°-1</sup> to 2<sup>°-5</sup>) injected with BM cells from primary recipients, mice A and B. (C, D) Representative semi-quantitative PCR analyses (4 months post-transplantation) of hematopoietic organs and/or sorted cell DNA from adult *Clasp2*<sup>-/-</sup> primary recipients injected with (C) 3x10<sup>6</sup> total BM cells or (D) 10,000 sorted LSK cells isolated from C57Bl/6 donor (two mice shown as example, mice 1 and 2). (E) Representative semi-quantitative PCR analysis (4 months post-transplantation) of peripheral blood DNA from 6 C57Bl/6 secondary recipients (2<sup>°-1</sup>-2<sup>°-6</sup>) injected with 3x10<sup>6</sup> total BM cells from *Clasp2*<sup>-/-</sup> primary recipients (mice 1 and 2) initially reconstituted with 10,000 C57Bl/6 LSK cells. (F) Representative semi-quantitative PCR analysis of hematopoietic organs of two secondary recipients (2<sup>°-1</sup> and 2<sup>°-2</sup>). Donor indicates the ymt (male chromosome marker) or *Clasp2* PCR fragment, and Myo indicates the myogenin DNA normalization control PCR fragment. DNA dilution controls (0 to 100%) were used to quantitate percentages of donor chimerism that are indicated below each lane. PB, peripheral blood; BM, bone marrow; Th, thymus; LN, lymph node; Sp, spleen, M, myeloid cells sorted from BM; E, erythroid cells sorted from BM; L, lymphoid cells sorted from BM; B, B cells sorted from spleen; T, T cells sorted from spleen; FL, fetal liver.

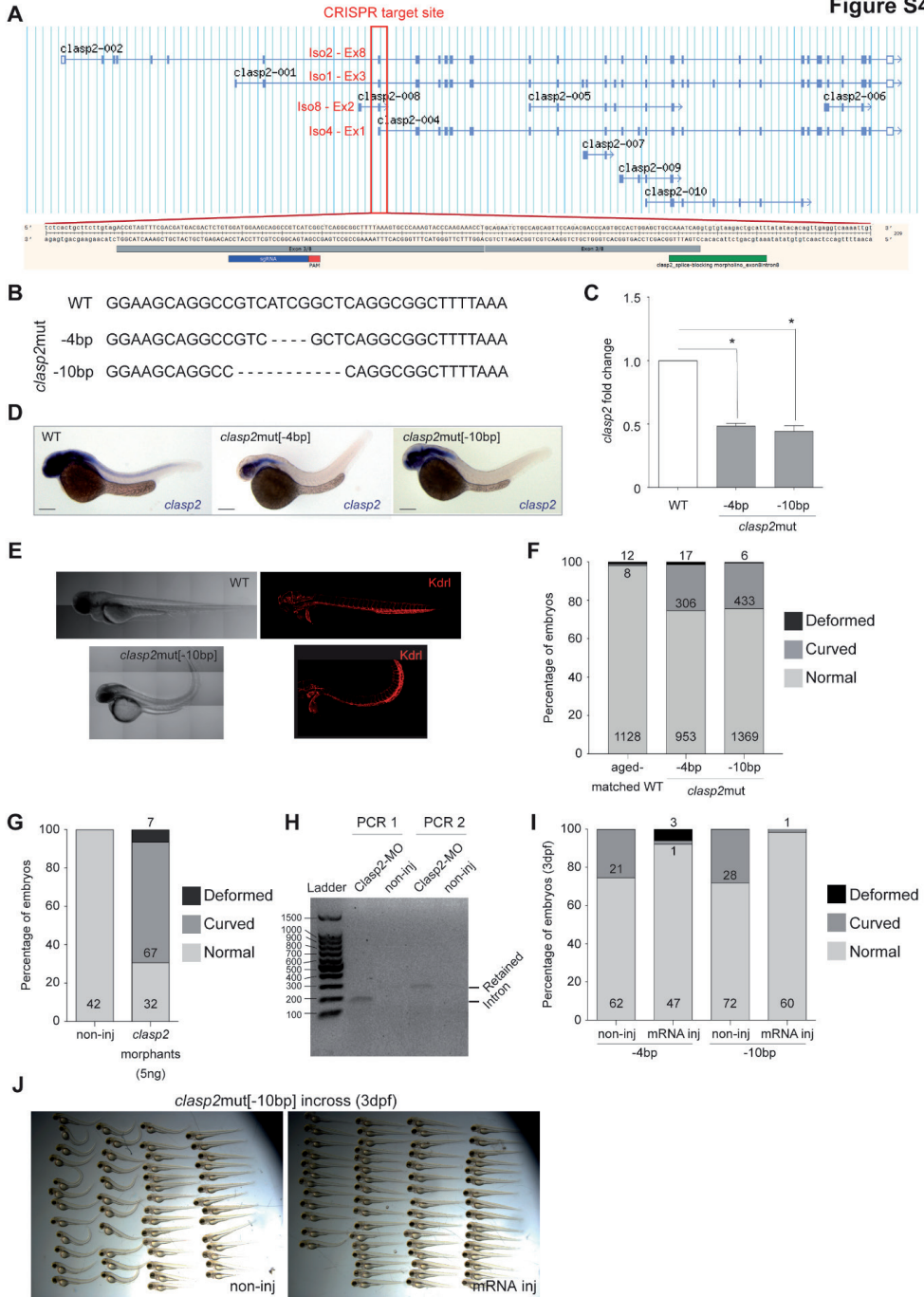
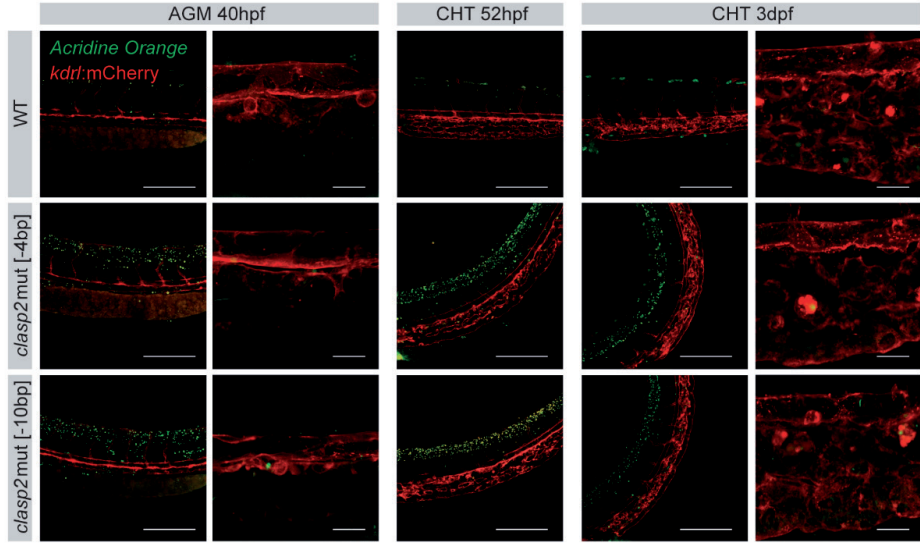


**Figure S4** (related to Figures 1 and 3). Generation and validation of *clasp2* loss-of-function zebrafish lines. (A) Sequence of zebrafish *clasp2* isoforms. Red box: location of the CRISPR target site in exons (Ex) 8, 3, 2 and 1 of the *clasp2* isoforms (iso) 002, 001, 008 and 004, respectively. (B) Indels obtained in the two *clasp2* mutant lines with a frame shift resulting in

premature STOP codon (*clasp2*mut[-4bp] and [-10bp]). (C) mRNA *clasp2* fold changes in WT and *clasp2*mut[-4bp] and [-10bp] zebrafish embryos. (D) Representative images of WISH for *clasp2* in WT, *clasp2*mut[-4bp] and [-10bp], at 40hpf. (E) Representative bright filter and fluorescent images of *Tg(kdrl:mCherry)* (WT) and *clasp2*mut[-10bp] zebrafish embryos at 40hpf. Red, mCherry fluorescence. (F) Proportion of aged-matched WT and *clasp2* mutant embryos (*clasp2*mut[-4bp] and [-10bp] mutations) with a normal or curved tail, or deformity. (G) Proportion of zebrafish non-injected (non-inj) or injected with *clasp2* morpholino (*clasp2* morphants) with a normal or curved tail, or deformity. (H) RT-PCR comparing *clasp2* intron retention and expression levels in non-injected control embryos and in MO-injected embryos at 40hpf. (I, J) Rescue experiments. (I) Proportion of *clasp2*mut[-4bp] and [-10bp] embryos with a normal or curved tail, or deformity, after non-injection (non-inj) or injection (inj) of *clasp2* mRNA at 3dpf. Numbers on column: number of zebrafish embryos analyzed. (J) Images of *clasp2*mut[-10bp] embryos, non-injected (left panel) or injected with *clasp2* mRNA (right panel), analyzed at 3dpf. Numbers on column: number of embryos with the corresponding phenotype (F, G, I). Error bars; mean  $\pm$  SEM (C). \*P<0.05, Unpaired t test with Welch's correction (C), Scale bar: 200 $\mu$ m (D). CHT, caudal hematopoietic tissue; dpf, day post-fertilization.

**A**



**B**

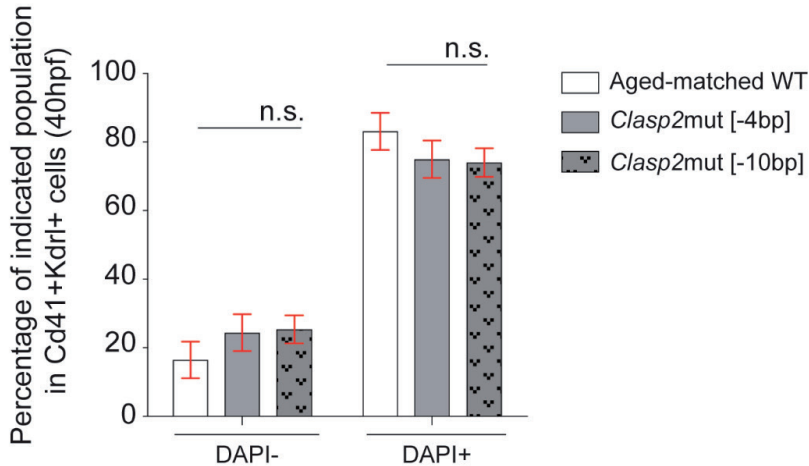


**Figure S5 (related to Figure 3). No abnormal apoptosis in the aorta of *clasp2mut* embryos.** (A) Double and single fluorescent images of *Tg(kdr1:mCherry)* (WT), *clasp2mut*[-4bp] and *clasp2mut*[-10bp] zebrafish (background *Tg(kdr1:mCherry)*) after staining with acridine orange and analyzed in the AGM at 40hpf, and the CHT at 52hpf and 3dpf. Red, mCherry; Green, acridine orange. (B) Graph representing the percentage of alive (DAPI-) and dead (DAPI+) cells in the aortic *cd41+kdr1+* hematopoietic population of aged-matched WT, *clasp2mut*[-4bp] and *clasp2mut*[-10bp] embryos at 40hpf (n=3). Error bars: mean  $\pm$  SEM (B). n.s., not significant, 2way ANOVA (B). Scale bars: 200 $\mu$ m and 20 $\mu$ m (A). WT, wildtype; AGM, aorta-gonad-mesonephros; CHT, caudal hematopoietic tissue; hpf, hour post-fertilization; dpf, day post fertilization.



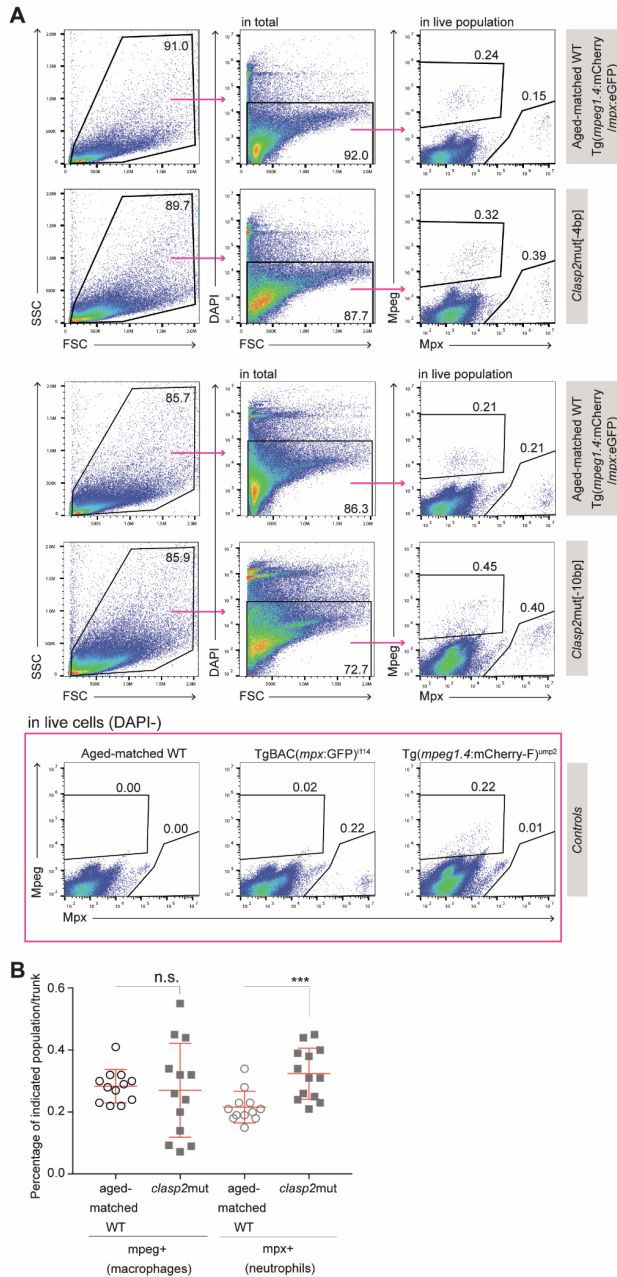


**Figure S6 (related to Figure 4). *clasp2mut* zebrafish embryos have more neutrophils.** (A) Representative flow cytometry plots showing the percentages of neutrophils (*mpx*<sup>+</sup>) and macrophages (*mpeg*<sup>+</sup>) in *clasp2mut*[-4bp] and *clasp2mut*[-10bp] zebrafish, compared to aged-matched WT (background *Tg(mpeg1.4:mCherry)*), at 3dpf (n=5, 5-20 embryos pooled per sample). Aged-matched WT, *TgBAC(mpx:eGFP)* and *Tg(mpx:eGFP/mpeg1.4:mCherry-F)* zebrafish embryos, were used as controls (pink box). (B) Percentages of neutrophils (*mpx*<sup>+</sup>) and macrophages (*mpeg*<sup>+</sup>) in *clasp2mut*[-4bp] and *clasp2mut*[-10bp] zebrafish, compared to aged-matched WT. \*\*\*P<0.001, n.s., not significant, Unpaired t test with Welch's correction (B). WT, wildtype; dpf, day post-fertilization.

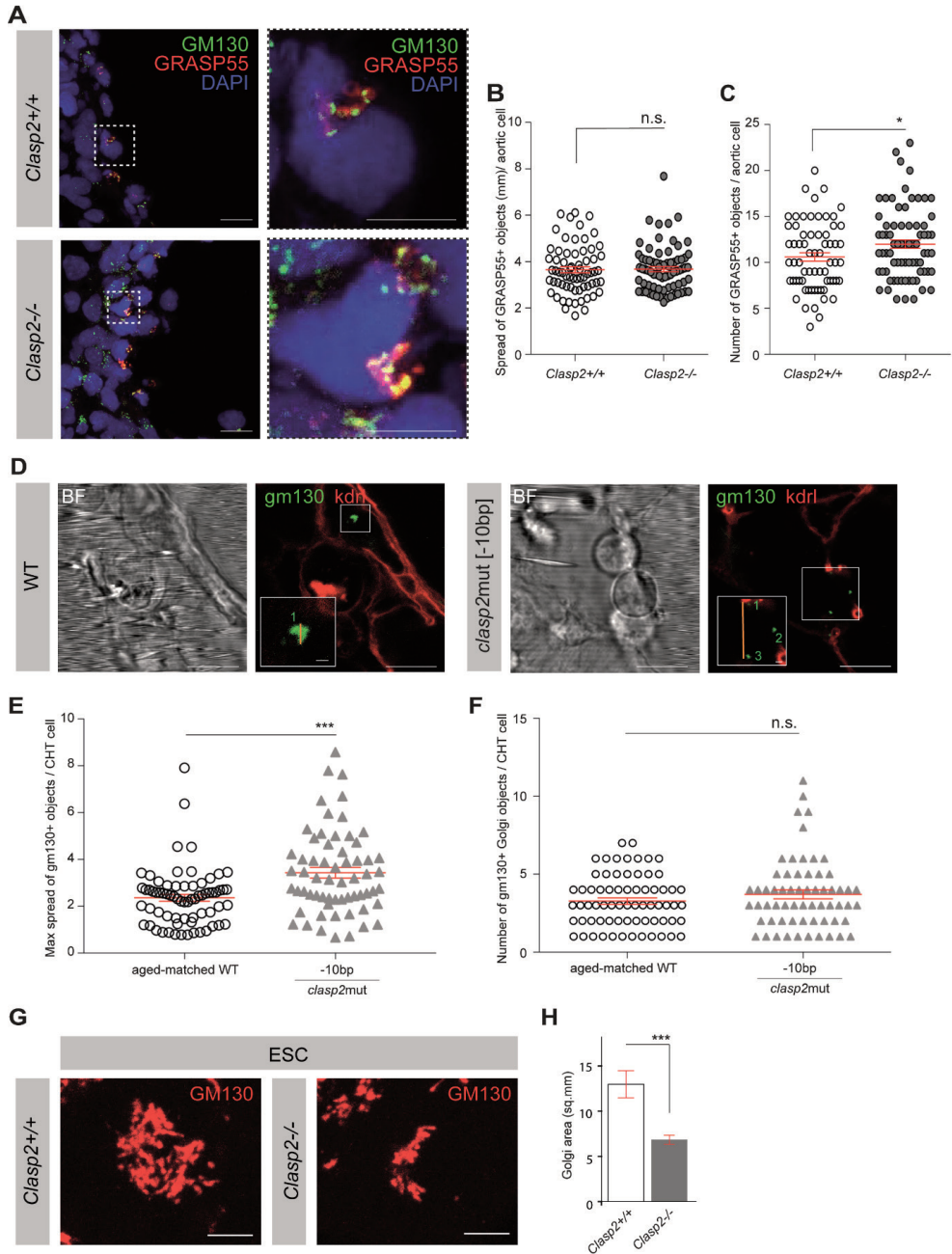
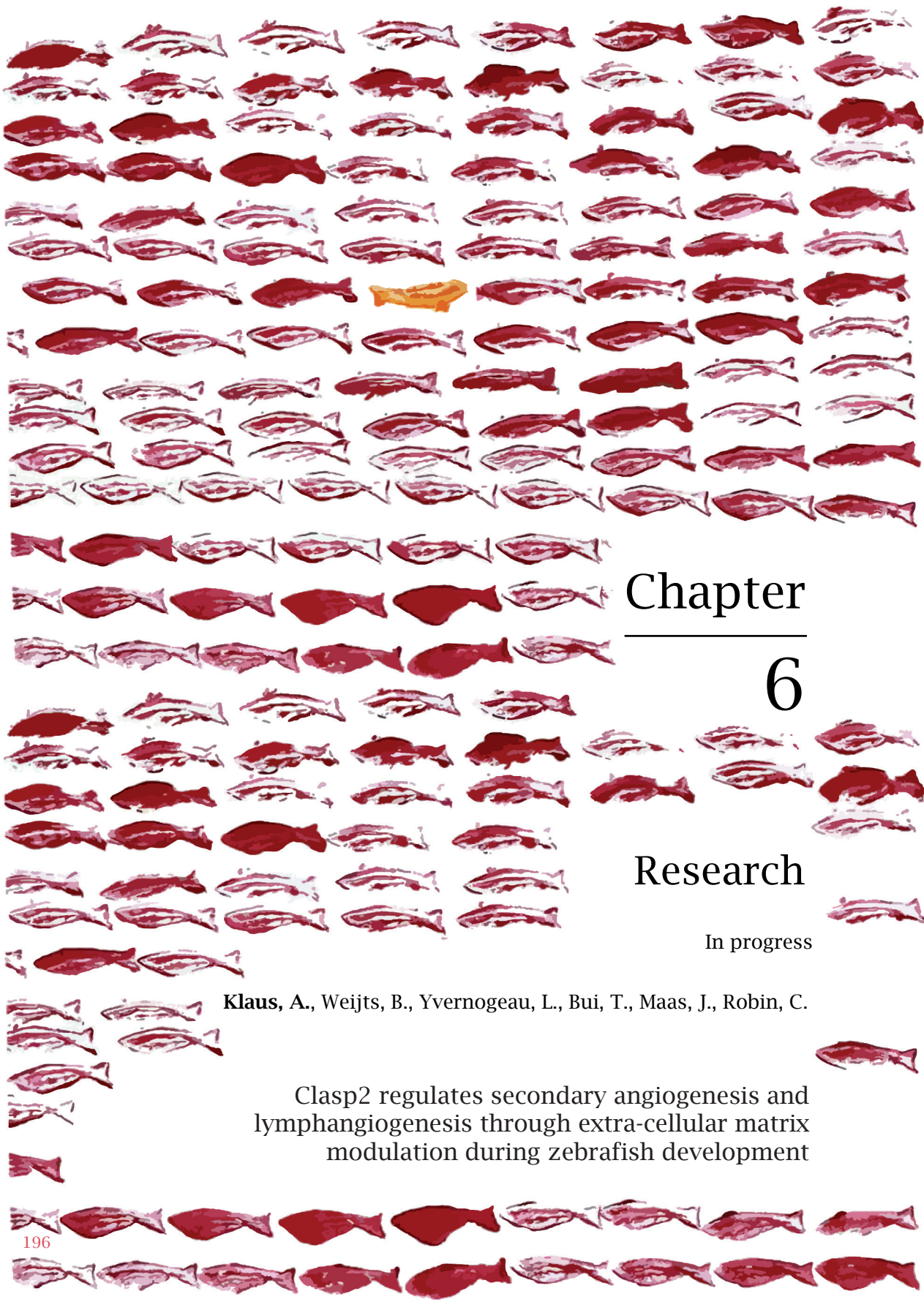


**Figure S7 (related to Figure 6). Increased c-Kit degradation and defective trafficking to the plasma membrane in *Clasp2*<sup>-/-</sup> mouse IAHC cells, zebrafish HSPCs and mouse embryonic stem cells.** (A) Representative immunofluorescent images of IAHCs in E10.5 *Clasp2*<sup>-/-</sup> and *Clasp2*<sup>+/+</sup> mouse embryos after staining with anti-GM130 (green), anti-GRASP55 (red) and DAPI (blue). Dashed boxes are shown enlarged on the right of each panel. (B, C) Graphs showing the spread (B, in  $\mu\text{m}$ ) and number (C) of GRASP55+ objects per aortic cells in E10.5 *Clasp2*<sup>-/-</sup> and *Clasp2*<sup>+/+</sup> embryos (n=2). Measurements were performed as illustrated in Fig.6B and C. (D) Representative bright field and fluorescent images of the CHT region of *Tg(kdrl:mCherry)* (WT)

and *clasp2*mut[-10bp] zebrafish embryos injected with GFP-*gm130* mRNA at 2dpf. Green, EGFP fluorescence; Red, mCherry fluorescence. One example is shown for each phenotype. Close-ups are shown in the inside bottom of the fluorescent images, with the spread of Golgi and the number of Golgi objects indicated by an orange line and green numbers, respectively. (E, F) Graphs representing the maximal spread of GFP+ Golgi objects (E, in  $\mu\text{m}$ ) and the number of GFP+ Golgi objects (F) in phenotypical round blood cells within the CHT of WT and *clasp2*mut[-10bp] injected embryos at 2dpf. (G) Representative immunofluorescent images of mESCs stained with anti-GM130 (red) (n=2). (H) Graphs showing the quantification of Golgi area (in  $\text{Sq.}\mu\text{m}$ ); n=29 *Clasp2*<sup>+/+</sup> and 30 *Clasp2*<sup>-/-</sup> ESCs. Data are represented as mean  $\pm$  SEM (B, C, E, F, H). \* $P < 0.05$ , \*\*\* $P < 0.001$ , n.s., not significant, Unpaired student t-test (B, C, H), Mann-Whitney U test (E, F). Scale bars, 10 $\mu\text{m}$  (A, D), 1 $\mu\text{m}$  (D, close-up), 2.5mm (G). CHT, caudal hematopoietic tissue; WT, wild type; dpf, day post-fertilization; BF, bright filter; mESC, mouse embryonic stem cells.

**Table S1. Sequences for genotyping, CRISPR/Cas9 genome editing, PCR, RT-qPCR, in situ hybridization and morpholino injection experiments.**

Purpose	Species	Name	Sequence
Genotyping	Mouse	ProbA5	TGACCACCAGCCTGACCTA
		Rev2	ACCTGAACAGAAGGAACATC
		#p2G1	CGGCATCAGAGCAGCCGATTG
	Zebrafish	zf_Cl2_F	CCTTTTCGTGCAGCTTATGTCA
		zf_Cl2_R	GGTTAATTGGGCAATCATTTGCT
		zf_Cl2_MHS	GAAGCAGGCCGTCAATCGGC
CRISPR/Cas9 genome editing	Zebrafish	sg RNA	TAATACGACTCACTATAGGATG GAAGCAGGCCGTCAATGTTTTAG AGCTAGAAATAGCAAAG
		constant oligo	AAAAGCACCGACTCGGTGCCA CTTTTCAAGTTGATAACGGAC TAGCCTTATTTAACTTGCTAT TTCTAGCTCTAAAAC
Semi-quantitative PCR (transplantation)	Mouse	YMT2-1	CTGGAGCTCTACAGTGATGA
		YMT2-2	CAGTTACCAATCAACACATCAC
		MYO-1	TTACGTCATCGTGGACAGC
		MYO-2	TGGGCTGGGTGTTAGCCTTA
RT-qPCR primer	Mouse	c-Kit-qF	GCGTTCCTCGCCTCCAAGAATT GTATT
		c-Kit-qRT	CACTTTCAAATGTGTACACGCA GCTG
		gammaTub_F	CCAGCGGATTCTCCCAGG
		gammaTub_R	GAATGACACAGTACAATCCC TCT
		pericentrin_F	ATGCAGAAGCAGCAGGAGTT
		pericentrin_R	CTTCAAGGAGGCCCTTAGCC
		mPgk1_RTq_Fw1	GGGTGGATGCTCTCAGCAAT
		mPgk1_RTq_Rv1	GTTCTGGTGCCACATCTCA
		mGusb_RTq_Fw1	AACAACACACTGACCCCTCA
		mGusb_RTq_Rv1	ACCACAGATCGATGCAGTCC
		Tbp_RTq_Fw1	CTACCGTGAATCTTGGCTGTAA AC
		Tbp_RTq_Rv1	AATCAACGCAGTTGTCCGTGGC
		mClasp2alpha_RTq_Fw1	CGGGTATCGTTGTAGGATTGG
		mClasp2alpha_RTq_Rv1	CAGGTTCTGAGCTTCTTCTCG
	mClasp2gamma_RTq_Fw1	CAGTGGTGGTTCTGTGGTTGTT TC	
	mClasp2gamma_RTq_Rv1	CCTCCGAATTTCCCTCACCTA	
	Zebrafish	RTzf_CLASP2bi_3to6_8to11_F	GCCACTGGAGCTGCCAAATC
		RTzf_CLASP2bi_3to6_8to11_R	CTTCAGCGCGTTTGCTCTGT
		qPCR_zf_ef1a_F	GATTGTGTGCTGGTGGTGTG
		qPCR_zf_ef1a_R	TGTATGCCTGACTTCTTGTG
		qPCR_zf_bact_F	CCACCTTAAATGGCTTAGCA
		qPCR_zf_bact_R	CATTGTGAGGAGGGCAAAGT
	ESCs	STAT3_F	TGTTGGAGCAGCATCTTCAG
		STAT3_R	GAGGTTCTCCACCACCTTCA
		GAPDH_F	AGGTCGGTGTGAACGGATT
		GAPDH_R	AACAATCTCCACTTGGCCACTG
	<i>In situ</i> hybridization, subcloning	Zebrafish	clasp2_ISH_F
clasp2_ISH_R			TCCCTCGAGGAAGTGCGCCAG AAGCATT
Morpholino	Zebrafish	zf_clasp2_i7e8	ACTACGGTCTACAAGAAGCAG TGAG
RT-PCR	Zebrafish	zfCl2e8e9F	TGCTTCATCCACAGAGTCG
		Reverse 3.2	AGACTGCATTTATATACACAGT TGAGG
		Reverse 3.3	TTTCTTCTCAGGCAAGTCTTAT TTGT



# Chapter

# 6

# Research

In progress

**Klaus, A., Weijts, B., Yvernogeu, L., Bui, T., Maas, J., Robin, C.**

Clasp2 regulates secondary angiogenesis and lymphangiogenesis through extra-cellular matrix modulation during zebrafish development



**D**uring early vertebrate embryonic development, a functional circulatory system is established, allowing blood cells to travel through the growing tissues to provide oxygen and nutrients. The formation of blood vessels, lymphatics and hematopoietic cells is ontogenetically linked, all deriving from the lateral plate mesoderm. A multitude of extrinsic and intrinsic regulatory signals controls the cellular specification of endothelial cells (ECs) and hematopoietic stem and progenitor cell (HSPC) production, including the cytoskeletal filament system. In particular, the microtubule (MT)-binding protein Clasp2 ensures hematopoietic stem cell (HSC) identity by regulating critical receptor trafficking at the plasma membrane. By using a Clasp2 loss-of-function zebrafish model, we uncover here a novel function of Clasp2 in modulating EC dynamics. We show that Clasp2 is involved in secondary venous angiogenesis and lymphangiogenesis originating from the posterior cardinal vein (PCV). Clasp2 regulates the extra-cellular matrix (ECM) composition by influencing the turnover of the hyaluronan network through the hyaluronan scavenger receptor Stabilin 2. We hypothesize that this reduces the availability of ECM-anchored cytokines, such as the key angiogenic signal vascular endothelial growth factor (VEGF), for binding to their receptors on EC surface. Clasp2 thus has an important role in influencing EC dynamics through modulation of the ECM composition and turnover.



## Introduction

The vascular system develops at an early stage of embryogenesis to supply the growing tissues with oxygen and nutrients and to remove metabolic products. Hematopoietic cells circulate through this vascular system to the tissues in need. With the constant growth of the embryo and the development of organs, the vascular system expands and remodels to provide continuous supply. The ability of ECs to migrate, guided by extracellular signaling cues, is key for the formation of a vascular network. All vascular ECs, which begin their journey from the paraxial mesoderm, initially migrate to the midline of the zebrafish embryo where they form the dorsal aorta (DA) and PCV, initiating the process of vasculogenesis (1, 2). In a next step, arterial ECs sprout from the DA and migrate further dorsally guided by Vegfa - Kdr/Kdrl-signaling to form the intersomitic vessels (ISVs). When the arterial ISVs (aISVs) reach the dorsal side, they anastomose to form an all-arterial network (reviewed in (3)). In order to build a functional circulatory network, venous ECs will then egress from the PCV guided by Vegfc-Flt4 signaling (4, 5). Venous sprouts then anastomose with an aISV to form a venous ISV (vISV). This event is semi-stochastic, resulting in a balanced ratio of aISVs and vISVs throughout the embryo body. However, if the sprout fails to connect, the venous and lymphatic progenitors migrate further dorsally to the horizontal myoseptum where they accumulate as parachordal lymphangioblasts (PL). These cells will later form the lymphatic system, consisting of lymphatic ISVs and the thoracic duct (TD), located between the DA and PCV (3, 6, 7).

The vascularization of an embryo is a complex, multistep process orchestrated by Vegf-Vegf receptor signaling (Vegfa/Kdrl/Kdrl and Vegfc/Flt4) and downstream activation of pErk (8, 9). Vegf availability is strictly controlled by a multitude of regulators. While much research has focused on these extracellular cues and their downstream pathways, relatively little is known about the cell-intrinsic cues and regulation of cellular structure. Cells are surrounded by an ECM that critically influences their responsiveness to cues in the environment. For instance, hyaluronan (HA) is an integral part of the ECM capable of inducing Vegf release through binding, in its short polymeric form (o-HA), to the low-affinity co-receptor CD44 (10, 11). Availability of o-HA is partly regulated by endocytosis and degradation following the binding to scavenger receptors such as Stabilin 2 (Stab2). Knockdown (KD) of *stab2* reduces pErk in arterial cells, which leads to defects in secondary angiogenesis and lymphangiogenesis in zebrafish (12, 13). Moreover, Vegf is known to act as a negative regulator of *stab2* expression (12), highlighting the interwoven regulatory actions of Vegf- and HA-signaling.

While the Vegf- and HA-signaling cascade has been uncovered, it remains unclear how cells intrinsically regulate ECM density and thereby their response to extra-cellular signaling cues such as Vegf. We found here that *stab2* expression is regulated by the MT-binding protein Clasp2. We have previously shown that loss of Clasp2 affects the stem cell properties of mouse and zebrafish HSPCs. In mouse, this occurs through the blockage of HSC precursor maturation, loss of self-renewing potential, and premature differentiation through enhanced lysosomal degradation and defective trafficking of the important cell surface receptor c-Kit (37). We also demonstrated that Clasp2 is critically involved in the formation of an centrosomal MT network emanating from the Golgi that is essential for the transport of vesicles as part of the secretory pathway. Here, using the zebrafish model, we show that loss of Clasp2 also has a strong impact on secondary angiogenesis and lymphangiogenesis via the deregulation of HA-signaling and thereby the composition of the ECM. We hypothesize that Clasp2 affects EC dynamics through defective ECM turnover as a result of an altered secretory and endosomal pathway, influencing EC migratory behaviors.

## Results

### Clasp2 is involved in the regulation of *stab2* expression in venous ECs

To approach the question whether Clasp2 plays a role in the regulation of migrating endothelial or endothelium-derived cells in an unbiased manner, we performed scRNA-seq of *kdr1:mCherry+cd41:eGFP+* HSPCs (Supplementary Figure 1A) and total *kdr1:mCherry+* ECs (Supplementary Figure 1B) from zebrafish embryos. Cells were sorted from the trunk, including AGM and CHT, of 40hpf *clasp2*mut[-4bp; -10bp] and age-matched wildtype (WT) embryos (Figure 1A, Supplementary Figure 1). An unsupervised clustering approach allowed for annotation of cellular identity, based on known marker genes (Figure 1A-D; of note, t-SNE displays both *kdr1:mCherry+cd41:eGFP+* and total *kdr1:mCherry+* cells sorted from WT and *clasp2*mut embryos). The expression of *sox18* (Figure 1B), *etsrp* and *dll4* (Supplementary Figure 1 C, C', C'') demarcates the vascular endothelium. This population could be further subdivided in arterial ECs based on *efnb2a* (Figure 1C) and *notch1b* (Supplementary Figure 1D, D') expression, and in venous ECs characterized by *dab2* (Figure 1D), *lyve1b* and *stab1* (Supplementary Figure 1 E, E', E'') expression. All populations encompassed WT and *clasp2*mut cells.

GO term biological process and KEGG analysis of the differentially expressed genes (DEGs) between all WT and *clasp2*mut cells (independent of sorted cell types) revealed an increased regulation of protein catabolic processes, associated with an increase in lysosomal and phagosomal pathways upon loss of Clasp2 (Supplementary Figure 1F, G). Accordingly, among the few upregulated genes in the vascular endothelium of *clasp2*mut embryos were *stabilin-2 (stab2)*, *TIMP metalloproteinase inhibitor 2b (timp2b)*, *legumain (lgmn)*, and *cathepsin La (ctsla)* (Supplementary Figure 1H), all being associated with ECM turnover and lysosomal degradation. Of note, the aforementioned upregulated genes were most highly expressed in the venous EC population (Figure 1E, Supplementary Figure 1I, J, K). Among the downregulated genes (Supplementary Figure 1H) was *hyaluronan and proteoglycan link protein 1a (hapln1a)*, an important connector of neurocan/versican and the hyaluronan network (18, 19), further indicating a regulatory role of Clasp2 in ECM composition.

Because the top upregulated gene upon loss of Clasp2 was *stab2*, a scavenger receptor for o-HA, connected to endocytosis and lysosomal degradation of this ECM component, we further investigated the potential role of this particular gene (20-22). Whole-mount *in situ* hybridization (WISH) for *stab2* verified its expression in the caudal vein and CHT region of 40hpf embryos (Figure 1F). Moreover, 40% of *clasp2*mut embryos expressed high levels of *stab2* in the CHT and caudal vein, while only 10% of WT siblings showed a comparably high expression level (Figure 1F, G), as expected from our DEG analysis.

Overall, our scRNA-seq data suggest a role for Clasp2 in maintaining a proper balance in ECM turnover and lysosomal degradation in venous vascular ECs, by controlling ECM-associated genes such as *stab2*.

### Clasp2 affects arterial-venous specification through regulation of the HA-network.

Given the requirement of Stab2 for both venous specification and lymphangiogenesis (12, 13), and HA's pivotal role in angiogenesis (23), we investigated the regulatory connection between Clasp2, Stab2 and the HA network. First, we focused on the role of Clasp2 in secondary venous sprouting. To visualize and quantify aISVs and vISVs, we used the transgenic reporter line *Tg(flt4:YFP/dll4:Gal4xUAS:RFP)* in which venous ECs are YFP+ and arterial ECs are RFP+. Morpholino-mediated KD of *clasp2 (clasp2MO)* in the above-mentioned line resulted in reduced venous *flt4:YFP* expression (Figure

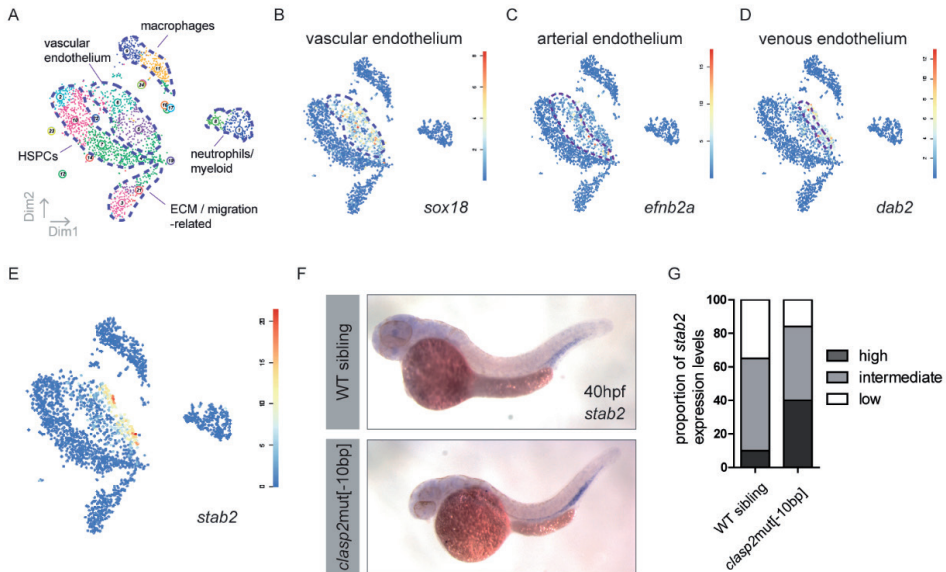


**Figure 1. Clasp2 is involved in the regulation of *stab2* expression in venous ECs.** (A) t-SNE representation of RaceID run on scRNA-seq data of 40hpf *kdrl:mCherry+* sorted ECs and *kdrl:mCherry+ cd41:eGFP+* sorted HSPCs from the trunk of 40hpf *clasp2* mutant and age-matched WT zebrafish embryos. Populations were assigned based on known marker genes. (B-D) The vascular EC population was denoted based on (B) *sox18* expression, (C) arterial endothelium based on *efnb2a* and (D) venous endothelium based on *dab2* expression levels among other genes (see supplementary figure 1C-E). (E) High *stab2* expression is confined to the venous EC population. (F) WISH for *stab2* on 40hpf WT and *clasp2mut[-10bp]* siblings. (G) Quantification of *stab2* expression levels by WISH on 40hpf WT and *clasp2mut[-10bp]* siblings (n=2; 20 wt, 25 *clasp2mut[-10bp]* embryos).

2A dark green arrows, Figure 2B light green arrows, middle panels) and increased arterial *dll4*:RFP expression when compared to non-injected siblings (Figure 2A light red arrows, Figure 2B dark red arrow, bottom panels, Figure 2D, E). Quantification of aISVs versus vISVs resulted in a ratio of 1 in non-injected sibling embryos and a ratio >1 in *clasp2* morphants (ratio aISV/vISV = 1.6), revealing a reduced number of vISVs in *clasp2* morphants (Figure 2C (non-injected compared to *clasp2*MO)).

To verify whether a similar effect on arterial-venous differentiation was detectable in *clasp2* mutant embryos, we performed WISH for arterial markers (Supplementary Figure 2A, B) on 40hpf embryos. *clasp2mut[-10bp]* showed increased numbers of *dll4* expressing aISVs compared to WT siblings, although not statistically significant (Supplementary Figure 2B, first panels, Figure 2C). The expression of other arterial markers such as *notch1b*, *notch3* and *efnb2a* was not changed in *clasp2mut[-10bp]* embryos (Supplementary Figure 2B, C). Similarly, we assayed the expression pattern of venous markers (Supplementary Figure 2D, E). While *vegfc* and *flt4* expression seemed reduced, *efnb4a* expression was not changed in *clasp2mut[-10bp]* embryos compared to their WT siblings (Supplementary Figure 2E, F). Of note, *clasp2* morphant and *clasp2* mutant embryos showed an increase in non-perfused ISVs at 2-4dpf, indicating that ISVs did not form a functional lumen with neither aorta nor vein (Supplementary Figure 3A, B). However, based on blood flow direction, the ratio of the remaining functional/perfused aISVs/vISVs was almost equal in *clasp2mut[-10bp]* embryos (Supplementary Figure 3C). These data indicate that a subtle impairment of venous sprouting and secondary vessel remodeling might occur in *clasp2mut* embryos.

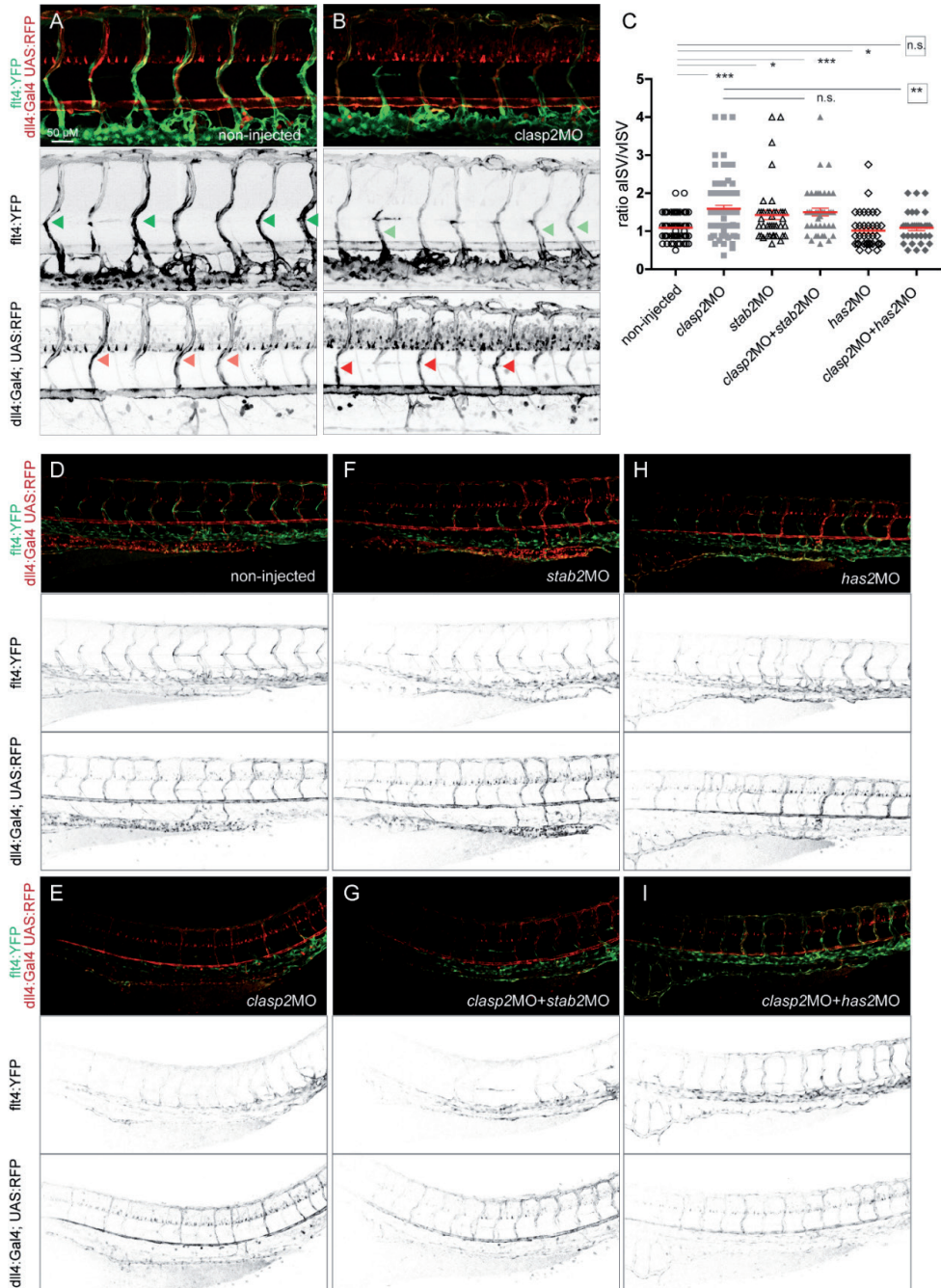


**Figure 2. Clasp2 influences arterial-venous specification through regulation of the HA-ECM network.** (A) Maximal projection of a confocal image of a non-injected *Tg(flt4:YFP/dll4:Gal4xUAS:RFP)* 3dpf embryo. Green arrow heads indicating venous (v)ISVs, red arrow heads indicating arterial (a)ISVs. (B) *clasp2MO* injected *Tg(flt4:YFP/dll4:Gal4xUAS:RFP)* sibling. Light green arrows indicating decreased *flt4:YFP* expression, dark red arrows indicating increased *dll4:RFP* expression compared to the non-injected sibling. (C) Ratio of aISVs versus vISVs in the 15 somites area, starting proximal at the yolk sac elongation, for both sides of the embryo



in non-injected (n=8, 44 embryos), and *clasp2* (n=5, 38 embryos), *stab2* (n=3, 20 embryos), *clasp2+stab2* (n=2, 20 embryos), *has2* (n=3, 18 embryos), *clasp2+has2* (n=3, 16 embryos) morphants at 3dpf. Error bars, mean  $\pm$  SEM. n.s., not significant. \*\*\*P<0.001, \*\*P<0.01, \*P<0.05, square indicates significant rescue. Mann-Whitney U test. (D-I) representative confocal images of (D) non-injected embryos, and (E) *clasp2*, (F) *stab2*, (G) *clasp2+stab2*, (H) *has2*, (I) *clasp2+has2* morphants at 3dpf. ISV, intersomitic vessels.

If loss of Clasp2 leads to an increase in the HA scavenger receptor *stab2* on RNA level, we hypothesized that a reduction of *stab2* expression might rescue the A/V specification phenotype in *clasp2* morphants. Morpholino-mediated KD of *stab2* at half the reported dosage resulted in a reduced number of vISVs (ratio(aISV/vISV)=1.4) (Figure 2C (non-injected compared to *stab2*MO), 2F), as previously reported (12). Notably, co-injection of *clasp2* and *stab2* morpholino did not rescue the A/V phenotype, nor strongly reduced the number of vISVs further (ratio aISV/vISV = 1.5) (Figure 2C (non-injected and *clasp2*MO compared to *clasp2*MO+*stab2*MO), G). However, while the KD of *has2*, the synthetase of HA in the vascular system, did not influence A/V specification alone (ratio aISV/vISV = 1.0) (Figure 2C (non-injected compared to *has2*MO), 2H), the co-injection of *has2*MO with *clasp2*MO rescued the venous impairment (ratio aISV/vISV = 1.1) (Figure 2C (non-injected and *clasp2*MO compared to *clasp2*MO+*has2*MO), 2I).

Our data thus show that Clasp2 regulates secondary venous sprouting. Furthermore, the inhibition of HA synthesis through *has2* KD rescued the arterial-venous specification defect phenotype observed in the absence of Clasp2.

### **Clasp2 is required for lymphangiogenesis partially acting through the Stab2 receptor**

Venous and lymphatic progenitors are ontogenetically closely related and possess a high degree of plasticity. *Stab2*, which is regulated by *HoxC9*, is also required for lymphangiogenesis, further highlighting the close relationship between venous and lymphatic angiogenesis (13). In line with our previous observation, *clasp2* mutant and morphant embryos develop severe oedema at 5dpf (data not shown), suggesting that lymphangiogenesis might be affected. To determine Clasp2 effects on lymphangiogenesis, we quantified the formation of PLs and TDs at 4dpf in *fli1a*:GFP+ embryos that express GFP in all vascular ECs. KD of *clasp2* led to a strong decrease in the number of PLs (orange arrows and line) and TDs (blue stars and line) as compared to non-injected siblings (Figure 3A, B, C, D, E). As previously reported, we found that the KD of *stab2* had a negative effect on lymphangiogenesis (fewer PLs and TDs), although less severely than with *clasp2* KD (Figure 3B, C, F). Loss of both *Stab2* and *Clasp2* (double morphants) partially rescued the formation of PLs (Figure 3B, G) but strikingly not of TDs (Figure 4C, G) when compared to non-injected siblings and *clasp2* morphants. These data suggest that a normalization of the *Stab2* levels in *clasp2* morphants is sufficient to rescue PL but not TD formation. KD of *has2* also reduced the numbers of PLs by a third and TDs by half (Figure 3B, C, H), but double KD of *has2* and *clasp2* only partially rescued PL formation (Figure 3B, I) and had no positive effect on TD formation (Figure 3C, I). While other factors can partially compensate the absence of *Clasp2* for PL formation, our data show that *Clasp2* is critically required for TD generation.

Upon close inspection of the aortic and venous segregation in *clasp2* morphants, it was apparent that the overall distance between the aorta and vein is drastically shorter (Figure 3A). This close connection between the major axial vessels raises the possibility that lymphatic progenitors might be sterically hindered from forming the TD. If *Clasp2* is indeed essential for the proper spacing, this would explain why the TD phenotype could not be rescued by altering ECM composition through KD

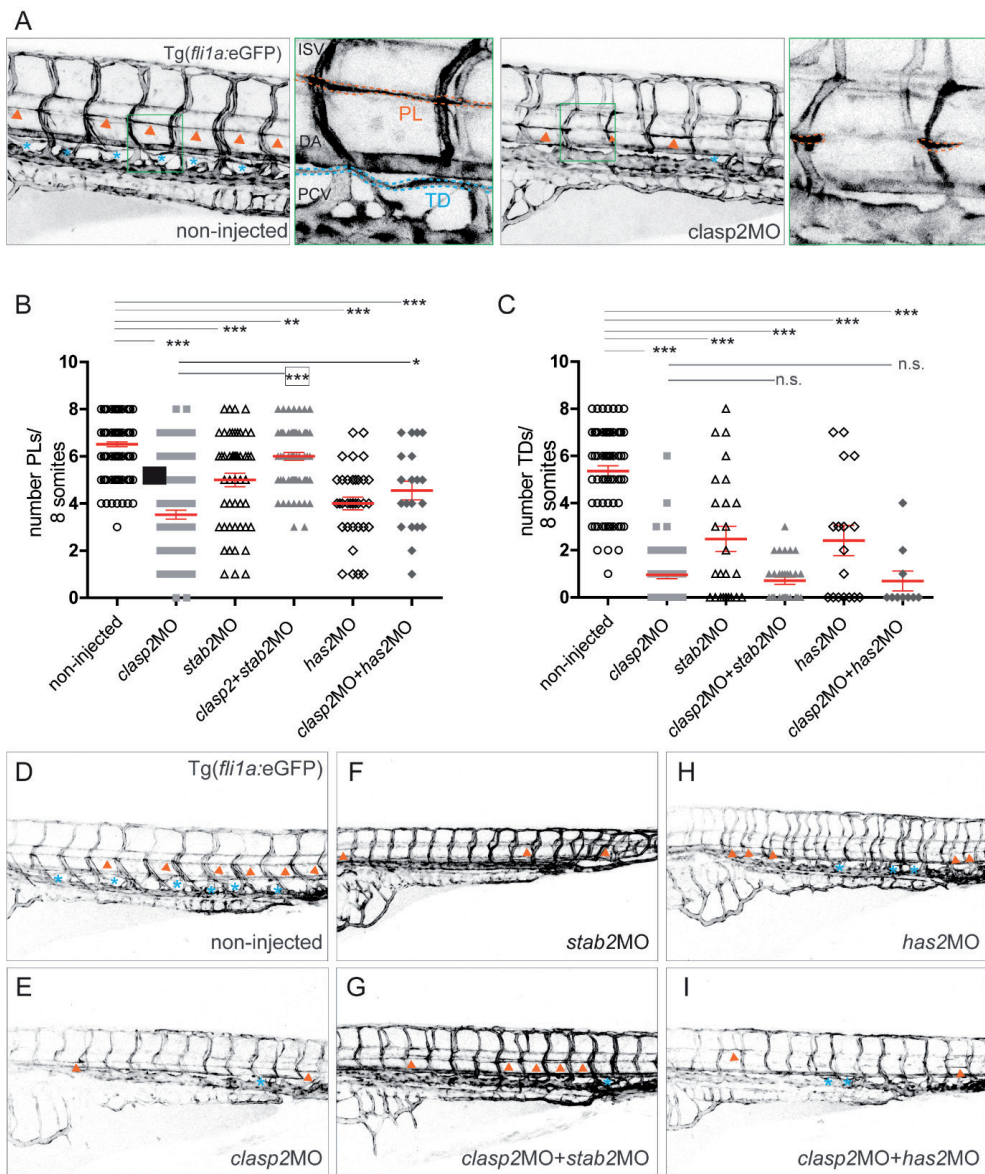


**Figure 3. Clasp2 acts on lymphangiogenesis through the regulation of Stab2 receptors and ECM composition.** (A) Representative confocal image of *Tg(fli1a:eGFP)* embryos at 4dpf, non-injected and *clasp2* morphants. Close-up region around the PL and TD is demarcated by a green square. Orange arrows and dotted lines indicating the PLs, blue stars and dotted lines the TDs. Dorsal aorta (DA), posterior cardinal vein (PCV), intersomitic vessel (ISV), PL (parachordal lymphangioblast), thoracic duct (TD) (B) Quantification of PLs corresponding in the region including the 8 somites over the yolk sac extension at both sides in non-injected (n=8, 79 embryos), *clasp2* (n=6, 61 embryos), *stab2* (n=3, 21 embryos), *clasp2+stab2* (n=3, 32 embryos), *has2* (n=3, 17 embryos), *clasp2+has2* (n=3, 10 embryos) morphants at 4dpf. \*\*\*P<0.001, \*\*P<0.01, \*P<0.05, square indicating the significant rescue. Mann-Whitney U test. (C) Quantification of TDs in the region including the 8 somites over the yolk sac extension in non-injected, *clasp2*, *stab2*, *clasp2+stab2*, *has2*, *clasp2+has2* morphants at 4dpf (same number of embryos as in (B)). n.s., not significant. \*\*\*P<0.001. Mann-Whitney U test. (D-I) Representative confocal images of *Tg(fli1a:eGFP)*+ (D) non-injected, (E) *clasp2*, (F) *stab2*, (G) *clasp2+stab2*, (H) *has2*, (I) *clasp2+has2* morphants at 4dpf.



of either *stab2* or *has2* in *clasp2* morphants. Importantly, while inhibition of HA synthesis through *has2* KD rescued A/V specification in *clasp2* morphants, it only partially improved PL formation. Only the inhibition of *Stab2*, the scavenger receptor that removes HA from the extracellular space, significantly improved PL formation in *clasp2* morphants. This important difference points to the need for a precisely balanced ECM composition and turnover for intact signaling and downstream migratory behavior of venous and lymphatic ECs.

### Clasp2 impacts the emergence dynamics and anchorage of HSPCs newly produced in the embryonic aorta

Our previous study has demonstrated the requirement of *Clasp2* in the efficient formation of HSPCs in the aorta (37). Indeed, *clasp2* mutant zebrafish, which display a curved body axis, had reduced numbers of *runx1+* and *cd41:eGFP+* cells in the aorta, both markers identifying HSPCs. In absence of *Clasp2*, hemogenic ECs underwent

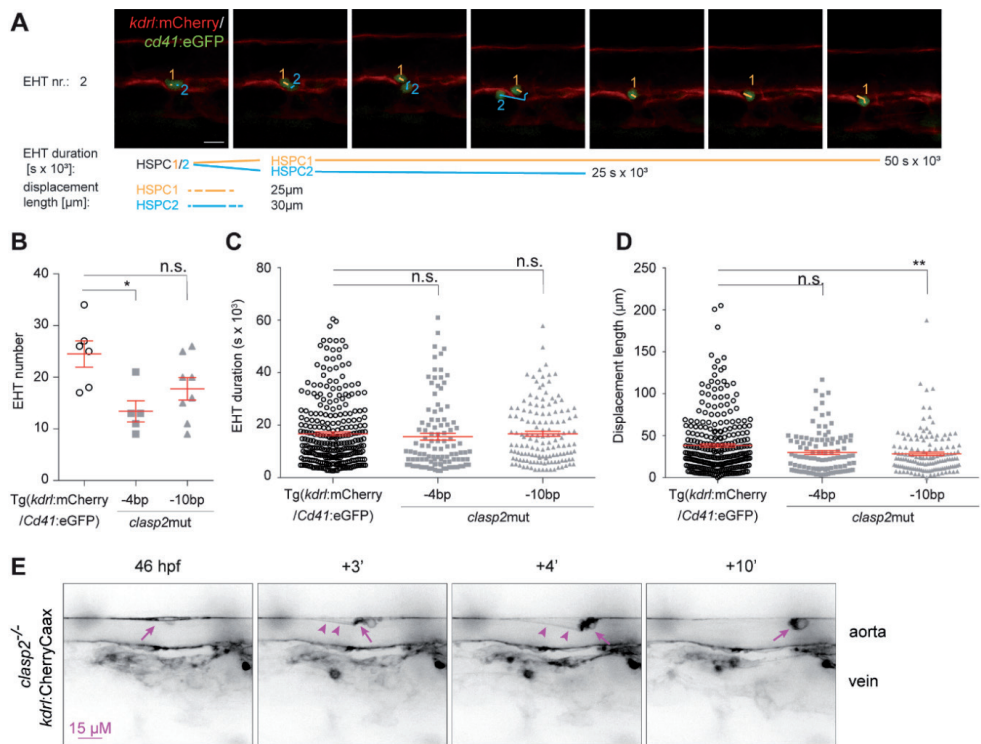


**Figure 4. Altered HSPC dynamics in the aorta in the absence of *Clasp2*.** (A) Stills of Movie 1 showing the emergence of *cd41:eGFP+* HSPCs from the *kdr1:mCherry+* floor of the aorta in a WT embryo. Exemplary schematics for the quantifications displayed in B, C and D; HSPC1 in orange, HSPC2 in blue. (B) Graph representing the number of newly emerging *cd41+* cells (representative of the number of EHT event) per stack after live imaging of WT and *clasp2mut* zebrafish at 36-53 hpf (n=7 independent experiments, with a total of 6 WT, 5 *clasp2mut*[-4bp] and 8 *clasp2mut*[-10bp] embryos). (C) Graph showing the emergence duration in seconds (s) of *cd41+* HSPCs in WT and *clasp2mut* embryos. (D) Graph representing the displacement length (in μm) of the newly emerged *cd41+* HSPCs in the sub-aortic space of WT and mutant zebrafish at 36-53 hpf. (E) Live confocal time-lapse imaging of a *kdr1:CherryCaax+ clasp2mut*[-10bp] embryo. Extrusion of an EC from the roof of the aorta. Arrows indicate cellular extension anchoring the EC to the endothelium. Scale bar, 15 μm. (B-D) n.s., not significant. \*\*P<0.01, \*P<0.05, Mann-Whitney U test.

EHT in the aorta, but at a lower frequency. Based on our current findings in venous and lymphatic ECs, we investigated whether other EC-derived cells, i.e., HSPCs, might display a similarly altered migratory pattern upon loss of Clasp2.

To determine whether the EHT dynamics were affected, we performed live time-lapse confocal imaging and different types of quantifications during the timeframe of active hematopoiesis in the aorta (40-52hpf). *clasp2*mut lines were crossed into a reporter background to identify HSPCs (*cd41:eGFP+*) emerging from the endothelium (*kdr1:mCherryCaax+*). First, we tracked the number of emerging HSPCs (hereafter referred to as EHT number); second, the duration between the emergence and the entering of *cd41:eGFP+* HSPCs into the vein circulation (thereafter referred to as EHT duration); and third, the displacement measuring the distance travelled by *cd41:eGFP+* HSPCs (referred to as displacement lengths) (Figure 4A). Fewer *cd41:eGFP+* HSPCs were found emerging from the ventral aortic endothelium in *clasp2*mut[-4bp] with curved body axis (Figure 4B), in line with our previous observations (37). Of note, the same tendency was detected for *clasp2*mut[-10bp] embryos, although not statistically significant (Figure 4B). The duration of HSPC emergence was similar in *clasp2*mut and WT embryos (Figure 4C), whereas the HSPC displacement was significantly decreased in *clasp2*mut aortas (Figure 4D). Therefore, fewer successful EHT events occur that allow HSPCs to emerge from the endothelium, there is also a change in EHT dynamics and HSPC migratory behavior.

To determine whether *clasp2*mut HSPCs are more tightly anchored to the endothelium after emergence, therefore affecting their detachment and subsequent migration through the sub-aortic space, the cellular shape and cellular extrusions of HSPCs were visualized with a higher optical resolution. Bridge-like extensions that locally anchored *clasp2*mut ECs while detaching from the endothelium were observed in the roof of the aorta (Figure 4E), which suggests that similar attachment might occur during HSPC emergence. Overall, our imaging data indicate that Clasp2 influences the anchorage of emerging HSPCs to the endothelium and thereby their detachment and/or mobility.

## Discussion

Fundamental insight into how ECs interact with their environment—and, more specifically, how the immediate microenvironment (such as the ECM) influences the migratory behavior of these cells—is of great importance, especially with regards to battling vascularization during tumorigenesis. Here we unravel that Clasp2, a MT-binding protein, is a modulator of ECM composition and turnover through regulation of ECM-associated proteins. Our data demonstrate that loss of Clasp2 leads to a deregulated expression of ECM-modulating molecules, for instance the scavenger receptor of hyaluronan Stab2, in vascular endothelial cells. Our data further suggest that Clasp2 has a role in secondary angiogenesis. Loss of Clasp2 leads to decreased venous secondary angiogenesis and lymphangiogenesis. Moreover, modulation of the HA network through downregulation of either the scavenger receptor or the synthetase of HA rescued different aspects of the vascular phenotypes associated with loss of Clasp2, suggesting that HA-ECM levels and composition are critical for secondary angiogenesis. A similar ECM modulation might be involved in the transient anchorage of hemogenic ECs/emerging HSPCs in the aortic endothelium upon loss of Clasp2 that leads to altered HSPC emergence dynamics.

## Clasp2 plays a role in ECM turnover and lysosomal degradation in vascular ECs

To determine a potential role of Clasp2 in the regulation of migrating ECs and EC-derived cells, such as HSPCs, we chose to sequence the transcriptome of these cell populations from WT and *clasp2*mut[-4; -10bp] embryos. This transcriptional profiling revealed a strong upregulation of ECM-associated genes in *clasp2*mut vascular ECs. Our results highlighted *stab2* as the most upregulated gene in *clasp2*mut venous vascular cells. Other upregulated genes included (i) *timp2*, a protease inhibitor and regulator of metalloproteinases (24), a class of enzymes that plays an important role in ECM remodeling and cell-cell anchorage (25), (ii) *lgmn*, a protease activator in the endo/lysosomal compartment involved in ECM remodeling through the degradation of fibronectin (26) and (iii) *ctsla* that plays a role in the degradation of ECM proteins in cancers (27). The obtained transcriptomic profile strongly suggests a role for Clasp2 in ECM turnover and degradation via the lysosomal pathway, with Stab2 as a key molecule linking the HA-ECM network with the endosomal pathway in venous vascular ECs (Figure 5A, B).

## Clasp2 regulates secondary angiogenesis via modulation of the HA-ECM network

As suggested by the strong upregulation of *stab2* that occurred exclusively within the venous compartment, we found no effect of loss of Clasp2 on vasculogenesis and primary angiogenesis. However, morpholino-mediated KD of *clasp2* unraveled its importance for venous sprouting. Typically, once a functional, perfused connection between venous sprout and the ISV is established, the venous blood flow will support the migration of venous ECs into the ISV that will ultimately displace the arterial ECs. Venous specification is therefore a process of active migration of venous cells rather than *trans*-differentiation (28). To better understand how Clasp2-deficient embryos come to lack vISVs at 3 dpf, further live imaging will be required to visualize whether venous sprouts are not properly generated, not able to connect, and/or not able to efficiently migrate up the ISV. Venous sprouts are initially formed, but they might not be efficient in anastomosing with the arterial ISVs. Under physiological conditions, failed venous anastomosis would typically lead to the migration of lymphatic progenitor cells along the arterial ISV towards the embryo midline to form the PL network. Other lymphatic progenitors would then migrate out to form the TD between the DA and PCV (3, 6, 7). Both parts of the lymphatic network are severely affected by the loss of Clasp2, indicating that indeed a migratory defect might preclude the formation of a functional lymphatic network.

In agreement with the literature, KD of *stab2* led to a venous sprouting defect (12). However, KD of both *clasp2* and *stab2* did not worsen the venous impairment, suggesting that they might be subjected to the same pathway/regulation. Strikingly, inhibition of HA synthesis through KD of *has2* rescued the A/V specification phenotype induced by loss of Clasp2 (Figure 5C). We hypothesize that a reduction in HA-network complexity either releases sequestered angiogenic factors (potentially also Vegfc) and/or leads to a decrease of Vegfa released via CD44 signaling. In turn, Vegfa will not exert its regulatory function on Stab2, allowing Stab2 to further remove HA from the extracellular space. Such reduction of HA and Vegfa might be required to allow venous ECs to sprout towards a Vegfc gradient. Further studies will be needed to determine the contribution of the CD44-Vegf signaling axis to this phenotype, e.g., by knocking down *tmem2*, the enzyme that digests long HA polymers into active o-HA (the ligand of CD44), or by inhibiting the CD44 pathway (29).

While the combined KD of *has2* and *clasp2* only partially rescued the development of PLs, the combined KD of *stab2* and *clasp2* reestablished PL numbers (Figure 5D). In this case, the injection of a lowly effective dosage of *Stab2* MO likely neutralized the overexpression of *stab2* resultant of the *clasp2* KD (as observed from the scRNA-seq data). Importantly, none of the combined KD approaches rescued the TD phenotype. *Clasp2* seems to play an essential role, potentially ECM-independent, in the establishment of a subaortic space. Upon detailed inspection at 3dpf and 4dpf, the DA and PCV remained located fairly close to each other in *clasp2* morphants and mutants. This proximity might sterically prevent TD progenitors from migrating into the space to form the duct. Further time-lapse imaging should shed light onto the development of this particular phenotype.

### **Clasp2 balances ECM density through regulation of the endo-/lysosomal pathway**

The finding that both the inhibition of *Has2* and the reestablishment of lower *Stab2* levels have a positive influence on PL lymphangiogenesis might indicate that a balance in the composition of HA ECM matrix is required. Recently, *Hapln1b* was shown to be important for the maintenance of such balance in ECM composition (30). Hyaluronan and proteoglycan link proteins (encoded by *hapln* genes) are connectors of the versican and HA network (31), which is the network that VEGF165 utilizes for binding (32). Of note, *HAPLN1* is required for immune cell motility (33) and lymphatic vessel integrity (34) in human fibroblasts. Mahony et al. showed that *Hapln1b*, at a specific level, is essential for HSPC specification in the zebrafish aorta. In this context, *Hapln1b* regulates the availability of the important hematopoietic ligand *Kitlb* to bind to its receptor *Kit* (30). Loss of *Hapln1b* reduces the HA network complexity, thereby also the amount of network-bound *Kitlb*, which is then not available for receptor binding. However, increased levels of *Hapln1b* will render the HA network too dense, trapping *Kitlb* and also preventing its binding to *Kit*. A similar mechanism for sequestering other cytokines has been reported (25). Moreover, not *hapln1b*, but *hapln1a* is one of the few differentially downregulated genes in the vascular endothelium of *clasp2* mutant embryos. This isoform was previously reported to be required for maintaining HA stability in zebrafish (35), further emphasizing a fundamental change of the ECM network upon loss of *Clasp2*.

How does a MT-binding protein then modulate ECM composition? *Clasp2* is a critical factor for the establishment of a functional endo-/lysosomal pathway and recycling of extracellular/cell surface proteins, as we have shown for the c-Kit receptor during hematopoiesis (37). Mechanistically, *Clasp2* is involved in anchoring non-centrosomal MTs at the *trans*-Golgi that are the highways for the secretory pathway. We have previously shown that loss of *Clasp2* is associated with dispersed Golgi morphology and an increase in lysosomal activity in HSPCs. The increased expression of lysosomal enzymes, which are associated with ECM degradation that was seen in our scRNA-seq data of vascular ECs, is in line with such a hypothesis. Support comes from a study where CLASP-tethered MTs provided a network for exocytic vesicle transport towards focal adhesions in migrating epithelial cells. The authors further suggested a role for CLASPs in regulating vesicular transport as part of a secretory pathway that would modulate cell-ECM interactions and thereby enable focal adhesion turnover (36). Thus, ECM-remodeling and turnover might indeed be disturbed by dysfunctional secretory and recycling pathways. The altered ECM composition likely prevents important cytokines from binding to their cognate receptors on the cellular surface. Further work will be needed to fully understand the mechanisms by which *Clasp2* modulates ECM composition and influences the migratory behavior of ECs.

## Clasp2 regulates HSPC migratory dynamics in the embryonic aorta

Modulation of the ECM might affect the migratory behavior of other EC-derived cell types such as HSPCs. We have previously shown that Clasp2 is required for the formation of HSPCs within the embryonic aorta, i.e., to obtain an appropriate number of functional HSPCs (Klaus et al., in revision). Through high-resolution imaging and *in vivo* tracing of the migratory behavior of emerging HSPCs, we now recorded that loss of Clasp2 not only affects the number of emerging HSPCs, but also the dynamics of the EHT event. While Clasp2-deficient HSPCs emerge at a normal speed, they travel significantly less far in the sub-aortic space, after egressing from the aortic endothelium and before joining the circulation in the PCV. High-resolution imaging revealed extensive cellular protrusions on the emerging HSPCs (data not shown) and ECs egressing from the endothelium, suggesting that inter-endothelial contacts are not resolved in a timely manner, and emerging cells remain transiently anchored to the endothelium. This might be one of the causes of the partial HSPC maturation blockage and premature differentiation that we previously reported in the aorta of Clasp2-deficient embryos (37).

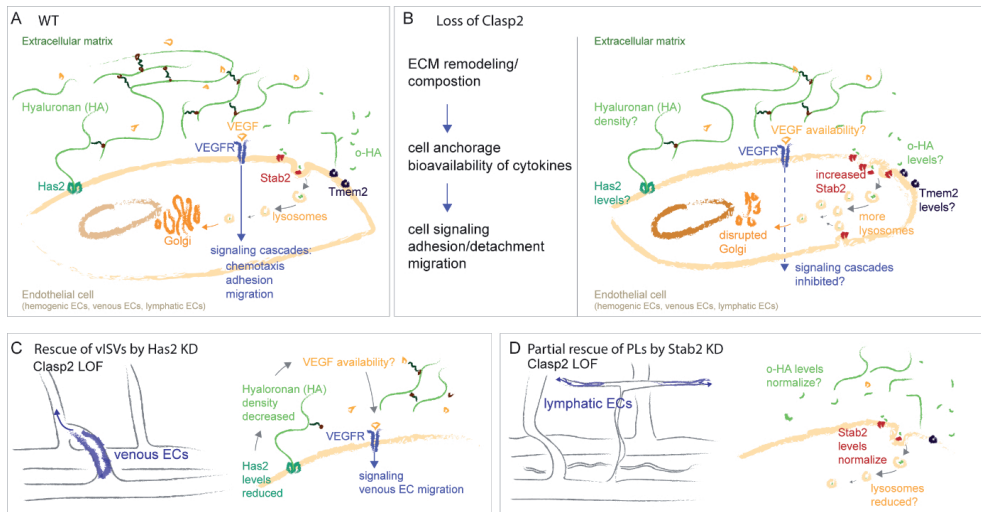


**Figure 5. Model proposing how loss of Clasp2 results in altered ECM composition.**

(A) Schematic of the ECM turnover in WT ECs. Hyaluronan (HA) is synthesized by Has2 and forms long polymers that anchor cytokines such as VEGF. VEGF is the ligand for VEGF receptors; binding of the ligand induces a downstream signaling cascade that controls chemotaxis, adhesion and migration. HA is depolymerized into smaller bioactive molecules by Tmem2. Stab2 is involved in the endocytosis of HA and the degradation in lysosomes. (B) Upon loss of Clasp2, Stab2 expression and lysosomal activity is increased, indicative of disrupted ECM turnover. It is yet unclear how this affects the other factors that are involved in ECM turnover and/or downstream signaling cascades. (C) In loss-of-function (LOF) Clasp2 embryos, venous EC migration is rescued by *has2* knockdown (KD). Reduction of Has2 likely results in decreased HA network density and potentially alters cytokine availability and downstream signaling. Venous intersomitic vessel (vISV). (D) In LOF Clasp2 embryos, the migration of parachordal lymphangioblasts (PLs) is partially rescued by *stab2* KD, likely normalizing Stab2 levels and potentially also balancing endocytosis and lysosomal degradation of HA.

## Concluding remarks

Importantly, all here mentioned cytokines and factors play essential roles and are often deregulated during tumor development. This underscores the importance of fundamental research into the mechanisms behind ECM stabilization, ECM-mediated sequestering of cytokines, and the influence on angiogenesis, to develop better targeted therapies for treating hematopoietic and lymphoid malignancies.

## Experimental model and subject details

### Animals

Experimental animals were maintained and propagated in line with the institutional guidelines. All procedures were executed following the Standards for Care and Use of Laboratory Animals that were approved by the ethical review board of the Hubrecht Institute.

### Zebrafish and embryos

Zebrafish were kept and bred following the guidelines of FELASA and the standard laboratory conditions of the Hubrecht Institute. The following zebrafish lines were used: embryos with *clasp2*mut [-4bp] and [-10bp] mutations (37) or wild type genetic background of the fish lines TL, AB, *Tg(kdr1:mCherry)* (ZFIN ID: ZDB-TGCONSTRUCT-110127-23), *Tg(cd41:eGFP)* (14) *Tg(kdr1:mCherry/cd41:eGFP)*, *Tg(dll4:Gal4;UAS:RFP/flt4:YFP)* and *Tg(dll4:EGFP/fli1a:lifeact-mCherry)*.

Embryos were raised in E3 medium until the required age, i.e., 40 hours post fertilization (hpf) 52hpf, 3 and 4 days post fertilization (dpf), as previously described in (15, 16). To inhibit the development of melanocytes for microscopic observations and in situ hybridizations (ISH), embryos were transferred to E3 supplemented with 0.003% 1-phenyl-2-thiourea (PTU) (15).

## Acknowledgements

The authors thank the present and past lab members for helpful discussion and technical help. We further thank the Hubrecht FACS Facility and Hubrecht Imaging Center for technical support, and Single Cell Discoveries for generating and analyzing the scRNA-sequencing data.

## Author contributions

C.R. and A.K.. conceived ideas and designed the research. with the help of the other authors B.W. and L.Y. A.K generated the *clasp2* mutant fish lines and performed all analyses with the help of L.Y. for cell sorting. B.W. performed time-lapse live-imaging with higher resolution. T.B and J.M. performed the WISH experiments. A.K. and C.R. analyzed and interpreted the experiments with the help of all authors; A.K. and C.R. created the figures and wrote the preliminary manuscript.



## References

1. B. Fouquet, B. M. Weinstein, F. C. Serluca, M. C. Fishman, Vessel patterning in the embryo of the zebrafish: guidance by notochord. *Dev Biol* 183, 37-48 (1997).
2. L. Sumoy, J. B. Keasey, T. D. Dittman, D. Kimelman, A role for notochord in axial vascular development revealed by analysis of phenotype and the expression of VEGF-2 in zebrafish *flh* and *ntl* mutant embryos. *Mech Dev* 63, 15-27 (1997).
3. B. M. Hogan, S. Schulte-Merker, How to Plumb a Pisces: Understanding Vascular Development and Disease Using Zebrafish Embryos. *Dev Cell* 42, 567-583 (2017).
4. L. D. Covassin, J. a. Villefranc, M. C. Kacergis, B. M. Weinstein, N. D. Lawson, Distinct genetic interactions between multiple Vegf receptors are required for development of different blood vessel types in zebrafish. *Proceedings of the National Academy of Sciences of the United States of America* 103, 6554-6559 (2006).
5. B. M. Hogan et al., Vegfc/Flt4 signalling is suppressed by Dll4 in developing zebrafish intersegmental arteries. *Development* 136, 4001-4009 (2009).
6. S. Isogai, J. Hitomi, K. Yaniv, B. M. Weinstein, Zebrafish as a new animal model to study lymphangiogenesis. *Anatomical science international* 84, 102-111 (2009).
7. S. Schulte-Merker, A. Sabine, T. V. Petrova, Lymphatic vascular morphogenesis in development, physiology, and disease. *The Journal of cell biology* 193, 607-618 (2011).
8. S. Koch, L. Claesson-Welsh, Signal transduction by vascular endothelial growth factor receptors. *Cold Spring Harb Perspect Med* 2, a006502 (2012).
9. M. Simons, E. Gordon, L. Claesson-Welsh, Mechanisms and regulation of endothelial VEGF receptor signalling. *Nat Rev Mol Cell Biol* 17, 611-625 (2016).
10. J. F. Murphy et al., Engagement of CD44 modulates cyclooxygenase induction, VEGF generation, and proliferation in human vascular endothelial cells. *FASEB J* 19, 446-448 (2005).
11. L. S. Rodgers et al., Depolymerized hyaluronan induces vascular endothelial growth factor, a negative regulator of developmental epithelial-to-mesenchymal transformation. *Circ Res* 99, 583-589 (2006).
12. M. S. Rost, S. Sumanas, Hyaluronic acid receptor Stabilin-2 regulates Erk phosphorylation and arterial-venous differentiation in zebrafish. *PLoS One* 9, e88614 (2014).
13. S. J. Stoll, S. Bartsch, J. Kroll, HOXC9 regulates formation of parachordal lymphangioplasts and the thoracic duct in zebrafish via stabilin 2. *PLoS One* 8, e58311 (2013).
14. H. F. Lin et al., Analysis of thrombocyte development in CD41-GFP transgenic zebrafish. *Blood* 106, 3803-3810 (2005).
15. M. Westerfield. (University of Oregon Press, Eugene, 2000), vol. 4th.
16. C. B. Kimmel, W. W. Ballard, S. R. Kimmel, B. Ullmann, T. F. Schilling, Stages of embryonic development of the zebrafish. *Developmental dynamics : an official publication of the American Association of Anatomists* 203, 253-310 (1995).
17. B. Weijts, E. Tkachenko, D. Traver, A. Groisman, A Four-Well Dish for High-Resolution Longitudinal Imaging of the Tail and Posterior Trunk of Larval Zebrafish. *Zebrafish* 14, 489-491 (2017).
18. S. Shi et al., Link protein has greater affinity for versican than aggrecan. *J Biol Chem* 279, 12060-12066 (2004).
19. U. Rauch, S. Hirakawa, T. Oohashi, J. Kappler, G. Roos, Cartilage link protein interacts with neurocan, which shows hyaluronan binding characteristics different from CD44 and TSG-6. *Matrix Biol* 22, 629-639 (2004).
20. E. N. Harris, E. Baker, Role of the Hyaluronan Receptor, Stabilin-2/HARE, in Health and Disease. *Int J Mol Sci* 21, (2020).
21. M. S. Pandey, P. H. Weigel, A hyaluronan receptor for endocytosis (HARE) link domain N-glycan is required for extracellular signal-regulated kinase (ERK) and nuclear factor- $\kappa$ B (NF- $\kappa$ B) signaling in response to the uptake of hyaluronan but not heparin, dermatan sulfate, or acetylated low density lipoprotein (LDL). *J Biol Chem* 289, 21807-21817 (2014).
22. M. S. Pandey, P. H. Weigel, Hyaluronic acid receptor for endocytosis (HARE)-mediated endocytosis of hyaluronan, heparin, dermatan sulfate, and acetylated low density lipoprotein (AcLDL), but not chondroitin sulfate types A, C, D, or E, activates NF- $\kappa$ B-regulated gene expression. *J Biol Chem* 289, 1756-1767 (2014).
23. E. L. Pardue, S. Ibrahim, A. Ramamurthi, Role of hyaluronan in angiogenesis and its utility to angiogenic tissue engineering. *Organogenesis* 4, 203-214 (2008).
24. M. M. Bernardo, R. Fridman, TIMP-2 (tissue inhibitor of metalloproteinase-2) regulates MMP-2 (matrix metalloproteinase-2) activity in the extracellular environment after pro-MMP-2 activation by MT1 (membrane type 1)-MMP. *Biochem J* 374, 739-745 (2003).
25. C. Bonnans, J. Chou, Z. Werb, Remodelling the extracellular matrix in development and disease. *Nat Rev Mol Cell Biol* 15, 786-801 (2014).
26. E. Dall, H. Brandstetter, Structure and function of legumain in health and disease. *Biochimie* 122, 126-150 (2016).
27. T. A. Tabish et al., Graphene Oxide-Based Targeting of Extracellular Cathepsin D and Cathepsin L As A Novel Anti-Metastatic Enzyme Cancer Therapy. *Cancers (Basel)* 11, (2019).
28. B. Weijts et al., Blood flow-induced Notch activation and endothelial migration enable vascular remodeling in zebrafish embryos. *Nat Commun* 9, 5314 (2018).
29. J. E. De Angelis et al., Tmem2 Regulates Embryonic Vegf Signaling by Controlling Hyalu-

- ronic Acid Turnover. *Dev Cell* 40, 123-136 (2017).
30. C. B. Mahony et al., Hapln1b, a central organizer of the extracellular matrix, modulates kit signalling to control developmental haematopoiesis. *Blood Adv*, (2021).
  31. A. P. Spicer, A. Joo, R. A. Bowling, A hyaluronan binding link protein gene family whose members are physically linked adjacent to chondroitin sulfate proteoglycan core protein genes: the missing links. *J Biol Chem* 278, 21083-21091 (2003).
  32. S. Nandadasa et al., The versican-hyaluronan complex provides an essential extracellular matrix niche for Flk1. *Matrix Biol* 97, 40-57 (2021).
  33. A. Kaur et al., Remodeling of the Collagen Matrix in Aging Skin Promotes Melanoma Metastasis and Affects Immune Cell Motility. *Cancer Discov* 9, 64-81 (2019).
  34. B. L. Ecker et al., Age-Related Changes in HAPLN1 Increase Lymphatic Permeability and Affect Routes of Melanoma Metastasis. *Cancer Discov* 9, 82-95 (2019).
  35. J. Govindan, M. K. Iovine, Hapln1a is required for connexin43-dependent growth and patterning in the regenerating fin skeleton. *PLoS One* 9, e88574 (2014).
  36. S. J. Stehbens et al., CLASPs link focal-adhesion-associated microtubule capture to localized exocytosis and adhesion site turnover. *Nature cell biology* 16, 561-573 (2014).
  37. A. Klaus et al., CLASP2 safeguards hematopoietic stem cell properties during mouse and fish development. *Cell Reports* 39, Issue 11, 110957 (2022).

## SUPPLEMENTAL DATA

### METHODS

#### Generation of *clasp2* mutant lines by CRISPR/Cas9-genome editing

*clasp2*mut fish were generated in Klaus et al. (37). Briefly, exon 3 in the *clasp2*-205 isoform (NM\_207072) (exon present in multiple isoforms, such as *clasp2*-202 exon8, *clasp2*-204 exon1, see <http://zfin.org/ZDB-GENE-040426-2343#transcripts>) was targeted by Cas9 via the sgRNA GGATGGAAGCAGGCCGTCAT, designed using chochop webtool. sgRNAs were transcribed using the MEGAscript T7 kit (Ambion). The plasmid pCS2-nCas9n (Addgene) was linearized by NotI (Promega) digestion and used as template to transcribe a capped Casp-mRNA using the SP6 mMessage Machine kit (Ambion). Wildtype AB embryos were microinjected at the one-cell stage with purified sgRNA (25ng/μl) and Cas9 mRNA (150ng/μl). Mutagenesis was assessed in the F1 generation (F0 crossed to TL) by PCR (primers: 5'-CCTTTTCG-TGCAGCTTATGTCA-3'; 5'-GGTTAATTGGGCAAATCATTGCT-3') and sequencing of the product. Genome editing resulted in the generation of two mutant lines with a deletion (-4 and -10bp) that resulted in a frameshift and premature stop-codon. *clasp2*mutant[-4bp] and [-10bp] lines were propagated as described above and all analyses were performed on generations >F2.

#### Genotyping

Adult fish >2 months were fin-clipped, or embryos were collected and DNA was isolated. Fish were genotyped by PCR using the primers described above for the F1 generation. Additionally, one primer complementary to the scarred region was used (primers see above, and 5'-GAAGCAGGCCGTCATCGGC-3').

#### Morpholino injections

The morpholino (MO) was designed to target the exon-intron boundary of exon 3 of *Clasp2* (sequence: ACTACGGTCTACAAGAAGCAGTGAG; GeneTools, LCC), which was also targeted by CRISPR/Cas9. For knockdowns, 5 pg of the *clasp2*MO, *stab2*MO (cocktail of 0.625 pg *stab2*MO1 (GTAATCATCATGCCGTTCTTCTAG), 1.75pg *stab2*MO2 (GAGCCAGAAAGAAGAAACTGAAA GT) (12) and 4 pg *has2*MO (12) (AGCTGACCGCTTTATCACATCTCAT) were microinjected per embryo, directly in the yolk of 1-2 cell stage embryos. The embryos were sorted at 3 dpf based on a curved body axis and imaged at 3 and 4 dpf with a Leica stereomicroscope MZ16FA and/or Leica SP8 confocal microscope.

#### Confocal fluorescence imaging of live zebrafish embryos (time-lapse)

Fluorescent images were acquired using a Leica SP8 confocal microscope. Time-lapse live-cell confocal imaging was performed with Zeiss 700 and 900 microscopes. For the image acquisition, embryos were immobilized through anesthesia with 1x tricaine (0.16 mg/ml ethyl 3-aminobenzoate methanesulfonate; Sigma E10521) and mounted in 0.8% low-melting agarose (Invitrogen) in filtered E3 with 0.003% PTU. Embryos were either embedded in 35mm glass bottom dish or in a modified Four-Well WillCo dish (17) covered with 0.8 % low-melting agarose and imaged with a 63x objective. Time-lapse imaging was done at 28.5°C overnight, starting from 30-32hpf, with a ×10.0 fluar dry lens and digital zoom. Confocal planes were typically 2μm and imaged every 10-15 minutes for about 17 hours. Embryos were recovered after imaging and genotyped. Movies were analyzed using the Imaris X software, automatically quantifying *kdrl*+*cd41*+ cells in the manually defined region of the aortic floor.

### Whole-mount *in situ* hybridization

All zebrafish antisense *in situ* hybridization (ISH) probes, except for *stab2*, were kindly provided by Prof. Schulte-Merker (WWU Münster, Germany) and Prof. Le Noble (Karlsruhe Institute of Technology, Germany). For the *stab2* ISH probe, a part of the coding region of *stab2* was PCR amplified (Forward GGAGAATTCTGTTCAGGG-TACTACGGCAG, Reverse CCAGAAGTTCCATGCCCAGTGAGCTCGGA) from a cDNA template and then cloned into pCS2+ plasmid (Addgene) using the XhoI, EcoRI cutting site. Plasmids were linearized and riboprobes were transcribed from the T7 promoter incorporating digoxigenin-11-UTP for detection via antibodies. Briefly, zebrafish embryos were fixed overnight in 4% PFA. Embryos were then dehydrated in methanol and stored at -20°C. In the first step of the ISH protocol, embryos were rehydrated in PBS with 0.1% Tween20 (PBST, Sigma-Aldrich) with decreasing levels of methanol. For permeabilization, embryos were incubated for 3-10 minutes in Proteinase K (10µg/ml) solution and re-fixed in 4% PFA for 20 minutes. The embryos were first equilibrated in hybridization buffer (hyb) for >1h, followed by the hybridization step, an overnight incubation with the anti-sense riboprobe supplemented with tRNA and heparin at 70°C. Next, the embryos were first washed into SSC, then PBST. Before adding the anti-digoxigenin antibody conjugated to alkaline phosphatase overnight at 4°C, embryos were blocked with BSA and sheep serum for 1 hour. The next day, embryos were extensively washed with PBST and transferred into PBST. The enzymatic detection required incubation in NBT/BCIP substrate buffer. Stained embryos were re-fixed in 4% PFA, washed and stepwise transferred into 80% glycerol/PBS for imaging and storage. Embryos were imaged using a Leica stereomicroscope MZ16FA with a Hamamatsu Flash4 LT digital camera.

### Flow cytometry analysis and cell sorting

Embryos were selected at 40hpf based on transgene expression or a curved body axis in the case of *clasp2*mut embryos. Embryos were anesthetized using tricaine before removing the yolk sac and heads with needles. The remaining residues of yolk were removed by pipetting up and down in calcium free Ringer's solution and washing with PBS0. Embryos were dissociated in TrypLE (Gibco, #12604054), by shaking at 800rpm for 1 hour at 32°C and vigorous pipetting. Cells were filtered and resuspended in PBSMQ containing 2mM EDTA, 2% sterile filtered FCS and 0.5µg/ml DAPI. Single cells were sorted on the BD Influx Cell Sorter (BD Bioscience) into 384-well plates containing mineral oil for single-cell RNA-sequencing (scRNA-seq).

### Single-cell RNA sequencing

scRNA-seq was performed and analyzed by the company Single Cell Discoveries, using RaceID according to their standard procedures. The datasets generated during and/or analyzed during the current study will be available in the Gene Expression Omnibus repository.

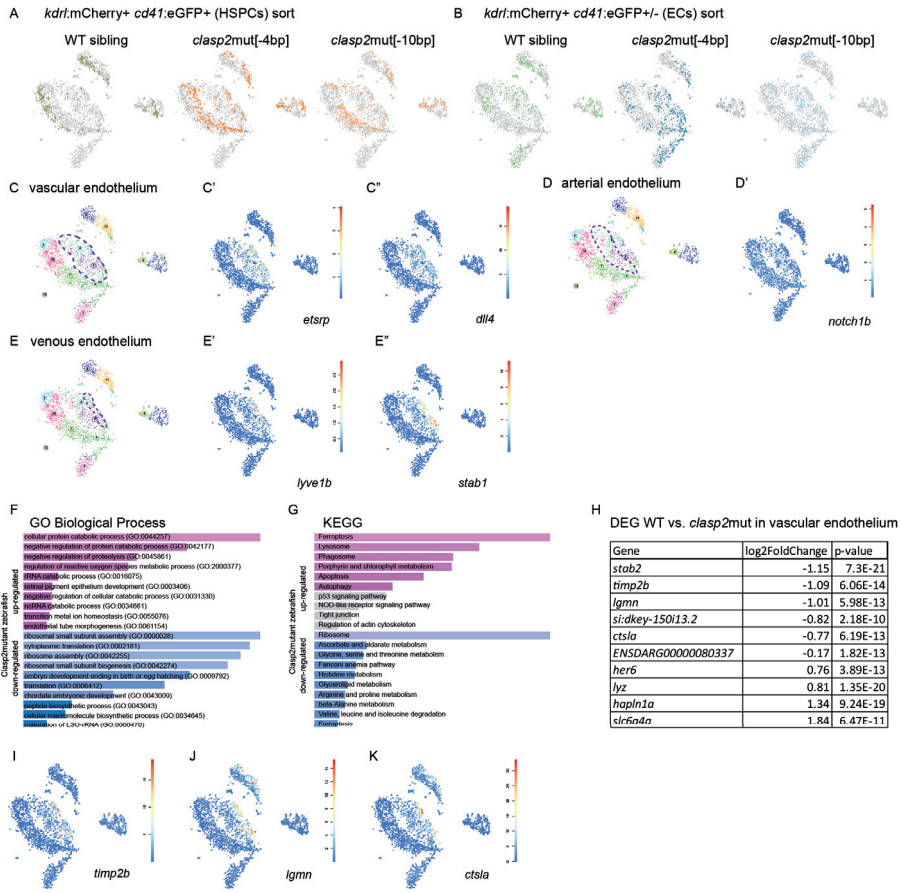
GO biological process and KEGG analysis were done online with FishEnrichr (<https://maayanlab.cloud/FishEnrichr/>).

### Quantification and statistical analysis

Time-lapse confocal live movies were analyzed using Imaris X software. Briefly, emerging HSPCs were recognized in the manually defined region of interest, the floor of the aorta, by dual fluorescent expression of *kdrt*:mCherry and *cd41*:eGFP. Emerging cells were automatically identified as new tracks and their trajectory tracked over the course of the movie. The parameters 'number of tracks', 'duration' and 'displacement' were used for statistical analyses. All other images were processed using FIJI software. For quantifications and statistical analyses, Prism7 software (GraphPad

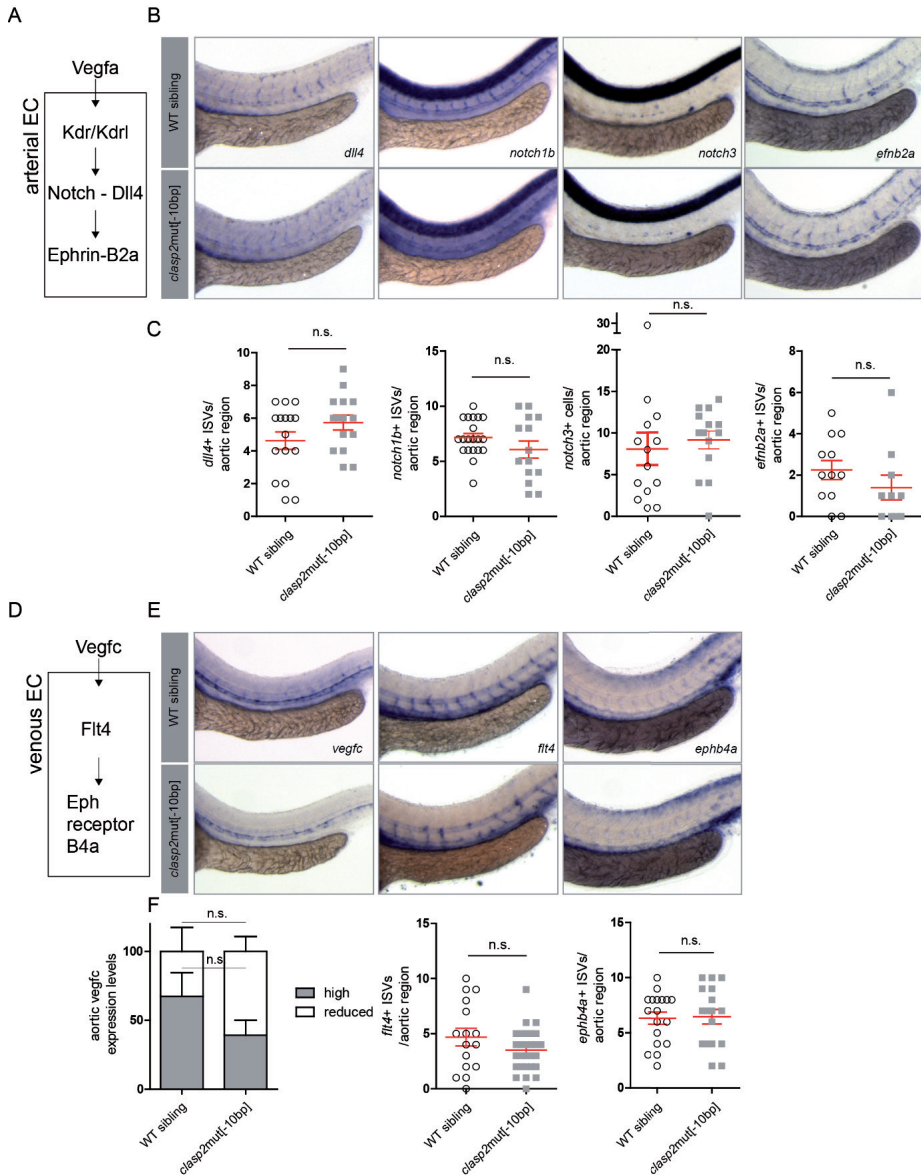
Software, Inc.) was used. Results were expressed as mean  $\pm$  SEM. Mann-Whitney U test was applied to determine the level of significance between two groups.  $P < 0.05$ , 0.01, 0.001 and 0.0001 were considered statistically significant and marked as \*, \*\*, \*\*\* and \*\*\*\*, respectively.  $P > 0.05$  is non-significant (n.s.).

## SUPPLEMENTARY FIGURES



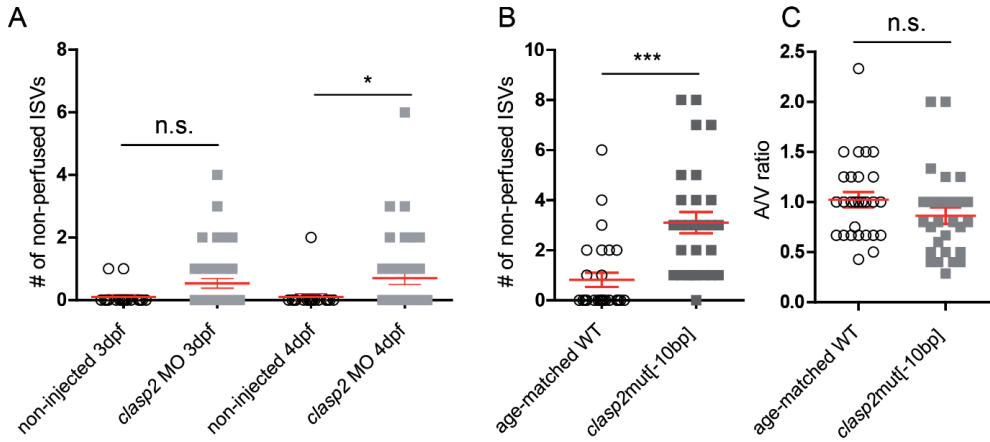
**Supplementary Figure 1. Genes associated with ECM turnover are differentially regulated in the venous endothelium in absence of Clasp2.** (A) t-SNE representation of scRNA-seq data from *kdr1:mCherry+ cd41:eGFP+* HSPCs and (B) *kdr1:mCherry+ cd41:eGFP+/-* ECs sorted from 40hpf trunk regions of WT, *clasp2mut[-4bp]* and *clasp2mut[-10bp]* from left to right. (C) t-SNE representation of all sorted populations. The dotted line indicates the vascular endothelium. (C') Expression of the vascular EC gene *etsrp*. (C'') Expression of the vascular EC gene *dll4*. (D) t-SNE displaying cells from arterial endothelium indicated with dotted line. (D') Expression of the arterial EC gene *notch1b*. (E) t-SNE displaying cells from venous endothelium indicated with dotted line. (E') Expression of the venous EC gene *lyve1b* and (E'') *stab1*. (F) GO biological process analysis of all DEGs between WT age-matched and *clasp2* mutant cells. In purple upregulated genes in *clasp2* mutants compared to WT, in blue downregulated genes. (G) KEGG analysis of all DEGs between WT age-matched and *clasp2* mutant cells. In purple upregulated genes in *clasp2* mutant compared to WT, in blue downregulated genes. (H) Table of DEGs specifically up- (negative log2foldchange) and down- (positive log2foldchange) regulated in the vascular endothelium of *clasp2* mutants compared to age-matched WT. (I-K) t-SNE representation of (I) *timp2b*, (J) *lgmn* and (K) *ctsla* expression.





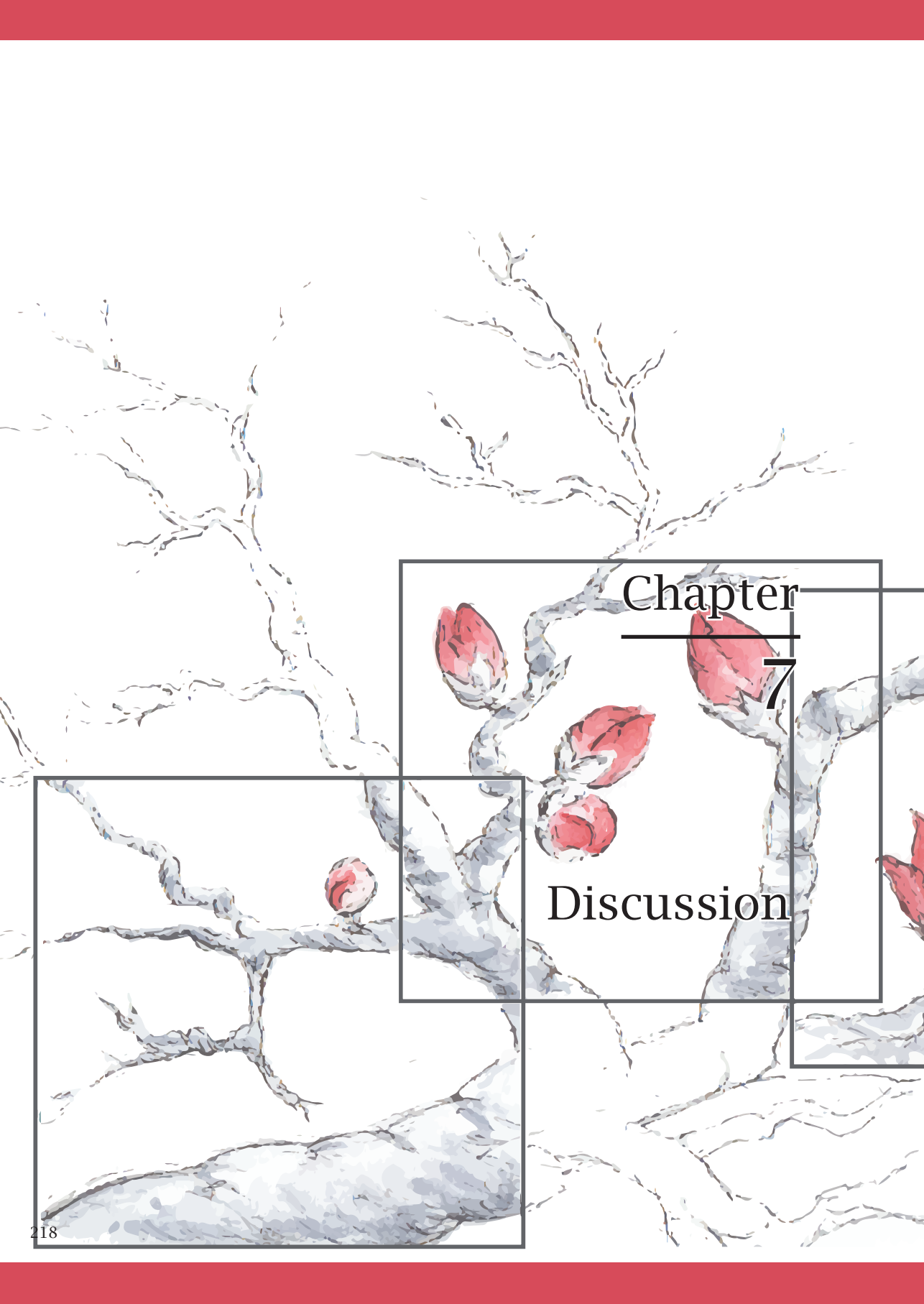
**Supplementary Figure 2. A/V specification is not markedly affected in *clasp2mut*[-10bp] embryos.** (A) Schematic of arterial EC signaling pathway induced by Vegfa. (B) WISH for arterial markers in WT siblings and *clasp2mut*[-10bp] embryos at 40hpf. From left to right: *dll4*, *notch1b*, *notch3*, *efnb2a*. (C) Quantifications of positive ISVs or aortic cells corresponding to the region of the yolk sac extension in WT siblings compared to *clasp2mut*[-10bp] embryos at 40hpf. From left to right *dll4*+ ISVs (n=1, 16 WT, 15 *clasp2mut*[-10bp] embryos), *notch1b*+ ISVs (n=1, 20 WT, 14 *clasp2mut*[-10bp] embryos), *notch3*+ positive aortic cells (n=1, 14 WT, 14 *clasp2mut*[-10bp] embryos), *efnb2a*+ ISVs (n=1, 12 WT, 10 *clasp2mut*[-10bp] embryos). (D) Schematic of venous EC signaling pathway induced by Vegfc. (E) WISH for venous markers in WT siblings and *clasp2mut*[-10bp] embryos at 40hpf. From left to right: *vegfc*, *flt4* and *ephb4a*. (F) Quantifications of expression levels or positive ISVs corresponding to the region of the yolk sac extension in WT siblings compared to *clasp2mut*[-10bp] embryos at 40hpf. From left to right expression levels of *vegfc* (n=2, 27 WT, 19 *clasp2mut*[-10bp] embryos), *flt4*+ ISVs (n=2, 16 WT, 28 *clasp2mut*[-10bp] embryos) and *ephb4a*+ ISVs (n=1, 18 WT, 17 *clasp2mut*[-10bp] embryos). n.s., not significant.





**Supplementary Figure 3. Loss of Clasp2 leads to an increased number of dysfunctional, non-perfused ISVs.** (A) Quantification of non-perfused ISVs corresponding to the region above the yolk sac extension in *clasp2* morphants compared to non-injected siblings at 3dpf (n=2; 10 WT non-injected., 20 *clasp2*MO) and 4dpf (n=2; 10 WT non-injected, 20 *clasp2*MO). (B) Quantification of non-perfused ISVs corresponding to the region above the yolk sac extension in *clasp2*mut[-10bp] embryos compared to age-matched WT embryos at 3dpf (n=3; 28 WT age-matched., 28 *clasp2*mut[-10bp]). (C) Quantification of perfused arterial versus venous ISVs based on the blood flow direction in *clasp2*mut[-10bp] embryos compared to age-matched WT embryos at 3dpf (same n as in (B)). n.s., not significant, \*\*\*P<0.001, \*P<0.05.

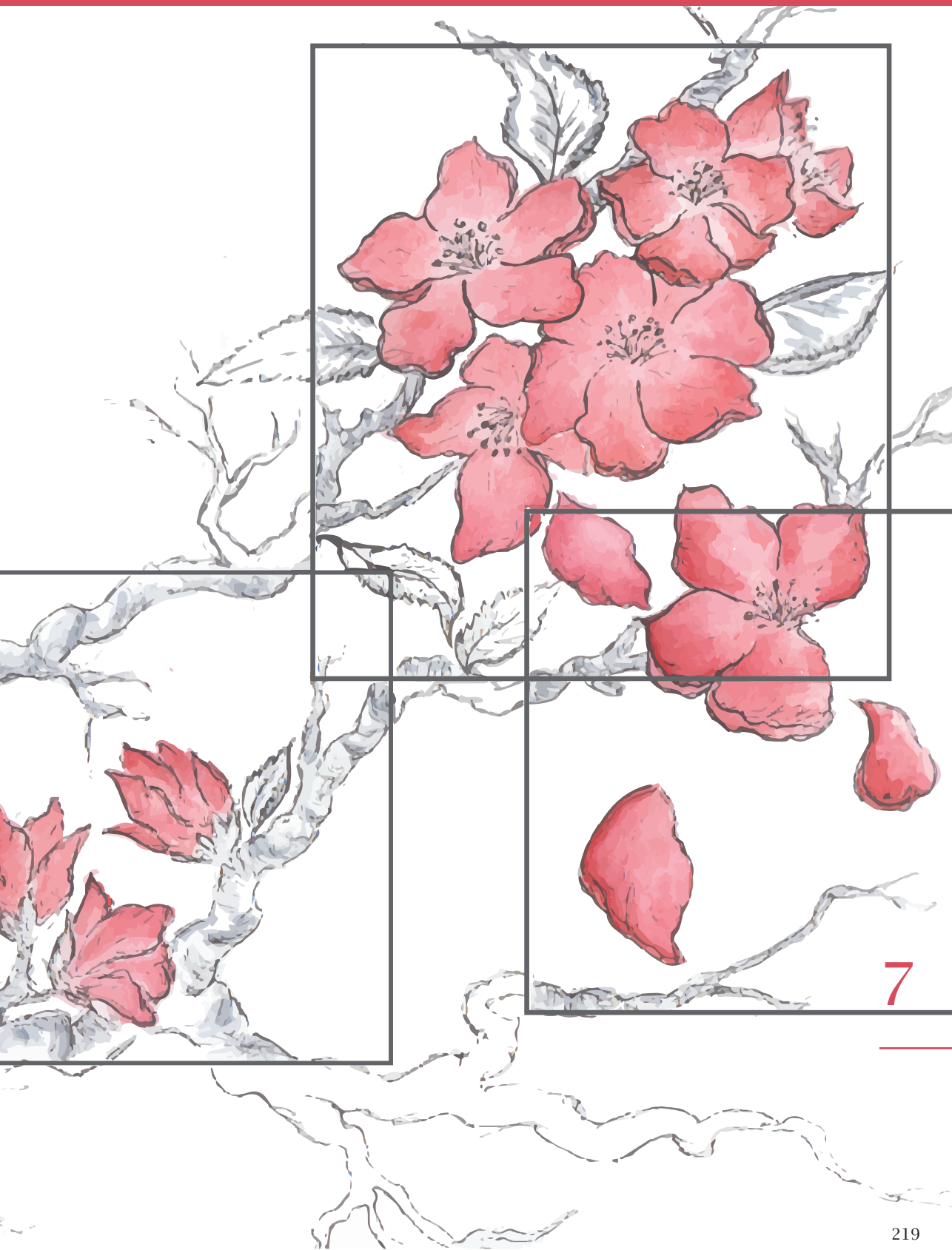




Chapter

7

Discussion



7

The central question of this thesis explores how HSC formation is regulated during embryonic development. In this study, we have seen how multiple cell-intrinsic and -extrinsic (niche) signals interact to form the basis of the regulatory landscape controlling HSC formation. We probed the cellular states leading from an originally endothelial cell, over pre-mature cellular intermediates, to a fully potent HSC state. Additionally, we questioned which factors control this shift in cell fate and whether those factors are intrinsic to the emerging cell, or cues from the surrounding cellular environment. We found previously unknown regulators of the complex network supporting developmental hematopoiesis, with a particular focus on the cytoskeletal regulator CLASP2.

Research has invested in uncovering the mechanisms underlying HSC generation and constant progress are made. However, we are still far from fully understanding this complex process as it occurs in the embryo *in vivo*, and even further away from recapitulating it *in vitro* to produce transplantable HSCs for a clinical use.

## 1. Dissecting developmental hematopoiesis *in vivo* to generate HSCs *in vitro*: the toolbox

### 1.1. Advances in single-cell omics

In recent years a multitude of important factors, developmental trajectories and bottlenecks have been identified through single-cell (or low cellular input) omics methods. The field continues to rapidly grow, and techniques are constantly improving. In **chapter 3, 4** and **6**, single-cell RNA sequencing and tomography sequencing (tomo-seq) were used to interrogate cell-intrinsic and -extrinsic regulatory landscapes, respectively.

Many single-cell transcriptomic studies, such as in **chapter 3**, focused on the identification of cell-intrinsic factors (for instance transcription factors) that control HSPC generation (1-11). From a multitude of species, i.e., mouse, chicken, zebrafish and human, single cells were sorted to enrich for ECs, HECs, EHT cells, pre-HSCs, HSCs and HPCs, and then sequenced. The dynamic molecular changes and regulatory networks as the cell develops from an EC to an HSC state could be followed. Importantly, these studies revealed the heterogeneous nature of the sorted cell populations that was previously underestimated, and allowed for *in silico* purification for further analysis, highlighting the power of such single-cell techniques. Moreover, the finding of new cell surface markers was used to further improve the purification of these rare cell types. However, one major drawback of single-cell techniques is the loss of spatial information upon tissue dissociation that does not allow for identification of the precise location of the cells or regulatory cues specifically coming from the microenvironment.

To address the cell-extrinsic regulatory landscape of HSPC formation in the aorta, we therefore used a tomo-seq approach in **chapter 4**. This sequencing technique was one of the first sequencing-based methods that combined spatial information with the transcriptome of a particular region of interest (12). By sequencing cryosections of thick transversal embryo slices or complete embryos, RNA expression profiles are generated along specific regions or the axis of the embryo. Through comparison of such profiles along the dorso-ventral axis of the embryo with single-cell transcriptomes of sorted HSPCs, we were able to identify ligand-receptor pairs (e.g.,

ADM-RAMP2) that are involved in HSPC-niche interactions (13). The transcriptomic comparison of multiple species yielded conserved environmental factors that regulate IAHC formation, among them SVEP1, which will be discussed in detail below.

With the same aim of identifying spatial transcriptomics, laser capture dissection was combined with RNA-seq of zebrafish (14) and human embryos (7). In the latter study by Crosse *et al.*, a similar approach to ours was chosen to identify cell-cell interactions. Briefly, the transcriptome of single cells sorted from the dorsal aorta was intersected with the transcriptomic profile of the ventral aortic microenvironment in human embryos. Endothelin (that we also highlighted by our tomo-seq approach) was identified as a potent novel ventrally secreted factor that promotes IAHC formation, highlighting the power of such spatial-sequencing approaches.

Current efforts focus on multiplexing these transcriptomic approaches with other single-cell measurements to increase the types or “modes” of information that can be obtained from one cell. Sequencing-based examples are DNA sequencing techniques such as ATAC-seq or ChIC-seq that respectively interrogate chromatin accessibility and epigenetic regulation, next to the transcriptomic readout. Recently, Zhou *et al.* identified two novel mechanistic events in aortic hemopoiesis by means of ATAC-seq: a RUNX1-dependent developmental bottleneck between the pre-HE and HE state and an early wave of CD45+ lymphomyeloid-biased progenitors (LMPs) emerging in the AGM before HSC generation (10).

Promising for the field of hematopoiesis are also the recent developments in the area of lineage tracing or cell fate sequencing technologies. Although these barcoding techniques are still far from perfect, they allowed to trace and study the fate of embryonic and fetal HSCs in adult mice (15, 16) and promise to be applicable to different developmental timepoints. Thus far, these approaches are highly dependent on labeling efficiency, barcode diversity and uniqueness and detection levels. Besides these breakthroughs in RNA- and DNA-sequencing methods, proteomic techniques are also of high interest. So far, flow cytometry analysis has been limited by the spectral overlap between fluorophores. However, new developments where the common fluorescent protein-conjugated antibodies are replaced by chelated antibody labels have improved the resolution (17). This so-called cytometry by time-of-flight (CyTOF) is also applicable to tissue sections. Much like in tomo-seq where spatial information is combined with transcriptomics, spatial information can be linked to the immunophenotype of a specific cell with CyTOF. Other methods stain cells with antibodies that are coupled to unique oligonucleotide sequences (CITE-sequencing) (18). These sequences are accounted for in the library and thereby allow for the correlation of immunophenotype and transcriptome. Yet another technique labels the surface of fixed tissue slides with DNA barcodes that are delivered by a microfluidic system (19). This technique termed DBiT-seq allows for multi-omics, including antibody labelling, imaging, and gene expression profiles at a resolution of 10- $\mu$ m pixels.

In an ideal experiment, we would like to be able to follow the specification and emergence of HSCs by live-cell imaging in the aorta *in vivo*, isolating the emerging cells plus the surrounding niche cells, and obtain transcriptomic, epigenetic and proteomic readouts, whilst retaining spatial information and cellular identity. Considering the advances that have been made solely in the last five years, starting with the sequencing of a mere 100 cells to state-of-the-art multimodal omics, this scenario is no longer unlikely. The newly gained knowledge on HSC production and regulation obtained from these studies has been instrumental for improving current culture techniques to amplify or *de novo* generate HSCs.



## 1.2. Advances in generating HSCs *in vitro*

To date, it remains challenging to generate HSCs. The *in vitro* production of HSCs from iPSCs, ESCs or somatic cells is still limited, providing very few HSC-like cells with restricted multilineage and/or self-renewal capacities. Culture techniques that facilitate the generation, maturation and amplification of HSCs often require native tissues rather than cell lines and are extremely limited in scale of cellular output. Examples that were used in this study are the culture of either intact embryonic tissue as explant (20) or dissociated and reaggregated cells (21, 22), both allowing for the maturation of pre-HSCs into HSCs in a 3D environment.

Another technique that is also based on the self-organization property of cells (basis for the reaggregation culture) are the so-called organoids or mini-organs in a dish (23). However, organoids are thus far not adapted to recapitulate the hematopoietic production *in vitro*. Indeed, these organoids mostly stem from one cellular source which is not the case in tissue explant culture, nor in reaggregates that usually also contain supportive cells, such as OP9 cells that will provide a hematopoietic niche. In contrast, organoids that mimic a hematopoietic stem cell niche with its complex composition out of multiple cell types, such as macrophages, MSCs, smooth muscle cells and ECs, have not yet been developed.

Interesting results were obtained from the culture of embryoid bodies (EBs), an aggregate of ESCs, whose differentiation is induced in presence of defined cytokine cocktails. For a long time, these EBs were only capable of mimicking the early steps of embryonic development such as the formation of the three germ layers. Hematopoiesis in those EBs further cultured with hematopoietic cytokines recapitulated the first primitive wave of blood cell production in the YS (24-29). However, newly adapted culture protocols with a hematopoietic cytokine/growth factor cocktail that includes the before-mentioned factors BMP4, VEGF, SCF, FLT3 and IL-3 among others, allowed for the generation of more definitive hematopoietic cells. Finally, key for an important step forward in the generation of transplantable HSCs *in vitro* was the induction of an intermediate endothelial step through an extended culture period allowing for the maturation along the pre-HE, HE, pro- and pre-HSC maturation axis, mimicking the *in vivo* situation (30). While this development is remarkable, the efficiency of the culture was lacking and the produced HSC-like cells remained molecularly different from their *in vivo* counterparts. Multiple reprogramming approaches tried to either circumvent an arterial endothelial state (31, 32) or to use non-ECs as the starting point for their culture (33, 34). None of these approaches yielded cells that were the exact equal of HSCs generated *in vivo*, emphasizing the importance of recapitulating the physiological sequence of the EHT process.

One promising culture technique that has gained much attention recently is the gastruloid formation. Essentially, EBs are supplemented with a pulse of WNT/ $\beta$ -catenin that is sufficient to induce the growth along an anteroposterior axis, much like an early embryo (35). These embryo-like structures develop somites and mesoderm-derived structures (36). A preliminary study reported the presence of few progenitors (mainly erythroid) and CFU-S in mouse gastruloids (37), indicating that the hematopoietic cells present at 168h of gastruloid differentiation most likely correspond to a developmental stage equivalent to E8.5 to E9.5 of embryonic development, which is one day before the HSC production starts *in vivo*. This shows that a more supportive culture protocol needs yet to be developed to potentially lead to the ultimate goal of generating functional HSCs in these gastruloids. Thus far, we have

only molecular indications of the formation of an endothelium in the gastruloids, but it remains unknown if it might become hemogenic and undergo EHT if cultured in the appropriate condition. Culture timing seems crucial and is thus far restricted to early development, which might preclude the formation of aortic-type HECs that are uniquely able to generate HSCs. Currently, HSC generation in gastruloids is still a distant goal. Nonetheless, the defined nature of the system in terms of cellular input and supplements holds promise to sub-dissect the regulatory landscape of HSC production during, at least, the first steps of embryonic development in the future, without the usage of animals.

To conclude, the discussed *in vitro* techniques and studies are constantly further developed, but to date none of them efficiently creates the appropriate environment to efficiently induce EHT and pre-HSC maturation, and/or to produce functional HSCs and/or to maintain HSC characteristics *in vitro*.

## 2. Intra-cellular regulation of hematopoietic specification

The role of a cell-intrinsic regulatory network of key transcription factors in initiating definitive hematopoiesis in the embryo could not possibly be more essential. To name a few, the actions of the regulatory network around foremost *Runx1*, *Notch*, *Gata2* and *Gfi1* are essential for hematopoietic specification in the aorta. In zebrafish embryos, Dll4-Notch induces the arterial program in *gata2a*-expressing ECs. This expression is required for the induction of *gata2b*, which in turn activates the master regulator *runx1*. Together with *cmyb*, *runx1* will govern the downregulation of the arterial program, including the high *notch* activity, to allow for the shift towards the hematopoietic fate to occur (reviewed in (38). This cell fate switch through the downregulation of arterial genes is conserved in mammals (39).

### 2.1. Balancing the arterial versus hematopoietic program in a continuum of maturation

In **chapter 2**, we described a cellular intermediate state of cells that are in the process of acquiring their adult HSC properties. These pre-HSCs are in a developmental state between HECs and HSCs. Pre-HSCs reside within IAHCs that are transiently attached to the endothelial wall of the DA, where they progressively mature towards a fully potent HSC state. **Chapter 3** highlighted the molecular steps of this maturation process in the embryonic aorta, leading to progressive downregulation of the endothelial program and upregulation of the hematopoietic program. Using scRNA-seq of sorted non-HE and HE cells, and IAHC cells, we could prove that pre-HSCs are indeed part of the IAHC cell population, next to more committed progenitors. On a molecular level, the different pre-HSC populations (type I and II) are relatively similar. Most transcriptional changes occurred between E10 and E11, capturing the program switch, EHT events and the pre-HSC maturation from type I into type II. Our data highlighted the critical regulation of the vascular, arterial, and hematopoietic programs for the various and successive fate switches to occur. However, successful maturation to potent HSCs requires the completion of a continuum of intermediate cellular states before the acquisition of a full stem cell potential. Recent studies underscore this developmental continuum by identifying more intermediate cell states such as pre-states of the hemogenic endothelium with dual angiogenic and hematopoietic potential that are defined by RUNX1 levels and cell cycle status (10, 40).

Of note, intermediate cellular states that would correspond to pre-HSCs in mammals have not yet been identified in zebrafish embryos, which might be due to a lack of reliable markers to identify these intermediate cell population and/or the rapid development of these embryos. Still, it also suggests that there truly is a continuum of maturation, rather than discrete steps, in which the angiogenic program is slowly switched off while the hematopoietic program is upregulated.

## 2.2. Role of the non-centrosomal MT network in receptor trafficking via the secretory pathway

### 2.2.1. c-Kit - hit the threshold

One factor that has an unexpected role in mediating HSC-niche interactions is the MT-binding protein CLASP2. In **chapter 5**, we found that CLASP2 is not only a regulator of adult hematopoiesis (41), but also an important regulator of pre-HSC maturation and of the balance between HSC self-renewal and differentiation in the embryo. Interestingly, CLASP2 seems to influence all of these processes through modulation of the c-Kit-SCF-signaling pathway. Loss of CLASP2 leads to decreased maturation of pre-HSC type I into type II, a loss of functional HSCs, and premature hematopoietic differentiation that ultimately leads to a severe pancytopenia in adult mice. In line with a role for SCF/c-Kit-signaling in pre-HSC maturation (42), SCF-deficient embryos show a reduction of pre-HSCs type II (43), similar to what we saw in *Clasp2*<sup>-/-</sup> mice. Of note, in *Scf* mutants, IAHCs contained fewer cells, which is in agreement with the observation of a (basal to apical) c-Kit gradient in IAHC architecture that correlates with maturation and proliferative status (44). Apical cells with corresponding high levels of c-Kit might be more dependent on SCF activation driving their proliferation; hence, IAHCs should remain smaller. c-Kit signaling not only drives proliferation but also cellular survival and migration (45). Consequently, it is of utmost importance for a cell to sustain appropriate c-Kit receptor levels on its cellular surface.

Recent research efforts in the field of developmental hematopoiesis have highlighted that finely tuned threshold levels and balances (rather than discrete on-off switches) in ligand-receptor expression serve as developmental bottlenecks. The most prominent example is NOTCH. Briefly, Notch signaling is required for HSC formation in the embryo. While it is an essential factor for the induction of the arterial program via Dll4/Notch1, high Dll4-induced Notch activation will later prevent the cellular fate switch towards the hematopoietic lineage (46). Hence, *in vivo* Notch activity is specifically downregulated in IAHC cells, while the endothelial environment maintains active Notch signaling (47, 48). I will come back to the role of Notch-signaling in IAHCs below. The role of SCF/c-Kit signaling in HSC formation is much less clear. While all IAHC cells express c-Kit, and the most potent HPCs and HSCs are found in the c-Kit-high fraction (9), the inhibition of SCF/c-Kit curiously does not affect HSPC formation (49, 50). Very recently, c-Kit expression was mostly associated with the CXCR4-negative HE cells that produce exclusively multipotent progenitors (MPPs), but not HSCs (51). In other words, CXCR4-positive HE cells, from which HSCs originate, have very low levels of c-Kit. However, other studies show that SCF/c-Kit signaling is a driver of hematopoietic maturation in the aorta, as mentioned above. Moreover, in the subsequent niche, the FL, c-Kit is essential for progenitor amplification of both MPPs (including erythro-myeloid progenitors (EMPs)) and HSPCs (52). SCF together with CXCL12 seems to control HSC retention in the FL niche (53). And finally in the BM, SCF/c-Kit activity is involved in maintaining the quiescent state to ensure HSC survival (54). Thus, SCF/c-Kit-signaling is one of the key regulators

during developmental hematopoiesis, involved in many steps along the developmental timeline. Our data indicate that functional c-Kit levels just below a certain threshold are sufficient to severely impact the pre-HSC maturation process, leading to a premature differentiation. Progressive loss of c-Kit results in the progressive loss of the HSC compartment.

c-Kit expression is not restricted to HSCs; multiple other cell types express this cell surface receptor, such as primordial germ cells (PGCs). Here, SCF/c-Kit signaling is crucial for PGC migration and survival within the gut region. Loss of SCF or c-Kit dramatically reduces PGC numbers and remaining PGCs are found mislocalized (55). Furthermore, c-Kit plays an essential role in the induction of differentiation during spermatogenesis (56). In line with these studies, *Clasp2*<sup>-/-</sup> mice are sterile (data not shown), suggesting that other SCF/c-Kit dependent cell types might also be affected in the mutants. In contrast, intestinal stem cells that are surrounded by c-Kit-expressing Paneth cells (57) were unaffected by the loss of CLASP2 (data not shown), potentially emphasizing a cell-intrinsic requirement of c-Kit expression in the stem cell, rather than by the environment.

Recently, an increasing body of evidence indicated that embryonic and fetal hematopoiesis is largely sustained by multipotent progenitors. It seems that, while the newly born HSCs are capable of self-renewal and multilineage differentiation, their initial progenitor output is minimal (58, 59). The multipotent progenitors include the above mentioned MPPs, EMPs and LMPs that derive from (CXCR4-negative) HE in the aorta (10, 52), but also EMPs derived from the YS (60). However, it is not fully clear to which extent YS-derived EMPs/GMPs and early aorta-derived MPPs (10, 51) contribute to the embryonic/fetal HPC pool. In line with the finding that c-Kit is highly expressed by aorta-derived MPPs but not essential for YS EMP production (52), *Clasp2* knockout mice have normal progenitor output from the YS. This indicates that CLASP2 is specifically required in the more definitive HE population in the aorta, rather than in the more lineage-restricted HE of the YS. This further underscores the possibility that hematopoietic specification in YS and aortic HE is mechanistically different, with a different regulatory role for the SCF/c-Kit-signaling axis.

### 2.2.2. Safeguarding Golgi and secretory pathway integrity with CLASP2

In **chapter 5**, we found that besides the above-discussed role of CLASP2 in maintaining c-Kit cell surface levels, CLASP2 also played a role in the maintenance of Golgi integrity *in vivo*. Moreover, loss of CLASP2 was associated with an increase in lysosomal activity. Synthesis, trafficking, degradation and recycling of essential receptors such as c-Kit need to be tightly regulated and balanced. We know that CLASP2 plays multiple crucial roles in the stabilization of the secretory pathway that is responsible for the trafficking of receptors to and from the cell surface.

First, the turnover of receptors at the cell surface via the secretory pathway is dependent on a MT-network that emanates from the *trans*-Golgi network (TGN) in polarized cells (reviewed in (61)). CLASP2 is involved in capturing the MTs in this non-centrosomal MT network. It is not fully clear if CLASP2 supports the nucleation at the Golgi-MTOC or is only involved in the tethering of the MT to the *trans*-Golgi membrane via interaction with the Golgi protein GCC185 (62, 63). The Golgi, and especially the TGN, is the key protein-sorting machinery and trafficking hub. Impairment of this Golgi-anchorage via CLASPs affects the directed transport of vesicles to the plasma membrane (64). Of note, CLASPs not only play a role in the formation

of Golgi-derived MTs, but also for Golgi organization itself. After cell division, when the Golgi needs to reassemble, MTs anchor at these dispersed mini-Golgi stacks, capture the stacks and pull them together (64, 65). Centrosome- and Golgi-derived MTs work together to assemble the fragmented Golgi stacks to the characteristically stacked ribbon structure. Hence, loss of CLASP leads to dispersed Golgi mini-stacks and failure to reassemble them, a phenotype that we also observed in HSPCs after E11 in *Clasp2*<sup>-/-</sup> embryos.

Second, in migrating cells, CLASP2 also mediates the tethering of MTs to the adhesion site of the cell. In this context, LL5 $\beta$  acts in concert with other proteins as a platform that recruits CLASP2 to the vicinity of the focal adhesions (FAs) (66). Here, CLASP aids in attaching and stabilizing the MT, enabling FA turnover. Importantly, loss of CLASP2 protein is associated with fewer MTs connecting to the cell cortex that will also affect vesicular transport and fusion with the plasma membrane.

Third, the MT-network is also important for the transport and tethering of endosomal organelles that are responsible for the degradation and recycling of cell surface material (67). As mentioned above, we see an increase of lysosomal activity upon loss of CLASP2 that contributes to the decrease of c-Kit at the plasma membrane.

We hypothesize that without the stabilizing function of CLASP2, the non-centrosomal MT-network is altered and thereby negatively influences receptor turnover at the cell surface *in vivo*. However, in an *in vitro* study, loss of CLASP1 and 2 by siRNA-mediated knockdown did not result in inefficient post-Golgi trafficking of vesicles to the plasma membrane, as likely assumed (64). Rather, it resulted in random, non-polarized transport, indicating that CLASPs are indispensable for the directionality of the secretory pathway. Consequently, CLASP-deficient cells lacked cellular polarization and persistent migration. Polarized vesicular trafficking and protrusion extension at the leading edge were directly linked, in a CLASP-dependent manner. Importantly, CLASP2-overexpressing cells show similar trafficking and migratory impairments, indicating that CLASP2 is the key factor linking Golgi ribbon assembly with polarized vesicular trafficking and directed migration of cells. In the role as linker, loss of CLASP2 in HSCs might also result in depolarized, random expression of cell surface receptors, such as c-Kit. One future direction yet to be addressed is the potential lack of polarization that might be part of the disrupted stem cell-niche interactions in the AGM, FL and BM.

### 2.2.3. Modes of HSC polarization and migration

Surprisingly, relatively little is known about polarized nature, directed vesicular trafficking and molecular mechanisms of migration in HSCs. Human HSPCs cultured on MSC feeders display a highly polarized morphology with a lamellipodium at the leading edge and a uropod at the rear side (68). Through extension of the lamellipodium and simultaneous retraction of the uropod, HSPCs are capable of migration along a CXCL12 gradient. While RhoA-ROCK1 regulate MT destabilization at the uropod, the authors did not describe the role of stabilizing factors, such as CLASP2, at the leading edge. It is tempting to speculate that, *in vivo*, HSPCs also show a similar mode of directed migration involving CLASPs. Recently, the essential role of another cytoskeletal component, a contractile actomyosin ring, was uncovered in the emergence of HSPCs from the aortic endothelium in zebrafish embryos (69, 70). Both inhibition of the actomyosin ring as well as blood flow led to misorientation of HSPCs towards the aortic space and retention of the cells in the aortic endothelium. However, the molecular mechanisms ensuring correct polarization towards the subaortic space remain unclear. Similarly, it is not yet resolved how the emerging cells then further

migrate through the subaortic space towards the vein from a mechanistic perspective on the subcellular level.

### 3. Extra-cellular regulation of definitive hematopoiesis

#### 3.1. Blood needs to flow

To characterize conserved extrinsic hematopoietic regulators from the immediate environment, i.e., the vascular niche, but also longer-range acting signals, we performed tomographic sequencing of mouse, chicken, zebrafish, and human embryos at the time of HSPC formation/emergence (**chapter 4**). Among many known factors, we identified common genes not previously known to regulate hematopoiesis. Comparison of these factors with the transcriptome of IAHC cells in a secretomic analysis emphasized the intricate interactions of IAHC cells with their vascular niche, through many ligand-receptor couples. Among others, we found the ligand-receptor pair ADM-RAMP2, ADM being specifically expressed in the niche while RAMP2 was expressed by ventral ECs and IAHC cells. Interestingly, ADM acts in the detection of hemodynamic forces via its receptor RAMP2 and the co-receptor CALCRL (71). It has long been known that blood flow is important for proper HSPC formation via a Nitric Oxide-signaling cascade (72, 73) and that downstream activation of PKA (74), prostaglandin E2 (75), adenosine receptor expression (76) and Klf2-mediated induction of *runx1* (77), support HSC generation. More recently cilia, that protrude into the lumen of the aorta to sense the shear stress, were shown to be important for hematopoietic induction (78). These cilia provide a platform for Notch signaling and as such they are downregulated in the process of commitment to the hematopoietic lineage. Less is known about the upstream mediators of NO-signaling. While described as a regulatory pathway for blood pressure (71), ADM-RAMP2/CALCRL activation might be a missing mechanistic link in hematopoietic regulation. As vasodilator, ADM is released in response to the activation of a mechanosensitive channel, PIEZO1. Upon binding to RAMP2/CALCRL and several intermediate steps, cAMP levels increase in the cell, leading to PKA activation, subsequent eNOS phosphorylation and NO release. ADM-RAMP2/CALCRL also act upstream of the PI3-K/AKT signaling pathway, similarly leading to the activation of eNOS and subsequent NO release (reviewed in (79)). Importantly, downregulation of *Nos1* in zebrafish and NOS3 inhibition or deficiency in mice result in the loss of IAHC cells and HSPCs (73). This finding is consistent with ADM-RAMP2/CALCRL being a potential upstream regulator of NOS activity in the formation of IAHC cells. These data emphasize the essential role of hemodynamic forces in HSPC formation, which is often disregarded in *in vitro* culture attempts. Activation of NO-signaling might be an important step for large-scale generation of functional HSCs.

#### 3.2. Extra-cellular matrix - a barrier and supplier

The microenvironment of a stem cell niche not only exerts its regulatory function via the secretion of ligands or biomechanical forces such as shear stress as we discussed above, but also via its biophysical properties. These properties are dependent on the ECM, a highly dynamic structure composed of proteins, glycoproteins, proteoglycans and polysaccharides such as hyaluronan. The ECM plays a pivotal role in stem cell anchorage and orientation in their niche, thereby facilitating asymmetric cell divisions that ensure self-renewal and controlled differentiation. It serves as a migration barrier and/or track, as a signal reservoir for cytokine retention, but the ECM is also



capable of inducing downstream signaling itself (reviewed in (80)). ECM modulation is particularly important during developmental hematopoiesis. For instance, when an HEC/pre-HSC is emerging from the endothelium, it first needs to resolve intracellular adhesion to the neighboring ECs, to form IAHCs and then to successfully detach and enter the blood stream.

### 3.2.1. SVEP1 – an ECM protein regulating IAHC architecture

In **chapter 4** of our studies, we found that the ECM protein SVEP1 regulates IAHC cellularity and HSC activity. SVEP1 is a ligand for  $\alpha 9\beta 1$  integrin (81). Loss of SVEP1 in mouse embryos results in the formation of fewer IAHC cells (in absolute number), but those cells are organized in larger IAHCs with a higher cellularity. It is known that Notch signaling is involved in regulating IAHC size, as discussed above (82). Importantly, *Svep1* mutant embryos have normal levels of downstream effectors of Notch signaling, suggesting that SVEP1 might act in a Notch-independent manner. We hypothesized that SVEP1, as ECM protein and integrin ligand, might influence the cell-cell adhesion of IAHC cells. This hypothesis is in line with our observation of large IAHCs that were still attached to the aortic endothelium at E12.5, when cells typically migrate to the FL (and only small IAHCs usually remain). Of note, large IAHCs seem to anti-correlate with HSC potential, indicating that IAHC size affects the maturation of the residing pre-HSCs or the maintenance of newly formed HSCs.

IAHC architecture was previously reported to relate to the proliferative status of the cells (44). Highly proliferative pre-HSCs are located apically, allowing for a less restricted accumulation of IAHC cells; for proper progression to an HSC state, a slower cell cycle is required. However, loss of SVEP1 did not seem to alter the cell cycle status of IAHC cells. While further research is needed to unravel the underlying mechanism, it is tempting to speculate that larger IAHCs shield the inner cells from necessary environmental cues to fully commit to the HSC fate. IAHC cellularity decreases from 1-19 cells at E10.5, to 1-11 cells at E11.5, which coincides with maturation of pre-HSC type I into type II. Moreover, at E11, HSCs were found to localize almost exclusively to small, ventral IAHCs that contained 1-2 cells (9). Although the early pre-HSC maturation step (type I into type II) was unaffected, the last maturation step towards HSCs could be inhibited in SVEP1-deficient embryos. It is still not fully resolved how, and in which order or manner, the matured IAHC cells detach to further migrate to the FL. Although it is unclear if IAHC architecture is determinant for the maturation status of pre-HSCs, it is somewhat surprising how different the organization is in different species. While mouse embryos have ventral and dorsal IAHCs of different sizes and shapes, ranging from single cells to mushroom-like structures ((83-84), see chapter 2), chicken and human IAHCs are ventrally restricted. Whereas the entire floor of the chicken aorta undergoes EHT (85-87), only a few cells that seem sporadically dispersed in the middle part of the aorta form IAHCs in human embryos (88). Lastly, in the zebrafish model, only single cells are formed, and emergence occurs away from the aortic lumen, towards the vein (89, 90). What controls these differences between species or if they result solely from anatomical constraints remains to be determined.

### 3.2.2. Clasp2 - secondary angiogenesis and lymphangiogenesis - ECM turnover

In **chapter 6**, we observed that loss of Clasp2 in zebrafish embryos not only results in the emergence of fewer HSPCs, but that their emergence dynamics were changed.

Emerging cells transiently remained in contact with neighboring cells through extensive cellular extrusions; they migrated less within the subaortic space. Interestingly, normal migration is facilitated through the degradation of the ECM surrounding the HSPC through the secretion of metalloproteinases (Mmps) (91, 92). Inhibition of Mmp2 activity is known to result in retention of HSPCs in the aortic endothelium, reminiscent of the phenotype that we observed transiently upon Clasp2 depletion. Consistently, depletion of macrophages that express Mmp2 led to a similar phenotype, indicating a role for the ECM in controlling HSPC emergence.

Loss of Clasp2 not only affects hematopoietic progenitors, but also the migratory behavior of other EC progenitors of venous and lymphatic fate. The formation of venous ISVs is strongly dependent on the migration of venous ECs (93). Upon loss of Clasp2, overall fewer vISVs were formed, indicating that Clasp2 influences this directional migration. In a similar migratory process, lymphatic progenitors will travel to the horizontal myoseptum and later further towards ventral and dorsal to form a lymphatic network. Clasp2 deficiency in zebrafish results in a complete failure to develop a functional lymphatic network, indicating a pivotal role of Clasp2 in lymphangiogenesis. Strikingly, genes associated with ECM, ECM-turnover and endosomal degradation were upregulated in venous/lymphatic progenitors upon loss of Clasp2. To highlight a few of them, *timp2b*, whose interaction with MMPs largely modulates ECM-turnover (94), was among those genes. The top upregulated gene was *stab2*, the scavenger receptor of HA, which is a key component of the ECM. We have earlier described how tightly interwoven HA and VEGF signaling are. Our functional data indicate that Clasp2 influences venous and lymphangiogenesis through the modulation of HA in the ECM via the induction of ECM-turnover proteins. This not only has an impact on the migratory path of HSPCs (as seen for instance upon Mmp inhibition), but likely influences the availability of ECM-sequestered cytokines to bind to their cognate surface receptors on hematopoietic, venous and lymphatic endothelial cells. The ligand binding induces downstream signaling that ultimately control the migratory behavior of ECs. Recently, Hapln1b was reported to be a key organizer of the ECM matrix by binding Kitlb and thereby regulating HSPC emergence in the aorta (95). Remarkably, a strict balance is required. Indeed, while loss of Hapln1b results in a reduced ECM network that binds too little Kitlb, gain of Hapln1b renders the ECM too dense, thereby preventing Kitlb to bind to kit on the surface of the emerging HSPCs. Of note, the other isoform *hap11a*, also required for HA network stability (96, 97), is upregulated upon loss of Clasp2. We hypothesized that Clasp2 influences the ECM turnover through the regulation of endosomal trafficking pathway and ECM-modulating proteins, and that the composition of the ECM is key for the migratory behavior of these EC populations.

An interesting sidenote is that Svep1, being an ECM protein, is also a conserved regulator of lymphangiogenesis in mouse and zebrafish development (98, 99). Loss of Svep1 affects the migration of lymphatic progenitors and the remodeling of the network further emphasizing the role of the ECM in modulating EC migration, particularly those of the venous/lymphatic lineage.

#### 4. Summary of emerging concepts and concluding remarks

To summarize the important regulatory concepts in this thesis, our data indicate that inefficient maturation of pre-HSCs as early as their emergence from the endothelium will affect the self-renewal and multilineage potential of HSCs (even if their immunop-

henotype is still indistinguishable from other HSCs by conventional techniques). The maturation of pre-HSCs in the aortic IAHCs seems extremely finetuned by SCF/c-Kit signaling activity. Rather than an on/off switch in terms of expression, a threshold level needs to be reached and maintained to support their maturation and to prevent premature differentiation. Since c-Kit signaling is mainly induced by membrane-bound SCF (100), it emphasizes the pivotal role of stem cell-niche interaction. Consequently, disturbance of this interaction by signaling activity under threshold levels induces premature differentiation bypassing a potent stem cell state. The secretory pathway plays an essential role in the regulation of protein levels at the surface. A lack of polarization and/or below-threshold level expression of cell surface receptors might suffice to disturb IAHC cell formation or other niche interactions, and thereby preclude the successful maturation, amplification, and maintenance of stem cells.

Another concept connected to cell-environment interaction that we described here is the modulation of the ECM. The matrix surrounding a cell is a highly dynamic structure with a rapid turnover that both shields and nurtures when it comes to signaling cues. Important cytokines, e.g., angiogenic or hematopoietic, are tethered to the network that allows their binding to their receptors on the cellular surface. However, increased density of the matrix can shield the cell, rendering it less responsive to the microenvironmental signaling cues. Metalloproteinases play an important role in the degradation of the ECM, which is a prerequisite for HSPCs to emerge from the aortic endothelium. The smaller ECM fragments are biologically active and also signal via low-affinity receptors that influence many cellular processes such as angiogenesis, migration, survival, but also invasiveness and metastasis.

In solid cancers, ECM dynamics are disrupted by an imbalance between synthesis, secretion, and changed expression of proteins that are involved in ECM turnover and degradation. Together, these changes alter the biomechanical properties of the matrix, rendering it stiffer. As an example, breast cancer stem cells often secrete high levels of HA. Interaction with CD44 (low affinity co-receptor) induces the expression of stem cell markers, which support stemness, increase invasiveness and alter the more chemoresistant cells. Hence, multiple targeted therapy strategies are aiming at “breaking down the barrier” (reviewed (101)). Among many ECM-degrading targets are the intra-tumoral treatment with hyaluronidases and hyaluronan synthetase-inhibitors. This example truly emphasizes how important it is to understand the fundamental processes governing organogenesis during embryonic development to improve our current treatment strategies of malignant diseases.

## References

1. F. Zhou et al., Tracing haematopoietic stem cell formation at single-cell resolution. *Nature* 533, 487-492 (2016).
2. Y. Hu et al., Single-cell RNA sequencing highlights transcription activity of autophagy-related genes during hematopoietic stem cell formation in mouse embryos. *Autophagy* 13, 770-771 (2017).
3. C. S. Baron et al., Single-cell transcriptomics reveal the dynamic of haematopoietic stem cell production in the aorta. *Nature Communications* 9, (2018).
4. I. Bergiers et al., Single-cell transcriptomics reveals a new dynamical function of transcription factors during embryonic hematopoiesis. *Elife* 7, (2018).
5. Y. Zeng et al., Tracing the first hematopoietic stem cell generation in human embryo by single-cell RNA sequencing. *Cell Res* 29, 881-894 (2019).
6. J. Zhou et al., Combined Single-Cell Profiling of lncRNAs and Functional Screening Reveals that H19 Is Pivotal for Embryonic Hematopoietic Stem Cell Development. *Cell Stem Cell* 24, 285-298.e285 (2019).
7. E. I. Crosse et al., Multi-layered Spatial Transcriptomics Identify Secretory Factors Pro-

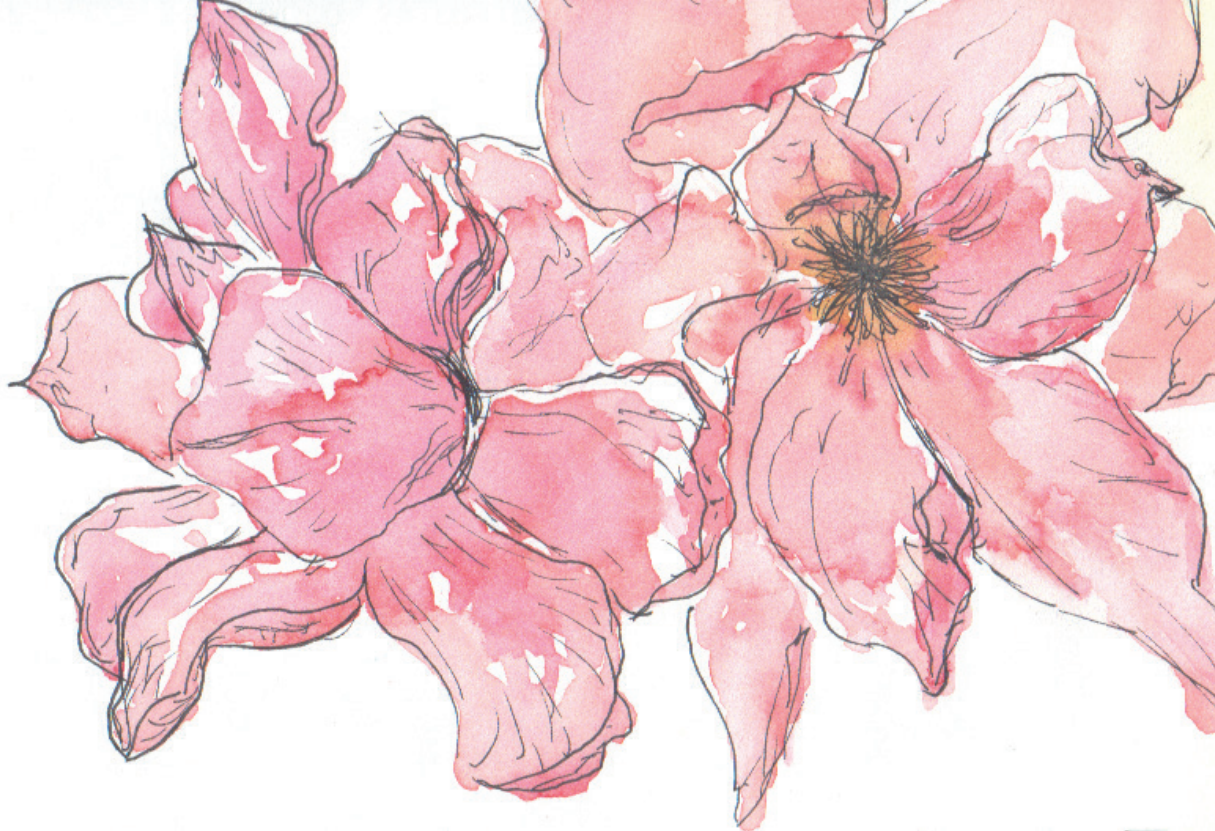
- moting Human Hematopoietic Stem Cell Development. *Cell Stem Cell* 27, 822-839.e828 (2020).
8. S. Hou et al., Embryonic endothelial evolution towards first hematopoietic stem cells revealed by single-cell transcriptomic and functional analyses. *Cell Res* 30, 376-392 (2020).
  9. C. S. Vink et al., Iterative Single-Cell Analyses Define the Transcriptome of the First Functional Hematopoietic Stem Cells. *Cell Rep* 31, 107627 (2020).
  10. Q. Zhu et al., Developmental trajectory of prehematopoietic stem cell formation from endothelium. *Blood* 136, 845-856 (2020).
  11. S. Blokzijl-Franke et al., Phosphatidylinositol-3 kinase signaling controls survival and stemness of hematopoietic stem and progenitor cells. *Oncogene* 40, 2741-2755 (2021).
  12. F. Kruse, J. P. Junker, A. van Oudenaarden, J. Bakkers, in *Methods in Cell Biology*, H. William Detrich, M. Westerfield, L. I. Zon, Eds. (Academic Press, 2016), vol. 135, pp. 299-307.
  13. L. Yvernogeu et al., Multispecies RNA tomography reveals regulators of hematopoietic stem cell birth in the embryonic aorta. *Blood* 136, 831-844 (2020).
  14. Y. Xue et al., A 3D Atlas of Hematopoietic Stem and Progenitor Cell Expansion by Multi-dimensional RNA-Seq Analysis. *Cell Rep* 27, 1567-1578.e1565 (2019).
  15. S. Bowling et al., An Engineered CRISPR-Cas9 Mouse Line for Simultaneous Readout of Lineage Histories and Gene Expression Profiles in Single Cells. *Cell* 181, 1410-1422.e1427 (2020).
  16. W. Pei et al., Resolving Fates and Single-Cell Transcriptomes of Hematopoietic Stem Cell Clones by PolyloxExpress Barcoding. *Cell Stem Cell* 27, 383-395.e388 (2020).
  17. R. Gadalla et al., Validation of CyTOF Against Flow Cytometry for Immunological Studies and Monitoring of Human Cancer Clinical Trials. *Front Oncol* 9, 415 (2019).
  18. M. Stoeckius et al., Simultaneous epitope and transcriptome measurement in single cells. *Nat Methods* 14, 865-868 (2017).
  19. Y. Liu et al., High-Spatial-Resolution Multi-Omics Sequencing via Deterministic Barcoding in Tissue. *Cell* 183, 1665-1681.e1618 (2020).
  20. J. Lv, F. Liu, Application of Aorta-gonad-mesonephros Explant Culture System in Developmental Hematopoiesis. *Journal of visualized experiments : JoVE*, 56557 (2017).
  21. S. Taoudi et al., Extensive hematopoietic stem cell generation in the AGM region via maturation of VE-cadherin+CD45+ pre-definitive HSCs. *Cell stem cell* 3, 99-108 (2008).
  22. J. M. Sheridan, S. Taoudi, A. Medvinsky, C. C. Blackburn, A novel method for the generation of reaggregated organotypic cultures that permits juxtaposition of defined cell populations. *Genesis (New York, N.Y. : 2000)* 47, 346-351 (2009).
  23. T. Sato et al., Single Lgr5 stem cells build crypt-villus structures *in vitro* without a mesenchymal niche. *Nature* 459, 262-265 (2009).
  24. G. Keller, M. Kennedy, T. Papayannopoulou, M. V. Wiles, Hematopoietic commitment during embryonic stem cell differentiation in culture. *Molecular and Cellular Biology* 13, 473-486 (1993).
  25. T. Nakano, H. Kodama, T. Honjo, *In vitro* development of primitive and definitive erythrocytes from different precursors. *Science* 272, 722-724 (1996).
  26. T. Yamaguchi et al., Two-Step Differentiation of Mast Cells from Induced Pluripotent Stem Cells. *Stem Cells and Development* 22, 726-734 (2012).
  27. M. V. Wiles, G. Keller, Multiple hematopoietic lineages develop from embryonic stem (ES) cells in culture. *Development* 111, 259-267 (1991).
  28. D. Vittet et al., Embryonic Stem Cells Differentiate *In vitro* to Endothelial Cells Through Successive Maturation Steps. *Blood* 88, 3424-3431 (1996).
  29. A. Subramanian et al., Macrophage differentiation from embryoid bodies derived from human embryonic stem cells. *J Stem Cells* 4, 29-45 (2009).
  30. L. Guyonneau-Harmand et al., Transgene-free hematopoietic stem and progenitor cells from human induced pluripotent stem cells. *bioRxiv*, 177691 (2017).
  31. A. Ditadi, C. M. Sturgeon, Directed differentiation of definitive hemogenic endothelium and hematopoietic progenitors from human pluripotent stem cells. *Methods* 101, 65-72 (2016).
  32. R. Lis et al., Conversion of adult endothelium to immunocompetent haematopoietic stem cells. *Nature* 545, 439-445 (2017).
  33. K. Batta, M. Florkowska, V. Kouskoff, G. Lacaud, Direct reprogramming of murine fibroblasts to hematopoietic progenitor cells. *Cell Rep* 9, 1871-1884 (2014).
  34. C. M. Sturgeon, A. Ditadi, G. Awong, M. Kennedy, G. Keller, Wnt signaling controls the specification of definitive and primitive hematopoiesis from human pluripotent stem cells. *Nat Biotechnol* 32, 554-561 (2014).
  35. D. A. Turner et al., Anteroposterior polarity and elongation in the absence of extra-embryonic tissues and of spatially localised signalling in gastruloids: mammalian embryonic organoids. *Development* 144, 3894-3906 (2017).
  36. S. C. van den Brink et al., Single-cell and spatial transcriptomics reveal somitogenesis in gastruloids. *Nature* 582, 405-409 (2020).
  37. G. Rossi, S. Giger, T. Huebscher, M. P. Lutolf. ([www.biorxiv.org](http://www.biorxiv.org), 2021).
  38. W. W. Sugden, T. E. North, Making Blood from the Vessel: Extrinsic and Environmental Cues Guiding the Endothelial-to-Hematopoietic Transition. *Life (Basel)* 11, (2021).
  39. C. O. Lizama et al., Repression of arterial genes in hemogenic endothelium is sufficient for haematopoietic fate acquisition. *Nature Communications* 6, 1-10 (2015).

40. M. Z. Fadlullah et al., Murine AGM single-cell profiling identifies a continuum of hemogenic endothelium differentiation marked by ACE. *Blood*, (2021).
41. K. Drabek et al., The microtubule plus-end tracking protein CLASP2 is required for hematopoiesis and hematopoietic stem cell maintenance. *Cell reports* 2, 781-788 (2012).
42. S. Rybtsov et al., Tracing the origin of the HSC hierarchy reveals an SCF-dependent, IL-3-independent CD43(-) embryonic precursor. *Stem cell reports* 3, 489-501 (2014).
43. E. Azzoni et al., Kit ligand has a critical role in mouse yolk sac and aorta-gonad-mesonephros hematopoiesis. *EMBO Rep* 19, (2018).
44. A. Batsivari et al., Understanding Hematopoietic Stem Cell Development through Functional Correlation of Their Proliferative Status with the Intra-aortic Cluster Architecture. *Stem Cell Reports* 8, 1549-1562 (2017).
45. S. Sharma et al., Stem cell c-KIT and HOXB4 genes: critical roles and mechanisms in self-renewal, proliferation, and differentiation. *Stem Cells Dev* 15, 755-778 (2006).
46. Y. Tang, H. Bai, S. Urs, Z. Wang, L. Liaw, Notch1 activation in embryonic VE-cadherin populations selectively blocks hematopoietic stem cell generation and fetal liver hematopoiesis. *Transgenic Res* 22, 403-410 (2013).
47. G. Del Monte, J. Grego-Bessa, A. González-Rajal, V. Bolós, J. L. De La Pompa, Monitoring Notch1 activity in development: evidence for a feedback regulatory loop. *Dev Dyn* 236, 2594-2614 (2007).
48. C. Richard et al., Endothelio-mesenchymal interaction controls runx1 expression and modulates the notch pathway to initiate aortic hematopoiesis. *Dev Cell* 24, 600-611 (2013).
49. M. Ogawa et al., Expression and function of c-Kit in fetal hematopoietic progenitor cells: transition from the early c-Kit-independent to the late c-Kit-dependent wave of hematopoiesis in the murine embryo. *Development* 117, 1089-1098 (1993).
50. F. Bernex et al., Spatial and temporal patterns of c-kit-expressing cells in WlacZ/+ and WlacZ/WlacZ mouse embryos. *Development* 122, 3023-3033 (1996).
51. T. Dignum et al., Multipotent progenitors and hematopoietic stem cells arise independently from hemogenic endothelium in the mouse embryo. *Cell Rep* 36, 109675 (2021).
52. A. Fantin et al., KIT Is Required for Fetal Liver Hematopoiesis. *Frontiers in Cell and Developmental Biology* 9, 1908 (2021).
53. K. Lewis, M. Yoshimoto, T. Takebe, Fetal liver hematopoiesis: from development to delivery. *Stem cell research & therapy* 12, 139-139 (2021).
54. L. A. Thorén et al., Kit regulates maintenance of quiescent hematopoietic stem cells. *J Immunol* 180, 2045-2053 (2008).
55. K. Molyneaux, C. Wylie, Primordial germ cell migration. *Int J Dev Biol* 48, 537-544 (2004).
56. L. Zhang et al., c-kit and its related genes in spermatogonial differentiation. *Spermatogenesis* 1, 186-194 (2011).
57. M. E. Rothenberg et al., Identification of a cKit(+) colonic crypt base secretory cell that supports Lgr5(+) stem cells in mice. *Gastroenterology* 142, 1195-1205.e1196 (2012).
58. L. Freyer, L. Iturri, A. Biton, E. G. Perdiguero, Overlapping Definitive Progenitor Waves Divide and Conquer to Build a Layered Hematopoietic System. *bioRxiv*, 2020.2012.2024.424302 (2020).
59. B. A. Ulloa et al., Definitive hematopoietic stem cells minimally contribute to embryonic hematopoiesis. *Cell Rep* 36, 109703 (2021).
60. J. M. Frame, K. H. Fegan, S. J. Conway, K. E. McGrath, J. Palis, Definitive Hematopoiesis in the Yolk Sac Emerges from Wnt-Responsive Hemogenic Endothelium Independently of Circulation and Arterial Identity. *Stem Cells* 34, 431-444 (2016).
61. L. Fourriere, A. J. Jimenez, F. Perez, G. Boncompain, The role of microtubules in secretory protein transport. *J Cell Sci* 133, (2020).
62. A. Efimov et al., Asymmetric CLASP-dependent nucleation of noncentrosomal microtubules at the trans-Golgi network. *Developmental cell* 12, 917-930 (2007).
63. Y. C. Lin et al., ARL4A acts with GCC185 to modulate Golgi complex organization. *J Cell Sci* 124, 4014-4026 (2011).
64. P. M. Miller et al., Golgi-derived CLASP-dependent microtubules control Golgi organization and polarized trafficking in motile cells. *Nature cell biology* 11, 1069-1080 (2009).
65. J. Thyberg, S. Moskalewski, Role of microtubules in the organization of the Golgi complex. *Exp Cell Res* 246, 263-279 (1999).
66. G. Lansbergen et al., CLASPs attach microtubule plus ends to the cell cortex through a complex with LL5beta. *Developmental cell* 11, 21-32 (2006).
67. R. Matteoni, T. E. Kreis, Translocation and clustering of endosomes and lysosomes depends on microtubules. *Journal of Cell Biology* 105, 1253-1265 (1987).
68. A. V. Fonseca, D. Corbeil, The hematopoietic stem cell polarization and migration: A dynamic link between rhoa signaling pathway, microtubule network and ganglioside-based membrane microdomains. *Communicative and Integrative Biology* 4, 201-204 (2011).
69. M. Lancino et al., Anisotropic organization of circumferential actomyosin characterizes hematopoietic stem cells emergence in the zebrafish. *Elife* 7, (2018).
70. D. Chalin et al., Modeling and live imaging of mechanical instabilities in the zebrafish aorta during hematopoiesis. *Scientific Reports* 11, 9316 (2021).
71. A. Iring et al., Shear stress-induced endothelial adrenomedullin signaling regulates vascular tone and blood pressure. *Journal of Clinical Investigation* 129, 2775-2791 (2019).
72. L. Adamo et al., Biomechanical forces promote embryonic haematopoiesis. *Nature* 459,



- 1131-1135 (2009).
73. T. E. North et al., Hematopoietic stem cell development is dependent on blood flow. *Cell* 137, 736-748 (2009).
  74. P. G. Kim et al., Flow-induced protein kinase A-CREB pathway acts via BMP signaling to promote HSC emergence. *Journal of Experimental Medicine* 212, 633-648 (2015).
  75. M. F. Diaz et al., Biomechanical forces promote blood development through prostaglandin E2 and the cAMP-PKA signaling axis. *The Journal of experimental medicine* 212, 665-680 (2015).
  76. L. Jing et al., Adenosine signaling promotes hematopoietic stem and progenitor cell emergence. *Journal of Experimental Medicine* 212, 649-663 (2015).
  77. L. Wang et al., A blood flow-dependent *klf2a*-NO signaling cascade is required for stabilization of hematopoietic stem cell programming in zebrafish embryos. *Blood* 118, 4102-4110 (2011).
  78. Z. Liu et al., Primary cilia regulate hematopoietic stem and progenitor cell specification through Notch signaling in zebrafish. *Nature Communications* 10, 1-11 (2019).
  79. C. Geven, M. Kox, P. Pickkers, Adrenomedullin and Adrenomedullin-Targeted Therapy As Treatment Strategies Relevant for Sepsis. *Frontiers in Immunology* 9, 292 (2018).
  80. P. Lu, V. M. Weaver, Z. Werb, The extracellular matrix: a dynamic niche in cancer progression. *J Cell Biol* 196, 395-406 (2012).
  81. R. Sato-Nishiuchi et al., Polydom/SVEP1 is a ligand for integrin  $\alpha 9 \beta 1$ . *J Biol Chem* 287, 25615-25630 (2012).
  82. C. Porcheri et al., Notch ligand Dll4 impairs cell recruitment to aortic clusters and limits blood stem cell generation. *The EMBO Journal* 39, 1-19 (2020).
  83. J. C. Boisset et al., Progressive maturation toward hematopoietic stem cells in the mouse embryo aorta. *Blood* 125, 465-469 (2015).
  84. T. Yokomizo et al., Whole-mount three-dimensional imaging of internally localized immunostained cells within mouse embryos. *Nature protocols* 7, 421-431 (2012).
  85. T. Jaffredo, R. Gautier, a. Eichmann, F. Dieterlen-Lièvre, Intraaortic hemopoietic cells are derived from endothelial cells during ontogeny. *Development (Cambridge, England)* 125, 4575-4583 (1998).
  86. T. Jaffredo, R. Gautier, V. Brajeul, F. Dieterlen-Lièvre, Tracing the progeny of the aortic hemangioblast in the avian embryo. *Developmental biology* 224, 204-214 (2000).
  87. F. Dieterlen-Lièvre, C. Pouget, K. Bollérot, T. Jaffredo, Are intra-aortic hemopoietic cells derived from endothelial cells during ontogeny? *Trends in cardiovascular medicine* 16, 128-139 (2006).
  88. M. Tavian et al., Aorta-associated CD34+ hematopoietic cells in the early human embryo. *Blood* 87, 67-72 (1996).
  89. J. Y. Bertrand et al., Haematopoietic stem cells derive directly from aortic endothelium during development. *Nature* 464, 108-111 (2010).
  90. K. Kissa, P. Herbomel, Blood stem cells emerge from aortic endothelium by a novel type of cell transition. *Nature* 464, 112-115 (2010).
  91. J. Travnickova et al., Primitive macrophages control HSPC mobilization and definitive haematopoiesis. *Nature Communications* 6, 1-9 (2015).
  92. L. N. Theodore et al., Distinct Roles for Matrix Metalloproteinases 2 and 9 in Embryonic Hematopoietic Stem Cell Emergence, Migration, and Niche Colonization. *Stem Cell Reports* 8, 1226-1241 (2017).
  93. B. Weijts et al., Blood flow-induced Notch activation and endothelial migration enable vascular remodeling in zebrafish embryos. *Nat Commun* 9, 5314 (2018).
  94. R. Avādaneî et al., High variability in MMP2/TIMP2 and MMP9/TIMP1 expression in secondary liver tumors. *Rom J Morphol Embryol* 54, 479-485 (2013).
  95. C. B. Mahony et al., Hapln1b, a central organizer of the extracellular matrix, modulates kit signalling to control developmental haematopoiesis. *Blood Adv*, (2021).
  96. K. Jeong Suk et al., Molecular Cloning and Developmental Expression of a Hyaluronan and Proteoglycan Link Protein Gene *crtl1/hapln1* in Zebrafish. *Zoological Science* 25, 912-918 (2008).
  97. J. Govindan, M. K. Iovine, Hapln1a is required for connexin43-dependent growth and patterning in the regenerating fin skeleton. *PLoS One* 9, e88574 (2014).
  98. T. Karpanen et al., An Evolutionarily Conserved Role for Polydom/Svep1 during Lymphatic Vessel Formation. *Circulation Research* 120, 1263-1275 (2017).
  99. N. Morooka et al., Polydom Is an Extracellular Matrix Protein Involved in Lymphatic Vessel Remodeling. *Circ Res* 120, 1276-1288 (2017).
  100. S. Takagi et al., Membrane-bound human SCF/KL promotes *in vivo* human hematopoietic engraftment and myeloid differentiation. *Blood* 119, 2768-2777 (2012).
  101. E. Henke, R. Nandigama, S. Ergün, Extracellular Matrix in the Tumor Microenvironment and Its Impact on Cancer Therapy. *Front Mol Biosci* 6, 160 (2019).





---

&

List of abbreviations  
Samenvatting in het Nederlands  
Zusammenfassung auf Deutsch  
List of publications  
Curriculum Vitae

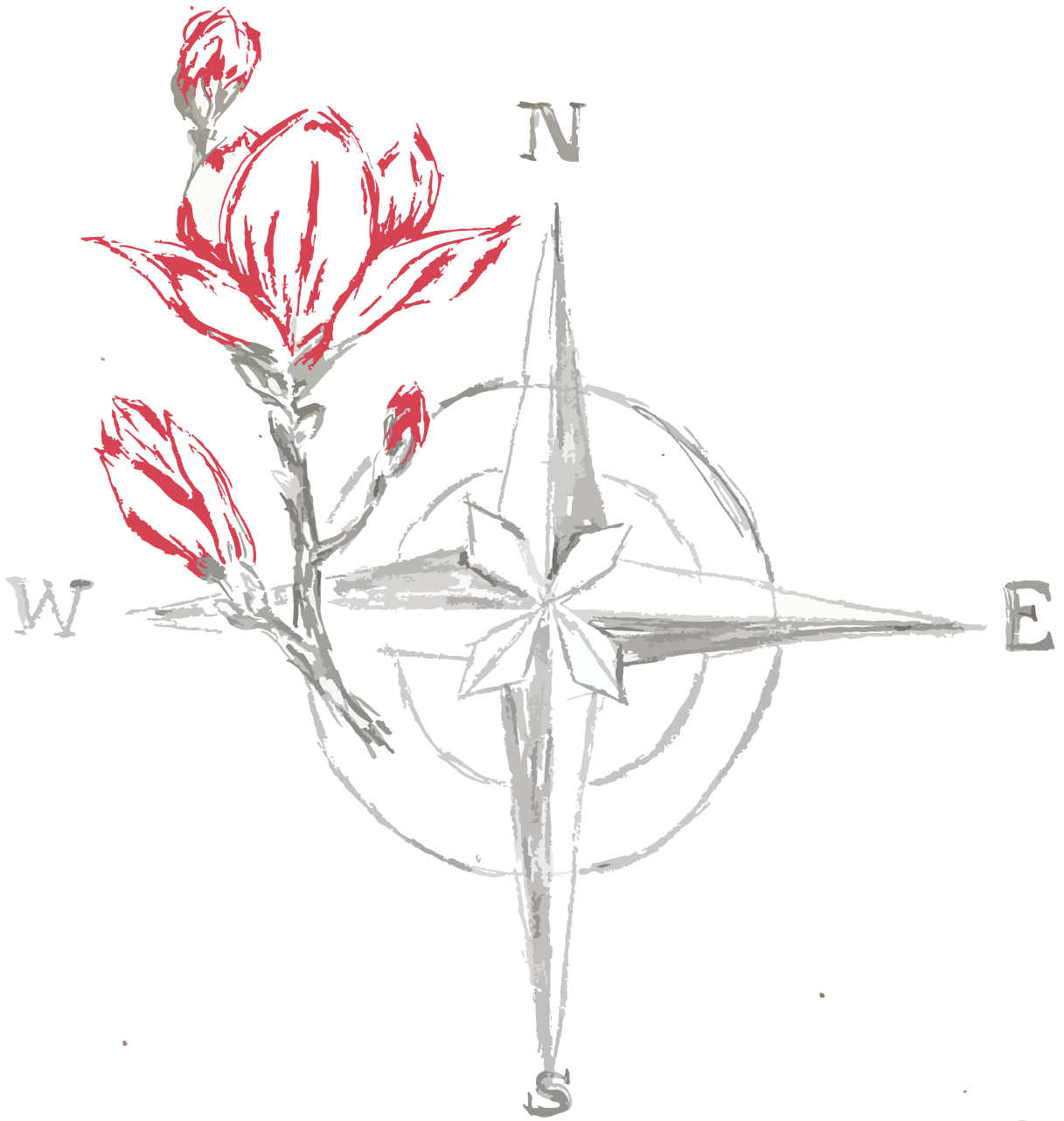


# List of abbreviations

+ tips	microtubule plus-end-tracking protein
Ac-LDL	acetylated-low density lipoprotein
ADM	adrenomedullin
AGM	aorta-gonad-mesonephros
aISV	arterial ISV
BafA	bafilomycin A1
BFU-E	burst forming unit erythroid
BM	bone marrow
CEL-seq	cell expression by linear amplification and sequencing
CFU	colony forming unit
CFU-C	colony-forming unit cell
CFU-E	CFU-erythroid
CFU-G	CFU-granulocyte
CFU-GEMM	CFU-granulocyte-erythrocyte-macrophage-megakaryocyte
CFU-GM	CFU-granulocyte-macrophage
CFU-M	CFU-macrophage
CFU-Mk	CFU-megakaryocyte
CHT	caudal hematopoietic tissue
CITE-seq	cellular indexing of transcriptomes and epitopes by sequencing
CLASP2	cytoplasmic linker associated protein 2
CLIP	cytoplasmic linker protein
CMP	common myeloid progenitor
ctsla	cathepsin La
CXCL12	C-X-C motif chemokine ligand 12
CXCR4	C-X-C motif chemokine receptor 4
CyTOF	cytometry by time-of-flight
d	days
DA	dorsal aorta
DEC	Dier Experimenten Commissie
DLAV	dorsal longitudinal anastomotic vessel
dpf	days post fertilization
E	embryonic day
e.e.	embryo equivalent
EB	embryoid body
EC	endothelial cell
ECM	extracellular matrix
EHT	endothelial-to-hematopoietic transition
EMP	erythro-myeloid progenitors
ESCs	embryonic stem cells
FA	focal adhesions
FACS	fluorescence-activated cell sorting
FL	fetal liver
GFP	green fluorescent protein
GO	gene ontology
GSK-3	glycogen synthase kinase-3
HA	hyaluronan
hapln1a	hyaluronan and proteoglycan link protein 1a
HEC	hemogenic endothelial cell

Hh	hedgehog
hpf	hours post fertilization
HSCs	hematopoietic stem cells
HSPCs	hematopoietic stem and progenitor cells
Hyb	hybridization
IAHC	intra-aortic hematopoietic cluster
IAS	intra-aortic staining
ISH	in situ hybridization
ISV	inter-somitic vessel
ITG	integrin
KD	knockdown
kitlb	kit ligand b
LECs	lymphatic endothelial cells
lgmn	legumain
Lin	lineage marker
LPM	lateral plate mesoderm
LSK	lineage marker negativ, SCA-1 positive and c-Kit positive
LTC-IC	long-term culture-initiating cell
Ly6-A	lymphocyte antigen 6 complex, or SCA-1 stem cell antigen-1
MAPs	microtubule-associated proteins
Mmps	matrix metalloproteinases
MO	morpholino
MPPs	multipotent progenitors
MSCs	mesenchymal stem cell
MT	microtubule
MTOC	microtubule-organizing center
n.s.	not significant
o-HA	oligosaccharides of hyaluronan
P	postnatal day
PCR	polymerase chain reaction
PCV	posterior cardinal vein
PGCs	primordial germ cells
PHH3	phospho-Histone H3
PI3-K	phosphatidylinositol-3-kinase
PL	placenta
PL	parachordal lymphangioblasts
pre-HSC	immature precursor of HSC
P-Sp	para-aortic splanchnopleural mesoderm
RA	retinoic acid
RAMP2	receptor activity modifying protein 2
RFP	red fluorescent protein
RTK	receptor tyrosine kinases
RT-qPCR	quantitative reverse transcription polymerase chain reaction
Runx1	runt-related transcription factor 1
Sca-1	stem cell antigen-1 or Ly6a, lymphocyte antigen 6 complex
SCF	stem cell factor
scRNA-seq	single-cell RNA sequencing
Sl	locus steel locus
Slam	signaling lymphocyte activation molecule
smRNA-FISH	single-molecule RNA <i>in situ</i> hybridization
sp	somite pair
stab2	stabilin-2

SVEP1	sushi von willebrand factor type A EGF and pentraxin domain containing 1
TD	thoracic duct
TF	transcription factor
timp2b	metalloproteinase inhibitor 2b
Tomo-seq	RNA tomography sequencing
TS	total staining
VE-cad	VE-cadherin, Cdh5
VEGF	vascular endothelial growth factor
VEGFR2	vascular endothelial growth factor receptor 2
vISV	venous ISV
vWF	von willebrand factor
W	locus dominant-white spotting locus
wIAHCs	whole intra-aortic hematopoietic clusters
WISH	whole-mount <i>in situ</i> hybridization
WT	wild type
YS	yolk sac
γ-TuRC	γ-tubulin ring complex



&



# Samenvatting in het Nederlands

## Cel-intrinsieke en -extrinsieke regulatie van hematopoëse tijdens embryonale ontwikkeling

**Hoofdstuk 1** Hematopoëse is het proces waarbij bloed wordt gemaakt. Hematopoëtische stamcellen (HSC's) vormen de basis van het hematopoëtische systeem: ze hebben zowel zelfvernieuwendende eigenschappen als de capaciteit te differentiëren naar verscheidene subtypen bloedcellen. Aangezien de gedifferentieerde bloedcellen kortdurend leven, hebben HSC's de cruciale functie het bloedsysteem continu aan te vullen. Bij alle gewervelde dieren ontstaan de eerste HSC's tijdens de embryonale ontwikkeling. Op embryonale dag (E)9.5 van de ontwikkeling van de muis, ontluiken gespecialiseerde hemogene endotheelcellen uit de endothele bekleding van de belangrijkste slagaders, zoals de aorta, om vervolgens een endothele-naar-hematopoëtische transitie (EHT) te ondergaan. EHT leidt tot de vorming van hematopoëtische cellen die zich organiseren in specifieke clusters (ook wel intra-aortische hematopoëtische clusters of IAHC's genaamd) die tijdelijk aan het endotheel gehecht blijven. Het aantal IAHC-cellen piekt op E10.5, wanneer de eerste HSC's in de aorta worden gedetecteerd. Op E11 bevatten IAHC's zeer weinig HSC's en erytroïde-myeloïde voorlopers; IAHC's zijn voornamelijk samengesteld uit HSC-precursoren (pre-HSC's) die zich geleidelijk ontwikkelen tot volledig transplanteerbare HSC's. De afname van het aantal IAHC-cellen in de aorta valt samen met het verschijnen van HSC's in de foetale lever (FL). Gezien het vergelijkbare aantal pre-HSC's in de aorta op E11.5 en HSC's in FL op E12.5, migreren pre-HSC's hoogstwaarschijnlijk van de aorta naar de FL om hun differentiatieproces daar te voltooien. Deze golf van pre-HSC-rijping, gevolgd door expansie, leidt tot de vorming van de volwassen HSC's die het beenmerg (BM), de belangrijkste plaats van hematopoëse op volwassen leeftijd, zullen koloniseren. De beperkte ruimtelijke en temporale productie van HSC's tijdens de embryonale ontwikkeling wordt strak gereguleerd door een complex netwerk van cel-intrinsieke en -extrinsieke factoren. Het verkrijgen van een beter begrip van HSC-regulatie is de belangrijkste focus van dit proefschrift.

**Hoofdstuk 2** IAHC's werden eerder beschreven als samengesteld uit HSC's en meer toegewijde voorlopercellen. Wij en anderen hebben echter aangetoond dat de overgrote meerderheid van IAHC-cellen in feite pre-HSC's (type I en II) zijn, die hun volledige transplantatie-potentieel pas vertonen na een rijpingsproces dat *in vitro* tot stand kan komen, of na transplantatie *in vivo* in een bevorderlijke micro-omgeving (i.e., neonatale lever).

**Hoofdstuk 3** Om een beter begrip te krijgen van het cel-intrinsieke regulerende netwerk en de moleculaire gebeurtenissen van IAHC-vorming en HSC-generatie in de aorta, hebben we het transcriptionele landschap van fenotypisch gedefinieerde populaties onderzocht. We hebben RNA-sequencing van individuele cellen toegepast op non-hemogeen endotheel, hemogeen endotheel, pre-HSC's type I, pre-HSC's type II en voorlopercellen. Ons doel was om meer inzicht te verkrijgen in waarom HSC-productie in de aorta ruimtelijk beperkt is. Terwijl IAHC's aan beide zijden van de aorta aanwezig zijn, is HSC-activiteit beperkt tot de ventrale zijde van de aorta (op E10.5). Daarom identificeerden we welke genen tijdens het rijpingsproces differentieel tot expressie werden gebracht in de bovengenoemde populaties geïsoleerd op E10.5 en E11.5. We onderzochten ook de ruimtelijke distributie door genexpressie te evalueren in IAHC's geïsoleerd van zowel de ventrale als dorsale zijden van de aorta,

en ontdekten dat ze moleculair erg vergelijkbaar zijn.

**Hoofdstuk 4** De stamcelomgeving, of niche, speelt een belangrijke rol bij de vorming van IAHC-cellen, en dus HSC-productie, in de aorta. Het HSC-potentieel is beperkt tot de ventrale zijde van de aorta tijdens embryonale hematopoëse. Om geconserveerde cel-extrinsieke moleculaire signalen te identificeren die betrokken zijn bij het regulerende landschap van HSC-generatie, voerden we tomografie-sequencing (tomo-seq) uit van verschillende embryosoorten, te weten humaan, muis, kip, en zebra. De embryo's werden gesegmenteerd langs de dorsoventrale en anteroposteriore assen, om zodoende inzicht te verkrijgen in de ruimtelijke regulatie van genexpressie. We ontdekten verschillende genen die actief zijn in de micro-omgeving van de ventrale aorta, en hun regulerende effect op de HSC-productie werd bevestigd door het uitvoeren van *loss- of gain-of-function* (LOF, GOF) experimenten in de verschillende dierspecies. We benadrukten de vaatverwijzende ADM en bijbehorende receptor RAMP-2, evenals SVEP1, een adhesiemolecuul, als belangrijke en geconserveerde micro-omgevingssignalen voor een correcte HSC-generatie in de embryonale aorta.

**Hoofdstuk 5** Van het eiwit CLASP2 is eerder aangetoond dat het een microtubulus (MT)-stabiliserende factor is die nodig is voor de instandhouding van HSC's in het beenmerg van volwassen muizen. Door de analyse van LOF-modellen van muizen en zebra's, ontrafelen we de cruciale betrokkenheid van CLASP2 bij het bewaken van de stamceleigenschappen van embryonale en foetale HSC's. Hoewel ze fenotypisch vergelijkbaar zijn met WT HSC's, hebben *Clasp2* knock-out HSC's geen zelfvernieuwend capaciteit en ondergaan ze voortijdige differentiatie naar bloedceltypen met een beperktere functie. Als gevolg daarvan zal de HSC-pool uiteindelijk uitgeput raken. We ontdekten dat het tekort aan zelfvernieuwing in *Clasp2* knock-out HSC's verband houdt met verminderde recirculatie van de c-Kit-receptor naar het plasmamembraan, als gevolg van een defect Golgi-netwerk en verhoogde lysosomale afbraak. We beschrijven voor het eerst een gradiënt van c-Kit-expressie (in plaats van een binaire afwezigheid of aanwezigheid) die de zelfvernieuwend eigenschappen van HSC sterk beïnvloedt door interactie met de stamcelniche.

**Hoofdstuk 6** *Clasp2* medieert niet alleen c-Kit expressie aan de oppervlakte van de cel (en daardoor de interactie van embryonale HSC's met hun respectievelijke niche); we onthullen ook dat *Clasp2* de dynamiek moduleert waarmee HSC-voorlopers opkomen uit het aorta-endotheel. Met behulp van *live-cell* beeldvorming hebben we waargenomen dat verlies van *Clasp2* leidt tot uitgebreide cellulaire uitsteeksels die cellen verankeren aan het endotheel van de aorta, waardoor hun migratiegedrag verandert. We gebruikten RNA-sequencing en daaropvolgende analyse van het vasculaire endotheel van zebra embryo's met een mutatie in het *clasp2* gen. De resultaten ondersteunen een rol van *Clasp2* in de endo/lysosomale route en suggereren een regulerende functie bij de herstructurering van de extracellulaire matrix in veneuze/lymfatische endotheelcellen. In overeenstemming met deze data, verminderde het verlies van *Clasp2* veneuze secundaire kieming en lymfangiogenese. We laten zien dat modulatie van het hyaluronan extracellulaire matrix (ECM)-netwerk verschillende aspecten van het veneuze/lymfatische fenotype in *Clasp2*-deficiënte embryo's kan redden, wat aangeeft dat *Clasp2* inderdaad betrokken is bij ECM-regulatie. We rapporteren hier een regulerende functie van *Clasp2* in het migratiegedrag van specifieke endotheelcelpopulaties door modulatie van ECM-samenstelling en omzet.



**Hoofdstuk 7 Discussie** "Hoe worden functionele HSC's gegenereerd tijdens de embryonale ontwikkeling en hoe wordt dit proces gereguleerd?" is de centrale vraag van dit proefschrift. Het huidige werk, samen met andere studies, begint het complexe netwerk op te helderen dat HSC-ontwikkeling op verschillende niveaus regelt. Cel-intrinsieke factoren, zoals moleculaire veranderingen in transcriptiefactoren, zorgen bijvoorbeeld voor de overgang van een endotheel naar een hematopoëtisch programma tijdens EHT. Op cellulair niveau zijn complexe herschikkingen van het cytoskelet nodig voor een succesvolle opkomst uit het endotheel. Het onderhoud van het gestarte stamcelprogramma is in grote mate afhankelijk van de interactie van de cel met de omringende micro-omgeving en het vermogen om te reageren op gradiënten van factoren in die omgeving. Verminderd intracellulair transport van receptoren zoals c-Kit, die de communicatie tussen HSC's en de nichefactoren bemiddelt, resulteert in het verlies van stamceleigenschappen. Hierin lijkt de juiste timing en het aantal receptoren op het cellulaire oppervlak, gedeeltelijk gecontroleerd door vesiculair transport via het golgicomplex en degradatie via de endo/lysosomale route, cruciaal. Cel-extrinsieke signalen, zoals uitgescheiden liganden uit de directe micro-omgeving, zijn een ander belangrijk onderdeel van het regulerende landschap van HSC-generatie. De beschikbaarheid van liganden in de extracellulaire ruimte, die vervolgens binden aan hun verwante receptoren op het celoppervlak, wordt gemoduleerd door de extracellulaire matrix en diër complexiteit. Het begrijpen van het regulerende netwerk dat *de novo* generatie van HSC's tijdens de embryonale ontwikkeling mogelijk maakt is cruciaal voor een verbetering van onze huidige inspanningen om deze kostbare cellen *in vitro* te produceren, met een bredere betekenis voor stamceltherapieën en regeneratieve geneeskunde.

# Zusammenfassung auf Deutsch

**Kapitel 1 Einführung** Hämatopoese ist der Prozess der Blutbildung. Dieser Prozess bringt hämatopoetische oder blutbildende Stammzellen (HSC) hervor, die die Grundlage des gesamten Blutzellsystems bilden. Durch ihre Fähigkeit in alle unterschiedlichen Blutzelltypen heranzureifen und sich dabei ständig selbst zu erneuern, können HSCs das gesamte Blutsystem wieder auffüllen. Dadurch kann lebenslang der konstante Bedarf an kurzlebigen Blutzelltypen gedeckt werden, ohne dass die Zahl dieser Stammzellen erschöpft wird. In Wirbeltieren entstehen die ersten HSCs während der Embryonalentwicklung. Bei Mäusen, durchlaufen besondere Endothelzellen in der Wand der Aorta (und anderen grossen Arterien) am neunten embryonalen Tag ((E)9,5) der Mausentwicklung eine Spezialisierung in Richtung Blutbildung. Dieser Übergang von Endothel- nach Blutzelle (EHT) führt zur Bildung von Blutzellen und Stammzellvorläuferzellen, die sich zunächst in Zellaggregaten (IAHCs) organisieren. Diese IAHCs bleiben vorübergehend an die Aortenwand gebunden. Einen Tag später (E10.5) erreicht die Anzahl dieser blutbildenden Zellen ihren Höhepunkt, gleichzeitig können nun die ersten richtigen, potenten HSCs nachgewiesen werden. Per se enthalten die IAHCs nur sehr wenige HSCs und wenige bereits weiter spezialisierte erythroid-myeloische Vorläuferzellen, denn hauptsächlich bestehen sie aus Stammzellvorläuferzellen (pre-HSCs). Diese reifen nach und nach vollständig zu transplantierbaren HSCs heran. Die Zahl der IAHCs in der Aorta nimmt erst ab wenn die ersten HSCs in der in der fötalen Leber (FL) zu finden sind. Aufgrund der ähnlichen Anzahl von pre-HSCs in der Aorta am Tag 11 im Vergleich zur Anzahl reifer HSCs in der FL am Tag 12, wird vermutet, dass pre-HSCs höchstwahrscheinlich von der Aorta zur FL wandern, um dort ihren Reifungsprozess abzuschließen. Diese Welle von heranreifenden pre-HSCs und die sich anschließende Expansion der reifen Stammzellen in der FL formt einen Pool von HSCs der später das Knochenmark, den Hauptort der adulten Blutbildung, besiedeln wird. Die begrenzte räumliche und zeitliche Produktion von HSCs während der Embryonalentwicklung wird streng durch ein komplexes Netzwerk von zelleigenen und extrinsischen Faktoren reguliert. Ein besseres Verständnis der HSC-Regulierung ist das Hauptaugenmerk dieser Arbeit.

**Kapitel 2** Früher nahm man an, dass die beschriebenen hämatopoietischen Zellanhäufungen in der Aorta ausschließlich aus blutbildenden Stammzellen und schon weiter differenzierten Vorläuferzellen der reifen Blutzellen zusammengesetzt sind. Wir und andere haben jedoch gezeigt, dass die überwiegende Mehrheit der IAHC-Zellen tatsächlich pre-HSCs (Typ I und II) sind, die ihr volles Potenzial erst nach einem Reifungsprozess entwickeln. Dieser Reifungsprozess kann ausschließlich in einer förderlichen Mikroumgebung (z.B. Neugeborenenleber) stattfinden, dies kann *in vitro* geschehen, oder aber nach der Transplantation in Neugeborene *in vivo* erfolgen.

**Kapitel 3** Um das zelleigene regulatorische Netzwerk und die molekularen Ereignisse, die der Entstehung der blutbildenden Zellen in der Aorta zu Grunde liegen besser zu verstehen, untersuchten wir das Transkriptom phänotypisch definierter Populationen. Hierfür sequenzierten wir die RNA von einzelnen Zellen des nicht-hämogenen Endothels, hämogenen Endothels, pre-HSCs Typus I, pre-HSCs Typus II und weiter differenzierten Vorläuferzellen an. Unser Hauptziel war es, mehr darüber zu erfahren, warum die HSC-Produktion in der Aorta so räumlich begrenzt ist. Während in der Maus IAHCs auf beiden Seiten der Aorta vorhanden sind (ventral und dorsal), ist die HSC-Aktivität ausschließlich auf die ventrale Seite der Aorta (bei E10.5) beschränkt. Um besser zu verstehen welche Gene in den oben genannten Popu-



lationen während des Reifungsprozesses am Tag E10.5 und E11.5 eine Rolle spielen, untersuchten wir ihr Expressionslevel. Hierbei haben wir zusätzlich unterschieden zwischen IAHCs, die von der ventralen oder dorsalen Seite der Aorta isoliert wurden. Dabei stellten wir fest, dass sie molekular sich sehr ähnlich sind.

**Kapitel 4** Die Stammzellumgebung oder Nische spielt eine wichtige Rolle bei der IAHC-Zellbildung und somit der HSC-Produktion in der Aorta. Wie bereits oben beschrieben, ist die Lokalisation der HSCs während der embryonalen Hämatopoese auf die ventrale Seite der Aorta begrenzt. Um die molekularen Signale in der Zellumgebung zu identifizieren, die Teil der regulatorischen Landschaft der HSC-Generation sind, führten wir eine so genannte Tomographie-Sequenzierung (tomo-seq) von Embryonen unterschiedlicher Spezien durch (nämlich Mensch, Maus, Huhn und Zebrafisch). Hierbei, um einen Einblick in die räumliche Regulation der Genexpression zu gewinnen, wurden die Embryonen entlang ihrer dorsoventralen und anteroposterioren Achse segmentiert. Dabei identifizierten wir mehrere Gene, die in der Mikroumgebung der ventralen Aorta aktiv sind. Die regulatorische Wirkung dieser Gene auf die HSC-Produktion testeten wir in Loss- oder Gain-of-Function (LOF, GOF)-Experimenten, in verschiedenen Tiermodellen. In Kapitel 4 beschreiben wir den Vasodilatator ADM und den zugehörigen Rezeptor RAMP-2 sowie SVEP1, ein Adhäsionsmolekül, als wichtige und konservierte Mikroumgebungssignale für die korrekte HSC-Erzeugung in der embryonalen Aorta.

**Kapitel 5** Es wurde zuvor gezeigt, dass das Protein CLASP2 welches ein stabilisierender Faktor für Mikrotubuli (MT) ist, auch für die Aufrechterhaltung und Erneuerung von HSCs im Knochenmark von erwachsenen Mäusen notwendig ist. Durch die Analyse von Maus- und Zebrafisch-LOF-Modellen, entdeckten wir die entscheidende Beteiligung von CLASP2 an der Erhaltung der Stammzeleigenschaften in embryonalen und fötalen HSCs. Obwohl sie WT-HSCs phänotypisch sehr ähnlich sind, fehlen *Clasp2*-Knockout-HSCs die Fähigkeit zur Selbsterneuerung und unterliegen daher einer vorzeitigen Differenzierung in Blutzelltypen mit eingeschränkter Funktion. Das hat zur Folge, dass der HSC-Pool irgendwann erschöpft ist. Wir fanden heraus, dass die Ursache für die gestörte Selbsterneuerung von *Clasp2*-Knockout-HSCs durch eine deregulierte Rezirkulation des c-Kit-Rezeptors zur Plasmamembran hervorgerufen wird. Der Grund dafür ist ein defektes Golgi-Netzwerks und ein erhöhter lysosomaler Abbau in den blutbildenden Stammzellen. Wir beschreiben somit zum ersten Mal einen Gradienten der c-kit-Expression (anstelle einer binären Abwesenheit oder Anwesenheit), der die Selbsterneuerungseigenschaften von HSC durch Interaktion mit der Stammzellnische stark beeinflusst.

**Kapitel 6** *Clasp2* vermittelt nicht nur die c-Kit-Expression an der Zelloberfläche (und damit die Interaktion embryonaler HSCs mit ihren jeweiligen Nischen); wir zeigen auch, dass *Clasp2* die dynamische Migration in welcher die HSC-Vorläufer aus dem Aortenendothel hervorgehen beeinflusst. Mithilfe von Live-Cell-Imaging beobachteten wir, dass der Verlust von *Clasp2* zu ausgedehnten Zellvorstülpungen führt, welche die knospenden Zellen am Endothel der Aorta verankern und damit ihr Migrationsverhalten einschränken. Um zu verstehen welche Faktoren auf molekularer Ebene dabei eine Rollen spielen, haben wir die RNA des vaskulären Endothels von Zebrafischembryos mit einer Mutation im *clasp2*-Gen sequenziert. Die Ergebnisse unterstützten die zuvor beschriebene Rolle von *Clasp2* im endo-/lysosomalen Signalweg. Insbesondere in venösen/lymphatischen Endothelzellen scheint *Clasp2* eine regulatorische Funktion bei der Umstrukturierung der extrazellulären Matrix zu haben. In Übereinstimmung mit diesen Daten verringerte der Verlust von *Clasp2*

die venöse, sekundäre Angiogenese und Lymphangiogenese. Außerdem konnten wir zeigen, dass die Modulation des extrazellulären Hyaluronan-Matrix-Netzwerks (ECM) mehrere Aspekte des venösen/lymphatischen Phänotyps in Clasp2-defizienten Embryonen wiederherstellen kann. Dies weist darauf hin, dass Clasp2 tatsächlich an der ECM-Regulierung beteiligt ist. Wir beschreiben hier eine regulatorische Funktion von Clasp2, die das Migrationsverhalten spezifischer Endothelzellpopulationen durch die Modulation der ECM-Zusammensetzung, Synthese und Abbau beeinflusst.

**Kapitel 7 Diskussion** „Wie entstehen funktionelle HSCs während der Embryonalentwicklung und wie wird dieser Prozess reguliert?“ ist die zentrale Frage dieser Arbeit. Diese Doktorarbeit, zusammen mit vielen anderen Studien, beginnt das komplexe Netzwerk welches die HSC-Entwicklung auf verschiedenen Ebenen reguliert aufzuklären. Beispielsweise während der EHT vermitteln zelleigene Faktoren, so wie molekulare Veränderungen der Transkriptionsfaktoren, den Übergang von einer Endothelzelle zu einem hämatopoetischen Programm. Auf zellulärer Ebene sind komplexe Umgestaltungen des Zytoskeletts für den erfolgreichen Austritt aus dem Endothel erforderlich. Die Aufrechterhaltung des initiierten Stammzellprogramms hängt stark von der Interaktion der Zelle mit der umgebenden Mikroumgebung und ihrer Fähigkeit ab, auf Gradienten von Faktoren in dieser Umgebung zu reagieren. Ein verminderter intrazellulärer Transport von Rezeptoren wie c-kit, welche die Kommunikation zwischen HSCs und den Nischenfaktoren vermitteln, führt zum Verlust der Stammzeleigenschaften. Hier scheinen der richtige Zeitpunkt und die richtige Anzahl von Rezeptoren auf der Zelloberfläche entscheidend zu sein, welche durch den vesikulären Transport über den Golgi-Komplex und den Abbau über einen endo/lysosomalen Weg kontrolliert werden. Zellexterne Signale, wie z. B. sekretierte Liganden aus der unmittelbaren Mikroumgebung, sind ein weiterer wichtiger Teil der regulatorischen Landschaft der HSC-Erzeugung. Die Verfügbarkeit von Liganden im extrazellulären Raum, die dann an ihre spezifischen Rezeptoren auf der Zelloberfläche binden, wird durch die Komplexität der extrazellulären Matrix moduliert. Das Verständnis dieses regulatorischen Netzwerks, dass die *de-novo*-Generierung von HSCs während der Embryonalentwicklung ermöglicht, ist auch entscheidend für die Verbesserung unserer derzeitigen Bemühungen diese wertvollen Zellen *in vitro* zu produzieren. Was wiederum von großer Bedeutung für unsere heutigen Stammzelltherapien und Ansätze in der regenerativen Medizin ist.



# List of publications

1. **Klaus A**, Clapes T, Yvernogeu L\*, Basu S\*, Weijts B\*, Maas J, Smal I, Galjart N, Robin C.  
CLASP2 safeguards hematopoietic stem cell properties during mouse and fish development.  
*Cell Reports*. 2022;39(11):110957.
2. Yvernogeu L, **Klaus A\***, Maas J\*, Morin-Poulard I\*, Weijts B, Schulte-Merker S, Berezikov E, Junker JP, Robin C.  
Multispecies RNA tomography reveals regulators of hematopoietic stem cell birth in the embryonic aorta.  
*Blood*. 2020;136(7):831-44.
3. Baron CS\*, Kester L\*, **Klaus A**, Boisset JC, Thambyrajah R, Yvernogeu L, Kouskoff V, Lacaud G, van Oudenaarden A, Robin C.  
Single-cell transcriptomics reveal the dynamic of haematopoietic stem cell production in the aorta.  
*Nature Communications*. 2018;9(1):2517.
4. **Klaus A**, Robin C.  
Embryonic hematopoiesis under microscopic observation.  
*Developmental Biology*. 2017;428(2):318-27.
5. Boisset JC, Clapes T, **Klaus A**, Papazian N, Onderwater J, Mommaas-Kienhuis M, Cupedo T, Robin C.  
Progressive maturation toward hematopoietic stem cells in the mouse embryo aorta.  
*Blood*. 2015;125(3):465-9.

# Curriculum Vitae

Anna Katharina Klaus was born on February 5<sup>th</sup> 1987 in Braunschweig, Germany. She received her Abitur (high school diploma) in 2006. Her Bachelor studies in Biology she conducted at the Technical University in Braunschweig, where she obtained her degree with a focus on neurobiology. In 2010 she moved to Rotterdam (the Netherlands) for her graduate studies in Molecular Medicine. There, in the lab of Dr. Catherine Robin, she investigated the emergence of blood stem cells in the embryo. After receiving her Master's degree in 2012, she gained knowledge and experience in zebrafish vascular and neuronal development as a research assistant in the group of Prof. Ferdinand le Noble at the Max-Delbrück Center in Berlin-Buch (Germany). In October 2014, Anna started her PhD at the Hubrecht Institute in the group of Dr. Catherine Robin. Her research focused on the cell-intrinsic and -extrinsic regulation of blood stem cell generation during development. The work she developed on that subject is presented in this thesis.